CRANFIELD UNIVERSITY

ROSS CHAPLIN

AERODYNAMIC INTERFERENCE BETWEEN HIGH-SPEED SLENDER BODIES

SCHOOL OF ENGINEERING

PHD THESIS

CRANFIELD UNIVERSITY

SCHOOL OF ENGINEERING

DEPARTMENT OF AEROSPACE SCIENCES

PhD THESIS

Academic Year 2009/2010

ROSS CHAPLIN

AERODYNAMIC INTERFERENCE BETWEEN HIGH-SPEED SLENDER BODIES

Supervisor Dr D. G. MacManus

December 2009

Abstract

Significant aerodynamic interference can occur between high-speed bodies in close proximity. A complex flowfield develops where shock and expansion waves from a generator body impinge upon the adjacent receiver body. The pressure and flow angularity changes which occur across these disturbances modify the body aerodynamics. The aim of this research is to quantify the aerodynamic interference effects for multi-body configurations and understand the relevant flow physics.

The interference aerodynamics for slender bodies in a supersonic flow were investigated through a parametric wind tunnel study. The receiver bodies were finned and un-finned configurations. The effect of lateral and axial body separations, receiver incidence and the strength of the disturbance field were investigated. Measurements included forces and moments, surface pressures and flow visualisations. Supporting computations using steady-state, viscous predictions provided a deeper understanding of the underlying aerodynamics and flow mechanisms. Good agreement was found between the measured and predicted interference loads and surface pressures for all configurations.

The interference loads are strongly dependent upon the axial impingement location of the primary shockwave. These induced loads change polarity as the impingement location moves aft over the receiver. The magnitude of the interference loads increase when the receiver is at incidence and are amplified by up to a factor of three when rear fins are attached. In general, the interference loads are larger for a stronger disturbance flowfield. The centre of pressure location is substantially affected and the static stability of the finned receiver changes in some configurations. The effect of the aerodynamic interference on the body trajectories was assessed using an unsteady, Euler prediction in combination with a 6DOF dynamic model. This shows aerodynamic

interference can cause a collision between the bodies. Moreover, the initial interference loads dominate the subsequent body trajectories and static modelling can be used to evaluate the dynamic trajectories.

Acknowledgments

Many people have contributed to the completion of this research. I would like to take time to thank them.

My supervisor David MacManus for his guidance and help throughout. I would especially like to thank him for the many occasions when he took my work home with him to read and provide feedback during the writing process.

I would like to acknowledge the financial support of the UK MOD. The investigation which is the subject of this report was initiated by the Air Systems Department Dstl and was carried out under the terms of Contract No RD025 – 1962. Additional funding was also provided through an ESPRC CASE award. I would also like to thank Dstl for the release of experimental data which greatly enhanced this research.

Trevor Birch for his constant support and guidance throughout. In particular, I would like to thank him for making arrangements for me to undertake two placements at Dstl. These aided my research and I enjoyed my time at Dstl immensely. Moreover, I would like to also thank Ben Shoesmith and Kristian Petterson who gave up alot of their own time in order to assist me. Their help with IMPNS and Cobalt was particularly useful.

The experimental tests in this research would not have been possible without the help of the following people at ISL: Freidrich Leopold, Bastien Martinez, Thibaut Guathier, Denis Bidino, Joseph Junker, Christophe Demeautis, Michel Meister, Dominique Willme. I am grateful for their help and generous assistance during my time at ISL.

Les Oswald for his more or less 24/7 high performance computing support. The technical staff of the Department of Aerospace Sciences for the manufacture of the wind tunnel models. Bob Tomaro and Cobalt Solutions LLC for the kind use of the overset solver. All the friends I have met whilst at Cranfield and those continuing friendships from home.

Most importantly, I would like to thank my Mum, Dad, Keith and Ben for their enduring love and support. The last 3½ years simply would not have been possible without them.

Finally, this thesis is dedicated to the memory of Uncle Jack who sadly passed away recently.

Table of contents

Notation

Nomenclature

English symbols

a	body translational acceleration	[ms^{-2}]
a_s	sonic velocity	[ms^{-1}]
A	Stern-Volmer calibration constant	
AR	Grid convergence asymptotic range parameter	
b	fin semi-span	[m]
B	Stern-Volmer calibration constant	
c	fin mean aerodynamic chord	[m]
c_f	fin root chord	[m]
C	approximate diffracted shockpath perimeter parameter	$C = \frac{D}{sin\theta_{obl}}$
C_f	skin friction coefficient vector	$C_f = \frac{\tau}{q_\infty}$
C_p	local pressure coefficient	$C_p = \frac{p - p_\infty}{q_\infty}$
ΔC_p	pressure coefficient difference from isolated at a given location	$\Delta C_p = C_p - C_{p,iso}$
$\Delta C_{p,near}$	pressure coefficient difference from isolated at ϕ=180°	
$\Delta C_{p,far}$	pressure coefficient difference from isolated at ϕ=0°	
$C_{X,t}$	total measured axial force coefficient (Figure 3.10)	$C_{X,t} = \frac{F_X}{q_\infty S}$

C_X	corrected axial force coefficient to freestream pressure over base area	$C_X = C_{X,t} + \frac{(p_b - p_\infty)\mathrm{S_b}}{q_\infty \mathrm{S}}$
C_Y	side force coefficient (Figure 3.10)	$C_Y = \frac{F_Y}{q_\infty S}$
C_Z	normal force coefficient (Figure 3.10)	$C_Z = \frac{F_Z}{q_\infty S}$
C_l	rolling moment coefficient about body leading edge (Figure 3.10)	$C_l = \frac{M_X}{q_\infty SD}$
C_m	pitching moment coefficient about body leading edge (Figure 3.10)	$C_m = \frac{M_Y}{q_\infty SD}$
C_n	yawing moment coefficient about body leading edge (Figure 3.10)	$C_n = \frac{M_Z}{q_\infty SD}$
ΔC_X	axial force interference load	$\Delta C_X = C_X - C_{X,iso}$
ΔC_Z	normal force interference load	$\Delta C_Z = C_Z - C_{Z,iso}$
ΔC_m	pitching moment interference load	$\Delta C_m = C_m - C_{m,iso}$
D	maximum body diameter at base (Figure 3.3)	[m]
D_s	sting diameter	[m]
$D\rho/Dt$	change in density with respect to solution time	[$kgs^{-1}m^{-3}$]
$D\omega/Dt$	change in turbulence model variable with respect to solution time	[s^{-2}]
dC_Z/dx	local normal force coefficient	[m^{-1}]
$\mathrm{EF\_\Delta C_Z}$	effect of fins on the normal force interference load	
$\mathrm{EF\_\Delta C_m}$	effect of fins on the pitching moment interference load	
F_s	grid convergence factor of safety	
F_X	total axial force	[N]
F_Y	side force	[N]
F_Z	normal force	[N]
g	grid resolution normalised by fine grid level	
$GCI_{\mathrm{g}=1,1.5}$	grid convergence index between fine and	

	medium grid	
$GCI_{g=1.5,2.25}$	grid convergence index between medium and coarse grid	
I	pixel luminescence intensity	
I_A	2nd moment of area	[m^4]
I_m	mass moment of inertia	[kgm^2]
I_{XX}, I_{YY}, I_{ZZ}	mass moment of inertia around body-fixed principle axes	[kgm^2]
L	body length (Figure 3.3)	[m]
m	body mass	[kg]
M	Mach number	$M = \frac{U}{a_s}$
M_c	crossflow Mach number	$M_c = Msin\sigma$
M_m	body rotational moment	[Nm]
M_X	rolling moment	[Nm]
M_Y	pitching moment	[Nm]
M_Z	yawing moment	[Nm]
N	number of computational time-steps	
$O_{Xw}, O_{Yw} O_{Zw}$	translation vector components w.r.t wind axes of body X_{cg} from t=0	[m]
p	static pressure	[Nm^{-2}]
p_b	pressure acting over base region	[Nm^{-2}]
p_{con}	observed order or convergence	
q	dynamic pressure	[Nm^{-2}]
r_b	body radius	[m]
r_{conv}	grid refinement parameter in all directions	
r_{eff}	effective grid refinement parameter	
r_g	generator bow shock radius	[m]
r_{sh}	distance from generator leading edge to receiver impingement location	[m]
R	maximum body radius at base	[m]

Re_D	freestream Reynolds number based on base diameter	$Re_D = \frac{\rho_\infty U_\infty D}{\mu_\infty}$
$Re_{\delta BL}$	Reynolds number based on approaching boundary-layer thickness	$Re_{\delta BL} = \frac{\rho_\infty U_\infty \delta_{BL}}{\mu_\infty}$
R_{gas}	Universal gas constant	[$Jkg^{-1}K^{-1}$]
s	entropy	[JK^{-1}]
S	body reference area	[m^2]
S_b	body base area	[m^2]
t	solution time	[s]
t_f	maximum fin thickness	[m]
Δt	solution global time-step	[s]
Δt_{char}	characteristic time-step	$\Delta t_{char} = D/U_\infty$
ΔT	total solution time	[s]
T	static temperature	[K]
U	velocity	[ms^{-1}]
$\forbidden{V}$	body volume	[m^3]
V	body translational velocity vector	[ms^{-1}]
V_{Xw}, V_{Yw} , V_{Zw}	body translational velocity components w.r.t wind axes	[ms^{-1}]
x'	axial impingement of the primary disturbance (Appendix B.3)	[m]
Δx	axial stagger between bodies, positive when generator upstream of receiver	[m]
x_f	chordwise distance measured from fin leading edge ($x_f = x - x_{LE}$)	[m]
$\Delta x'_f$	distance from lifting fin leading edge upstream to the location where the diffracted shock crosses the body centreline ($x_f = x_{LE} - x$)	[m]
x_{LE}	axial distance from receiver leading edge to fin leading edge	[m]

x_{res}	horizontal spatial resolution in the PSP 2D image space	[m]
X, Y, Z	body-fixed axes (Figure 3.7)	[m]
$X_w, Y_w,$ Z_w	wind axes (Figure 3.7)	[m]
X_{cp}	longitudinal centre of pressure measured from body leading edge	[m]
X_{cg}	longitudinal centre of gravity measured from body leading edge	[m]
X_{sm}	body static margin ($X_{cp} - X_{cg}$) measured from body leading edge	[m]
Δy	spanwise offset between bodies, positive when receiver is starboard of generator	[m]
y_{res}	vertical spatial resolution in the PSP 2D image space	[m]
y_f	spanwise distance measured from fin root ($y_f = y - r_b$)	[m]
y_1	normal distance from a solid boundary	[m]
y^+	non-dimensional boundary-layer co-ordinate	$y^+ = \sqrt{\left(\frac{\tau}{\rho}\right)_{y_1=0}} \frac{y_1}{\upsilon}$
Δz	lateral separation between bodies, positive when generator top dead centre above receiver	[m]

Greek symbols

α	body angle of attack (Figure 3.9)	[°]
α_{rot}	body rotational acceleration	[s^{-2}]
β	body angle of sideslip (Figure 3.9)	[°]
γ	ratio of specific heats	

Γ	shock diffraction attenuation parameter	$\frac{\Delta C_{p,near} - \Delta C_{p,far}}{\Delta C_{p,near}}$
δ	uncertainty in a given parameter	
δ_{refl}	flow turning angle necessary for a regular shockwave reflection	[°]
δ_{BL}	boundary-layer thickness	[m]
ε	body surface curvature angle relative to X-Y plane (Appendix B.3)	[°]
ζ	body surface curvature angle relative to X_w-Y_w plane (Appendix B.3)	[°]
η	local expansion field strength	$\eta = \frac{dp}{dx} * \frac{L}{p_\infty}$
θ_f	fin leading edge wedge angle	[°]
θ_s	bow shockwave angle relative to X_w-Y_w plane (Appendix B.3)	[°]
θ_{obl}	shock obliqueness angle ($\theta_{obl} = \theta_s - \sigma$) (Appendix B.3)	[°]
λ	body roll angle (Figure 3.9)	[°]
μ	dynamic viscosity	[$kgm^{-1}s^{-1}$]
ν	kinematic viscosity	[m^2s^{-1}]
ρ	air density	[kgm^{-3}]
ρ_m	body material density	[kgm^{-3}]
σ	body total incidence angle (Figure 3.9)	[°]
σ_p	local flow incidence	[°]
$\sigma_p{}'$	local flow incidence on body centreline	[°]
$\sigma_{p,up}$	local flow upstream of fin leading edge	[°]
σ_{cor}	incidence angle correction due to local flow angularity	[°]
σ_y	material yield stress	[Nm^{-2}]
τ	surface shear stress vector	[Nm^{-2}]
ϕ	body azimuth angle from receiver farside (Figure 3.3)	[°]
$\mathbf{\Phi}$	receiver azimuth set-up position relative to generator body	[°]
ψ	local shock strength (ΔC_p across impinging and reflected	

	shockwaves)	
ψ_{imp}	impinging shock strength (ΔC_p across impinging shock)	
ψ_{refl}	reflected shock strength (ΔC_p across reflected shock)	
χ	reflected shock triple point trajectory path angle	[°]
ω	body rotational velocity vector	[s^{-1}]
$\omega_{Xw}, \omega_{Yw}, \omega_{Zw}$	body rotational velocity components w.r.t wind axes	[s^{-1}]

Subscripts

0	stagnation conditions
∞	freestream conditions (inf)
R	receiver body
G	generator body
iso	isolated body condition
$near$	receiver nearside (ϕ=180°) conditions
far	receiver farside (ϕ=0°) conditions
imp	impinging shock conditions
$refl$	reflected shock conditions
ref	PSP calibration reference conditions
amb	ambient conditions
bod	receiver forebody and afterbody (excluding fins)
fin	receiver fins

Superscripts

*	instantaneous value of a given parameter

Abbreviations

CFD	Computational Fluid Dynamics
PSP	Pressure Sensitive Paint
ARA	Aircraft Research Association

ISL	French-German research Institute of Saint-Louis
RANS	Reynolds Averaged Navier-Stokes
S20 SWT	S20 supersonic wind tunnel at ISL
ARA SWT	Supersonic wind tunnel at ARA
DSTL	Defence Science and Technology Laboratory
MOD	UK Ministry of Defence
SL	Sea Level conditions
RBM	Rigid Body Motion
6DOF	6 Degrees of Freedom
RR	Regular shockwave Reflection
SMR	Single Mach Reflection
BAT	Brilliant Anti-armour Technology
DARPA	Defence Advanced Research Projects Agency
RATTLRS	Revolutionary Approach To Time-critical Long Range Strike
JDAM	Joint Direct Attack Munition
AFRL	Air Force Research Laboratory

Further details of notation can be found in Appendix B.3

Chapter 1 Introduction

In a high-speed flow, significant aerodynamic interference can occur when two bodies are placed in close proximity. The complex interference flowfield is primarily dominated by the impinging shock and expansion waves. These disturbances originate from a generator body and impinge upon the receiver body of interest (Figure 1.1). The interference aerodynamics are further complicated by the presence of multiple shock reflections, shock diffractions as well as shock interactions with the viscous body vortex and boundary-layer flows. The induced changes in static pressure and flow angularity across the impinging disturbances modify both the local and overall aerodynamics of the slender body in comparison to the isolated body case. The primary focus of this research is to quantify the magnitude of these effects and understand the associated flow physics.

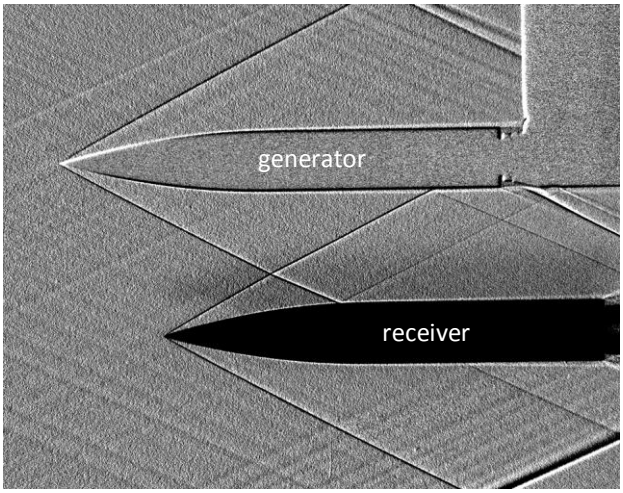

Figure 1.1 A typical multi-body interference flowfield

1.1 Practical situations which involve aerodynamic interference

The main practical application of this research is for weapons which dispense multiple submunition payloads from a bus vehicle at supersonic speeds. An example of this is the Block II ATACMS missile which dispenses 13 Brilliant Anti-armour Technology (BAT)

submunitions[1-3] at M=1.2. These guided munitions then glide towards and destroy moving armoured targets (Figure 1.2).

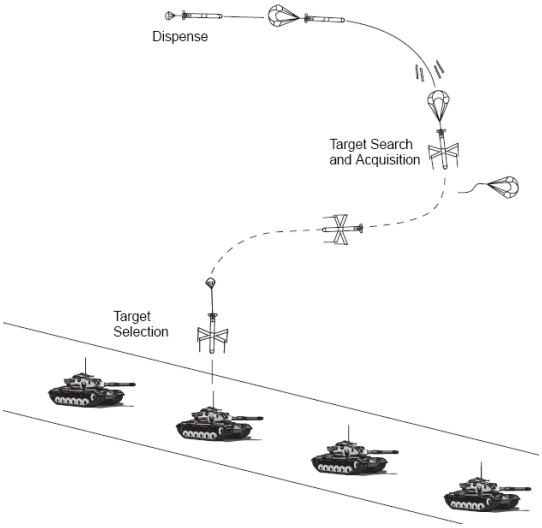

Figure 1.2 Schematic of the BAT submunition system[4]

Other practical applications are future high-speed, long-range strike weapons which are currently under development. Such weapons typically cruise at super/hypersonic speeds and are effective against time-critical targets. The multiple submunition bodies are encased within the larger bus vehicle and are dispensed at supersonic speeds close to the target. Two demonstrator examples are the Revolutionary Approach To Time-critical Long Range Strike (RATTLRS) system[5] and the HyFly Hypersonic flight demonstrator[6]. The RATTLRS demonstrator project aims to test a vehicle which launches from subsonic speeds and accelerates to cruise at Mach 3. It has the option to dispense submunitions at supersonic speeds and a successful demonstration of this aspect of the program has been completed recently in sled tests[5] at M=1.8 (Figure 1.3). In a similar set of tests, a Boeing/Air Force Research Laboratory (AFRL) program also successfully dispensed a MK-82 Joint Direct Attack Munition (JDAM) from a sled[7] at Mach 2 (Figure 1.4).

Figure 1.3 Lockheed Martin sled dispense tests[5] at M=1.8

Figure 1.4 Boeing/AFRL sled dispense tests[7] at M=2.0

HyFly is a hypersonic missile technology demonstrator program from the Defence Advanced Research Projects Agency (DARPA) which aims to achieve sustained cruise flight at M=6 under the power of a dual combustion ramjet[6] (Figure 1.5 (a)). Another key objective of this program is to demonstrate submunition delivery at supersonic speeds. Recent tests in 2007 and 2008 launched the HyFly missile from a F-15E[8] and it reached speeds up to M=3.5 (Figure 1.5 (b)). Further tests are scheduled which aim to achieve M=6 and test the submunition dispense system.

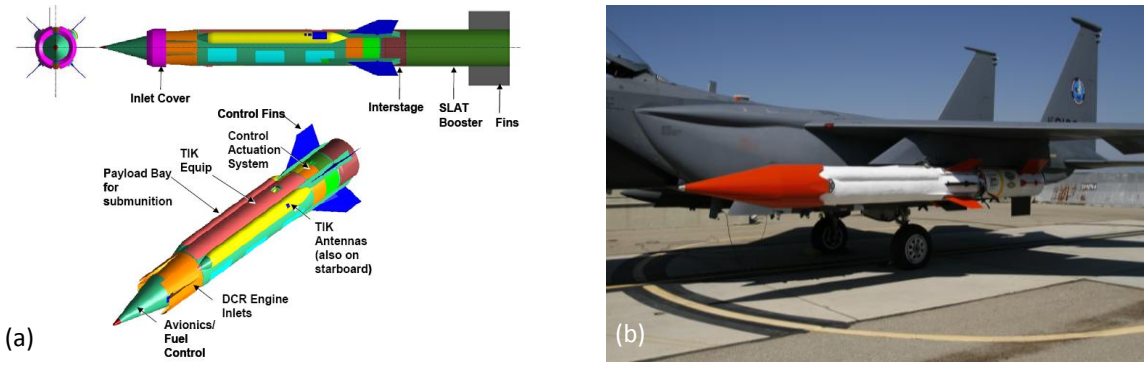

Figure 1.5 (a) Schematic of the HyFly demonstrator components[6] (b) HyFly demonstrator attached to an F-15E[8],

The brief examples provided above are some of the few reported weapon systems which may involve the dispense of submunitions at high speeds. Due to the incentive to package as many munitions as possible in weapons of this sort there is likely to be aerodynamic interference between the bodies post-dispense. This becomes particularly important in situations where the interference loads significantly change the trajectory of the bodies. This may decrease the accuracy of the weapon, or worse, result in a collision. Finally, this research is focused on the mutual aerodynamic interference between the bodies post-dispense. The current investigation does not consider the aerodynamic effects on the bodies from the bus-vehicle. All in all, there is a limited amount of quantitative information in the open literature on this subject[9-12] and since modern weapon systems may utilise high-speed submunitions, this area requires further research.

1.2 Research aim and objectives

1.2.1 Research aim

The overall research aim is to quantify the aerodynamic interference effects between two slender bodies in a high-speed flow and understand the flow physics mechanisms, which cause these effects.

1.2.2 Research objectives

In order the meet the research aim, the following specific objectives are established to give the research a well-defined framework.

1. Design, manufacture and test a finned and un-finned slender body of interest over a wide range of multi-body configurations. Quantify the interference effects through force and moment measurements.
2. Evaluate the capability of the CFD prediction method to capture the relevant interference aerodynamics and use the flowfield predictions in an appropriate way to better understand the measured trends.
3. Understand the topology of the interference flowfield and the propagation of the disturbance waves around the bodies.

4. Investigate the origins of the interference loads and the fundamental flowfield mechanisms which cause the interference effects.
5. Quantity the sensitivity of the interference loads to the following key non-dimensional parameters: lateral separation between the bodies, axial impingement location of the primary interaction, receiver body incidence and the disturbance field strength.
6. Assess the impact of viscous shock interactions on the characteristics of the interference effects.
7. Quantify the effect that control fins have on the interference effects and understand the underlying flowfield mechanisms relevant to a finned body.
8. Evaluate how well the research findings apply to the problem at full-scale.
9. Assess the implications of the research findings for the design of submunition bodies which dispense from a bus vehicle.

1.3 Thesis structure

The structure of this thesis is outlined below.

- The relevant literature pertaining to this problem is reviewed Chapter 2.
- Chapter 3 begins with a description of the research approach and then describes the experimental and computational method.
- The results for a simplified, un-finned body are presented in Chapter 4, with a subsequent discussion of the principal findings.
- The results and discussion for a finned body follow in Chapter 5.
- In Chapter 6, a synthesis discussion brings together the main research findings. The applicability of these findings to the full-scale problem is then assessed, followed by an evaluation of the research implications.
- Finally, conclusions are drawn from the presented findings and recommendations are made for the direction of future study in Chapter 7.

Chapter 2 Literature Review

An important factor which contributes to the novelty of this research is that the interference effects between two bodies are investigated under supersonic conditions. Many studies of mutual interference between bodies, predominantly stores and aircraft, at subsonic speeds have been conducted previously[13]. Unfortunately, limited information is available in the open literature on aerodynamic interference between slender bodies in a high-speed flow. This is surprising since a number of future high-speed vehicles may include the option of dispensing stores or submunitions at supersonic speeds[1,5-7]. Additional pertinent literature is available for other high-speed multi-body configurations such as the Two-Stage-To-Orbit concept[14,15] and sabot discard[16,17] (Figure 2.1).

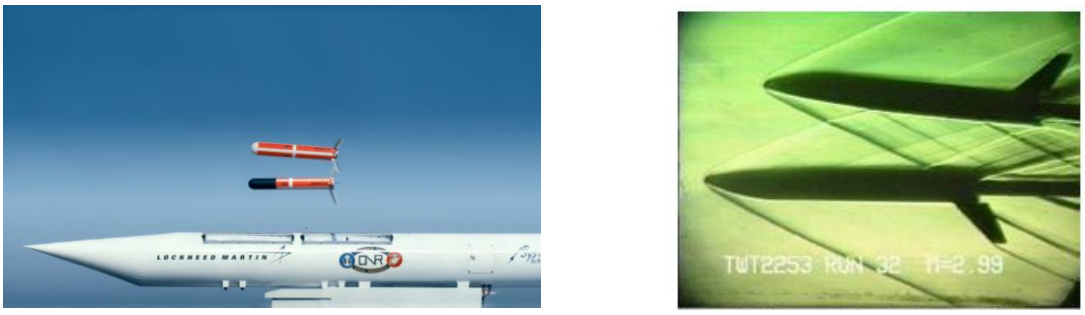

Figure 2.1 (a) RATTLRS high-speed munitions dispense[5] and (b) Two Stage to Orbit Concept[15]

Previous studies of aerodynamic interference were frequently found to focus on the validation of CFD codes[10] or analytical prediction methods[18,19]. There has, until now, been little focus on the underlying aerodynamics which cause the interference effects between two slender bodies. Nevertheless, a summary of the most relevant literature available is now given. The chapter outline is as follows.

- Force and moment effects of aerodynamic interference (§2.1)
- Flow physics of aerodynamic interference (§2.2)

- Summary of knowledge gaps (§2.3.1)

2.1 Multi-body forces and moments

A limited amount of literature is available which discusses the effect of aerodynamic interference on the force and moment characteristics of a slender body. The findings from investigations which consider several practical arrangements of different slender bodies, wings and flat plates are now summarised.

2.1.1 Mutual slender body interference

An early consideration of aerodynamic interference between two slender bodies was reported by Gapcynski[9] in 1955. Gapcynski measured pressures and forces on a parabolic body of revolution at zero incidence[a] in close proximity to a solid wall with a freestream flow of M=1.41 and M=2.01. These tests investigated the effect of the distance between the body centrelines, henceforth known as the lateral separation (Figure 2.2 (a)) for two axially aligned bodies. When the body was close to the wall (small $\Delta z/D$), the normal force induced through aerodynamic interference attracted the body further towards the wall. The induced pitching moment around the body centre of gravity tended to pitch the body away from the wall. As the lateral separation increased over the range ($2.5 \leq \Delta z/D \leq 7$) Gapcynski observed that both of the interference loads changed polarity. Moreover, the normal force loads varied non-monotonically with lateral separation, whereas there was a continuous relationship with pitching moment. Overall, maximum interference normal force and pitching moment loads were observed to be in the order of ΔC_Z=0.12 and ΔC_m=-0.04[b]. Unfortunately, since these tests were used to validate an analytical model, there was very little analysis to interpret the observed trends in the induced force and moments, even though there was a wealth of local normal force and pressure data available on the body of interest.

A more recent example of mutual slender body interference is reported by Volkov[11]. Volkov predominantly used computational predictions to investigate the interference

[a] Measurements were also taken with the body at ±3° but no analysis of these results was presented
[b] Note that the body length was used as the characteristic length in the non-dimensionalisation of C_m

flowfield between two, axially aligned, cone-cylinder bodies at M=4.03 (Figure 2.2 (b)). Volkov was able to use the detail of the wave structures predicted by CFD to interpret the effect of the impinging disturbances on the body of interest. Volkov observed that when the bodies were very close ($\Delta z/D<2$) multiple reflected shockwaves were induced between the bodies and the interference flowfield was extremely complex. In addition, the effect of the diffracted waves on the shielded side of the body can significantly affect the overall body loads. At the minimum lateral separation ($\Delta z/D=1.2$), Volkov reported that the interference normal force tended to force the bodies apart. This remained the case over the range of lateral separations considered ($1.2 \leq \Delta z/D \leq 2$) and is due to the very high impinging shock strengths. As in Gapcynski[9] the polarity of the interference moment changed from one which pitched the bodies together to one which pitched the bodies apart as $\Delta z/D$ increased. Maximum interference loads observed by Volkov were in the order of ΔC_Z=-0.12 and ΔC_m=0.04.

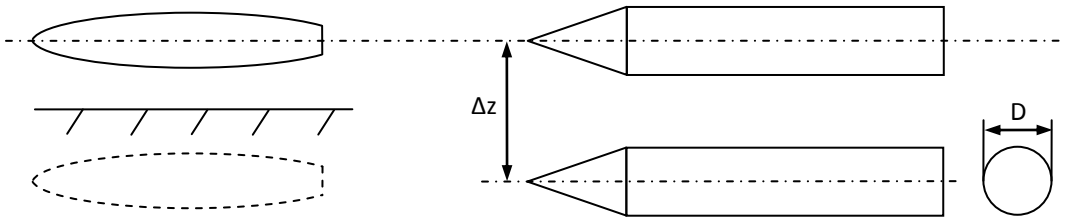

(a) Gapcynski (b) Volkov

Figure 2.2 Schematic showing the definition of lateral separation for bodies investigated by (a) Gapcynski[9] and (b) Volkov[11]

2.1.2 Traverse of stores through a disturbance flowfield

Another aspect of high-speed mutual interference is to place the slender body of interest in the disturbance flowfield of a 2D wing (Figure 2.3) to help understand the practical situation of supersonic weapon release. A handful of researchers[18-23] have reported the measured forces and moments on stores as they were traversed in either the lateral (Figure 2.3 (a)) or axial direction (Figure 2.3 (b)) through a disturbance flowfield. These configurations are for bodies at zero incidence and some included control fins.

Gapcynski[20] continued his previous work and tested the same parabolic body of revolution close to a wing in a freestream flow at M=2.01. Gapcynski axially traversed the body at a fixed lateral separation. He found that when the impinging shock was near the body trailing edge, the normal force interference was negative (which repelled the body from the wing) and was accompanied by a positive pitching moment interference (which pitched the body towards the wing). As the body moved aftward through the wing disturbance flowfield, both the normal force and pitching moment changed polarity. This is in line with Gapcynski's previous observations[9] where a similar geometric effect was achieved by a variation in lateral separation at a fixed axial stagger. Maximum interference loads were in the order of ΔC_Z=0.3 and ΔC_m=0.4, and in some cases an effective incidence of σ_{eff}=8° was observed based on ΔC_Z[21]. As in the previous Gapcynski paper, little or no analysis is offered to help interpret why these changes occur. Corder et al.[22] investigated an un-finned store which traversed axially through the disturbance flowfield from a tangent ogive body. They reported similar characteristics to Gapcynski with maximum interference loads in the order of ΔC_Z=-0.2 and ΔC_m=0.4. Newman et al.[24] noted that the axial force interference was as much as 20% of the isolated configuration for an un-finned ogive-cylinder body as it traversed through a 2D wedge shock. The normal force and pitching moment interference were as much as ΔC_Z=0.8 and ΔC_m=0.3 and changes of this order could significantly affect the body trajectory[24].

Cenko et al.[18] and Waskiewicz[19] investigated a finned store adjacent to a flat plate at incidence with a freestream flow at M=1.9. They both recorded that the interference loads were highly sensitive to where the shock impinged axially on the body as it traversed aftward through the disturbance field, as noted in the un-finned investigations. Maximum interference effects for a finned store were ΔC_Z=1 and ΔC_m=0.3. Corder et al.[22] recorded a similar importance of axial impingement location for a finned store in a freestream flow at M=2.5. The disturbance field was 3D and provided by a tangent-ogive body in Corder's investigation and maximum interference effects were in the order of ΔC_Z=-0.35 and ΔC_m=0.8. Perkins[23] noted similar findings for a finned store as it traversed in the lateral direction through a disturbance field. In

this case, the freestream Mach number was M=1.81 and maximum interference effects were ΔC_Z=0.4 and ΔC_m=1.

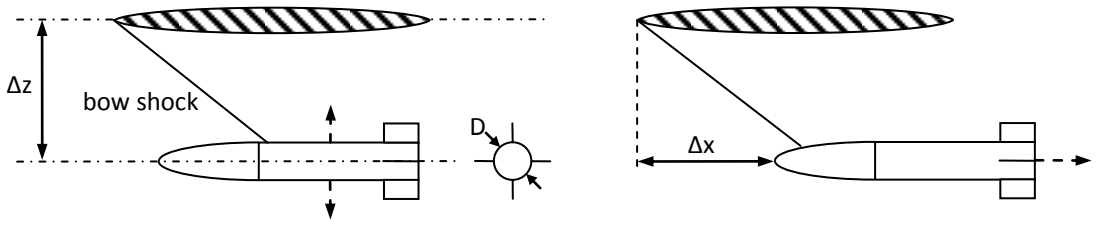

(a) lateral traverse (b) axial traverse

Figure 2.3 Schematic of a generic finned stored which traverses through a disturbance flowfield from a 2D wing in the (a) lateral and (b) axial direction

Lastly, Wilcox[25] and August et al.[26] have investigated the situation where a cone-cylinder body traverses through the leeside flowfield of a flat plate at incidence in a freestream flow at M=6. This investigation aimed to help understand the aerodynamic complexities involved with hypersonic weapon dispense. Both researchers noted that the flow angularity upstream of the body was the primary interference mechanism which affected the body loads.

Overall, notable changes in the body aerodynamic loads as a consequence of high-speed interference effects have been reported by a number of researchers. Two recent publications by Malmuth[27] and Fedorov et al.[28] have constructed analytical prediction methods based on weak shock scattering and asymptotic methods. These provide estimates of ΔC_Z and ΔC_m for a slender body at zero incidence in a disturbance flowfield which involves a shock interaction with the body of interest. Good agreement is found by both researchers with measured data when the interference effects are dominated by a primary interaction (i.e. a single disturbance shockwave) and become less accurate when the bodies are very close where the flowfield exhibits multiple shock reflections. Other researchers who have developed analytical predictions methods for this problem include Cenko et al.[18] and Waskiewicz[19] through the influence function method and again good agreement is observed with measured data for the majority of configurations.

A number of researchers have hypothesised that the observed interference loads could significantly affect the subsequent body trajectory[27,29]. One of the few to test

this is the work of Malmuth[27] where predictions were made of the trajectory of a store in the disturbance flowfield of a 2D wing in a freestream flow at M=3.9. The body trajectory is reported to be significantly altered when either the leading edge or trailing edge wing shockwaves impinge on the body.

2.2 Multi-body flow physics

In addition to the overall interference loads, it is important to understand the detailed underlying flow physics. Very few literature examples have been found which document the interaction of an oblique shockwave with a body of revolution in steady flow. As a result, only the findings of one investigation will be highlighted in any detail in the forthcoming discussion. This involved a number of the flowfield interactions typically found in high-speed multi-body interference flowfield.

Brosh et al.[10,30,31] investigated the impingement of a 2D oblique shockwave on a cylinder at zero incidence, with a turbulent boundary-layer in a freestream flow at Mach 3 and a Reynolds number based on the cylinder length of $Re_L=18.2x10^6$ (Figure 2.4). Extensive measurements of surface pressure, surface oil flow were conducted as well as flowfield static and total pressure surveys. This data was used to investigate the interaction flowfield and served as a validation dataset for computational predictions of the flowfield.

Brosh et al. reported that the impinging shock induced large pressure gradients on the cylinder nearside. These resulted in a notable local pressure rise which contributed to a shock-induced separation region on the nearside. This primary separation bubble acted as an obstacle to the oncoming nearside flow and caused a secondary separation bubble immediately upstream of the first. However, for a weaker impinging shock (when the wedge was placed further from the cylinder) only a single separation bubble is observed[30]. The nearside pressure gradients induced by the impinging shock were observed to be as large in the crossflow direction as in the axial direction. This lead to the development of a severe crossflow from nearside to farside (orientated at as much as 45° to freestream flow direction). In this sense, and with consideration of the oil flow structures on the cylinder farside, the interaction effect of the impinging shock

acts like an effective incidence. The crossflow thickened the farside boundary-layer. Dual separation regions were observed but this time with a crossflow separated flow structure. Wake-type flow resulted on the farside and as a result significant upstream influence of the diffracted shock occurred (up to 6 times the un-disturbed boundary-layer thickness). Similar observations of large upstream influence were made by Morkovin[32] for a similar study at M=1.9. The farside pressure rise was approximately a quarter of that of the nearside and remained at approximately the same level along the body downstream of the farside interaction, another indicator of a region of separated flow. Moreover, the shock attenuates significantly as it diffracts around the body.

Overall, the work of Brosh et al. is important as it is a first attempt to understand the underlying flow physics behind shock-wave impingement on a cylindrical body. It is clear from the findings presented that the flow physics even in a simplified arrangement (Figure 2.4) can be highly complex. It also highlights some of the important physical reasons for the pressure footprints which induce the changes in body loads observed in previous studies which were more focussed on force and moment measurements. Brosh et al. have shown that alot of information about the flowfield is required to understand the underlying aerodynamics of shockwave-cylindrical body interactions.

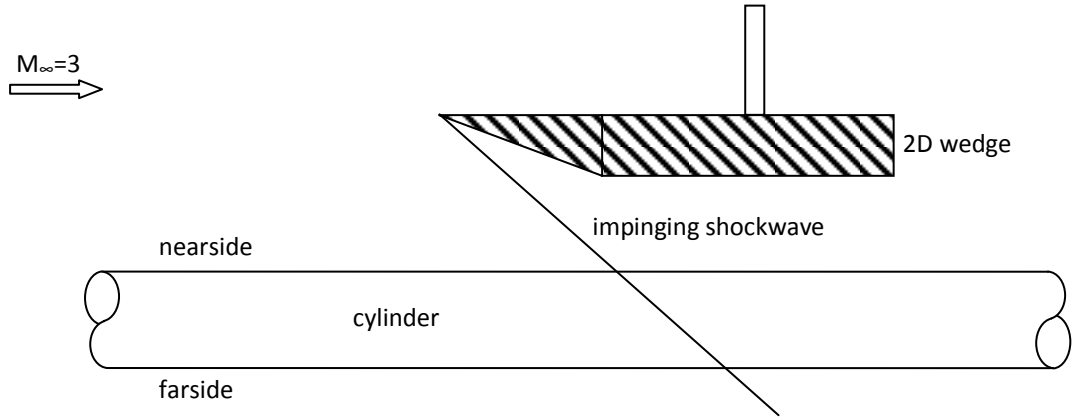

Figure 2.4 Schematic of the experiment set-up, adapted from Brosh[30]

Another similar configuration of a 2D shock interaction with a cylindrical body at zero incidence was predicted computationally by Hung[12] for a freestream flow at M=4 and

Re_D=0.32x10^6. Many of Hung's findings were similar to Brosh with large regions of complex flow on both sides of the cylinder observed. Hung did do more to explain the shock diffraction around the body and observed that the regular shock reflection on the nearside transitioned into so called "lambda" shock structures as the shock reached the cylinder farside and beyond[12,33]. The use of CFD allowed Hung to compare the axial pressure distributions at various azimuth locations for both laminar and turbulent flows. On the cylinder nearside, there was no difference between laminar and turbulent flows. However further towards the farside, there is significantly more upstream influence for the laminar predictions but the local pressure rise due to the shock is not as large as the turbulent case. Moreover, there was also a more severe crossflow in the laminar computation.

The general characteristics of shockwave boundary-layer interactions can be found in comprehensive review papers by Dolling[34] and Settles[35]. More particularly, similar to Brosh et al. and Hung, highly complex separated flow as the result of interactions between 3D shockwaves and planar and axi-symmetric boundary-layers are also reported by Derunov et al.[36], Gai[37] and Kussoy et al.[38].

2.3 Summary

The previous research published on the topic of high-speed aerodynamic interference between slender bodies has been reviewed. In general, limited information is available in the open literature and from which a list is provided below for areas which are not well understood and require further research.

2.3.1 Gaps in current knowledge

- A more detailed understanding is required about the flow physics of the elemental interactions which occur in a multiple slender body flowfield and how these combine to bring about the overall interference loads.

- Further evaluation of the capability of CFD to predict high-speed interference flows is needed. This must include validation of measured and predicted

interference loads and surface pressures over a wider range of configurations than currently exists.

- More quantitative measurements are needed to evaluate the interference loads on slender bodies over a greater range of axial and lateral separation distances between the bodies than currently exists.

- There is limited information available on the quantitative effect of control fins, disturbance field strength or body incidence on the interference loads for the body of interest.

- There is limited information available on whether interference effects can be large enough to change the static stability of a finned body.

- Very few investigations have studied the interference effects on the trajectory of a slender body. Little is known about the nature of the unsteady interference flowfield.

- Limited information exists to guide the designer of a submunition weapon system with respect to the problems of aerodynamic interference. Recommendations are needed based on the research-based points above, in order to better inform the designer.

The areas which require further research (above) have been used as the motivation for the specific research objectives in the current research (§1.2.2). This will develop understanding in these areas and progress the scientific field of high-speed aerodynamic interference.

Chapter 3 Research Approach and Method

This chapter describes how the research aim will be achieved through the collection and interpretation of quantitative experimental and computational data. The bodies under investigation are described along with the arrangement of the multi-body configurations and the frames of reference. The experimental and computational method provides details about the way in which the measurements and predictions were performed. Finally, estimates of the uncertainties in the measured and predicted parameters are provided.

These discussions are grouped into the following sections.

- Research approach (§3.1)
- Slender body descriptions (§3.2)
- Multi-body arrangements and reference frames (§3.3)
- Experimental method: S20 wind tunnel and data acquisition (§3.4)
- Experimental method: ARA wind tunnel and data acquisition (§3.5)
- Computational method (§3.6)
- Uncertainty analysis (§3.7)

3.1 Research approach

In order to meet the overall research aim (§1.2.1) this investigation required quantitative data to determine and interpret the interference effects between two slender bodies. This was supplied through a comprehensive wind tunnel study completed by the author as well as measurements from a previous experimental dataset[39]. Further to these measurements, Computational Fluid Dynamics (CFD) was used extensively to interpret the measured trends and understand the underlying aerodynamics of the interference flowfield. The CFD allowed flexibility to extend beyond the experimental test matrix and to analyse configurations where no measurements were possible.

This research provides quantitative information relevant to the practical application of multiple bodies which dispense from a larger bus vehicle. The current approach assumes that the bodies dispense safely and that the bus vehicle has a negligible aerodynamic effect on the bodies. Therefore, the aerodynamics of different post-dispense geometric configurations are investigated and the interference effects are evaluated.

Three main experimental design decisions were taken to simplify the configurations under investigation from the full-scale problem. As is the norm in wind tunnel experiments, the models were tested at a reduced tunnel-scale from what would be expected in a full-scale application ($1/5^{th}$ scale). All measurements and the majority of CFD predictions assume steady-state conditions. The majority of data was taken at a fixed Mach number of $M_\infty=2.43$. A full-scale dispense Mach number is expected to be in the supersonic regime[1,5-7]. The extension of the tunnel-scale research findings to the full-scale problem is investigated in §6.2.

3.2 Description of bodies under investigation

The four bodies which were investigated were all slender in profile ($L/D \gg 1$). Each body is designated as either a receiver or a generator. The investigation focuses on

the aerodynamics of the receiver bodies, whilst the generator bodies provide the disturbance flowfield.

3.2.1 Receiver bodies

All quantitative measurements were taken on the receiver bodies. Two receiver bodies were investigated, one un-finned (*m2651*) and the other finned (*m2652*) and these are shown in Figure 3.1 and Figure 3.2 respectively. The un-finned receiver consists of a 3.5D tangent ogive forebody. The afterbody is cylindrical and the overall length of the body is L/D=7.358, where D is the base diameter of D=20mm (Figure 3.3). In addition to the un-finned receiver, an equivalent body was designed in order to exhibit static stability. To achieve this, a set of cruciform control fins were designed using Missile Datcom[40] and CFD. These fins were positioned at the aft of the body with the fin leading edge located at $x_{LE}/D=6.358$ (Figure 3.4). The fins have a hexagonal profile (0.2-0.6-0.2c), a total chord length of c=20mm (c/D=1), a semi-span of b=13mm (b/D=0.65) and a thickness to chord ratio of $t_f/c=0.1$ (Figure 3.5). Further details on the design of the finned receiver can be seen in Appendix A.1.

Figure 3.1 The un-finned receiver body (*m2651*)

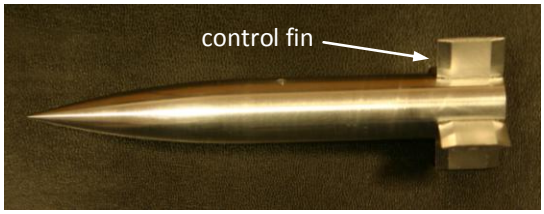

Figure 3.2 The finned receiver body (*m2652*)

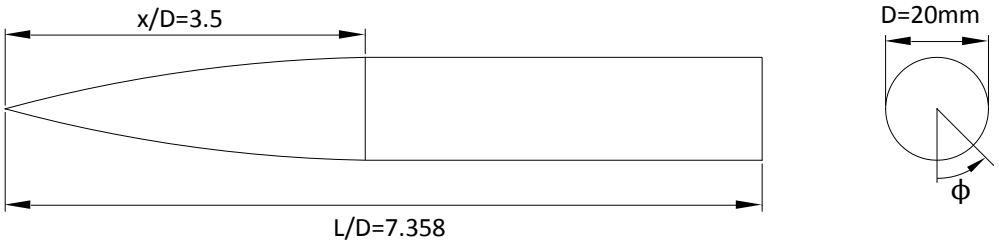

Figure 3.3 Schematic of the un-finned receiver body and definition of azimuth angle (ϕ)

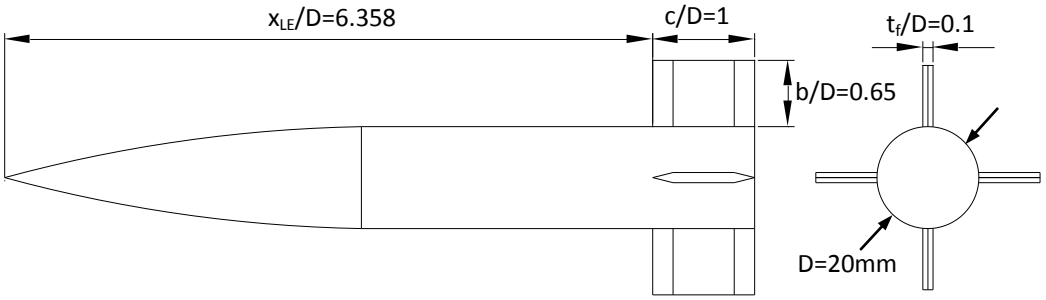

Figure 3.4 Schematic of the finned receiver body

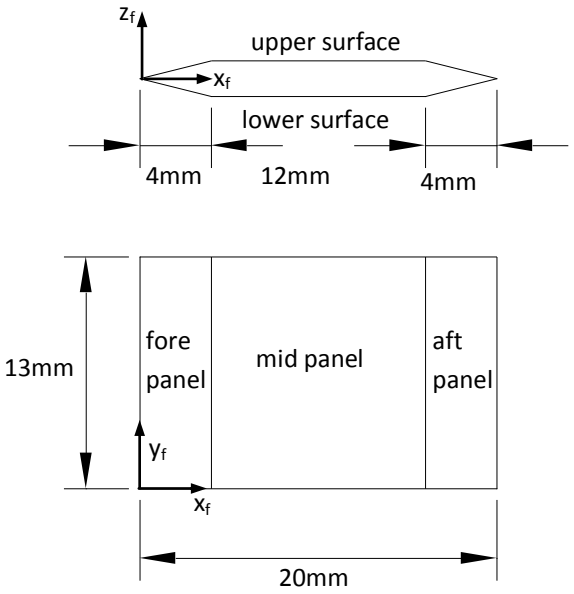

Figure 3.5 Schematic of the receiver fin and fin axes system

3.2.2 Generator bodies

No measurements were taken on the generator bodies. Instead, these provided the disturbance flowfield. The sharp generator (*m2653*) is identical to the un-finned receiver (Figure 3.1). In addition to the sharp generator, a blunt generator was designed which allowed testing of a stronger disturbance flowfield. The blunt generator (*m2654*) is the same overall length as the sharp generator (L/D=7.358, D=20mm) but includes a hemi-spherical forebody which induces a stronger bow shock and expansion wave field (Figure 3.6).

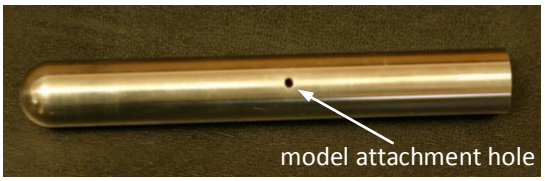

Figure 3.6 The blunt generator body (*m2654*)

All of the bodies described above were tested in the S20 Supersonic Wind Tunnel (S20 SWT) at the French-German Research Institute of Saint-Louis (ISL). These bodies were manufactured within a tolerance of 0.1mm out of high-strength aluminium (H30 6082-T6) and included a small model attachment screw hole (Figure 3.6). Finally, the un-finned receiver and sharp generator were also tested in the Supersonic Wind Tunnel (ARA SWT) at the Aircraft Research Association (ARA) at a larger dimensional scale of D=25.4mm (§3.5). Although only a subset of this data is used in the forthcoming chapters, the bodies tested in the ARA SWT are designated *m265r* and *m265g* respectively, to avoid any confusion with bodies tested in the S20 SWT.

3.3 Multi-body arrangements and reference frames

This research includes a parametric study which covers many different isolated and multi-body configurations. In order to identify the geometric arrangement of the bodies under investigation, the following section describes several definitions. In addition, the reference frames used in the chapters ahead are also briefly discussed. This information applies to the measured and predicted data.

3.3.1 Geometric arrangements

Only one receiver body and one generator body are investigated at any one time in a single multi-body configuration. The geometric arrangement for a given configuration is based on the relative positions of the bodies at zero incidence in the wind-axes reference frame (X_w,Y_w,Z_w). Since the models are bodies of revolution, a cylindrical reference frame is logical and the important dimension in any configuration is the minimum distance between the body centrelines, the radial separation (Δr). In practice, this distance is set by placing the receiver at an appropriate lateral separation (Δz), spanwise offset (Δy) and axial stagger (Δx) relative to the generator (Figure 3.7 (a)). The lateral separation is defined as positive when the generator is top dead centre of the receiver. The spanwise offset and axial stagger are defined as positive relative to the wind-axes reference frame (Figure 3.8). In all tests, no spanwise offset ($\Delta y=0$) was used and thus $\Delta r=\Delta z$ (Figure 3.7 (b)). This decision was taken for two reasons. Firstly, it avoided the practical complications in the wind tunnel associated

with installing the bodies at a non-zero spanwise offset. The second was that since the receiver azimuthal set-up location is zero (**Φ**=0°), the receiver forces and moments reported by the body-fixed cartesian reference frame (X,Y,Z) can be used directly to interpret whether the interference effects cause the receiver to pitch towards or away from the generator. This is because the body fixed Z axis is aligned with the radial separation line.

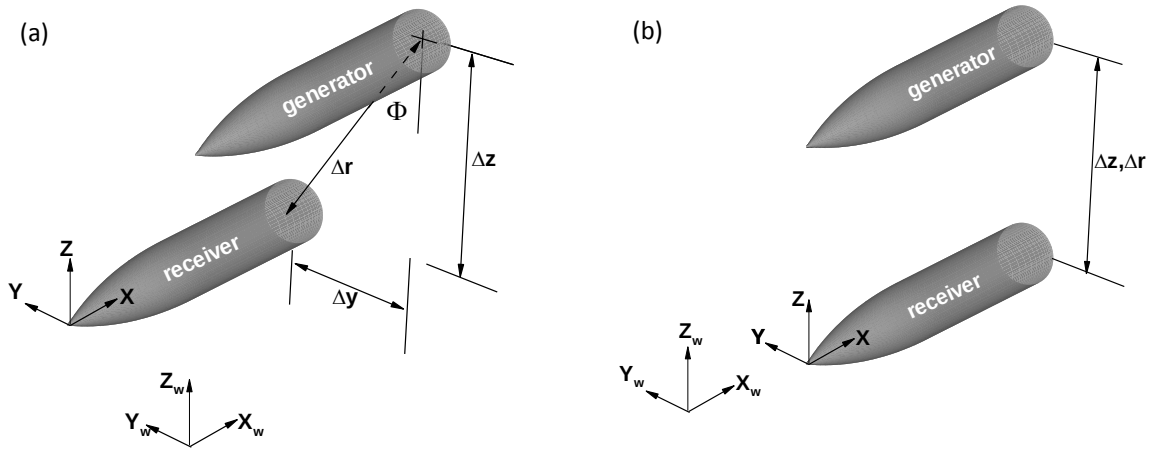

Figure 3.7 Schematic of the cylindrical reference frame with no axial stagger when (a) **Φ**>0°, (b) **Φ**=0° and shows the wind axes (X_w,Y_w,Z_w) and body axes (X,Y,Z)

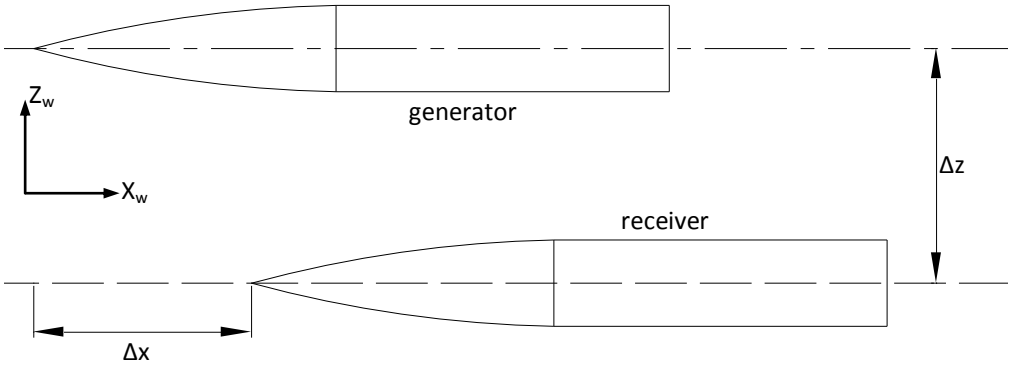

Figure 3.8 Definitions of positive axial stagger (Δx) and positive lateral separation (Δz)

3.3.2 Angle definitions

The attitude of a body is described by the angle between the body axial centreline and the freestream velocity vector. The freestream velocity vector (U_∞) is aligned with the streamwise (X_w) direction in the wind-axes reference frame. A positive angle of attack is defined as body nose up relative to the freestream flow (Figure 3.9 (a)). A positive roll angle is defined as anti-clockwise looking upstream into wind (Figure 3.9 (b)). A

positive sideslip is defined as wind into the starboard side of the body (Figure 3.9 (c)). The total incidence angle is the total included angle between the body axial centreline and the freestream velocity vector[41] (Figure 3.9 (d)).

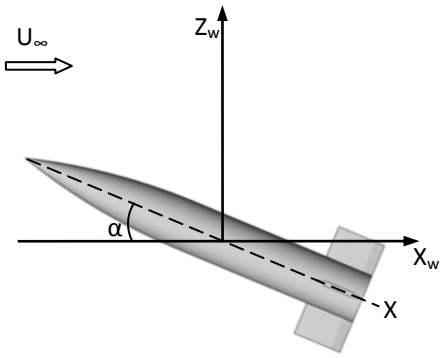

(a) positive angle of attack (Y_w,Y into page)

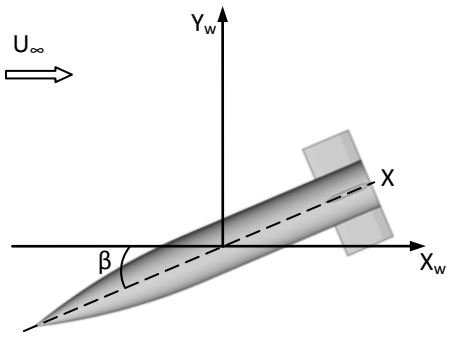

(c) positive sideslip (Z_w,Z out of page)

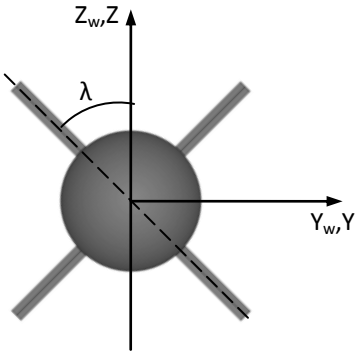

(b) positive roll (X_w,X and U_∞ out of page)

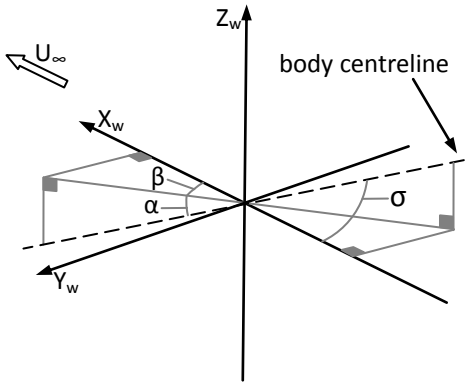

(d) total incidence angle

Figure 3.9 Angles of the body centreline (dashed) relative to wind axes reference frame (solid) for (a) positive angle of attack, (b) positive roll angle, (c) positive sideslip and (d) total incidence angle

The receiver roll angle and sideslip remain zero throughout all experiments in this research (β_R=0°, λ_R=0°). As a result, the total incidence angle (σ_R) is frequently used to defined the pitch attitude of the body instead of the angle of attack. The generator body roll and incidence also remain zero for all experiments (σ_G=0°, λ_G=0°).

3.3.3 Data reduction

The steady-state force and moment data (measured and predicted) are reported for the receiver bodies only. The receiver forces and moments are defined using a body-fixed cartesian reference frame (X,Y,Z) with the moment reference location at the body

leading edge (Figure 3.10). These axes pitch with the body but do not roll with the body. All measured and predicted forces and moments are non-dimensionalised using the base area (S) as the characteristic area and the base diameter (D) as the characteristic length (Equation 3.1-3.3). The axial force is further corrected to assume freestream pressure acts over the base area (S_b=S) using a measurement of the base pressure[42] (p_b), Equation 3.4.

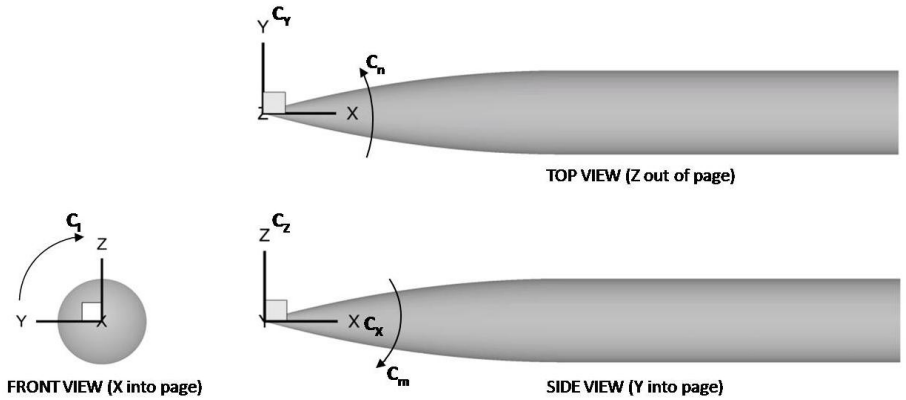

Figure 3.10 Receiver body force and moment sign convention using body-fixed reference frame

$$C_Z = \frac{F_Z}{q_\infty S} \quad 3.1$$

$$C_{X,t} = \frac{F_X}{q_\infty S} \quad 3.2$$

$$C_m = \frac{M_Y}{q_\infty SD} \quad 3.3$$

$$C_X = C_{X,t} + \frac{S_b(p_b - p_\infty)}{q_\infty S} \quad 3.4$$

As with previous mutual interference studies[13] the isolated body loads are recorded, but the focus of the investigation will be to understand the trends of the interference loads. The interference loads are defined as the load difference from the isolated case as a result of the disturbance flowfield (i.e. $\Delta C_Z = C_Z - C_{Z,iso}$). This allows the comparative magnitude of the interference effects across different configurations to be easily established.

3.4 Experimental method: ISL S20 Supersonic Wind Tunnel

3.4.1 Wind tunnel set-up and operating conditions

The majority of measurements reported in this research were conducted in the 0.2m x 0.2m, blowdown S20 Supersonic Wind Tunnel (S20 SWT) at ISL (Figure 3.11). The working section operating conditions are listed below in Table 3.1 and Appendix A.2. The tunnel run time was typicaly 50s.

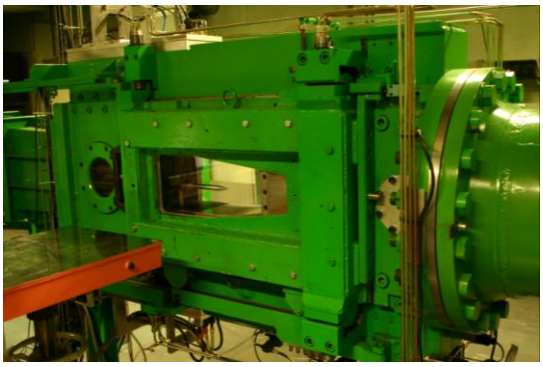

Figure 3.11 The S20 Supersonic Wind Tunnel

Parameter	Value
M_∞	2.43
p_0	0.675 MPa
T_0	293 K
Re_D	1.4×10^6

Table 3.1 Freestream operating conditions in the S20 SWT

Multi-body testing was performed with a dual-support sting system (Figure 3.12). A traverse mechanism allowed the upper generator body and lower receiver body to be translated relative to one another in the streamwise direction. The receiver body incidence was controlled using the lower support sting, which rotated about a centre of rotation point 1.65D upstream of the base on the body centreline. Two D_s=16mm diameter stings connected each body to their respective supports (Figure 3.12). The upper support was removed when testing the receiver bodies in isolation.

On the whole, no boundary-layer transition devices were used on the bodies tested in the S20 SWT. However, a small number of additional tests of the isolated un-finned receiver configuration were performed with a wire transition strip attached 2mm from the leading edge of the forebody. These demonstrated that fixed transition had a negligible effect on the normal force and pitching moment coefficients and a small increase in axial force of C_X=0.01 (Appendix A.3). It is therefore assumed that the boundary-layer was naturally turbulent during tests in the S20 SWT.

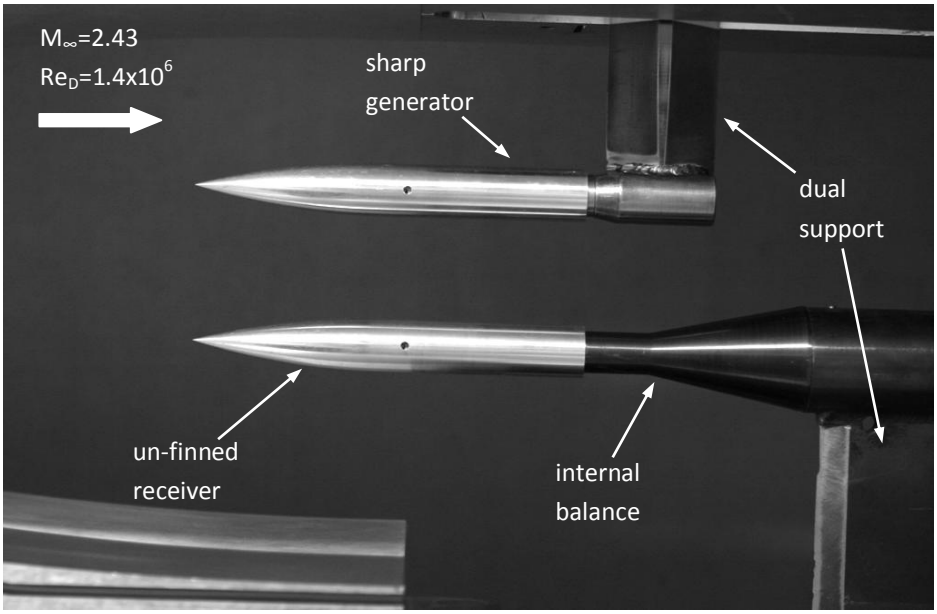

Figure 3.12 Un-finned receiver (*m2651*) set-up adjacent to the sharp generator (*m2653*) in the S20 SWT

3.4.2 Data acquisition and measurement procedure

For each test, the settling chamber total pressure and total temperature were measured with a Druck PMP-4070 20bar, absolute pressure transducer (S/N 1069985) and a total temperature probe respectively. The calibration data for these are shown in Appendix A.4. The total pressure measurement and the Mach number based on the tunnel nozzle geometry of M_∞=2.43 were used to calculate the freestream dynamic pressure (q_∞) used in the subsequent data reduction. This Mach number assumption was assessed through measurement of the wave angles from the working section liner which indicated Mach numbers of M=2.41 and M=2.42 on the upper and lower liners respectively. In addition, for a single test the Mach number was calculated from the measurement of the working section static pressure using a Druck PMP-4070 10bar absolute pressure transducer (S/N 1378924), the total pressure measurement and isentropic relations. In this case the measured Mach number was M_∞=2.40. In all other tests, the working section static pressure was not measured[a]. Instead, the Druck PMP-4070 10bar pressure transducer was used to measure the base pressure of the receiver body. The tunnel total pressure and total temperature measurements were

[a] Measuring the working section static pressure required a wind tunnel door that was incompatible with the shadowgraph visualisation measurement system.

also used to calculate the freestream Reynolds number in each configuration (Re_D=1.4x10^6).

To assess the interference aerodynamics, different multi-body configurations were tested to evaluate the effects of the axial stagger, disturbance field strength and receiver incidence. For a multi-body configuration, the measurement procedure was as follows. The receiver and generator bodies were arranged in the tunnel at a lateral separation of $\Delta z/D$=2.94 and zero incidence (σ_R=0°, σ_G=0°). When the finned receiver was tested the fins were in arranged in the + configuration (λ=0°). The bodies were then traversed to the axial stagger under investigation ($\Delta x/D$). The wind tunnel started with a short period of settle time where no measurements were taken (<5s). After which, the receiver body incidence was varied (typically) between $-15 \leq \sigma_R \leq 15°$ in increments of 1° and 2°.

The receiver body paused at each incidence setting where the forces and moments were measured using an ABLE MKXIV 6-component, balance (Figure 3.12). This balance was fitted internally in the lower support and central cavity of the receiver. The balance had been calibrated by Able a-priori and was proof loaded before and after use, which demonstrated good accuracy to within 0.5% of the applied load. The force and moment balance outputs (as well as p_0, p_b and T_0) were acquired using a 16bit Racal instruments 6062 DAQ board at a sample rate of 100 kHz with a sample duration of 2s. The signal was filtered by a low-pass 5Hz filter. For one run, the sample time was doubled and this showed negligible effect on the measured forces and moments (Appendix A.5) which indicates that 2s was suitable.

A shadowgraph image was also taken at each incidence setting. A light source was focussed using a 0.38m diameter lens (Figure 3.13 (a)) and the illuminated flowfield was projected onto a transparent screen on the opposite tunnel window where a still image was taken with a PCO Sensicam qe camera (Figure 3.13 (b)). Images were then post-processed offline using image division to accentuate the shock structures. This used a reference image of the tunnel running with no receiver body present.

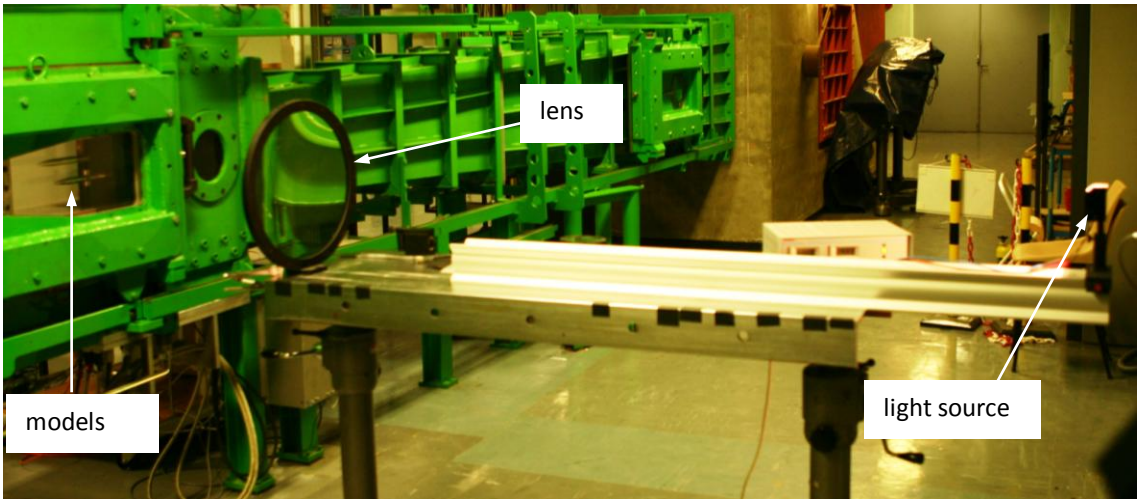

(a) light source and lens

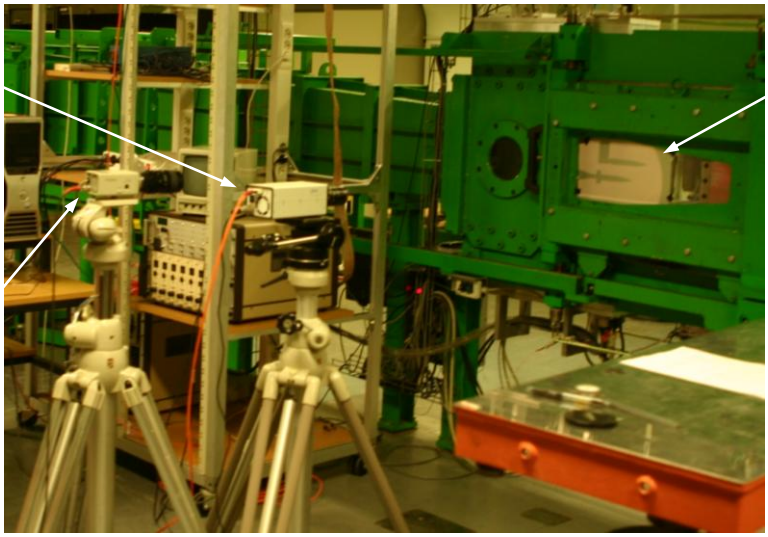

(b) cameras and screen

Figure 3.13 Set-up of the shadowgraph measurement system (a) light source, lens and (b) cameras, screen

The above procedure was repeated for all combinations of receiver and generator bodies (*m2651-m2654*) at 5 different axial stagger configurations. In the sharp generator configurations these were Δx/D=-1.65, 0, 1.67, 2.68, 3.679. For the blunt generator tests the axial stagger was adjusted to ensure the same axial impingement location of the primary disturbance as the equivalent sharp generator configuration. The blunt generator configurations were tested at axial staggers of Δx/D=-3.81, -2.16, -0.53, 0.44, 1.2. This approach helped to simply the analysis so that the interference effects could be compared as a function of the disturbance field strength alone. The receiver bodies in isolation were tested without the upper sting support but on the same lower sting and in the same position in the tunnel as the multi-body

configurations. This provided data to gain an understanding of the underlying isolated aerodynamics of the receiver bodies and provided a reference dataset for comparison with the CFD predictions

Finally, the details of the set-up, calibration and procedure for the PSP measurements can be found in Appendix A.6

3.4.3 Experimental test matrix

Details of the S20 SWT experimental test matrix are listed below in Table 3.2. A total of 434 configurations were investigated. In the multi-body configurations, the lateral separation and generator incidence were equal to $\Delta z/D=2.94$ and $\sigma_G=0°$ respectively in all tests. The force and moment results for these configurations can be found in Appendix B.6,B.7 and Appendix C.3,C.4.

Receiver	Generator	Configuration	Incidence range	F+M	Shadow-graph	PSP
Un-finned	-	isolated	$-15 \le \sigma_R \le 15°$	✓	✓	✗
Un-finned	Sharp	$\Delta x/D=-1.65$,	$-12 \le \sigma_R \le 15°$	✓	✓	✗
		0, 2.68, 3.679	$-15 \le \sigma_R \le 15°$	✓	✓	✗
Un-finned	Sharp	$\Delta x/D=1.67$	$-15 \le \sigma_R \le 15°$	✓	✓	
			σ_R=-15,-8,0,8,15°			✓
Un-finned	Blunt	$\Delta x/D=-3.81,-2.16,$	$-10 \le \sigma_R \le 15°$	✓	✓	✗
		0.44, 1.2	$-15 \le \sigma_R \le 15°$	✓	✓	✗
Un-finned	Blunt	$\Delta x/D=-0.53$	$-15 \le \sigma_R \le 15°$	✓	✓	
			σ_R=-15,-8,0,8,15°			✓
Finned	-	isolated	$-15 \le \sigma_R \le 15°$	✓	✓	✗
Finned	Sharp	$\Delta x/D=-1.65$,	$-12 \le \sigma_R \le 15°$	✓	✓	✗
		0, 2.68	$-15 \le \sigma_R \le 15°$	✓	✓	✗
Finned	Sharp	$\Delta x/D=1.67$	$-15 \le \sigma_R \le 15°$	✓	✓	
			σ_R=-15,-8,0,8,15°			✓
Finned	Blunt	$\Delta x/D=-3.81, -2.16,$	$-10 \le \sigma_R \le 15°$	✓	✓	✗
		0.44	$-15 \le \sigma_R \le 15°$	✓	✓	✗
Finned	Blunt	$\Delta x/D=-0.53$	$-15 \le \sigma_R \le 15°$	✓	✓	
			σ_R=-15,-8,0,8,15°			✓

Table 3.2 S20 SWT experimental test matrix

3.5 Experimental method: ARA Supersonic Wind Tunnel

3.5.1 Wind tunnel set-up and operating conditions

The author did not conduct the measurements taken in the 0.69m x 0.76m, continuous Supersonic Wind Tunnel (ARA SWT) at ARA[39]. Only a subset of this experimental dataset, which tested the un-finned receiver (*m265r*) and the sharp generator (*m265g*), are included in this research. A discussion of the full measurement database can be found in Chaplin et al.[43]. The working section operating conditions for the ARA SWT are listed in Table 3.3 and Appendix A.7.

Parameter	Value
M_∞	2.5
p_0	0.08 MPa
T_0	308 K
Re_D	1.93×10^5

Table 3.3 Freestream operating conditions in the ARA SWT

The multi-body test arrangement is illustrated in Figure 3.14. The sharp generator body was mounted on the main support quadrant. The receiver body was mounted using a D_s=12.7mm diameter sting to a M67/7 6-component, internal strain gauge balance. A separation rig allowed translational movement of the receiver body parallel and normal to the tunnel axis. Transition was fixed on both bodies using a 2mm wide circumferential strip of 0.1 – 0.3mm diameter Ballotini grit attached 12mm from the leading edge. The boundary-layer was assumed to be turbulent in the ARA SWT tests.

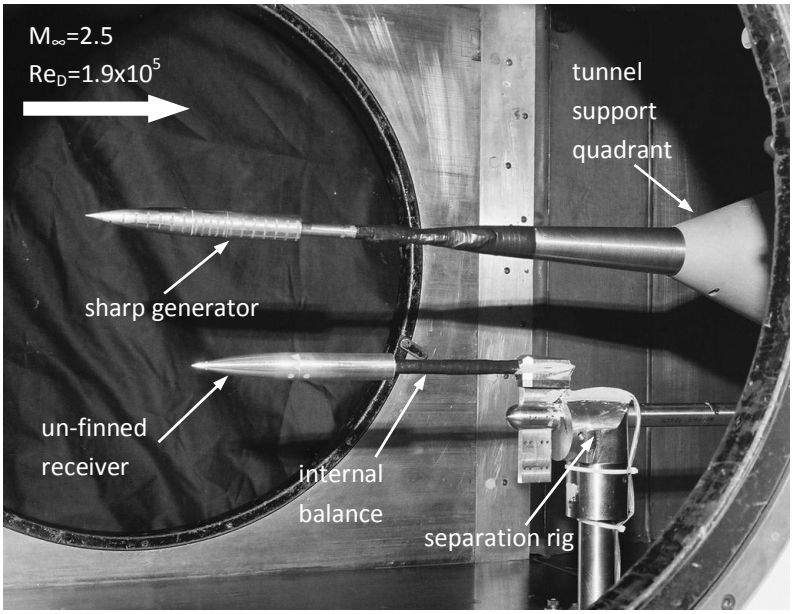

Figure 3.14 Un-finned receiver (*m265r*) set-up adjacent to the sharp generator (*m265g*) in the ARA SWT

3.5.2 Data acquisition and measurement procedure

Force and moment measurements for the receiver body were taken using the 6-component internal balance. No details of the data acquisition system are available from the original test report[39]. To provide a basic evaluation of the aerodynamic characteristics of the slender body, as well as a baseline validation dataset for the CFD prediction method, the forces and moments for the receiver in isolation were measured over the incidence range $-7 \leq \sigma_R \leq 16°$. The six forces and moments were measured at each incidence setting under nominally steady conditions during a pitch-pause sweep. However, the axial force measurements were deemed not credible based on poor repeatability over two consecutive runs (see Appendix B.1). As a result all axial force data presented in the forthcoming chapters originates from measurements taken in the S20 SWT and not the ARA SWT.

In the multi-body configurations, the receiver body was arranged at different axial and lateral locations relative to the generator. This allowed the effect of lateral separation to be evaluated. Two axial staggers were tested: $\Delta x/D=0$ and $\Delta x/D=3.679$. Four lateral separations were tested: $\Delta z/D=1.94$, $\Delta z/D=2.94$, $\Delta z/D=3.94$ and $\Delta z/D=4.96$. In each configuration, the generator and receiver bodies remained at zero incidence and the receiver force and moments were measured. Finally, schlieren images of the flowfield

were taken in selected configurations using a horizontal knife-edge arrangement. No other details of the schlieren set-up are available.

3.5.3 Experimental test matrix

Details of the ARA SWT experimental test matrix are listed below in Table 3.4. A total of 20 configurations were investigated. In the multi-body configurations the receiver and generator incidence angles were equal to zero in all tests.

Receiver	Generator	Configuration	Incidence range	F+M	Schlieren
Un-finned	-	isolated	$-7 \leq \sigma_R \leq 16°$	✓	✓
Un-finned	Sharp	$\Delta x/D=0$ $\Delta z/D=1.94,2.94,3.94.4.96$	$\sigma_R=0°$	✓	✓
Un-finned	Sharp	$\Delta x/D=3.679$ $\Delta z/D=1.94,2.94,3.94.4.96$	$\sigma_R=0°$	✓	✓

Table 3.4 ARA SWT experimental test matrix

3.6 Computational method

This section describes the computational method used for the steady-state predictions in this research. The flow solver is introduced first, followed by a discussion of the gridding approach and the boundary conditions used. To avoid confusion, the method and description of the unsteady predictions are not included in this chapter but can be found in §6.2.2 and Appendix D.1

3.6.1 Flow solver description

All computational predictions in this research were conducted using the commercial flow solver Cobalt[44]. This is an unstructured, implicit solver based on a finite volume formulation and further details can be found in Tomaro[45]. This solver has demonstrated its capability in the prediction of slender bodies flowfields at high incidence. Turpault[46] compared predictions using each of the Reynolds averaged Navier-Stokes (RANS) turbulence models available in Cobalt with a detailed experimental database for a 15 calibre slender body at σ=10°. The measurements included surface pressures, flowfield total pressure and flow angularity measurements as well as boundary-layer flow surveys. Turpault's conclusion was that Menter's SST 2-equation turbulence model[47] performed the best of the turbulence models tested in terms of agreement with the experimental data. In this research, the viscous predictions solved the steady-state Navier-Stokes equations and turbulence was modelled using the SST turbulence model. The solutions were obtained using 2nd order spatial accuracy.

A subset of the experimental configurations were modelled computationally. This provided integrated force and moment data for comparison with the measured results as well as more detailed flowfield information to help understand the flow physics of the interference aerodynamics.

3.6.2 Gridding approach

All 3D computational grids were created using the grid generation software Gridgen[48]. Two gridding approaches were used for the steady-state predictions in this research. The experimental configurations in the ARA SWT involved both bodies arranged at zero incidence. Therefore, basic structured grids were used to model these configurations. The experimental configurations in the S20 SWT were more geometrically complex and involved the receiver body arranged at incidence. Consequently, structured grids would have been inefficient and labour-intensive so a hybrid gridding approach was adopted which included structured and unstructured cells.

All computational domains modelled one half of the flowfield since the body sideslip angles were both zero. This helped to minimise computational requirements. The surfaces of the receiver and generator bodies were generated using a CAD database of the wind tunnel models (with the model attachment hole removed). The computational domain extended from a short distance upstream of the leading edge of the foremost body to approximately 3D downstream of the base of the aftmost body. The base and supporting sting were also included for each body where appropriate. The surrounding flowfield domain contained the bow shock of both bodies so that they exited through the outlet face. Overall, the grids increased in complexity and size when the finned receiver was used (Table 3.5).

Configuration	Receiver	Grid type	Cells
isolated	un-finned	hybrid	8m
isolated	finned	hybrid	12m
multi-body	un-finned	hybrid	19m
multi-body	finned	hybrid	21m
isolated	un-finned	structured	4m
multi-body	un-finned	structured	14m

Table 3.5 Maximum grid sizes for the computational configurations

3.6.2.1 Structured grids

The structured grids contained hexahedral cells. In the isolated body configurations, a single block, O-type topology was used (Figure 3.15 (a)). For the multi-body configurations, a multi-block arrangement of H-type blocks was used (Figure 3.15 (b))

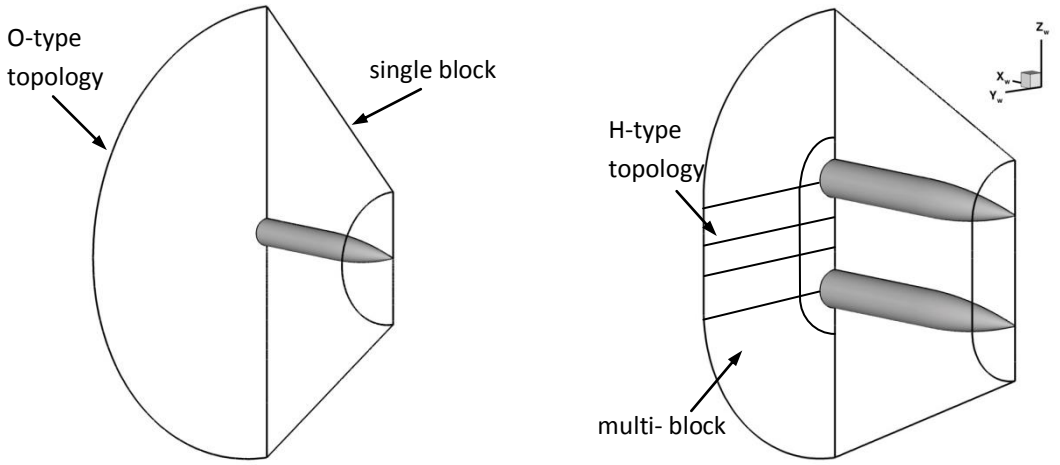

Figure 3.15 Structured grid block topologies shown on the outlet face for the ARA SWT (a) isolated and (b) multi-body computational configurations

In order to fully resolve the boundary-layer flows, a first cell spacing in the radial direction was chosen to ensure an average y^+ value over each body of $y^+ \leq 1$[44]. The local y^+ over the receiver surface is shown for a typical configuration at $\sigma_R=0°$ in Figure 3.16 and highlights that the maximum local y^+ at the leading edge is equal to $y^+=2$. Finally, a progression ratio of approximately 1.1 was used to cluster the grid points radially outward from the body surface and typically, 25-30 cells spanned the boundary-layer maximum thickness[49].

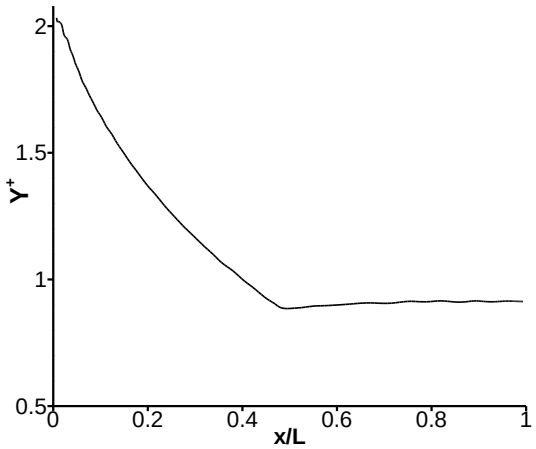

Figure 3.16 Local distribution of y^+ along receiver nearside ($\phi=180°$): m2651 isolated $\sigma_R=0°$

3.6.2.2 Hybrid grids

The hybrid grids contained both structured and unstructured blocks and used hexahedral, tetrahedral and prismatic cell types. The body surfaces, and a region close to the each body, were gridded using structured cells in order to maintain the boundary-layer resolution described above. Moreover, the structured cells allowed more control for the spatial refinements necessary in the inter-fin region for the finned receiver (Figure 3.17). Fine and coarse blocks of unstructured cells covered the rest of the flowfield domain. The fine region covered the most important area, the interference flowfield in between and around the bodies. The coarse unstructured region covered the less important farfield (Figure 3.18). Special care was taken to ensure there was smooth cell size progression across all block boundaries.

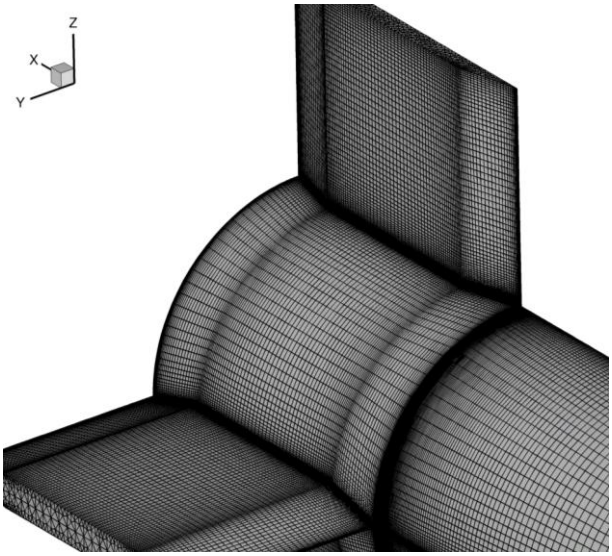

Figure 3.17 Inter-fin spatial resolution

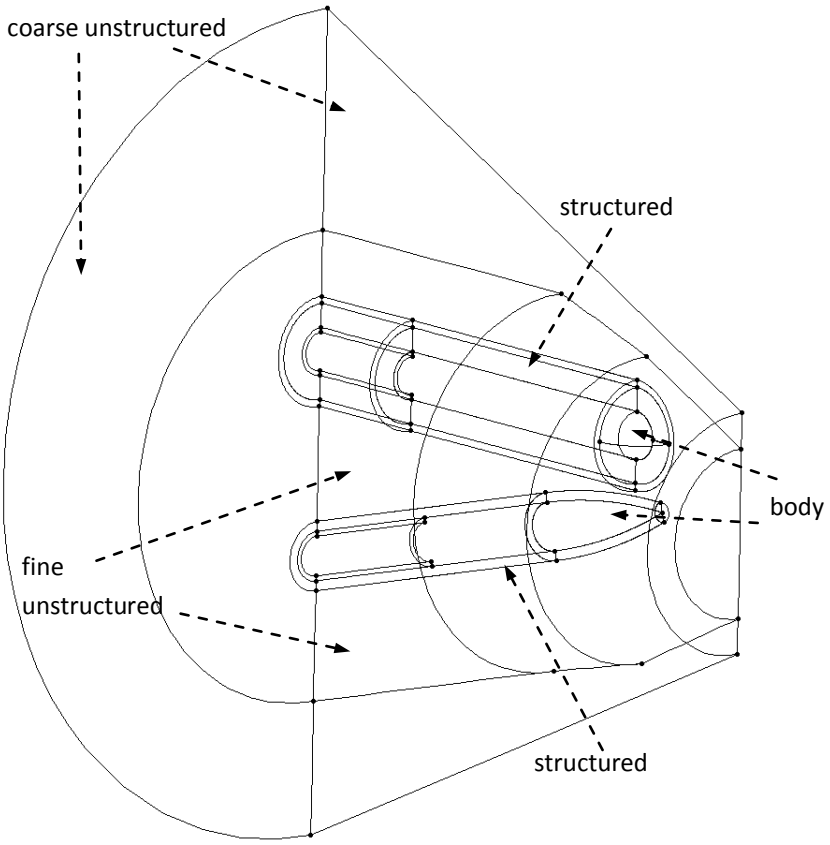

Figure 3.18 Hybrid multi-block topology

There are two main advantages of the hybrid gridding approach. Firstly, it eliminates the complex task to fit a structured grid around a multi-body configuration where the receiver body is at high-incidence and in close proximity to the generator body. Secondly, for a configuration where the receiver is placed at incidence, equal spatial resolution can be applied across the entire interference region (Figure 3.19). This is important in order to resolve the shock and expansion reflections on the aft of the bodies and this would have been extremely inefficient if a structured grid had been used.

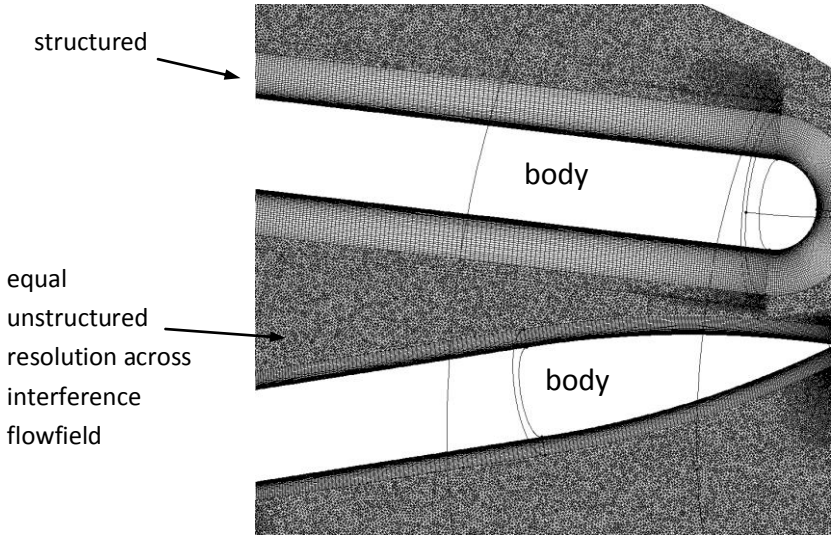

Figure 3.19 Equal spatial resolution throughout the inter-body region, cells shown on the symmetry plane

The degree of spatial resolution in the unstructured interference region was set in order to adequately resolve bow shock and expansion disturbances to the same extent as was achieved in the structured grids. This was verified through comparison of the axial pressure distributions across the bow shockwave at various distances from the sharp generator body. Various levels of unstructured resolution were tested, and this information was used to guide the degree of unstructured resolution in the inter-body region. The resolution shown in Figure 3.19 was as adequate as the structured grids and was typical of the used in the multi-body grids (Figure 3.20).

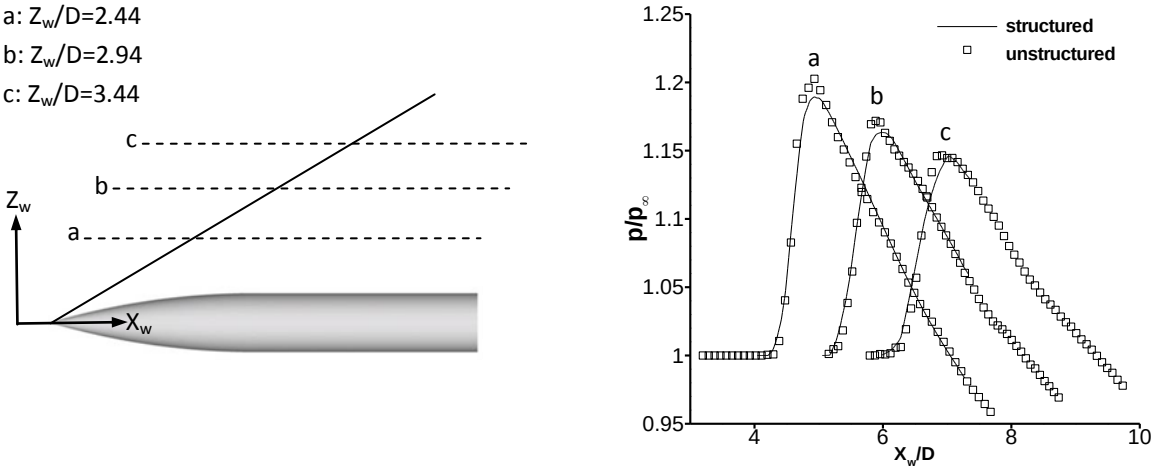

Figure 3.20 Bow shock pressure rises at different distances from sharp generator for both structured and unstructured grids

3.6.3 Boundary conditions

All body and sting surfaces were defined as no-slip solid walls which assumed turbulent flow (Figure 3.21). A symmetry condition was applied on the X_w-Z_w plane since the sideslip of the bodies were zero throughout. Both the inlet and farfield boundary conditions were prescribed as fixed supersonic inflows at the relevant tunnel freestream operating conditions to match the experiment. The outlet boundary values were calculated using a modified Riemann invariants condition[44].

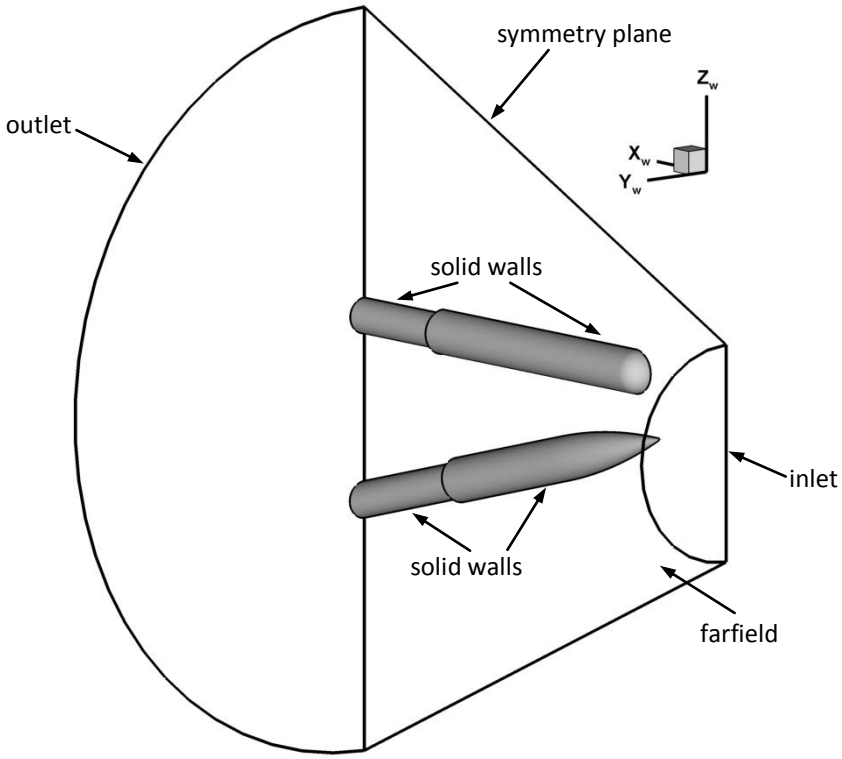

Figure 3.21 Illustration of boundary conditions applied in the computational predictions

3.6.4 Computational test matrix

Details of the steady-state computational configurations predicted using CFD are listed below in Table 3.6. A total of 78 configurations were studied. The freestream flow conditions are indicated to identify whether the predictions simulated the S20 SWT (Table 3.1) or the ARA SWT (Table 3.3) experiments. As in all experiments, the generator remained at zero incidence (σ_G=0°) throughout.

Receiver	Generator	Configuration	Incidence range	Conditions
Un-finned	-	isolated	$-15 \le \sigma_R \le 15°$	S20 SWT
Un-finned	Sharp	Δz/D=2.94	σ_R=0,15°	S20 SWT
		Δx/D=-1.65,0,2.68		
Un-finned	Sharp	Δz/D=2.94, Δx/D=1.67	σ_R=-15,-8,0,8,15°	S20 SWT
Un-finned	Blunt	Δz/D=2.94, Δx/D=-0.53	σ_R=-15,-8,0,8,15°	S20 SWT
Finned	-	isolated	$-15 \le \sigma_R \le 15°$	S20 SWT
Finned	Sharp	Δz/D=2.94	σ_R=0°	S20 SWT
		Δx/D=-1.65,-0.83,0,		
		0.835,2.68,		
Finned	Sharp	Δz/D=2.94, Δx/D=1.67	σ_R=-15,-8,0,8,15°	S20 SWT
Finned	Blunt	Δz/D=2.94, Δx/D=-0.53	σ_R=-15,-8,0,8,15°	S20 SWT
Un-finned	-	isolated	$0 \le \sigma_R \le 16°$	ARA SWT
Un-finned	Sharp	Δx/D=0	σ_R=0°	ARA SWT
		Δz/D=1.94,2.94,3.94,4.96		
Un-finned	Sharp	Δx/D=3.679	σ_R=0°	ARA SWT
		Δz/D=1.94,2.94,3.94,4.96		

Table 3.6 Computational test matrix of the steady-state configurations

3.7 Uncertainty analysis

Uncertainty estimates are presented for the measured and predicted parameters used in the forthcoming chapters.

3.7.1 Experimental uncertainty

The experimental uncertainties were calculated using the approach of Taylor[50]. For the measurements taken in the S20 SWT these are mostly expressed as a fractional uncertainty of the measured value (Table 3.7). All measurement uncertainties were estimated from systematic and random sources of error which included the instrument calibration, instrument accuracy given by the manufacturer and the data acquisition resolution. The uncertainty in the PSP measurement is based on the difference between the measured PSP and an in-situ static pressure measurement taken on the balance near the model base. Full details of the uncertainty calculations are recorded in Appendix A.8.

Tunnel arrangement		Freestream conditions		Forces and moments		PSP	
$\Delta x/D$	±0.7-5.7%	M_∞	2.43 ± 1.2%	C_X	±2.6%	p	±10%
$\Delta z/D$	±0.1%	Re_D	$1.4x10^6$ ± 0.4%	C_Z	±0.6%		
$\sigma_{R,unfin}$	± 0.1°			C_m	±0.6%		
$\sigma_{R,fin}$	± 0.2°			ΔC_X	±3.7%		
σ_G	± 0.1°			ΔC_Z	±0.9%		
x'/L	± 0.01			ΔC_m	±0.9%		

Table 3.7 Summary of experimental uncertainty in measurements performed in the S20 SWT

Limited information is known about the uncertainties in the measurements taken in the ARA SWT. The uncertainties in the force and moment measurements were estimated from the balance measurement resolution and reference measurements taken on the receiver body when no shock interaction occurred (Table 3.8). No information was available for the uncertainties associated with the freestream flow conditions. Full details on these calculations can be seen in Appendix A.8.

Parameter	Uncertainty
C_Z	0.015
C_m	0.12
ΔC_Z	0.021
ΔC_m	0.17

Table 3.8 Summary of experimental uncertainties in measurements performed in the ARA SWT

3.7.2 Computational uncertainty

For the steady-state computations, a discussion of the iterative convergence and spatial discretisation error are given below. All other sources of computational uncertainty such as geometry modelling errors, computer round-off and programming errors are assumed to be negligible.

3.7.2.1 Iterative convergence

Iterative convergence was assessed by examination of the solution residuals and the forces and moments on the receiver body over the solution time. For all computational solutions, satisfactory iterative convergence of the solution residuals was observed and the forces and moments converged to within 0.5% of the reported values. An example plot is shown below in Figure 3.22 for a typical configuration which shows adequate convergence of the receiver normal force coefficient. The full criteria applied for an iteratively converged solution can be seen in Appendix A.9.

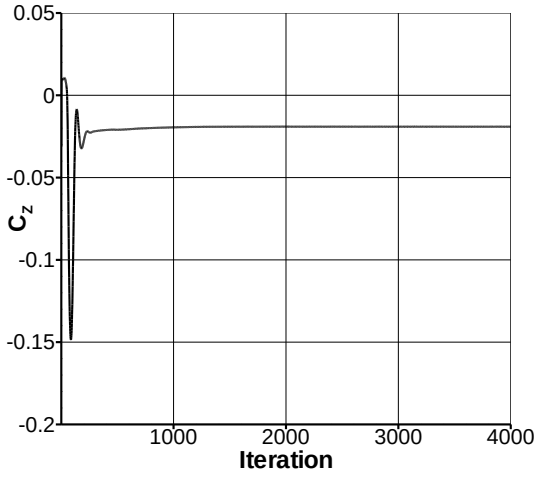

Figure 3.22 Iterative convergence study of a typical configuration: m265r m265g, Δx/D=0 Δz/D=1.94, σ_R=0° σ_G=0°

3.7.2.2 Grid convergence

A selection of configurations representative of the dataset as a whole were further investigated to assess the solution sensitivity to spatial resolution and provide an estimate of the ordered discretisation error using the approach of Roache[51] (Appendix A.9). A grid convergence study was completed for each of the selected configurations over three grid levels in order of decreasing spatial resolution: fine, medium and coarse. For the structured grids a grid refinement ratio of r_{conv}=1.5 was used in all three grid directions. For the hybrid grids, an effective grid refinement ratio, based on the relative total grid sizes, of approximately r_{eff}≈1.5 was used (Equation 3.5 shows r_{eff} between the fine and medium grid levels).

$$r_{eff} = \left(\frac{N_{fine}}{N_{\text{med}}}\right)^{1/3} \quad 3.5$$

The integrated force and moment coefficients (C_X,C_Z,C_m) were used as the comparison parameters. The results for the datum interference configuration (discussed in §4.2.1) are presented in Figure 3.23 an example of a typical grid convergence assessment. The normal force coefficient (C_Z) is reported for the coarse (g=2.25), medium (g=1.5) and fine (g=1) grid levels. The continuum value at zero grid spacing from Richardson's extrapolation (g=0) is also included[51]. It can be seen in this example that the medium grid solution is close to the fine solution ($GCI_{g=1,1.5}$=0.27%) and within the asymptotic range.

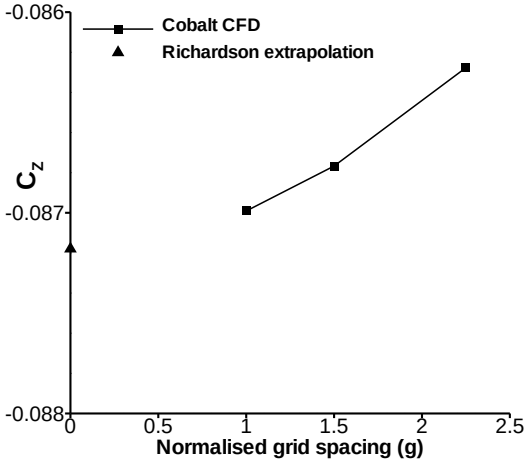

Figure 3.23 Grid convergence study of datum configuration: m265r m265g, Δx/D=0 Δz/D=2.94, σ_R=0° σ_G=0°

In this and all of the other configurations examined, a typical grid convergence index between the fine and medium grids was less than 0.5%. This is considered a reasonable estimate of the discretisation error and the results of the fine grid solutions are presented in the forthcoming chapters. Overall, the fine grid solutions were considered grid independent of further spatial refinement.

Chapter 4 Origins and Sensitivity of the Interference Loads

Placing one slender body in close proximity to another will induce a complex interference flowfield. This is expected to significantly change the local and overall receiver aerodynamics compared to the isolated configuration. This chapter investigates the nature of the resulting interference effects for an un-finned receiver. Although this receiver body is a relatively simple configuraiton, it is used to introduce the basic concepts involved in the problem of multi-body interference. This discussion will begin with analysis of simple configurations and then develop an understanding of the more complex aerodynamics as the chapter progresses. It will also provide a reference for the discussion of the finned receiver aerodynamics to follow in Chapter 5.

This chapter begins with a description of the aerodynamics of the un-finned receiver in isolation (§4.1). A subsequent discussion of the multi-body interference aerodynamics begins by investigating two simple configurations, in detail, to understand the nature of the disturbance flowfield and the origins of the interference loads (§4.2). Additional aspects are also investigated which include the effects of

- lateral separation (Δz) between two bodies (§4.3).
- receiver incidence (σ_R), §4.4.
- a stronger disturbance flowfield (§4.5).
- axial impingement location (x'), §4.6.

Finally, the chapter closes with a discussion of the viscous shockwave interactions observed in this problem and their effect on the interference aerodynamics (§4.7).

The interference aerodynamics and elemental flow features tend to be bespoke to each configuration and the extraction of simple and general trends is difficult. Consequently, this chapter (as well as Chapter 5) is structured in such a way as to simplify the non-linear nature of the multi-body problem in order to aid understanding. This approach considers separately the main parameters of interest and allows the flowfield to be discussed in detail in order to explain the reasons behind the observed interference loads. In addition, for a given configuration under investigation, all available data is used (experimental and computational) in the discussion of the underlying aerodynamics.

Two datasets of measurements taken on the un-finned receiver in the ARA SWT (at M_∞=2.5, Re_D=1.9x10^5) and the S20 SWT(at M_∞=2.43, Re_D=1.4x10^6) are utilised in this chapter. Although at different freestream conditions, the force and moment measurements are combined in the forthcoming analysis. This is justified because the difference in Mach number between the two datasets (M_∞=0.07) has a negligible effect on C_Z and C_m. The Reynolds number differs by an order of magnitude between the two datasets. However, since the boundary-layer is turbulent in both the current datasets this Reynolds number difference does not affect the C_Z and C_m characteristics of the receiver body[52]. The ARA SWT axial force measurements are deemed unreliable (Appendix B.1) and thus the only axial force data presented in this chapter are taken in the S20 SWT where the C_X measurements are credible. The S20 SWT PSP measurements are used where appropriate. Finally, viscous CFD predictions were conducted at the appropriate flow conditions for each configuration. With more than 400 experimental configurations in total it was impractical to model all of these using CFD so a subset of experimental configurations were modelled with the receiver at σ_R=-15, -8, 0, 8, 15° and used to further investigate the underlying aerodynamics.

4.1 Isolated aerodynamics of the un-finned receiver

Before discussing the complicated aerodynamics involved in the multi-body configurations, the force and moment (§4.1.1) and flowfield characteristics (§4.1.2) of the un-finned receiver in isolation are first discussed. This gives an introduction into how the aerodynamic characteristics of this body change as a function of incidence.

4.1.1 Un-finned receiver force and moment characteristics

Due to a small asymmetry in the working section flow of the S20 SWT and ARA SWT, angularity corrections of σ_{cor}=-0.1° and σ_{cor}=-0.3°, respectively, are applied to the measured data presented in Figure 4.1 - Figure 4.4. This ensures zero normal force at zero incidence. The measured force and moment characteristics of the un-finned receiver are typical of a high-speed slender body[41,53]. The normal force (C_Z) and pitching moment (C_m) increase approximately linearly over the low incidence range (-6 ≤ σ_R ≤ 6°) where the flow around the body is generally attached (Figure 4.1, Figure 4.2). This variation becomes non-linear when the vortex–lift is significant at the higher incidence angles. The theoretical predictions included a slender body potential term and an empirical viscous crossflow term[41], and are generally close to the measurements especially at low incidence. There is negligible difference between the predicted normal force and pitching moment values at the different flow conditions. There is good agreement between the predicted C_Z, C_m and the measurements taken in the ARA SWT. However, there is a non-negligible discrepancy between the measurements in the S20 SWT and the predicted data (up to 13% difference in C_Z at σ_R=-15°). This discrepancy has been thoroughly investigated and is attributed to an unknown systematic bias in the S20 SWT measurement system (see Appendix B.2 for details). However, this bias has no effect on the interference loads presented in §4.2-4.6 since it was present when measuring both the isolated and multi-body loads.

4.1.1.1 Axial force

The axial force measurements taken in the ARA SWT are deemed unreliable due to poor repeatability over two successive runs (see Appendix B.1). Therefore, the only measurements presented in Figure 4.3 are taken in the S20 SWT. The trend of the

measured axial force corrected for base pressure (C_X) with incidence is typical, remaining roughly constant over the incidence range with a small increase at higher angles of incidence ($\sigma_R \geq 8°$). This trend is predicted well by the CFD, although the predictions under-estimate the magnitude of the measured loads. The discrepancy, although larger than the experimental uncertainty, is relatively small to within an average of 10% of the measured loads. This discrepancy is not expected to be associated with transition since the CFD modelled turbulent flow over the receiver surface and the experiemental set-up resulted in a naturally turbulent boundary-layer. The variations of side force (C_Y), yawing moment (C_n) and rolling moment (C_l) with incidence are not presented here as they all are nominally zero since the un-finned receiver is a body of revolution tested at zero sideslip ($\beta=0°$).

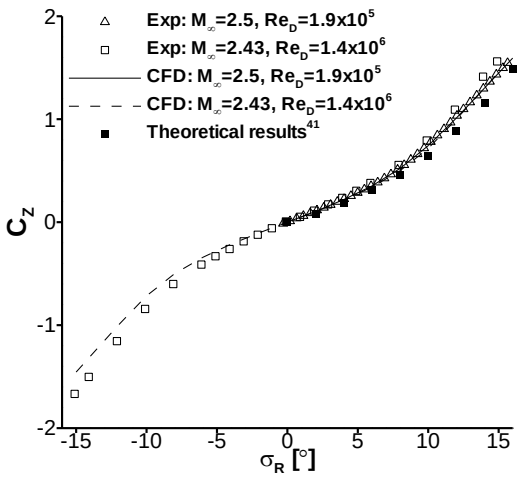

Figure 4.1 Normal force characteristics for the un-finned receiver in isolation (error bars omitted)

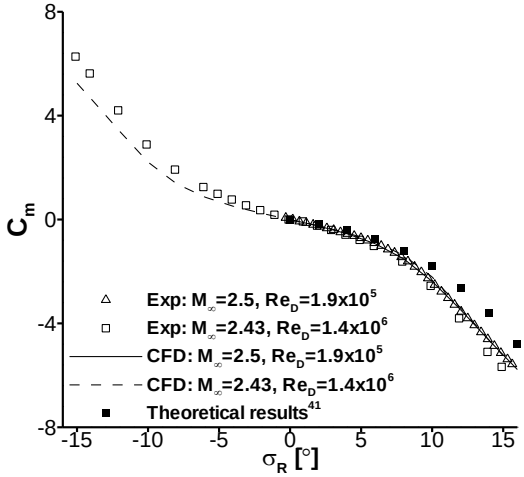

Figure 4.2 Pitching moment characteristics for the un-finned receiver in isolation (error bars omitted)

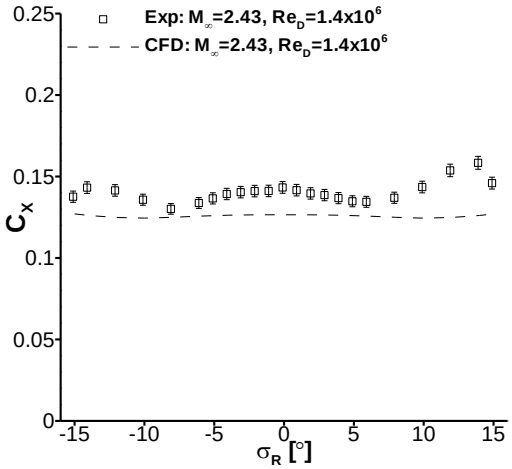

Figure 4.3 Axial force (corrected for base pressure) characteristics for the un-finned receiver in isolation

4.1.1.2 Centre of pressure location

The longitudinal centre of pressure (X_{cp}) is located at approximately two-thirds the length of the forebody at low incidence and the measured values agree moderately well with the theoretical predictions. As the angle of incidence increases, the centre of pressure moves aft as the streamwise local normal force distribution becomes more aftward loaded due to the effects of the body vortices[41,54] (Figure 4.4). Over the incidence range tested, the un-finned receiver remains statically unstable with a negative static margin ($X_{sm} < 0$) defined as the centre of pressure located forward of the centre of gravity (X_{cg}=4.438). These stability characteristics are expected since the body has no aft-located stabilising device (such as a set of control surfaces or flare) as well as the receiver being relatively short in length (L/D=7.358). Another point worth noting is the large movement in X_{cp} over the incidence range, which is a characteristic the aerodynamics of a slender body.

At positive incidence, both sets of predictions and measurements agree in terms of trend and magnitude. The negative incidence range shows that the CFD captures the trend of the measurements whilst under-estimating the magnitude of X_{cp}. However, it is likely this discrepancy is the result of the previously discrepancy in C_Z (Figure 4.1) and C_m (Figure 4.2) propagating through the calculation of the measured X_{cp}=-C_m/C_Z. In addition, one would have more confidence in the predicted values since the X_{cp} distributions are expected to be symmetric for both positive and negative incidence for a body of revolution.

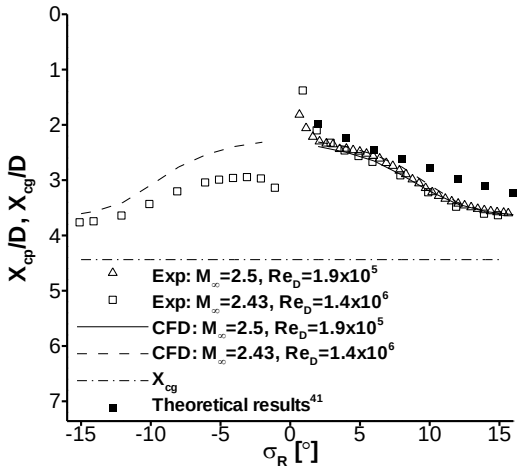

Figure 4.4 Longitudinal centre of pressure location for the un-finned receiver

4.1.2 Flowfield features of the un-finned receiver at σ_R=0,15°

The viscous CFD predictions demonstrate good agreement with the measured forces and moments. The solutions are now used to understand the basic flowfield features of the un-finned receiver of importance in the forthcoming discussion of the interference aerodynamics (§4.2-4.7). Two configurations at σ_R=0,15° are used to demonstrate the flowfield features at different incidence angles.

4.1.2.1 Receiver flowfield at zero incidence (σ_R=0°)

When the receiver is at zero incidence (σ_R=0°), the leading-edge produces a bow shockwave which begins curved due to the ogival forebody shape, and becomes approximately conical as the distance from the body centreline increases (Figure 4.5). The bow shock initially increases the local pressure by an equal amount along any azimuthal plane at a given axial location on the body (Figure 4.6). A fan of expansion waves emanate from the receiver forebody and decrease the local pressure over the length of the forebody (x/L=0.48). Aft of the forebody, the local pressure re-compresses towards the freestream value (C_p=0). The elevated pressure which acts over the forebody (due to the bow shock) makes a majority contribution to the overall axial force as wave drag[55] (Figure 4.7). Only the skin friction component of axial force acts over the afterbody since there is no available x-directed projected area over which the pressure force can act. The overall normal force is zero since σ_R=0° and thus dC_Z/dx=0 over the length of the body.

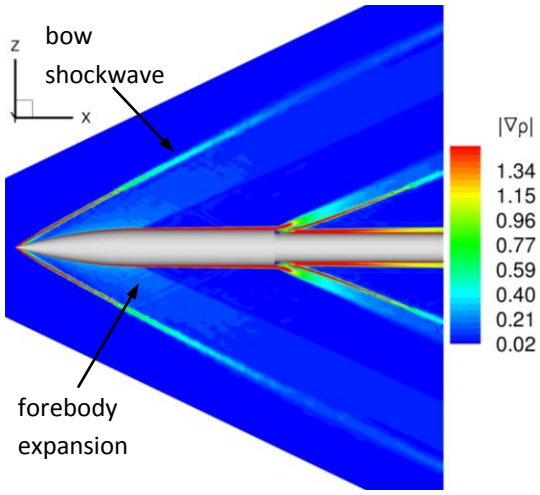

Figure 4.5 Predicted contours of |∇ρ| on the x-z symmetry plane: m2651 isolated σ_R=0°

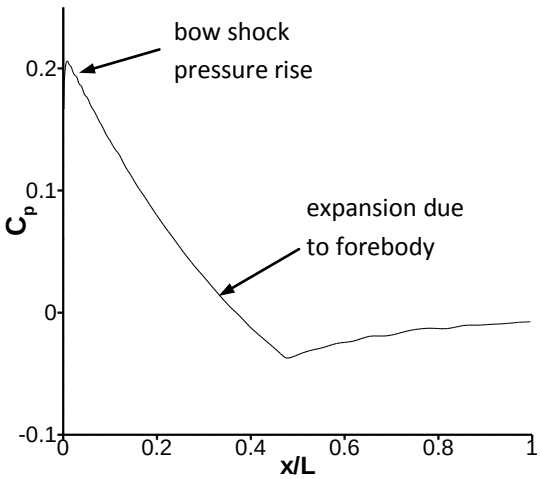

Figure 4.6 Predicted axial pressure distribution for a given azimuth angle: m2651 isolated σ_R=0°

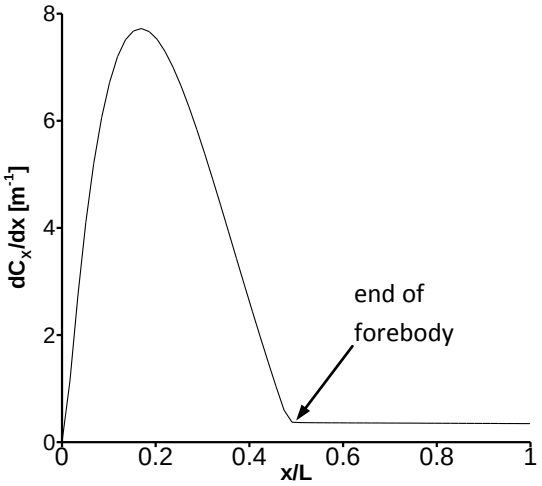

Figure 4.7 Predicted local axial force distribution: m2651 isolated σ_R=0°

4.1.2.2 Receiver flowfield at high incidence (σ_R=15°)

When the receiver incidence is increased to σ_R=15°, the overall normal force is positive (C_Z=1.56). The windward surface (ϕ<90°) experiences an augmented pressure due to the stronger, lower portion of the bow shockwave (Figure 4.8). On the other hand, the leeward surface (ϕ>90°) pressure is lower than the windward and this pressure difference creates the positive local normal force distribution over the length of the receiver body seen in Figure 4.8. The forebody generates the majority of the overall normal force, which is typical of short slender body at this incidence[41,53]. Nevertheless, the afterbody does generate a moderate amount of positive local normal force since it experiences a component of the freestream as crossflow. At lower incidence angles, the crossflow on the after body is less and this helps to explain why, although the body is statically unstable, the static margin decreases as incidence increases since the crossflow acting over the afterbody aft of X_{cg} acts to stabilise the body (Figure 4.4).

The main interest in this high-incidence configuration, though, is the nature of the leeward flowfield. The circumferential pressure distributions (Figure 4.9) show the presence of two symmetric primary leeside vortices on either side of the body (Figure 4.10). The skin friction lines show a well-established and definitive primary separation line (S1) in Figure 4.11 which is induced by a crossflow shockwave (Figure 4.12). Although the separation line stretches over half of the body length, the flow remains attached at the x/D=3 location (Figure 4.10). Further aft at x/D=5, the crossflow shock initiates an adverse pressure gradient at $\phi \approx 90°$ which causes an induced crossflow

separation. As a result, a primary vortex forms on the leeside of the body (Figure 4.10) and this significantly affects the circumferential pressure distribution where a primary vortex suction peak is observed at ϕ=150° (Figure 4.9). The azimuthal location of the primary separation line (S1) moves windward for locations further aft along the body and is located at $\phi \approx 80°$ for x/D=7. At this crossflow location, the vortex sheet feeds the primary vortex which is more developed than at x/D=5 and is located further from the leeside surface and re-attaches on the symmetry plane (A2). A small counter-rotating secondary vortex is formed from (S2) underneath the primary vortex core and there is also a further tertiary vortex rotating in the same sense as the primary vortex and re-attaching at A3 (Figure 4.10). The primary, secondary and tertiary vortex features all induce suction peaks observed in the leeside pressure distribution for x/D=7 at $\phi \approx 156°$, $\phi \approx 132°$ and $\phi \approx 115°$ respectively (Figure 4.9). These give rise to the so-called 'vortex-lift' component of the overall normal force which varies in a non-linear way with incidence.

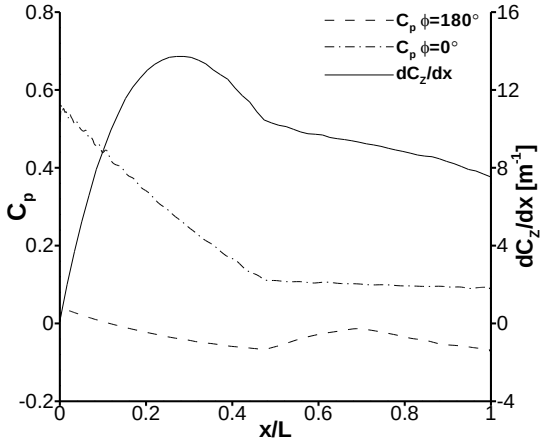

Figure 4.8 Predicted axial pressure and local normal force distribution: m2651 isolated σ_R=15°:

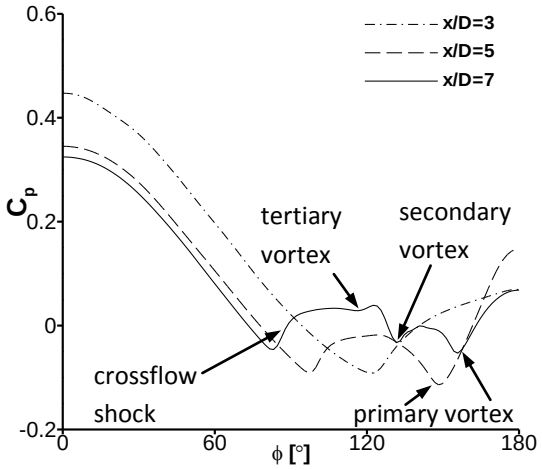

Figure 4.9 Predicted circumferential pressure distribution at x/D=3,5,7: m2651 isolated σ_R=15°

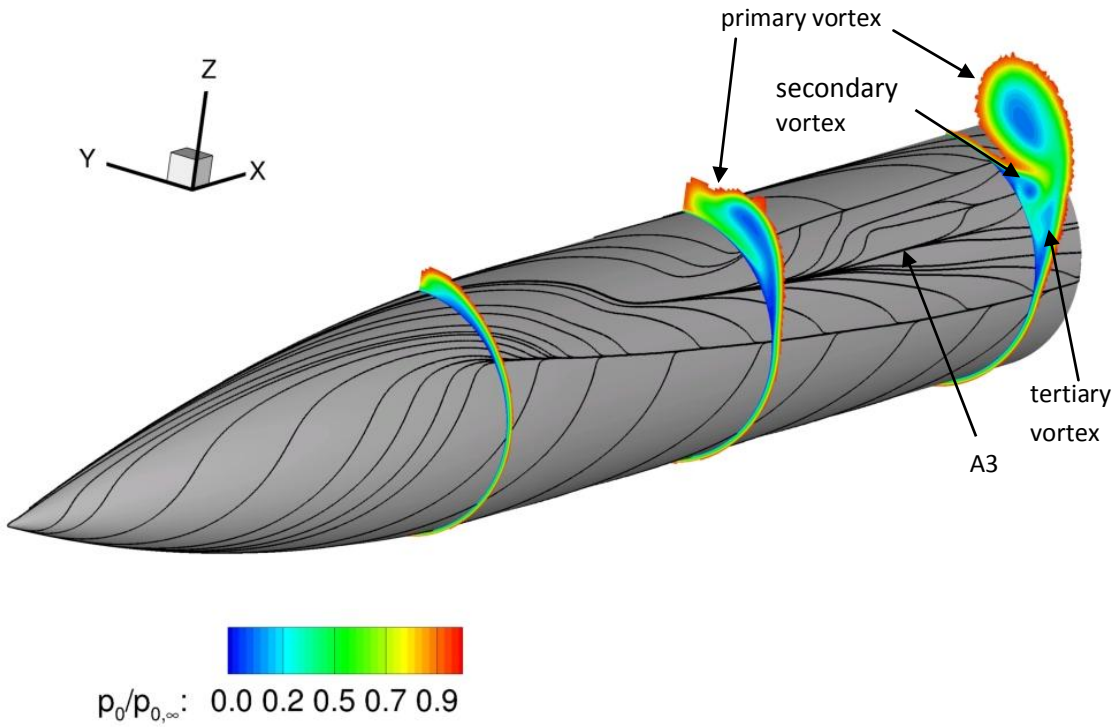

Figure 4.10 Predicted surface skin friction vector lines and crossflow slices of total pressure at x/D=3,5,7: m2651 isolated σ_R=15°

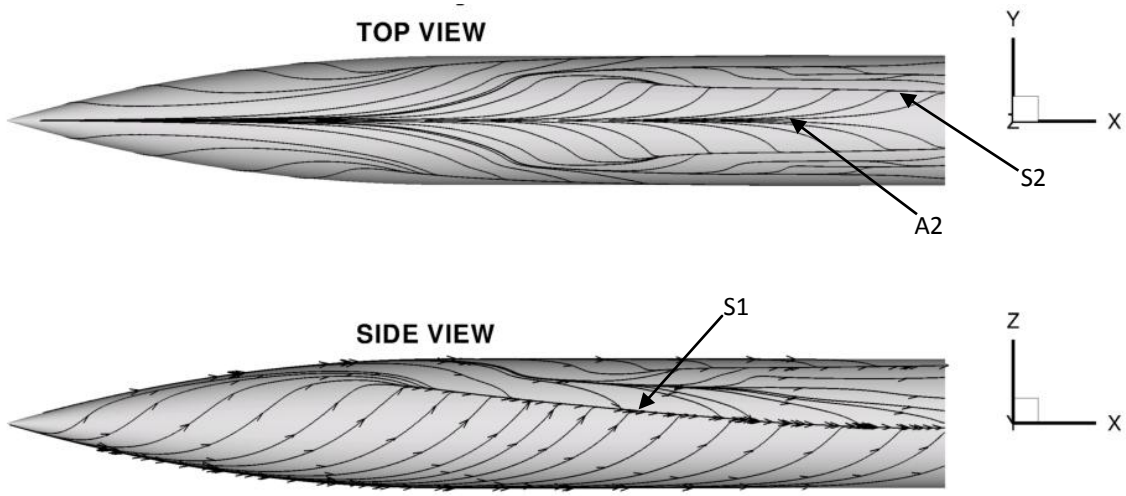

Figure 4.11 Predicted surface skin friction vector lines: m2651 isolated σ_R=15°

The primary crossflow separation for the σ_R=15° case is induced by a crossflow shock. The origin of this flow feature is the deflection of supersonic flow caused by the modified leeside body shape in the region of leeside primary vortices[56]. Whether a crossflow shock develops or not depends on the crossflow Mach number ($M_c \geq 0.44$). This is equal to M_c=0.63 for the σ_R=15° configuration and according to the criterion laid out by Prince[56] a crossflow shock will develop for $\sigma_R \geq 11°$.

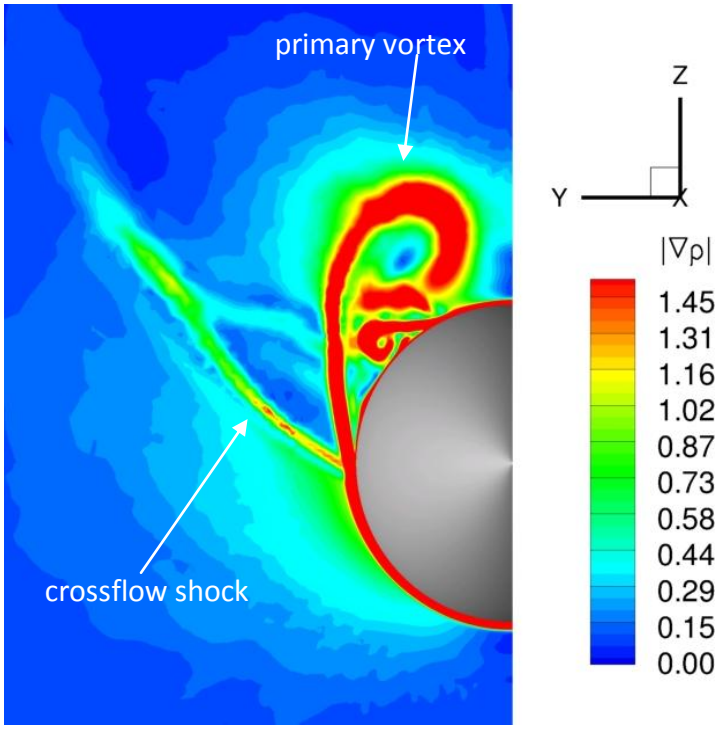

Figure 4.12 Predicted contours of |∇ρ| on a crossflow slice at x/D=7 showing evidence of crossflow shock: m2651 isolated σ_R=15°

Overall, the aerodynamics of the un-finned receiver are assessed using force and moment measurements and CFD predictions of the flowfield. The non-linear variation of normal force and pitching moment with incidence, as well as the body remaining statically unstable are typical characteristics of an un-finned slender body under supersonic conditions. The complex leeside flow structure is increasingly important as the body incidence increases. At high incidence (σ_R=15°) large regions of separated flow are observed on the leeside of the body where primary, secondary and tertiary vortices are present. Good agreement between the measured and predicted forces and moments is observed.

4.2 Interference flowfield characteristics and mechanisms

Changes to the local and overall receiver aerodynamics are expected as a result of a disturbance flowfield induced by a generator body. In this section, two multi-body configurations are investigated in detail to understand the origins of the interference loads and how the propagation of disturbances around the bodies influences the underlying aerodynamics. The first is the datum interference configuration of two identical bodies which are axially aligned at zero incidence. The second configuration is at a closer lateral separation where there is extensive propagation of the different wavefronts around the bodies. These configurations have been selected as they highlight some of the key features which are fundamental to understanding of the interference aerodynamics and will aid all forthcoming discussions.

4.2.1 Datum interference configuration, $\Delta x/D=0$ $\Delta z/D=2.94$

The datum interference configuration is where the bodies are axially aligned ($\Delta x/D=0$), with a lateral separation of $\Delta z/D=2.94$ and both bodies are at zero degrees incidence. The flowfield structure for this configuration is highlighted by the measured schlieren image (Figure 4.13) and the predicted flowfield density-gradient contours ($\partial\rho/\partial z$) on the X-Z symmetry plane (Figure 4.14). The primary disturbance impinges on the receiver nearside at approximately x'/L=0.66. The CFD predicts this to within 1% of the measured location and shows that the CFD accurately captures the topology of the interference region. A portion of the impinging shock reflects back towards the generator and the rest diffracts around the receiver body.

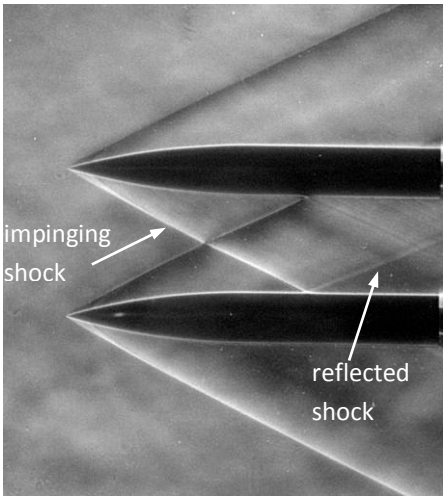

Figure 4.13 Measured schlieren visualisation: m265r m265g, Δx/D=0 Δz/D=2.94, σ_R=0° σ_G=0°

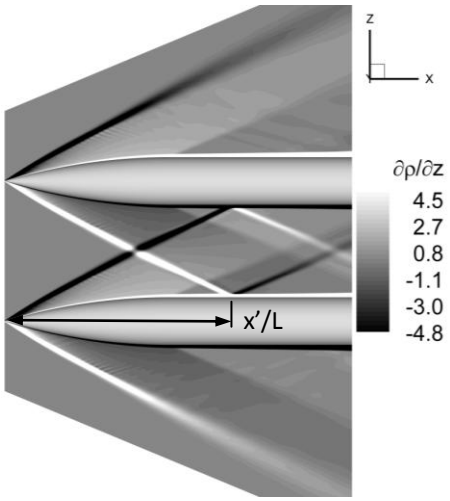

Figure 4.14 Predicted symmetry-plane contours of ∂ρ/∂z: m265r m265g, Δx/D=0 Δz/D=2.94, σ_R=0° σ_G=0°

4.2.1.1 Receiver pressure distribution and origins of the interference loads

The predicted surface pressure contours on the receiver body (Figure 4.15) highlight the impact of the impinging shock on the nearside flowfield, as well as the attenuating shock footprint as it diffracts around the body. In this case, the diffracted portion of the impinging shock has only a small influence on the farside pressure distribution (Figure 4.15). The impinging shock causes an initial nearside (ϕ=180°) pressure rise of $\Delta C_{p,near}$=0.11 which is closely followed by a drop in pressure due to the impinging expansion waves originating from the generator forebody (Figure 4.16). This nearside region of positive differential pressure (i.e. a difference from the isolated values) results in an initial reduction in local normal force (dC_Z/dx) before recovering and leading to a small region of positive local normal force at the aft end of the body (Figure 4.17). The increase in local normal force over the aft region is due to the combined effect of the farside influence of the diffracted shock and the nearside influence of the expansion waves. The associated three-dimensional static pressure field also drives a strong crossflow from nearside to farside, which is seen in the surface skin friction vector lines (Figure 4.18). The interference loads (ΔC_Z, ΔC_m) are defined as the changes in force and moment from the isolated configuration ($\Delta C_Z = C_Z - C_{Z,iso}$) at a given incidence. These primarily depend on the strength and location of the induced changes to the static pressure field on the body and in this configuration are ΔC_Z=-0.07, ΔC_m=0.4 which equate to an effective incidence over the isolated body of

σ_{eff}=-1.2° based on ΔC_Z and σ_{eff}=-2.3° based on ΔC_m. This illustrates that the pitching moment is more affected by the interference flowfield than the normal force due to the induced changes in the local force distribution.

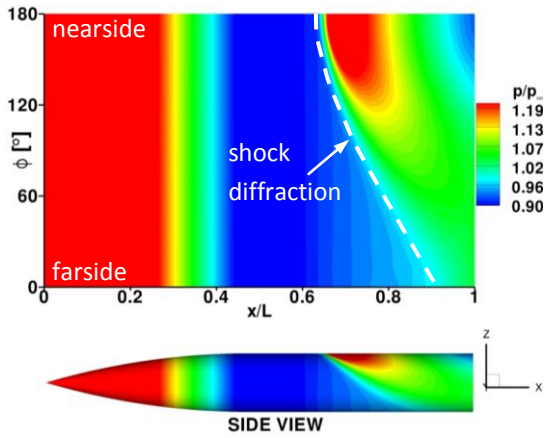

Figure 4.15 Predicted receiver surface pressure contours: m265r m265g, Δx/D=0 Δz/D=2.94, σ_R=0° σ_G=0°

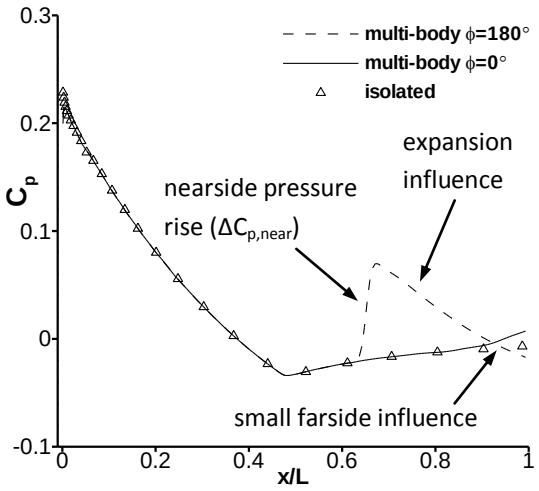

Figure 4.16 Predicted receiver axial pressure distribution: m265r m265g, Δx/D=0 Δz/D=2.94, σ_R=0° σ_G=0°

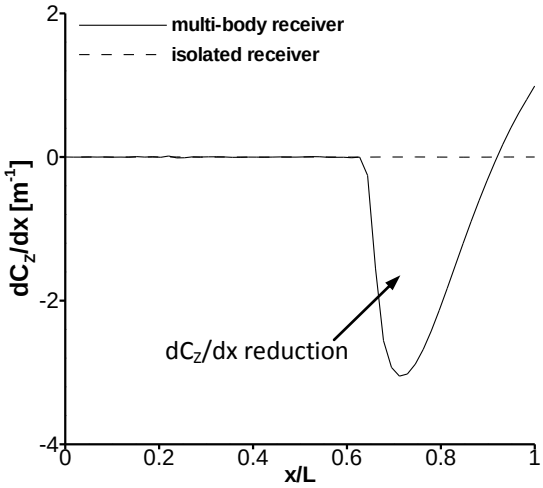

Figure 4.17 Predicted receiver axial dC_Z/dx distribution: m265r m265g, Δx/D=0 Δz/D=2.94, σ_R=0° σ_G=0°

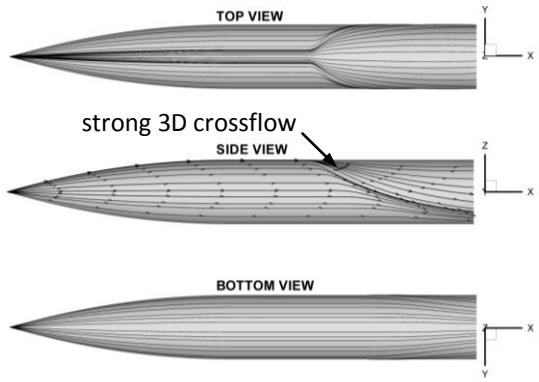

Figure 4.18 Predicted receiver surface skin friction vector lines: m265r m265g, Δx/D=0 Δz/D=2.94, σ_R=0° σ_G=0°

4.2.2 Closest lateral configuration, $\Delta x/D=0$ $\Delta z/D=1.94$

When the bodies are in closer proximity (i.e. a reduction in lateral separation from $\Delta z/D=2.94$ to $\Delta z/D=1.94$), the flowfield becomes more intricate due to the appearance of multiple shock reflections, complex shock diffraction and significant influence of the diffracted shock on the farside of the receiver body (Figure 4.19). To understand the wave structure development, a sequence of crossflow data planes at various streamwise locations are examined for the predicted flowfield (Figure 4.20 (a-g)).

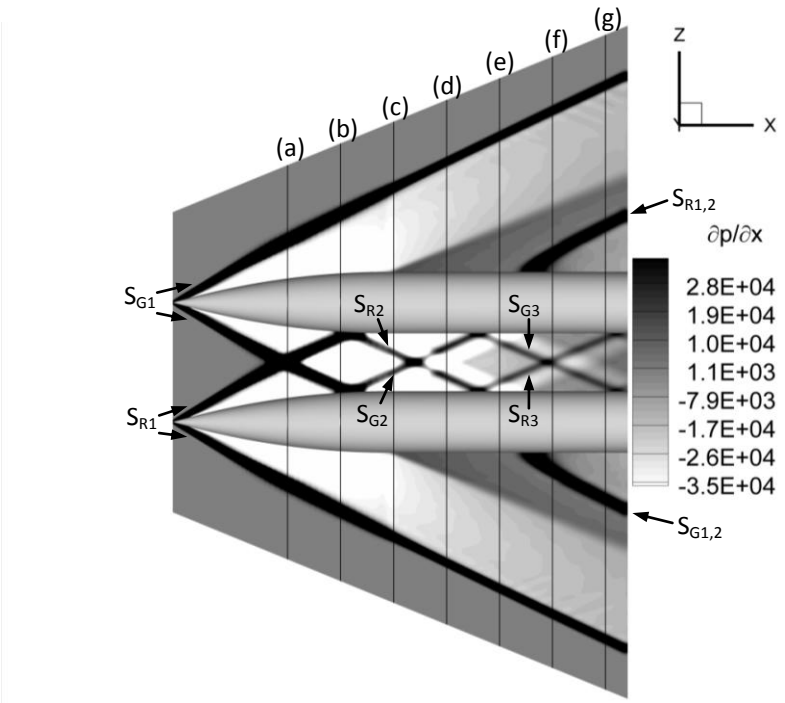

Figure 4.19 Predicted symmetry plane ∂p/∂x contours showing crossflow slice locations (a-g): m265r m265g, Δx/D=0 Δz/D=1.94, σ_R=0° σ_G=0°

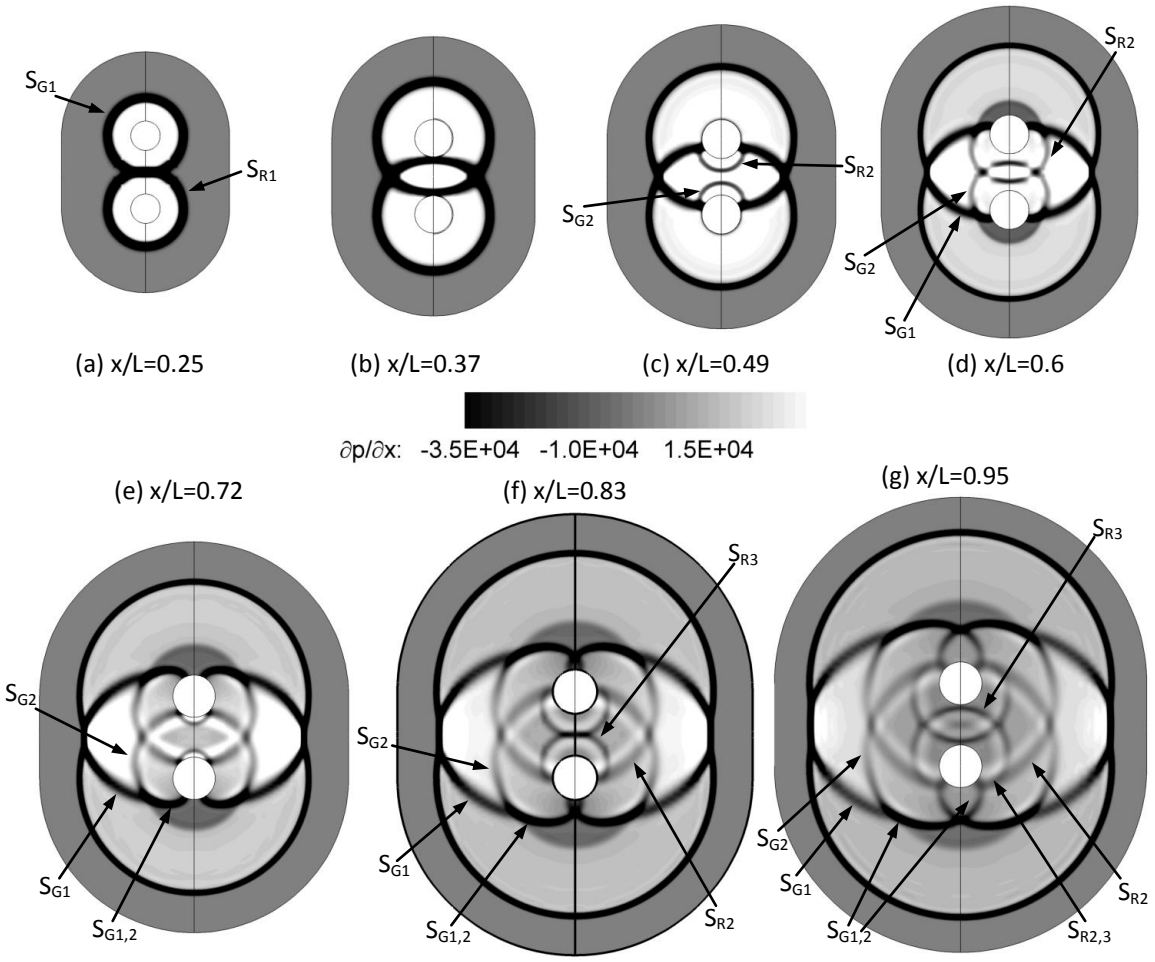

Figure 4.20 Predicted crossflow slice ∂p/∂x contours: m265r m265g, Δx/D=0 Δz/D=1.94, σ_R=0° σ_G=0°

4.2.2.1 Flowfield disturbance wave structure

The flowfield shock structure is investigated by examining the progress of different wavefronts through the interaction regions. The bow shockwaves waves which originate from the receiver (denoted by S_R) and generator (denoted by S_G) bodies result in reflections between the bodies as well as diffractions around the bodies. Subsequent wave reflections are indicated by an increase in the subscript from 1 at the source to 3 near the trailing edge of each body (Figure 4.19). Since the incidence of both bodies is zero, the flowfield is symmetric about an X_w-Y_w plane mid-way between the bodies. Therefore, only the disturbances which interact with the receiver body are noted here, followed by a subsequent discussion on their effect on the local receiver aerodynamics. The impinging shock (S_{G1}) strikes the receiver body and a portion of it is reflected to form S_{G2} (Figure 4.20 (a-c)). When the local Mach number can longer sustain regular reflection a Mach reflection is formed and the subsequent Mach stem ($S_{G1,2}$) continues to diffract around the body (Figure 4.20 (d-e)). Further details on the transition from regular to Mach reflection can be found in §6.1.4. At x/L=0.6, it is also noted that S_{R2} has reflected from the generator body and is travelling back towards the receiver body. The Mach stem ($S_{G1,2}$) then diffracts to the farside of the receiver body and S_{R2} reflects from the receiver body to form S_{R3} (Figure 4.20 (f)). The aftmost crossflow plane illustrates just how complex the interference pattern is for this configuration (Figure 4.20 (g)). Another Mach stem ($S_{R2,3}$) begins to diffract around the receiver body. In addition, $S_{G1,2}$ crosses with its opposing lateral leg from the other side of the body. This highlights the influence of the impinging shock onto the initially shielded farside of the receiver body and shows why there can be an increase in the farside pressure[57] which affects both the local and overall aerodynamics.

4.2.2.2 Receiver pressure distribution

It is clear from the flowfield description above that the three main disturbances which affect the receiver body are S_{G1}, S_{R2}, S_{G3}. Each of these is accompanied by a local nearside pressure rise of approximately $\Delta C_{p,near}$=0.11, 0.03 and 0.01 respectively (I, IV and VI in Figure 4.21). The impinging shock (S_{G1}) initially strikes the nearside of the receiver body at approximately x'/L=0.4 and the portion of the shock diffracts around

the receiver body and causes a notable local pressure increase on the farside (region V in Figure 4.21). As noted in the datum configuration (§4.2.1), the initial pressure rise associated with the impinging bow shock, is immediately followed by a drop in nearside pressure. Over the receiver forebody ($x/L \leq 0.48$), the local surface is affected by both the expansion waves which originate from the receiver forebody and those from the generator forebody (Figure 4.19). However, downstream of the receiver forebody ($0.48 \leq x/L \leq 1$), only the expansion waves which emanate from the generator forebody impinge upon the nearside surface. As a result, the local negative pressure gradient (dp/dx) is less severe for the latter region (III) in comparison to region II. It should also be remembered that this dual slope characteristic does not occur for the datum configuration because the generator shock impinges downstream of the receiver forebody. Finally, the increase in farside pressure associated with the diffracted shock ($S_{G1,2}$) is different from the nearside characteristic and remains approximately constant after the initial rise (region V). This suggests that the expansion waves originating from the generator forebody do not diffract to the same extent as the bow compression waves. This characteristic has a large effect on the local normal force induced over the aft region of the body. Similar results for a cylinder in the presence of an impinging shock are observed by Brosh[10].

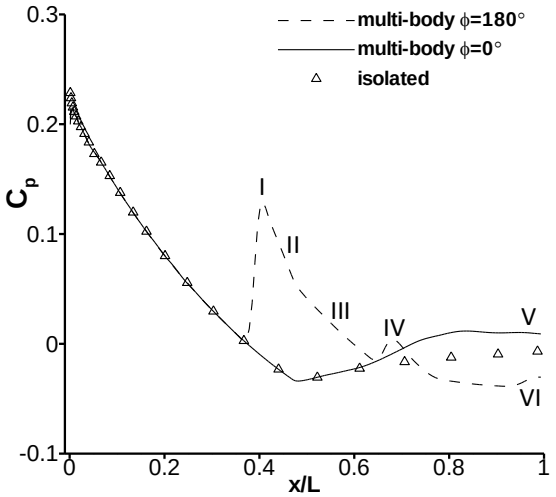

Figure 4.21 Predicted receiver axial pressure distribution: m265r m265g, $\Delta x/D=0$ $\Delta z/D=1.94$, $\sigma_R=0°$ $\sigma_G=0°$

4.2.2.3 Origins of the interference loads

As with the datum configuration, the nearside region of positive differential pressure due to the impinging shock, produces a substantial region of negative local normal

force. However, the diffracted shock extensively propagates around the body and increases the farside pressure (Figure 4.21). The effect of this is augmented by the expansion waves which impinge on the nearside and result in a positive local normal force region near the aft end of the body (Figure 4.22). This reduces the impact of the nearside pressure rise and explains why the magnitude of the normal force interference reduces from ΔC_Z=-0.07 for the datum configuration to ΔC_Z=-0.04 for this configuration where the bodies are closer together. The pitching moment interference (ΔC_m) also reduces from ΔC_m=0.4 to ΔC_m=-0.1. Overall, the changes in normal force on the receiver body can be thought of as a 'balancing act' between the relative dominance and location of the nearside and farside regions of differential pressure.

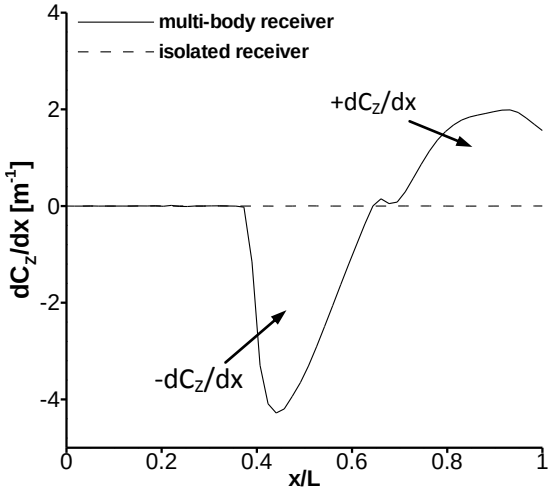

Figure 4.22 Predicted receiver axial local normal force distribution: m265r m265g, Δx/D=0 Δz/D=1.94, σ_R=0° σ_G=0°

In summary, the interference effects have been investigated for two simple configurations where both bodies are at zero incidence. The interference loads which act on the receiver body are a function of the complex local regions of differential pressure induced by the disturbance flowfield. The aerodynamics become more complicated for the closest lateral separation case where there is extensive propagation of the impinging disturbances and thus significant influence on the farside flowfield.

4.3 Effect of lateral separation

For a multi-body configuration, the lateral separation between the two bodies is an important variable in the design of a submunition dispense process from a bus vehicle. It is therefore important to understand the aerodynamic relationship between the interference effects and this parameter. The lateral separation affects the axial impingement location and the strength of the impinging disturbances, both of which are expected to have a significant impact on the receiver aerodynamics. This is investigated in this section for two different configurations. The first is when the two bodies are axially aligned (Δx/D=0) and the second is when the generator is placed upstream of the receiver (Δx/D=3.679).

4.3.1 Axial stagger of Δx/D=0

When the bodies are at zero incidence and axially aligned (Δx/D=0), the induced normal force and pitching moment acting on the receiver body vary non-monotonically with increasing lateral separation (Figure 4.23). The largest measured interference effects are observed for the datum configuration where the lateral separation is Δz/D=2.94. There is modestly good agreement between the measurements and predictions where the CFD broadly captures the trend of both ΔC_Z and ΔC_m. Moreover, the CFD generally under-predicts the magnitude of the normal force changes and over-predicts the pitching moment.

The previous section (§4.2) showed that for the closest lateral separation (Δz/D=1.94) both the nearside and farside interactions are important contributors to the overall interference loads. As Δz increases beyond the datum configuration (Δz/D=2.94), the influence of the diffracted shock diminishes for the Δz/D=3.94 case. The induced interference loads tend to zero for Δz/D=4.96 at which point the bow shock misses the receiver body altogether (Figure 4.23).

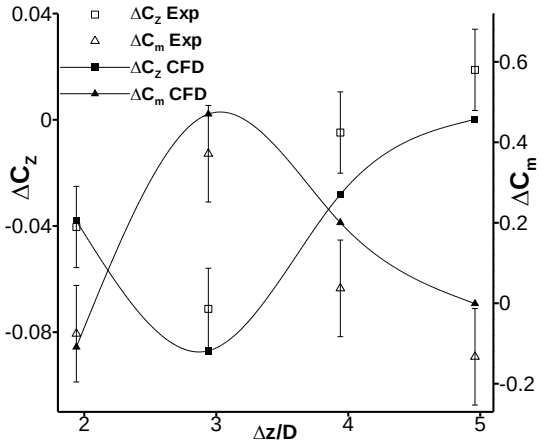

Figure 4.23 Effect of lateral separation on the receiver interference loads: m265r m265g, Δx/D=0, σ_R=0° σ_G=0°

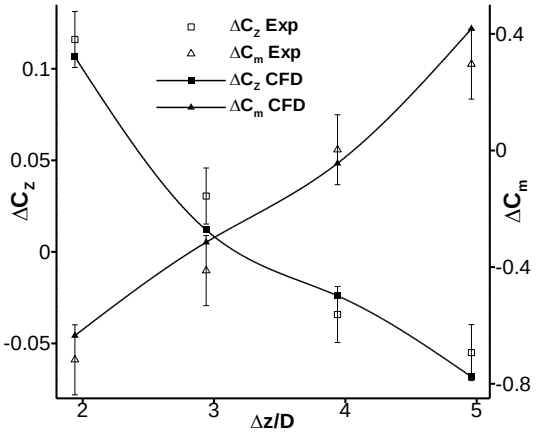

Figure 4.24 Effect of lateral separation on the receiver interference loads: m265r m265g, Δx/D=3.679, σ_R=0° σ_G=0°

4.3.2 Axial stagger of Δx/D=3.679

The interference aerodynamics depend on both the axial stagger and lateral separation and when the generator is placed half a body length upstream of the receiver (Δx/D=3.679) the largest effects are found when the bodies are in closest lateral proximity (Δz/D=1.94, Figure 4.24). For this configuration, the generator bow shock strikes the receiver at the leading edge and the generator base expansion fan impinges onto the receiver (Figure 4.25). This causes a region of positive local normal force near the aft end of the body (Figure 4.26). This strongly influences the overall impact and the measured induced normal force and pitching moment of ΔC_Z=0.12 and ΔC_m=-0.72. This equates to an effective incidence of 2.2° based on ΔC_Z or 5.1° based on ΔC_m and again shows that the pitching moment is more affected by the interference effects due to the change in local normal force distribution.

As the lateral separation increases, the induced normal force decreases and the pitching moment increases monotonically (Figure 4.24). This is primarily due to the diminishing effect of the interference mechanisms which specifically generate regions of positive local normal force. Consequently, as the lateral separation increases there is less influence of the diffracted shock on the receiver farside and the extent of the nearside region of negative differential pressure is reduced (Figure 4.26).

The normal force coefficient changes polarity as the lateral separation increases. At the smallest lateral separation, the interference attracts the bodies drawn closer

together while at the larger separations there is a repulsive normal force acting on the receiver. A similar change in polarity of the pitching moment is also observed where ΔC_m switches from negative at a close lateral separation to a positive value for the largest spacing. This finding is in agreement with the observations made by other researchers[11] in an investigation involving two axially aligned slender bodies. The CFD predictions capture the trend and magnitude of the measured interference loads for this axial stagger, and both normal force and pitching moment lie within the experimental uncertainty (Figure 4.24).

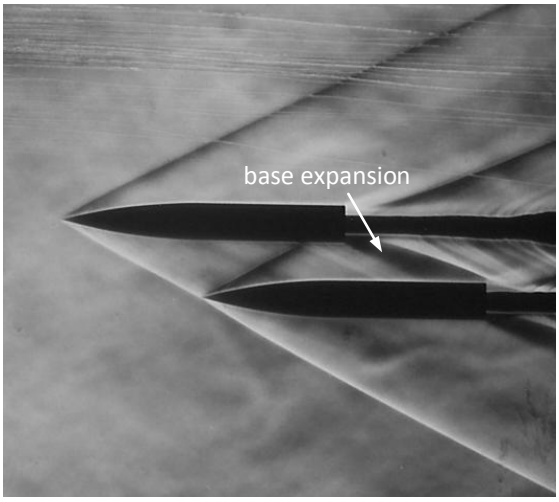

Figure 4.25 Measured schlieren visualisation: m265r m265g, Δx/D=3.679 Δz/D=1.94, σ_R=0° σ_G=0°

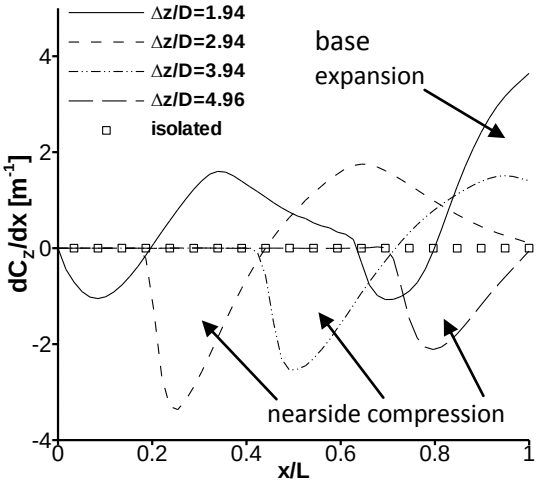

Figure 4.26 Predicted receiver axial dC_Z/dx distribution: m265r m265g, Δx/D=3.679, σ_R=0° σ_G=0°

Overall, the effect of lateral separation is not simple and is dependent upon the initial axial stagger. This is due to the number of variables changing as the lateral separation increases, namely the axial impingement location and the strength of the impinging disturbances (both shock and expansion waves). In order to make this problem simpler to understand these parameters need to be decomposed and assessed independently where possible, this is addressed in §4.5 and 4.6. Finally, the lateral separation does have a significant influence on whether secondary interactions occur, where disturbances which originate from the receiver reflect from the generator and impinge on the aft end of the receiver. These secondary interactions can have a significant influence on the static pressure distribution as seen in §4.2.2.

4.4 Effect of receiver incidence

As the receiver incidence increases from zero, there is a change in the underlying isolated aerodynamics where the effects of flow separations, body vortices and a streamwise load distribution become more significant. Furthermore, for multi-body configurations, the induced interference flowfield is modified along with a change to the location and strength of the impinging disturbances and the shock obliqueness angle. Consequently, as both the isolated receiver aerodynamics and the disturbance flowfield are significantly different, it is expected that the interference loads will also depend on the receiver incidence setting.

All of the forthcoming multi-body configurations discussed in §4.4-4.7 are at a lateral separation of $\Delta z/D=2.94$. A large part of this section will utilise measured and predicted data for a subset of configurations at one axial stagger ($\Delta x/D=1.67$). In doing so, parameters will be introduced to aid in the analysis of configurations where the body of interest is at incidence. Furthermore, the subset of configurations will be discussed, in detail, in order to understand the complex relationship between the elemental interactions and how these contribute to the overall changes in the interference loads. A summary discussion then discusses the effect of receiver incidence using data from across the experimental test matrix.

4.4.1 Receiver force and moment characteristics

The un-finned receiver and sharp generator were arranged with an axial stagger of $\Delta x/D=1.67$ and $\sigma_G=0°$ while the receiver incidence was varied from $\sigma_R=-15°$ to $\sigma_R=15°$. The interference ΔC_Z and ΔC_m are found to vary non-monotonically with incidence and the effects are a minimum when the receiver is at approximately zero incidence (Figure 4.27). The magnitude of the interference loads generally increases as the receiver is pitched either up or down. Moreover, the interference is typically larger at positive rather than negative incidence with maximum loads of $\Delta C_Z=-0.18$ and $\Delta C_m=0.43$ observed at $\sigma_R=14°$. This equates to a change of effective incidence of $\sigma_{eff}=-1.1°$ based on ΔC_Z and $\sigma_{eff}=-0.6°$ based on ΔC_m. For this configuration, the longitudinal centre of pressure location moves aft from $X_{cp}/D=3.6$ to 3.8 between the isolated and

multi-body cases (Figure 4.28). Moreover, across the positive incidence range the interference effects always result in an aftward movement of X_{cp}. This stabilising change in X_{cp} significantly increases for lower positive incidence settings and can be as large as $\Delta X_{cp}/D=5$. For the simple, un-finned receiver, the reference $X_{cg}/D=4.44$ is included for comparison. A different characteristic is observed for the configurations with the receiver at negative incidence. At large negative incidence there is no change in X_{cp} but in the range $-1 \leq \sigma_R \leq 6°$, the centre of pressure moves forward up to $\Delta X_{cp}/D=2$. Finally, the axial force interference is effectively zero except at high, positive incidence but the magnitudes are generally small with a maximum of $\Delta C_X=0.03$ (Figure 4.27). Overall, excellent agreement is observed between the measured and predicted interference loads.

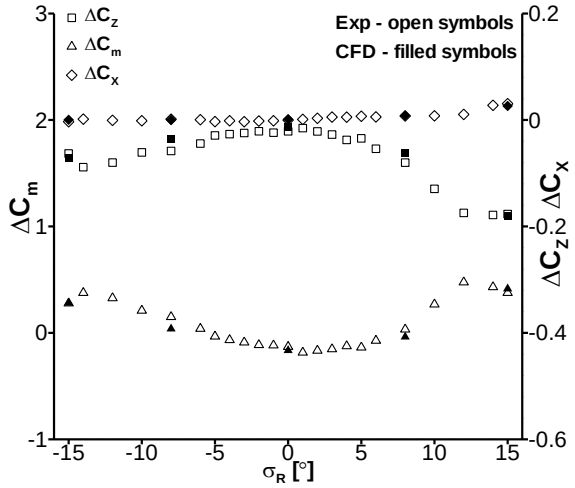

Figure 4.27 Effect of receiver incidence on receiver interference loads: m2651 m2653, $\Delta x/D=1.67$ $\Delta z/D=2.94$, $\sigma_G=0°$. Error bars omitted

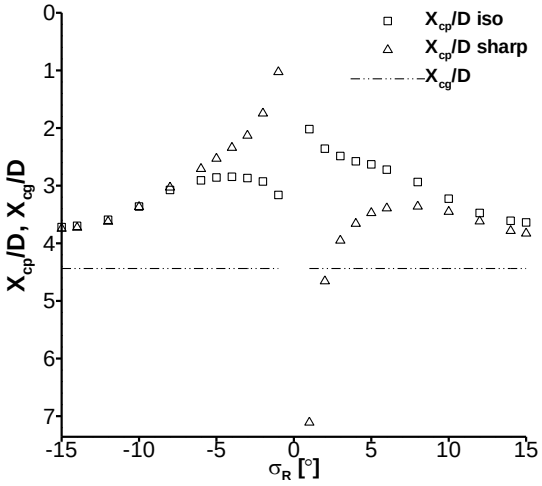

Figure 4.28 Effect of receiver incidence on measured receiver X_{cp}: m2651 m2653, $\Delta x/D=1.67$ $\Delta z/D=2.94$, $\sigma_G=0°$

4.4.2 Interference flowfield structure

The underlying aerodynamic mechanisms are examined using measured data and CFD predictions for a selection of configurations ($\sigma_R=0, \pm 8, \pm 15°$). A change in receiver incidence affects five important parameters which characterise the interference aerodynamics (Table 4.1). These are the axial impingement location (x'/L), the impinging shock strength, the reflected shock strength, the local expansion field strength and the shock obliqueness angle (θ_{obl}).

As the receiver incidence increases over the range $-15 \leq \sigma_R \leq 15°$, the axial impingement location moves significantly forward from x'/L=0.55 to x'/L=0.09 (Figure 4.29). The shadowgraph visualisation (Figure 4.29 (a)) and the associated surface pressure contours (Figure 4.30 (a)) for the σ_R=15° configuration show that the impinging shock does not diffract to the farside of the receiver body as a result of the shock obliqueness angle and geometric arrangement. However, the shock structure for the other incidence settings is similar to the datum topology where the shock influences the farside flow. The shock obliqueness angle is defined as the included angle between the generator conical bow shock angle and the receiver body axis ($\theta_{obl}=\theta_{s,G}-\sigma_R$) both measured from the streamwise flow direction on the X_w-Y_w pitching plane. This decreases from θ_{obl}=43° to θ_{obl}=13° as the incidence increases from σ_R=-15° to σ_R=15° (Figure 4.30 (a)–(e)). An increase in the obliqueness angle increases the extent of the farside footprint for a given x'/L to a maximum at σ_R=-15° where the shock reaches the farside furthest fore compared to the other incidence settings.

Figure 4.29 also illustrates that the conical distance between the generator leading edge and the receiver impingement location (Δr_{sh}) decreases as the receiver incidence increases. This parameter characterises the decay in strength of the impinging shock which is listed for each configuration listed in Table 4.1 using analysis of the isolated disturbance flowfield. The reflected shock strength, is determined by the amount of flow turning (δ_{refl}) necessary to return the flow tangent to the downstream surface aft of the impinging shock and this decreases as the receiver incidence increases. This is also predicted from analysis of the isolated disturbance flowfield and is a function of the local flow pitch caused by the impinging shock (σ_p), the local surface curvature (ζ) and the receiver incidence (σ_R). All of the parameters used in this discussion are defined in Appendix B.3.

Excellent agreement is observed between the predicted and measured pressure contours for the configurations considered in this section (Appendix B.4). This demonstrates that the CFD prediction method is firstly, capable of predicting the high incidence leeside flow structure for a slender body, in particular the low pressure regions induced beneath the body vortices. Secondly, the interaction pressure

footprints are accurately predicted in the correct locations and with the correct magnitudes in all incidence configurations. This shows that the CFD is capable of accurately predicting the qualitative impact of the disturbance flowfield and increases confidence in using the CFD to understand the underlying aerodynamics.

σ_R [°]	x'/L	θ_{obl} [°]	$\Delta C_{p,near}$	$\Delta r_{sh}/D$	$\Delta C_{p,imp}$ (% of $\Delta C_{p,near}$)	δ_{refl} [°]
-15	0.54	43.2	0.133	6.42	0.040 (30%)	17.5
-8	0.49	36.2	0.121	6.02	0.043 (35%)	10.6
0	0.40	28.2	0.090	5.22	0.048 (53%)	5.4
8	0.26	20.2	0.095	4.21	0.056 (59%)	2.9
15	0.08	13.2	0.116	2.88	0.072 (62%)	2.6

Table 4.1 Effect of receiver incidence on the predicted interference parameters: m2651 m2653, $\Delta x/D=1.67$ $\Delta z/D=2.94$, $\sigma_G=0°$

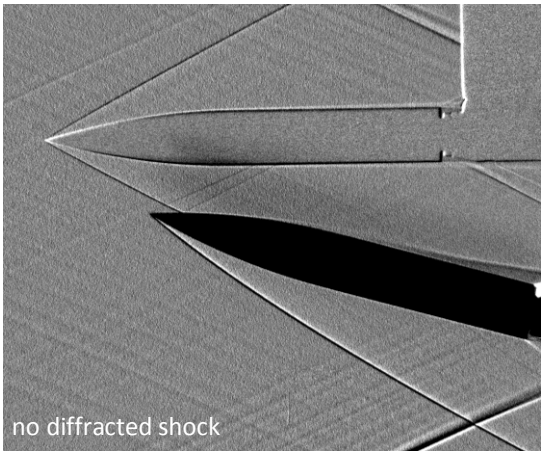

(a) σ_R=15°

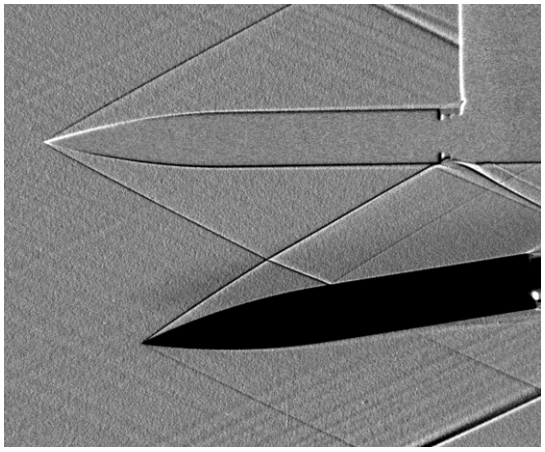

(d) σ_R=-8°

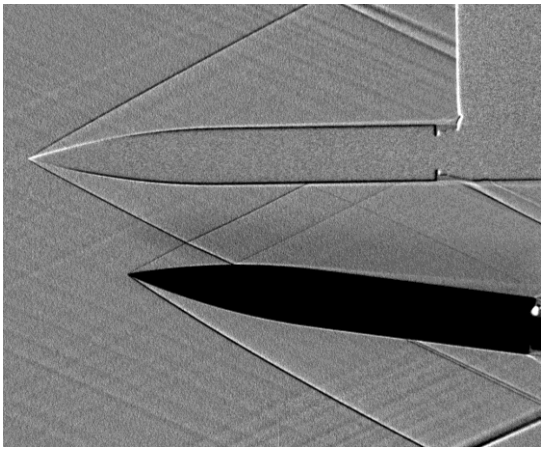

(b) σ_R=8°

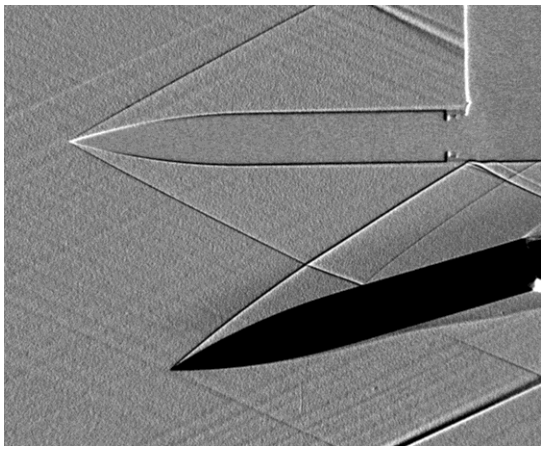

(e) σ_R=-15°

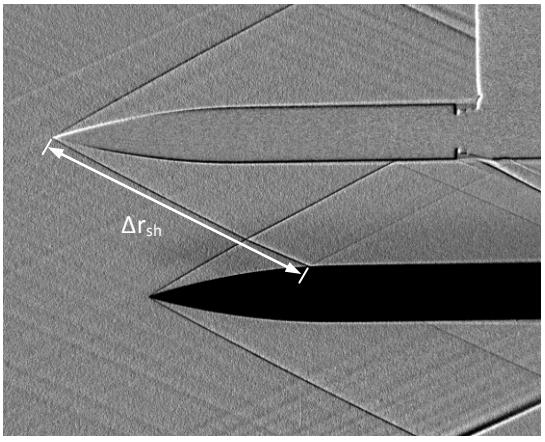

(c) σ_R=0°

Figure 4.29 Measured shadowgraph visualisations for different receiver incidence settings (a-e): m2651 m2653, $\Delta x/D$=1.67 $\Delta z/D$=2.94, σ_G=0°

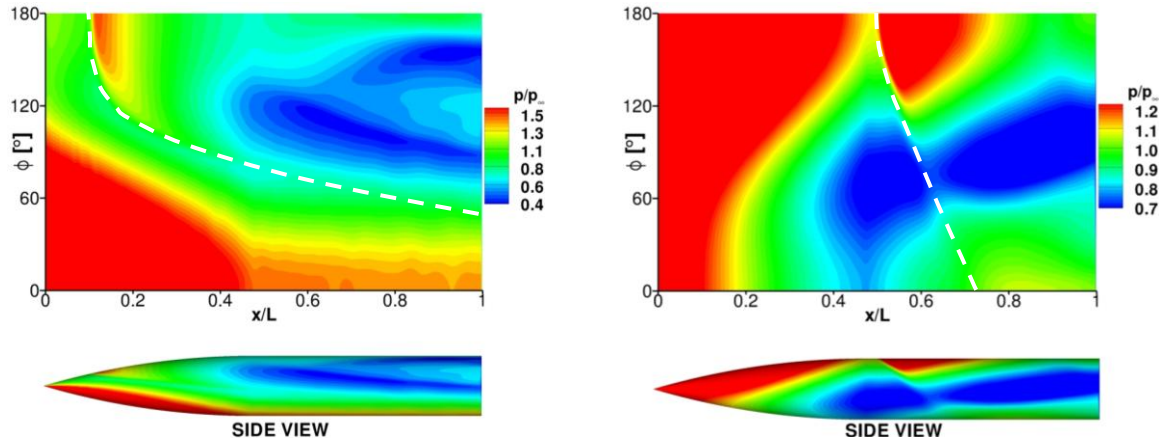

(a) σ_R=15°

(d) σ_R=-8°

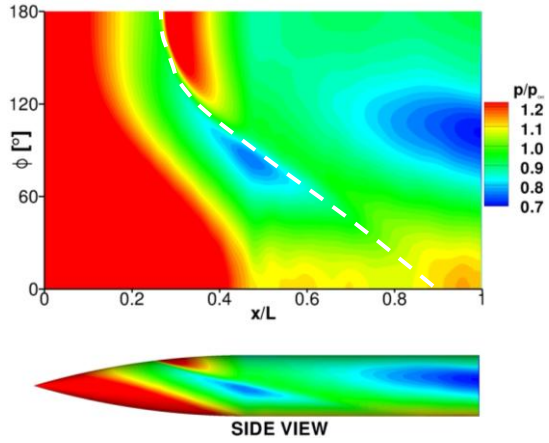

(b) σ_R=8°

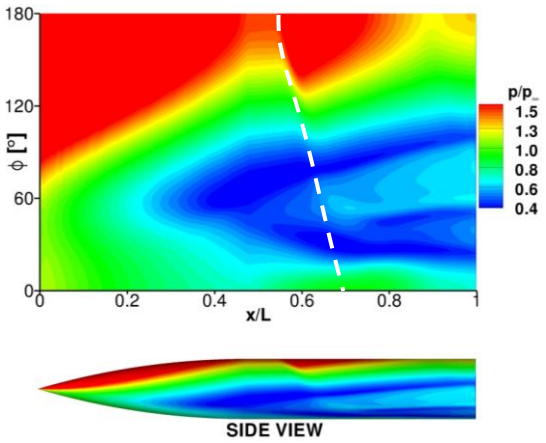

(e) σ_R=-15°

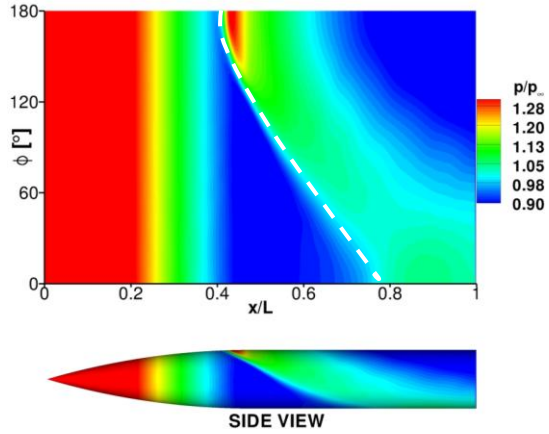

(c) σ_R=0°

Figure 4.30 Predicted receiver surface pressure contours highlighting the impinging shock paths (dashed) for different receiver incidence settings (a-e): m2651 m2653, Δx/D=1.67 Δz/D=2.94, σ_G=0°

4.4.3 Effect of receiver incidence on the underlying flowfield mechanisms

The interference loads are up to an order of magnitude greater for the receiver at incidence (both positive and negative) in comparison to the zero incidence case. It is known that the interference flowfield comprises of a range of elements, which individually either increase or decrease the receiver local normal force distribution. These are investigated for the configuration at zero incidence (§4.4.3.1) and then for bodies at negative (§4.4.3.2) and positive (§4.4.3.3) incidence.

4.4.3.1 Interference effects for the receiver at zero incidence

For the zero incidence case the impinging shock strikes the receiver body at approximately x'/L=0.4 (Figure 4.29 (c)) which leads to a total nearside pressure rise of $\Delta C_{p,near}$=0.09 (Figure 4.31 (c)). This is a function of a predicted impinging shock strength of $\Delta C_{p,imp}$=0.05 and a predicted reflected shock strength of $\Delta C_{p,refl}$=0.04 due to moderate $\Delta r_{sh}/D$ and δ_{refl} values (Table 4.1). The shock diffracts around the body and induces the local normal force distribution seen in Figure 4.32 (c) and leads to overall interference loads of ΔC_Z=-0.02 and ΔC_m=-0.13 (Figure 4.27).

4.4.3.2 Interference effects for the receiver at negative incidence

Two main differences are observed for the receiver at negative incidence in comparison to the zero incidence configuration. Firstly, the reflected shock strength dominates the augmented nearside pressure rise (δ_{refl} increases from 5.4° to 17.5°, Table 4.1). This is due to the high flow turning necessary to maintain tangency with the downstream receiver surface and results in a $\Delta C_{p,near}$=0.12 for σ_R=-8° and $\Delta C_{p,near}$=0.13 for σ_R=-15° (Figure 4.31 (d),(e)). Secondly, the strength of the expansion waves which impinge on the nearside are weaker since the receiver is further from the generator (Figure 4.29 (c)–(e)). Finally, for the receiver at σ_R=-15° the impact of the diffracted shock on the farside region of positive differential pressure is reduced because this shock interacts with the body vortex flows (Figure 4.31 (e)). This interaction tempers the expected region of positive differential pressure in comparison to similar incidence cases without an interaction. All of these aspects augment the signifinace of the interactions which induce regions of negative local normal force and

diminish those which produce regions of positive local normal force in comparison to the zero incidence configuration (Figure 4.32 (c)-(f)). This leads to a more negative ΔC_Z for the negative incidence cases. The pitching moment interference load over the negative incidence range is dominated by the nearside region of positive differential pressure and results in positive values of ΔC_m.

4.4.3.3 Interference effects for the receiver at positive incidence

The interference loads are also larger at positive incidence in comparison to the zero incidence configuration. At positive incidence, the receiver is closer to the generator body ($\Delta r_{sh}/D$ reduces from 5.2 to 2.9, Table 4.1), the nearside pressure rise is dominated by the subsequent increase in impinging shock strength and reaches $\Delta C_{p,near}$=0.095 for σ_R=8° and $\Delta C_{p,near}$=0.116 for σ_R=15° (Figure 4.31 (a),(b)). In addition, as σ_R increases the shock obliqueness angle (θ_{obl}) reduces (Figure 4.30 (b)) and ultimately results in the diffracted shock not extending to the farside of the receiver (Figure 4.30 (a)). This eliminates the farside region of differential pressure which makes a positive contribution to the normal force when the body is at zero incidence (Figure 4.31 (a)). The increases in the magnitude of the region of nearside positive differential pressure for bodies at positive incidence leads to a more significant region of negative local normal force compared to the configuration at zero incidence (Figure 4.32 (a)-(c)). This leads to a more negative ΔC_Z than observed at zero incidence. Over the positive incidence range, the normal force interference acts near the receiver leading edge and induces large changes to the pitching moment interference loads up to ΔC_m=0.48 at σ_R=12°.

Overall, the interference loads are larger when the body is at incidence because of the augmented total nearside shock strength and the declining significance of the interactions which cause regions of positive local normal force relative to the zero incidence configuration (Figure 4.32 (f)).

4.4.3.4 Comparison between positive and negative incidence

In general, the interference loads are greater at positive than negative incidence. For example, the configuration at σ_R=15° induces a ΔC_Z which is three-times larger than the σ_R=-15° case.

When the receiver is at σ_R=15° (x'/L=0.09) the extent of the nearside region of positive differential pressure is much larger than for the σ_R=-15° case (x'/L=0.55) and the force contribution is increased accordingly (Figure 4.32 (a),(e)). In addition, for σ_R=15° there is no influence of the impinging shock on the farside pressure distribution (Figure 4.30 (a)) whereas for the σ_R=-15° case, the extent of the farside interaction is extended due to the increased shock obliqueness angle (θ_{obl}). Consequently, the diffracted shock reaches the receiver farside further upstream and this increases the positive normal force contribution and therefore reduces the overall magnitude of the interference load for the σ_R=-15° case (Figure 4.32 (e)). Both of the above, augment the significance of the interactions which induce regions of negative local normal force when the receiver is at positive incidence ($\sigma_R > 0°$). They also show the diminishing contribution of the interactions which induce regions of positive local normal force, which also acts to increase the magnitude of ΔC_Z for $\sigma_R > 0°$ (Figure 4.32 (f)).

Overall, there is not as marked a difference between the pitching moment at negative and positive incidence as there is for normal force due to the influence of changes in x'/L (Figure 4.32 (f))

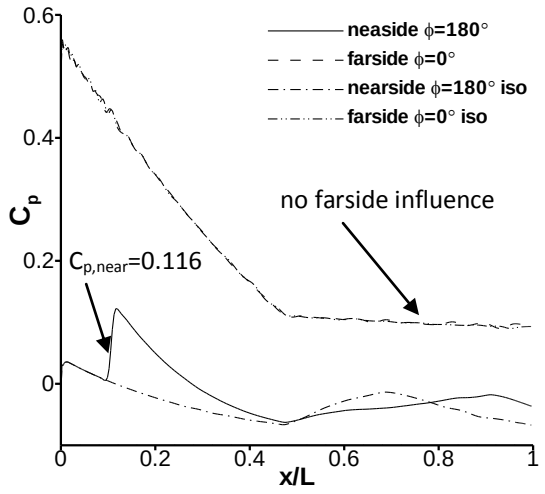

(a) σ_R=15°

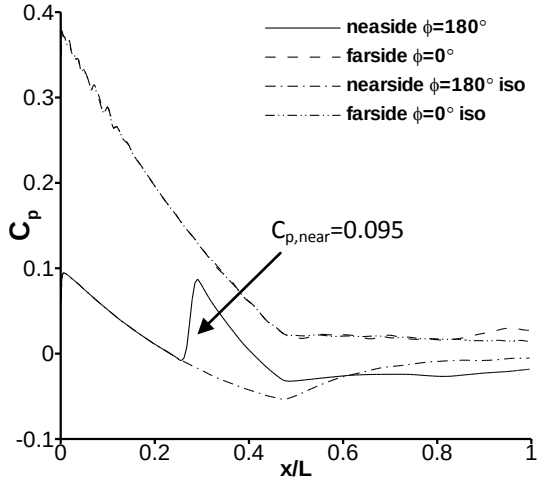

(b) σ_R=8°

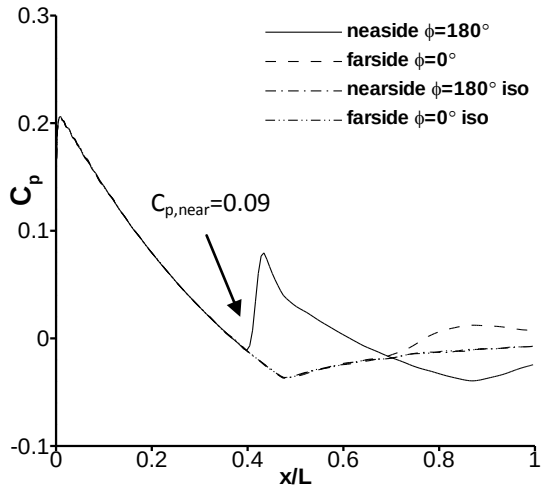

(c) σ_R=0°

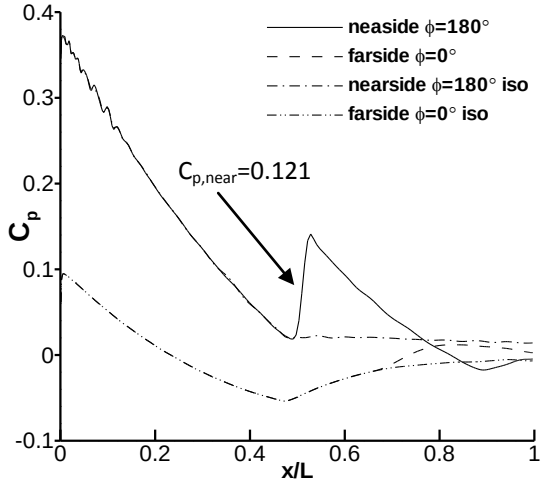

(d) σ_R=-8°

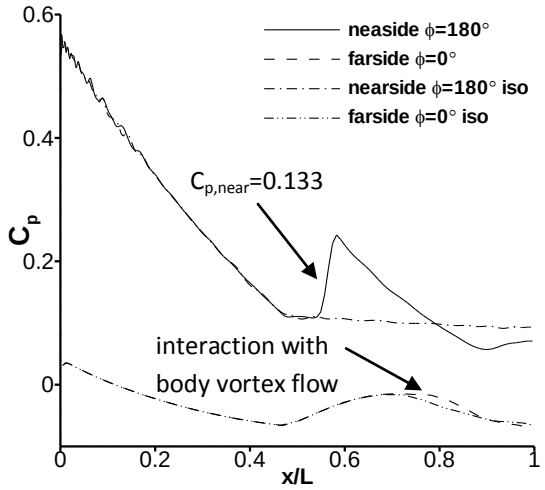

(e) σ_R=-15°

Figure 4.31 Predicted receiver axial pressure distribution for different receiver incidence settings (a-e): m2651 m2653, Δx/D=1.67 Δz/D=2.94, σ_G=0°. Note the different y-axis scaels

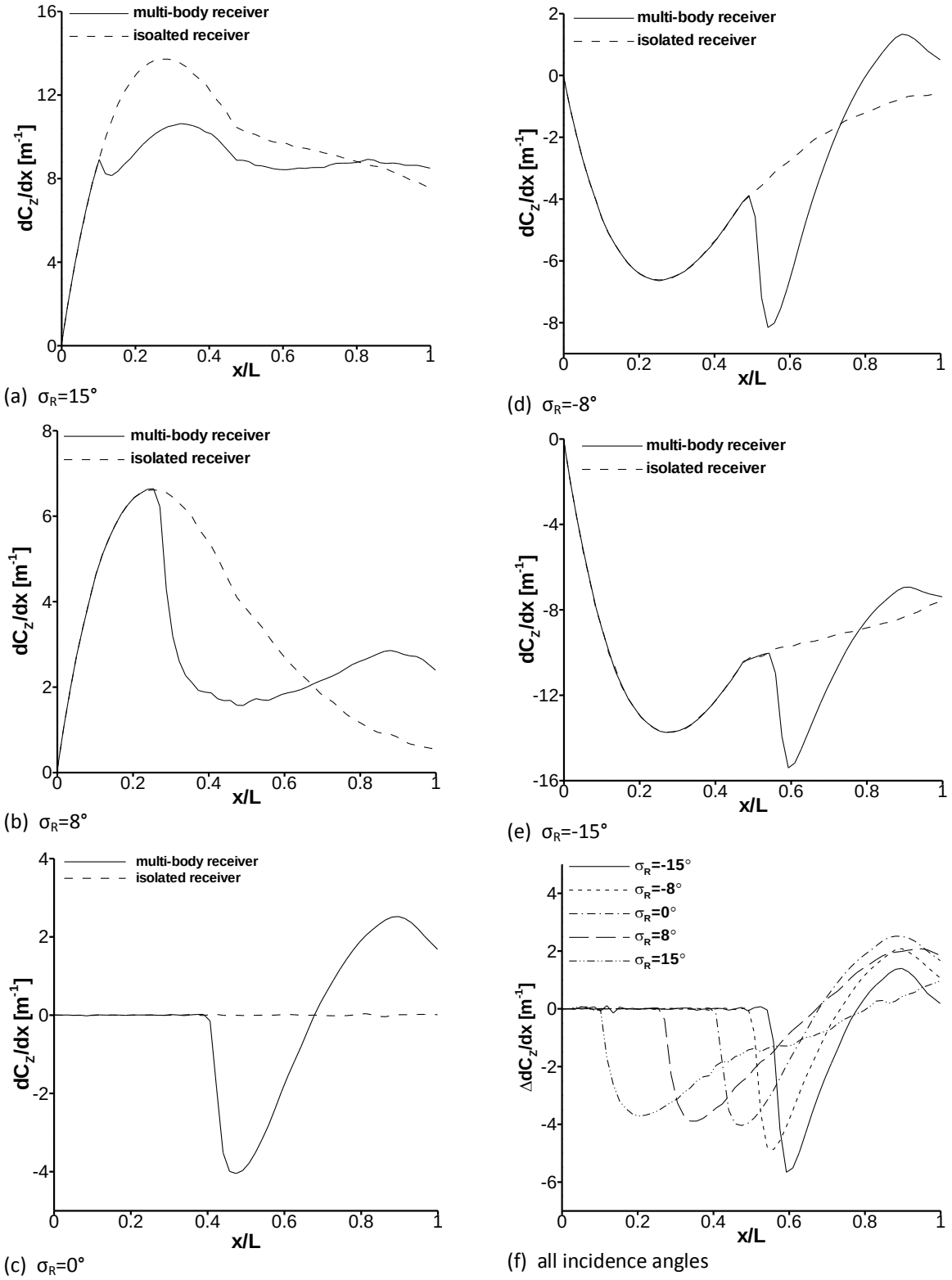

Figure 4.32 Predicted receiver axial local normal force distribution for (a-e) different receiver incidence settings and (f) combined change in local normal force from the isolated configuration: m2651 m2653, $\Delta x/D=1.67$ $\Delta z/D=2.94$, $\sigma_G=0°$. Note the different y-axis scales

4.4.4 Summary discussion on the effect of receiver incidence

Varying the receiver incidence setting has a significant effect on the interference characteristics. It is one of the most complex variables investigated in this research. This parameter plays a crucial role in determining the axial impingement location which affects the extent of the nearside regions of differential pressure, the impinging shock obliqueness angle which affects the extent of the farside regions of differential pressure and the relative position of the receiver body within the disturbance flowfield which affects the magnitude of all impinging disturbances. These individual elements change the local pressure distribution in comparison to the isolated configuration and combine to give the overall interference loads.

In general, the interference effects are generally larger when the receiver incidence either increases or decreases from zero. This interference almost always acts to reduce the normal force from the isolated value ($\Delta C_Z < 0$). This is due to the augmentation of the magnitude of the nearside region of positive differential pressure and diminishing significance of the interactions which cause positive changes to the local normal force distribution for cases at both positive and negative incidence. Figure 4.33 underlines this finding for configurations at different axial stagger arrangements, except for the small number of configurations where the axial impingement location is very close (if not upstream) of the receiver leading edge. The effect on pitching moment is extremely sensitive to the local changes in the normal force distribution induced by the interactions, but (as with normal force) the trend is generally the same and increases in magnitude when the receiver is placed at incidence (Figure 4.34).

Another key finding is that the largest interference loads are typically found at high, positive incidence ($\sigma_R > 10°$). This is because an increase in receiver incidence from zero, reduces the shock obliqueness angle and translates the axial impingement location forward. This, in turn, means that there is no room for the impinging shock to diffract to the receiver farside and that the nearside regions of differential pressure act over a large extent. Both of these features induce large, negative changes in normal

force (Figure 4.33). This is in opposition to the configurations at negative incidence where the extent of the farside region of positive differential pressure increases (due to a rising θ_{obl}) and there is a subsequent relative increase in the positive local normal force contribution.

The extraction of general trends can be difficult when discussing the effect of receiver incidence and not all configurations demonstrate the findings identified above. A good example of this is when the generator is downstream of the receiver ($\Delta x/D=-1.65$). In this case, there is little variation in axial impingement location ($x'/L < 20\%$) because x'/L is close to the centre of rotation point of the wind tunnel support structure. Over the incidence range considered, there is also little change to the impinging shock strength due to approximately constant $\Delta r_{sh}/D$ values. Moreover, there is no influence of the impinging shock on the farside flow, and the interference loads are solely the result of the nearside region of positive differential pressure. The interference loads are thus insensitive to receiver incidence because the important parameters are either approximately fixed or redundant (x'/L, θ_{obl}, $\Delta r_{sh}/D$). This is a helpful reminder that the crucial aspect in understanding the influence of σ_R is to understand the elemental changes in the parameters which characterise the interference effects.

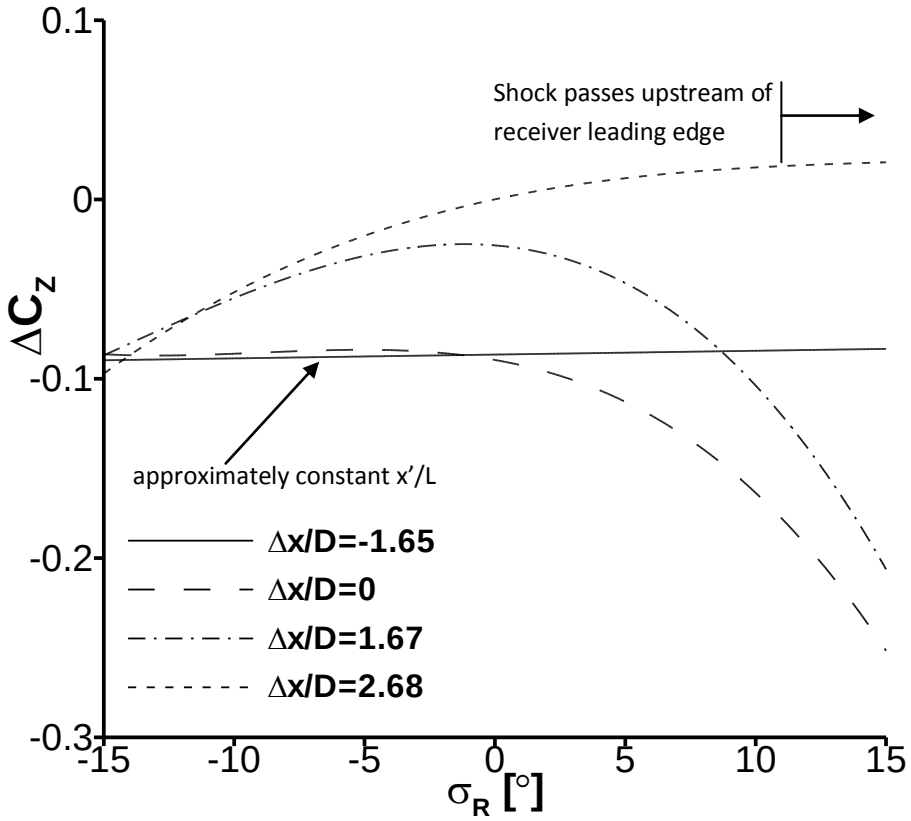

Figure 4.33 Effect of receiver incidence on measured normal force interference: m2651 m2653, Δz/D=2.94, σ_G=0°

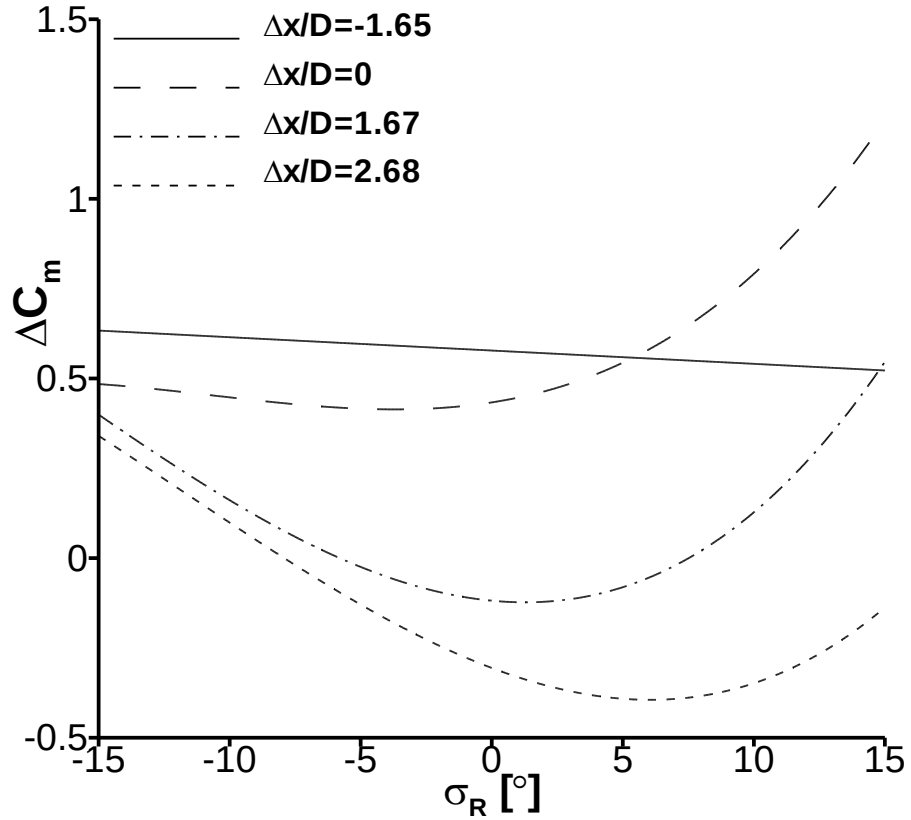

Figure 4.34 Effect of receiver incidence on measured pitching moment interference: m2651 m2653, Δz/D=2.94, σ_G=0°

4.5 Effect of a stronger disturbance flowfield

An increase in the strength of the disturbance flowfield is achieved through the use of a blunt generator with a hemi-spherical forebody. This augments the strength of the bow shock and expansion wave field. In particular, the pressure rise across the impinging shock (ΔC_p) increases by a factor of three compared to when the sharp generator is used. Since the interference effects have been shown (§4.4) to be sensitive to the strength of the impinging disturbances, it is expected that the stronger disturbance flowfield produced by the blunt generator will have a significant impact on the receiver aerodynamics.

As with the sharp generator, the effect of incidence is examined over the range $-15 \leq \sigma_R \leq 15°$ for a single axial stagger. As a result of the different bow shock structures, the axial stagger is changed from $\Delta x/D=1.67$ to $\Delta x/D=-0.53$ to maintain a constant axial impingement location of $x'/L=0.4$ at $\sigma_R=0°$ in comparison to the sharp generator so that the results are genuinely comparable as a function of disturbance field strength alone. This subset of configurations will be discussed, before a summary discussion of the strength of the disturbance flowfield using data from across the experimental test matrix.

4.5.1 Receiver force and moment characteristics

Relative to the sharp generator configurations, and depending on the receiver incidence angle, the blunt generator produces significant changes in both the ΔC_Z and ΔC_m. At positive incidence ($\sigma_R > 0°$) there are relatively minor changes in ΔC_Z while at negative incidence ($\sigma_R < 0°$) the interference loads are almost doubled in some cases (e.g. $\sigma_R=-12°$ in Figure 4.35). In addition, as with the configurations which involve the sharp generator, the interference loads increase as the receiver body is placed at either positive or negative incidence. Unlike the sharp generator configurations, the ΔC_Z distribution is more symmetric across the incidence range. The changes in ΔC_m due to the effect of the blunt generator can be significant but also depend on the receiver incidence. At positive incidence, ΔC_m is approximately tripled at $\sigma_R=5°$ and at a negative incidence of $\sigma_R=-14°$ the ΔC_m is almost doubled from 0.38 to 0.66 (Figure

4.36). When using the blunt generator, the pitching moment changes are not symmetric about σ_R=0° as the local minimum ΔC_m occurs at σ_R=5°. Similar characteristics in the movement of X_{cp} are observed as for the sharp generator configurations (Figure 4.37). However, the effects of both the forward and aftward movement of X_{cp} are amplified by up to a factor two. For the blunt generator configurations between $1 \leq \sigma_R \leq 5°$ the interference flowfield moves the centre of pressure further aftward than the equivalent sharp generator configurations and so much so, that the body is statically stable over this range. Finally, the axial force interference load follows a similar trend to that observed for the sharp generator but reaches a larger maximum of ΔC_X=0.06 at σ_R=15°.

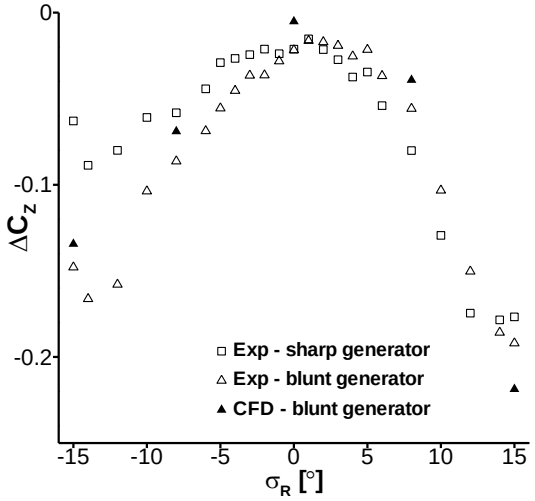

Figure 4.35 Effect of blunt generator on the measured receiver normal force interference load: m2651, Δz/D=2.94, σ_G=0° (error bars omitted)

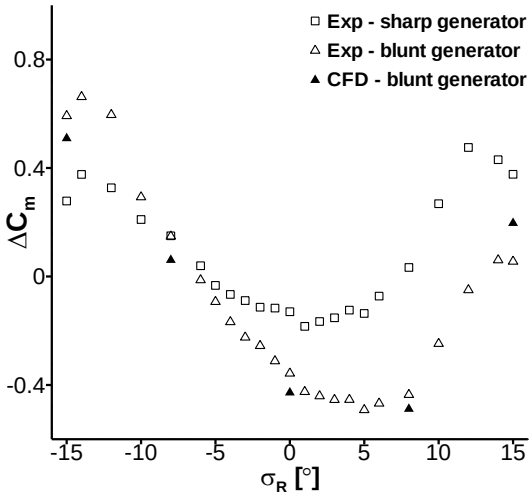

Figure 4.36 Effect of blunt generator on the measured receiver pitching moment interference load: m2651, Δz/D=2.94, σ_G=0° (error bars omitted)

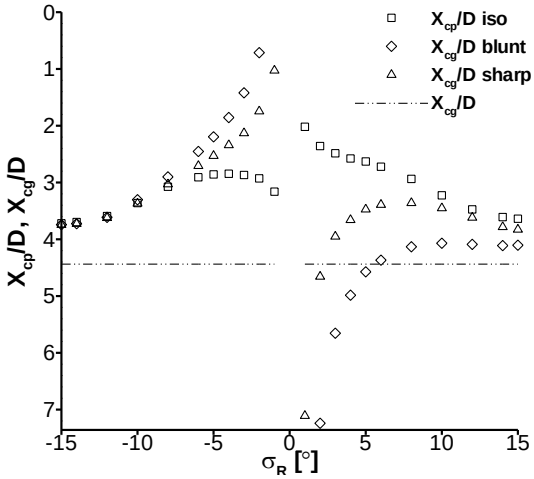

Figure 4.37 Effect of a blunt generator on measured receiver X_{cp}: m2651, Δz/D=2.94, σ_G=0°

4.5.2 Interference flowfield structure

Using the blunt generator increases the impinging shock strength (ΔC_p across shock) at σ_R=0° by a factor of three compared to the when the sharp generator is used. The shock angle for the approximately conical portion of the blunt generator bow shock is $\theta_{s,G}$=28.6° which is similar to that for the sharp generator ($\theta_{s,G}$=28.2°). Consequently, over the incidence range tested there is a negligible difference in axial impingement location between most configurations using the sharp and blunt generator bodies. The largest difference in impingement location is x'/L=0.07 which occurs at σ_R=15° (Table 4.2). As well as changing the shock strength, the blunt generator also has a different expansion wave field, which affects the interference aerodynamics. The hemispherical forebody induces stronger expansion waves, which act over a smaller extent compared to the sharp generator flowfield.

The principal features of the interference flowfield in the blunt generator configurations are generally similar to those which involve the sharp generator (Figure 4.38 (a)-(e)). A notable exception is for σ_R=15° where the impinging shock diffracts to the farside of the receiver body (Figure 4.38 (a)) whereas for the sharp generator it does not (Figure 4.29 (a)). This is due to the propagation of the double-shock structure on either side of a separated flow region induced by the impinging shock around the receiver body (see §4.7 for details). Similarly, the interaction footprints highlighted by the receiver surface pressure contours (Figure 4.39 (a)-(e)) show comparable flow structures to the sharp generator cases, except for σ_R=15° and σ_R=8°. In these cases there is evidence of a local shock-induced crossflow separation of the boundary-layer occurring on the receiver nearside. The low-pressure plateau (Figure 4.39 (a),(b)) along with the double-reflected shock structure (Figure 4.38 (a),(b)) either side of the separation region were also observed by Brosh[10,12,30]. The horseshoe vortex flow feature (Figure 4.38 (a)) and the double diffracted shock structure in the σ_R=15° case also support this interpretation.

As in the sharp generator configurations, there is excellent agreement between the measured and predicted pressure contours, and importantly the CFD captures the

suspected regions of local flow separation (Appendix B.4). This indicates that the CFD prediction method is also able to predict some of the more complex flow situations involving shock boundary-layer interactions and extensive regions of separated flow. The predicted flowfield solutions are now used to investigate the σ_R=0, ±8, ±15° configurations to better understand the effect of a stronger disturbance flowfield.

σ_R [°]	x'/L	θ_{obl} [°]	$\Delta C_{p,near}$	$\Delta z_{sh}/D$[a]	$\Delta C_{p,imp}$ (% of $\Delta C_{p,near}$)	δ_{refl} [°]
-15	0.54	43.6	0.343	2.88	0.115 (34%)	21.3
-8	0.49	36.6	0.313	2.68	0.129 (41%)	14.8
0	0.39	28.6	0.289	2.34	0.157 (54%)	10.8
8	0.28	20.6	0.313	1.94	0.204 (65%)	8.4
15	0.15	13.6	0.467	1.20	0.363 (78%)	12

[a] $\Delta z_{sh}/D$ is an equivalent parameter of $\Delta r_{sh}/D$ for the blunt generator to characterise shock decay

Table 4.2 Effect of receiver incidence on the predicted interference parameters: m2651 m2654, Δx/D=-0.53 Δz/D=2.94, σ_G=0°

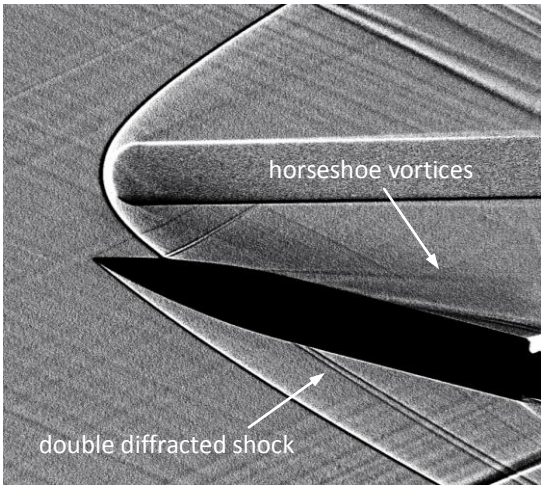

(a) σ_R=15°

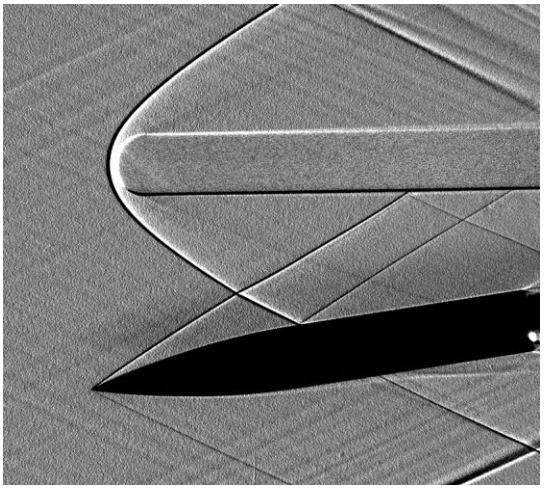

(d) σ_R=-8°

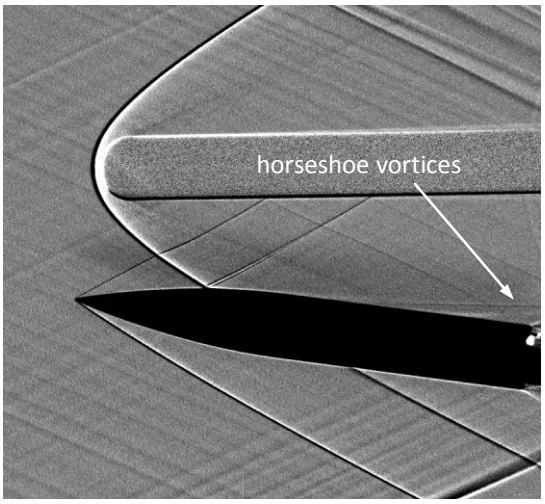

(b) σ_R=8°

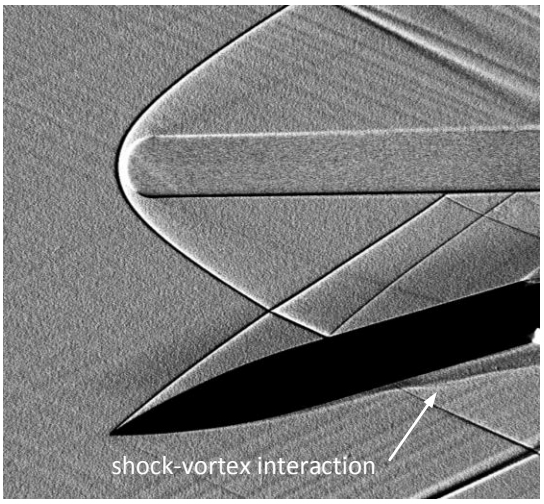

(e) σ_R=-15°

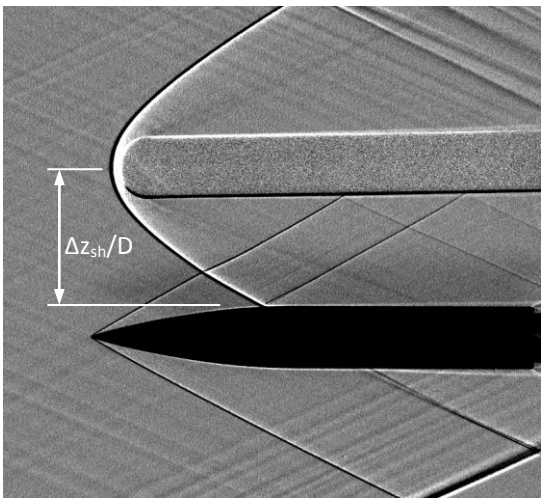

(c) σ_R=0°

Figure 4.38 Measured shadowgraph visualisations for different receiver incidence settings (a-e): m2651 m2654, Δx/D=-0.53 Δz/D=2.94, σ_G=0°

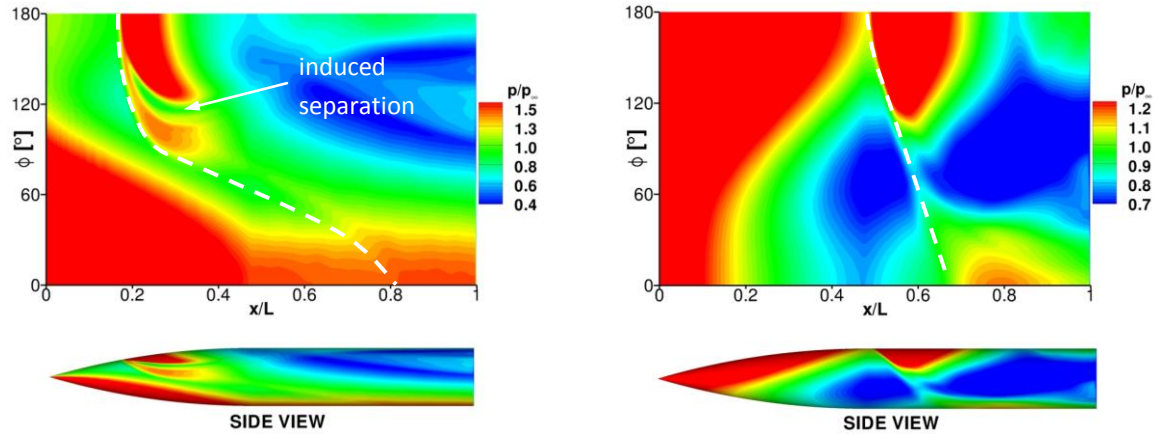

(a) σ_R=15°

(d) σ_R=-8°

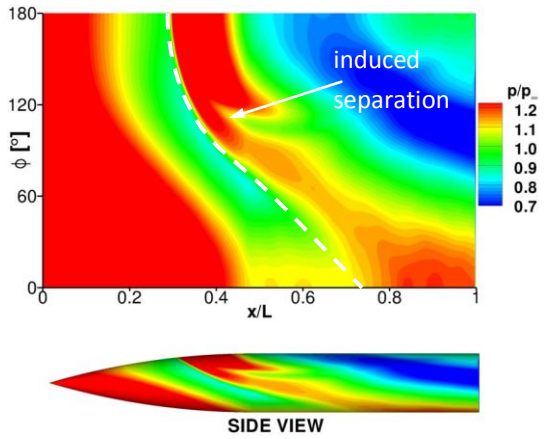

(b) σ_R=8°

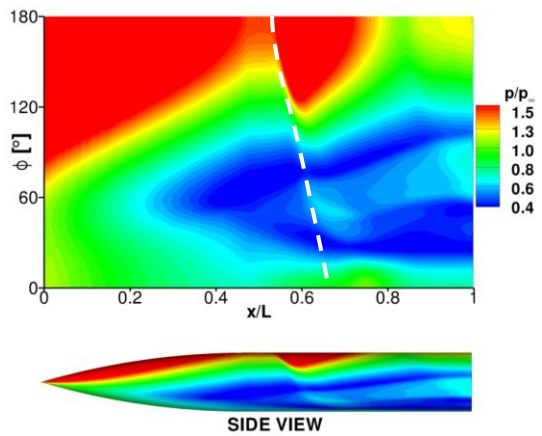

(e) σ_R=-15°

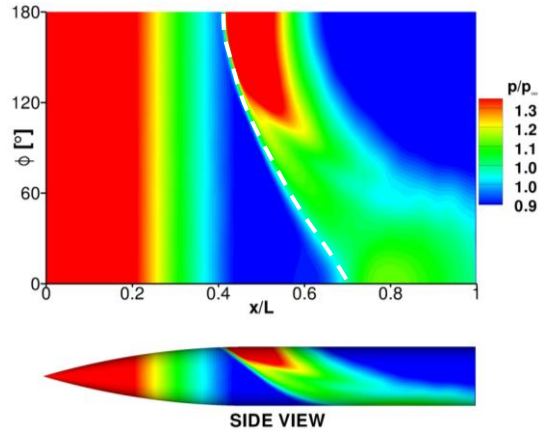

(c) σ_R=0°

Figure 4.39 Predicted receiver surface pressure contours highlighting the impinging shock paths (dashed) for different receiver incidence settings (a-e): m2651 m2654, Δx/D=-0.53 Δz/D=2.94, σ_G=0°

4.5.3 Effect of a stronger disturbance flowfield on the underlying flowfield mechanisms

The effect of a stronger disturbance flowfield on the interference effects is first investigated for three configurations where the interference characteristics are different (σ_R=-15°,0°,15°).

4.5.3.1 Receiver body at σ_R=-15°

When the receiver is at σ_R=-15° and the blunt generator is used, the normal force interference load more than doubles (to ΔC_Z=-0.15) in comparison to the equivalent configuration using the sharp generator. The bow shock impinges at approximately the same location (x'/L=0.54) in both cases, but the initial nearside pressure rise is larger by a factor of 2.5 ($\Delta C_{p,near}$=0.34) in comparison to when the blunt generator is used (Figure 4.40 (c)). Consequently, this leads to a larger change in negative local normal force as a result of a more significant nearside region of positive differential pressure (Figure 4.41 (c)). The local nearside pressure reduces at a greater rate than the sharp generator configuration, due to the influence of the stronger expansion field associated with the hemi-spherical forebody. The shock diffracts to the receiver farside, and induces a local region of positive differential pressure (Figure 4.40 (f)). However, this farside compression is affected by the body vortex flow on the leeside (farside) of the body and reduces shortly after rising. Overall, the blunt generator increases the magnitude of the regions of the receiver which experience changes in both positive and negative local normal force (Figure 4.41 (c)). However, the farside compression is tempered by the shock vortex interaction and the increase in the magnitude of the nearside compression dominates the overall reduction in ΔC_Z compared to the sharp generator case. The dominance of the nearside region of differential pressure concurrently leads to an increase in the overall pitching moment of ΔC_m=0.3 compared to the sharp case.

4.5.3.2 Receiver body at σ_R=0°

At σ_R=0°, the stronger disturbance flowfield produces a negligible overall change in ΔC_Z relative to the sharp generator configuration, and a reduction in pitching moment from ΔC_m=-0.13 to ΔC_m=-0.36. The blunt generator augments the nearside pressure rise compared to when the sharp generator is used (Figure 4.40 (b)) and induces a greater magnitude of the negative change in local normal force (Figure 4.41 (b)). However, because the receiver is close to the generator body, the interactions which induce regions of positive local normal force are also significant. The strong impinging expansion waves along with the augmented farside region of positive differential pressure (Figure 4.40 (b), (e)), induce a significant region of positive local normal force (Figure 4.41 (b)). This balances the reduction in C_Z caused by the stronger nearside region of positive differential pressure and overall there is effectively no change in normal force compared to the sharp case. The pitching moment is dominated by the region of positive local normal force acting near the trailing edge of the receiver body and there is an increase in the magnitude of the pitching moment interference (ΔC_m) compared to the sharp generator case by a factor of three.

4.5.3.3 Receiver incidence σ_R=15°

Different aerodynamic characteristics are observed for the high positive incidence configurations ($\sigma_R \geq 12°$) where the diffracted shock reaches beyond the receiver farside as a result of a viscous shock interaction (see §4.7.1 for further analysis). This did not occur for the equivalent configurations involving the sharp generator and is a significant effect of the stronger disturbance flowfield. For σ_R=15°, the impinging shock diffracts to the receiver farside and leads to a compression of the local pressure (Figure 4.40 (d)). The increase in the magnitude of the nearside compression (Figure 4.40 (a), from the sharp generator case, is offset by the increase in the strength of the local impinging expansion waves and the presence of the farside compression (Figure 4.41 (a)). As a result, these competing aspects balance and there is little difference to the normal force between the sharp and blunt generator cases for this incidence setting.

In general, the blunt generator increases the magnitude of normal force interference compared to the sharp cases. However, due to the impact of competing local interactions and the intricacies relating to shock diffraction, there are some configurations where there is only a small effect on the interference loads.

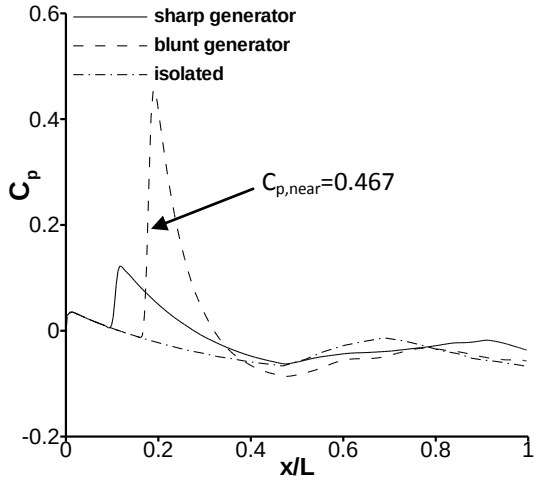

(a) σ_R=15° nearside

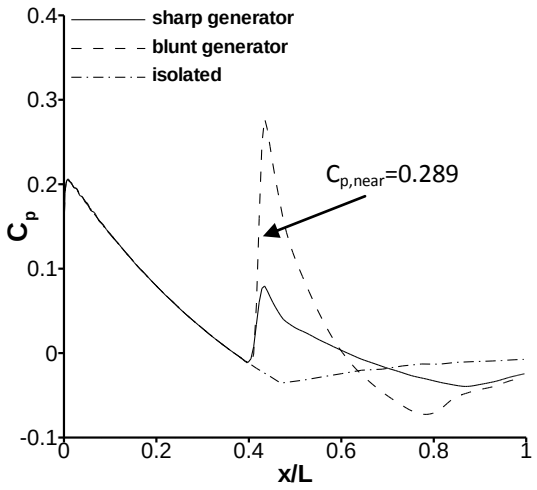

(b) σ_R=0° nearside

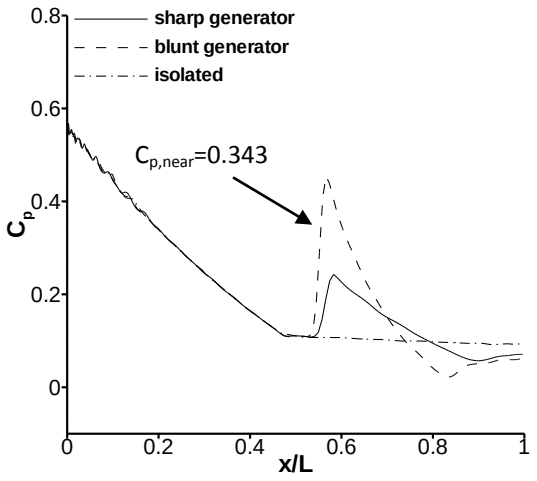

(c) σ_R=-15° nearside

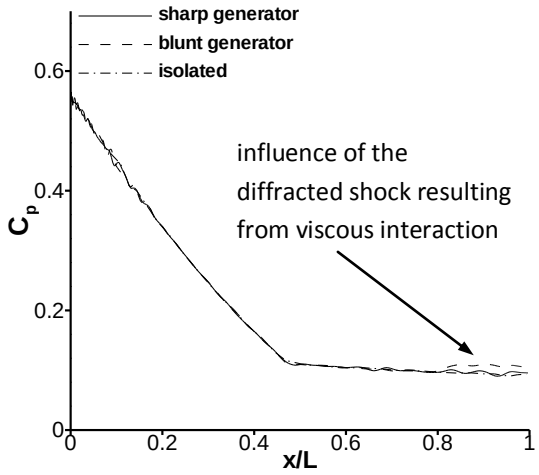

(d) σ_R=15° farside

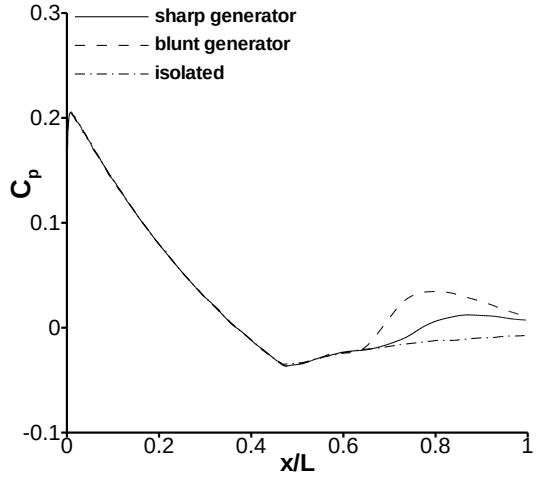

(e) σ_R=0° farside

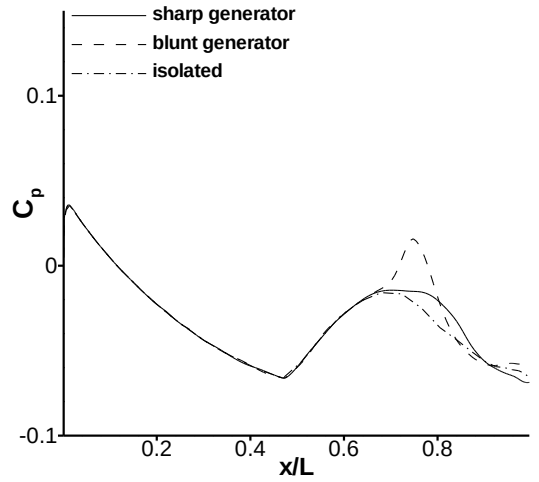

(f) σ_R=-15° farside

Figure 4.40 Effect of blunt generator on the predicted receiver axial pressure distribution for different receiver incidence settings (a-f): m2651, $\Delta z/D$=2.94, σ_G=0°

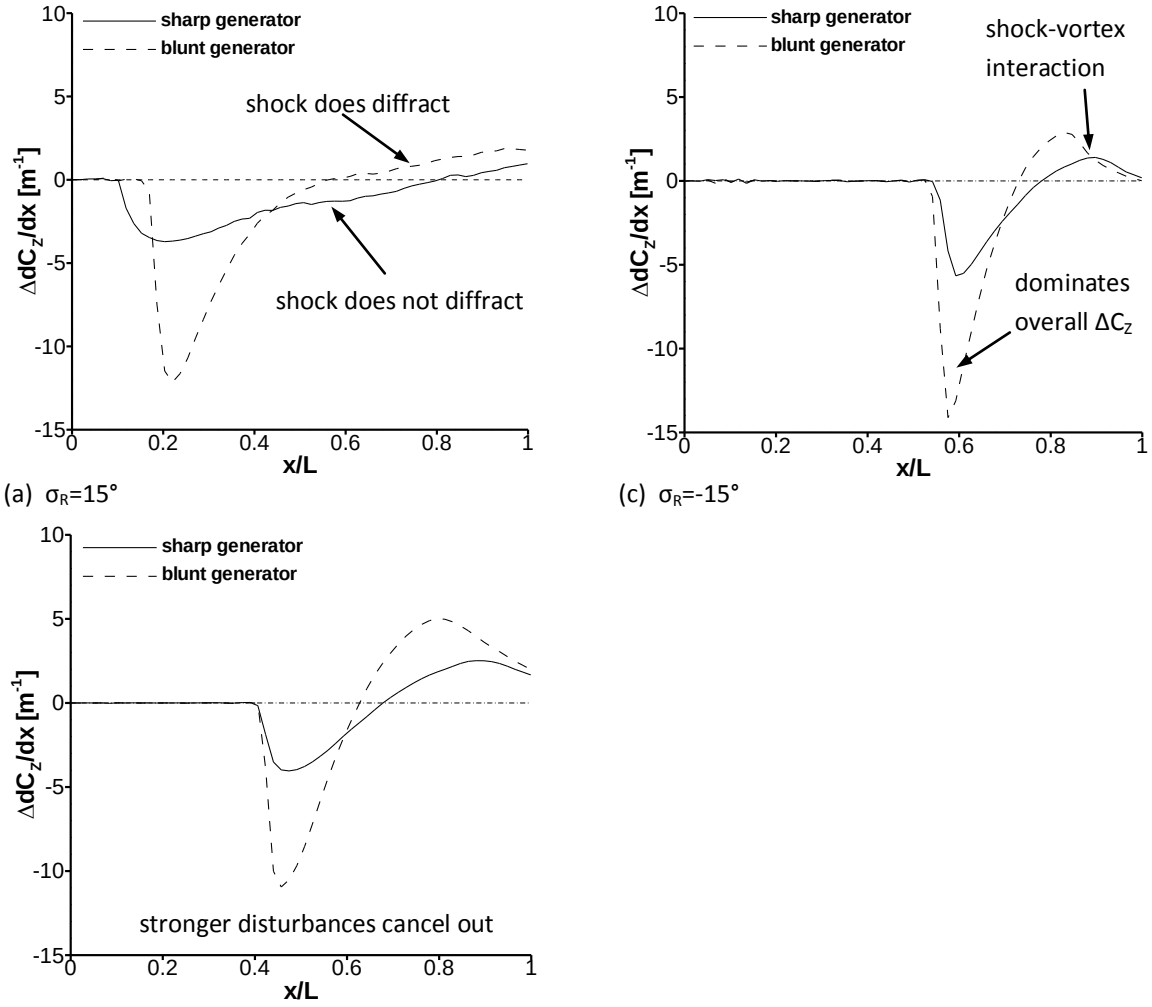

Figure 4.41 Effect of the blunt generator on the predicted change in the local normal force distribution from the isolated configuration (no change to the isolated configuration is highlighted as dash-dot) for different receiver incidence settings (a-c): m2651, Δz/D=2.94, σ_G=0°

4.5.4 Summary discussion on the effect of a stronger disturbance flowfield

The use of a blunt generator changes the disturbance flowfield by increasing the strength of the bow shockwave and forebody expansion field in comparison to the sharp generator flowfield. The design of the experimental configurations minimised changes in x'/L and θ_{obl} in this part of the investigation so that the comparisons with the sharp generator results would be a genuine (as far as possible) comparison of the strength of the disturbance flowfield.

In general, this comparison showed that the stronger disturbance flowfield does not change the trend of the interference effects but it did increase the magnitude of the normal force interference. This is due to the dominance of the nearside region of positive differential pressure which simply increases for a larger impinging shock strength. The stronger disturbance flowfield has a particularly strong effect on configurations where the impinging shock does not diffract to the farside of the receiver body.

This can be seen when opening out the discussion to include data from configurations where the bodies are at different axial staggers to the subset discussed in §4.5.1-4.5.3 (Figure 4.42 (a)-(d)). It should be noted that although on the whole, the stronger disturbance flowfield does increase the magnitude of the interference effects, this does not happen in every case. There are configurations (Figure 4.42 (a)-(b)) where the blunt generator induces little or no difference compared when the sharp generator is used. However, this is not because the potency of the elemental interactions are weak. It is simply because these elemental contributions can cancel one another out in the overall calculation of the interference load. It is further evidence of the complexity of the problem of multi-body interference and it's inherit dependence of the combined effects of many different parameters.

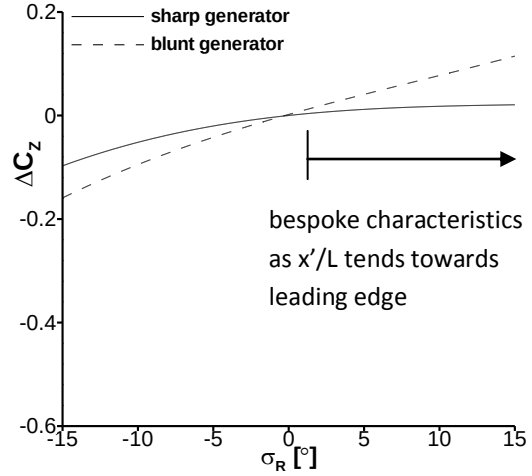

(a) Δx/D=2.68 (sharp), Δx/D=0.44

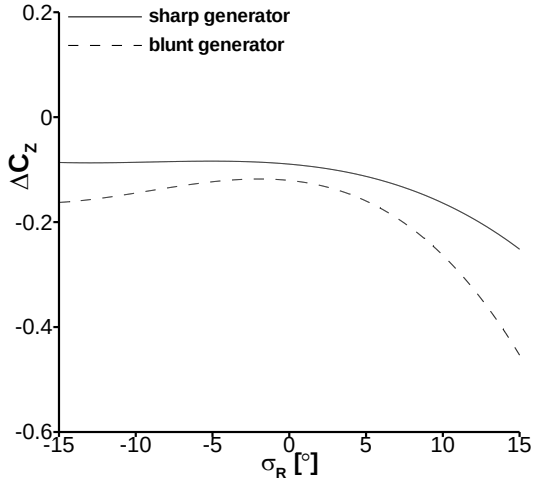

(c) Δx/D=0 (sharp), Δx/D=-2.16 (blunt)

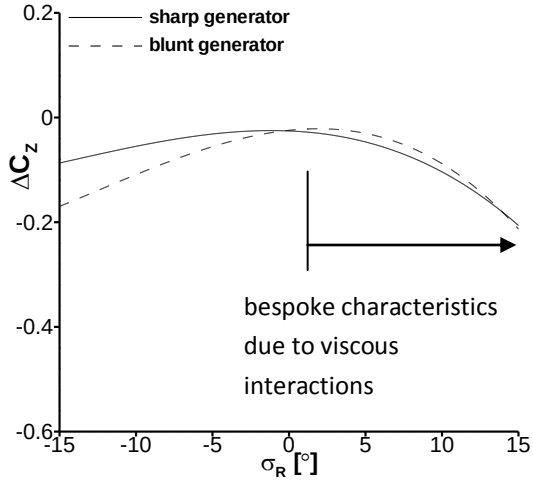

(b) Δx/D=1.67 (sharp), Δx/D=-0.53 (blunt)

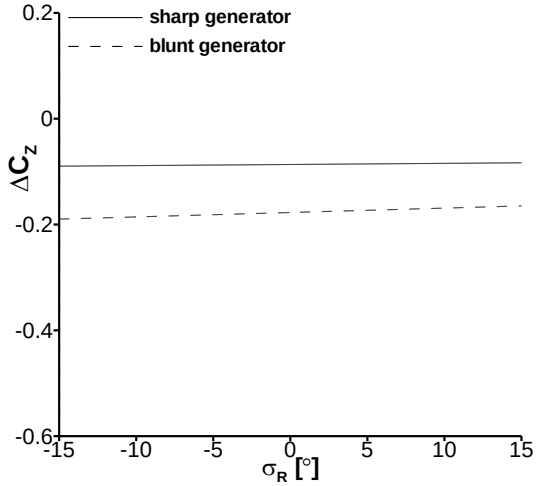

(d) Δx/D=-1.65 (sharp), Δx/D=-3.81 (blunt)

Figure 4.42 Effect of blunt generator on the measured receiver normal force interference for different axial stagger settings (a-d): m2651, Δz/D=2.94, σ_G=0°

4.6 Effect of axial impingement location

For a multi-body arrangement, the axial impingement location (x'/L) strongly impacts the extent of the nearside and farside regions of differential pressure. Consequently, a change in the axial impingement location is expected to have a significant effect on the interference loads of the receiver body. This is evaluated for a cross-section of the experimental test matrix where the receiver incidence (σ_R) is fixed and the axial stagger (Δx) is varied. The configurations considered are for the un-finned receiver and sharp generator at five incidence angles (σ_R=-15, -8, 0, 8, 15°) over a range of 5 axial staggers ($\Delta x/D$=-1.65, 0, 1.67, 2.68, 3.679). The CFD flow solutions are then used to understand the aerodynamics induced by a change in axial impingement location for two groups of representative configurations first when σ_R=0° and then for cases where σ_R=15°.

4.6.1 Receiver force and moment characteristics

The measured normal force interference (ΔC_Z) becomes more negative as the generator (and axial impingement location) moves aftward for the majority of the presented incidence angles (Figure 4.43). There is a concomitant increase in the pitching moment interference load (ΔC_m), Figure 4.44. However, the only exceptional configurations are those where the receiver is placed at σ_R=15°. These show a characteristically different, non-monotonic trend of normal force and pitching moment interference with axial stagger.

The significance of these results becomes more apparent if the abscissa is changed to the axial impingement parameter, x'/L (Figure 4.45 and Figure 4.46). The effect of x'/L on the interference loads remains similar for $-15 \leq \sigma_R \leq 8°$ and the data points group moderately well together which further underlines the primary significance of this parameter (§4.2-4.5). Figure 4.45 and Figure 4.46 further emphasise that the σ_R=15° configurations are characteristically different to those at the other incidence settings. As a result, representative examples of the different trends observed (σ_R=0° and σ_R=15°) are further investigated using the predicted flowfield to firstly understand the nominal effect of axial impingement location and secondly to understand why the

σ_R=15° configurations are different. Finally, the equivalent configurations involving the blunt generator were also assessed but showed similar trends to those presented here for the sharp generator. Therefore, these results will not be discussed but instead can be referred to in Appendix B.5.

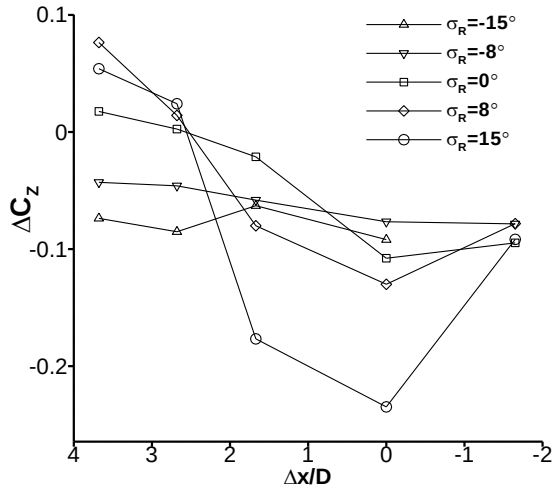

Figure 4.43 Effect of axial stagger on measured receiver normal force interference load: m2651 m2653, Δz/D=2.94, σ_G=0°

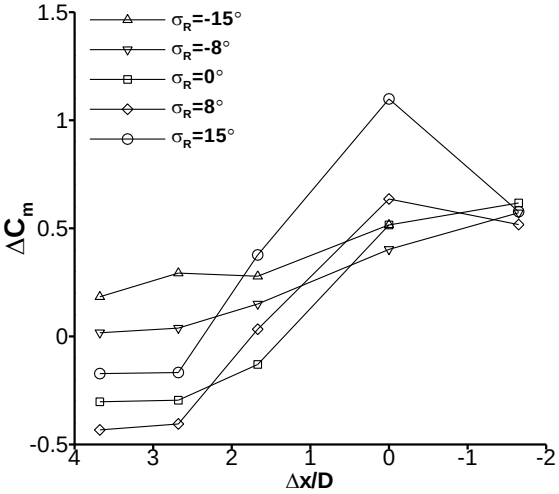

Figure 4.44 Effect of axial stagger on measured receiver pitching moment interference load: m2651 m2653, Δz/D=2.94, σ_G=0°

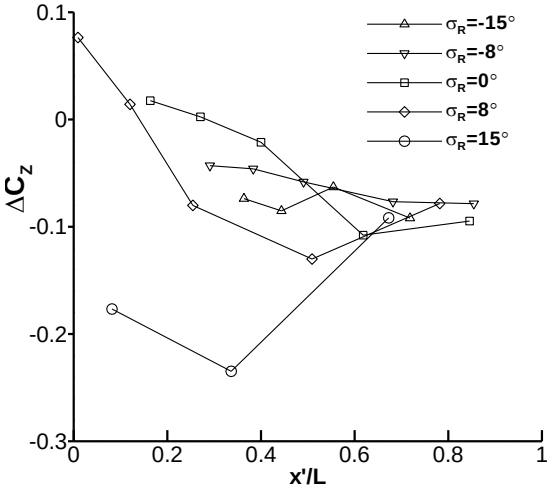

Figure 4.45 Effect of axial impingement location on measured receiver normal force interference load: m2651 m2653, Δz/D=2.94, σ_G=0°

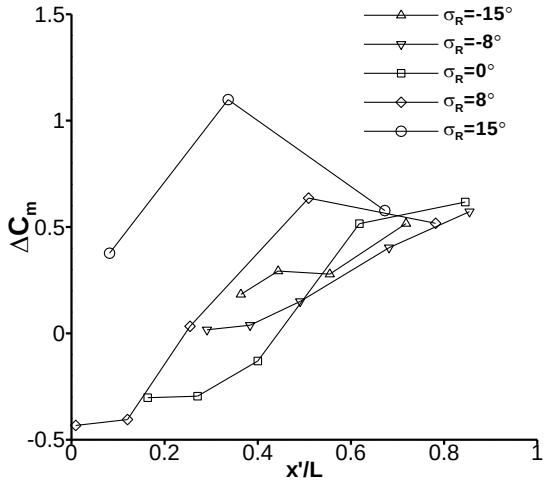

Figure 4.46 Effect of axial impingement location on measured receiver pitching moment interference load: m2651 m2653, Δz/D=2.94, σ_G=0°

4.6.2 Nominal effect of axial impingement location for configurations at $\sigma_R=0°$

Over the axial stagger range considered, the generator moves aftward and leads to a total axial impingement range covering 75% of the receiver body length (Figure 4.47 (a)-(e)). As the generator moves from Δx/D=3.679 (upstream of receiver) to Δx/D=-1.65 (downstream of receiver), there is a change in polarity of the induced interference loads (Figure 4.48, Figure 4.49). This significant finding was also observed by other researchers in similar studies[9,11,18]. This implies that the disturbance flowfield has a characteristically different impact on the receiver body aerodynamics and subsequent trajectory depending on the axial impingement location. For example, when the impingement location is near the leading edge, there is an interference force (ΔC_Z) which attracts the receiver towards the generator body. This changes, however, to a repulsive force when the shock impinges near the trailing edge. The induced pitch-down for an x'/L near the leading edge also changes to a pitch towards the generator when x'/L is near the tailing edge. Overall, there is good agreement between the measured and predicted interference loads and the flowfield CFD solutions are now used to understand why the observed change in polarity occurs for both bodies at zero incidence.

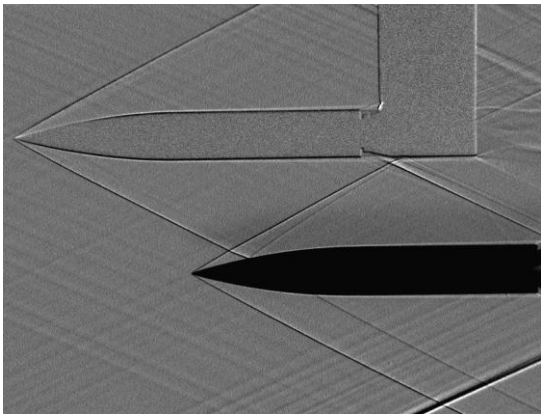

(a) Δx/D=3.679

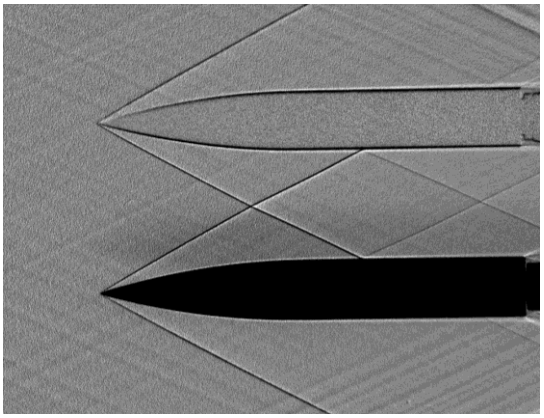

(d) Δx/D=0

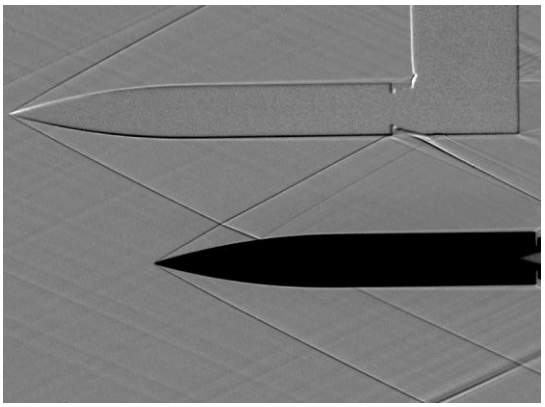

(b) Δx/D=2.68

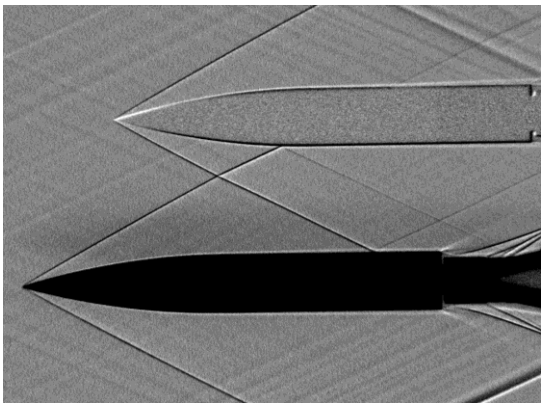

(e) Δx/D=-1.65

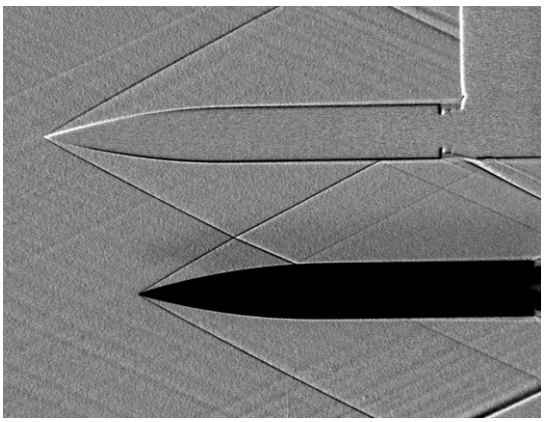

(c) Δx/D=1.67

Figure 4.47 Measured shadowgraph visualisations for different axial stagger settings (a-e): m2651 m2653, Δz/D=2.94, σ_R=0° σ_G=0°

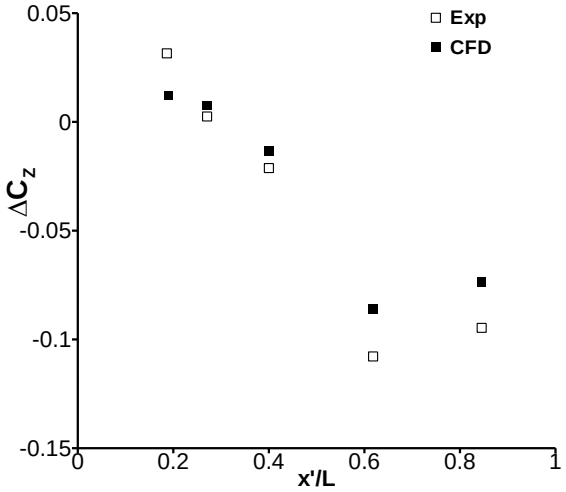

Figure 4.48 Effect of axial impingement location on receiver normal force interference load: m2651 m2653, Δz/D=2.94, σ_R=0° σ_G=0° (error bars omitted)

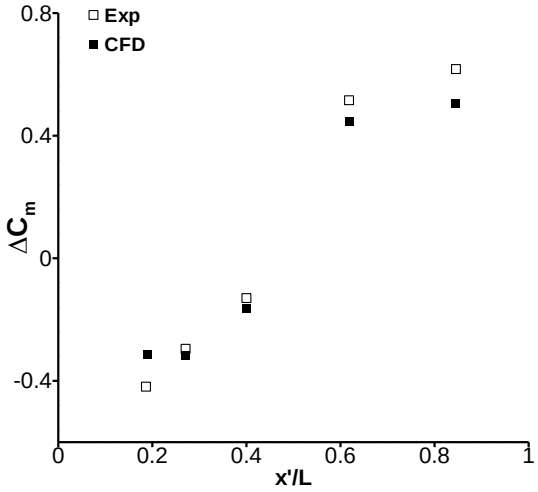

Figure 4.49 Effect of axial impingement location on receiver pitching moment interference load: m2651 m2653, Δz/D=2.94, σ_R=0° σ_G=0° (error bars omitted)

4.6.2.1 Flowfield mechanisms for the configurations at σ_R=0°

In all five configurations, a portion of the impinging shock diffracts around the receiver body. The diffracted wavefront reaches the receiver farside for all configurations except Δx/D=-1.65 where it crosses the body centreline (ϕ≈90°) at the trailing edge of the body. Since the lateral separation is fixed, the distance from the generator leading edge to the impingement location (Δr_{sh}/D) is approximately the same for each axial stagger configuration and this leads to nearside pressure rises of approximately equal magnitude ($\Delta C_{p,near}$≈0.1), Figure 4.50. The axial impingement location has a significant influence on the interaction of the impinging expansion waves. When x'/L is near the leading edge the local expansion field is stronger (Δx/D=3.679, Δx/D=2.68) due to the influence of the receiver forebody expansion field on the local nearside pressure. A more moderate negative pressure gradient is observed when x'/L is further aft (Δx/D=1.67, Δx/D=0 and Δx/D=-1.65).

The farside pressure distributions show similar characteristics (in terms of magnitude and trend of the local pressure) for all axial stagger configurations (Figure 4.51). Moreover, the expansion waves do not diffract to the farside of the receiver to the same extent as the compression waves and although the local pressure reduces after

the initial rise, there are no configurations studied in the computational test matrix that exhibit a farside region of negative differential pressure.

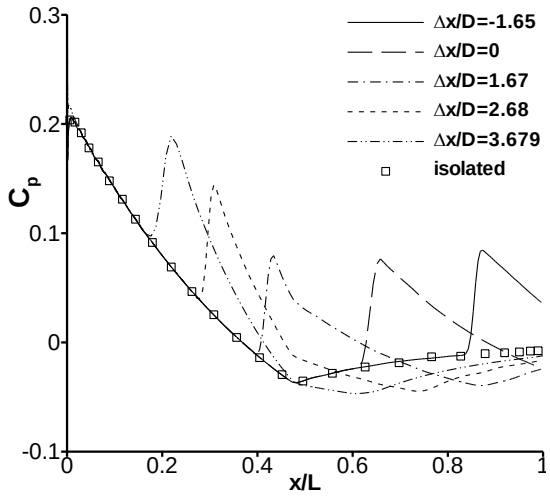

Figure 4.50 Effect of axial stagger on predicted receiver nearside pressure distribution: m2651 m2653, Δz/D=2.94 σ_R=0° σ_G=0°

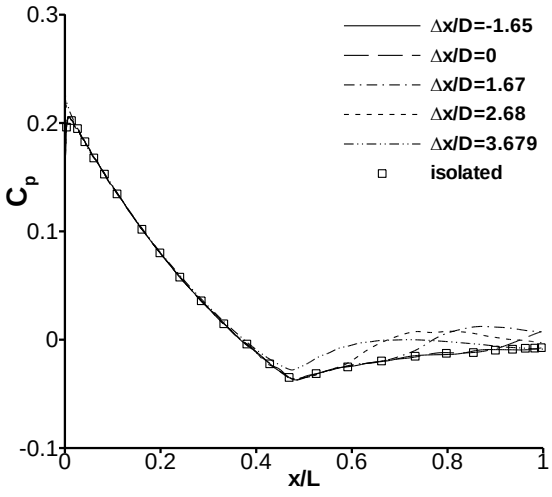

Figure 4.51 Effect of axial stagger on predicted receiver farside pressure distribution: m2651 m2653, Δz/D=2.94, σ_R=0° σ_G=0°

The local normal force distribution which acts on the receiver body is strongly influenced by the axial impingement location and is a function of both the magnitude of the regions of differential pressure and the projected area over which these differential pressure regions act (Figure 4.52). As the axial impingement location moves further aft, the extent of the regions of positive local normal force diminish. As a result, the overall ΔC_Z reduces as the $\Delta dC_Z/dx < 0$ region becomes a larger portion of the overall interference load. Moreover, because the nearside region of positive differential pressure occurs further aft along the body as x'/L increases the moment arm increases for a similar magnitude of local normal force, this coupled with the reduction in the $\Delta dC_Z/dx > 0$ regions leads to an increase in ΔC_m.

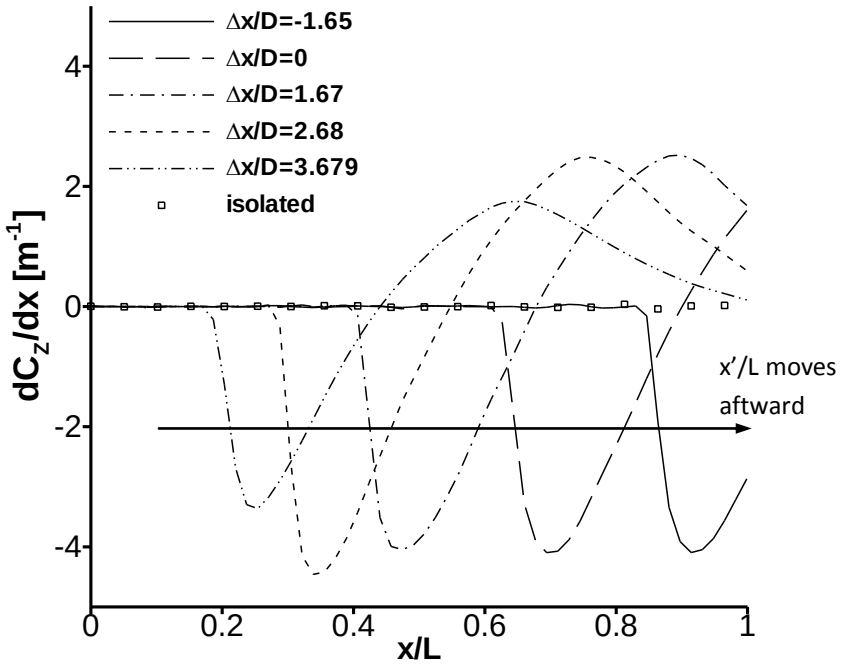

Figure 4.52 Effect of axial stagger on predicted receiver local normal force distribution: m2651 m2653, Δz/D=2.94, σ_R=0° σ_G=0°

4.6.3 Effect of axial impingement location on the underlying flowfield mechanisms when σ_R=15°

It is clear from Figure 4.45 and Figure 4.46, that the configurations where the receiver incidence is σ_R=15° exhibit a characteristically different trend than the other cases and this section aims to find out the reason for this.

As a result of the geometric arrangement, the impinging shock passes far upstream of the receiver leading edge for the configuration where the generator is furthest upstream of the receiver (Δx/D=3.679) and this configuration will not be discussed. Instead for an axial stagger of Δx/D=2.68 the generator bow shock passes sufficiently close to the receiver leading edge to influence the receiver flowfield (Figure 4.53 (a). For the other axial configurations (Figure 4.53 (b)-(d)) the generator bow shock impinges onto the nearside (and leeside) flow structure. However, no diffracted shock is visible on the farside of the receiver body for any of these configurations.

Overall, a non-monotonic trend of interference load as a function of axial impingement location is observed in Figure 4.54 and Figure 4.55. Moreover, there is good

agreement between the measured and predicted forces and moments and the predicted flowfield solutions are able to evaluate the interaction of the impinging shockwave with the receiver leeside to assess the effect of axial impingement location.

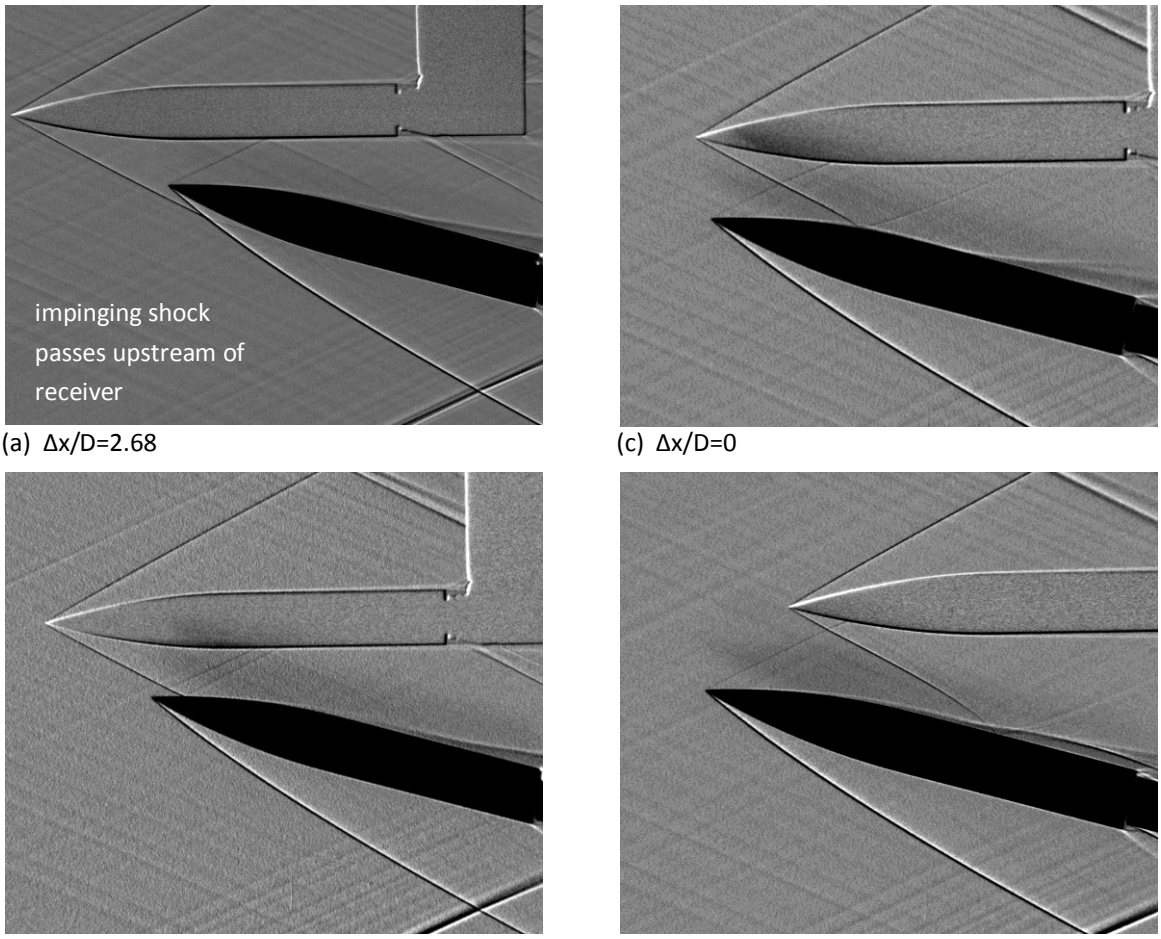

(a) Δx/D=2.68 (c) Δx/D=0

(b) Δx/D=1.67 (d) Δx/D=-1.65

Figure 4.53 Measured shadowgraph visualisations for different axial stagger settings (a-d): m2651 m2653, Δz/D=2.94, σ_R=15° σ_G=0°

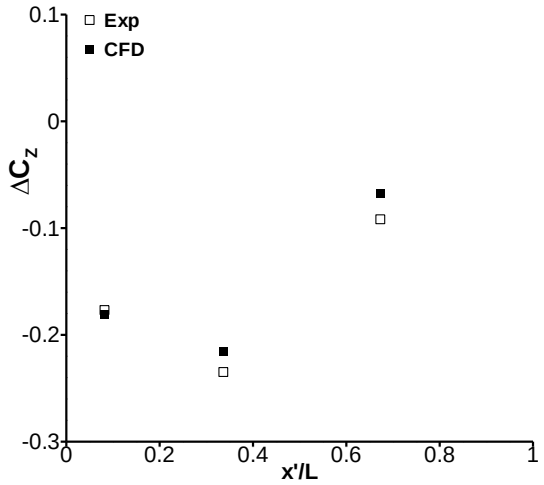

Figure 4.54 Effect of axial impingement location on receiver normal force interference load: m2651 m2653, Δz/D=2.94, σ_R=15° σ_G=0°

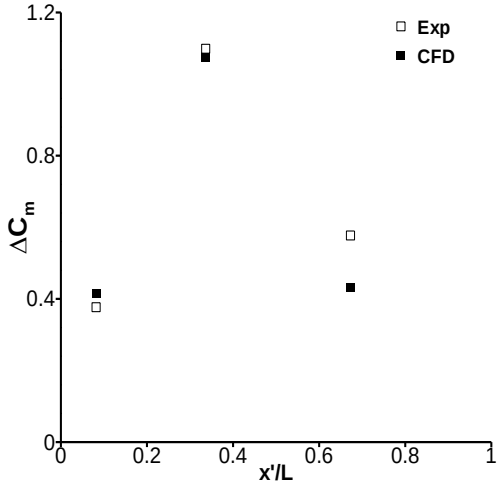

Figure 4.55 Effect of axial impingement location on receiver pitching moment interference load: m2651 m2653, Δz/D=2.94, σ_R=15° σ_G=0°

4.6.3.1 Flowfield structure

A first analysis of the shock structure for the four axial stagger configurations studied (Figure 4.53) reveals the characteristic difference from the σ_R=0° cases in the previous section; there is no shock diffraction to the farside of the receiver. In the three configurations where the generator bow shock impinges on the receiver, the shock obliqueness angle (θ_{obl}≈13°) and geometric arrangement are such that the diffracted shock passes over the base of the receiver and does not reach the farside (Figure 4.30 (a), Figure 4.56 and Figure 4.57). This observation is confirmed with examination of the farside pressure distribution where there is negligible influence of the diffracted shock for all axial configurations (Figure 4.58). Consequently, the effect of axial impingement location on the interference loads is determined solely by the nature of the interactions between the impinging disturbances and the nearside flowfield (Figure 4.59).

4.6.3.2 Flowfield characteristics for the configurations at σ_R=15°

A nearside pressure rise is observed in all configurations, induced by the impinging shock with the exception of the Δx/D=2.68 configuration where it is the result of the pre-compression from the generator bow shock passing upstream of the receiver leading edge. The characteristics of the nearside interactions for the two configurations where the generator is upstream of the receiver (Δx/D=2.68 and

Δx/D=1.67) are different from the other two configurations where the generator is axially aligned (Δx/D=0) and downstream of the receiver (Δx/D=-1.65). When the axial impingement location is upstream of the axial roll-up location of the body vortices (as for Δx/D=2.68 and Δx/D=1.67), the expansion waves from the generator forebody strongly reduce the receiver nearside pressure after the initial rise. Moreover, the skin friction footprint of the impinging shock tends to turn the flow in the opposite-direction to the natural crossflow induced by the body incidence. This has the effect of delaying the axial roll-up location of the primary vortices further aft along the receiver than the isolated configuration (Figure 4.60 (a)-(c)). The influence of this can be seen in the corresponding nearside pressure distribution for both configurations in Figure 4.59 where the pressure footprints show that the development of the body vortices occur further aft on the body.

When the impingement location is aft of the roll-up location of the body vortices (as in Δx/D=0 and Δx/D=-1.65) then the impinging expansion waves have little effect of the nearside flowfield and the body vortex is the dominant flow feature in determining the leeside (nearside) pressure distribution (Figure 4.59) after the initial compression. For example, the local pressure trend after the initial rise is similar to the isolated configuration where the body vortices dominate the local pressure distribution. The predicted skin friction line plots (Figure 4.60 (d)-(e)) show little effect on the vortex roll-up location since the impingement location is aft of the roll-up location for the isolated configuration and this is also reflected in the nearside pressure distributions for configurations where Δx/D=0 and Δx/D=-1.65.

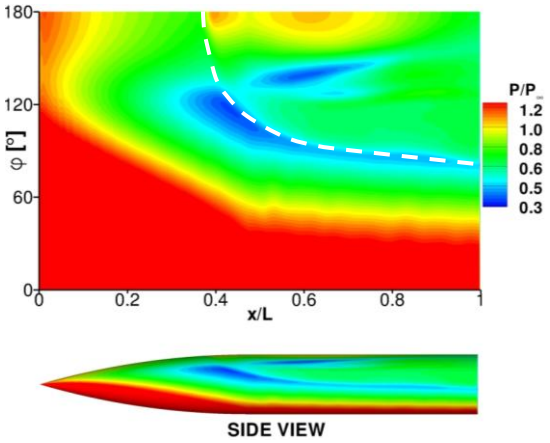

Figure 4.56 Predicted receiver surface pressure contours highlighting approximate impinging shock path (dashed): m2651 m2653, Δx/D=0 Δz/D=2.94, σ_R=15° σ_G=0°

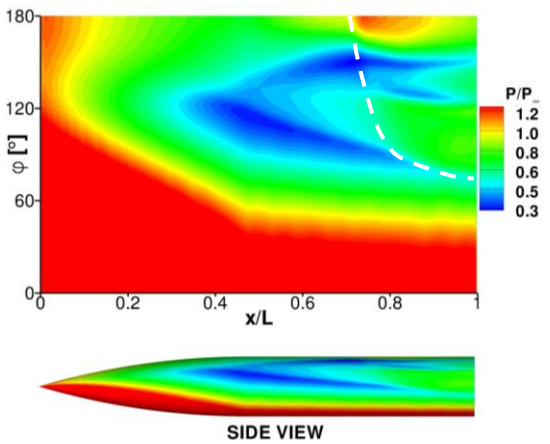

Figure 4.57 Predicted receiver surface pressure contours highlighting approximate impinging shock path (dashed): m2651 m2653, Δx/D=-1.65 Δz/D=2.94, σ_R=15° σ_G=0°

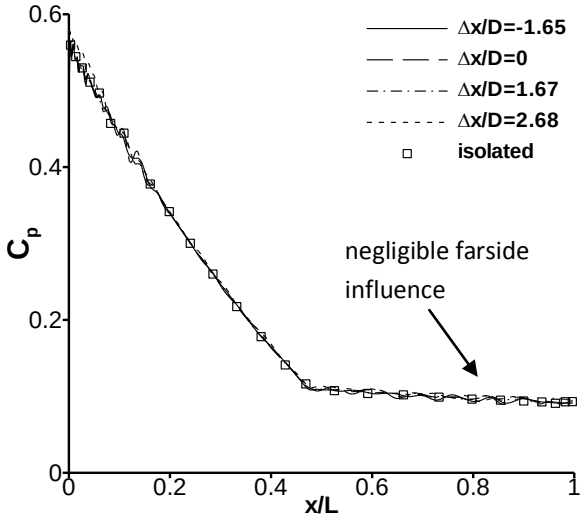

Figure 4.58 Effect of axial stagger on predicted receiver farside pressure distribution: m2651 m2653, Δz/D=2.94 σ_R=15° σ_G=0°

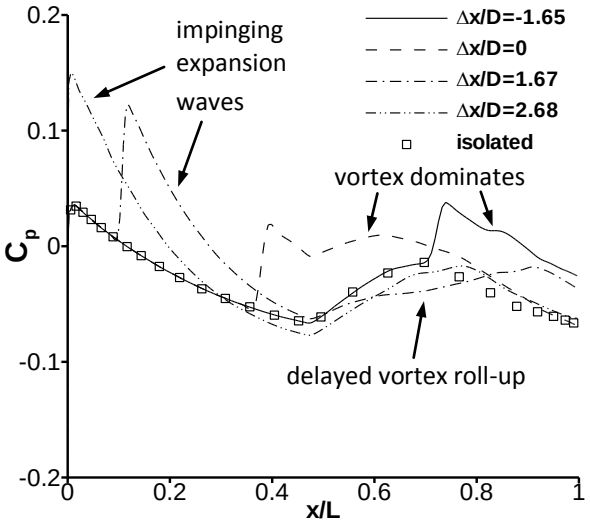

Figure 4.59 Effect of axial stagger on predicted receiver nearside pressure distribution: m2651 m2653, Δz/D=2.94 σ_R=15° σ_G=0°

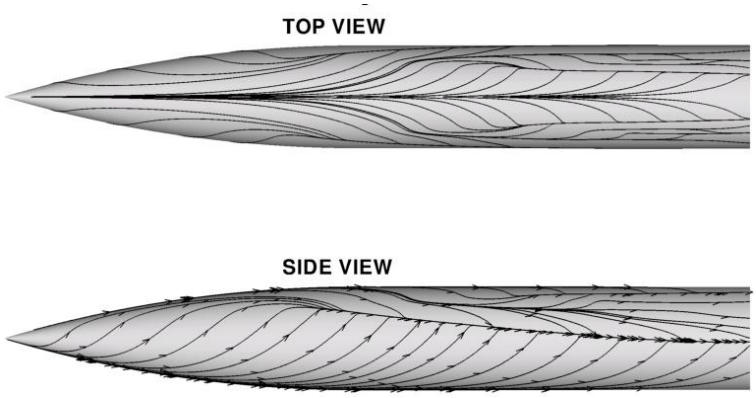

(a) m2651 isolated σ_R=15°

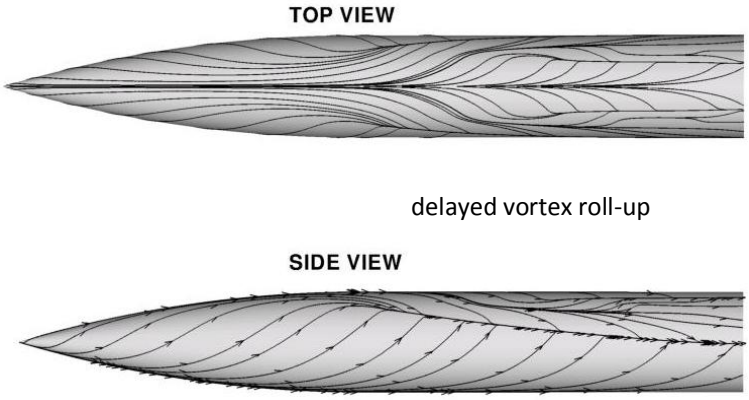

(b) Δx/D=2.68

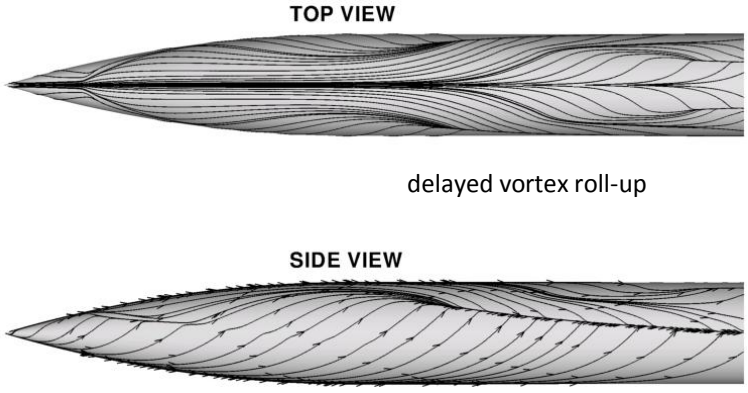

(c) Δx/D=1.67

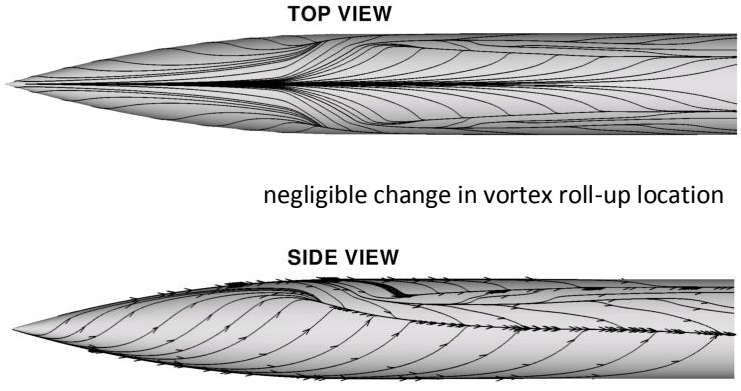

(d) Δx/D=0

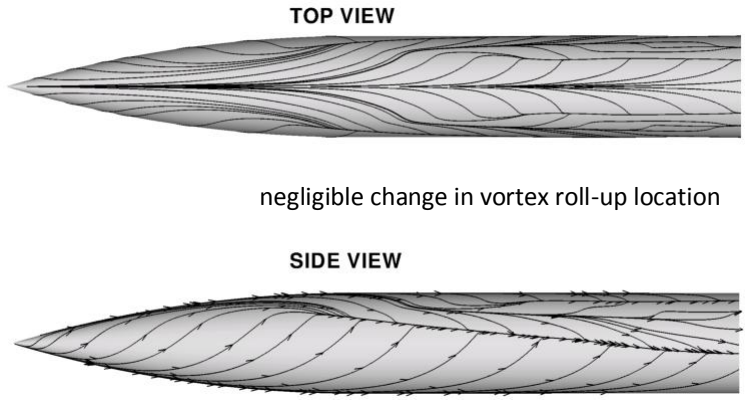

(e) Δx/D=-1.65

Figure 4.60 Predicted surface skin friction vector lines for the (a) isolated configuration and (b-e) different axial stagger settings: m2651 m2653, Δz/D=2.94, σ_R=15° σ_G=0°

4.6.3.3 Receiver local normal force distributions for configurations at σ_R=15°

The axial impingement location has a significant effect on the receiver nearside pressure distribution and these regions of differential pressure, in turn, affect the local normal force distribution (Figure 4.61). This is expressed as a change in the local normal force distribution from the isolated configuration in Figure 4.62 in order to see the interaction characteristics more clearly. When the generator bow shock misses the receiver (Δx/D=2.68) the local normal force distribution is dominated by an increase in the positive local normal force region induced by the impinging expansion waves acting over a large portion of the body nearside. This leads to an overall positive normal force interference load (ΔC_Z=0.03) and negative pitching moment interference (ΔC_m=-0.17). As the impingement location moves aft, the influence of the impinging expansion waves diminishes (acting over a smaller extent for Δx/D=1.67) until they have a negligible effect (as in Δx/D=0 and Δx/D=-1.65). For the latter two configurations there are no regions of positive $\Delta dC_Z/dx$ induced at all and the interference footprints contribute solely to a negative overall normal force interference load. Finally, the Δx/D=1.67 and Δx/D=0 configurations induce the largest magnitude of interference loads (Figure 4.62) as a result of large extent over which the nearside region of positive differential pressure acts over the body (Figure 4.54 and Figure 4.55).

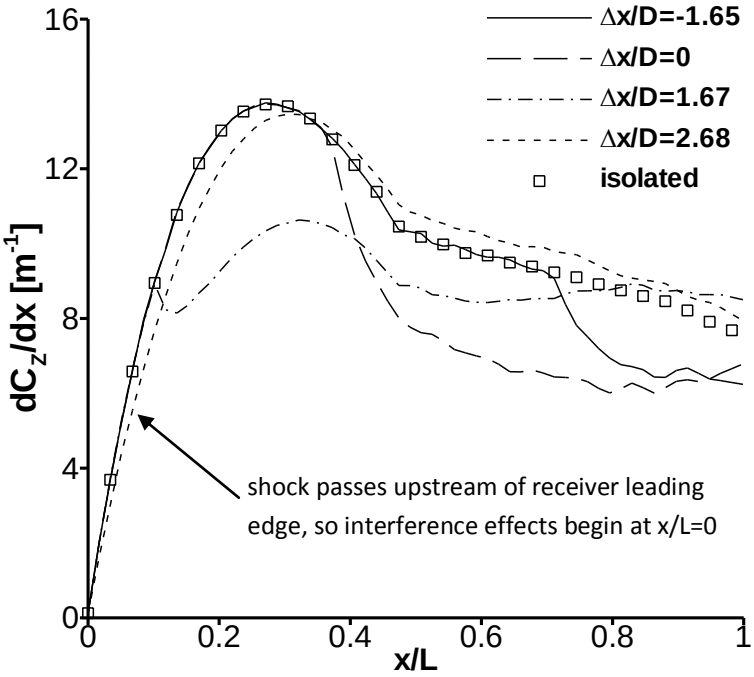

Figure 4.61 Effect of axial stagger on predicted receiver local normal force distribution: m2651 m2653, Δz/D=2.94, σ_R=15° σ_G=0°

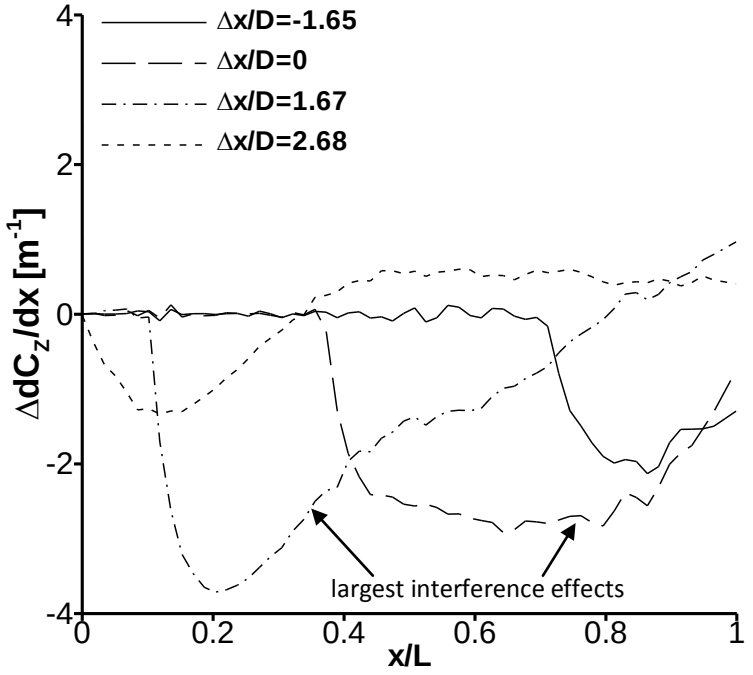

Figure 4.62 Effect of axial stagger on predicted receiver change in local normal force distribution from the isolated configuration: m2651 m2653, Δz/D=2.94, σ_R=15° σ_G=0°

4.6.4 Summary discussion on the effect of axial impingement location

The axial impingement location has a profound effect on the magnitude and polarity of the interference loads induced by the disturbance flowfield. When the impingement

location (x'/L) is close to the leading edge, the interactions which induce regions of positive local normal force over the body dominate and there is a positive overall normal force interference ($\Delta C_Z > 0$) and a negative pitching moment interference ($\Delta C_m < 0$). As the impingement location moves aftward, the normal force interference becomes more negative with a concomitant increase in pitching moment interference. This is due to the diminishing extent of the nearside region of negative differential pressure and farside region of positive differential pressure.

The change in polarity is significant as it shows that the interference effects initially attract ($\Delta C_Z > 0$) the receiver towards the generator when x'/L is close to the leading edge. However, this changes to a repulsive interference force ($\Delta C_Z < 0$) when the impingement location is towards the trailing edge. Moreover, the interference effects cause the receiver to pitch-up towards the generator when x'/L is aft of the body centre of gravity location ($x'/L > 0.6$), thus increasing the likelihood of a collision.

The only examples of where these observations are different is when the receiver is placed at $\sigma_R = 15°$. For these configurations, the diffracted shock does not reach the receiver farside as a result of the shock obliqueness angle and this is the characteristic difference to the other cases. As a result the effect of axial stagger is much more case specific and non-monotonic. It is observed, however, that the resulting interference loads are closely related to x'/L and whether this is fore or aft of the body vortex roll-up location. The latter situation results in the largest observed interference effects of up to $\Delta C_Z = -0.235$ ($\sigma_{eff} = -1.8°$) and $\Delta C_m = 1.1$ ($\sigma_{eff} = -2°$) for $\Delta x/D = 0$.

4.7 The impact of a viscous interaction on the interference effects

The discussion thus far, has shown that shock interactions with viscous flow features can significantly influence the nature of the interference effects. The importance of the viscous flow features is expected due to their significant impact on the surface pressure distribution and thus the body loads of a slender body (§4.1). Moreover, in other multi-body studies, impinging shockwaves have been observed to interact with, and significantly alter, the nominal flow structure of the boundary–layer[34,58]. Consequently, a selection of relevant configurations exhibiting strong interactions with the viscous flow features are now investigated using CFD predictions to understand the underlying flow physics.

4.7.1 A supercritical shockwave boundary-layer interaction

One configuration which involves a supercritical Shock Boundary-Layer Interaction (SBLI) is when the un-finned receiver is placed adjacent to the blunt generator at an axial stagger of $\Delta x/D=-0.53$ and at an incidence of $\sigma_R=15°$ (Figure 4.63 (a)). The language 'supercritical' is used here to indicate that there is a local shock-induced separation of the receiver nearside boundary-layer. The impinging generator bow shock induces a large nearside pressure rise ($\Delta C_{p,near}=0.47$) as a result of the close proximity between the impingement location and the generator leading edge ($\Delta z_{sh}/D=1.2$). The induced adverse pressure gradient across the impinging shock results in a thickening of the local boundary-layer and a region of separated flow.

A simplified sketch of a 2D oblique shock interaction with a boundary-layer is shown in Figure 4.63 (c) to highlight the likely characteristics of the local flowfield on the receiver nearside symmetry plane more clearly. The separation bubble contains locally recirculating flow and is bounded by a streamline, which separates from point S and re-attaches at the attachment point A in Figure 4.63 (c). The presence of the region of separated flow leads to the formation of a separation shockwave upstream of point S in order to turn the oncoming flow around the 'obstacle'. Downstream of the separation bubble, the separated shear layer re-attaches and a re-attachement shock is formed to re-align the local flow with the solid surface. This is the reason why a

double-shock structure (separation and re-attachment shock) is visible in the close up of the receiver nearside flowfield in Figure 4.63 (b). Finally, this flowfield feature was also observed in similar studies of a shock impinging on a cylindrical body by Brosh[10,30] and Morkovin[32].

4.7.1.1 Horse-shoe vortex system

The local separation region described above leads to a horse-shoe vortex on either side of the body (Figure 4.63 (a), Figure 4.64 (a)). A well defined separation line, S1 line is observed (Figure 4.64 (b)). A vortex feeding sheet rolls-up into a small horse-shoe vortex structure with its core close to the surface and re-attaches further leeward at A2. There is also evidence of a weaker secondary vortex underneath the horse-shoe vortex with the secondary separation and attachment lines S2 and A3 respectively.

The horse-shoe vortex structure initially spans windward in the direction of the shock path as x/L increases. After a short distance along the body, the momentum of the natural crossflow begins to dominate the local flow structure and forces the horse-shoe vortex leeward. It reaches close to the symmetry plane and then travels towards the base of the receiver as shown by the red streamtrace ribbons in Figure 4.64 (a). This is significant because the horseshoe vortex trails a low pressure region underneath the core as can be seen in Figure 4.64 (b). This has a moderate vortex suction effect on the local pressure distribution and is a direct consequence of the viscous interaction rather than the presence of an impinging shock (i.e. this doesn't occur for the equivalent configuration using the sharp generator).

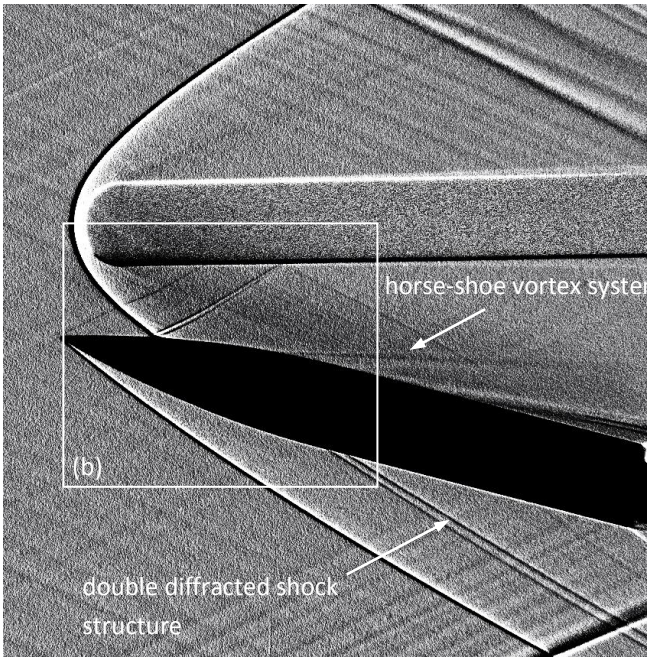

(a) Full flowfield

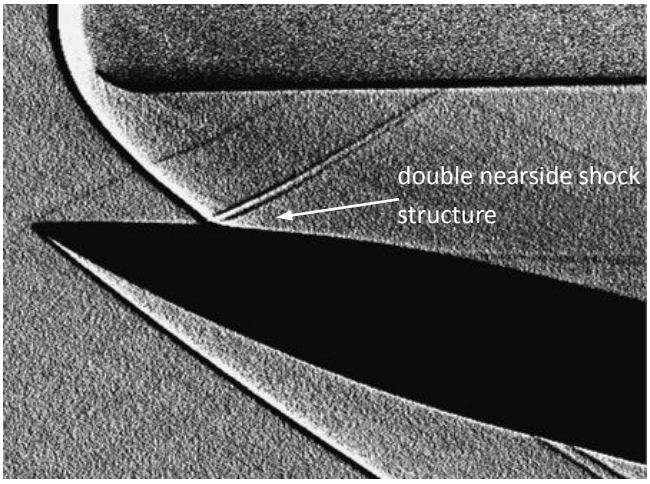

(b) Close-up of the nearside interaction region

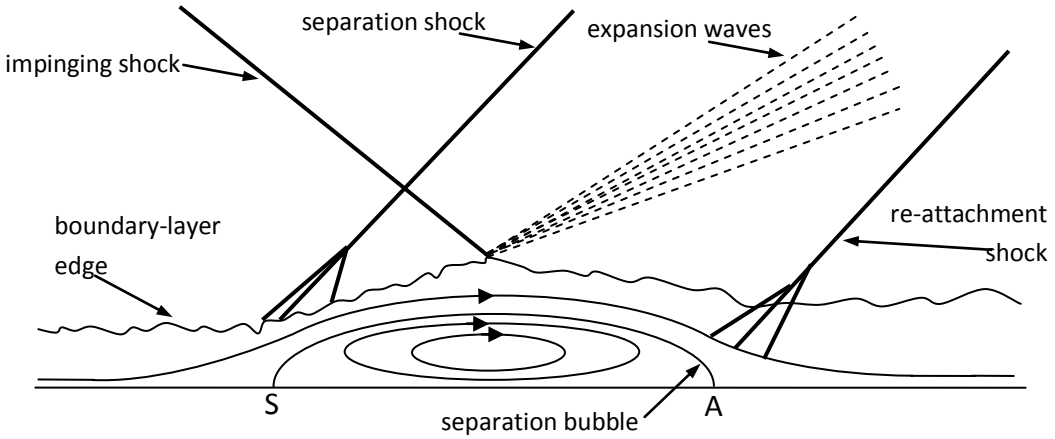

(c) Sketch of the SBLI on the nearside symmetry plane and the double shock structure

Figure 4.63 (a,b) Measured shadowgraph visualisation: m2651 m2654, Δx/D=-0.53 Δz/D=2.94, σ_R=15° σ_G=0° and (c) a sketch of the local itneraction

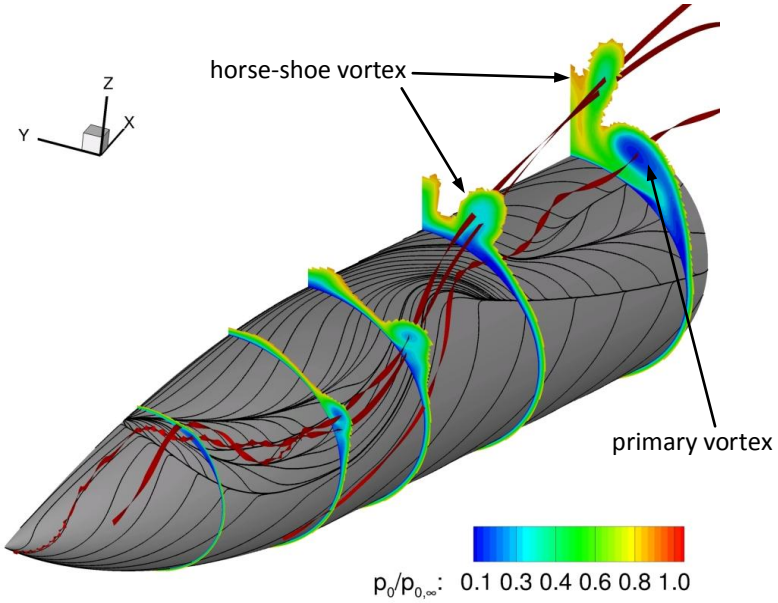

(a) Surface skin friction vector lines, crossflow slices contours of $p_0/p_{0,\infty}$, highlighting streamtraces ribbons coloured red

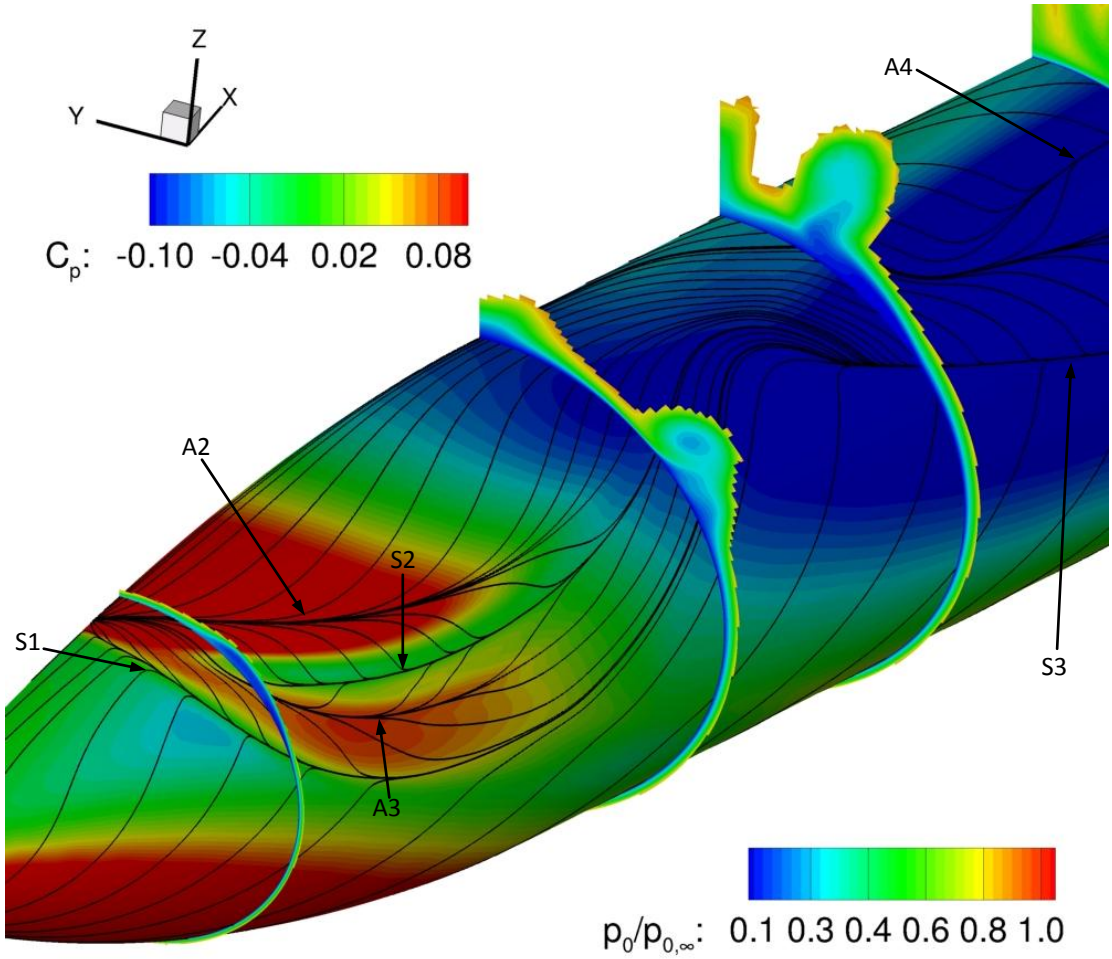

(b) Surface skin friction vector lines, crossflow slices of total pressure ($p_0/p_{0,\infty}$) contours, surface pressure contours of static pressure coefficient (C_p)

Figure 4.64 Predicted flowfield features highlighting the viscous flow structure: m2651 m2654, Δx/D=-0.53 Δz/D=2.94, σ_R=15° σ_G=0°

4.7.1.2 Body vortex roll-up location

As a result of the substantive re-organisation of the body crossflow due to the local separation region, the body vortex roll-up location (Figure 4.65 (a)) is much further aft than both the isolated configuration (Figure 4.65 (b)) and the equivalent multi-body configuration using the sharp generator where there is no supercritical interaction (Figure 4.65 (c)). Therefore, the presence of the horse-shoe vortex and the characteristic differences in body vortex development has a notable effect on the receiver pressure distribution. The decrease in area over which the body vortices act reduces the vortex-lift component of the normal force compared with the sharp generator configuration (with a subcritical interaction) and the isolated configuration (with no interaction). Moreover, the primary vortex is smaller and closer to the surface (Figure 4.64 (a)) in comparison to the isolated configuration (Figure 4.10).

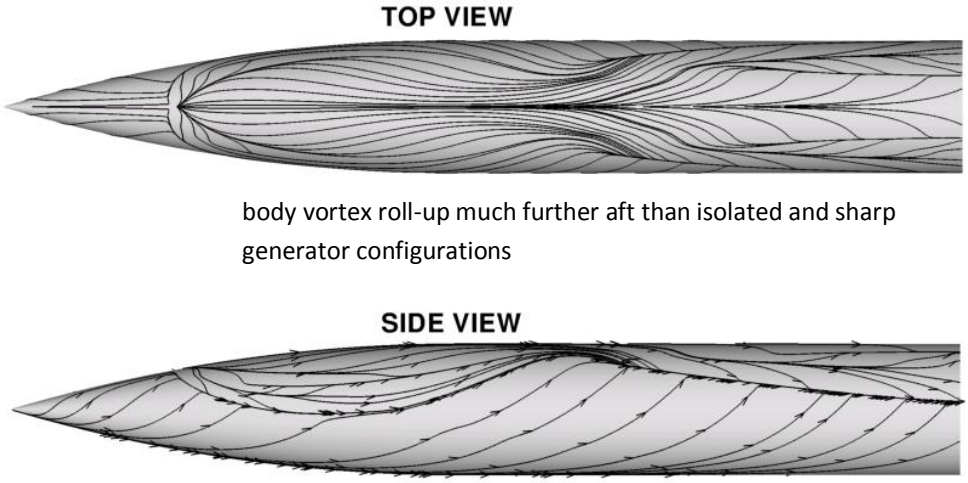

(a) blunt generator: m2651 m2654, Δx/D=-0.53 Δz/D=2.94, σ_R=15° σ_G=0°

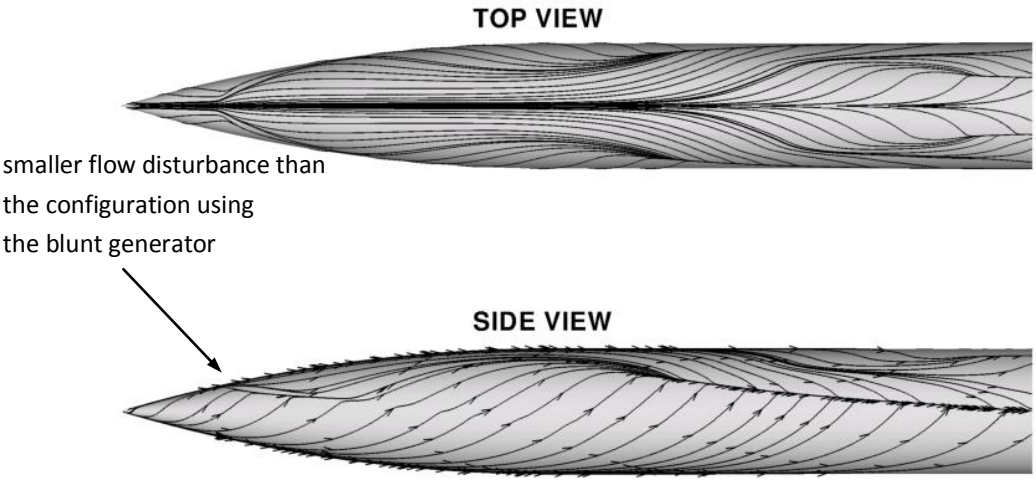

(b) sharp generator: m2651 m2653, Δx/D=1.67 Δz/D=2.94, σ_R=15° σ_G=0°

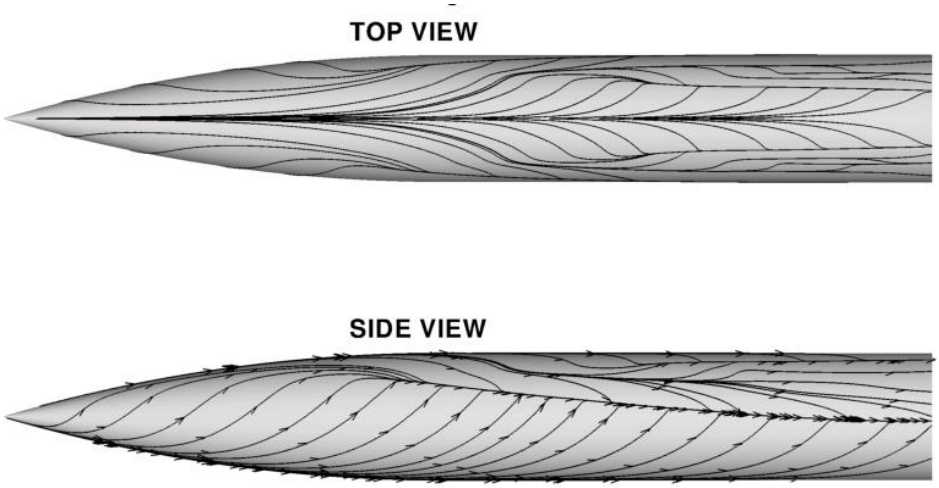

(c) isolated: m2651 σ_R=15°

Figure 4.65 Predicted receiver surface skin friction vector lines for different configurations

4.7.1.3 Effect on diffracted shockpath

The differences discussed above due to the supercritical interaction are important as they will affect the surface pressure distribution and thus the body loads. However, there is another important observation for this configuration. A significant consequence of the viscous interaction is that the shock now diffracts to the farside whereas for the configuration involving the sharp generator it does not. The natural shock path for the equivalent configuration with the sharp generator is for the diffracted shock to exit through the receiver base (Figure 4.30 (a)) and there is no influence on the receiver farside (Figure 4.31 (a)). The viscous interaction characteristically changes this and the resulting separation region acts as a further obstacle to the flow. A separation shock forms forward of the separation region and primary impinging shock. Both of these shockwaves then diffract to the farside where the double shock structure on the receiver farside can be seen in Figure 4.63 (a).

As a result of the viscous interaction, a farside region of positive differential pressure will act to reduce the negative change in normal force induced by the nearside region of positive differential pressure, the importance of which has been previously described. A similar characteristic is observed for another pair of configurations for the same axial stagger and a receiver incidence of σ_R=8° (Figure 4.66, Figure 4.67). The diffracted shock reaches the receiver farside for both of these cases, but the induced crossflow separation for the blunt generator case leads to the diffracted shock

reaching the farside further fore than the sharp case. This difference is too large to be due to the small differences in the shock obliqueness angles between the sharp and blunt generator bow shocks and the extent of the farside region of positive differential pressure doubles (Figure 4.68).

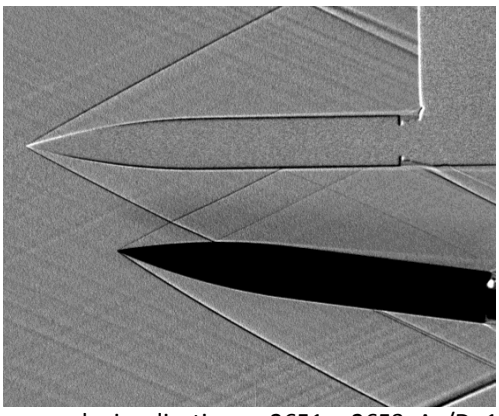

Figure 4.66 Measured shadowgraph visualisation: m2651 m2653, Δx/D=1.67 Δz/D=2.94, σ_R=8° σ_G=0°

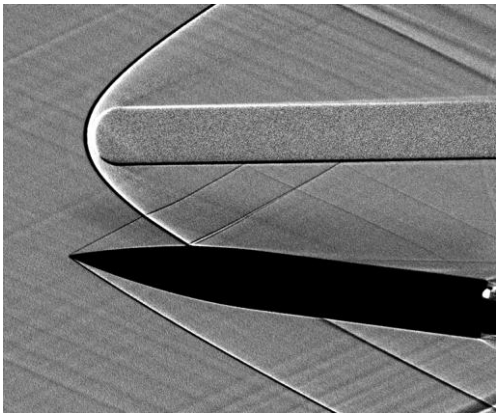

Figure 4.67 Measured shadowgraph visualisation: m2651 m2654, Δx/D=-0.53 Δz/D=2.94, σ_R=8° σ_G=0°

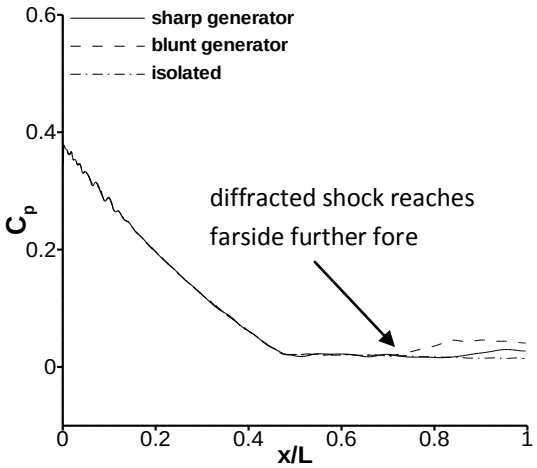

Figure 4.68 Effect of the blunt generator on the predicted farside receiver pressure distribution: m2651, Δz/D=2.94, σ_R=8° σ_G=0°

4.7.2 Summary

In summary, the viscous shock interactions have a significant impact on the leeside flow structure and thus the receiver body pressure distribution. A complex horse-shoe vortex system is observed in a number of configurations as well as a delay in the roll-up of the body vortices. Most importantly, the size and location of the separation regions can influence the impinging shock path and thus promote the diffraction of the impinging shock around the receiver body. All of these specific changes as a result of the viscous flow behaviour alters the local normal force distribution along the body and thus also the interference loads. Finally, it is clear that the viscous interactions can have a 1st order effect on the characteristics of interference effects.

4.8 Summary of chapter findings

The aerodynamics of the un-finned receiver have been investigated for the body in isolation and a number of multi-body arrangements. The isolated aerodynamics are typical of a slender body under supersonic conditions where the streamwise load distribution and complex leeside flow structure become more significant as the body incidence increases. When a generator body is placed in close proximity, the interference loads acting on the receiver body are a function of the complex local regions of differential pressure induced by the disturbance flowfield. The aerodynamics become more complicated for configurations where there is extensive propagation of the impinging disturbances to the farside of the receiver body.

Understanding how the interference loads vary with different geometric parameters is not simple. However, the interference loads are found to be a function of three main parameters for a given configuration which characterise the interference effects. These are

- the axial impingement location which primarily affects the extent of the nearside regions of differential pressure
- the impinging shock obliqueness angle which affects the extent of the farside regions of differential pressure
- the relative position of the receiver body within the disturbance flowfield which affects the strength of all impinging disturbances

General trends are often hard to extract and the interference characteristics tend to be bespoke to each configuration. Nevertheless, the following conclusions are drawn from the results in this chapter.

- The interference effects decrease with increasing lateral separation. This also depends on the initial axial arrangement of the bodies.
- The interference effects are larger when the receiver is at incidence.

- The interference effects generally increase for a stronger disturbance flowfield. However, there are notable configurations where interference loads are insensitive to the disturbance flowfield strength.
- The axial impingement location has a profound effect on the magnitude and polarity of the interference loads. Completely opposing effects in the forces and moments are observed when the impingement point changes.
- Shock interactions with the viscous flow features have been found to characteristically change the interference effects.
- Shock induced separation can occur and has a significant effect on the interference loads.
- Very good agreement is found between the measured and predicted interference loads throughout.
- The pressure footprints are predicted well in terms of location and magnitude in comparison to the PSP measurements. This gives confidence that the CFD is predicting the correct interference loads for the correct reasons.

Chapter 5 The Changing Nature of the Interference Effects for Bodies with Control Surfaces

A receiver body with fins attached at the trailing edge is investigated in this chapter. The finned receiver is statically stable over a large incidence range and is therefore more interesting and relevant than the simplified investigation presented in Chapter 4. This chapter investigates how the addition of fins changes the nature of the interference flowfield in comparison with the un-finned receiver configurations and what impact this has on the interference effects.

This chapter focuses on the following key areas for discussion:

- The aerodynamics of the finned receiver in isolation (§5.1)
- The effect of axial impingement location on the interference effects for a finned receiver in comparison to an un-finned body (§5.2)
- The effect of receiver incidence on the interference effects for a finned receiver in comparison to an un-finned body (§5.3)
- A summary of the chapter findings (§5.4)

As in the previous chapter, the interference aerodynamics and elemental flow features tend to be bespoke to each configuration and the extraction of simple and general trends is difficult. The flow physics involved in the finned receiver configurations tend to be even more complicated than what has been presented thus far. In order to clarify the effects as much as possible, this discussion is structured in such a way as to breakdown the non-linear nature of the problem and make it easier to understand. To this end, the discussion of the interference effects initially focuses on simpler configurations where the receiver incidence is zero. Further analysis is then devoted to configurations where the receiver is at incidence and where the aerodynamics

becomes more complex. For any given configuration, the elements of the interference flowfield already discussed in the previous chapter for the equivalent un-finned receiver configuration will not be repeated here. Instead, this chapter will primarily focus on the differences induced by the presence of the fins on the interference effects. Finally, both the experimental and computational datasets are used in the discussion of the underlying aerodynamics.

The only measured data for the finned receiver was taken in the S20 SWT tunnel (at M_∞=2.43, Re_D=1.4x10^6). These tests repeated many of the un-finned configurations using both the sharp and blunt generator and the measurements were taken on the finned receiver. Throughout this chapter, the finned receiver is orientated at zero sideslip (β=0°) and in the roll configuration where the fins are in a '+' arrangement (λ=0°) in order to simplify the problem as much as possible. Furthermore, the lateral separation and generator incidence are maintained at Δz/D=2.94 and σ_G=0° respectively throughout. As in the previous chapter, a subset of the experimental configurations are modelled using CFD (at σ_R=-15, -8, 0, 8, 15°) and are used to further investigate the underlying aerodynamics.

5.1 Isolated aerodynamics of the finned receiver

This chapter begins with an evaluation of the aerodynamics of the finned receiver body in isolation. This includes a description of the force and moment characteristics as a function of incidence (§5.1.1) and the important flowfield features (§5.1.2) pertinent to the forthcoming analysis of the multi-body configurations. This section also gives an insight into the basic aerodynamic differences between the finned and un-finned receiver bodies in isolation.

5.1.1 Force and moment characteristics of the finned receiver as a function of incidence

A flow angularity correction of σ_{cor}=-0.05° is applied to the measured data presented in Figure 5.1 - Figure 5.4, which ensures zero normal force at zero incidence. As expected, the addition of fins increases the magnitude of the receiver normal force and pitching moment loads in comparison to the un-finned receiver for a given incidence (Figure 5.1, Figure 5.2). The normal force increases by as much as 60% at σ_R=15°. In this configuration, the fins account for a third (35%) of the total normal force load and half (49%) of the total pitching moment load (Table 5.1). The trend of both normal force and pitching moment with incidence is more linear than the un-finned receiver as a result of the additional loads produced by the fins. Good agreement is observed between the measured and predicted C_Z and C_m. However, as in the un-finned configuration (§4.1.1), there remains a small discrepancy between the measured and predicted loads, predominately at high negative incidence. The measurements of C_Z are a maximum of 7% larger than the predictions at σ_R=-15°. As stated in the discussion of the un-finned results (Appendix B.2) this is most likely due to a systematic measurement error and does not affect the interference loads presented in §5.2-5.3.

The axial force remains roughly constant across the incidence range, which is similar to the un-finned receiver trend. This trend is predicted well by the CFD (Figure 5.3). However, the CFD under-predicts the magnitude of the measured values by an average of 11% across the incidence range and these lie outside the stated experimental

uncertainty. Moreover, the predicted values show that the fins account for approximately half of the total axial force loads for most incidence angles. The measured and predicted values of C_Y, C_l, and C_n are all zero and not presented here.

	σ_R=0°			σ_R=8°			σ_R=15°		
	C_X	C_Z	C_m	C_X	C_Z	C_m	C_X	C_Z	C_m
body	0.18	0	0	0.18	0.59	-2	0.18	1.59	-6.16
fin	0.15	0	0	0.15	0.55	-3.68	0.17	0.86	-5.81
total	0.33	0	0	0.33	1.14	-5.68	0.35	2.45	-11.97

Table 5.1 Predicted force contributions from the body and fins for different incidence settings: m2652 isolated

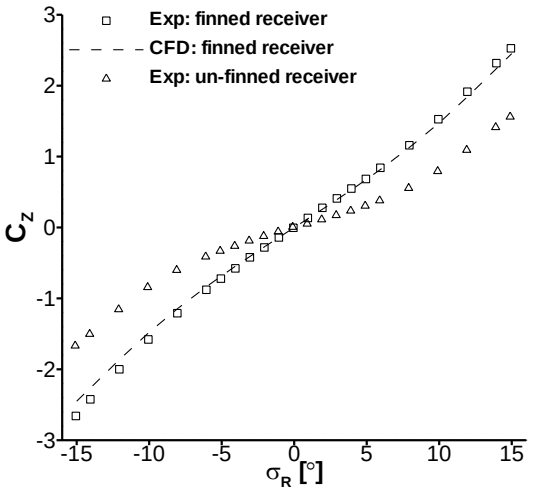

Figure 5.1 Normal force as a function of incidence for the finned and un-fined receiver bodies in isolation (error bars removed for clarity)

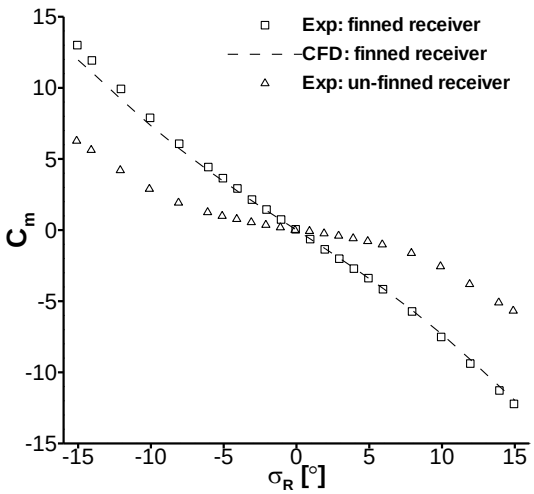

Figure 5.2 Pitching moment as a function of incidence for the finned and un-finned receiver bodies in isolation (error bars removed)

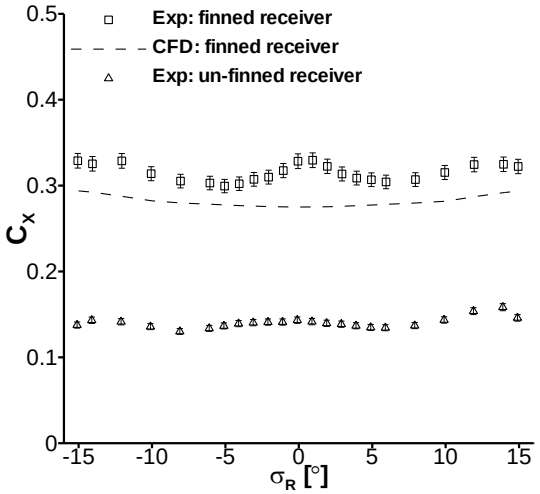

Figure 5.3 Axial force (corrected for base pressure) as a function of incidence for the finned and un-finned receiver bodies in isolation

The addition of fins to the trailing edge of the receiver body moves the centre of pressure aftward to a position of $X_{cp}/D \approx 5$ which remains approximately fixed across the incidence range (Figure 5.4). Importantly, this is aft of the centre of gravity location ($X_{cg}/D=4.55$) and results in a positive static margin, meaning that the body is statically stable over the incidence range studied. A typical magnitude of the marginal static margin is equal to $X_{sm}/D=0.3$ for a receiver incidence of $\sigma_R=\pm 15°$. Moreover, good agreement is observed between the measured and predicted values of X_{cp} with a maximum difference in the order of 0.1 calibres.

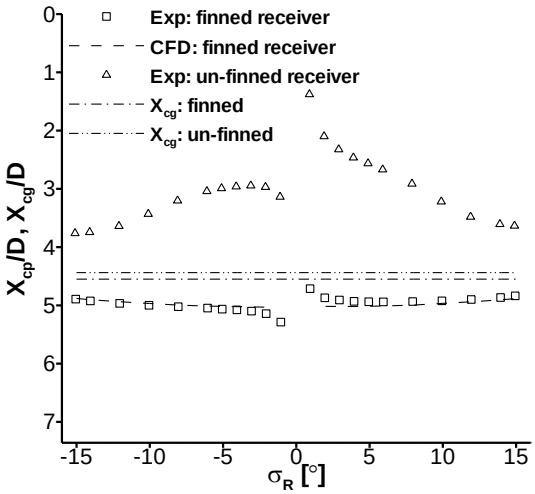

Figure 5.4 Longitudinal centre of pressure location as a function of incidence for the finned and un-finned receiver bodies in isolation

5.1.2 Flowfield features of the finned receiver at $\sigma_R=0,8,15°$

Good agreement is seen between the measured and predicted forces and moments, and the predicted flowfield solutions are now used to understand the important flowfield features introduced by the fins for $\sigma_R=0,8,15°$. Upstream of the receiver fins, a description of the bow-shock and forebody expansion structure, as well as the pressure distribution over the body is given in §4.1.2 and will not be repeated here. Instead, the inter-fin shock structure and accompanying pressure distributions are briefly described. In the finned receiver configurations discussed throughout this chapter, the lifting fins are positioned at $\phi=90°,270°$ on the body. Since the receiver body is at zero roll ($\lambda=0°$), these are located on the body-fixed pitching plane. The body is always at zero sideslip and although the reported fin loads in this chapter include all 4 fins, the subsequent in-depth analysis focuses on the lifting fins.

Moreover, these are usually referred to from here on as a lifting *fin* rather than fins, recognising the symmetry about the X-Z axis.

The leading edge shock structure on the lifting fin is important as it influences the surface pressures on both the fin itself and the body within the inter-fin region. When the receiver incidence is zero, the strength of the upper and lower portions of the shock emanating from the leading edge of the lifting fin are equal. Both of these shocks intersect with the equivalent shocks emanating from the normal fins located on the X-Z symmetry plane at $\phi=0,180°$ (Figure 5.5 (a)). This leads to a high pressure region in the inter-fin region bounded by both shocks and this is also seen in the axial pressure distributions on the body taken at $\phi=45,135°$ (Figure 5.6 (a), (b)). Since the effect of the fins on the body are equal in the upper and lower inter-fin regions there is no change in local normal force induced by this region.

As the receiver incidence increases, the lower portion of the lifting fin leading edge shock strengthens and the upper portion weakens (Figure 5.5 (b),(c)). Moreover, the shock angle at which the shock propagates increases for the lower portion of the leading edge shock as the incidence increases. The augmented shock strength leads to regions of elevated pressure in the lower inter-fin region (Figure 5.6 (b),(c)). The opposite is observed in the upper fin region where the local shock footprint decreases in magnitude as incidence increases (Figure 5.6 (a),(c)).

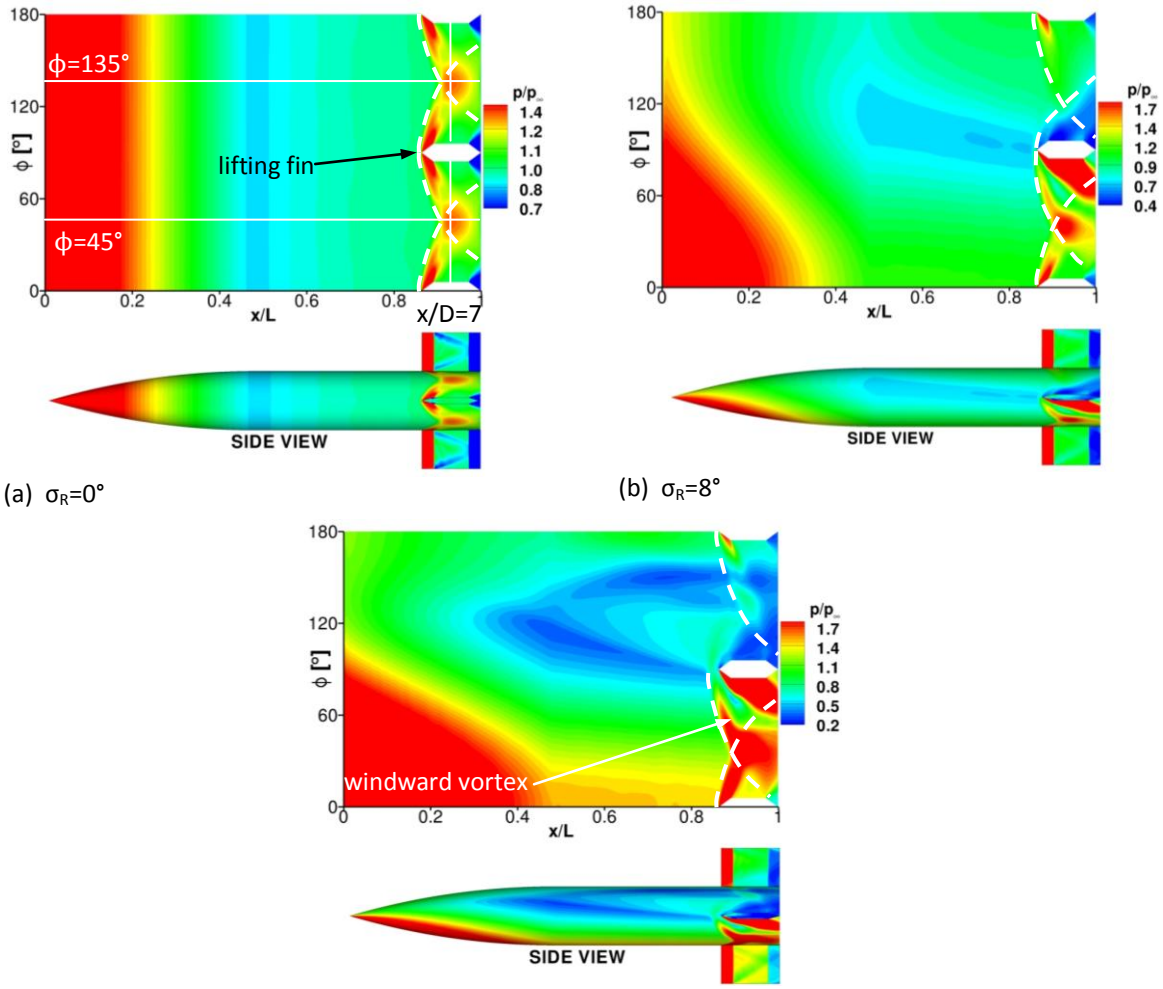

(a) σ_R=0°

(b) σ_R=8°

(c) σ_R=15°

Figure 5.5 Predicted receiver surface pressure contours highlighting the approximate inter-fin shock paths (dashed) for different receiver incidence settings (a-c): m2652 isolated. Note the different contour levels.

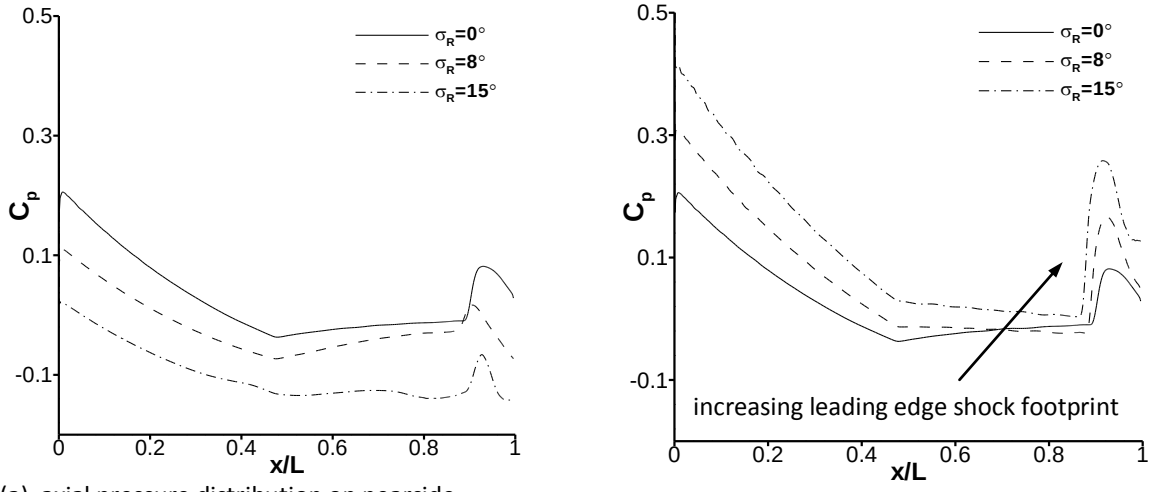

(a) axial pressure distribution on nearside (ϕ=135°)

(b) axial pressure distribution on farside (ϕ=45°)

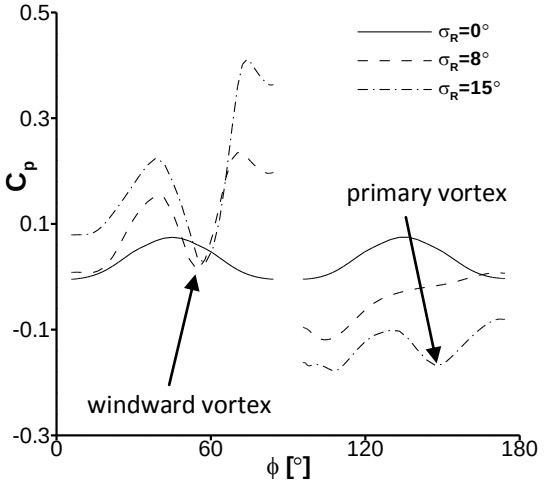

(c) circumferential pressure distribution at x/D=7

Figure 5.6 Predicted receiver surface pressure distributions along different planes (a-c) and for different incidence angles: m2652 isolated

Finally, a shock-induced windward vortex develops in the lower inter-fin region for a receiver incidence of σ_R=8 and 15°. This is the result of a glancing shock interaction between the leading edge shock from the lower surface of the lifting fin and the local boundary-layer (Figure 5.7 (a)). This flow feature is not observed at σ_R=0°. However, as the incidence increases, so does the strength of the leading edge shock from the lower surface of the lifting fin. When the receiver incidence is σ_R=15°, this leads to a well defined separation line (Figure 5.7 (b)) from which the local flow separates and rolls up into a small vortex close to the surface. The windward vortex is not as large as the primary vortex but it does have a noticeable effect on the inter-fin pressure distribution (Figure 5.6 (c)) and acts to reduce the local contribution of the inter-fin region to normal force.

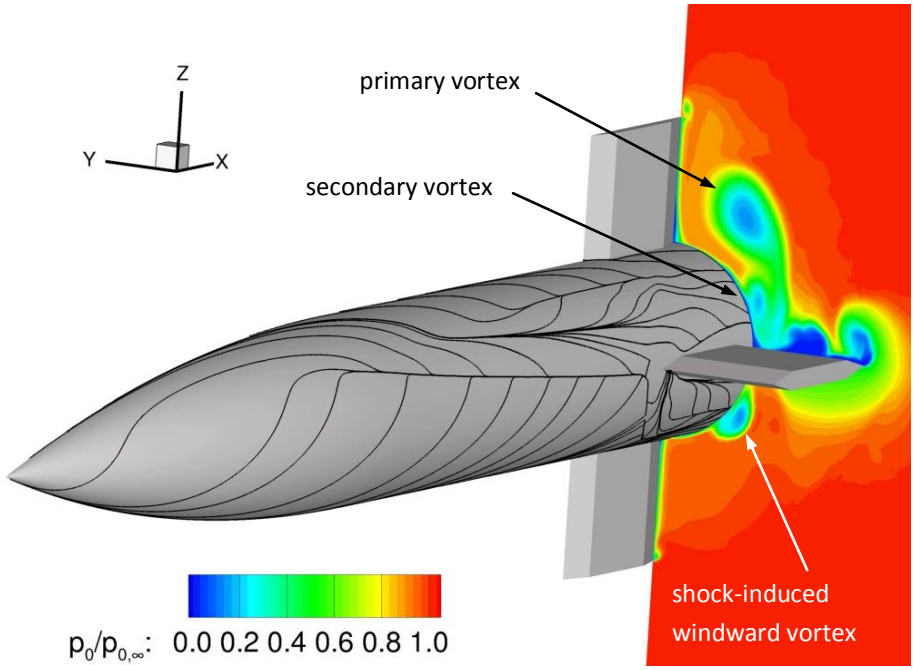

(a) full domain

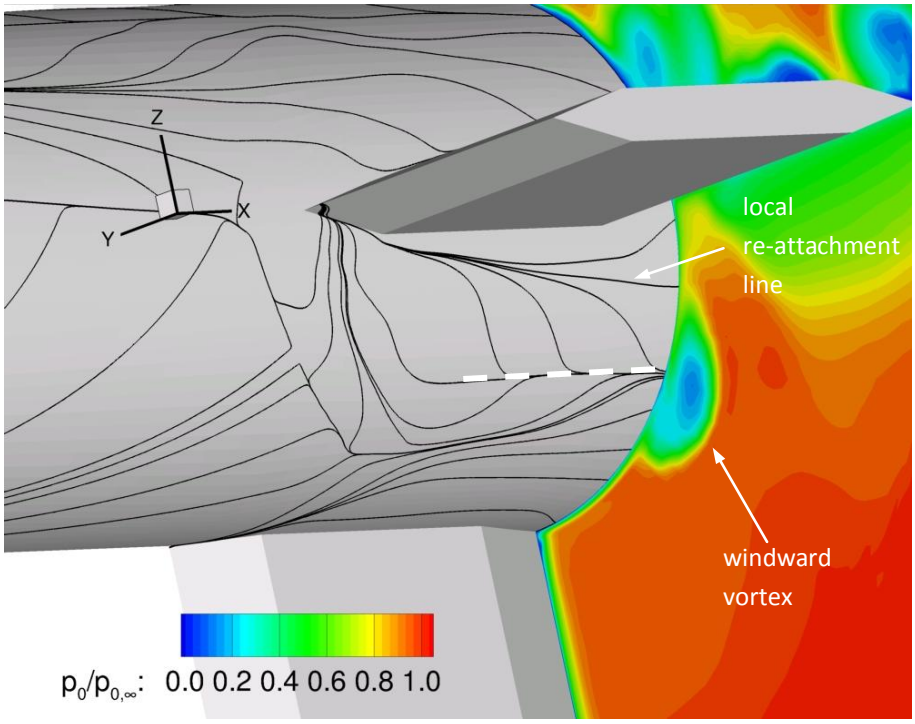

(b) close-up of the windward vortex highlighting local flow separation line (dashed)

Figure 5.7 Predicted surface skin friction vector lines and contours of $p_0/p_{0,\infty}$ on a crossflow slice at x/L=1: m2652 isolated σ_R=15°

5.2 The effect of axial impingement location on the interference effects for a finned receiver in comparison to an un-finned body

The axial impingement location is known to have a profound effect on the magnitude and polarity of the interference loads acting on the un-finned receiver (§4.6). The addition of fins to the receiver body is expected to intensify the sensitivity of the interference loads to the axial impingement location. The effect that the fins have on the interference loads is investigated for a cross-section of the measurement database. This section discusses configurations which involve the finned receiver and sharp generator and covers five different incidence angles (σ_R=-15, -8, 0, 8, 15°) placed at four axial stagger arrangements ($\Delta x/D$=-1.65, 0, 1.67, 2.68). The predicted flowfield solutions are then used to further understand the effect of fins for a subset of configurations at σ_R=0°.

5.2.1 Effect of axial stagger on the finned receiver force and moment characteristics in comparison to an un-finned body

The finned receiver interference loads are sensitive to the axial stagger between the bodies (Figure 5.8, Figure 5.9) and show the same change in polarity of the interference loads over this axial stagger range as observed in the un-finned receiver cases (§4.6). Non-monotonic trends of both normal force and pitching moment interference are observed as the sharp generator moves aft from upstream of the receiver ($\Delta x/D$=2.68) to downstream of the receiver ($\Delta x/D$=-1.65). In general, the fins only have a notable effect in comparison to the un-finned receiver, when the bodies are axially aligned ($\Delta x/D$=0). However, in this configuration the magnitudes of the interference loads are significantly larger than the un-finned case. These characteristics are the same when the blunt generator is used and the results are not presented here, instead they can be referred to in Appendix C.1.

Since, the finned receiver trends are common for all incidence angles presented, a subset of cases at σ_R=0° will be investigated in this section. However, before doing so a datum finned configuration is first analysed to understand the relevant flow physics

for a finned body. Then some metrics and concepts are introduced which will be used throughout the rest of the chapter.

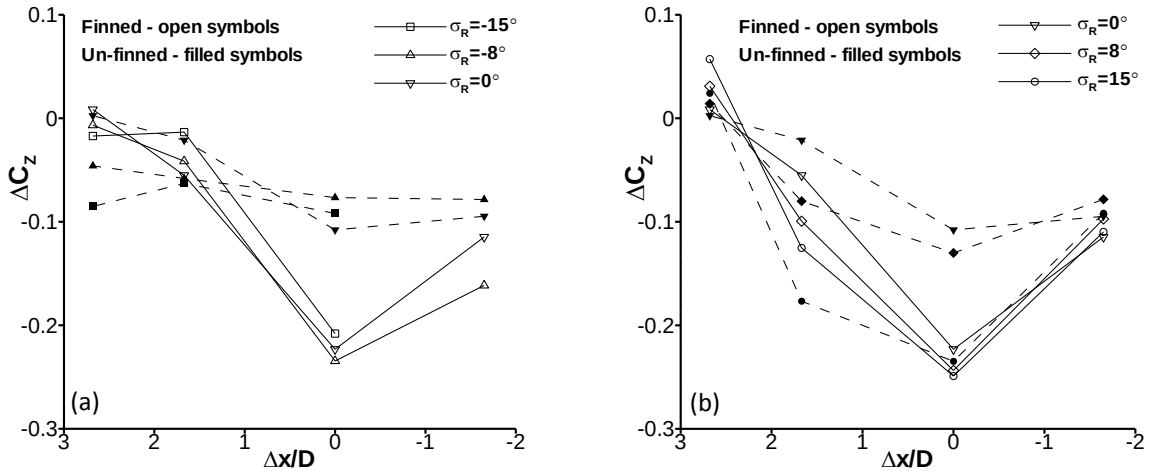

Figure 5.8 Effect of axial stagger on measured receiver normal force interference load for the finned receiver (solid lines) in comparison to the un-finned receiver (dashed lines): m2653, Δz/D=2.94, σ_G=0° for (a) σ_R=-15,-8,0° and (b) σ_R=0,8,15 (error bars removed for clarity)

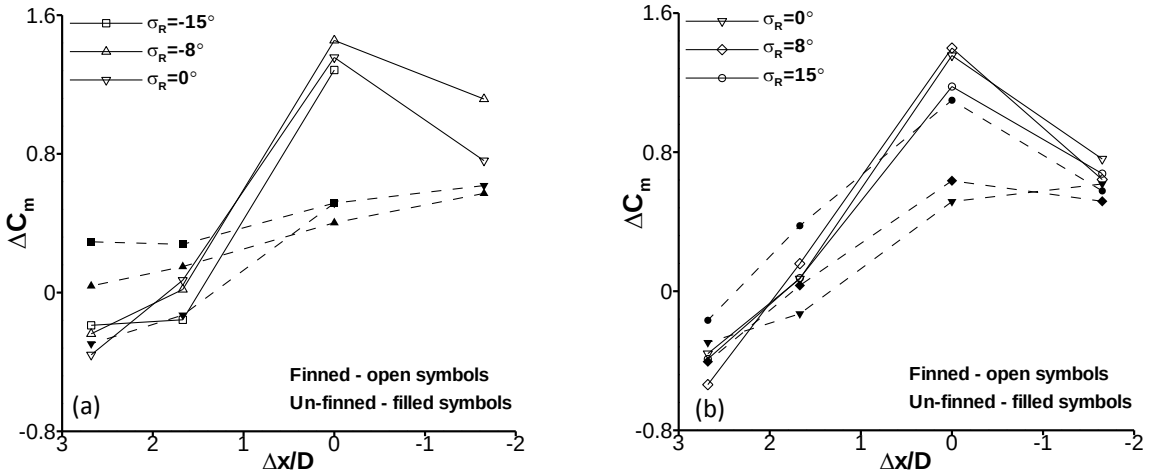

Figure 5.9 Effect of axial stagger on measured receiver pitching moment interference load for the finned receiver (solid lines) in comparison to the un-finned receiver (dashed lines): m2653, Δz/D=2.94, σ_G=0° for (a) σ_R=-15,-8,0° and (b) σ_R=0,8,15 (error bars removed for clarity)

5.2.2 Investigation into the datum finned configuration

The underlying aerodynamics involved in the finned receiver configurations can be highly complex. This section discusses the datum finned configuration to help explain the associated flow physics and introduce some metrics and concepts which will help interpret the results presented in the remainder of the chapter.

The finned datum configuration involves the finned receiver and sharp generator axially aligned (Δx/D=0), with a lateral separation of Δz/D=2.94 and both bodies at zero incidence (Figure 5.10). An important characteristic in this configuration is that the bow shock passes close to the lifting fins as it diffracts around the receiver body. The use of CFD is essential to understand the finned receiver configurations since no fin loads were measured in the experiments. This allows evaluation of the comparative contribution of the body and fin loads to the total interference loads. In this datum configuration, the fins account for 53% of the total normal force interference and 58% of the pitching moment interference (Table 5.2). This underlines the effect the fins can have on the magnitude of the interference loads.

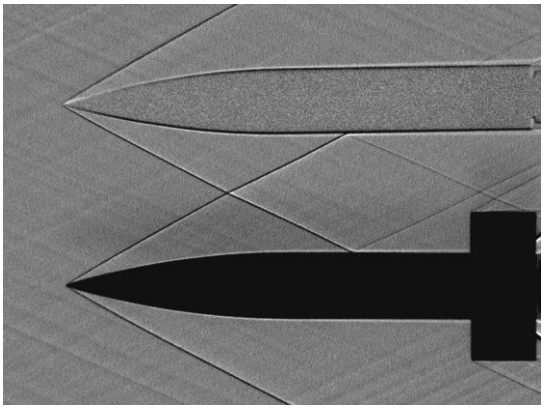

Figure 5.10 Measured shadowgraph visualisations for the datum finned configuration: m2652 m2653, Δx/D=0 Δz/D=2.94, σ_R=0° σ_G=0°

receiver	Δx/D	$\Delta C_{Z,bod}$	$\Delta C_{Z,fin}$	ΔC_Z	$\Delta C_{m,bod}$	$\Delta C_{m,fin}$	ΔC_m
finned	0	-0.108	-0.122	-0.23	0.598	0.814	1.412
un-finned	0	-0.086	-	-0.086	0.445	-	0.445

Table 5.2 Component breakdown of the predicted receiver interference loads for the finned datum configuration and the equivalent un-finned case: m2652 m2653, Δx/D=0 Δz/D=2.94, σ_R=0° σ_G=0°

5.2.2.1 The effect of fins metric

A quantitative method used to express the difference between the finned and un-finned receiver interference loads (as observed in Figure 5.8 and Figure 5.9) is detailed in Equation 5.1. This states that the effect of the fins on a given interference load ($EF\_\Delta C_Z$ in this example) is approximately equal to the *change* in the interference load acting on the body from the un-finned configuration (term shown in brackets), added to the fin interference load[a]. As an example, this is calculated for the datum finned configuration below and shows that the fins more than double the magnitude of the normal force interference by a factor of 2.67. They also triple the magnitude of the pitching moment interference (by a factor of 3.17) in comparison to the un-finned configuration (Table 5.2).

$$EF\_\Delta C_Z \approx \left(\Delta C_{Z,bod,finned} - \Delta C_{Z,bod,unfin}\right) + \Delta C_{Z,fin} \qquad 5.1$$

$$EF\_\Delta C_Z \approx (-0.108 + 0.086) - 0.122$$

$$EF\_\Delta C_Z \approx -0.144$$

5.2.2.2 Second order interference effects

Another interesting observation from the breakdown of the datum configuration interference loads is that the body interference loads (excluding the fins) are different from the un-finned body interference loads. This is even though the body is at the same attitude at the same location within the same disturbance flowfield and suggests the existence of a 2nd order interference effect. Second order interference effects occur in configurations where the presence of the fins changes the impact of the primary interactions i.e. the impinging shock and expansion field. The only means available to achieve this is the shock and expansion wave structure emanating from the fin leading edge and panel blend points. When the body is at zero roll (λ=0°), the lifting fins are on the body-fixed pitching plane (X-Y). Therefore, any change in strength of the leading edge shock in comparison with the isolated configuration will

[a] Comparing the body interference loads of the finned receiver to the un-finned receiver is not strictly accurate since the body wetted area is slightly smaller for the finned receiver due to the missing fin root areas. However, the change in wetted area is small (1.5%) and is not expected to affect the overall interference loads. Moreover, this is why the ≈ sign is used in Equation 5.1.

introduce a modified pressure field in both the lower and upper inter-fin regions and thus change the impact of the primary interaction. This is brought about through a change in the local flow pitch upstream of the fin leading edge ($\Delta\sigma_{p,up}$).

This is a notable finding because the axial impingement location and strength of the local flow pitch flowfield strongly influence whether 2nd order interference effects occur. It should be noted that the above only holds for the finned body orientated in the + configuration (λ=0°). If the roll orientation changes, then the induced change in upstream Mach number (ΔM_{up}) will also contribute to the magnitude of the 2nd order interference effects.

5.2.2.3 Datum configuration flowfield mechanisms

As in the un-finned configurations, the total interference loads are a complex function of different elemental changes in the local aerodynamics. This is investigated in detail for the datum configuration as an introduction to the effect of the fins.

A comparison of the surface pressure contours for the isolated (Figure 5.11) and datum (Figure 5.12) configurations illustrates the diffracted shock path in the vicinity of the lifting fins ($\Delta x'_f/D$ =0.7). This results in elevated pressures in the upper and lower inter-fin regions. It also induces a local flow pitch[a] close to the lifting fins of $\Delta\sigma_{p,up}$=-2.6°. Both inter-fin regions are mostly in compression as a result of the impinging shock front (Figure 5.13 (a),(b)). Moreover, the negative flow pitch leads to an augmented region of positive differential pressure on the nearside, inter-fin body surface but a region of expanded flow which acts to temper the impact of the diffracted shockwave (Figure 5.14). Both of these observations demonstrate the impact of the 2nd order interference effects where the strength of the fin leading edge shocks are modified from the isolated case and this, in turn, modifes the impact of the primary interaction.

A 1st order estimate[53] of the normal force acting on a 3D fin of zero thickness at an incidence of σ=-2.6° is equal to C_Z=-0.055. Since this agrees well with the predicted

[a] This value is predicted at the fin mid-span location (y_f/b=0.5), a short distance upstream of the fin leading edge ($\Delta x_f/D$=0.05)

normal force interference for *one* of the lifting fins ($\Delta C_{Z,fin}/2$=-0.061) one may assume the fin $\Delta C_{Z,fin}$ is solely influenced by the flow pitch. However, further analysis of the fin pressure distributions reveal that the fin loads are, in fact, a more complex function of more than one element. The upper surface of the lifting fin is indeed dominated by the augmented strength of the leading edge shock as a result of the negative flow pitch (Figure 5.15 (a)). However, the local pressure, especially on the fore panel, is further increased by the impinging shock compression footprint, as noticed in the regions of inter-fin surface close to the fin upper surface (Figure 5.14). There is little change to the fore panel pressure on the fin lower surface (Figure 5.15 (b)). This is unexpected since the negative flow pitch acts to reduce the pressure in this region. However, the diffracted shock tempers the impact of the flow pitch on the lower surface and overall, there is a negligible change from the isolated pressure distribution.

All in all, the influence of the flow pitch on the upper surface dominates the total fin normal force interference ($\Delta C_{Z,fin}$=-0.122). Due to the distance of the fins from the receiver leading edge, this results in a large total pitching moment interference ($\Delta C_{m,fin}$=0.814)

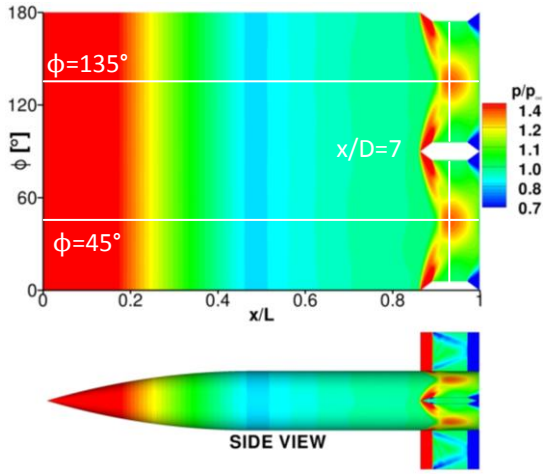

Figure 5.11 Predicted receiver surface pressure contours highlighting the extracted pressure distributions: m2652 isolated σ_R=0°

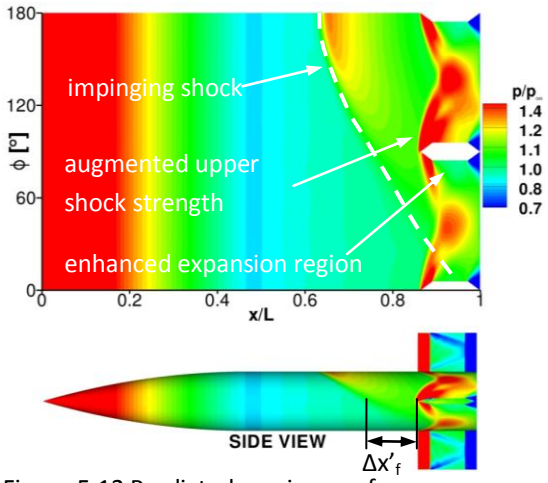

Figure 5.12 Predicted receiver surface pressure contours highlighting the approximate impinging shock location (dashed) and distance from fin leading edge to centreline impingement point ($\Delta x'_f$): m2652 m2653, $\Delta x/D$=0 $\Delta z/D$=2.94, σ_R=0° σ_G=0°

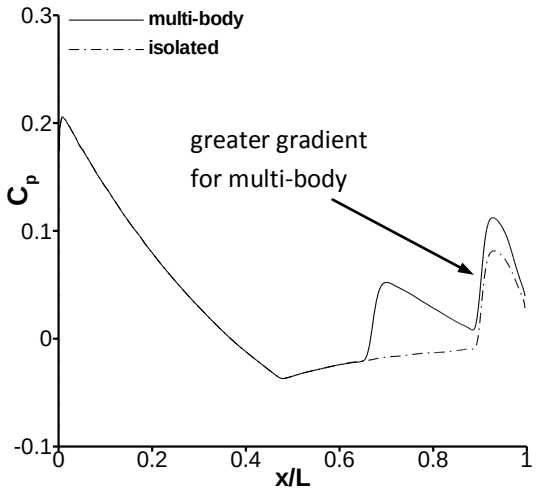

(a) axial pressure distribution, nearside ϕ=135°

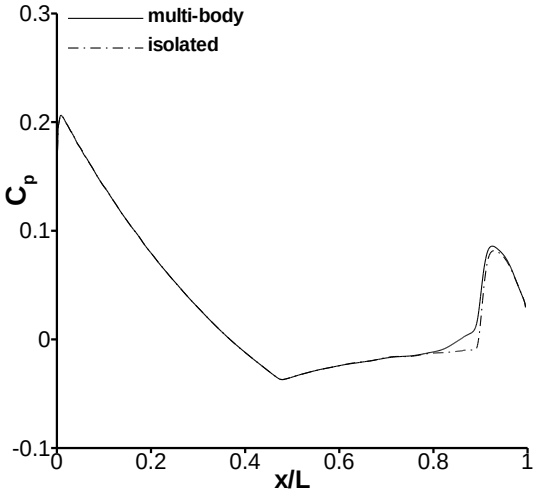

(b) axial pressure distribution, farside ϕ=45°

Figure 5.13 Predicted receiver body surface pressure distributions (a-b): m2652 m2653, $\Delta x/D$=0 $\Delta z/D$=2.94, σ_R=0° σ_G=0° (see Figure above for location)

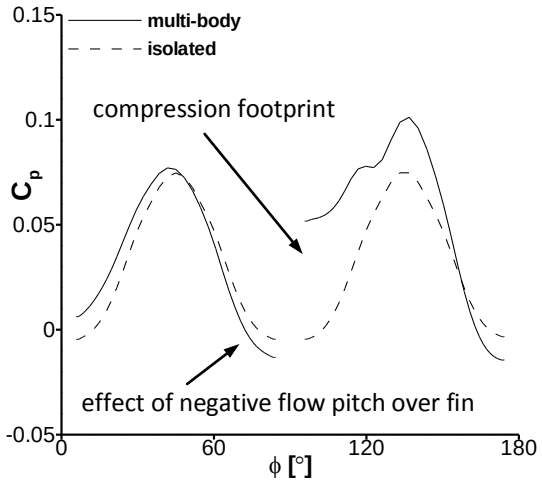

Figure 5.14 Predicted receiver body circumferential surface pressure distribution at x/D=7: m2652 m2653, Δx/D=0 Δz/D=2.94, σ_R=0° σ_G=0°

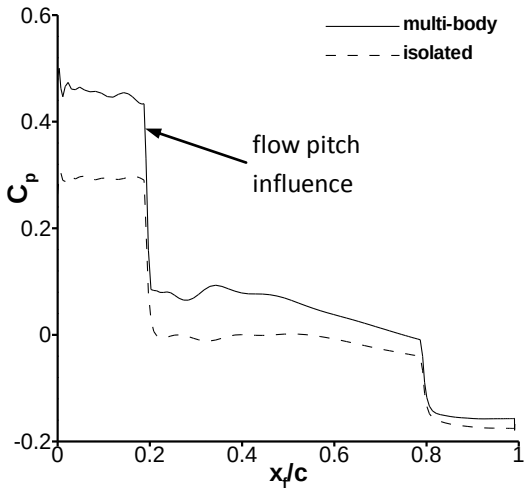

(a) chordwise pressure distribution on upper surface

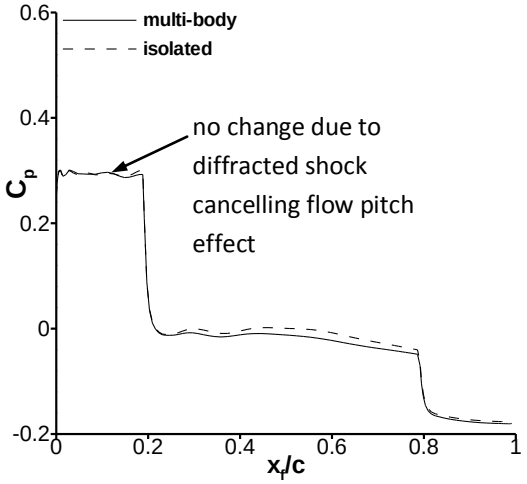

(b) chordwise pressure distribution on lower surface

Figure 5.15 Predicted receiver fin surface pressure distributions (a-b) at y_f/b=0.5: m2652 m2653, Δx/D=0 Δz/D=2.94, σ_R=0° σ_G=0°

5.2.3 Effect of axial impingement location on the finned receiver in comparison to a finned body for configurations where σ_R=0°

This section investigates a subset of the configurations shown in Figure 5.8 and Figure 5.9 for the finned receiver at zero incidence. The CFD solutions are used to investigate the underlying aerodynamics in four axial stagger configurations for the finned receiver and sharp generator (Figure 5.16). In these configurations, the generator is placed upstream of the receiver (Figure 5.16 (a), (b)), in the datum arrangement (Figure 5.16 (c)) and also downstream of the receiver (Figure 5.16 (d)).

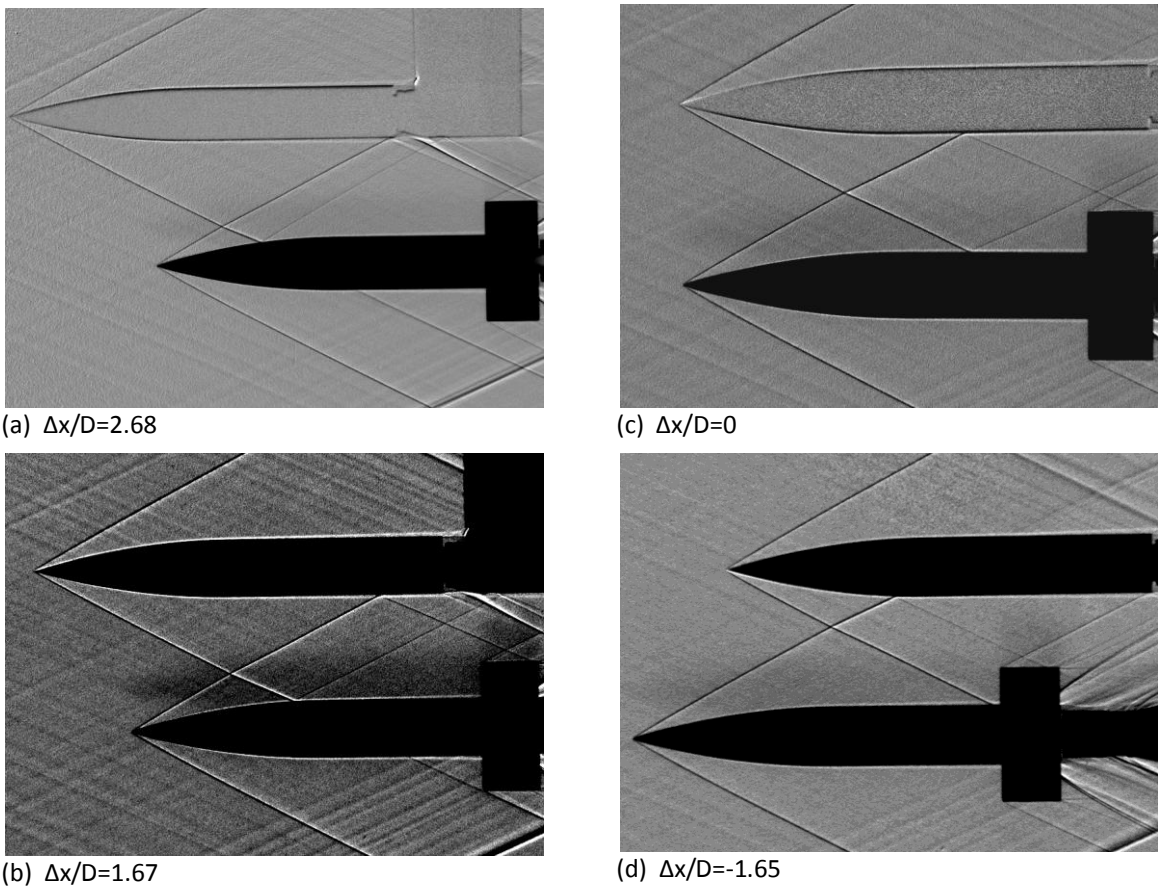

(a) Δx/D=2.68 (c) Δx/D=0

(b) Δx/D=1.67 (d) Δx/D=-1.65

Figure 5.16 Measured shadowgraph visualisations for different axial stagger settings (a-d): m2652 m2653, Δz/D=2.94, σ_R=0° σ_G=0°

5.2.3.1 Forces and moments in comparison to the un-finned receiver for configurations at σ_R=0°

Analysis of the datum configuration (§5.2.2) has shown that the effect of adding fins to the receiver for a given configuration is a function of the fin interference loads and also how much the body interference loads change from the un-finned case. The fins can as much as triple the interference loads and the sensitivity of the interference loads to the axial impingement location is increased when the finned receiver is used (Figure 5.17, Figure 5.18). Moreover, the effect of axial impingement location is more configuration specific in comparison to the un-finned cases. In particular, the fins induce large interference effects for configurations where the diffracted shock passes close to the leading edge of the lifting fins. This is evident in the datum configuration and to a lesser extend when Δx/D=1.67. Good agreement is observed between the measured and predicted interference loads and the CFD solutions are used to understand the effect of axial impingement location for the finned receiver.

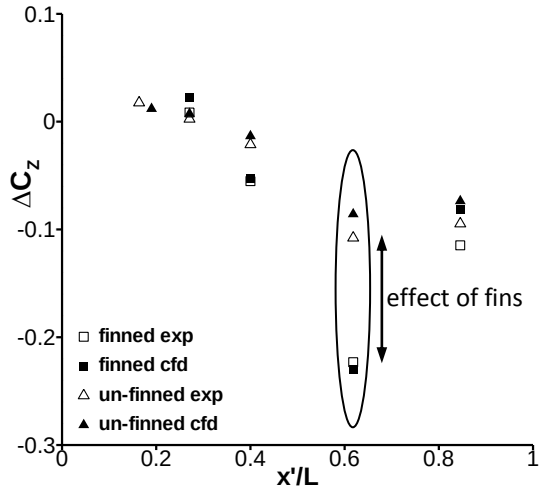

Figure 5.17 Effect of fins on measured receiver normal force interference load: m2653, Δz/D=2.94, σ_R=0°σ_G=0°

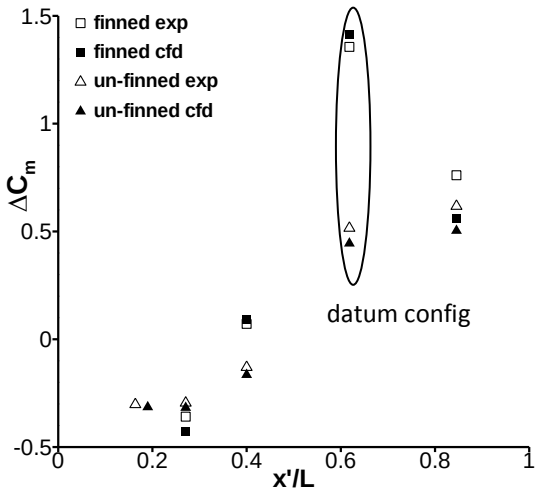

Figure 5.18 Effect of fins on measured receiver pitching moment interference load: m2653, Δz/D=2.94, σ_R=0° σ_G=0°

The predicted interference loads are split into the contributions from the receiver body and fins to aid the analysis (Table 5.3). In many of the configurations the fin loads are a significant portion of both the total normal force and total pitching moment interference loads (Figure 5.19, Figure 5.20). The fin interference loads also dominate the change in total interference load between the finned and un-finned configurations (Table 5.4) i.e. they are the primary influence on the effect that the fins have. The effect of the fins reduces as the impingement location moves from the datum towards the receiver leading edge. In addition, it also reduces when the shock impinges onto the upper surface of the lifting fin as in Δx/D=-1.65 (Figure 5.16 (d)). Although, there are still minor differences for the cases where the impingement location is near the receiver leading edge (EF_ΔC_Z=-0.1) and on the lifting fin (EF_ΔC_Z=0.06), the interference loads for these configurations are generally close to the un-finned values (Figure 5.17, Figure 5.18). This is because the distance from the centreline impingement location to the fin leading edge increases (from $\Delta x'_f/D$=0.8 for the datum configuration to $\Delta x'_f/D$=3.4 at Δx/D=2.68). Consequently, the magnitude of the induced flow pitch close to the lifting fin reduces to zero (Table 5.4) and the pressure footprints have little effect. Therefore, in the configurations at zero incidence the fins only have a noticeable effect when the axial impingement location is such that the diffracted shock passes close to the lifting fin leading edge. Otherwise, the

interference loads are generally close to the un-finned values. Finally, 2nd order interference effects are only prominent in the datum configuration and to a lesser extent when the axial stagger Δx/D=1.67 configuration.

Δx/D	$\Delta\sigma_{p,up}$ [°]	$\Delta C_{Z,bod}$	$\Delta C_{Z,fin}$	ΔC_Z	$\Delta C_{m,bod}$	$\Delta C_{m,fin}$	ΔC_m
-1.65	0	-0.071	-0.010	-0.081	0.484	0.074	0.559
0	-2.6	-0.108	-0.122	-0.23	0.598	0.814	1.412
1.67	-1.2	-0.020	-0.033	-0.053	-0.120	0.213	0.094
2.68	-0.3	0.009	0.013	0.023	-0.330	-0.096	-0.426

Table 5.3 Tabulated component breakdown of the predicted receiver interference loads for different axial stagger settings: m2652 m2653, Δz/D=2.94, σ_R=0° σ_G=0°

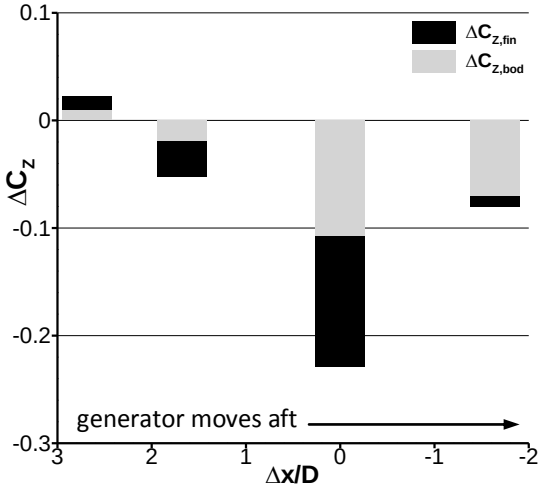

Figure 5.19 Graphical breakdown of the predicted receiver normal force interference loads for Δx/D=-1.65, 0, 1.67, 2.68: m2652 m2653, Δz/D=2.94, σ_R=0° σ_G=0°

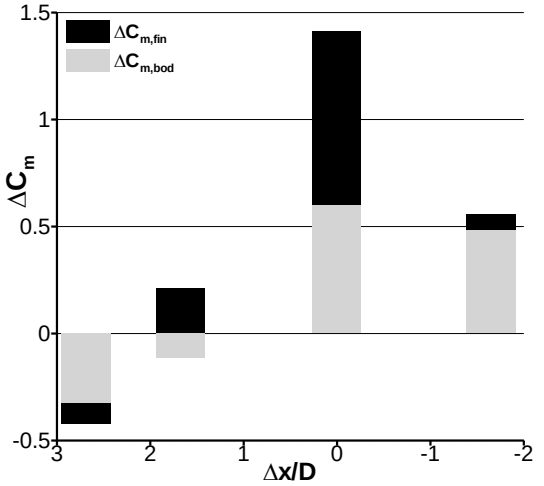

Figure 5.20 Graphical breakdown of the predicted receiver pitching moment interference loads for Δx/D=-1.65, 0, 1.67, 2.68: m2652 m2653, Δz/D=2.94, σ_R=0° σ_G=0°

$\Delta x/D$	$\Delta\sigma_{p,up}$ [°]	$\Delta C_{Z,finned}$	$\Delta C_{Z,unfinned}$	$EF\_\Delta C_Z$	$\Delta C_{m,finned}$	$\Delta C_{m,unfinned}$	$EF\_\Delta C_m$
-1.65	0	-0.081	-0.074	-0.007	0.559	0.504	0.055
0	-2.6	-0.23	-0.086	-0.144	1.412	0.445	0.967
1.67	-1.2	-0.053	-0.013	-0.040	0.094	-0.165	0.259
2.68	-0.3	0.023	0.007	0.016	-0.426	-0.318	-0.108

Table 5.4 Effect of fins on the predicted receiver interference loads for different axial stagger settings: m2653, $\Delta z/D=2.94$, $\sigma_R=0°$ $\sigma_G=0°$

5.2.3.2 Flowfield mechanisms

The dominant interference mechanism acting on the lifting fin loads changes as a function of the axial impingement location. The flowfield analysis of the datum configuration has shown that the fin interference loads are a complex function of the pressure footprints as well as the upstream flow pitch. The potency of these three individual mechanisms vary as the generator is moved forward or aft from the datum configuration and the overall fin interference loads are frequently influenced by all three. However, it is possible to say that in general, the fin loads are dominated by the generator forebody expansion waves when the generator is furthest upstream of the receiver with an axial stagger of $\Delta x/D=2.68$ (Figure 5.21 (a)). The dominant mechanism changes to flow pitch when $\Delta x/D=1.67$ and $\Delta x/D=0$ as a result of the proximity of the diffracted shock to the fin leading edge. Evidence of this is also seen in the circumferential pressure distribution (Figure 5.22) in the inter-fin region at $x/D=7$, where small region of negative differential pressure is observed close to the lower fin surface (fin leeside). Finally, the generator bow shockwave dominates the fin interference loads when the generator is aft of the receiver ($\Delta x/D=-1.65$), although the footprint extent is small and the fin interference loads are limited (Table 5.3). The data for this configuration is not included in Figure 5.21 and Figure 5.22.

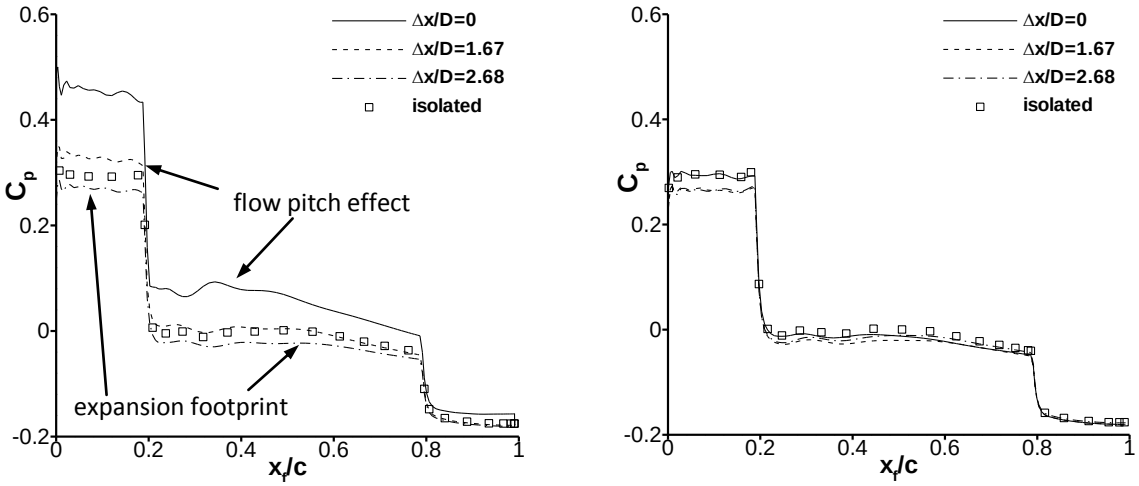

(a) chordwise pressure distribution on upper surface

(b) chordwise pressure distribution on lower surface

Figure 5.21 Predicted receiver fin surface pressure distributions (a-b) at $y_f/b=0.5$ for different axial stagger settings: m2652 m2653, $\Delta z/D=2.94$, $\sigma_R=0°$ $\sigma_G=0°$

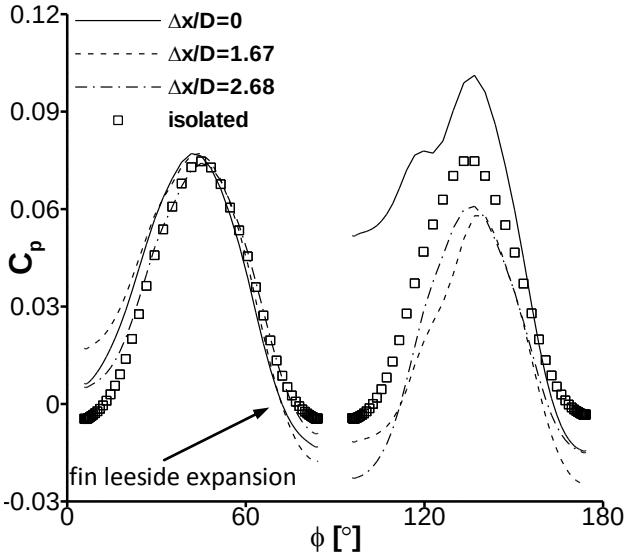

Figure 5.22 Predicted receiver body circumferential surface pressure distribution at x/D=7: m2652 m2653, $\Delta x/D=0$ $\Delta z/D=2.94$, $\sigma_R=0°$ $\sigma_G=0°$

5.2.4 Summary discussion on the relationship between the axial impingement location and the effect of fins

In summary, the addition of fins to the receiver body can have a large effect on the magnitude of the interference loads. In particular, the magnitude of the interference loads increase in configurations where the diffracted shock passes close to the leading edge of the lifting fins. Conversely, in configurations where the diffracted shock is far from the fins, the interference loads are generally close to the un-finned values and the presence of the fins does not have a substantial effect.

When the interference loads on the forebody and afterbody of the finned receiver (i.e. excluding the fins) differ noticeably from the un-finned values, the interference is classified as 2nd order. This is where the presence of the fins changes the impact of the primary interaction as a result of the leading edge shock structure. This is caused by a local flow pitch upstream of the leading edge of the lifting fins. The induced flow pitch for the datum configuration is equal to $\Delta\sigma_{p,up}$=-2.6° and results in large fin interference loads. This flow angularity acting as an interference mechanism in this way is not observed in the un-finned receiver configurations since the generator bow shock rarely passed upstream of the body leading edge. Overall, the fins loads are a complex function of the local flow pitch upstream of the leading and the pressure-based interference mechanisms as discussed extensively in the previous chapter.

Finally, to better understand the relationship between the proximity of the diffracted shock to the fin leading edge and the effect the fins have on the interference loads, Figure 5.23 and Figure 5.24 are presented. Figure 5.23 shows that there is little difference between finned and un-finned interference loads when the impingement location on the nearside is near the leading and trailing edges. A notable increase is seen in the region of x'/L=0.6. Another way to illustrate this effect is shown in Figure 5.24 in terms of the effect of the fins on the interference loads (EF_ΔC_Z and EF_ΔC_m) as a function of the distance from the fin leading edge to the location where the diffracted shock crosses the body centreline ($\Delta x'_f/D$). It can be seen that when the

diffracted shock passes within 1 calibre of the fin leading edge the effect of the fins is considerable.

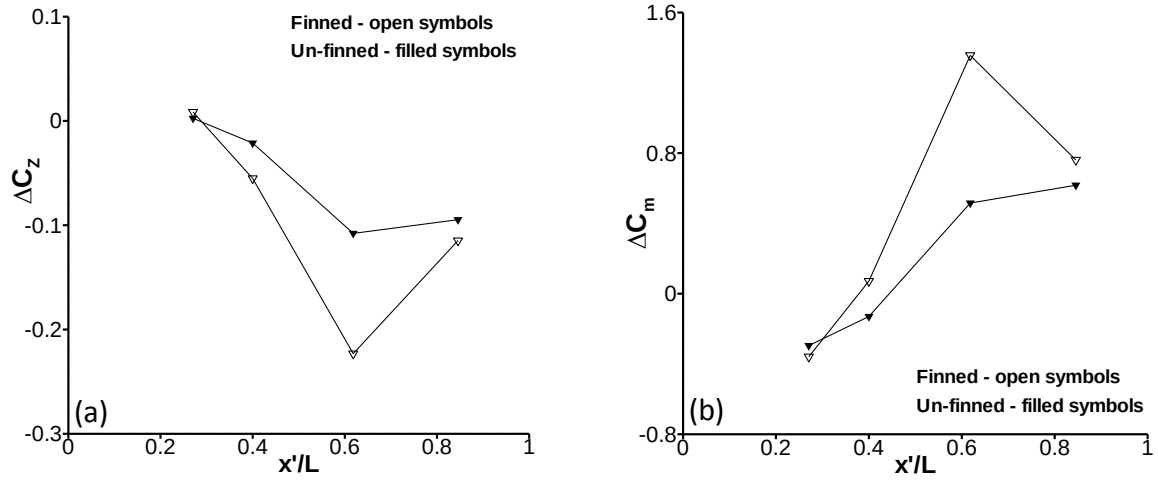

Figure 5.23 Comparison between the measured finned and un-finned (a) normal force and (b) pitching moment interference loads: m2653, $\Delta z/D=2.94$, $\sigma_R=0°$ $\sigma_G=0°$

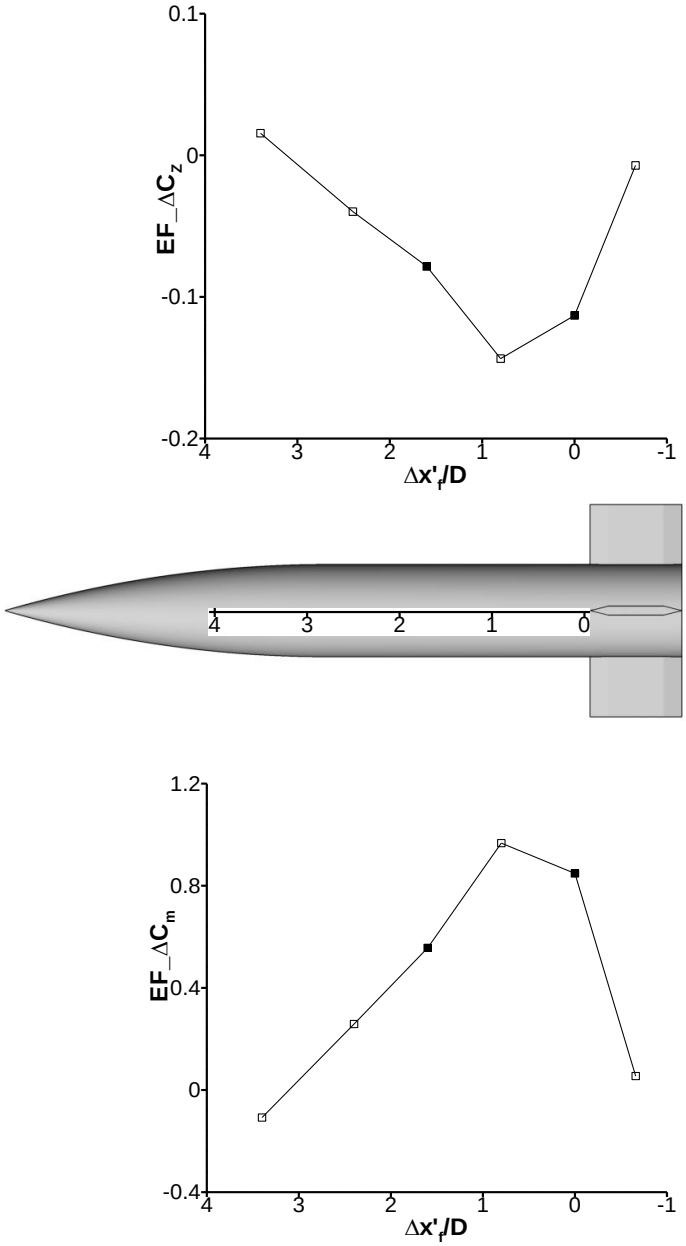

Figure 5.24 Analysis showing the effect of fins as a function of the distance from fin leading edge to the diffracted shock, measured data open symbols, predicted data filled symbols: m2652 m2653, Δz/D=2.94, σ_R=0° σ_G=0°

5.3 The effect of receiver incidence on the interference effects for a finned receiver in comparison to an un-finned body

It has been observed in Chapter 4 that the local flow conditions vary in different regions of the disturbance flowfield. Therefore, the aerodynamics of the finned receiver are expected to be different from the un-finned receiver cases because of the sensitivity of the fin loads to where they are located in the disturbance flowfield. Another finding from the previous chapter is that the centre of pressure location can move by three calibres or more as a result of the interference. This section also investigates whether this effect is seen in the configurations involving the finned receiver and whether the interference effects are large enough to change the static stability of the body.

This section uses measured and predicted data for a subset of the experimental test matrix at one axial stagger ($\Delta x/D=1.67$) for the finned receiver alongside the sharp generator. As in the previous section, the effect of a stronger disturbance flowfield is generally known to maintain the observed trend in the sharp generator configurations and increase the magnitude of the interference loads. Therefore, the configurations involving the blunt generator are not generally discussed although the full results are given in Appendix C.4.

5.3.1 Effect of incidence on the finned receiver forces and moments

5.3.1.1 Forces and moments

The normal force interference load becomes more negative as the receiver incidence increases from σ_R=-15° to σ_R=15°. There is a concomitant increase in pitching moment interference (Figure 5.25). As in the un-finned receiver configurations, the axial force interference is small. Moreover, good agreement is observed between the measured and predicted interference loads and demonstrates that the CFD is as capable of predicting the interference effects for the finned receiver at incidence. The effect that the fins have on the interference loads can be seen in Figure 5.26 where the normal force and pitching moment interference are compared between configurations

involving the finned and un-finned receiver bodies alongside the sharp generator. The trend of both interference loads as a function of incidence are more monotonic than the un-finned receiver configurations. There are strong differences when the receiver is at high negative incidence. These characteristics are investigated in §5.3.2 using predictions of the configurations at σ_R=-15, -8, 0, 8, 15°.

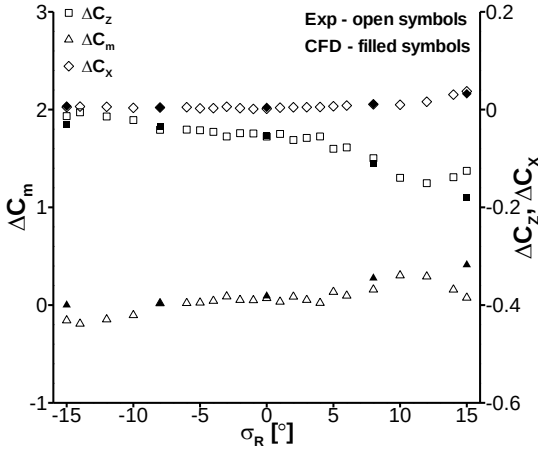

Figure 5.25 Effect of receiver incidence on the receiver body interference loads: m2652 m2653, Δx/D=1.67 Δz/D=2.94, σ_G=0° (error bars removed)

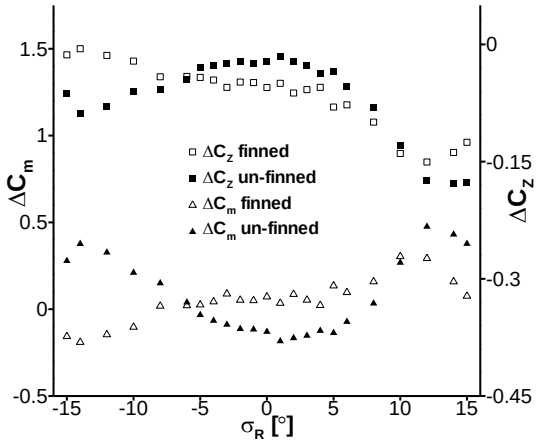

Figure 5.26 Effect of fins on the measured receiver body interference loads: m2653, Δx/D=1.67 Δz/D=2.94, σ_G=0°(error bars removed)

5.3.1.2 Static stability characteristics

The induced movement of X_{cp} is an important aspect of the interference effects for the marginally stable finned receiver. The disturbance flowfield from the sharp generator moves the centre of pressure on the finned receiver by up to two calibres over the incidence range considered (Figure 5.27). As a result in the receiver becomes statically unstable for σ_R=-1, 2°. This change in stability is a significant finding. Previous observations indicate that the centre of pressure movement is greater if the blunt generator is used. Therefore, the data for the equivalent configuration involving the finned receiver adjacent to the blunt generator are added to Figure 5.27. The increase in disturbance field strength does not change the trends observed in the weaker disturbance field but simply amplifies the effect. Consequently, the finned receiver is statically unstable for over a third of the negative incidence range.

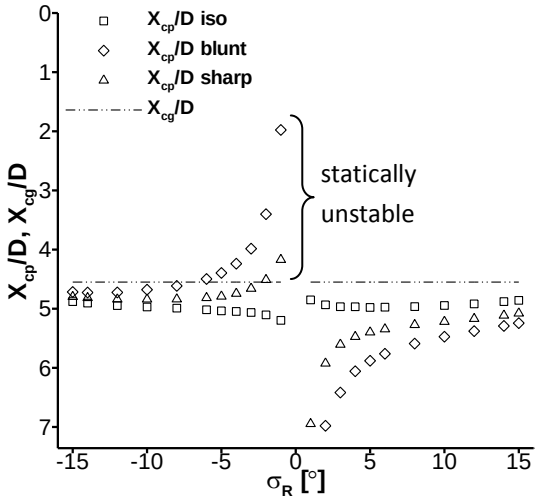

Figure 5.27 Effect of receiver incidence on the measured receiver X_{cp} using data from both the sharp and blunt generator configurations: m2652, $\Delta z/D$=2.94, σ_G=0°

5.3.2 Effect of receiver incidence on the flowfield mechanisms for the finned receiver

The local flow conditions in the disturbance flowfield are expected to strongly influence the fin loads based on the fin location in the disturbance field. The CFD predictions of the finned receiver at σ_R=-15, -8, 0, 8, 15° (Figure 5.28) are used to understand the change in trend of the interference loads as a function of incidence (Figure 5.26). Good agreement is observed between the surface pressures measured by the PSP and the predictions (Appendix C.2). This is in terms of the qualitative size and location of the interference footprints and also the quantitative pressure comparisons even in the highly complex inter-fin regions. This demonstrates further that the CFD is capable of predicting the local interference aerodynamics for configurations which involve the finned receiver.

The previous section has shown that the local fin loads are the dominant factor in the effect that the fins have on the total interference loads. Therefore, the difference between the two trends in Figure 5.26 is generally made up by the fin interference loads (Table 5.5). The complicated aspect of these configurations is the underlying aerodynamics of the fin interference loads. These are a function of three interference mechanisms which combine in different ways as the receiver incidence changes. The mechanisms include the compression footprint from the impinging shock, the

expansion footprint from the impinging expansion wave field and the flow angularity mechanism induced by the flow turning across the impinging shock.

5.3.2.1 Receiver at low incidence

When the receiver incidence is low (Figure 5.28 (c)), the fin loads are dominated by the flow pitch ($\sigma_{p,up}$=-1.2°) as shown by the high pressures on the fore panel of the upper surface. The upper surface is also affected to a smaller extent by the expansion waves (Figure 5.29 (a),(b)). This is the reason why the normal force interference between incidence angles of $-6 \leq \sigma_R \leq 6°$ is more negative than the un-finned loads.

5.3.2.2 Receiver at high negative incidence

As the incidence decreases from zero to σ_R=-15° the fins are located closer to the generator and are in the stronger part of the disturbance flowfield (Figure 5.28 (d),(e)). This enhances the effect of the expansion waves on the upper surface of the fin. The effects of this can be seen for the receiver placed at σ_R=-8°. In this configuration, the fin is influenced by a moderate flow pitch ($\sigma_{p,up}$=-1.3°) and this is clearly seen in the pressure distribution on the fin lower surface (Figure 5.30 (b)) as expected. However, the expansion waves are strong enough to cancel out the pressure rise on the fin upper surface (Figure 5.30 (a)) so much so that there is no overall fin interference load for this configuration (Table 5.5). As the incidence reduces further, the fins moves closer to the generator and the fin loads are further dominated by a stronger expansion field. This is the reason for the more positive interference loads for the finned receiver cases at high negative incidence.

5.3.2.3 Receiver at high positive incidence

Finally, as the incidence increase from zero to σ_R=15° the diffracted compression shock moves closer to the fin lower surface (Figure 5.28 (a),(b)). The flow pitch when the receiver is placed at σ_R=8° is twice as large as the configuration at zero incidence ($\sigma_{p,up}$=-2.1°) yet the fin normal force interference is approximately the same. The reason for this is due to the influence of the diffracted shockwave on the lower surface of the fin (Figure 5.31 (a)). The upper surface shows the expected pressure rise due to the flow pitch (Figure 5.31 (b)) but the compression footprint from the diffracted shock

cancels out the reduction in pressure as a result of the flow pitch. When the incidence increases further to σ_R=15°, the compression footprint augments the lower fin surface more and the fin loads become positive. This explains the more positive interference loads for the finned receiver at high positive incidence.

Overall, the dominant interference mechanism changes over the receiver incidence range due to the location of the receiver body in the disturbance flowfield. Subtly, this increases the sensitivity of the interference effects to incidence for the finned receiver because it is important which part of the finned receiver is in which part of the disturbance flowfield. At high negative incidence the expansion waves dominate, at low incidence the flow pitch dominates and at high positive incidence the shockwave compression footprint dominates. The effect of these mechanisms determines the observed changes in trend of interference loads as a function of incidence.

σ_R [°]	$\Delta\sigma_{p,up}$ [°]	$\Delta C_{Z,bod}$	$\Delta C_{Z,fin}$	ΔC_Z	$\Delta C_{m,bod}$	$\Delta C_{m,fin}$	ΔC_m
-15	-0.3	-0.063	0.033	-0.030	0.236	-0.235	0.001
-8	-1.3	-0.033	-0.001	-0.034	0.024	-0.008	0.016
0	-1.2	-0.020	-0.033	-0.053	-0.120	0.213	0.094
8	-2.1	-0.076	-0.035	-0.111	0.051	0.225	0.277
15	-1.2	-0.192	0.011	-0.181	0.484	-0.071	0.412

Table 5.5 Tabulated component breakdown of the predicted receiver interference loads for different receiver incidence settings: m2652 m2653, Δx/D=1.67 Δz/D=2.94, σ_G=0°

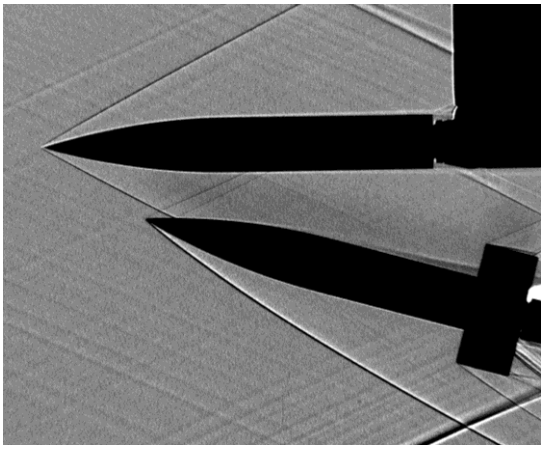

(a) σ_R=15°

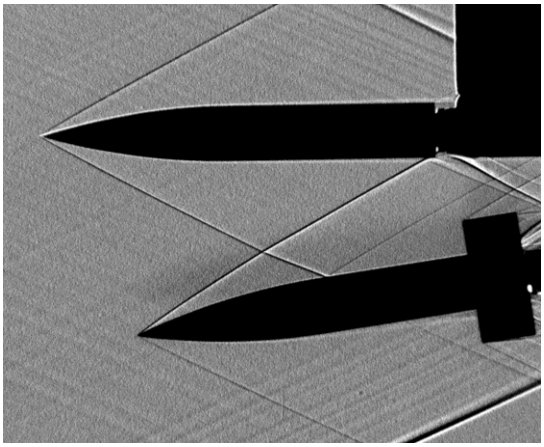

(d) σ_R=-8°

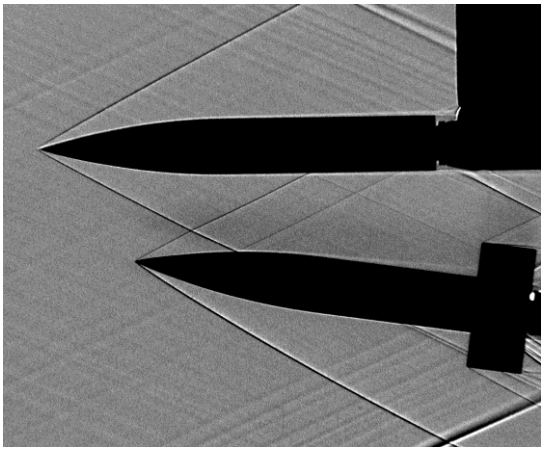

(b) σ_R=8°

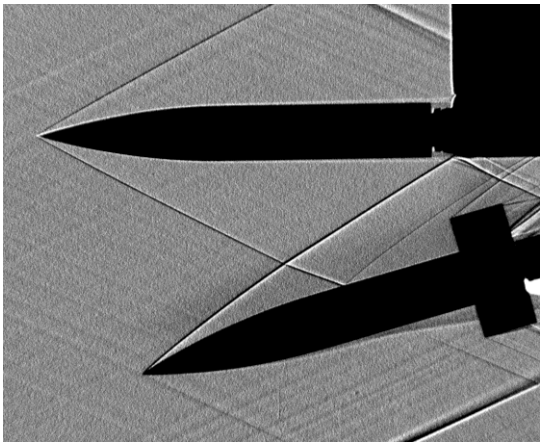

(e) σ_R=-15°

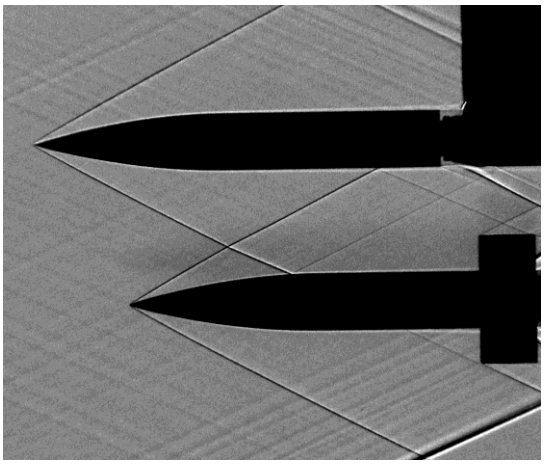

(c) σ_R=0°

Figure 5.28 Measured shadowgraph visualisations for different receiver incidence settings (a-e): m2652 m2653, $\Delta x/D$=1.67 $\Delta z/D$=2.94, σ_G=0°

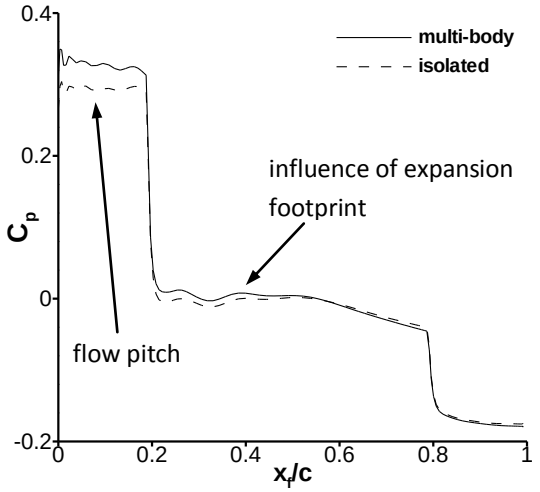

(a) chordwise pressure distribution on upper surface

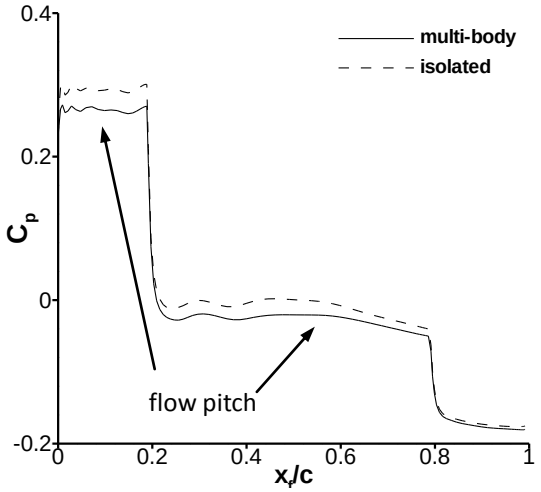

(b) chordwise pressure distribution on lower surface

Figure 5.29 Predicted receiver fin surface pressure distributions (a-b) at y_f/b=0.5: m2652 m2653, $\Delta z/D$=2.94, σ_R=0° σ_G=0°

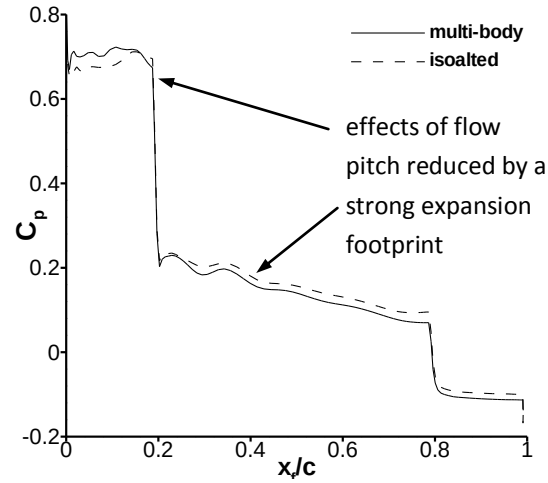

(a) chordwise pressure distribution on upper surface

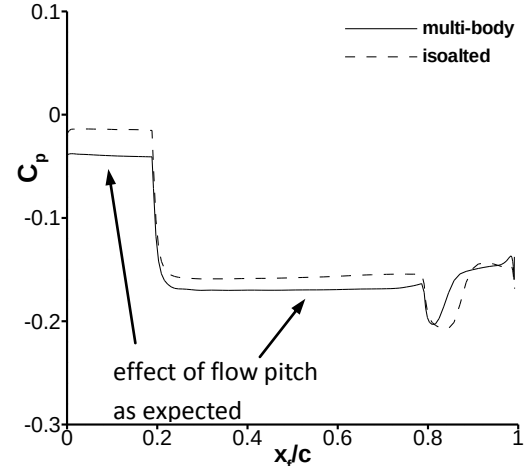

(b) chordwise pressure distribution on lower surface

Figure 5.30 Predicted receiver fin surface pressure distributions (a-b) at y_f/b=0.5: m2652 m2653, $\Delta z/D$=2.94, σ_R=-8° σ_G=0°. Note the different y-axis scales.

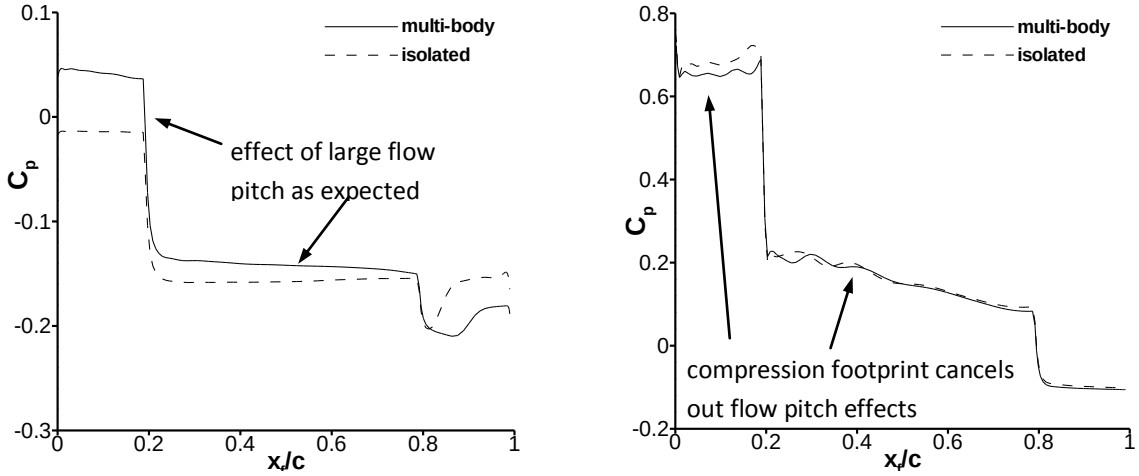

(a) chordwise pressure distribution on upper surface

(b) chordwise pressure distribution on lower surface

Figure 5.31 Predicted receiver fin surface pressure distributions (a-b) at $y_f/b=0.5$: m2652 m2653, $\Delta z/D=2.94$, $\sigma_R=8°$ $\sigma_G=0°$. Note the different y-axis scales.

5.3.3 Summary of the effect of receiver incidence on a finned receiver

The underlying aerodynamics of the finned receiver become increasingly complex when the receiver is placed at incidence. This leads to important differences in the aerodynamic characteristics in comparison to the un-finned configurations. First, the interference effects can change the stability of the finned receiver to be statically unstable. This is the case for a third of the negative incidence range when the blunt generator is used. Second, the trend of the interference loads for the finned receiver as a function of incidence is different from the equivalent un-finned case. The difference is primarily due to the fin interference loads. The interference loads which act on the fin are due to the complex combination of the angularity and pressure mechanisms. The dominant mechanism which influences the effect of the fins is observed to change over the receiver incidence range. This is the expansion footprint at high negative incidence, the induced flow angularity a low incidence, and the compression footprint at high positive incidence. Finally, the receiver incidence subtly has a more significant impact on the aerodynamic characteristics than for the un-finned configurations. This is because, for the finned receiver configurations it is important which part of the receiver body is in which part of the disturbance flowfield. For example, at high negative incidence, the fins are placed in the strong expansion wave field and this induces large fin normal force loads towards the generator body.

5.4 Summary of chapter findings

Some of the most interesting and complicated aerodynamics found in this research are presented in this chapter. The fins only have a notable effect in comparison to the un-finned case when the diffracted shock is close to the fins. In such configurations, the addition of fins to the receiver body can increase the magnitude of the interference loads by up to a factor of three. In essence, although the fins provide a vital role in ensuring static stability, they can have a detrimental influence on the interference characteristics. For example, in some configurations, the interference loads will induce in a large pitch-up moment towards the generator body, thus increasing the likelihood of a collision. Furthermore and equally as importantly, the interference effects in some configurations cause the receiver to become statically unstable. This is an important finding since the body could potentially become uncontrollable for a third of the total negative incidence range considered when the finned receiver is placed alongside the blunt generator.

The presence of fins also fundamentally changes the nature of the interference effects. This is primarily achieved through a flow angularity-based interference mechanism which does not act in the same way in the un-finned configurations. When the diffracted shock passes close to the leading edge of the lifting fins, there is an induced flow pitch and this results in large fin interference loads. The fin interference loads are the most significant contributor to the effect that the fins have on the total interference loads. These fin interference loads are a complex function of the three interference mechanisms of flow angularity and the two pressure-based mechanisms due to the impinging shock and expansion waves. The dominant interference mechanism which influences the fin loads is found to change over the axial stagger and receiver incidence range considered. This gives an indication of the complexity of the problem.

The receiver incidence parameter subtly plays a more significant role than in the un-finned configuration. This is because it is important, which part of the receiver body is placed in which location of the disturbance flowfield – large loads can develop on the

fins when the body is at high negative incidence and the fins are in close proximity to the generator body.

In some configurations, 2nd order interference effects are important where the presence of the fins reduce the effect of the primary interaction. This is caused by the flow pitch disturbance field upstream of the leading edge of the lifting fins which modifies the leading edge shock structure. For the majority of the configurations, where 2nd order effects are negligible the total interference loads can be treated as a superposition of the un-finned body interference loads and an estimate of the fin interference loads.

Finally, very good agreement is found between the measured and predicted interference loads. Moreover, the qualitative and quantitative comparisons of the measured and predicted surface pressures agree well, even in the complex inter-fin flow regions.

Chapter 6 Further Discussion and Implications of Research Findings

A large amount of detailed and often complex information is presented in the preceding discussion (§4,5). This chapter begins by bringing together the most important research findings for further investigation. After which the analysis broadens out to promote a higher-level understanding of the interference aerodynamics. In order to achieve this, the outline of the chapter is as follows:

- A further discussion of the research findings presented thus far (§6.1)
- An investigation into how well the research findings apply to a full-scale problem (§6.2)
- A summary of the chapter findings and a discussion of the implications of research findings (§6.3)

This chapter includes all measured and predicted data and the discussion utilises data across all configurations. This includes results for both the finned and un-finned receiver and uses both the sharp and blunt generator bodies. Finally, to assess the full-scale interference effects unsteady trajectory predictions of two finned bodies are reported.

6.1 Summary discussion of the research findings

With the complex nature of the discussion presented thus far, it is important at this point to summarise the most important characteristics of the interference aerodynamics. This begins with an illustration of the relationship between the main geometric parameters, which may include several of the key design variables, and the elemental interaction parameters. This is followed by a discussion of characteristics which relate to the finned receiver and a further discussion of the diffraction mechanism. This section ends with a brief outline of the limitations of the current dataset.

6.1.1 The relationship between the geometric and interaction parameters

The variation of a typical geometric parameter leads to multiple changes in the elemental interaction parameters which contribute to the overall interference loads. This can be highly complex and it is sometimes difficult to gain an overview of what the most important parameters are. This section aims to simplify this through graphical means. This gives a clear picture of the inter-dependent nature of the interference aerodynamics and extracts the most important interaction parameters (Figure 6.1).

In the vast majority of configurations studied there are no secondary interaction effects[a]. The receiver interference loads are the result of the primary interactions alone. Therefore, the characteristics of the primary interactions are studied for a representative configuration under supersonic flow conditions (M_∞, Re_D). This assumes a given disturbance field strength related to the generator geometry, which is characterised by the impinging shock strength (ψ_G), expansion field strength (η_G) and local flow pitch ($\sigma_{p,G}$) at the generator leading edge (highlighted purple in Figure 6.1). The dependents of the four main geometric parameters are traced to understand what elemental interaction parameters they influence. These geometric parameters are listed below and highlighted green in Figure 6.1.

[a] This is where disturbances emanating from the receiver body reflect from the generator body and impinge onto the aft end of the receiver.

- axial stagger between bodies (Δx/D)
- lateral separation between bodies (Δz/D)
- receiver incidence (σ_R)
- generator incidence (σ_G)

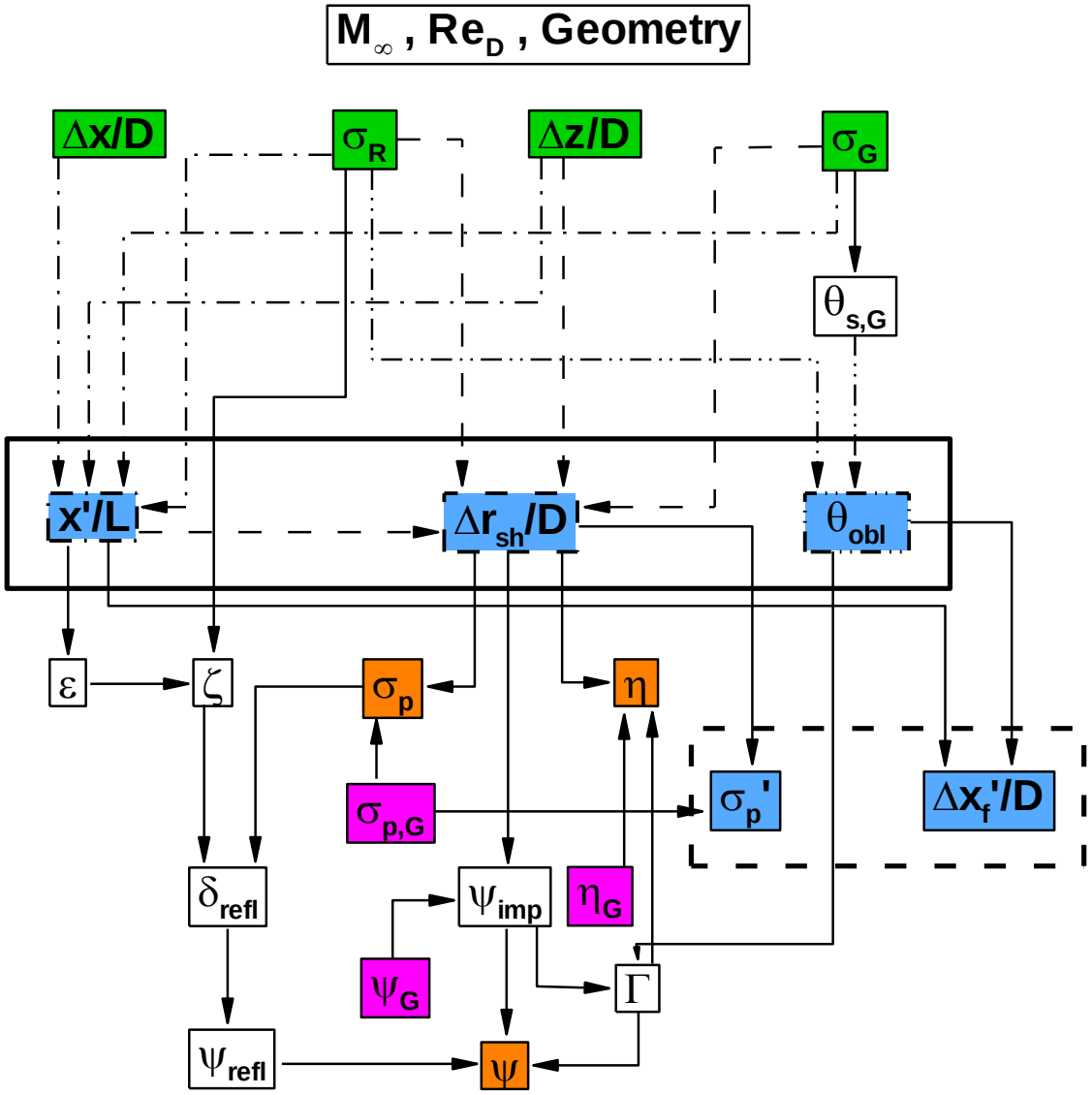

Figure 6.1 Diagram illustrating the inter-dependent nature of the geometric parameters, the interaction parameters and the overall interference loads. Note a description of the parameters can be found in Appendix B.3

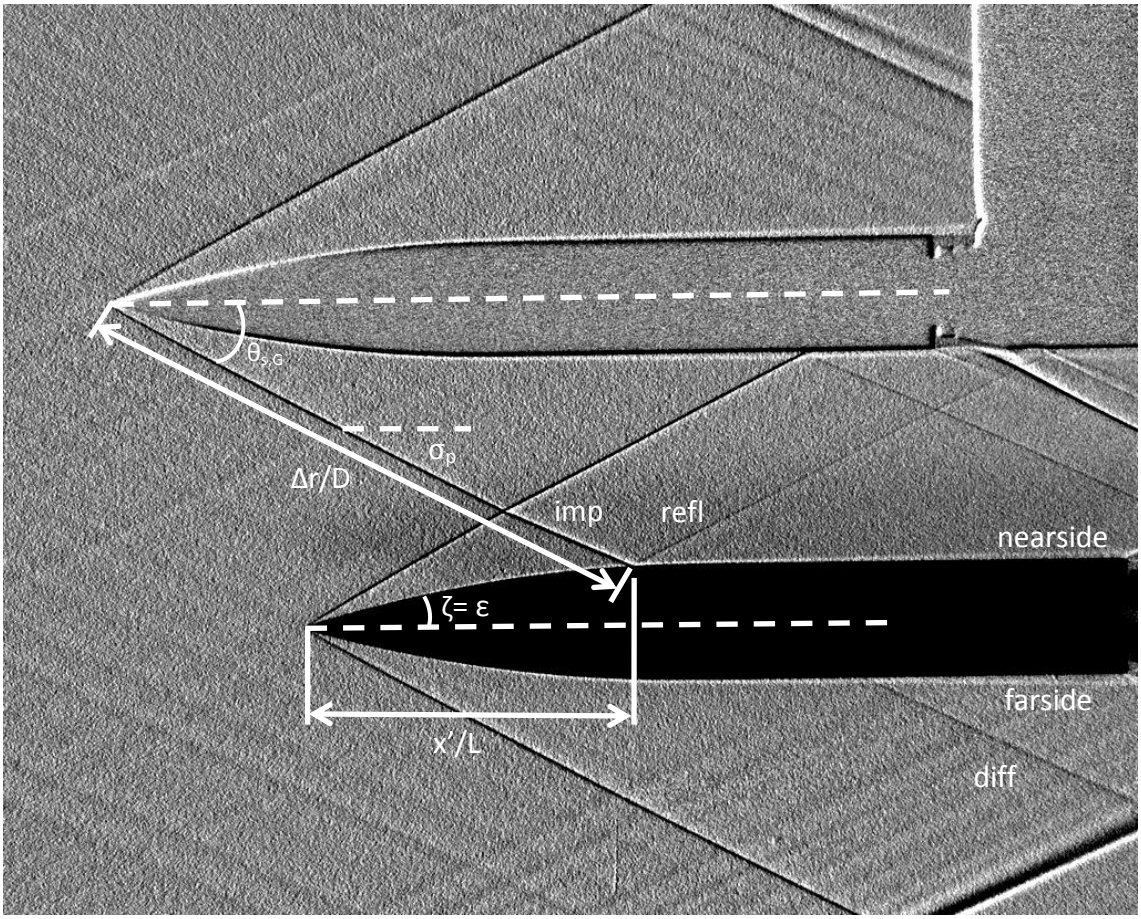

Figure 6.2 Shadowgraph of a typical multi-body configuration showing parameters used in the results analysis

Many of the parameters are defined in the previous and following sections but the others are as follows.

- ε is the included angle between the local surface curvature and the body centreline. ζ is the pitch angle the local surface curvature makes with the wind reference X_w-Y_w plane (Figure 6.2).

- δ_{refl} is the flow turning necessary to maintain a regular reflection downstream of the impinging shock. ψ_{imp} and ψ_{refl} are the strength of the impinging and reflected shocks respectively

- $\theta_{s,G}$ is the conical generator bow shock angle. Γ is the shock diffraction attenuation parameter and will be discussed in §6.1.4.2

6.1.1.1 Un-finned receiver discussion

The overall interference loads are a function of multiple regions of differential pressure where a change in pressure from the isolated configuration (Δp) acts over the extent of the affected surface area. The nearside and farside interactions induce different positive (p > piso) or negative (p < piso) regions of differential pressure and these contribute to a change in the local normal force distribution, $\Delta dC_Z/dx$ (Figure 6.3). The extent of the differential pressure regions is linked to the magnitude of the dependent interactions and the geometric parameters such as x'/L and θ_{obl}.

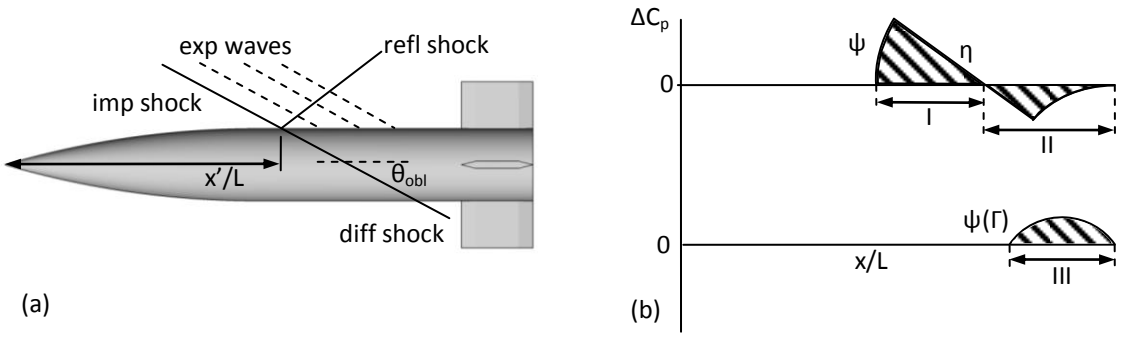

Figure 6.3 Sketch illustrating the (a) interaction parameters and (b) differential pressure rgions of the I) nearside positive differential pressure, II) nearside negative differential pressure, III) farside positive differential pressure

It is clear from Figure 6.1 that the differential pressure regions which contribute to the overall interference loads can be reduced to be primarily affected by certain interaction parameters. This is summarised below.

Nearside region of positive differential pressure ($p>p_{iso}$ which induces $\Delta dC_Z/dx<0$):

- Extent is a f(x'/L, ψ, σ_p, η)
- Magnitude is a f(ψ, σ_p)

Nearside region of negative differential pressure ($p<p_{iso}$ which induces $\Delta dC_Z/dx>0$):

- Extent is a f(x'/L, ψ, σ_p,η)
- Magnitude is a f(ψ, σ_p, η)

Farside region of positive differential pressure ($p>p_{iso}$ which induces $\Delta dC_Z/dx>0$):

- Extent is a f(x'/L, θ_{obl}, ψ(Γ), η)

- Magnitude is a f(ψ(Γ))

Farside region of negative differential pressure ($p<p_{iso}$ which induces $\Delta dC_Z/dx<0$):

- Extent is a f(x'/L, θ_{obl}, ψ(Γ), η)
- Magnitude is a f(ψ(Γ),η)

These differential pressure regions combine to give the overall interference loads:

- ΔC_Z,C_m are a f(x'/L, θ_{obl}, ψ, σ_p, η, Γ)
- ΔC_Z,C_m are a f(x'/L, $\Delta r_{sh}/D$, θ_{obl} ,Γ)

In summary, for a given disturbance field strength (ψ_G, η_G, $\sigma_{p,G}$) the un-finned receiver interference loads are a function of 3 main interaction parameters. These are listed below and coloured blue in the solid box in Figure 6.1.

- the axial impingement location (x'/L)
- the distance of the impingement location from the generator body ($\Delta r_{sh}/D$)
- the shock obliqueness angle (θ_{obl})

The axial impingement location and shock obliqueness angle dominate the extent of the interaction footprints. The magnitude of the change in pressure from the isolated values (Δp) is a function of the disturbance field strength and the decay of the local shock strength (ψ), expansion field strength (η) and the flow pitch (σ_p) as the distance increases from the generator body (coloured orange in Figure 6.1).

6.1.1.2 Finned receiver discussion

For the finned receiver in a given disturbance field, more interaction parameters exist due to the contribution of the fin interference loads to the overall interference effects. The fin interference loads are a function of the local flow pitch immediately upstream of the leading edge of the lifting fins ($\sigma_{p,up}$). This in turn, is a function of the local flow pitch at the centreline impingement location (σ_p') and the distance from this point to the fin leading edge ($\Delta x_f'/D$). These are coloured blue and contained within the dashed

box in Figure 6.1. The finned receiver interference loads are, of course, also a function of the interaction parameters shown in the solid box in Figure 6.1

6.1.1.3 The dominance of the axial impingement location

Assessing the sensitivity of the interference loads to the different interaction parameters is not easy as many interaction parameters can change when a geometric parameter is varied (§6.1.1). However, the previous chapters (§4,5) have identified that the interference loads are more sensitive to the axial impingement location than the other interaction parameters. The strength of the impinging disturbances and the shock obliqueness angle also have a moderate effect. However, the axial impingement location can change both the polarity and magnitude of the interference loads over its range (§4.6). This is particularly important with regards to the pitching moment interference. The interference loads are strongly sensitive to x'/L when the finned receiver is used (§5.2). This is because the interference loads increase makedly when the impinging shock is close to the fins.

The main reason for the dominance of the axial impingement parameter is that due to the relatively short length of the receiver body, it has a significant influence on the extent of the nearside regions of differential pressure. It also plays a large part in determining whether or not the farside differential pressure regions occur at all. The disturbance field can involve strong interactions, but if there is little or no extent on the receiver body over which to act, the interference effects will be limited. Finally, the fact that the axial impingement location can change the polarity of the interference effects is likely to have a significant bearing on the subsequent trajectories of the bodies (this is investigated in §6.2.4).

6.1.2 Dimensional analysis and dataset trends

A dimensional analysis is carried out for the un-finned body and uses the irreducible interaction parameters discussed in §6.1.1.1. In the dimensional analysis the repeated variables are ρ,U,D. The parameters which characterise interference aerodynamics are as follows. The interference effects are characterised by a change in normal force (ΔF_Z) from the isolated configuration. The axial impingement location is characterised by x'.

The impinging shock strength is characterised by Δp across the primary disturbance. The reflected shock strength is characterised by the flow turning to maintain a regular reflection (δ_{refl}). The impinging expansion strength is characterised by the local pressure gradient (dp/dx). The farside extent is characterised by the shock obliqueness angle (θ_{obl}). Flow compressibility is characterised by the freestream sonic velocity (a_s). Skin friction effects are characterised by the freestream dynamic viscosity (μ). The non-dimensional outputs form the following groupings. The magnitude of the angle parameters (δ_{refl},θ_{obl}) are minimised when they equal 0 and maximised when they equal 90°, so the sine of the angles are used.

$$\frac{\Delta F_Z}{\rho U^2 D^2} = f(\frac{x^{'}}{D}, \theta_{obl}, \delta_{refl}, \frac{\Delta p}{\rho U^2}, \frac{dp}{dx} * \frac{D}{\rho U^2}, \frac{U}{a_s}, \frac{\rho U D}{\mu})$$

$$\Delta C_Z = f(\frac{x^{'}}{L}, \sin(\theta_{obl}), \sin(\delta_{refl}), \Delta C_{p,imp}, \frac{dp}{dx} * \frac{L}{\rho U^2}, M, Re_D)$$

The entire dataset for the un-finned receiver (nearly 300 configurations) is now analysed for fixed tunnel freestream conditions (M and Re_D are disregarded). The interference loads are expected to be a linear function of x'/L, $\Delta C_{p,imp}$, $\sin(\delta_{refl})$, since these all increase either the extent or magnitude (Δp) of the differential pressure regions and these are now examined.

If the measured normal force (ΔC_Z) and pitching moment (ΔC_m) interference loads are plotted as a function of axial impingement location (x'/L) there is a notable amount of data scatter (Figure 6.4, Figure 6.5). However, if two small configuration-based restrictions are applied, the data groups more favourably and an approximately linear trend is observed as expected (Figure 6.6, Figure 6.7). Figure 6.6 and Figure 6.7 restrict the data to an incidence range of $-10 \leq \sigma_R \leq 6°$ and Δz/D=2.94. The high positive incidence configurations excluded were found to exhibit distinct trends from the majority of the data since the impinging shock did not diffract to the farside of the receiver body. However, within the stated bounds, a linear best-fit line is fitted to the data and gives an empirical estimate of ΔC_Z and ΔC_m to within an *rms* difference from the measured values of 0.03 and 0.2 respectively (Equation 6.1 and 6.2). Finally, there is still a moderate amount of data scatter which is due to dependence of the

interference loads on the other parameters outlined in the dimensional analysis above. However, these empirical estimates give a tentative first estimation of the interference loads within reasonable uncertainty bounds.

$$\Delta C_Z = 0.056 - 0.239\frac{x'}{L} \quad 6.1$$

$$\Delta C_m = -0.854 + 2.053\frac{x'}{L} \quad 6.2$$

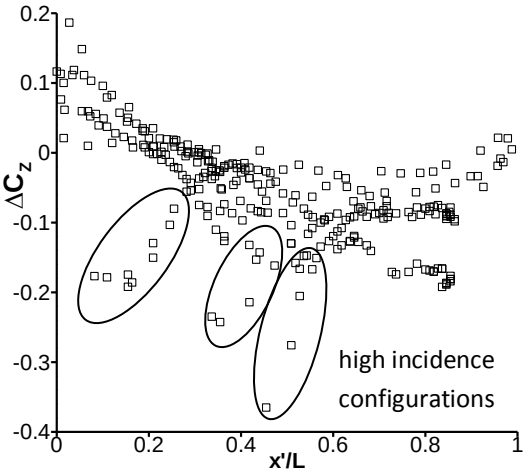

Figure 6.4 Measured ΔC_Z for the un-finned receiver as a function of axial impingement location. All data

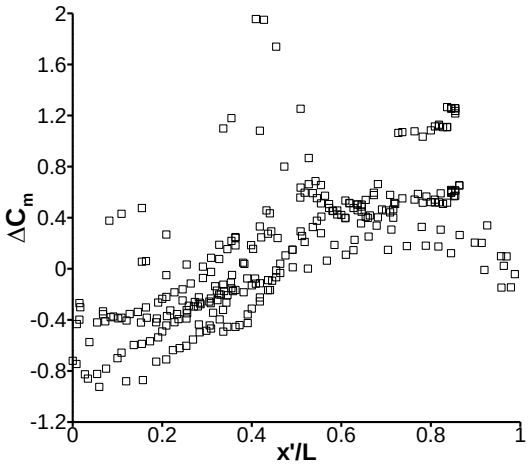

Figure 6.5 Measured ΔC_m for the un-finned receiver as a function of axial impingement location. All data

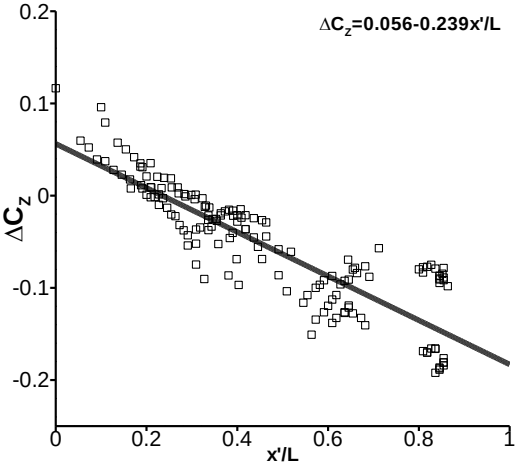

Figure 6.6 Measured ΔC_Z for the un-finned receiver as a function of axial impingement location. Selected data.

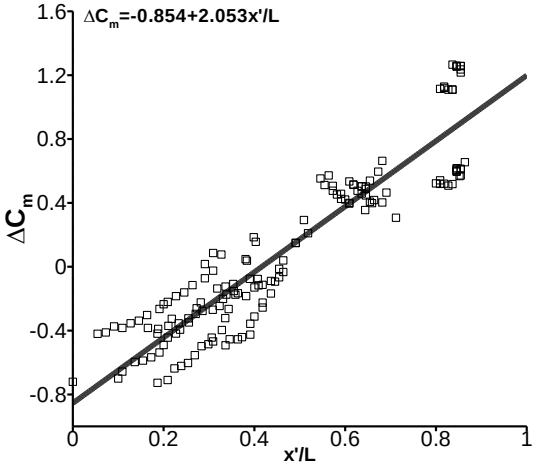

Figure 6.7 Measured ΔC_m for the un-finned receiver as a function of axial impingement location. Selected data.

The dependence of ΔC_Z on two of the other parameters are now discussed. When ΔC_Z is plotted as a function of $\Delta C_{p,imp}$ (Figure 6.8), δ_{refl} (Figure 6.9) there is no clear trend

and alot of data scatter when one would expect a roughly linear dependence. The load is expected to increase proportionally for an increase in pressure. It becomes clear from the above analysis that a simple correlation to predict the interference loads is difficult to achieve. This is most likely due to the complex nature of the interference problem, especially relating to the shock diffraction to the receiver farside. Even though data scatter is evident in Figure 6.6 and Figure 6.7, the central dependence on x'/L is exposed. Moreover, a tentative prediction of the interference loads can be made on this basis.

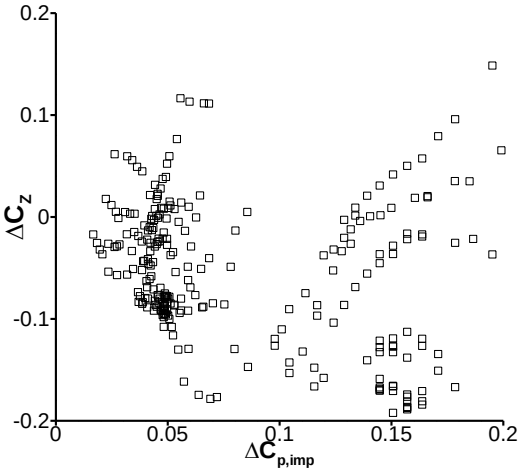

Figure 6.8 Measured ΔC_Z for the un-finned receiver as a function of impinging shock strength. All data

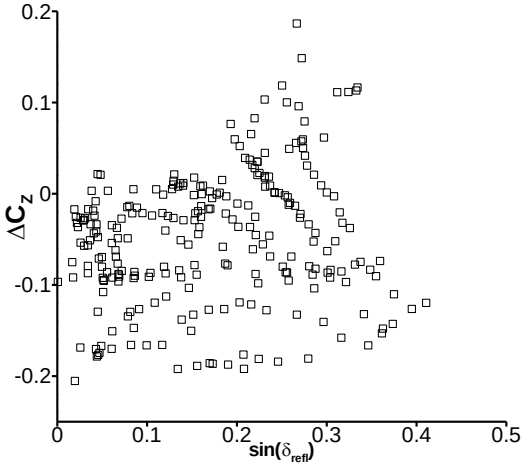

Figure 6.9 Measured ΔC_Z for the un-finned receiver as a function of a characteristic of reflected shock strength. All data

6.1.3 Discussion of the finned receiver aerodynamics

6.1.3.1 Interference effects on static stability

The significance of the normal force and pitching moment interference loads has been discussed at length in §4 and 5. Also of prime interest, is the effect of the interference on the static stability of the finned receiver. This is because if the body were to become unstable and uncontrollable as a result of the disturbance flowfield then this would be a highly undesirable and problematic outcome.

The location of the longitudinal centre of pressure is plotted for the entire experimental dataset for the finned receiver in Figure 6.10, which covers approximately 200 configurations in total. The finned receiver body in isolation is statically stable across an incidence range of $-15 \leq \sigma_R \leq 15°$ (black symbols in Figure

6.10). However, the aerodynamic interference changes the stability of the body to become unstable for approximately 20% of the multi-body configurations. The stability changes occur entirely at low incidence ($|\sigma_R| < 6°$). This is because at these low incidence angles, the magnitude of the interference loads are comparable to the isolated body loads and can have an appreciable effect (movements in X_{cp} of up to 4.5 calibres). Reciprocally, at high incidence the isolated body loads are up to an order of magnitude larger than the interference loads, there are only small movements in X_{cp} (typically in the order of 0.1 or 0.2 calibres).

For a given incidence angle, whether the disturbance field has a de-stabilising ($\Delta X_{cp}<0$) or a stabilising ($\Delta X_{cp}>0$) effect is largely determined by the axial impingement location. In the positive incidence range (Figure 6.10), when x'/L is on the forward half of the body (x'/L < 0.5) the interference has a stabilising effect (green symbols). This is because the induced pitching moment around the centre of gravity acts in the same direction as the isolated pitching moment and this moves the X_{cp} aft. The opposite is the case when x'/L is close to the trailing edge, x'/L > 0.5, shown as the red symbols in Figure 6.10.

These findings emphasize that the issue of static stability is of critical importance in the design of submunition bodies. This is especially important since an ideal dispense configuration is likely to include the bodies orientated at low incidence where the changes in stability are largest and most likely to occur. These findings also further underline the importance of the axial impingement parameter and this knowledge could be utilised to avoid changes in stability. For example, in the low positive incidence range any design should ensure that the impingement location of the primary disturbance is over the forebody to avoid a de-stabilising effect.

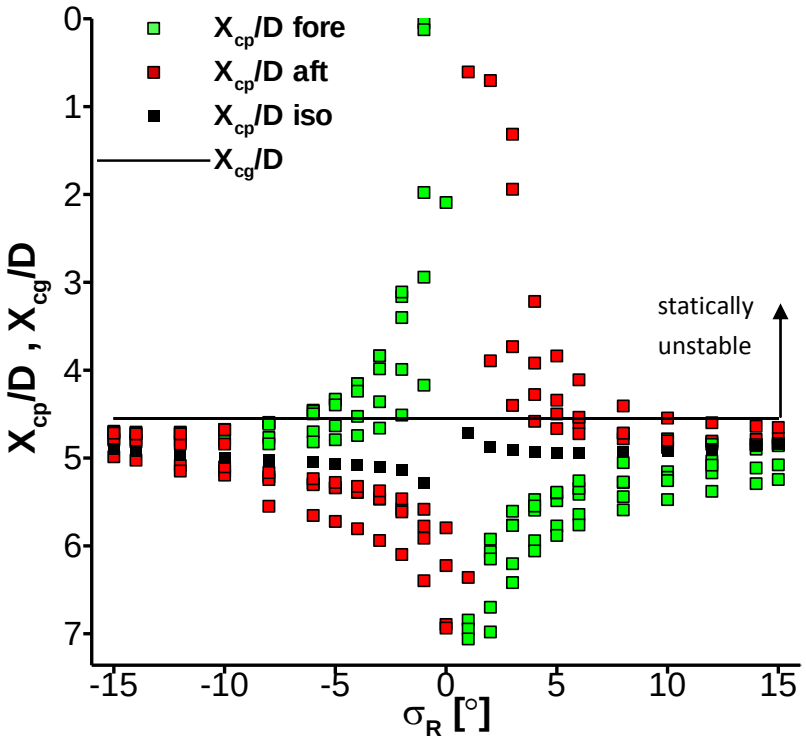

Figure 6.10 Measured longitudinal centre of pressure locations, red symbols indicate x'/L>0.5, green symbols indicate x'/L<0.5: includes data for the finned receiver and both generators

6.1.3.2 Control fins: competing interests of stability and interference

The design of any slender body involves consideration of the size and location of the control fins to ensure static stability[41,53]. The larger the planform area of the fins, and the further they are located from the body centre of gravity, the greater their contribution will be to the pitching moment which stabilises the body. However, the discussion in §5 has shown that when the diffracted shock passes close to the fin leading edge, large interference loads are observed. Therefore, it is logical to infer that these fin characteristics (a large planform area, located far from the X_{cg}) will result in larger interference effects.

This presents a design challenge for the engineer. Frequently, body fins are designed to be as small as possible but located at the trailing edge of the body to maximise their contribution to stability. It is recommended that the design objective to minimize the fin planform area should remain. In addition, another design objective should be to minimize the distance the fins are located from the X_{cg} whilst maintaining overall static stability.

It is also difficult to see how the issues surrounding fin interference would be avoided using alternative stabilising devices. One alternative is wraparound fins[1], although these would suffer from the same problems outlined for the body-fixed fins. However, wraparound fins would be able to be packaged more efficiently than body-fixed fins and they would also be a more practical solution for a dispense manoeuvre as they would deploy once the body had cleared the influence of the bus vehicle[a]. A second alternative would be a flare. This would also induce the interference problems associated with the flow pitch downstream of the impinging shock. This option is likely to be as inefficient to package as the body-fixed fins, if not more.

Assessing the control options are out of the scope of this research, but it is clear that when the impingement location is close to a set of control devices which are located aft of the X_{cg} the interference effects are likely to induce large moments towards the generator body. The induced pitching moment has a substantial influence on the subsequent unsteady motion of the bodies (§6.2).

6.1.4 Further discussion on shock diffraction

6.1.4.1 Revisit of the closest (Δz/D=1.94) un-finned configuration

The propagation of the disturbance shockwaves are described in §4.2.2 for a simple configuration where the bodies are in close proximity. In this section, an analogy is drawn between two related examples of shock diffraction in order to better understand the physical mechanism. The first is the predicted steady-state configuration from §4.2.2 where an oblique impinging shock diffracts around the un-finned receiver (Figure 6.11 (a)). The second is an experimental study reported by Kaca[59]. Kaca recorded interferograms of the shock structures which develop for a moving planar shock wave as it diffracts around a semi-circular cylinder for a similar Mach number of M_∞=2.81 (Figure 6.11 (b)). This allows insight into the phenomenon of shock reflections and diffraction around a cylindrical body as the flow features are similar for a steady, pseudo-steady and unsteady flowfields[60]. Figure 6.11 shows a

[a] Pop-up fins would also have similar properties but packaging would mean the allowed fin semi-span was small (typically <0.5D)

close-up of a given crossflow plane and identifies the principle flow features in both the steady and unsteady cases.

The left hand side of Figure 6.12 shows crossflow slices of ∂p/∂x to highlight the predicted shock structures as x/L increases along the receiver body (a-d). The illustrations of the right hand side of Figure 6.12 are interpretations of the Kaca measurements and progress in time (e-h). At each individual time, the flowfield is assumed to be pseudo-steady with the reference frame fixed to the reflection point (or triple point[60]). Overall, the shock structures are very similar between the two examples. As the impinging shock (I) strikes the receiver body a regular reflection (RR) is observed and the reflected shock (R) travels back towards the generator body (Figure 6.12 (a),(e)). The two shocks meet at the reflection point on the body surface (G). As the angle between the impinging shock and the cylinder tangent increases (as the shock diffracts around the body) there is a point on the receiver nearside where the RR can no longer be sustained by the local Mach number. In this situation, the amount of flow turning necessary is too great and since the flow is steady, a Single Mach Reflection (SMR) is formed[61] (Figure 6.12 (b,f)). Another study by Yang[57] involves a planar shock travelling at M_∞=2.81 which diffracts around a cylinder. Yang predicted the azimuthal location where transition to SMR first occurs to be within the band $130 \leq \phi \leq 140°$. Yang's actual observed transition location was ϕ=138° and for the steady configuration studied in this section the value is ϕ=133° (Figure 6.10 (b)) which falls within the stated band. The SMR flow structure now includes the impinging and reflected shocks as before, but also (in the early stages) a straight Mach stem (M) protruding from G. These three waves meet at a triple point (T) a small distance from the surface. Downstream of the SMR the flow remains supersonic. As the shock diffracts to the receiver farside surface, the triple point moves further from the surface and the Mach stem becomes more and more curved (Figure 6.12 (c),(g)). Eventually, the diffracted shock propagates beyond the receiver farside and the Mach stem (M') from the opposite side of the body crosses the axis of symmetry (Figure 6.12 (d)). In the Kaca experiments, this was the reflection of the Mach stem from the tunnel wall (Figure 6.12 (h)). Finally, one of Kaca's other interesting findings was that the path of

the triple point as it moves to the farside of the cylinder is collinear with a line inclined at χ=33° to the symmetry plane (dash-dot in Figure 6.12 (e)-(h)) and that this path is independent of freestream conditions[59]. This path angle is observed by Yang[57] to be χ=31°, however in the current predictions this angle is greater and closer to χ=43° (Figure 6.12 (c)).

Two notable differences between the two datasets are that the impinging wave is curved in the predictions but planar in the experiments. The other is that on further investigation into the predicted flowfield, no slip-lines (S) are visible. Overall, this analogy shows that shock diffraction mechanism for the current problem is strongly related to the nature of the impinging shock reflection. The type of reflection transitions from a RR to a SMR as the shock diffracts around the receiver body and beyond the farside.

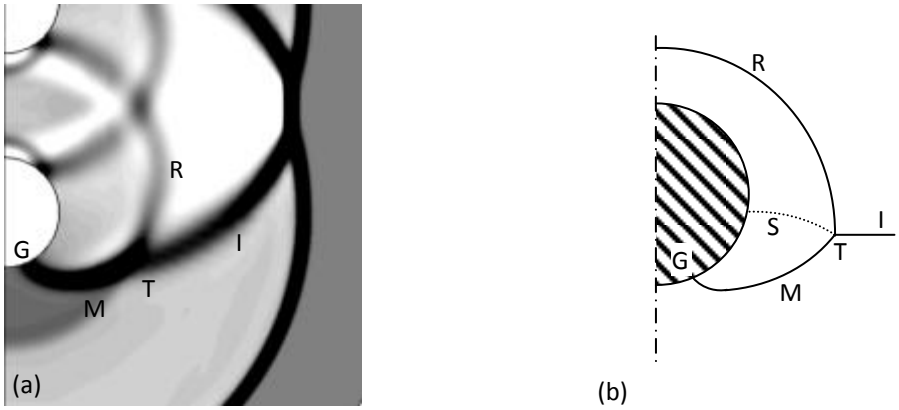

Figure 6.11 Close-up analysis of (a) predicted shock wave propagation at x/L=2 and (b) equivalent interpretation of planar wave diffraction[59]

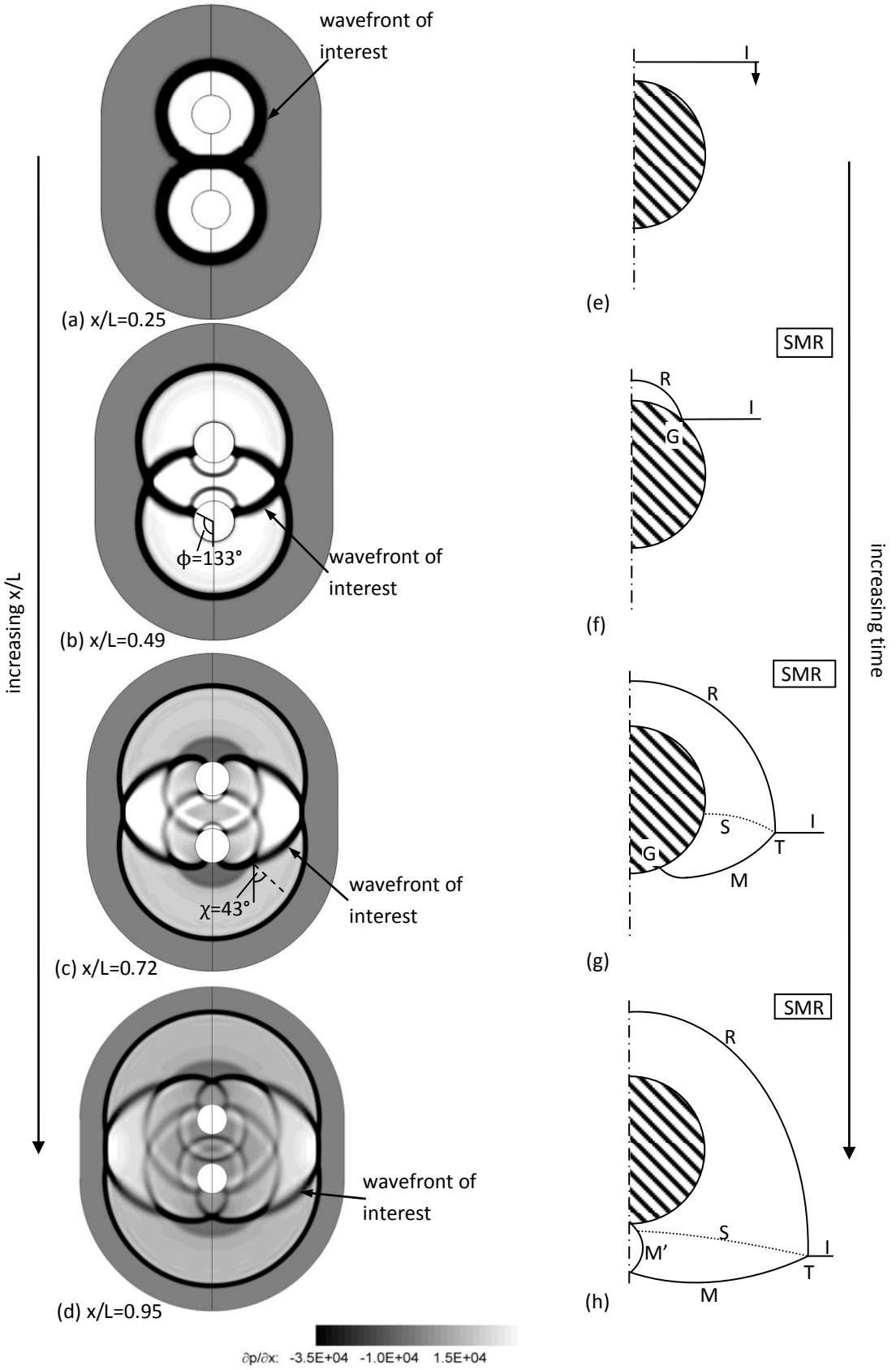

Figure 6.12 Predicted shock wave propagation (a-d), interpretations of planar wave diffraction[59] (e-h)

6.1.4.2 The shock diffraction attenuation parameter (Γ)

The impinging shock attenuates as it diffracts around the receiver body. The amount of attenuation is characterised by the difference between the initial nearside pressure rise from the isolated body measured on the ϕ=180° and the farside pressure rise at ϕ=0° (Equation 6.3). The amount that the shock is weakened by diffraction is important because it determines the magnitude of the farside region of differential pressure for a given initial shock strength. However, after a thorough literature search, no information has been found to detail what parameters might influence this attenuation. This section investigates the effect of two interaction parameters which are likely to affect the attenuation. These interaction parameters are the overall nearside pressure rise as a characteristic of the initial shock strength ($\Delta C_{p,near}$) and the second is an estimate of the shock path perimeter which the shock covers as it diffracts to the receiver farside ($C/D=1/\sin\theta_{obl}$). The parameter C is an estimation of this diffracted shock path perimeter and D is the body diameter. The shock path perimeter is the total contact path length over which the diffracted shock is in contact with the receiver body. This curved perimeter begins at the axial impingement point (x'/L) on the receiver nearside centreline (ϕ=180°) and then finishes on the farside centreline (ϕ=0°). The shock path perimeter is defined by the shock obliqueness angle (θ_{obl}). A low value of θ_{obl} means that the impinging shock is in contact with a large amount of the receiver surface before it reaches the farside, and hence leads to a high value of shock path perimeter. A high value of θ_{obl} means that the impinging shock is in contact with a small amount of the receiver body and thus leads to a low value of C. A subset of predicted solutions which cover a wide range of shock obliqueness angles ($13 \leq \theta_{obl} \leq 43°$) and different initial shock strengths ($0.1 \leq \Delta C_{p,near} \leq 0.47$) are considered to give some initial understanding about the attenuation associated with diffraction.

$$\Delta C_{p,near} - \Delta C_{p,far} \tag{6.3}$$

$$\Gamma = \frac{\Delta C_{p,near} - \Delta C_{p,far}}{\Delta C_{p,near}} \tag{6.4}$$

The attenuation of the diffracted shock is initially plotted against the shock path perimeter (Figure 6.13). It is clear that the amount of attenuation is a function of the

initial shock strength (shown by the larger initial shock strengths when the blunt generator is used). Moreover, although non-linear, the amount of attenuation generally increases as the shock path perimeter increases as might be expected. The y-axis is changed to show the shock diffraction attenuation parameter (Figure 6.14) which non-dimensionalises the attenuation by the initial shock strength (Equation 6.4). However, there remains data scatter and no overall trend which indicates that the data is a function of a further parameter. If both the shock diffraction attenuation parameter and the shock path perimeter are multiplied by the shock obliqueness angle measured in radians (θ_{obl}) a clear trend develops with reduced scatter (Figure 6.15). This shows more clearly that the attenuation associated with diffraction increases with shock path perimeter.

Nevertheless, it should be remembered that although these configurations include a wide range of initial shock strengths and shock obliqueness angles, these data points are only a subset of configurations and intended as a first step in understanding the attenuation associated with diffraction. Over the nine configurations presented here, the amount of attenuation only changes by a maximum of 20% between the different cases ($0.77 \leq \Gamma \leq 0.97$). Moreover, in all cases a significant proportion of the initial shock strength is weakened by the diffraction process.

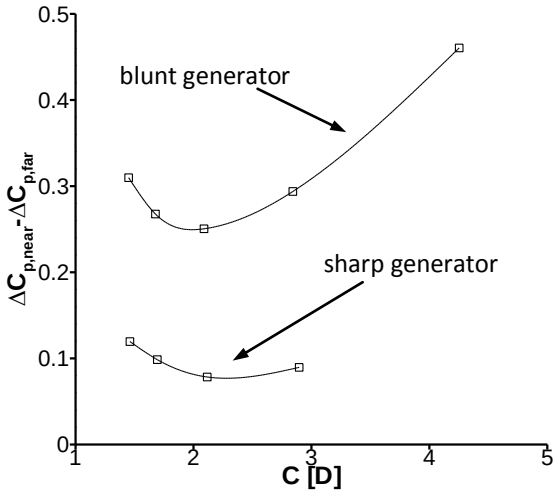

Figure 6.13 Shock diffraction attenuation as a function of shock path perimeter

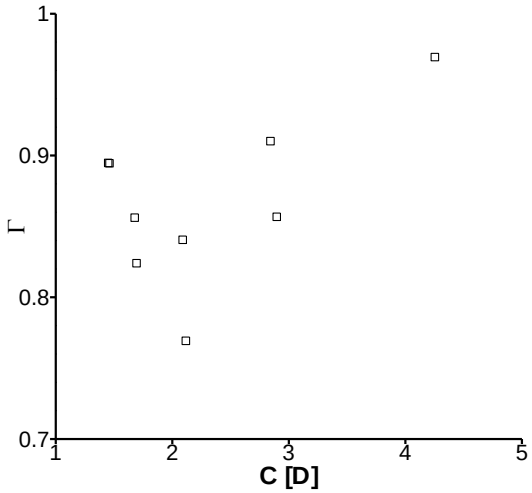

Figure 6.14 Shock diffraction attenuation parameter as a function of shock path perimeter. Note y-axis scale

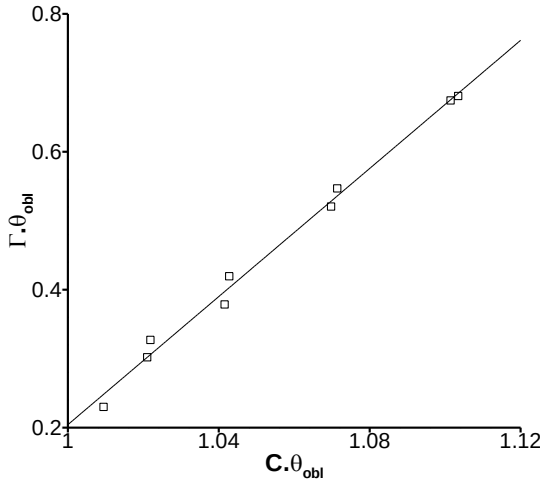

Figure 6.15 Shock diffraction attenuation parameter as a function of shock path perimeter

6.1.5 Other parameters relevant to the interference aerodynamics

The dataset obtained in this research allows the investigation of a wide range of parameters and includes almost 500 different configurations. However, not every aspect of the interference problem has been evaluated. Instead, the research objectives (§1.2.2) concentrated the available resources in the most efficient way to understand the underlying aerodynamics and the influence of the most important interaction parameters. This section briefly touches on the other parameters which have not been fully investigated. An estimation of their likely impact on the interference effects for a given initial configuration is also given based on the knowledge gained thus far.

6.1.5.1 Aspects of the interference problem which have not been investigated

Mach number: The main limitation of this dataset is that the majority of configurations are tested at a single Mach number (M_∞=2.43). One aspect which is Mach number insensitive is the diffraction mechanism which has been shown[57] to be very similar for M_∞=2.81 and M_∞=20. Nevertheless, the interaction parameters that a change in Mach number would influence have been discussed at some length. These are namely, the strength of the primary disturbance shock wave which in turn affects the expansion wave field and local flow pitch field. This would also change the disturbance shock angle which modifies both the shock obliqueness angle and the axial

impingement location. Consequently, it is expected that the Mach number will have a high impact on the interference loads (Table 6.1).

Reynolds number: The current dataset includes data at two Reynolds numbers (Re_D=1.4x10^6, Re_D=1.9x10^5). A change in Reynolds number will modify the nature of the body boundary-layer and will affect the viscous shock interactions. For example, at a given shock strength, the nature of a shock boundary-layer interaction is a function of the Reynolds number based on the approaching boundary-layer height ($Re_{\delta BL}$). The viscous interactions have been shown to have a moderate impact on the interference loads (§4.7).

r_G/r_b: The ratio (r_G/r_b) of the radius of the primary disturbance to the radius of the receiver body (Figure 6.16) is assessed as part of the investigation into the effect of lateral separation (§4.2). For the majority of configurations this is equal to 2.94, the same as the lateral separation since the spanwise offset is zero ($\Delta y/D=0$). A change in r_G/r_b modifies the extent of the nearside and farside interactions. However, over the range considered ($1.94 \leq r_G/r_b \leq 4.96$) it has only a small effect on the impinging shock path. If $r_G/r_b<1.94$ the bodies would be very close and this would not be a practical configuration. For $r_G/r_b>5$ the impinging shock will become more planar. Therefore, this parameter is expected to have a low impact on the interference loads.

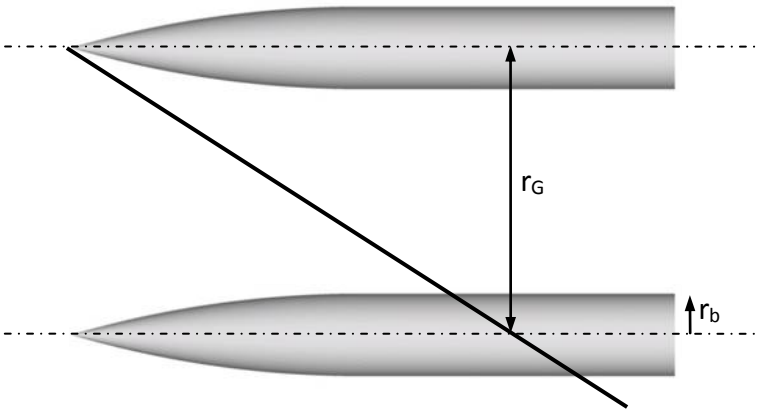

Figure 6.16 Schematic illustrating the generator bow shock radius (r_G) and body radius (r_b)

Sideslip angle: All bodies are tested at zero sideslip in order to simply the analysis and the experimental set-up. A variation in sideslip would make the

configuration asymmetric. As a result a component of the interference loads would be induced as side force and yawing moment interference. This is expected to have a moderate impact on the interference loads.

Roll angle: The receiver roll angle has no effect for un-finned receiver since it is a body of revolution. For the finned receiver a change in roll angle is expected to have a moderate impact on the interference loads. The non-zero roll angle will induce side force interference (ΔC_Y), yawing moment interference (ΔC_n) and rolling moment interference loads (ΔC_l) which have been zero for the configurations thus far.

Spanwise offset: All configurations have been tested at zero spanwise offset ($\Delta y/D=0$). A non-zero spanwise offset would modify the strength of the impinging disturbances and also the axial impingement location. A portion of the initial interference loads (ΔC_Z, ΔC_m) will be converted into ΔC_Y and ΔC_n and is expected to have a moderate impact on the interference loads.

Unsteady effects: All measured and predicted data is obtained under steady-state conditions. The practical application of this research is unsteady in nature and this requires a more detailed analysis before the likely impact can be estimated (§6.2)

Scale effects: The scale has no effect on the interference load coefficients as long as geometric and dynamic similarities are maintained. However, scale does have an effect on the subsequent motion of the bodies as a result of the aerodynamic interference and this is discussed further in §6.2.1.

Parameter	What the parameter changes	Impact on interference effects
M_∞	bow shock strength expansion field strength flow pitch distribution shock obliqueness angle impingement location	high
Re_D	body boundary-layer (δ_{BL})	moderate (viscous only)
r_G/r_b	extent of nearside and farside interactions	low

β	extent and magnitude of nearside and farside interactions	moderate
λ	-	none (un-finned)
	fin orientation	moderate (finned)
Δy/D	radial distance	moderate
d/dt	flowfield characteristics	discussed in §6.2.3- §6.2.4
D	body scale	discussed in §6.2.1

Table 6.1 Summary of the parameters not investigated which affect the interference aerodynamics

6.2 How the research findings apply to full-scale

Until this point, the discussion has primarily focussed on quasi-steady interference effects where measurements were obtained at a fixed body attitude with respect to time and predictions of the flowfield assumed steady-state conditions. This has been incredibly useful in order to simplify the underlying aerodynamics to gain a fundamental understanding about the nature of the interference effects (§4 and §5). However, any practical application at 'full-scale' which involves interference effects is unsteady in nature. For example, a primary application of this research relates to multiple submunitions which dispense from a larger bus vehicle and whose trajectory may be modified by the interference flowfield. This section aims to understand to what extent the research findings at steady-state 'tunnel-scale' apply at full-scale.

Although no unsteady (or dynamic) measurements were possible within the resources available to this research, a small number of unsteady CFD predictions have been completed. These model the trajectories of two finned bodies resulting from different initial multi-body arrangements. The two finned bodies were chosen as they are approximately representative of a submunition i.e. a statically stable, slender body with a moderate fineness ratio. The unsteady predictions were performed using the Cobalt Overset flow solver[44]. Previous studies have demonstrated the competence of this solver in evaluating the trajectory of a store released from an aircraft body[62]. This allows multiple overlapping grids to be assembled into a single grid after each time-step and also models the Rigid Body Motion (RBM) of the bodies in 6 Degrees of Freedom (6DOF), see Appendix D.1 for further details.

6.2.1 Scale effects

For the predictions of the bodies at full-scale to be genuinely analogous to the previous steady-state analysis, an appropriate set of full-scale conditions must be chosen. In order for the force coefficients to scale, geometric and dynamic similarity must be maintained. The finned bodies under investigation are the same non-dimensional geometry as the finned receiver in Chapter 5. The freestream Mach number is chosen to match the tunnel-scale condition as this is a representative

dispense Mach number for this application. Since the Reynolds number has little or no effect on the trajectory of the bodies[13] the unsteady flowfield is computed using the Euler equations. This assumption saved considerable computational resource for an acceptable reduction in fidelity[57].

How the translational and rotational motion of the bodies scale is investigated below in Equation 6.5 - 6.8. A dimensional approach is used to identify the parameters which affect the body motion, as characterised by the translational (a) and rotational accelerations (α_{rot}). It is clear from Equation 6.7 and 6.8 that the body motion is dependent on the full-scale conditions. The body motion is proportional to a characteristic of the operating conditions (p_∞) and inversely proportional to a characteristic of the dimensional body scale (L, L^2) and a characteristic of the material type (ρ_m).

The inputs to the calculation are M_∞,p_∞,T_∞,L,ρ_m and since M_∞ does not change between tunnel-scale and full-scale conditions:

$$U \propto \sqrt{T}\,, \rho \propto \frac{p}{T}$$

Translational motion		Rotational motion	
$a = \frac{F}{m}$	6.5	$\alpha_{rot} = \frac{M_m}{I_m}$	6.6
$F = f(\rho U^2 L^2)$		$M_m = f(\rho U^2 L^3)$	
$F \propto pL^2$		$M_m \propto pL^3$	
$m = f(\rho_m V)$		$I_m = f(mL^2)$	
$m \propto \rho_m L^3$		$I_m \propto \rho_m L^5$	

Giving:

$a \propto \frac{pL^2}{\rho_m L^3}$		$\alpha_{rot} \propto \frac{pL^3}{\rho_m L^5}$	
$a \propto \frac{p}{\rho_m L}$	6.7	$\alpha_{rot} \propto \frac{p}{\rho_m L^2}$	6.8

6.2.2 Unsteady calculations

Due to the importance of scale effects (§6.2.1) appropriate values of the parameters in Equations 6.7 and 6.8 are chosen and listed below. A summary of the tunnel-scale and full-scale conditions is also given in Table 6.2.

- The full-scale finned body diameter is equal to D=0.1m which is a representative size for the envisaged application and results in a overall length of L=0.74m
- Sea Level flow conditions are chosen (p_∞=101,325Pa) since the vehicle is likely to be ground targeted (Appendix D.2)
- The body material is chosen to be steel with a density of ρ_m=7860 kgm^{-3} and is a credible material for a warheaded submunition of this type

Parameter	Tunnel-scale	Full-scale
M_∞	2.43	2.43
p_∞	44,077.4 Pa	101,325 Pa
T_∞	134.2 K	288.2 K
Re_D	$1.4x10^6$	∞
D	0.02 m	0.1 m

Table 6.2 Flow conditions and geometric differences at tunnel-scale and full-scale

Following the decisions outlined above, the resultant mass properties for the finned bodies are summarised in Table 6.3. Although unlikely for an actual submunition, the body material is assumed to be homogeneous. This is accepted due to the dearth of any reliable information about an alternative and will suffice for this study.

Parameter	Value	Units
Material	Steel	-
ρ_m	7860	kgm^{-3}
m	37.06	kg
X_{cg}	0.455	m
I_{XX}	0.053	kgm^2
I_{YY},I_{ZZ}	1.194	kgm^2

Table 6.3 Mass and inertia properties for the full-scale finned body

The trajectory predictions do not take account of forces due to gravity since the focus is on the relative trajectory between the bodies. The unsteady calculations use a

global, implicit time-step of $\Delta t=3x10^{-4}s$[a] and cover a total solution time of $\Delta T=0.12s$. The full domain is large enough to allow one body length of translation in the Z_w-direction and half a body length of streamwise translation for the bodies experiencing the steady-state interference loads over the solution time. Further details about the grids and boundary conditions use in the unsteady calculations can be seen in Appendix D.1. On this basis there are 68 time-steps per calibre of translational motion and this is expected to be sufficient to resolve the time-dependent forces and moments.

The bodies are first arranged at t=0 in a multi-body arrangement and the flow is initialised to the freestream conditions. The subsequent body trajectories are calculated from the aerodynamic forces and moments acting on the bodies and the RBM equations are solved using a 3rd order Runge-Kutta scheme. At each of the time-steps (N=400), five Newton sub-iterations are used to reduce the temporal errors due to implicit integration[44]. Convergence information relating to the degree of iterative convergence at each time-step is not reported by Cobalt. Finally, all reported forces and moments are relative to the body fixed axes which move with the body and whose moment reference origin is fixed to the leading edge of the moving body. In the non-dimensionalisation of the forces and moments, the characteristic area and length used are the full-scale base area and base diameter respectively.

The configurations described in the following sections (§6.2.3 - §6.2.4) assume that the bodies undergo an ideal dispense from the bus vehicle. This assumes that the bus vehicle no longer has any aerodynamic influence on the bodies. It is also assumed that the streamwise direction is co-incident with the target line-of-sight and the focus is on the relative trajectory between the bodies and any deviation from this direction.

6.2.3 Results and discussion of the datum unsteady configuration

The datum unsteady configuration consists of two identical finned bodies which are initially axially aligned ($\Delta x/D=0$) with a lateral separation of $\Delta z/D=2.94$ and no spanwise

[a] This is 2.5 times the characteristic time of the problem ($\Delta t_{char}=U_\infty/D=1.2x10^{-4}s$). For an Euler calculation focussed on resolving the body integrated forces and moments, this is expected to be sufficient.

offset (Δy/D=0), Figure 6.17. Both bodies are placed at zero incidence at t=0 and the usual receiver and generator designations are retained in the following discussion. The measured steady-state interference loads for the finned receiver and sharp generator are ΔC_Z=-0.22, ΔC_m=1.35 (§5.2.2). This suggests that the bodies will translate away from one another but pitch towards each other, which increases the likelihood of a collision. An unsteady prediction of the flowfield is now discussed to assess the importance of the initial interference effects and thus how much insight into the unsteady motion can be gained from a steady-state analysis. Since this configuration is geometrically symmetrical, it is a good test case to assess the capability of the Cobalt Overset solver in the absence of any measured unsteady data.

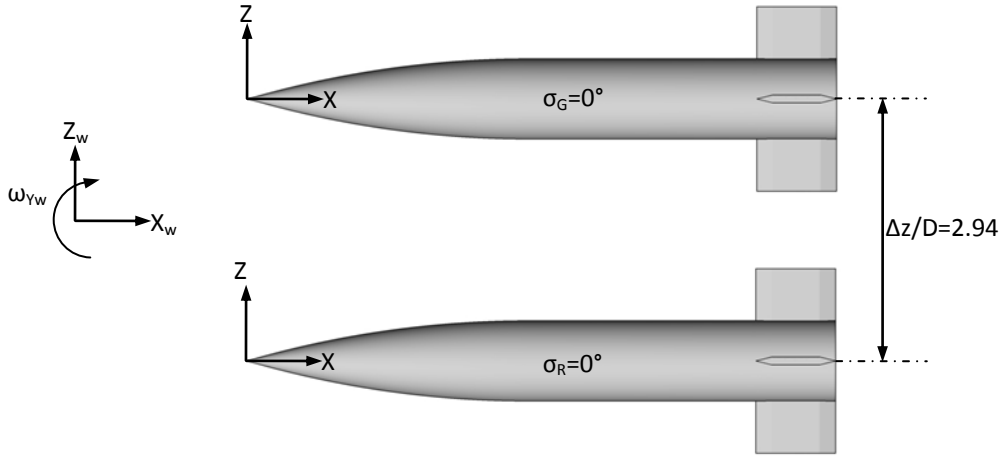

Figure 6.17 Datum unsteady configuration, finned body arrangement at t=0 and reference frames

6.2.3.1 Analysis of the body trajectories

The predicted longitudinal motion of both bodies is equal and opposite since the configuration is symmetric about the X_w-Y_w plane. As a result, the analysis in this section will only report the motion of the receiver body for simplicity. The equivalent data for the generator body are still included in the plots below to demonstrate the mutual nature of the interference aerodynamics. As expected C_Y*≈0, C_l*≈0 and C_n*≈0 for both bodies, as both were initially arranged at zero sideslip (β=0°) and zero roll (λ=0°) and remain so throughout the solution time. The * syperscript indicates an instantaneous value of a given parameter.

Overall, the aerodynamic interference in this datum unsteady configuration causes a collision between the bodies. The characteristics of the receiver body motion over the total solution time (ΔT=97.8ms) are broken down into four distinct phases (I - IV) to make it easier to understand the body trajectory and the influence of the interference effects. These are indicated in Figure 6.18 (a) and described below:

I. flowfield initialisation
II. initial influence of the interference loads and body motion away from generator
III. limited interference influence and body motion towards the generator
IV. in close proximity to the generator and fin collision

To help analyse the above phases of motion, Figure 6.18 plots different instantaneous parameters as a function of the solution time. Note that the loads and centre of pressure parameters are reported in a body-axes reference frame whilst the body velocities and displacements are reported in the wind-axes reference frame (Figure 6.17). Figure 6.19 shows snapshots of the flowfield at various instants throughout the solution time.

6.2.3.2 Phase I ($0 \leq t \leq 5ms$)

The flowfield is initialised to the freestream conditions at t=0. It takes approximately 5ms for the bow shock and expansion wave structures in the disturbance field to have any notable effect (Figure 6.19 (a)). Consequently, since the bodies are initially at zero incidence (and gravitational forces are neglected) the receiver normal force and pitching moment loads are zero in phase I (Figure 6.18 (a)).

6.2.3.3 Phase II ($5 \leq t \leq 50ms$)

After t=5ms, the disturbance field modifies the receiver normal force and pitching moment loads but has no effect on axial force. The predicted instantaneous interference loads are equal to C_Z*=-0.21, C_m*=1.26. These are close to the measured steady-state values of ΔC_Z=-0.22 and ΔC_m=1.36 and this lends confidence to the unsteady calculation that it captures the interference effects. The axial force on both

bodies remains roughly constant across the entire solution time (Figure 6.18 (a)). The predicted instantaneous axial force C_X*=0.42 is very close to the equivalent steady-state Euler prediction of C_X=0.41. Again, this gives confidence to the ability of the unsteady calculations to predict the basic aerodynamics of the receiver body. The constant axial force induces a negligible streamwise acceleration and thus the body streamwise velocity (V_{Xw}) increases linearly over the solution time (Figure 6.18 (d)).

The interference normal force accelerates the receiver body from rest in the downward, negative Z_w-direction. The resultant vertical velocity remains negative (Figure 6.18 (d)) for all of phase II and the receiver X_{cg} moves away from the generator (Figure 6.18 (e)). The pitching moment induced by the interference loads on the receiver lifting fins gives rise to an angular acceleration around the body centre of gravity. This increases the rotational velocity around the body pitching axis (Figure 6.18 (b)) and the receiver angle of attack increases accordingly (Figure 6.18 (c), (Figure 6.19(b)).

There is no significant lag between the changes in body attitude and the re-alignment of the static pressure field over the body and the instantaneous loads (Figure 6.18 (a)). Beyond a solution time of t≈30ms, the body normal force and pitching moment caused by the positive angle of attack become greater than the interference loads. These forces act in opposition to the interference loads and arrest the initial translational motion of the receiver away from the generator (Figure 6.18 (d)). At the end of phase II, the receiver reaches its maximum displacement from the generator body (Figure 6.19 (b)). Moreover, near the end of phase II when the receiver body is at low incidence, the interference effects change the static stability of the body to unstable (Figure 6.18 (f)) but when the angle of attack increases further in phase III, the centre of pressure moves rearward and the body becomes statically stable again.

6.2.3.4 Phase III ($50 \leq t \leq 87$ms)

In phase III, the receiver continues to pitch-up as a result of the dominance of the body normal force compared to the normal force produced by the fins. The body centre of pressure is upstream of the body centre of gravity and thus the body pitches towards

the generator and the angle of attack increases (Figure 6.18 (b),(c)). In doing so, the receiver normal force and pitching moment loads become many times greater than the interference loads which still act on the receiver. As a result, it is the angle of attack which now dominates the body motion. Consequently, this leads to a positive translational vertical velocity (Figure 6.18 (d)) and, for the first time, the receiver moves towards the generator body (Figure 6.18 (e), Figure 6.19 (c)). As the solution time increases, the receiver angle of attack increases further by the same process (Figure 6.18 (c)) and reaches a maximum of $\alpha^*=8.6°$ at t=87ms. At this time in the solution, the receiver is in close proximity to the generator body (Figure 6.19 (d)).

6.2.3.5 Phase IV ($87 \leq t \leq 98$ms)

Due to the proximity of the two bodies in phase IV, the impingement location of the primary disturbance is close to the receiver leading edge. The elevated pressure as a result of the interference and the proximity of the bodies leads to a negative angular velocity (Figure 6.18 (b)) and a small reduction in the receiver angle of attack (Figure 6.18 (c)). This acts to arrest the upward motion of the receiver body. However, this has little effect because the receiver momentum towards the generator body at this time in the solution is substantial. Finally, at t=98ms the upper receiver fin collides with the lower generator fin (Figure 6.19 (e)).

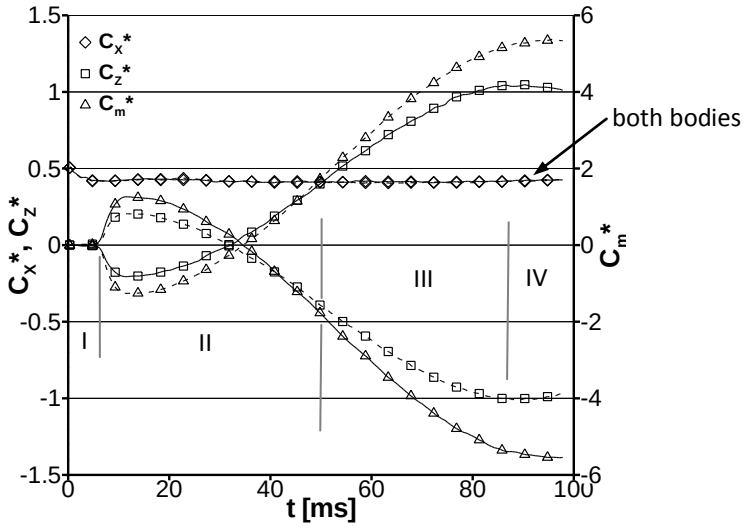

(a) axial force, normal force and pitching moment (relative to the body-axes reference frame)

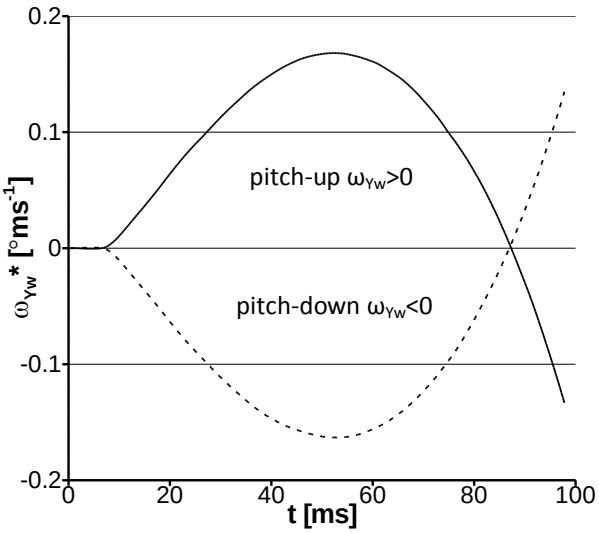

(b) rotational body velocity (relative to the wind-axes reference frame)

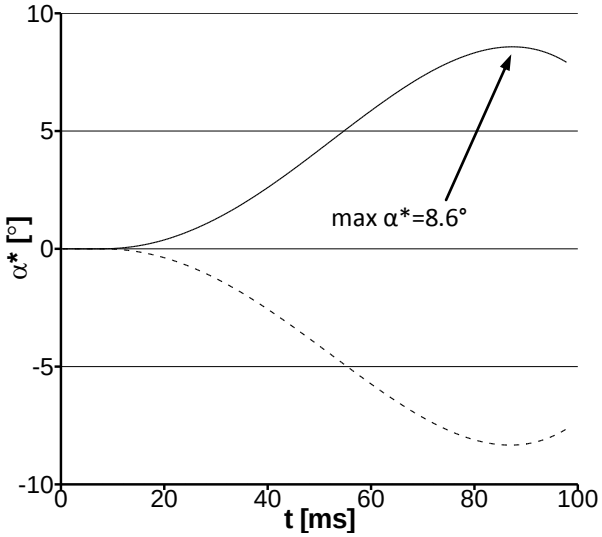

(c) angle of attack (relative to the wind-axes reference frame)

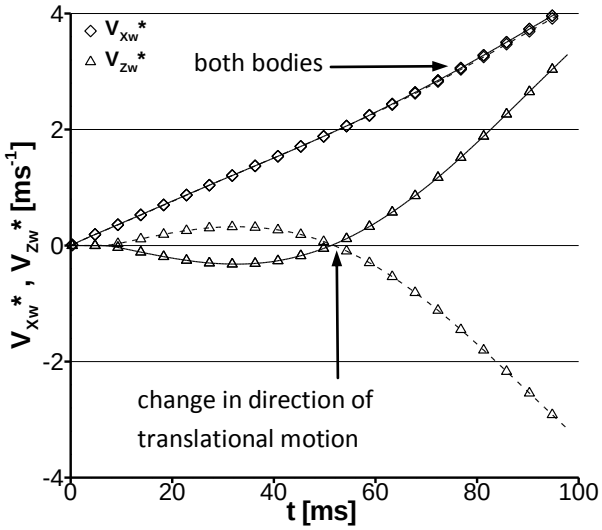

(d) streamwise and vertical translational body velocity (relative to the wind-axes reference frame)

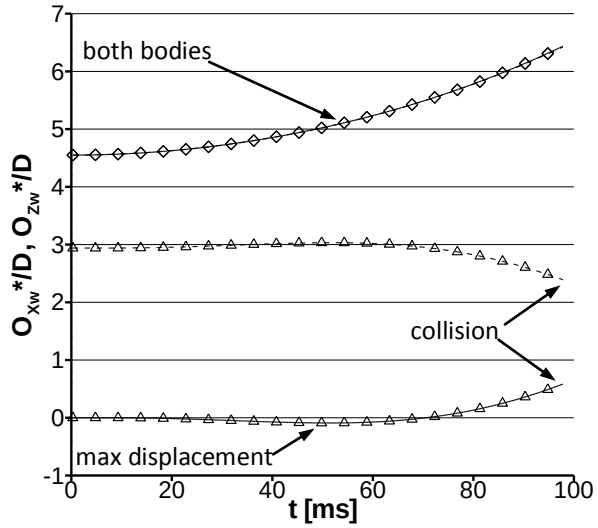

(e) streamwise and vertical body X_{cg} location (relative to the wind-axes reference frame)

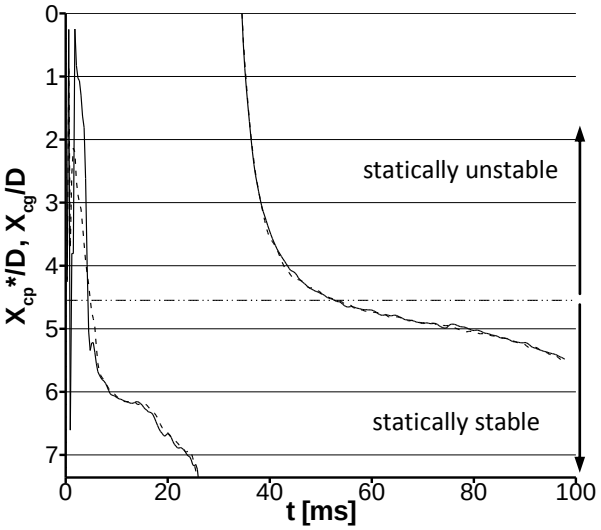

(f) longitudinal centre of pressure (relative to the body-axes reference frame)

Figure 6.18 Predicted instantaneous parameters as a function of the solution time for the receiver (solid line) and generator (dashed line) bodies: m2652, Δx/D=0 Δz/D=2.94, σ_R=0° σ_G=0° at t=0

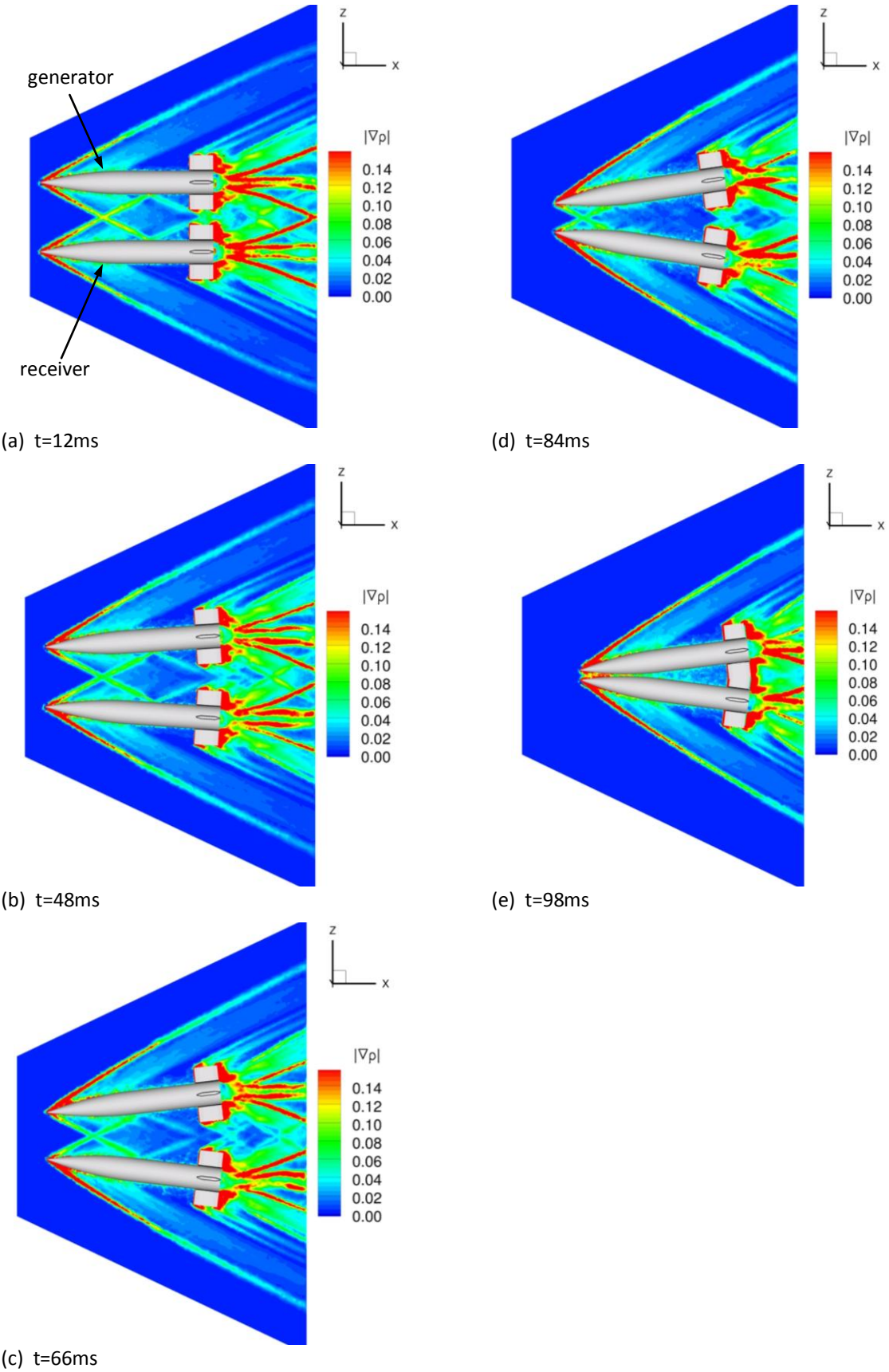

(a) t=12ms

(d) t=84ms

(b) t=48ms

(e) t=98ms

(c) t=66ms

Figure 6.19 Instantaneous snapshots of the predicted flowfield as a function of the solution time, (a-e) shows contours of $|\nabla\rho|$ on the X_w-Z_w plane: m2652, $\Delta x/D=0$ $\Delta z/D=2.94$, $\sigma_R=0°$ $\sigma_G=0°$ at t=0

The aerodynamic interference causes a collision between the two bodies which would be disastrous in a practical situation. This is a substantial finding of this research. Importantly in this configuration, it is the initial interference loads which determine and dominate the subsequent motion of the bodies and this can be accurately predicted by a steady-steady analysis of the initial configuration. Finally, there is very little lag (in the order of 2ms) between a change in body attitude and the subsequent change in body forces and moments. This means that steady-state snapshots throughout the solution time give an accurate representation of the unsteady flowfield.

The Cobalt Overset solver demonstrates a physically realistic prediction (symmetric motion) of the datum unsteady configuration. Although no unsteady measurements were available for direct comparison, the instantaneous interference loads were close to the steady-state measurements and predictions. Moreover, the forces and moments under an induced pitch were in-line with isolated values. A small amount of motion asymmetry between the two bodies is noticed (a difference in α^*=0.2°, C_Z^*=0.04, C_m^*=0.2). This is attributed to asymmetries in the grid assembly process of the inter-body flowfield grid. Overall, the important flow physics are captured using the Euler assumption in the unsteady predictions.

6.2.4 Effect of initial axial impingement location on body trajectory

The discussion of the steady-state configurations in §4.6 and §5.2 concluded that the axial impingement location of the primary disturbance has a profound effect on the magnitude and polarity of the steady-state interference loads. The discussion in this section evaluates whether this parameter is as important to the subsequent trajectories of the bodies. This is of interest because in a practical situation, the axial stagger between the bodies is a key design parameter and how the unsteady characteristics vary with this must be understood.

The configuration discussed in this section involves the bodies initially arranged with a lateral separation of $\Delta z/D=2.94$ and with the generator placed upstream of the receiver ($\Delta x/D=2.68$). The bodies are both initially at zero incidence and are without a spanwise offset ($\Delta y/D=0$). The measured steady-state interference loads for the finned receiver and sharp generator are equal to $\Delta C_Z=0.01$, $\Delta C_m=-0.36$. These do not include the effects of the generator fins onto the receiver body but it does suggest that the receiver will pitch away from the generator. This is examined with the prediction of the unsteady flowfield and is compared to the datum configuration to establish the effect of initial axial impingement location. Since the configuration is asymmetric the motion of the receiver body will be described followed by a description of the generator body motion.

6.2.4.1 Analysis of the unsteady configuration where Δx/D=2.68

The flow is initialised over a period of t=5ms where the receiver normal force and pitching moment are zero (Figure 6.20 (a)). An increase in normal force and pitching moment magnitude is observed when the impinging shock is formed. Shortly after, the impinging expansion waves have an effect and the predicted instantaneous interference loads are arrive at settled values of $C_Z^*=-0.01$ and $C_m^*=-0.21$ at t=15ms. These are close to the measured and predicted values for a similar steady-state configuration ($\Delta C_Z=0.01$, $\Delta C_m=-0.36$). This pitching moment interference is largely the result of the region of negative differential pressure that acts on the receiver nearside and the farside region of positive differential pressure which tend to pitch the receiver

nose-down. There is only a small amount of interference on the generator body since the receiver bow shock impinges near the trailing edge (Figure 6.21 (a)).

The pitching moment interference on the receiver induces a negative angular velocity (Figure 6.20 (b)) and leads to a negative angle of attack (Figure 6.20 (c)). As the solution time increases, similar characteristics are observed to those in the datum configuration. Namely that after the initial interference, the receiver angle of attack becomes more negative and this determines the subsequent trajectory. As the receiver angle of attack becomes more negative, the negative normal force and positive pitching moment become larger (Figure 6.20 (a)) and this leads to a downward translational velocity (Figure 6.20 (d)) and a further pitch away from the generator. This in turn, moves the receiver away from the generator body (Figure 6.21 (b)). This process is repeated for the receiver body with the angle of attack becomes more negative (to a minimum of α^*=-7.2°) as the solution time increases and the separation distance between the bodies becomes larger (Figure 6.20 (e), Figure 6.21 (c)). Consequently, there is no collision between the bodies in this configuration (Figure 6.21 (d)).

The generator body motion is only affected after t=40ms. The receiver bow shock impinges at the body trailing edge which results in a modest angular velocity (Figure 6.20 (b)) which leads to a negative angle of attack (Figure 6.20 (c)). This negative angle of attack remains constant as the receiver bow shock moves aft of the generator and there is no further interference as the solution time increases. Even though a small negative normal force and positive pitching moment act on the generator, the centre of gravity does not notably move towards the receiver body (Figure 6.20 (e)).

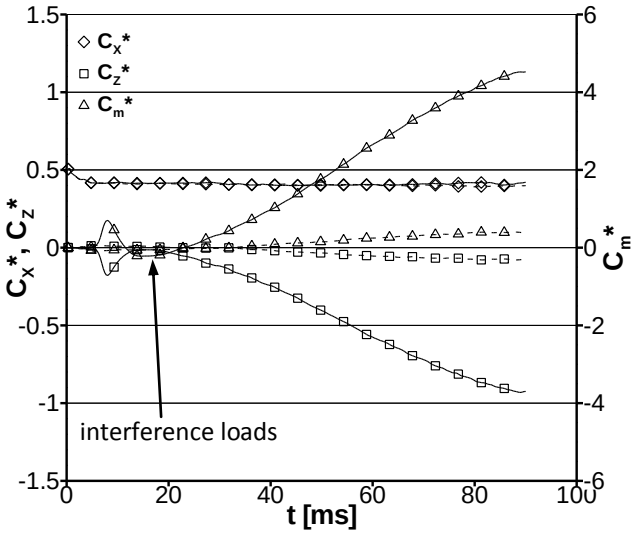

(a) axial force, normal force and pitching moment (relative to the body-axes reference frame)

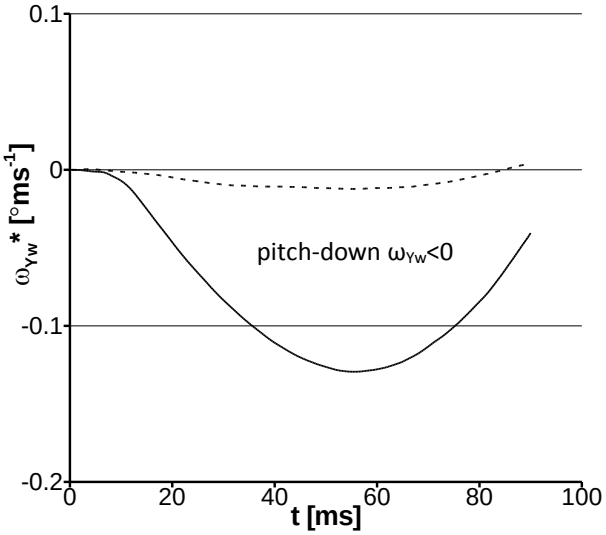

(b) rotational body velocity (relative to the wind-axes reference frame)

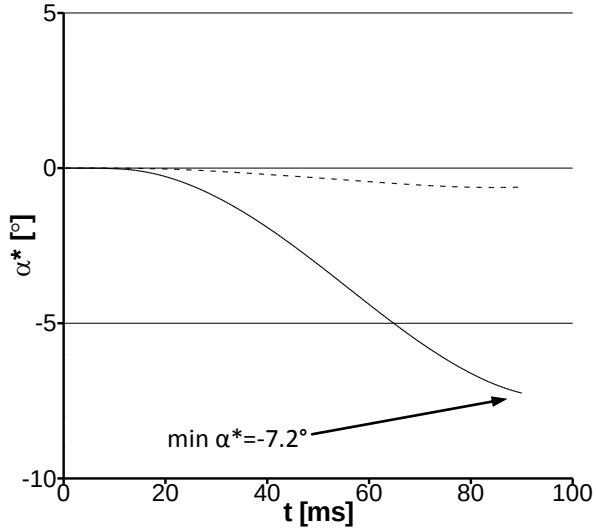

(c) angle of attack (relative to the wind-axes reference frame)

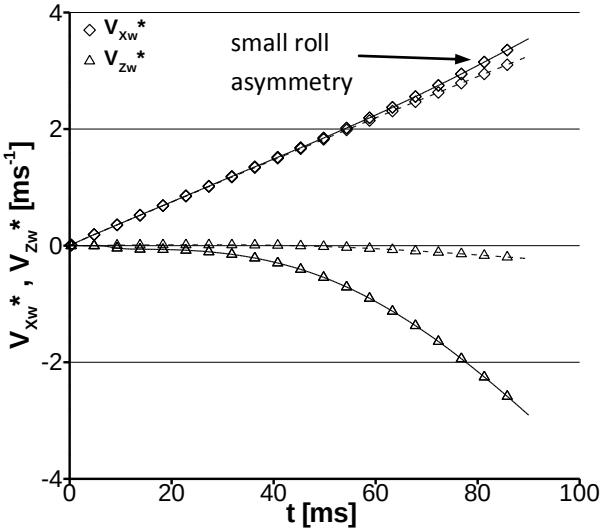

(d) streamwise and vertical translational body velocity (relative to the wind-axes reference frame)

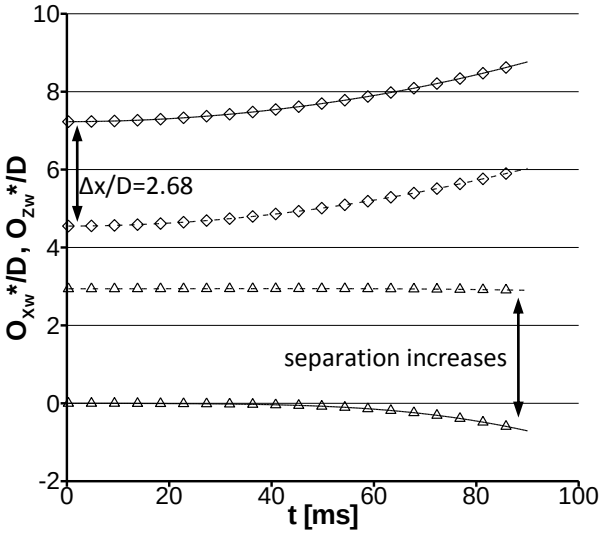

(e) streamwise and vertical body X_{cg} location (relative to the wind-axes reference frame)

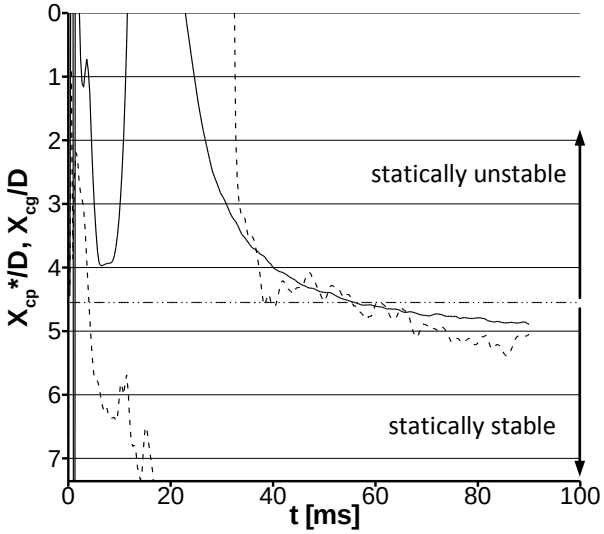

(f) longitudinal centre of pressure (relative to the body-axes reference frame)

Figure 6.20 Predicted instantaneous values of parameters as a function of the solution time for the receiver (solid line) and generator (dashed line) bodies: m2652, Δx/D=2.68 Δz/D=2.94, σ_R=0° σ_G=0° at t=0

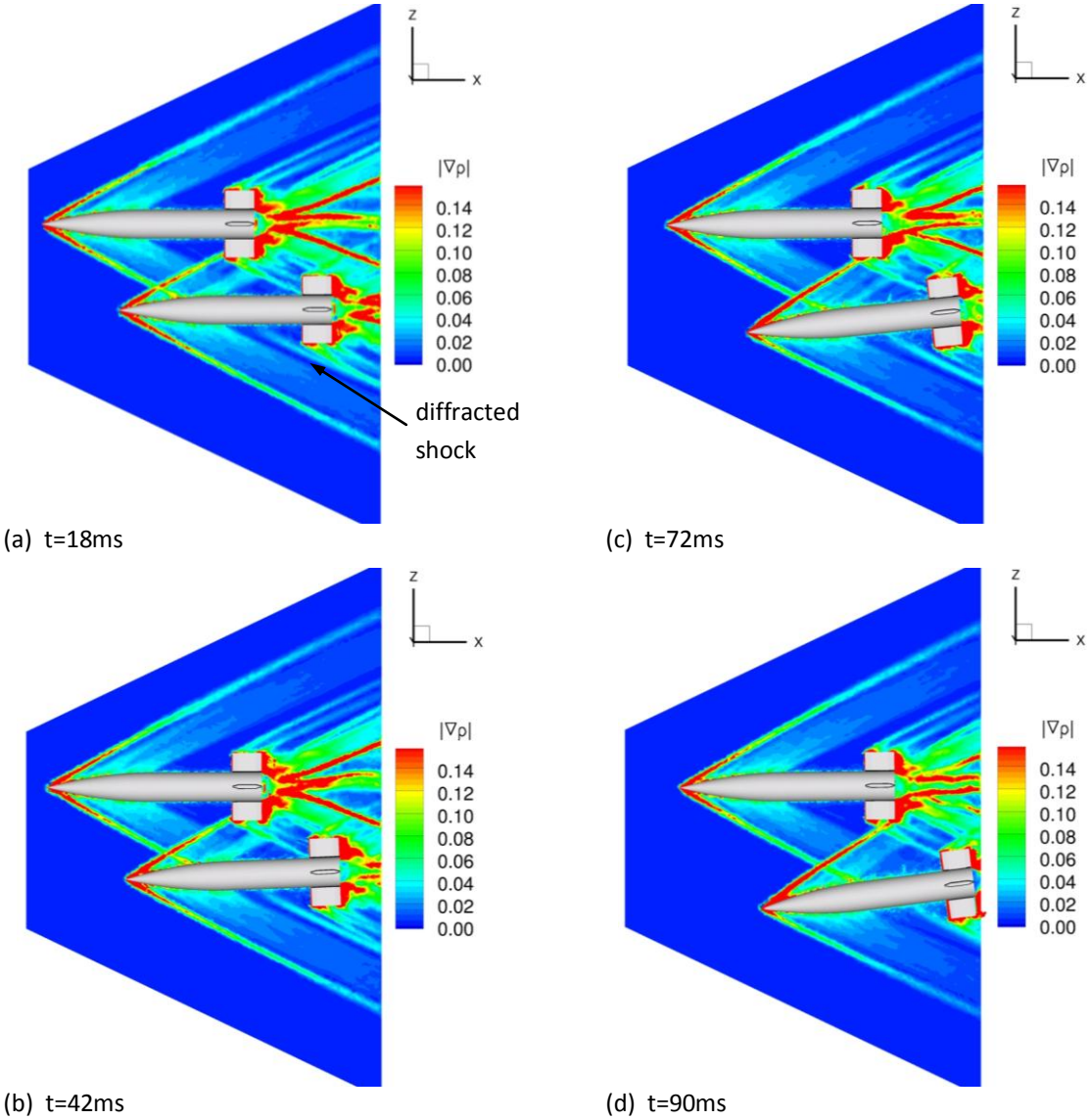

Figure 6.21 Instantaneous snapshots of the predicted flowfield as a function of the solution time, (a-d) shows contours of $|\nabla\rho|$ on the X_w-Z_w plane: m2652, $\Delta x/D=2.68$ $\Delta z/D=2.94$, $\sigma_R=0°$ $\sigma_G=0°$ at t=0

6.2.4.2 The effect of axial impingement location on the body trajectories

The initial axial impingement location has a profound effect on the subsequent trajectories of the two bodies. When the generator is placed upstream of the receiver, the trajectory of the bodies is very different to the datum configuration. When the axial stagger is $\Delta x/D=2.68$, there is no collision between the bodies. In this configuration the initial interference loads pitch the receiver away from the generator and the separation between the bodies increases for the rest of the solution time. This is another important finding because in a practical situation the difference in

geometric terms between Δx/D=0 and Δx/D=2.68 is not alot, yet one results in a collision and the other does not. Moreover, the analysis in this section gives credibility to the assumptions based on the steady-state analysis which indicate exactly what is observed in the unsteady results.

As with the prediction of the datum configuration, the instantaneous interference loads are close to the measured steady-state values, giving confidence to the CFD prediction method. A small asymmetry is noticed in this configuration which induces a maximum receiver roll angle of $\lambda^*=0.3°$, and leads to a $C_Y^*=0.02$ and $C_n^*=0.1$. These are relatively small and this is attributed to the complex interaction of the shocks which emanate from the generator lower fin onto the receiver upper fin

6.2.5 Summary of unsteady trajectory predictions

In summary, some very significant findings have been discussed in this section. The datum unsteady configuration shows that the aerodynamic interference between two bodies can result in a collision. Furthermore, the body trajectories are largely determined by the initial interference loads, particularly the induced pitching moment. This is important, as the initial interference effects can be accurately predicted with a steady-state prediction of the initial configuration.

The initial axial impingement location is critical in determining the subsequent trajectories of the bodies. This is because this parameter has a profound impact on the polarity of the steady-state interference loads and the body trajectories are known to strongly depend on the initial interference. This analysis confirms that the axial impingement location also has a large impact on the unsteady flowfield characteristics and there is no collision when the generator is initially placed upstream of the receiver. Finally, even though there is no collision, the bodies depart from the original streamwise axis. This may be detrimental to the accuracy of the weapon since the streamwise axis is assumed aligned with the target line-of-sight. Finally, it is seen throughout this section that the lessons learned in the research findings presented in the previous chapters do apply to the full scale problem because the body trajectories are dominated by the initial interference.

Overall, the unsteady CFD prediction of the instantaneous interference loads are close to the measured steady-state loads for equivalent configurations. Moreover, no significant lag is observed between a change in body attitude and the instantaneous loads. This indicates that steady-state snapshots throughout the solution time will give an accurate representation of the unsteady flowfield.

6.3 Summary and implications of research findings

This chapter summarises the key chapter findings and further discusses some of the most important themes. The interference loads for the un-finned receiver in a given disturbance field are primarily a function of of the axial impingement location (x'/L) the strength of the impinging disturbances (ψ, η, σ_p) and the shock obliqueness angle (θ_{obl}). In addition to these parameters, the interference loads which act on a finned receiver are also a function of the strength of the local flow pitch field on the body centreline (σ_p') and the proximity of the diffracted shock and the fin leading edge ($\Delta x_f'/D$). The relationship between these interaction parameters and the geometric parameters (such as $\Delta x/D$, $\Delta z/D$ and σ_R) has been simplified by graphical means. Overall, the interference loads are most strongly affected by the axial impingement location of the primary disturbance especially for configurations which involve fins. This is emphasised with a basic empirical method to estimate ΔC_Z within ±0.02 and ΔC_m to within ±0.2 as a function of x'/L alone. Due to the complexity of the underlying aerodynamics, particularly in relation to the influence of the diffracted shock, some data scatter still exists and a more generalised correlation is difficult to obtain. The physics of the diffraction process are found to be similar to an unsteady planar wave as it reflects and diffracts around a cylinder. The initial regular reflection seen on the nearside surface transitions into a Single Mach Reflection and this Mach stem diffracts to the receiver farside and crosses with its opposite on the other side of the body. The parameters which have been investigated in this research were chosen to allow the greatest understanding of the underlying aerodynamics of the interference problem within the resources available. Those areas which have not investigated have been summarised and their likely influence on the interference effects estimated.

For two axially aligned finned bodies at full-scale, the unsteady aerodynamic interference effects result in a collision. A large pitching moment is induced by the interference on the body fins and this pitches the bodies towards one another. The research findings apply well to full-scale because the initial interference loads (ΔC_Z, ΔC_m) dominate the subsequent body trajectories and are relatively insensitive to Reynolds number effects for a turbulent boundary-layer. Furthermore, the initial

interference effects can be accurately predicted by a steady-state analysis of the initial configuration. When the initial axial stagger between the bodies is changed so that the axial impingement location is on the receiver forebody (away from the fins), a markedly different trajectory occurs. In this case, the receiver pitches and translates away from the generator body and no collision occurs. This further underlines the significance of the axial impingement location to the subsequent body trajectories. Finally, no significant lag is observed between changes in body attitude and the instantaneous body loads and thus steady-state predictions throughout the solution time will give an accurate representation of the unsteady flowfield.

The main implications of the research findings are summarised as follows.

- A collision between two bodies can result from aerodynamic interference between two finned bodies. The designer must take significant steps to ensure that this does not happen, and pay particular attention to the sensitivity of the subsequent body trajectories to the initial axial impingement location.

- Even when no collision occurs, the interference effects can cause the bodies to pitch and translate away from one another. This may degrade the accuracy of the weapon and could require large control inputs to change the heading of the bodies back towards the target line-of-sight.

- The finned receiver can become statically unstable as a result of interference with movement of X_{cp}/D of up to 4.5 calibres. This happens exclusively at low incidence $|\sigma_R| < 6$ which is a typical operating range for an initial dispense orientation and it would again be disastrous if one or more bodies became uncontrollable.

- When x'/L is near the trailing edge, the fin interference loads cause large pitching moments towards the generator body. The size of control surfaces and their distance from the X_{cg} should be minimised to avoid large interference effects.

- A key design aim should be to obtain a dispense configuration where the x'/L is near the leading edge of the receiver, i.e. far away from the fins. Due to the length of the body, this may be difficult to achieve but it is nonetheless very important.

- To minimise body motion for a given interference load, the body scale should be as large as possible, the body materials should be the most dense possible, the dispense altitude should be as high as possible.

- The latter two implications above are difficult to satisfy in a realistic design. Warheaded submunitions are likely to be made from as light material as possible in order to allow more payload and reduce overall weight. The weapon is likely to be ground targeted, so the dispense pressure condition will be at its maximum. However, there is some room for the body scale to be a key design factor. This is particularly important because the rotational motion is proportional to $1/L^2$ and the pitching moment interference plays a significant role in determining the subsequent body trajectories.

Chapter 7 Conclusions and Future Work

Aerodynamic interference between multiple slender bodies in a high-seed flow has been investigated. To date, the flow physics associated with this high-speed interference problem have not been commonly reported in the open literature. To address this, the current research has studied in detail, the underlying aerodynamics of slender bodies in close proximity and quantified the effects on the body force and moment as well as static stability characteristics. Predictions of the effect of aerodynamic interference on the subsequent body trajectories are also conducted.

Four different slender bodies were designed, manufactured and tested in a comprehensive wind tunnel study. This included two receiver bodies of interest one finned and the other un-finned. Moreover, sharp and blunt generator bodies produced the disturbance flowfield. The forces and moments on the receiver body were measured along with the surface pressure distribution using Pressure Sensitive Paint. Shadowgraph visualisations of the flowfield were also taken. This measurement set allowed the assessment of the following important non-dimensional parameters: lateral separation between the bodies, axial impingement location of the primary disturbance, receiver incidence, and the disturbance field strength for the finned and un-finned receivers. Both steady-state and unsteady CFD predictions of the flowfield were successfully used to further understand the measured characteristics.

7.1 Research conclusions

The conclusions drawn from the results and discussions related to the specific research objectives are summarised below.

7.1.1 Assessment of the CFD prediction method

- Very good agreement is observed between the measured and predicted interference loads in all configurations studied. The predictions were successfully used to understand the underlying flow physics of the interference effects.

- Good qualitative and quantitative agreement is found between the predicted and measured surface pressures for both receiver bodies.

- In the vast majority of the configurations studied, the viscous interaction effects were negligible and Euler computations could rapidly predict accurate values of the interference loads.

- The effects of viscosity must be predicted to accurately resolve the more complex flow physics such as the shock interactions with the boundary-layer and body vortex flows which are prevalent when the body is at high incidence.

7.1.2 Topology of the interference flowfield and the diffraction mechanism

- This interference flowfield is primarily dominated by the impinging shock and expansion waves. The topology of the interference flowfield is further complicated by multiple reflections and diffraction of the impinging disturbances around the bodies.

- The diffracted shock severely attenuates as it diffracts around the body by as much as 90% of its initial strength. The expansion waves did not have as much of an impact on the farside flowfield as the diffracted shock waves.

- The steady-state shock diffraction mechanism is similar to that observed for an unsteady shockwave as it diffracts around a cylindrical obstacle at supersonic

speeds. The initial regular reflection on the receiver nearside transitions into a single mach reflection when the local Mach number can no longer support the necessary flow turning.

- The diffracted Mach stem becomes more curved as it diffracts around the body and eventually crosses with its opposite on the farside of the body and has a notable effect on the farside pressure distribution.

7.1.3 Origins of the interference loads

- The impinging disturbances induce a differential local pressure from the isolated configuration (Δp) over an affected surface area on the receiver body. The complexity of the regions of differential pressure increases for configurations where there is extensive propagation of the impinging disturbances to the receiver farside. These elemental regions of differential pressure combine to give the integrated interference loads.

- For a configuration affected by a primary interaction, the interference loads are primarily influence by a set of interaction parameters which define the extent and magnitude of the regions of differential pressure. These are the axial impingement location, the strength of the impinging disturbances, the shock obliqueness angle and the attenuation associated with diffraction.

- For the finned receiver, the interference loads are observed also be a function of the strength of the flow pitch upstream of the fin leading edge.

7.1.4 Un-finned receiver body

- The relationship between the measured interference loads and the geometric parameters was highly complex. General trends were difficult to extract since a change in a given geometric parameter (such as body incidence) led to a variation in a number of the individual interaction parameters.

- The effect of lateral separation is dependent upon the initial axial stagger between the bodies. However, this parameter has a large effect on whether secondary interactions exist.

- In general, the interference effects are larger when the receiver is placed at high incidence. In some configurations, the difference in interference loads are up to an order of magnitude in comparison the zero incidence case.

- In general, a stronger disturbance flowfield does not change the measured trends but amplifies the magnitude of the interference effects. However, some notable configurations are insensitive to disturbance field strength.

- The interference loads are most sensitive to the axial impingement location as it has a profound effect on both the magnitude and polarity of the interference loads. Completely opposing induced forces and moments are observed as the impingement location moves over the receiver body.

- A preliminary estimate of the interference loads can be made as a function of axial impingement location to within $\Delta C_Z=\pm 0.03$ and $\Delta C_m=\pm 0.2$.

- Maximum measured interference loads for the un-finned receiver were in the order of $\Delta C_Z=-0.4$ and $\Delta C_m=2$. These equate to an equivalent incidence of $\sigma_{eff}=-2.7°$ and $\sigma_{eff}=-1.8°$ respectively.

7.1.5 Viscous effects

- The interference aerodynamics are further complicated by interactions between the impinging shockwaves and the boundary-layer and body vortex flows.

- Several examples of a supercritical shock boundary-layer interaction are observed. As a result of the re-organisation of the leeward flowfield, this significantly delays the roll-up location of the body vortex and thus makes a notable contribution to the overall interference load.

- The separated flow regions which result from the shock boundary-layer interaction can affect the propagation angle of the impinging shock and this modifies the extent of the farside region of differential pressure which has a notable impact on the interference loads.

- In a configuration where the receiver is high negative incidence, the potency of the diffracted shock diminishes due to an interaction with the farside (leeside) body vortex and this has a notable impact on the interference loads.

7.1.6 Finned receiver body

- When the impinging shock passes close to the fins, the magnitude of the interference loads can increase by a factor of three in comparison to the un-finned receiver case. However, when the diffracted shock is far upstream of the fins the interference effects are similar to those for the un-finned receiver.

- The fin interference loads are induced by a complex combination of the effect of the local flow pitch upstream of the fin and the effect of the compression and expansion disturbance waves. It is therefore unlikely that a simple preliminary prediction technique could be based on the flow pitch alone.

- The dominant interference mechanism which determines the fin interference loads (flow pitch or pressure footprint) depends on the axial stagger configurations and the receiver incidence.

- The effect of receiver incidence is subtly more important for the finned configurations than the un-finned receiver cases. This is because it is more important which part of the finned receiver body is located in the strong region of the disturbance flowfield.

- In some configurations, 2nd order interference effects are observed when the flow pitch upstream of the fins changes the fin shock structure and thus the body interference loads (excluding the fins).

- The longitudinal centre of pressure is substantially affected by the aerodynamic interference and can lead to a change in static stability of the finned receiver. This is observed for the body at low incidence only ($|\sigma_R < 6|$) where for a given incidence, the axial impingement location determines whether the interference has a stabilising or de-stabilising effect.

7.1.7 Application of research findings to full-scale

- When the bodies are initially axially aligned ($\Delta x/D=0$), the aerodynamic interference between the bodies results in a collision.

- For bodies which have no initial momentum, the subsequent body trajectories are dominated by the initial interference loads, particularly the induced pitching moment. This is significant because the initial interference effects can be accurately predicted by a steady-state analysis of the initial configuration.

- For a configuration where the generator is placed ahead of the receiver, a collision does not occur and this demonstrates the sensitivity of the subsequent body trajectories to the initial axial impingement location.

- No significant lag is observed between a change in body attitude and the re-alignment of the static pressure field and the instantaneous loads. Therefore, this implies that steady-state snapshots throughout the solution time will give an accurate representation of the unsteady flowfield.

- Overall, based on the unsteady configurations studied the research findings for the bodies under steady-state conditions are found to apply to the full scale, unsteady problem.

7.1.8 Research implications design recommendations

- The designer must take account of the effects of aerodynamic interference in order to avoid a collision between the bodies in a dispense situation. Even when a collision does not occur, the interference effects may degrade the accuracy of the weapon.

- Changes in stability can occur at low incidence which is a typical operating range for an initial dispense orientation and one or more bodies become uncontrollable. The designer must reduce the likelihood of this happening through the control of the axial impingement location.

- The size of control surfaces and their distance from the X_{cg} should be minimised to avoid large interference effects.

- A key design aim should be to obtain a dispense configuration where the impingment location of the primary interaction is near the leading edge of the receiver. Due to the length of the body, this may be difficult to achieve but it is nonetheless very important.

- The body motion does not scale with the interference loads. Consequently, the body scale should be as large as possible, the body materials should be the most dense possible, the dispense altitude should be as high as possible.

Based on the conclusions drawn from the specific research objectives, this research has met its overall aim. Namely, this investigation has quantified the aerodynamic interference effects between two slender bodies for a wide range of configurations and explained the associated flow physics mechanisms which cause the interference effects. In these terms, the research can be considered a success.

7.2 Recommendations for future study

Although many of the knowledge gaps identified in §2 have been addressed by the current research, there remain areas of interest which require future study. Suggestions for some of these are listed below.

7.2.1 Experimental work

1) Conduct quasi-steady experiments similar to those in this research to assess the influence of the freestream Mach number on the interference effects.

2) Conduct experiments using the Captive Trajectory Support system to measure the actual flight trajectories of the two finned bodies in the tunnel. A test of

the axially aligned configuration will verify whether a collision occurs. Further tests could investigate the effect of initial axial stagger between the bodies and would be used to validate the unsteady predictions presented in this research.

3) Conduct simplified wind-tunnel tests for a single finned body as it traverses through the flowfield of a cavity representative of the bay of a bus vehicle. Investigate the unsteady aero-acoustic interference between the cavity and slender body which are likely to result during a dispense motion.

4) An alternative to the CTS experiments could be a set flight tests where two bodies are dispensed from a sled at supersonic speeds. This would be as realistic as possible to the full-scale problem and include the aerodynamic complexities which relate to the dispense motion and those which relate to interference effects with other slender bodies

7.2.2 Computational work

1) Compute further unsteady predictions to assess the impact of different initial configuration arrangements on the subsequent body trajectories. Variables to be investigated could include lateral separation between the bodies, body incidence, body sideslip and body roll. This would give the designer a fuller knowledge of the key dispense design parameters and a knowledge of factors which affect operational repeatability.

2) Compute a small number of unsteady predictions which include the effects of viscosity. This will identify if there are any significant unsteady viscous effects.

3) Use CFD to understand the flow physics associated with a slender body as it dispenses from a high-speed weapon bay.

4) Based on the existing experimental dataset, use CFD to investigate whether it is possible to counter the interference effects by control surface inputs. Assess the fin-effectiveness in this context and identify limits where the interference can no longer be controlled.

5) Use CFD to assess the different control surface options for the application of submunition dispense. Use the knowledge gained in this research concerning the body-fixed fins used and assess whether others option such as wraparound fins, a flare or lateral jets would have the same magnitude of interference effects. Moreover, the investigation should also identify what control options are best suited to the constraints of packaging and dispense motion.

6) Further CFD validation is needed to fully assess the capability to predict viscous interaction effects. This will require flowfield detailed measurements similar to those conducted by Brosh et al.[30] and should focus on simplified examples of shockwave boundary-layer and shockwave vortex interactions.

7.2.3 Empirical work

1) Use the current experimental database as a foundation to develop an empirical model to predict the interference loads. This should be based on the fundamental understanding of the interference aerodynamics exposed in this research and must be able to account for the influence of the diffracted shock on the receiver farside.

References

[1] Edge, H., Sahu, J. and Heavey, K., "Computational fluid dynamics modelling of submunition separation from missile", US Army Research Laboratory TR 1981, Maryland USA, 1999.

[2] Ferry, E., Sahu, J. and Heavey, K., "Navier-stokes computations of sabot discard using a chimera scheme", AIAA 1998-0752, Washington D.C. USA, 1998.

[3] Wooden, P., McQuillen, E. and Brooks, W., "Evaluation of a simplified multiple store interference model", AIAA Paper 1998-2800, Washington D.C. USA, 1998.

[4] Rodrigues, L., "Briliant antiarmor submunition: Opportunity exists to conduct critical test prior to production decision", General Accounting Office NSIAD 98-16, Washington D.C. USA, 1997.

[5] Lockheed Martin., *Lockheed martin demonstrates supersonic payload dispense during rattlers sled testing,* Available at: http://www.lockheedmartin.com/news/press_releases/2006/LOCKHEEDMARTINDEMONSTRATESSUPERSONI.html (Accessed 2nd December 2009).

[6] Erbland, P., "Current and near-term RLV/Hypersonic vehicle programs (paper 2)", *Critical Technologies for Hypersonic Vehicle Development (AVT/VKI Lecture Series EN-116),* Rhode-St-Genèse Belgium, December 2005, NATO RTO, New York USA, pp2.1-2.14.

[7] Boeing., *Boeing and AFRL demonstrate first-ever supersonic munitions release,* Available at: http://www.boeing.com/news/releases/2007/q4/071126a_nr.html (Accessed 2nd December 2009).

[8] DARPA., *Hyfly flight,* Available at: http://www.darpa.mil/news/2008/hyfly_flight.html (Accessed 10 December 2009).

[9] Gapcynski, J., Carlson, H., "A pressure-distribution investigation of the aerodynamic characteristics of a body of revolution in the vicinity of a reflection plane at mach numbers of 1.41 and 2.01", NACA RM L54J29, Washington D.C. USA, 1955.

[10] Brosh, A., Kussoy, M. and Hung, C., "Experimental and numerical investigation of a shock wave impingement on a cylinder", *AIAA Journal,* Vol. 23 (No. 6) 1985, pp840-846.

[11] Volkov, V., Derunov, E., "Interaction of a combination of bodies in supersonic flow. interference and diffraction of shock waves in flow over two bodies of revolution", *Journal of Engineering Physics and Thermophysics,* Vol. 79 (No. 4) 2006, pp712-721.

[12] Hung, C., "Impingement of an oblique shock wave on a cylinder", AIAA Paper 1982-0025, Washington D.C. USA, 1982.

[13] Keen, S., Morgret, C., Langham, F., *et al*., "Trajectory simulations should match flight tests and other lessons learned in 30 years of store-separation analysis", AIAA Paper 2009-0099, Washington D.C. USA, 2009.

[14] Bordelon, W., Frost, A. and Reed, D., "Stage separation wind tunnel tests of a generic two-stage-to-orbit launch vehicle", AIAA Paper 2003-4227, Washington D.C. USA, 2003.

[15] Pamadi, B., Neirynck, T., Hotchko, N., *et al*., "Simulation and analyses of stage separation of two-stage reusable launch vehicles", AIAA Paper 2005-3247, Washington D.C. USA, 2005.

[16] Lesage, F., Girard, B., "Wind tunnel and CFD investigation of aerodynamic interactions during sabot separation", AIAA 1996-0193, Washington D.C. USA, 1996.

[17] Schmidt, E., Plostins, P., "Aerodynamics of asymmetric sabot discard", AIAA 1982-1301, Washington D.C. USA, 1982.

[18] Cenko, A., Waskiewicz, J., "Recent improvements in prediction techniques for supersonic weapon separation", *Journal of Aircraft,* Vol. 20 (No. 8) 1983, pp659-666.

[19] Waskiewicz, J., DeJongh, J. and Cenko, A., "Application of panel methods to external stores at supersonic speeds", *Journal of Aircraft,* Vol. 20 (No. 2) 1983, pp153-158.

[20] Gapcynski, J., Carlson, H., "The aerodynamic characteristics of a body in the two-dimensional flow field of a circular-arc wing at a mach number of 2.01", NACA RM L54E14, Washington D.C. USA, 1957.

[21] Gapcynski, J., "The aerodynamic characteristics of a body in the flow field near the tip of a circular-arc wing of rectangular plan form at a mach number of 2.01", NASA TM X-211, Washington D.C. USA, 1960.

[22] Corder, D., Est, B. and Landingham, G., "Prediction of submunition dispense aerodynamics", AIAA Paper 1995-0331, Washington D.C. USA, 1995.

[23] Perkins, S., Dillenius, M. and Sims, J., "Supersonic submunition aerodynamics during dispense", AIAA Paper 1988-0335, Washington D.C. USA, 1988.

[24] Newman, G., Fulcher, K., Ray, R.*, et al*., "On the aerodynamics/dynamics of store separation from a hypersonic aircraft", AIAA Paper 1992-2722, Washington D.C. USA, 1992.

[25] Wilcox, F., "Separation characteristics of generic stores from lee side of an inclined flat plate at mach 6", NASA TM 4652, Washington D.C. USA, 1995.

[26] August, H., Hardy, F., Wilcox, F.*, et al*., "Leeside separation of hypersonic weapons", Wright Lab Wright-Patterson AFB A 447813, Ohio USA, 1996.

[27] Malmuth, N., Shaleav, V., "Theoretical modelling of interaction of multiple slender bodies in supersonic flows", AIAA Paper 2004-1127, Washington D.C. USA, 2004.

[28] Fedorov, A., Malmuth, N. and Soudakov, V., "Supersonic scattering of a wing-induced incident shock by a slender body of revolution", *Journal of Fluid Mechanics,* Vol. 585 2007, pp305-322.

[29] Meakin, R., "A general simulation model for multiple bodies in proximate flight", AIAA Paper 2003-3831, Washington D.C. USA, 2003.

[30] Brosh, A., Kussoy, M., "An experimental investigation of the impingement of a planar shock wave on an axisymmetric body at mach 3", NASA TM 84410, Washington D.C. USA, 1983.

[31] Hung, C., "Computation of three-dimensional shock wave and boundary-layer interactions", NASA TM 86780, Washington D.C. USA, 1985.

[32] Morkovin, M., Migotsky, E., Bailey, H.*, et al*., "Experiments on interaction of shock waves and cylindrical bodies at supersonic speeds", *Journal of Aerospace Sciences,* Vol. 19 (No. 4) 1952, pp237-247.

[33] Marconi, F., "Shock reflection transition in three-dimensional steady flow about interfering bodies", *AIAA Journal,* Vol. 21 (No. 5) 1983, pp707-713.

[34] Dolling, D., "Fifty years of shock-Wave/Boundary-layer interaction research: What next?", *AIAA Journal,* Vol. 39 (No. 8) 2001, pp1517-1531.

[35] Settles, G., Dolling, D., "Swept shock-wave/boundary-layer interactions" In: *Tactical missile aerodynamics: General topics,* Hemsch, M. ed, AIAA, Washington D.C. USA, 1992, pp505-574.

[36] Derunov, E., Zheltovodov, A. and Maksimov, A., "Development of three-dimensional turbulent separation in the neighborhood of incident crossing shock waves", *Thermophysics and Aeromechanics,* Vol. 15 (No. 1) 2008, pp29-54.

[37] Gai, S., Teh, S., "Interaction between a conical shock wave and a plane turbulent boundary layer", *AIAA Journal,* Vol. 38 (No. 5) 2000, pp804-811.

[38] Kussoy, M., Viegas, J. and Hortsman, C., "An experimental and numerical investigation of a 3-D shock separated turbulent boundary layer", AIAA Paper 1980-0002, Washington D.C. USA, 1980.

[39] Wright, M., Wathen, A. and Bone, M., "Details of mutual interference tests in the ARA 0.69m x 0.76m supersonic wind tunnel", Unpublished Contractor Report M265/2, Aircraft Research Association Bedford UK, 1994.

[40] Blake, W., "Missile datcom: Users manual - 1997 fortran 90 revision", Air Force Research Laboratory VA-WP-TR 1998-3009, Ohio USA, 1998.

[41] Nielsen, J., *Missile aerodynamics,* 1st Ed, McGraw-Hill Book Company Inc., New York USA, 1960, p450.

[42] Pope, A., Goin, K., *High-speed wind tunnel testing,* 1st Ed, John Wiley and Sons Inc., New York USA, 1965, p474.

[43] Chaplin, R., MacManus, D. and Birch, T., "Aerodynamic interference between two high-speed bodies in close proximity", Cranfield University NFP 0802, Bedford UK, 2009.

[44] "Cobalt users manual user manual" v4.0, Cobalt LLC, Ohio USA, 2007.

[45] Strang, W., Tomaro, R. and Grismer, M., "The defining methods of $Cobalt_{60}$: A parallel, implicit, unstructured Euler/Navier-stokes solver", AIAA Paper 1999-0786, Washington D.C. USA, 1999.

[46] Turpault, J., "Supersonic multi-body interactions", Unpublished MSc Thesis, Cranfield University, Bedford UK, 2009.

[47] Menter, F., "Zonal two equation k-w turbulence models for aerodynamic flows", AIAA Paper 1993-2906, Washington D.C. USA, 1993.

[48] "Gridgen user manual" v15.11, Pointwise, Texas USA, 2006.

[49] Cummings, R., Morton, S. and McDaniel, D., "Experiences in accurately predicting time-dependent flows", *Progress in Aerospace Sciences,* Vol. 44 (No. 4) 2008, pp241-257.

[50] Taylor, J., *An introduction to error analysis,* 2nd Ed, University Science Books, California USA, 1997, p327.

[51] Roache, P., *Verification and validation in computational science and engineering,* 1st Ed, Hermosa Publishers, New Mexico USA, 1998, p446.

[52] Ward, L., Brich, T., "An investigation of reynolds number effects on a tangent-ogive cylinder body", Defence Research Agency TM Aero/Prop 4, Bedford UK, 1992.

[53] Chin, S., *Missile configuration design,* 1st Ed, McGraw-Hill Book Company Inc., New York USA, 1961, p279.

[54] Birch, T., Allen, J. and Wilcox, F., "Force, surface pressure and flowfield measurements on slender missiles at supersonic speeds", AIAA Paper 2000-4207, Washington D.C. USA, 2000.

[55] Krieger, R., Vukelich, S., "Tactical missile drag" In: *Tactical missile aerodynamics: Prediction methodology,* Mendenhall, M. ed, AIAA, Washington D.C. USA, 1992, pp1-36.

[56] Prince, S., "The aerodynamics of high speed aerial weapons", Unpublished PhD Thesis, Cranfield University, Bedford UK, 1999.

[57] Yang, J., Lui, Y. and Lomax, H., "Computation of shock-wave reflection by circular cylinders", *AIAA Journal,* Vol. 25 (No. 5) 1987, pp683-690.

[58] Delery, J., Marvin, J. G., "Shock-wave boundary-layer interactions", AGARD AG 280, Neuille-Sur-Seine France, 1986.

[59] Kaca, J., "An interferometric investigation of the diffraction of a planar shock wave over a semicircular cylinder", Institute for Aerospace Studies University of Toronto TN 269, Toronto Canada, 1988.

[60] Ben-Dor, G., Dewey, J., "The mach reflection phenomenon: A suggestion for an international nomenclature", *AIAA Journal,* Vol. 23 (No. 10) 1985, pp1650-1652.

[61] Ben-Dor, G., Takayama, K. and Kawauchi, T., "The transition from regular to mach reflection and from mach to regular reflection in truly non-stationary flows", *Journal of Fluid Mechanics,* Vol. 100 (No. 1) 1980, pp147-160.

[62] Tomaro, R., Witzeman, F. and Strang, W., "A solution on the F-18C for store separation simulation using $Cobalt_{60}$", AIAA Paper 1999-0122, Washington D.C. USA, 1999.

[63] Gregory, J., Asai, K., Kameda, M.*, et al*., "A review of pressure-sensitive paint for high-speed and unsteady aerodynamics", *Proceedings of the IMechE, Part G: Journal of Aerospace Engineering,* Vol. 222 2008, pp249-290.

[64] Lui, T., Sullivan, J., *Pressure and temperature sensitive paints,* 1st Ed, Springer-Verlag, Berlin Germany, 2005, p309.

[65] Pulkin, E., Carlson, B., Gouin, S.*, et al*., "Ideality of pressure-sensitive paint. 1. platinum tetra(pentafluorophenyl)porphine in fluoroacrylic polymer", *Journal of Applied Polymer Science,* Vol. 77 2000, pp2795-2804.

[66] *GE sensing (druck) pressure sensors,* Available at: http://www.gesensing.com/druckproducts/ (Accessed 31 July 2009).

[67] *EADS NA test and services,* Available at: http://www.eads-nadefense.com/products.htm (Accessed 31 July 2009).

[68] *Able corp balances,* Available at: www.windtunnels.arc.nasa.gov/balcallab/ablebalance.html (Accessed 31 July 2009).

[69] Lui, T., Guille, M. and Sullivan, P., "Accuracy of pressure sensitive paint", *AIAA Journal,* Vol. 39 (No. 1) 2001, pp103-112.

Bibliography

Anderson, J., *Computational fluid dynamics,* 1st Ed, McGraw-Hill Book Company Inc., New York USA, 1995, p547.

Anderson, J., *Modern compressible flow with historical perspective,* 2nd Ed, McGraw-Hill Book Company Inc., New York USA, 1990, p479.

Chin, S., *Missile configuration design,* 1st Ed, McGraw-Hill Book Company Inc., New York USA, 1961, p279.

Figliola, R., Beasley, D., *Theory and design for mechanical measurements,* 2nd Ed, John Wiley and Sons Inc., New York USA, 1995, p542.

Hemsch, M., *Tactical missile aerodynamics: General topics,* 2nd Ed, AIAA, Washington D.C. USA, 1992, p731.

Lui, T., Sullivan, J., *Pressure and temperature sensitive paints,* 1st Ed, Springer-Verlag, Berlin Germany, 2005, p309.

Mendenhall, M., *Tactical missile aerodynamics: Prediction methodology,* 2nd Ed, AIAA, Washington D.C. USA, 1992, p766.

Nielsen, J., *Missile aerodynamics,* 1st Ed, McGraw-Hill Book Company Inc., New York USA, 1960, p450.

Pope, A., Goin, K., *High-speed wind tunnel testing,* 1st Ed, John Wiley and Sons Inc., New York USA, 1965, p474.

Schlichting, H., *Boundary layer theory,* 1st Ed, McGraw-Hill Book Company Inc., New York, USA, 1960, p769.

Shapiro, A., *The dynamics and thermodynamics of compressible fluid flow: Vol 1,* 1st Ed, John Wiley and Sons Inc., New York USA, 1977, p672.

White, F., *Viscous fluid flow,* 3rd Ed, McGraw-Hill Book Company Inc., New York USA, 2005, p640.

Zucker, R., Biblarz, O., *Fundamentals of gas dynamics,* 2nd Ed, John Wiley and Sons Inc., New York USA, 2002, p493.

Appendix A

A.1 Finned receiver design

The control fins on the finned receiver were designed using Missile Datcom[40] and Cobalt CFD predictions[44]. The objective was to design a set of cruciform control fins to stabilise (i.e. $X_{cp} > X_{cg}$) the un-finned receiver over an incidence range of $-15 \leq \sigma \leq 15°$. The design variables include fin profile, semi-span (b), chord length (c) and thickness (t). The initial trade-off studies were conducted using Missile Datcom where the effect of the design variables on the centre of pressure locations over the above incidence range was assessed.

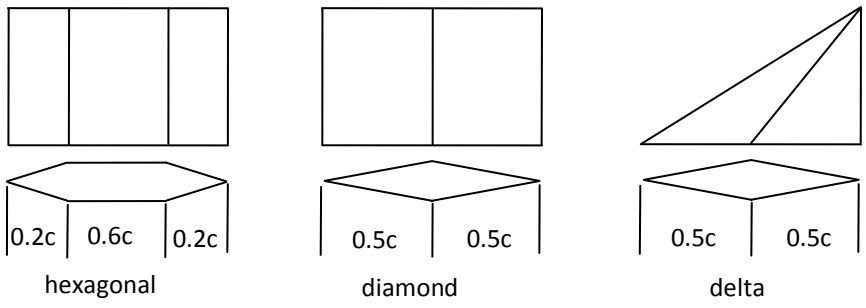

Figure A.1 Fin profiles

A.1.1 Phase 1

Three different thickness profiles were assessed: diamond, hexagonal and a delta fin (Figure A.1). The semi-span was limited to a maximum of b/D=1 by the fact that adequate space must be left between the bodies in a multi-body configuration in the S20 SWT. A nominal thickness to chord ratio was fixed at 8%, which was typical for a supersonic thin wing. The root chord was varied $c_{rt}/D=0.75,1,1.25$ for each profile (Figure A.2).

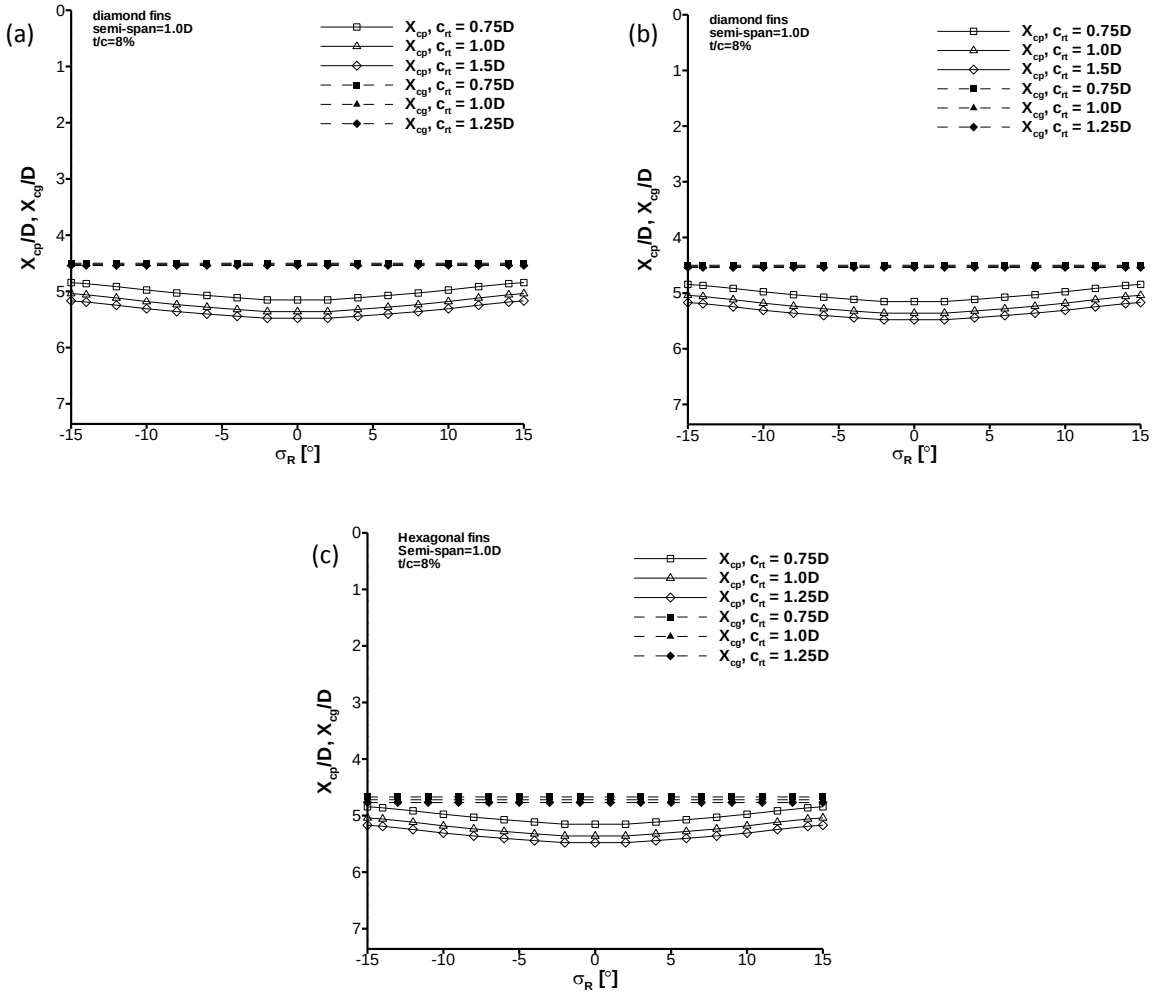

Figure A.2 Effect of root chord size for (a) delta, (b) diamond and (c) hexagonal profiles

A root chord of $c_{rt}/D=1$ was chosen since it provided adequate stability for all fin profiles. However the static stability of the delta fins for a root chord of $c_{rt}/D=1$ was considered too marginal so this profile was discounted for the next design phase.

A.1.2 Phase 2

A semi-span of b/D=1 caused large values of axial force and the effect of reducing this parameter was assessed. The parameters from phase 1 remained fixed ($c_{rt}/D=1$, t/c=8%) and the effect of fin semi-span was varied b/D=0.65, 0.75, 1 for the hexagonal and diamond profile (Figure A.3).

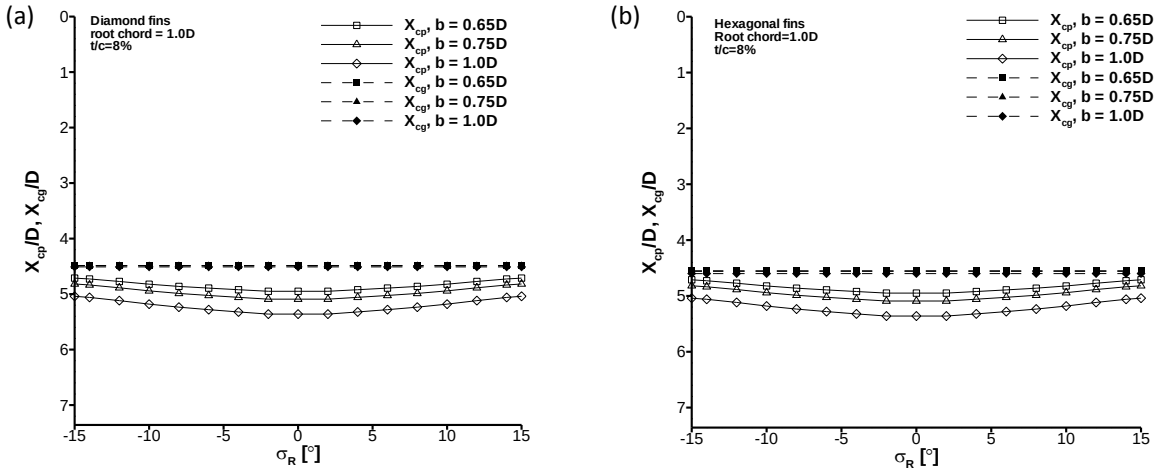

Figure A.3 Effect of semi-span size for (a) diamond and (b) hexagonal profiles

It is clear that a semi-span of b/D=0.65 for both profiles provides adequate stability.

A.1.3 Phase 3

Therefore two candidate designs remain. Either a hexagonal or diamond profile with the following characteristics, c/D=1, b/D=0.65. The thickness has a negligible effect on the centre of pressure location but a large effect on the axial force of the resultant design. Therefore, this is evaluated for a range of thickness to chord ratios t/c=4%,6%,8%,10%,12% in Figure A.4 which reports the C_X for the receiver body configuration as a whole (i.e. for the body and fins).

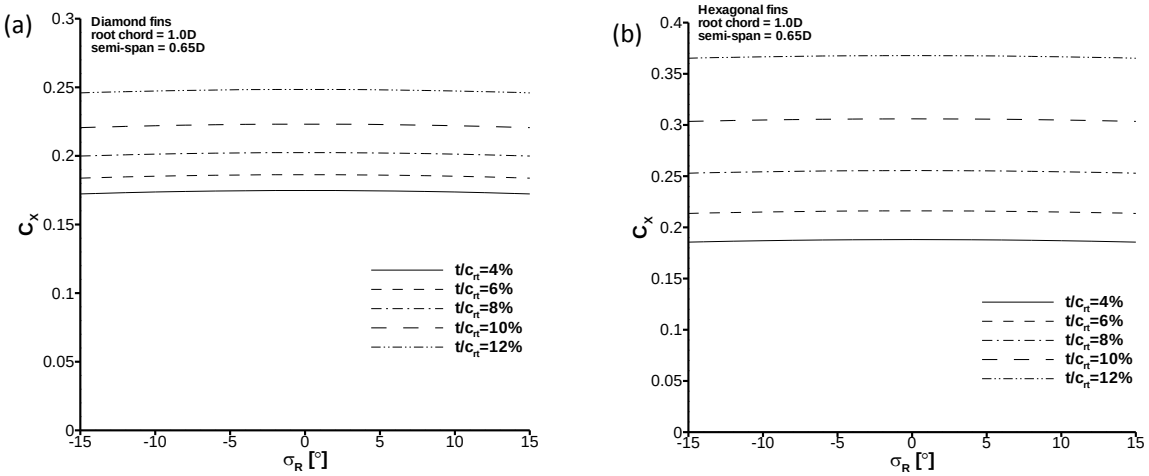

Figure A.4 Effect of thickness for (a) diamond and (b) hexagonal profiles

To provide a lower design limit for the fin thickness, a bending stress analysis of the two candidate fin profiles were conducted. This assumed a cantilever, homogeneous fin made from high-grade aluminium(6068 T6), with a critical yield stress of σ_y=250MPa, a factor of safety of 3, a stress concentration factor of 1.5 under a bending moment load equal to what the fin experiences at its maximum incidence of σ=15°. The minimum thickness for the hexagonal profile was t=0.81mm (t/c=4%) and was t=1.37mm (t/c=6.9%) for the diamond profile. Therefore, the hexagonal profile was chosen for the final design since it was more easily manufactured than the diamond profile and allowed a smaller thickness. A final thickness of 10% was chosen as it provided balance of low axial force and high strength.

A.1.4 Final design summary

The final design parameters are listed in Table A.1. The corresponding centre of pressure location on the body was predicted using Cobalt and confirmed that the finned receiver is statically stable over desired incidence range (Figure A.5).

Parameter	Value
Profile	Hexagonal (0.2c,0.6c,0.2c)
Planform	Rectangular
Chord	c=20mm (c/D=1)
Semi-span	b=13mm (b/D=0.65)
Thickness	t=2mm (t/c=10%)

Table A.1 Final fin design for the finned receiver

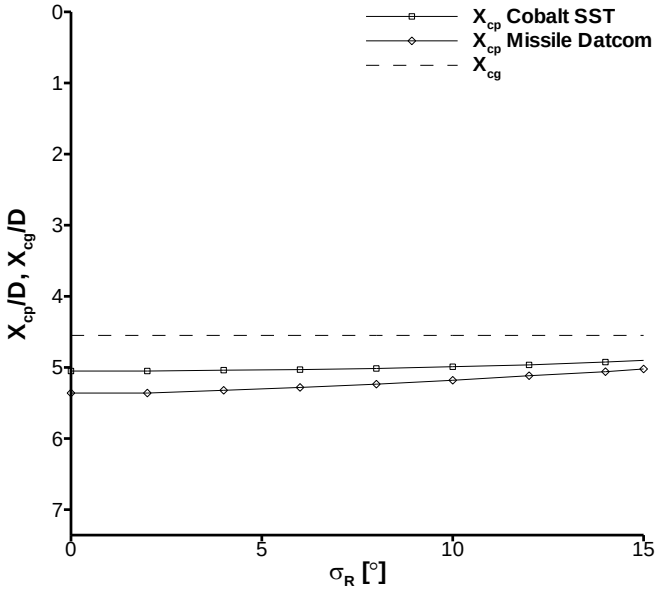

Figure A.5 Centre of pressure predictions for the finned receiver design

A.2 ISL S20 freestream flow conditions

The freestream flow conditions in the S20 SWT and used in the steady-state CFD calculations of the ISL configurations are listed below in Table A.2.

Parameter	Value	Units
Mach number	2.43	
Stagnation pressure	675,300	Nm^{-2}
Stagnation temperature	292.76	K
Static pressure	44,077.39	Nm^{-2}
Static temperature	134.23	K
Static density	1.144	kgm^{-3}
Velocity	564.34	ms^{-1}
Sonic velocity	232.24	ms^{-1}
Dynamic pressure	182,190.8	Nm^{-2}
Dynamic viscosity	$9.27x10^{-6}$	$kgm^{-1}s^{-1}$
Reynolds number based on diameter (D=0.02m)	$1.39x10^{6}$	
Reynolds number per meter	$6.95x10^{7}$	m^{-1}
Force coefficient denominator	57.24	N
Moment coefficient denominator	1.15	Nm

Table A.2 ISL S20 freestream flow conditions

A.3 Boundary-layer transition in the S20 SWT

Two tests of the isolated un-finned receiver body were conducted under identical conditions in the S20 SWT. In the first, natural free transition of the body boundary-layer occurred. In the second test, a small wire boundary-layer transition device was fixed approximately 2mm from the leading-edge (Figure A.6). The effect of fixing transition on the normal force, pitching moment and axial force was evaluated (Figure A.7 - Figure A.9).

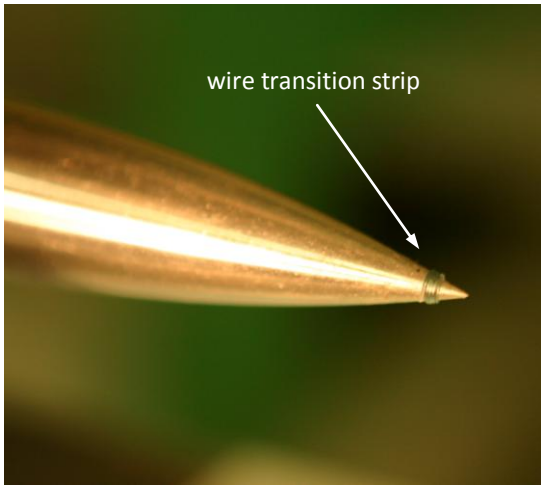

Figure A.6Model with transition fixed approximately 2mm from leading edge

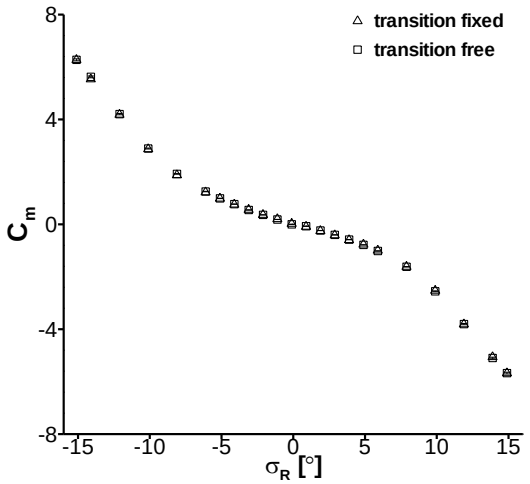

Figure A.8 Effect of fixing transition on pitching moment: m2651 isolated

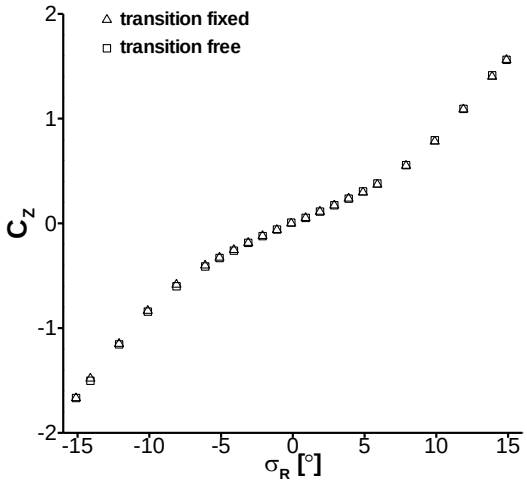

Figure A.7 Effect of fixing transition on normal force: m2651 isolated

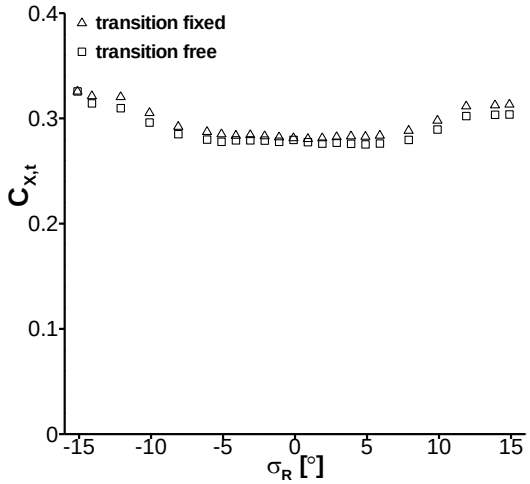

Figure A.9 Effect of fixing transition on axial force: m2651 isolated

The results above show that there is negligible effect of fixing transition on C_Z and C_m and only a small increase in axial force of $C_{X,t}$=0.01. Therefore, the receiver boundary-layer under the S20 SWT test conditions is assumed to be naturally turbulent.

A.4 S20 SWT calibration curves

The S20 SWT total pressure (p_0) and total temperature (T_0) in the settling chamber were measured in each run. In addition, the receiver body base pressure (p_b) was also measured at each incidence setting. The calibration curves for the two pressure transducers and the total temperature probe are shown in (Figure A.10 - Figure A.12). The transducer serial number for the total pressure measurement is #1069985. The transducer serial number for the base pressure measurement is #1378924.

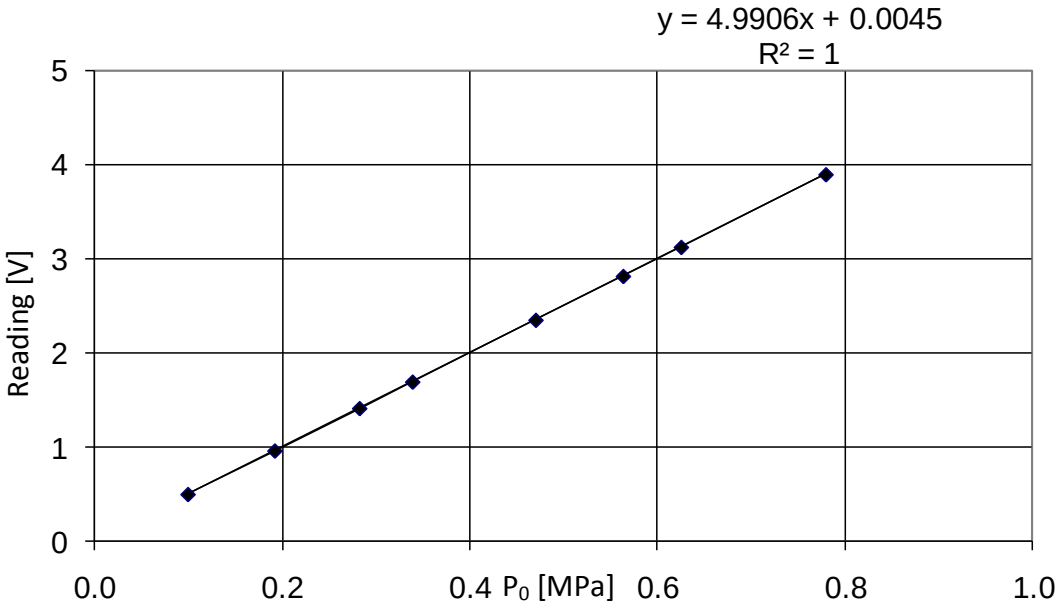

Figure A.10 Calibration curve for the total pressure measurement (#1069985)

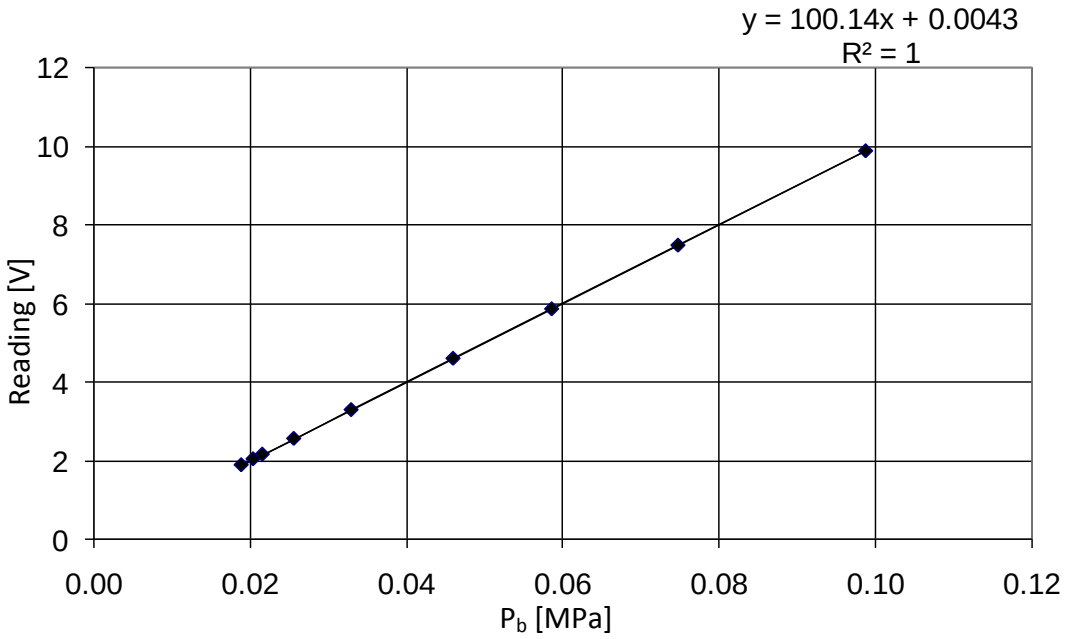

Figure A.11 Calibration curve for the base pressure measurement (#1378924)

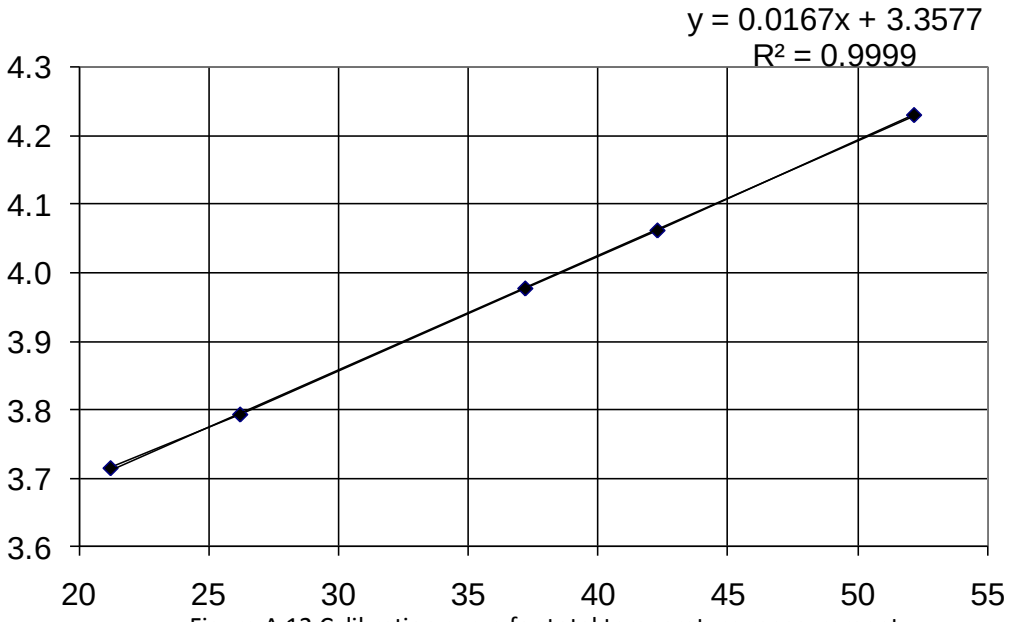

Figure A.12 Calibration curve for total temperature measurement

A linear fit is applied to the calibration data and the equations shown were used in the data processing. The deviation from the best fit line in each measurement is $\delta_{p0,cal}$=177Pa, $\delta_{pB,cal}$=20.5Pa, $\delta_{T0,cal}$=0.16K. These values are used in the uncertainty analysis.

A.5 Analysis of data acquisition sample duration

The nominal sample duration for the receiver body force and moment measurements in the S20 SWT was 2s. A test with an extended sample duration of 4s was run and the results compared (Figure A.13 - Figure A.15) to assess the adequacy of the nominal sample duration. In each case the sample rate remained fixed at 100kHz.

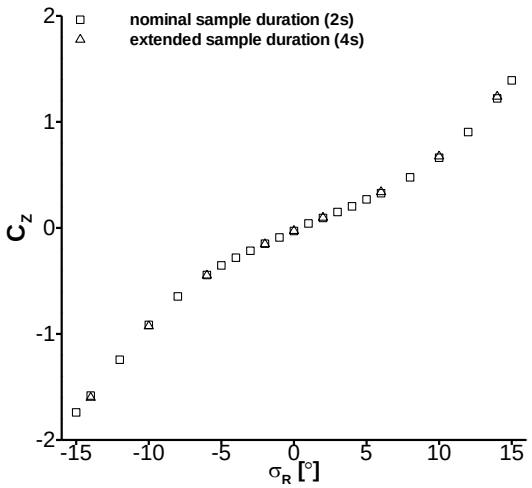

Figure A.13 Effect of sample duration on measured normal force: m2651 m2653, Δx/D=1.67 Δz/D=2.94, σ_G=0°.

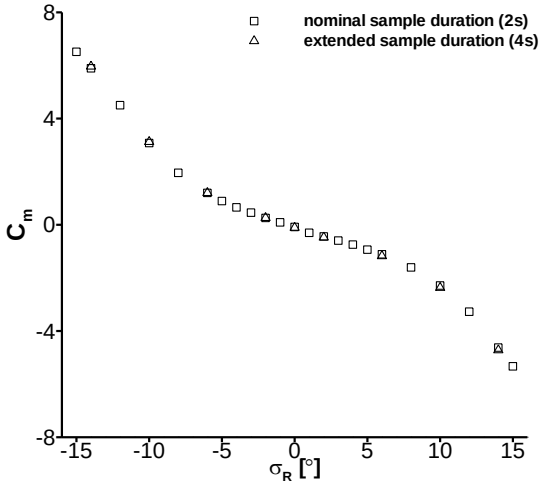

Figure A.14 Effect of sample duration on measured pitching moment: m2651 m2653, Δx/D=1.67 Δz/D=2.94, σ_G=0°.

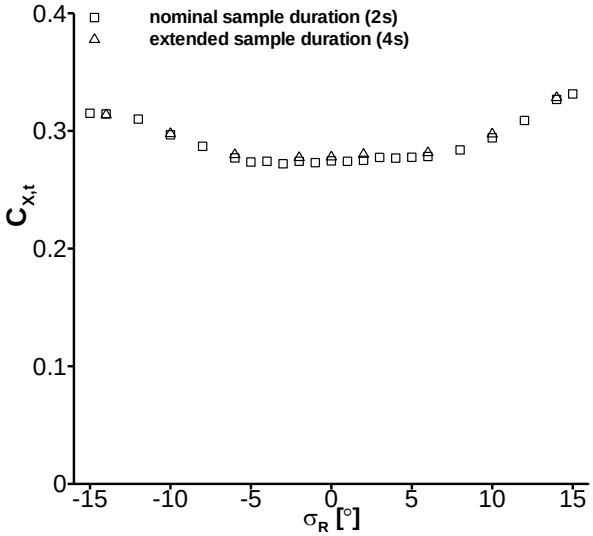

Figure A.15 Effect of sample duration on measured axial force: m2651 m2653, Δx/D=1.67 Δz/D=2.94, σ_G=0°.

The results above show that there is very little effect of an extended sample on the normal force, pitching moment and axial force coefficients. The r.m.s differences for each were $C_{Z,rms}$=0.03, $C_{m,rms}$=0.17 and $C_{X,t,rms}$=0.01 respectively. Therefore, a sample duration of 2s is considered adequate.

A.6 Methodology details of the Pressure Sensitive Paint measurements

In this research, a Bi-Luminophore PSP developed by Innovative Scientific Solutions Incorporated (ISSI) was used to obtain surface pressure measurements on both receiver bodies at selected incidence angles (Figure A.16 - Figure A.17).

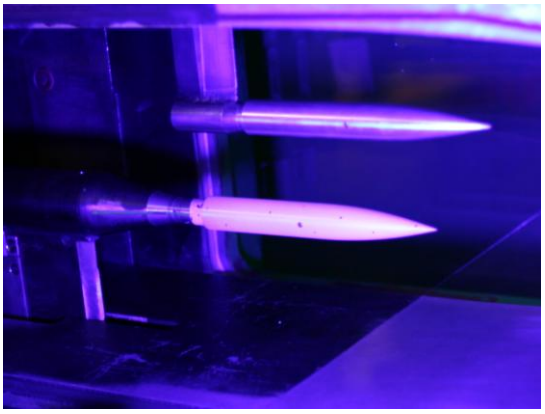

Figure A.16 The painted un-finned receiver set-up adjacent to the sharp generator

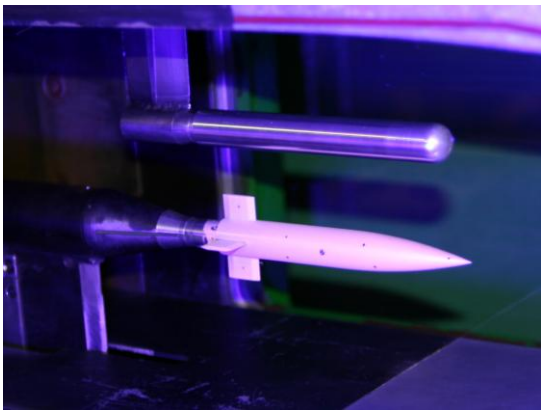

Figure A.17 The painted finned receiver set-up adjacent to the blunt generator

Binary-FIB BF405 contains two luminophore probes, a signal probe (platinum meso-tetra(pentafluorophenyl) porphyrine, Pt(TfPP)) which is sensitive to pressure and a reference probe which is sensitive to illumination but relatively insensitive to pressure. The binder is a FIB (Fluoro/Isopropyl/Butyl) polymer. The luminophore and polymer binder were dissolved in a benzene solvent and a uniform coat was applied by spray-painting the receiver model, which was first cleaned with acetone and polished. The model was cured for 20-30mins at 65°C to evaporate the solvent and immobilise the luminophore probes in the binder. As the Binary-FIB PSP contains TiO_2 particles, there was no need for a screen-layer to mask the natural luminescence of the model or to

increase the luminescence reflection of the paint. The Binary-FIB is therefore a uni-coat paint.

A.6.1 Brief PSP theory

The PSP technique relies upon the photo-physical processes involved in luminescence in particular oxygen quenching[63]. The underlying principle is expressed in Henry's law[64], which states that the concentration of oxygen molecules in the binder is proportional to the partial pressure of the oxygen adjacent to the paint layer. For air, this is proportional to the total air pressure. Consequently, a higher air pressure adjacent to the model surface, results in a reduced intensity of luminescence (Figure A.18). The expression that most conveniently describes the relationship between air pressure and luminescence intensity is the Stern-Volmer relation[64]. The constants A and B are experimentally determined calibration coefficients, I_{ref} and I are the intensities for a known and unknown pressure condition respectively. Similarly, p_{ref} and p are the pressures associated with a known and unknown test condition respectively (Equation A.1).

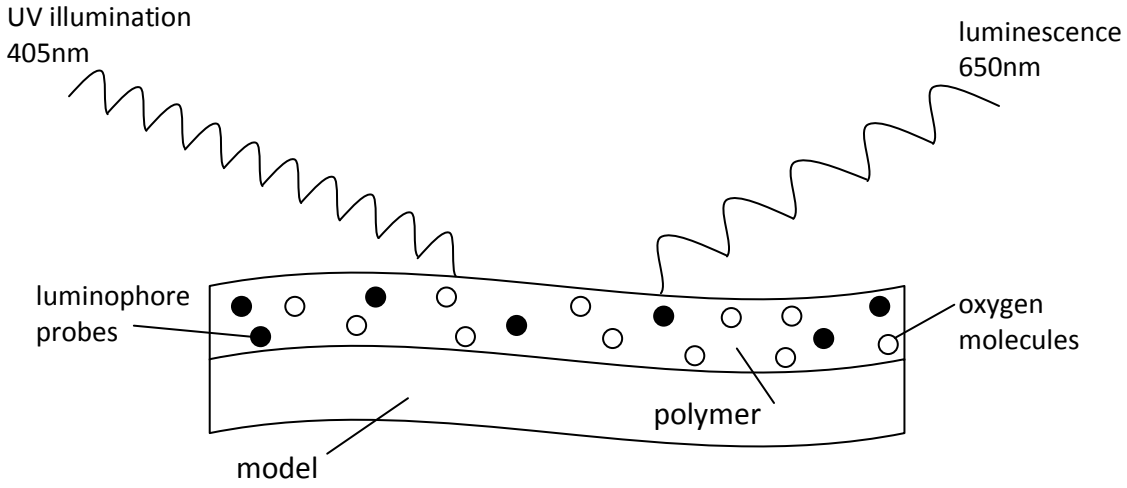

Figure A.18 Schematic of the physical mechanism involved in Pressure sensitive paint

$$\frac{I_{ref}}{I} = A + B\frac{p}{p_{ref}} \qquad \text{A.1}$$

A.6.2 Measurement set-up and procedure

For a given configuration, the painted receiver model was placed on the lower support and approximately 10 reference points were marked on the surface to aid with the post-test image re-alignment. Two ISSI UV LM2X-405 LED lamp modules were placed on an optics bench immediately adjacent to the working section. These were positioned approximately ±45° to the camera line of sight, which was set-up normal to the tunnel axis in the lateral direction (Figure A.19, Figure A.20). These provided illumination light at a wavelength of 405nm. The emitted luminescence was measured with a 12-bit PCO Sensicam qe camera, a Cosmicar TV manual zoom lens (12.5-75mm 1:1.8) and an Andover FS20-50 bandwidth optical filter with a pass wavelength of 650nm.

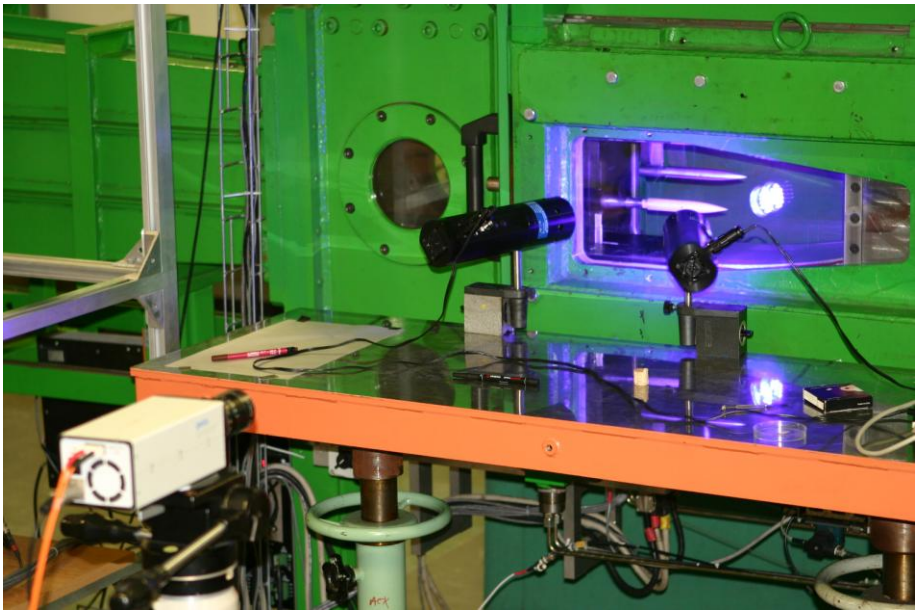

Figure A.19 PSP set-up in the S20 SWT

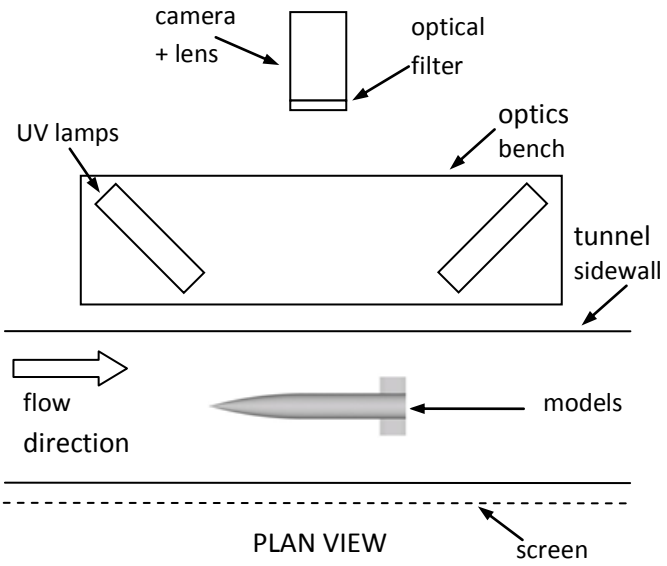

Figure A.20 Schematic of the PSP set-up in the S20 SWT

'Wind-off' images were acquired at each incidence (σ_R=0, ±8°, ±15°) which provided the reference intensity (I_{ref}) values for each pixel, where the reference atmospheric conditions were known ($p_{ref}=p_{amb}$=1atm and T_{amb}=20°C). Under 'wind-on' conditions the receiver was pitched through each of the incidence settings with a 5s pause at each. This was sufficient for time-independent pressure measurements as the Binary-FIB paint has a time response of 0.3s[65]. A wind-on image was acquired which measured the light intensity (I) and is related to the associated unknown pressure (p) for each pixel. At the end of each run, the models were removed and replaced by a 3D check-board with 10x10x10mm squares. The acquired image of this calibration model was used to transform the 2D image space into a known 3D co-ordinate system and was large enough to cover the complete movement of the receiver body. Finally, a 'black image' was also taken with the lens covered to identify the baseline noise level in the camera measurement system.

A.6.3 PSP data processing

An intensity–based PSP method was used to calculate the unknown pressures on the receiver body. In general, a ratio of the wind-off and wind-on images is used to mitigate the effects of uneven PSP coating, non-homogeneous luminophore concentration in the PSP layer and non-uniform illumination[64]. The use of LED lamps further ensured that there was a negligible change in the illumination intensity

between the wind-off and wind-on images. Due to aeroelastic deformation of the receiver body under aerodynamic loading and wind tunnel vibrations, the wind-on image was offset from the wind-off image. Therefore, the wind-on image was re-aligned to fit precisely over the wind-off image by using the reference marker points. The black image intensity (typically in the order of 0.5% of the total intensity levels) for each pixel was subtracted from both images and then a pixel-on-pixel intensity ratio was calculated (I_{ref}/I). For a given intensity ratio (I_{ref}/I) the associated pressure (p) was found from the Stern-Volmer calibration curve and knowledge of p_{ref} (Equation A.1). The pressure data in the 2D image space was mapped onto a 3D surface mesh of the receiver body, which contained approximately 200,000 nodes for the un-finned receiver and 450,000 nodes for the finned receiver. The spatial resolution in the 2D image space was estimated to be $x_{res}=y_{res}=0.13$mm, based on the number of camera pixels (1376x1040). Since only one camera was used, its spatial position with respect to the model was used to determine whether a given node was in view or not. All hidden nodes were assigned zero pressure.

A.6.4 PSP calibration

The Stern-Volmer calibration curve was determined from an a-priori calibration of a sample of Binary-FIB tested over a controlled pressure and temperature range. In this research, the calibration chamber tested a paint sample on a 40mm x 40mm copper plate for which the local temperature was regulated using a two-stage Peltier cell (Figure A.21 (a)). The sample temperature was measured with a thermistor, which was placed in a hollow moulding under the paint sample. The chamber pressure was regulated and measured using a piezoresistive sensor (Figure A.21 (b)). The reference intensity (I_{ref}) was first measured under ambient conditions of $p_{amb}=p_{ref}=1$bar and $T_{amb}=20°$. At constant temperature, different pressure levels were applied over a range of $2\text{mbar} \leq p \leq 5\text{bar}$ and the intensity recorded using the same acquisition system as previously described. This was repeated for different temperature settings. A 5^{th} order polynomial was fitted to the Stern-Volmer relation (Figure A.22, Equation A.2). Due to the ideality of the Binary-FIB paint[65], the resulting Stern-Volmer curves were relatively insensitive to temperature (0.03%/K) but showed a large sensitivity to

pressure (4.5%/psi). To aid post-run data validation, a small region of the sting was also painted. This region covered a static pressure port where the base pressure was measured during the PSP tests (Figure A.20). The static pressure port measurements were compared with the PSP measurements in the uncertainty analysis.

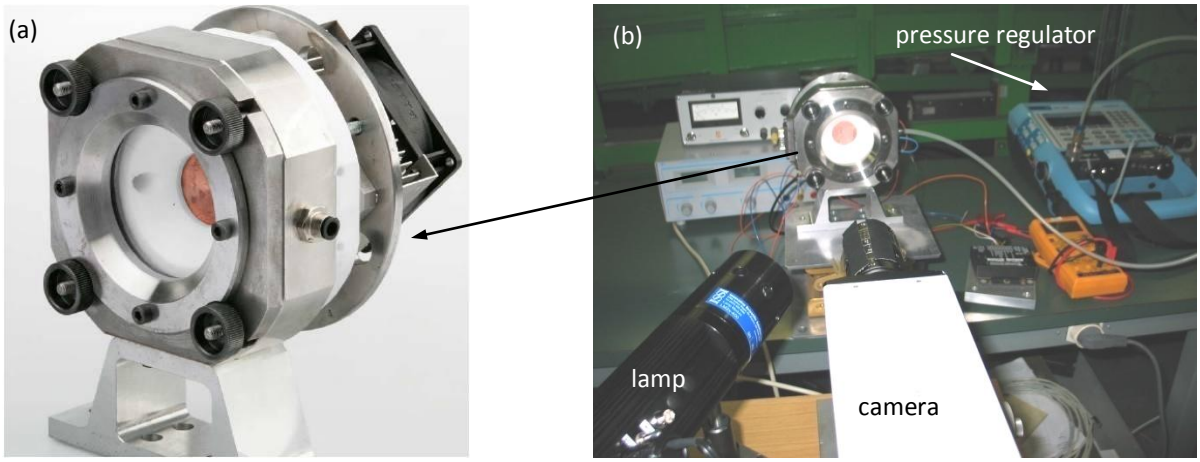

Figure A.21 (a) Calibration chamber and (b) calibration set-up

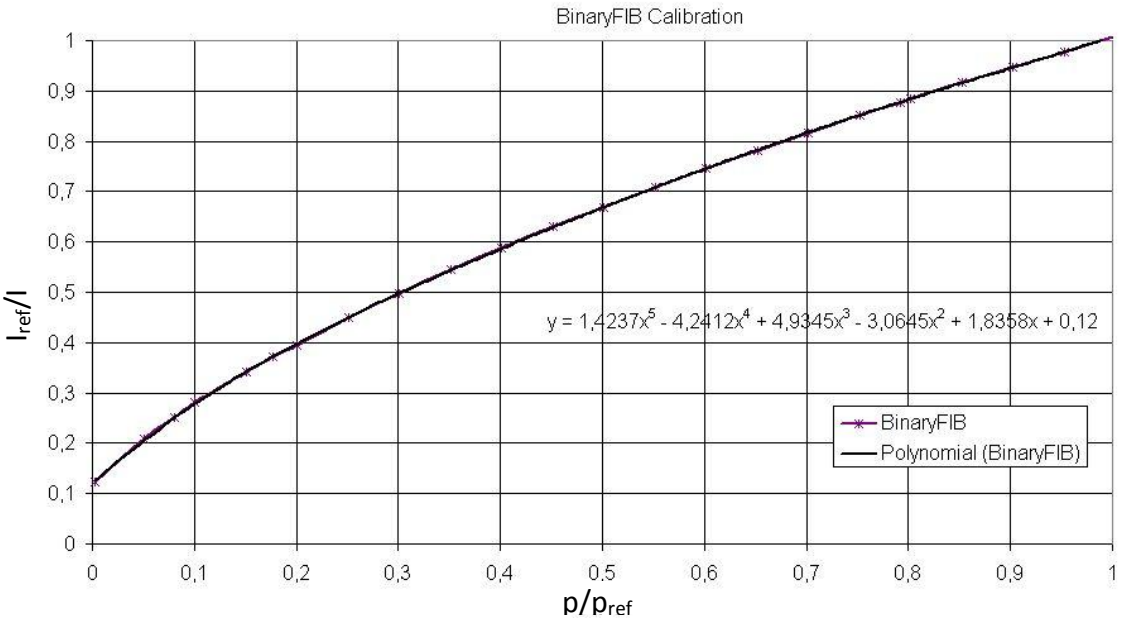

Figure A.22 Calibration curve for the Binary-Fib paint

$$\frac{I_{ref}}{I} = 0.12 + 1.8358\frac{P}{P_{ref}} - 3.0645\frac{P}{P_{ref}}^{2} + 4.9345\frac{P}{P_{ref}}^{3} - 4.2412\frac{P}{P_{ref}}^{4} + 1.4237\frac{P}{P_{ref}}^{5}$$

A.2

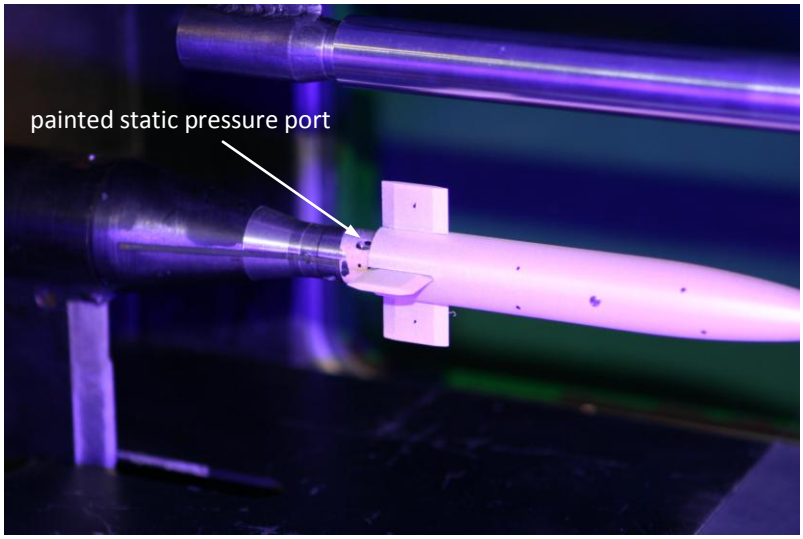

Figure A.23 The painted static pressure port on the balance sting

A.7 ARA SWT freestream flow conditions

The freestream flow conditions in the ARA SWT and used in the steady-state CFD calculations of the ARA configurations are listed below in Table A.3.

Parameter	Value	Units
Mach number	2.5	
Stagnation pressure	80,119.2	Nm^{-2}
Stagnation temperature	307.9	K
Static pressure	4689.9	Nm^{-2}
Static temperature	136.9	K
Static density	0.119	kgm^{-3}
Velocity	586.2	ms^{-1}
Sonic velocity	234.5	ms^{-1}
Dynamic pressure	20,516	Nm^{-2}
Dynamic viscosity	$9.438x10^{-6}$	$kgm^{-1}s^{-1}$
Reynolds number based on diameter (D=0.0254m)	$1.93x10^{5}$	
Reynolds number per meter	$7.6x10^{6}$	m^{-1}
Force coefficient denominator	10.4	N
Moment coefficient denominator	0.26	Nm

Table A.3 ARA SWT freestream flow conditions

A.8 Experimental Uncertainty analysis

Experimental Uncertainty - S20 SWT measurements

The experimental uncertainty for each parameter is estimated using the approach of Taylor[50]. The different parameters are grouped into four sections: those associated with the tunnel set-up and model attitude, the nominal freestream flow conditions, the force and moment measurements and the Pressure Sensitive Paint measurements. The elemental uncertainties result from systematic (or bias) and random measurement errors.

A.8.1 Tunnel set-up and model attitude

A.8.1.1 Axial stagger (Δx/D)

The elemental measurements required to calculate the non-dimensional form of the axial stagger parameter were Δx and D (Equation A.3).

$$\frac{\Delta x}{D}$$

$$\delta_{\Delta x/D} = f(\delta_{\Delta x}, \delta_D) \qquad \text{A.3}$$

The axial stagger between the receiver and generator bodies was controlled by the traverse mechanism, which varied the streamwise location of upper and lower model supports. The relative streamwise distance (Δx) between the leading edge of the receiver and generator bodies at zero incidence (σ_R=0°, σ_G=0°) was adjusted before each run. The remote mechanism was calibrated a-priori and gave Δx within an uncertainty of $\delta_{\Delta x,cal}$=±0.5mm. This was checked in each case with a pair of digital callipers. The scale resolution of the digital callipers was $\delta_{\Delta x,res}$=±0.005mm. The wind tunnel models were manufactured using a CNC machine within a tolerance of approximately δ_D=±0.005mm.

The sources of uncertainty in the axial stagger parameter are as follows:

1. Error associated with the accuracy of the remote displacement mechanism ($\delta_{\Delta x,cal}$)
2. Resolution of the digital callipers ($\delta_{\Delta x,res}$)
3. Uncertainty in the base diameter dimension (δ_D)

Ten axial stagger configurations are considered for the different generator bodies tested: Δx/D=-3.81, -2.16, -1.65, -0.53, 0, 0.44, 1.2, 1.67, 2.68, 3.679. Using the approach set out in Taylor[50] and assuming that the error sources are independent and random, the uncertainty of the axial stagger parameter ($\delta_{\Delta x/D}$) is estimated below for a sample case of Δx/D=-0.44 with all cases listed in Table A.4. The overall fractional uncertainty ranges between ±0.7%-5.7%.

$$\delta_{\Delta x} = \sqrt{\left(\delta_{\Delta x,cal}\right)^2 + \left(\delta_{\Delta x,res}\right)^2}$$

$$\delta_{\Delta x} = \sqrt{(0.5)^2 + (0.005)^2} = \pm 0.500025mm \cong \pm 0.5\ mm$$

$$\frac{\delta_{\Delta x/D}}{|\Delta x/D|} = \sqrt{\left(\frac{\delta_{\Delta x}}{\Delta x}\right)^2 + \left(\frac{\delta_{\Delta D}}{\Delta D}\right)^2}$$

$$\frac{\delta_{\Delta x/D}}{|-0.44|} = \sqrt{\left(\frac{0.5}{8.8}\right)^2 + \left(\frac{0.005}{20}\right)^2}$$

$$\frac{\delta_{\Delta x/D}}{|-0.44|} = 0.057 = \pm 5.7\%$$

Δx/D	Δx [mm]	$\delta_{\Delta x/D}$ /Δx/D	$\delta_{\Delta x/D}$ /Δx/D [%]	$\delta_{\Delta x/D}$
-3.81	-76.2	0.0066	0.7	0.03
-2.16	-43.2	0.0116	1.2	0.03
-1.65	-33	0.0152	1.5	0.03
-0.53	-10.6	0.0472	4.7	0.03
0	0	-	-	-
0.44	8.8	0.0568	5.7	0.03
1.2	24	0.0208	2.1	0.03
1.67	33.4	0.0150	1.5	0.03
2.68	53.6	0.0093	0.9	0.03
3.679	73.6	0.0068	0.7	0.03

Table A.4 Axial stagger uncertainty

A.8.1.2 Lateral separation (Δz/D)

The elemental measurements required to calculate the non-dimensional form of the lateral separation parameter were Δz and D (Equation A.4).

$$\frac{\Delta z}{D}$$

$$\delta_{\Delta z/D} = f(\delta_{\Delta z}, \delta_D) \quad \text{A.4}$$

The lateral separation is defined as the distance perpendicular to the tunnel axis between the centrelines of the receiver and generator bodies at zero incidence (σ_R=0°, σ_G=0°). This distance is fixed at the beginning of the test programme through the lateral positioning of the upper and lower supports. This was manually adjusted and measured with a spacer tool with a high degree of accuracy to within $\delta_{\Delta z}$=±0.055mm. The uncertainty in the body base diameter is the same as previously stated (δ_D=±0.005mm). The error sources for the lateral separation parameter are as follows:

1. Human error in approximating ($\delta_{\Delta z}$)
2. Uncertainty in model base diameter (δ_D)

The total uncertainty in the lateral separation parameter is calculated using the same method as Equation A.3 and shown below in Table A.5.

Δz/D	Δz [mm]	$\delta_{\Delta z/D}$ /Δz/D	$\delta_{\Delta z/D}$
2.94	58.8	0.1	0.003

Table A.5 Lateral separation uncertainty

A.8.1.3 Receiver body incidence (σ_R)

The receiver body incidence (σ_R) was controlled by the incidence regulator of the lower support. An a-priori calibration of the remote mechanism was conducted giving uncertainty of the set-up incidence to within $\delta_{\sigma,cal}$=±0.05°. This was confirmed at each incidence with a digital inclinometer. The effect of aerodynamic loading on the set-up angle was analysed using the shadowgraph visualisation for the isolated configurations using a horizontal reference plane. The maximum difference from the set-up incidence was $\delta_{\sigma,ld,m2651}$=±0.13° at σ_R=±15° for the un-finned receiver and $\delta_{\sigma,ld,m2652}$=±0.23° at σ_R=±15° for the finned receiver.

The sources of uncertainty for the receiver incidence parameter are as follows.

1. The error in the set-up incidence ($\delta_{\sigma,cal}$)
2. The error introduced by aerodynamic loading ($\delta_{\sigma,ld}$)

The combined receiver incidence uncertainty is calculated by combining the two elemental uncertainties above for the un-finned ($\delta_{\sigma R,m2651}$) and finned bodies ($\delta_{\sigma R,m2652}$).

$$\delta_{\alpha R,m2651} = \sqrt{\left(\delta_{\alpha,cal}\right)^2 + \left(\delta_{\alpha,ld,m2651}\right)^2}$$

$$\delta_{\alpha R,m2651} = \sqrt{(0.05)^2 + (0.13)^2} = \pm 0.14°$$

$$\delta_{\alpha R,m2652} = \pm 0.24°$$

A.8.1.4 Generator body incidence (σ_G)

The incidence of the upper support was fixed at σ_G=0° for all configurations. This was manually adjusted and checked with a digital inclinometer to within an uncertainty of $\delta_{\sigma,res}$=±0.05°. There was negligible longitudinal aerodynamic loading acting on the body and thus $\delta_{\sigma,ld,m2653}$= $\delta_{\sigma,ld,m2654}$=0°.

The only source of uncertainty for the generator incidence parameter is as follows.

1. The error in the set-up incidence at σ_G=0° ($\delta_{\sigma,res}$)

As this is the only elemental uncertainty the generator incidence uncertainty is $\delta_{\sigma G,m2653}$=$\delta_{\sigma G,m2654}$=±0.05°

A.8.1.5 Axial impingement location (x'/L)

The elemental measurements required to calculate the non-dimensional form of the axial impingement location parameter are x' and L (Equation A.5).

$$\frac{x'}{L}$$

$$\delta_{x'/L} = f(\delta_{x'}, \delta_L) \qquad \text{A.5}$$

The axial impingement location (x') is defined as the X body-coordinate location where the impinging shock strikes the receiver. This was measured from a scaled-down shadowgraph visualisation with a steel rule for each configuration to within $\delta_{x'}$=±0.5mm. The scale factor between the print-out and full size was k_{shad}=2.68. The

wind tunnel model was manufactured using a CNC machine within a tolerance of δ_L=±0.005mm.

The sources of uncertainty for the axial impingement parameter were as follows.

1. The uncertainty associated with the measurement of x' on print-out ($\delta_{x'}$)
2. The propagation of $\delta_{x'}$ introduced by the scale factor of the print out (k_{shad})
3. The uncertainty associated with the body length (δ_L)

These are combined in the following way to calculate the overall uncertainty in the axial impingement location parameter. The uncertainty in the length of the body was neglected since δ_L was much smaller than $\delta_{x'}$.

$$\delta_{x'} = \delta_{x'} * k_{shad}$$

$$\delta_{x'} = 0.5 * 2.68 = \pm 1.34\ mm$$

$$\delta_{x'/L} = \pm 0.01$$

A.8.2 Nominal freestream flow conditions

A.8.2.1 Freestream Mach number (M_∞)

The freestream Mach number (M_∞) was calculated from the elemental measurements of freestream static pressure (p_∞) and freestream total pressure ($p_{0,\infty}$) and the isentropic compressible flow relation for an ideal gas.

$$M_\infty = \sqrt{\frac{2}{\gamma}\left(\left(\frac{p_{0,\infty}}{p_\infty}\right)^{\gamma-1/\gamma} - 1\right)}$$

$$\delta_{M_\infty} = f(\delta_{p_{0,\infty}}, \delta_{p_\infty})$$

The Mach number was measured in only one experimental run. Therefore, all results presented in this document assume a freestream Mach number of M_∞=2.43 based on the wind tunnel liner geometry. The actual Mach number in the working section was verified through a single run measuring p_∞ and $p_{0,\infty}$ as well as analysis of the nozzle disturbance wave angles.

The freestream total pressure was measured in the wind tunnel settling chamber upstream of the nozzle. The freestream static pressure was measured using a static pressure port on the working section side-wall. The total pressure was measured with Druck absolute pressure transducer (PMP 4070, #1069985) with a full range of 2MPa. The accuracy of the total pressure measurement given by the manufacturer[66] was ±0.08% of the full range ($\delta_{p0,man}$=±1.6kPa) and included errors due to repeatability, hysteresis and non-linearity. The transducer calibration uncertainty was calculated by the least squares fitting approach of a best-fit straight line ($\delta_{p0,cal}$=±177Pa). Finally, the system resolution for the pressure and temperature measurements was based on a voltage range of 10V and the 15-bit Racal instruments Pro DAQ board to acquire the data. The minimum measureable voltage (V_{min}) was calculated using Equation A.6. The minimum measureable pressure was calculated using V_{min} as an input to the calibration curve and gives $\delta_{p0,res}$=±61.31Pa.

$$V_{min} = \frac{10V}{2^{15}}$$

$$V_{min} = 0.00031\,V \qquad \text{A.6}$$

In a similar fashion, a Druck absolute pressure transducer measuring the static pressure (PMP 4070, S/N 1378924) had a full range of 1MPa and a manufacturer's accuracy[66] of 0.08% full range giving: $\delta_{p,man}$=±800Pa, $\delta_{p,cal}$=±20.45Pa and $\delta_{p,res}$=±3.08Pa.

The sources of uncertainty for the freestream Mach number are as follows

1. The pressure measurement resolution for both transducers ($\delta_{p0,res}$, $\delta_{p,res}$)
2. The calibration uncertainty for both pressure transducers ($\delta_{p0,cal}$, $\delta_{p,cal}$)
3. The manufacturer's accuracy of both pressure transducers ($\delta_{p0,man}$, $\delta_{p,man}$)

The elemental uncertainties are combined to give the overall uncertainty for the static and total pressure measurements.

$$\delta_{p_{0,\infty}} = \sqrt{{\delta_{p_{0,cal}}}^2 + {\delta_{p_{0,man}}}^2 + {\delta_{p_{0,res}}}^2}$$

$$\delta_{p_0} = \pm 1611\ Pa$$

$$\delta_{p_\infty} = \sqrt{{\delta_{p_{cal}}}^2 + {\delta_{p_{man}}}^2 + {\delta_{p_{res}}}^2}$$

$$\delta_p = \pm 800\ Pa$$

The uncertainty in the freestream Mach number is calculated through the propagation of the elemental uncertainties. The ratio of freestream total to static pressure is denoted by the parameter PR. The average freestream measurements over this run are summarised in Table A.6 and lead to the following fractional uncertainties: δ_p/p_∞=1.7% and $\delta_{p0}/p_{0,\infty}$=0.2%.

Parameter	Quantity
$p_{0,\infty}$	0.678 MPa
p_∞	0.046 MPa
M_∞	2.40
PR_∞	14.61

Table A.6 Freestream conditions

$$M_\infty = \sqrt{\frac{2}{\gamma}\left(\left(\frac{p_{0,\infty}}{p_\infty}\right)^{\gamma-1/\gamma} - 1\right)}$$

$$\frac{\delta_{M_\infty}}{M_\infty} = \frac{\gamma - 1}{\gamma} * \frac{\delta_{PR_\infty}}{PR_\infty} * 0.5$$

$$\frac{\delta_{PR_\infty}}{PR_\infty} = \sqrt{\left(\frac{\delta_{p_0}}{p_{0,\infty}}\right)^2 + \left(\frac{\delta_{p_s}}{p_{s,\infty}}\right)^2} = 1.7\%$$

$$\frac{\delta_{M_\infty}}{M_\infty} = \frac{\gamma - 1}{\gamma} * 0.017 * 0.5 = \pm 0.2\%$$

The calculation of freestream Mach number (M_∞=2.40±0.01) assumed isentropic conditions between the settling chamber and working section. This does not take account of the loss in total pressure due to friction in the boundary-layer and this approach tends to underestimate the working section Mach number. Consequently, the actual Mach is estimated to be closer to the value based on the nozzle geometry (M_∞=2.43). This is supported through analysis of the measured disturbance wave angles ($\theta_s=\sin^{-1}(1/M_\infty)$) induced by the end of the nozzle geometry which were measured to give M_∞=2.42 and M_∞=2.41 for the upper and lower liners respectively. As a result, the value of 0.2% is deemed too conservative and the best estimate for the freestream Mach number is the one based on the liner M_∞=2.43±0.3 or ±1.3%.

A.8.2.2 Freestream Reynolds number (Re_D)

The freestream Reynolds number was calculated using the elemental measurements of total pressure and total temperature (T_0).

$$Re_D = \frac{\rho U D}{\mu}$$

$$\delta_{ReD} = f(\delta_{p0}, \delta_{T0}, \delta_D)$$

The total temperature was measured in the settling chamber with a total temperature probe. The manufacturer's accuracy was estimated to be $\delta_{T0,man}$=±0.5K. The calibration uncertainty was estimated using least square fitting for a best-fit straight line to be $\delta_{T0,cal}$=±0.16K. The system resolution was estimated, in the same way as previously described, to be $\delta_{T0,res}$=±0.02K.

The sources of uncertainty for the freestream unit Reynolds number are as follows.

1. The measurement resolution for p_0 pressure transducer ($\delta_{p0,res}$)
2. The calibration uncertainty for p_0 pressure transducer ($\delta_{p0,cal}$)
3. The manufacturer accuracy of p_0 pressure transducer ($\delta_{p0,man}$)
4. The measurement resolution for T_0 probe ($\delta_{T0,res}$)
5. The calibration uncertainty for T_0 probe ($\delta_{T0,cal}$)
6. The manufacturer accuracy of T_0 probe ($\delta_{T0,man}$)
7. Uncertainty in the base diameter dimension (δ_D)

$$\delta_{T_0} = \sqrt{{\delta_{T_{0,cal}}}^2 + {\delta_{T_{0,man}}}^2 + {\delta_{T_{0,res}}}^2}$$

$$\delta_{T_0} = \pm 0.5\ K$$

$$\delta_{p_0} = \pm 1611\ Pa$$

The nominal freestream conditions averaged over all runs conducted in the experimental test programme are summarised in Table A.7.

Parameter	Quantity
$p_{0,\infty}$	0.675 MPa
p_∞	0.044 MPa
T_0	292.8 K
T	134.2K
M_∞	2.43
ρ_∞	1.14 kgm^{-3}
U_∞	564.3 ms^{-1}
μ_∞	$9.27x10^{-6}$ $kgm^{-1}s^{-1}$
Re_D	$1.4x10^6$

Table A.7 Nominal freestream conditions in the S20SWT

The fractional uncertainty in the unit Reynolds number (δ_{ReD}/Re_D) is calculated from δ_U/U, δ_ρ/ρ, δ_μ/μ δ_D/D based on the elemental measurement uncertainties of δ_{p0} and δ_{T0}.

$$Re_D = \frac{\rho U D}{\mu}$$

$$\frac{\delta_{ReD}}{Re_D} = \sqrt{\left(\frac{\delta_\rho}{\rho}\right)^2 + \left(\frac{\delta_U}{U}\right)^2 + \left(\frac{\delta_\mu}{\mu}\right)^2 + \left(\frac{\delta_D}{D}\right)^2}$$

$$\rho = \frac{p}{RT}$$

$$p_\infty = \frac{p_{0,\infty}}{\left(1 + \frac{\gamma-1}{2} M_\infty{}^2\right)^{\frac{\gamma}{\gamma-1}}} \qquad \frac{\delta_p}{p_\infty} = \frac{\delta_{p_0}}{p_{0,\infty}} = \pm 0.2\%$$

$$T_\infty = \frac{T_{0,\infty}}{\left(1 + \frac{\gamma-1}{2} M_\infty{}^2\right)} \qquad \frac{\delta_T}{T_\infty} = \frac{\delta_{T_0}}{T_{0,\infty}} = \pm 0.2\%$$

$$\frac{\delta_\rho}{\rho} = \sqrt{\left(\frac{\delta_{p_0}}{p_0}\right)^2 + \left(\frac{\delta_T}{T}\right)^2} = \pm 0.3\%$$

$$U = M\sqrt{\gamma R T}$$

$$U = M\sqrt{\gamma R}\sqrt{T}$$

$$\frac{\delta_U}{U} = \frac{\delta_T}{T} * 0.5 = \pm 0.1\%$$

$$\mu = \frac{1.458x10^{-6}\sqrt{T}}{1 + \frac{110.4}{T}}$$

$$\delta_\mu = \frac{\partial \mu}{\partial T}\delta T$$

$$\frac{\partial \mu}{\partial T} = \frac{\mu(T_{135K}) - \mu(T_{133K})}{135 - 133} = 6.57x10^{-8}\ kg/ms.K$$

$$\delta_\mu = 6.57x10^{-8} * 0.2 = 1.58x10^{-8}\, kg/ms$$

$$\frac{\delta_\mu}{\mu} = \pm 0.2\%$$

$$\frac{\delta_{ReD}}{Re_D} = \sqrt{(0.3\%)^2 + (0.1\%)^2 + (0.2\%)^2 + (0.03\%)^2} = \pm 0.4\%$$

A.8.3 Force and moment measurements

The force and moment measurement uncertainties included estimations of both systematic and random errors. The random errors were estimated using a statistical approach and the systematic error sources were similar to those described previously. The receiver normal force (C_Z) and pitching moment (C_m) coefficients are calculated as an example. All force and moment coefficients were calculated using the elemental measurements of force (F_Z) or moment (M_Y), dynamic pressure (q_∞), characteristic area (S) and characteristic length (D) where applicable.

$$C_Z = \frac{F_Z}{q_\infty S} \qquad\qquad C_m = \frac{M_Y}{q_\infty SD}$$

$$\delta_{C_Z} = f(\delta_{F_Z}, \delta_{q_\infty}, \delta_S)$$

$$\delta_{C_m} = f(\delta_{M_Y}, \delta_{q_\infty}, \delta_S, \delta_D)$$

All force and moment measurements were taken using the ABLE MKIV, 6-component internal balance. A 15-bit Racal Instruments 6062 DAQ board was used to acquire the measurements[67]. The balance manufacturer's estimated accuracy[68] ±0.5% of the applied load compared to a best-fit straight line and accounts for all data scatter, hysteresis and non-linearity. The system resolution was estimated using the minimum measurable voltage as the input reading for all components and the resulting forces were calculated using the calibration matrix (see Table A.8).

Component	Resolution uncertainty [N,Nm]
F_X	$\delta_{FX,res}$=0.0192
F_Y	$\delta_{FY,res}$=0.0191
F_Z	$\delta_{FZ,res}$=0.0108
M_X	$\delta_{MX,res}$=0.0092
M_Y	$\delta_{MY,res}$=0.0109
M_Z	$\delta_{MZ,res}$=0.0002

Table A.8 Force and moment resolution uncertainly

The random uncertainties for each balance measurement were estimate for the datum (§4.2) at σ_R=8° and σ_R=15°. A statistical analysis assumed a normal distribution of the repeated measurements around the mean ($F_{\bar{Z}}$) value over the sample time history of 1 and 2s respectively. The standard deviation (σ_{FZ}) of 100,000 and 200,000 repeated measurement points (N) was first calculated. The random uncertainties were then calculated as the standard deviation of the mean with a confidence level of 95%[50]. The random uncertainties for all force and moment measurements were small and a summary of the random uncertainties are given in Table A.9.

$$\sigma_{F_Z} = \sqrt{\frac{\sum(F_Z - F_{\bar{Z}})^2}{N-1}}$$

$$\sigma_{\overline{F_Z}} = \frac{\sigma_{F_Z}}{\sqrt{N}}$$

$$\delta_{F_{Z,pre}} = \sigma_{\overline{F_Z}} * 1.96$$

Component	Random uncertainty [N,Nm]
F_X	$\delta_{FX,pre}$=0.0033
F_Y	$\delta_{FY,pre}$=0.0061
F_Z	$\delta_{FZ,pre}$=0.0088
M_X	$\delta_{MX,pre}$=0.00005
M_Y	$\delta_{MY,pre}$=0.0009
M_Z	$\delta_{MZ,pre}$=0.0007

Table A.9 Force and moment precision uncertainly

It can be seen that the system resolution uncertainties and random uncertainties for each component were negligible thus the overall uncertainty in all force and moment measurements is taken as 0.5% of the applied load.

The average freestream conditions used to non-dimensionalise the forces and moments are listed in Table A.10. The fractional uncertainties are also included for the denominators.

Parameter	Quantity	Uncertainty [%]
q_∞	0.182 MPa	0.2
S	0.00031 m^2	0.1
D	0.02 m	0.03
$q_\infty S$	57.23 N	0.2
$q_\infty SD$	1.14 Nm	0.2

Table A.10 Force and moment coefficient denominator uncertainly

$$\frac{\delta_{C_Z}}{C_Z} = \sqrt{\left(\frac{\delta_{F_Z}}{F_z}\right)^2 + \left(\frac{\delta_{q_\infty S}}{q_\infty S}\right)^2}$$

$$\frac{\delta_{C_Z}}{C_Z} = \sqrt{(0.6\%)^2 + (0.2\%)^2} = \pm 0.6\%$$

$$\frac{\delta_{C_m}}{C_m} = \sqrt{\left(\frac{\delta_{M_Y}}{M_Y}\right)^2 + \left(\frac{\delta_{q_\infty SD}}{q_\infty SD}\right)^2}$$

$$\frac{\delta_{C_m}}{C_m} = \sqrt{(0.6\%)^2 + (0.2\%)^2} = \pm 0.6\%$$

The other components are calculated in a similar fashion and a summary is given in Table A.11

Component	Uncertainty [%]
$\delta C_{X,t} / C_{X,t}$	0.6
$\delta C_{X,b} / C_{X,b}$	2.5
$\delta C_X / C_X$	2.6
$\delta C_Y / C_Y$	0.6
$\delta C_Z / C_Z$	0.6
$\delta C_l / C_l$	0.6
$\delta C_m / C_m$	0.6
$\delta C_n / C_n$	0.6

Table A.11 Force and moment coefficient uncertainly

The measured axial force coefficient ($C_{X,t}$) was corrected to assume freestream pressure acting over the base area. The axial force base correction ($C_{X,b}$) was calculated using the elemental measurements of average pressure (p_b) acting over the

base area (S_b), freestream static pressure (p_∞), freestream dynamic pressure (q_∞) and total base area (S).

The base pressure was measured using the same transducer as described for the freestream static pressure and had a total uncertainty of $\delta_{pb}=\delta_p=800Pa$. The freestream static pressure used was based on the measured freestream total pressure and an assumed Mach number of $M_\infty=2.43$. As a result the fractional uncertainty for the freestream static pressure was that of the freestream total pressure (0.2%), giving $\delta_{ps,\infty}=105Pa$. When calculating (p_b-$p_{s,\infty}$) fractional uncertainty, the minimum measured base pressure for a typical run ($p_b=0.012MPa$) and the freestream total pressure were used in the analysis below.

$$C_X = C_{X,t} + \frac{S_b(p_b - p_{s,\infty})}{q_\infty S}$$

$$C_{X,b} = \frac{S_b(p_b - p_\infty)}{q_\infty S}$$

$$\delta_{C_{X,b}} = f(\delta_{S_b}, \delta_{p_b}, \delta_{p_0}, \delta_{qS})$$

$$S = \frac{\pi D^2}{4} \qquad S_b = \frac{\pi}{4}(D^2 - D_s^2)$$

$$\frac{\delta_{D^2}}{D^2} = 2 * \frac{\delta_D}{D} = 0.1\% \qquad \frac{\delta_{D_s^2}}{D_s^2} = 2 * \frac{\delta_{D_s}}{D_s} = 0.1\%$$

$$\delta_{D^2} = 2x10^{-7}\ m^2 \qquad \delta_{D_s^2} = 1.6x10^{-7}\ m^2$$

$$\delta_{(D^2 - D_s^2)} = \sqrt{\delta_{D^2} + \delta_{D_s^2}} = 2.6x10^{-7}\ m^2$$

$$D^2 - D_s^2 = 1.4x10^{-4}\ m^2$$

$$\frac{\delta_{S_b}}{S_b} = \frac{2.6x10^{-7}}{1.4x10^{-4}} = \pm 0.2\%$$

$$\frac{\delta_{p_s}}{p_{s,\infty}} = \frac{\delta_{p_0}}{p_{0,\infty}} = 0.2\%$$

$$\delta_{p_b} = 800\ Pa \qquad \delta_{p_s} = 105\ Pa$$

$$\delta_{(p_b - p_{s,\infty})} = \sqrt{\delta_{p_b} + \delta_{p_s}} = 807\ Pa$$

$$\frac{\delta_{(p_b - p_{s,\infty})}}{|p_b - p_{s,\infty}|} = \frac{807}{32076} = \pm 2.5\%$$

$$\frac{\delta_{qS}}{qS} = \pm 0.2\%$$

$$\frac{\delta_{C_{X,b}}}{C_{X,b}} = \sqrt{\left(\frac{\delta_{S_b}}{S_b}\right)^2 + \left(\frac{\delta_{(p_b - p_{s,\infty})}}{|p_b - p_{s,\infty}|}\right)^2 + \left(\frac{\delta_{qS}}{qS}\right)^2}$$

$$\frac{\delta_{C_{X,b}}}{C_{X,b}} = \sqrt{(0.2\%)^2 + (2.5\%)^2 + (0.2\%)^2} = \pm 2.5\%$$

The interference loads were calculated by addition in quadrature. This was because the measurements of a given force under isolated and multi-body configurations were independent of one another. This gave the following interference load uncertainties

Component	Uncertainty [%]
$\delta\Delta C_X / \Delta C_X$	3.7
$\delta\Delta C_Z / \Delta C_Z$	0.9
$\delta\Delta C_m / \Delta C_m$	0.9

Table A.12 Force and moment interference load uncertainly

A.8.4 Pressure Sensitive Paint measurements

The uncertainty associated with PSP measurements is affected by many different factors. To reduce these sources of uncertainty an intensity ratio method was used to mitigate the effects of uneven PSP coating, non-homogeneous luminophore concentration in the PSP layer and non-uniform illumination[64]. The use of LED lamps further ensured that there was a negligible change in the illumination intensity between the wind-off and wind-on images. All images were re-aligned before calculating the intensity ratio so that wind-off and wind-on images overlay precisely and the effects of model deflection were reduced as much as possible. The black image intensity (typically in the order of 0.5% of the total intensity levels) was taken into account and subtracted from each image intensity in the data processing algorithm.

An estimate of the minimum pressure difference measureable from a single frame of image was made using the full well capacity of the CCD camera and the approach of Lui[69], giving $\delta_{p,min}/\delta_p$=1.2%. Further to this, the PSP measurement in the region of the model base is compared with the static pressure port measurement for all configurations in Table A.13. The PSP results exhibited a non-uniform pressure field in

this region but in general It can be seen that the minimum pressure uncertainty is too conservative and a better an estimation of the PSP measurement uncertainty is in the order of $\delta_p/p=10\%$.

PSP (p/p_∞)	Pressure port (p/p_∞)	Difference [%]
0.31	0.32	-4.41
0.36	0.4	-8.93
0.45	0.43	3.96
0.42	0.41	1.63
0.36	0.34	6.15
0.37	0.37	-0.24
0.48	0.44	8.91
0.42	0.4	6.32
0.36	0.33	9.61
0.42	0.4	6.16
0.46	0.52	-10.69
0.45	0.43	4.00
0.37	0.37	0.79
0.41	0.37	10.11
0.42	0.43	-3.20
0.39	0.4	-1.89
0.38	0.41	-6.47

Table A.13 PSP comparisons of base pressure

A.8.5 Experimental Uncertainty-ARA SWT measurements

The systematic uncertainties measured by the internal strain gauge balance were only based on the balance component resolutions due to a lack of information about the ARA SWT tests and are detailed in TableA.14.

$\delta_{CX,sys}$	$\delta_{CY,sys}$	$\delta_{CZ,sys}$	$\delta_{Cl,sys}$	$\delta_{Cm,sys}$	$\delta_{Cn,sys}$
± 0.0064	± 0.0154	± 0.0153	± 0.0199	± 0.0189	± 0.0193

TableA.14 Systematic uncertainties in the force and moment measurements

A statistical analysis is conducted for selected configurations where enough repeated sample measurements (N>20) were available. The configurations chosen are characteristic multi-body cases representative of the ARA SWT dataset as a whole and provided an estimate of the random component of the force and moment measurement uncertainties. In each configuration, the standard deviation (Equation A.7) and standard deviation of the mean value (Equation A.8) are calculated for over a sample of N repeated measurements (TableA.15).

$$\sigma_x = \sqrt{\frac{1}{N-1}\sum_{i=1}^{N}(x_i - \bar{x})} \quad \text{A.7}$$

$$\overline{\sigma_x} = \frac{\sigma_x}{\sqrt{N}} \quad \text{A.8}$$

Where: x is the measurement and $\bar{x}$ is the mean measurement value over the sample range.

Configuration	N	$C_{X,\sigma}$	$C_{X,\bar{\sigma}}$	$C_{Z,\sigma}$	$C_{Z,\bar{\sigma}}$	$C_{m,\sigma}$	$C_{m,\bar{\sigma}}$
Δx/L=0.5, Δz/D=1.94	22	0.00198	0.00042	0.00147	0.00031	0.00288	0.00061
Δx/L=0, Δz/D=1.94	22	0.00056	0.00012	0.00075	0.00016	0.00649	0.00138
Δx/L=0, Δz/D=2.94	22	0.00043	0.00009	0.00164	0.00035	0.00405	0.00086
Δx/L=0, Δz/D=3.94	22	0.00036	0.00008	0.00101	0.00022	0.00279	0.00059
Δx/L=0, Δz/D=4.96	22	0.00103	0.00022	0.00107	0.00023	0.00226	0.00048
Maximum	-	0.00198	0.00042	0.00164	0.00035	0.00649	0.00138

TableA.15 Statistical analysis for selected multi-body configurations

A normal distribution around the mean measurement value was assumed. The maximum standard deviation of the mean values with a confidence level of 95%[50] ($1.96 \times \overline{\sigma_x}$) are selected as characteristic values for the random component of uncertainty in the force and moment measurements (TableA.16).

$\delta_{CX,ran}$	$\delta_{CZ,ran}$	$\delta_{Cm,ran}$
± 0.00084	± 0.00069	± 0.00271

TableA.16 Random uncertainties in the force and moment measurements

The systematic and random components of uncertainty are combined by addition in quadrature to give the total uncertainty estimate for the force and moment measurements.

$$\delta_{CX} = \sqrt{\delta_{CXran}{}^2 + \delta_{CXsys}{}^2} = 0.00645$$

$$\delta_{CZ} = \sqrt{\delta_{CZran}{}^2 + \delta_{CZsys}{}^2} = 0.01532$$

$$\delta_{Cm} = \sqrt{\delta_{Cmran}{}^2 + \delta_{Cmsys}{}^2} = 0.01909$$

However, analysis of configurations where the impinging shock misses the receiver body have shown that the above estimate of the pitching moment uncertainty is too low. A more realistic estimate is δ_{Cm}=0.12. No information is known about uncertainty in the freestream flow measurements.

A.9 Computational uncertainty

A.9.1 Iterative convergence

The Cobalt flow solver outputs several parameters to aid assessment of the solution's dependence on the number of iterations completed (solution time). In this research, a solution is judged to be adequately iteratively converged when the following criteria are satisfied for 300 consecutive iterations.

- The normal force, pitching moment and axial force (F_Z, M_Y, F_X) which act on the receiver body must stabilise within a deviation limit of ±0.5% from the values reported.
- The density based solution residual ($D\rho/Dt$) must drop several orders of magnitude and stabilise at a constant value < 10^{-3}.
- The turbulence model residual ($D\omega/Dt$) must drop several orders of magnitude and stabilise at a constant value close to zero.
- The total number of supersonic cells in the computational domain must stabilise at a constant value.
- The average non-dimensional boundary-layer co-ordinate (y^+) over the receiver body must stabilise at a constant value $y^+ \leq 1$.

All steady-state computations in this research met the above criteria and are considered adequately iteratively converged.

A.9.2 Grid convergence

The receiver body axial force coefficient (C_X), pitching moment coefficient (C_m) and normal force coefficients (C_Z) are compared for a series of three grids for different configurations representative of the computational dataset as a whole. This grid convergence assessment follows the approach advocated by Roache[51] which is now summarised. The subscript g denotes the level of spatial resolution for the current grid which is non-dimensionalised by the fine grid resolution (g=2.25 for the coarse grid, g=1.5 for the medium grid g=1 for the fine grid, etc). In the configurations which used structured grids, the grid refinement ratio between grid levels was r_{conv}=1.5. In the configurations which used hybrid grids, an approximate grid refinement ratio of r_{eff}≈1.5 based on the total grid sizes was used (Equation A.9). The observed order of convergence (p_{con}) was calculated using Equation A.10 with C_X as an example parameter. Since Cobalt was run with 2nd order of spatial accuracy, if the observed order of accuracy exceeded two or was negative, then p_{con}=2 was used.

$$r_{eff} = \left(\frac{N_{fine}}{N_{\text{med}}}\right)^{1/3} \quad \text{A.9}$$

$$p_{con} = \ln\left(\frac{C_{X,g=2.25} - C_{X,g=1.5}}{C_{X,g=1.5} - C_{X,g=1}}\right)/\ln \text{r} \quad \text{A.10}$$

Richardson's extrapolation was then used to estimate the value of the chosen parameter for a grid spacing of zero (g=0) using the fine grid (Equation A.11).

$$C_{X,g=0} \cong C_{X,g=1} + \frac{C_{X,g=1} - C_{X,g=1.5}}{r^{p_{con}} - 1} \quad \text{A.11}$$

The grid convergence index was calculated between the fine and medium ($GCI_{g=1,1.5}$) as well as between the medium and coarse grids ($GCI_{g=1.5,2.25}$) (Equations A.12 and A.13). This assumed a factor of safety of F_s=1.25 since three grid levels were considered[51].

$$GCI_{1,1.5} = \frac{F_s \left|\frac{C_{X,g=1} - C_{X,g=1.5}}{C_{X,g=1}}\right|}{r^{p_{con}} - 1} \quad \text{A.12}$$

$$GCI_{1.5,2.25} = \frac{F_s \left| \frac{C_{X,g=1.5} - C_{X,g=2.25}}{C_{X,g=1.5}} \right|}{r^{p_{con}} - 1} \quad \text{A.13}$$

These were then used to judge whether the solutions are within the asymptotic range, such that Equation A.14 is satisfied.

$$AR \simeq \frac{GCI_{g=1.5,2.25}}{GCI_{g=1,1.5}\, r^{p_{con}}} \simeq 1 \quad \text{A.14}$$

The results of the grid convergence studies are now presented in Table A.17 - Table A.22.

m265r isolated σ_R=8° (structured grid)

	coarse (g=2.25)	medium (g=1.5)	fine (g=1)	zero (g=0)	$GCI_{1,1.5}$	AR	p_{con}
C_X	0.1431	0.1456	0.1461	0.1463	0.38%	1.97	2
C_Z	0.5188	0.5199	0.5211	0.522	0.23%	0.4	2
C_m	-1.5251	-1.5133	-1.5150	-	0.11%	-	-

Table A.17 Grid convergence: m265r isolated σ_R=8°

m265r m265g, Δx/D=0 Δz/D=2.94, σ_R=0° σ_G=0° (structured grid)

	coarse (g=2.25)	medium (g=1.5)	fine (g=1)	zero (g=0)	$GCI_{1,1.5}$	AR	p_{con}
C_X	0.14694	0.14767	0.14809	0.1487	0.48%	1.002	1.36
C_Z	-0.0863	-0.0868	-0.0870	-0.0872	0.27%	1.003	1.93
C_m	0.4648	0.4685	0.4702	0.4716	0.39%	1.004	1.91

Table A.18 Grid convergence: m265r m265g, Δx/D=0 Δz/D=2.94, σ_R=0° σ_G=0°

m2652 isolated σ_R=8° (hybrid grid)

	coarse (g=2.25)	medium (g=1.5)	fine (g=1)	zero (g=0)	$GCI_{1,1.5}$	AR	p_{con}
C_X	0.3273	0.3342	0.3377	0.3414	1.37%	1.01	1.65
C_Z	1.1382	1.1391	1.1373	-	0.16%	-	-
C_m	-5.6947	-5.6964	-5.6803	-	0.28%	-	-

Table A.19 Grid convergence: m2652 isolated σ_R=8°

m2651 m2654, Δx/D=-0.53 Δz/D=2.94, σ_R=15° σ_G=0° (hybrid grid)

	coarse (g=2.25)	medium (g=1.5)	fine (g=1)	zero (g=0)	$GCI_{1,1.5}$	AR	p_{con}
C_X	0.5530	0.5528	0.5514	0.5502	0.25%	0.08	2

C_Z	1.1332	1.1343	1.1325	-	0.16%	-	-
C_m	-5.0646	-5.0664	-5.0495	-	0.33%	-	-

Table A.20 Grid convergence: m2651 m2654, Δx/D=-0.53 Δz/D=2.94, σ_R=15° σ_G=0°

m2651 m2654, Δx/D=-3.81 Δz/D=2.94, σ_R=15° σ_G=0° (hybrid grid)

	coarse (g=2.25)	medium (g=1.5)	fine (g=1)	zero (g=0)	$GCI_{1,1.5}$	AR	p_{con}
C_X	0.5161	0.5157	0.5146	0.5138	0.2%	0.17	2
C_Z	1.2131	1.2141	1.2132	-	0.07%	-	-
C_m	-4.2957	-4.2960	-4.2903	-	0.13%	-	-

Table A.21 Grid convergence: m2651 m2654, Δx/D=-3.81 Δz/D=2.94, σ_R=15° σ_G=0°

m2652 m2653, Δx/D=1.67 Δz/D=2.94, σ_R=15° σ_G=0° (hybrid grid)

	coarse (g=2.25)	medium (g=1.5)	fine (g=1)	zero (g=0)	$GCI_{1,1.5}$	AR	p_{con}
C_X	0.9653	0.9678	0.9624	-	0.56%	-	-
C_Z	2.0933	2.0940	2.0931	-	0.04%	-	-
C_m	-11.569	-11.571	-11.557	-	0.12%	-	-

Table A.22 Grid convergence: m2652 m2653, Δx/D=1.67 Δz/D=2.94, σ_R=15° σ_G=0°

The configurations studied above covered some highly complex interference aerodynamics with the body at high incidence and with the finned receiver. The configurations predicted using structured grids generally demonstrated grid convergence. However, for the unstructured cases, less control of the grid resolution was available. Therefore, the relatively poor resolution of the impinging disturbances in the coarse grid frequently lead to a situation where a series of non-monotonic values for the parameters across the three grid levels was observed. In these cases, the grid convergence index between the fine and medium grid $GCI_{1,1.5}$ reported the percentage difference for a given parameter between the medium and fine grid. In general, it is clear that typical values of $GCI_{1,1.5}$ were less than 0.5% for all parameters across the configurations studied. As a result, the fine solutions are considered to be independent of further spatial refinement even if the solutions were not strictly grid

converged in the terms outlined by Roache. Overall, a discretisation error of <0.5% is considered a reasonable estimate.

Appendix B

B.1 Axial force measurements in the ARA SWT

Axial force measurements taken in the ARA SWT are shown in Figure B.1. The isolated un-finned receiver (*m265r*) is pitched through an incidence sweep for two consecutive runs (a and b).

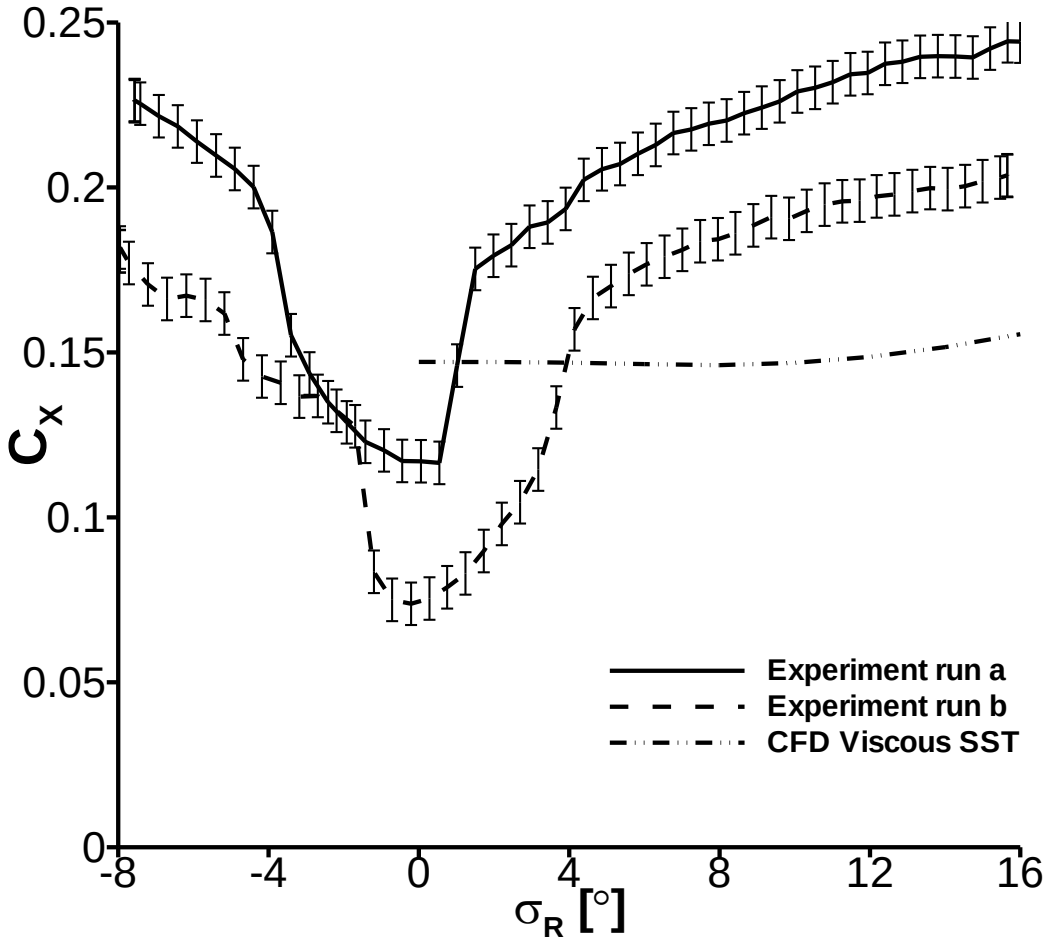

Figure B.1 Axial force repeatability in the ARA SWT

Poor experimental repeatability is observed for the corrected axial force coefficient between two these two consecutive runs. As a result, the axial force measurements in

the ARA SWT deemed unreliable and are not presented in the main body of this research.

B.2 Discrepancy between the measured and predicted loads for the isolated receiver bodies

This section investigates the reason for the discrepancy between the measurements and predictions of normal force and pitching moment for both receiver bodies in isolation. The results for the un-finned receiver as a function of incidence are shown in Figure B.2 and Figure B.3. The data at M_∞=2.43 and Re_D=1.4x10^6 are tests conducted in the S20 SWT. The data at M_∞=2.5 and Re_D=1.9x10^5 are tests conducted in the ARA SWT. Similar differences between ISL S20 and the CFD predictions are noted for tests of the finned receiver as well.

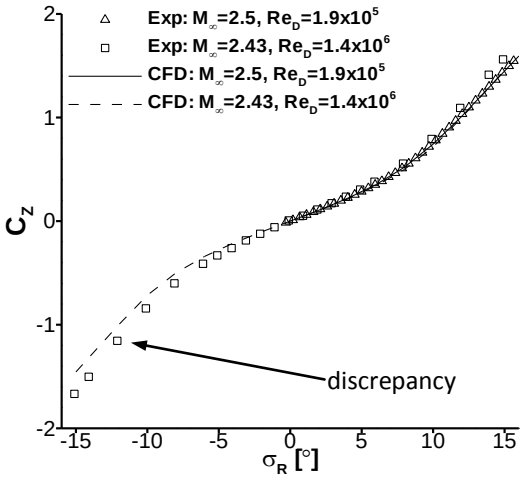

Figure B.2 Normal force characteristics for the un-finned receiver in isolation

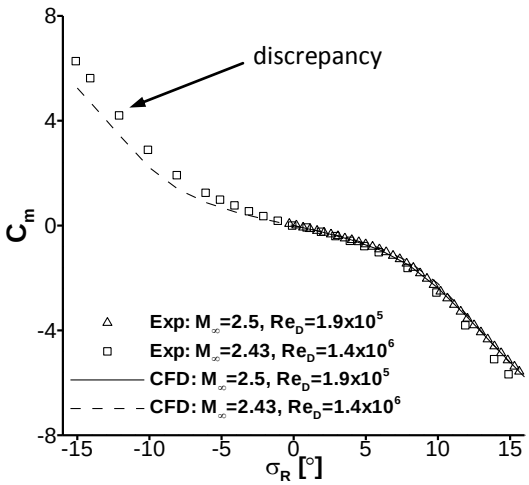

Figure B.3 Pitching moment characteristics for the un-finned receiver in isolation

The unexpected differences between the ISL S20 measurements and the predicted normal force loads are listed below in Table B.1. These differences are larger at negative incidence than at positive incidence for both bodies and are not proportional to normal force. Moreover, these non-negligible differences and must be investigated.

Receiver incidence (σ_R)	$(C_{Z,exp}-C_{Z,cfd})/C_{Z,cfd}$ Un-finned [%]	$(C_{Z,exp}-C_{Z,cfd})/C_{Z,cfd}$ Un-finned [%]
-15	14.7	8.9
-14	13.7	7.9
-12	14.7	8
-10	15.7	7.3
-8	16.2	6.87
-6	17.2	7
-4	18	8
-2	15.5	7.3
2	8.08	5.8
4	10.78	3
6	8.30	2.6
8	9.49	2.5
10	8.51	3.7
12	8.76	3.5
14	7.57	3.2
15	7.34	3.5

Table B.1 Percentage differences between the measured and predicted isolated receiver normal force loads

After several initial book-keeping checks were made, the following areas were further investigated to try and identify the source of the above discrepancies.

- Credibility of the predicted data
- Measurement repeatability
- Tests on the tunnel centerline
- S20 SWT freestream Mach number
- Balance proof testing

B.2.1 Credibility of the predicted data

The S20 SWT predictions for the un-finned receiver was consistent with measurements in the ARA SWT tunnel (Figure B.4). In addition, this data agreed with the other

predictions for different grid topologies and for both the ARA SWT conditions and the ISL S20 conditions.

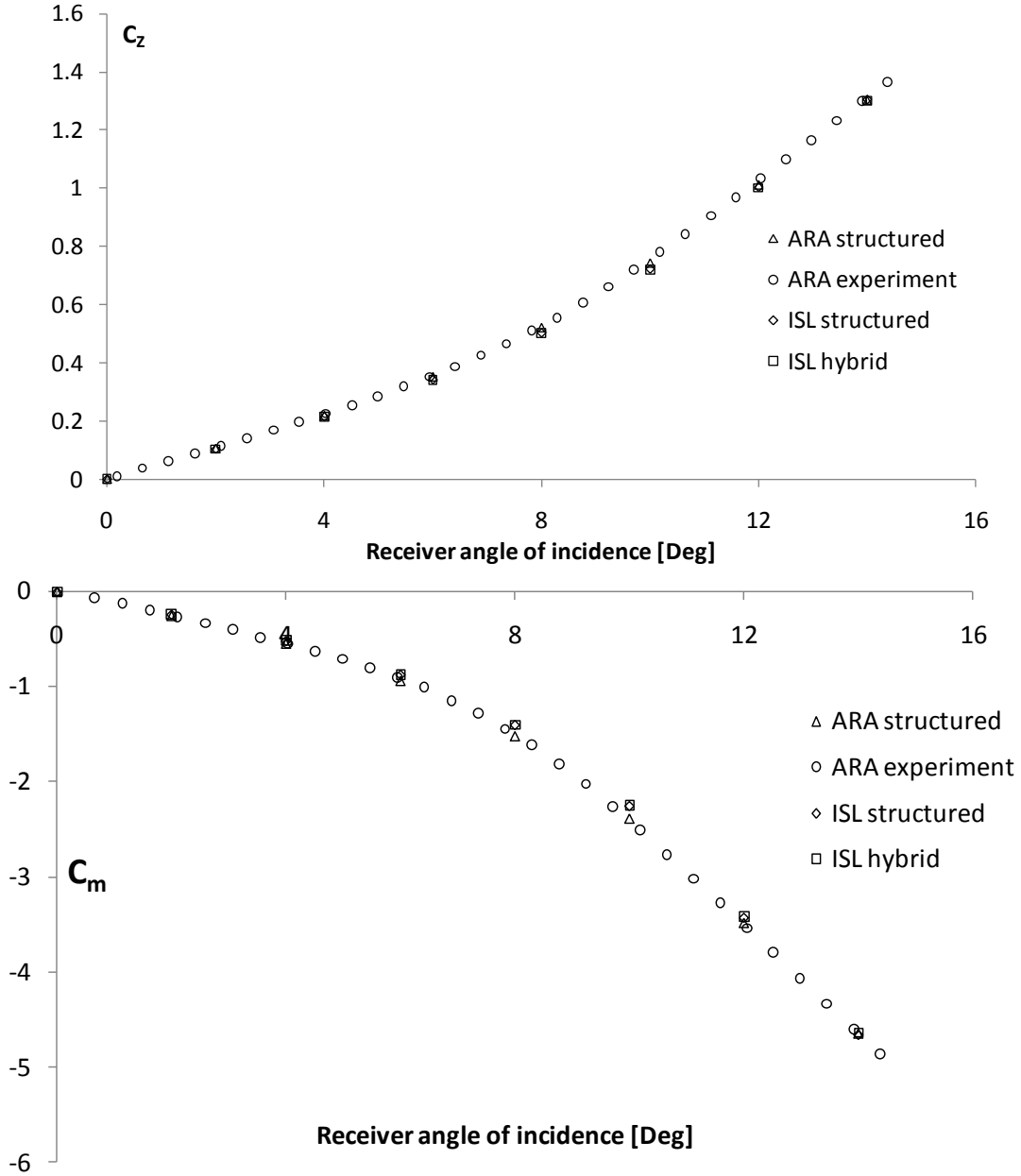

Figure B.4 Measurements and predictions (showing both structured and hybrid gridding topologies) of the un-finned receiver

It is clear from the data presented above that the source of the original discrepancy lies with the S20 SWT measurements. A mixture of measurements in another tunnel and many different CFD approaches give a reasonable indication of the what the correct data for the un-finned receiver should be.

B.2.2 Measurement repeatability

Since it thought the original discrepancy is caused by the measured data, the degree of measurement repeatability was evaluated over a series of repeated tests (runs a-d) of the un-finned receiver in isolation (Figure B.5).

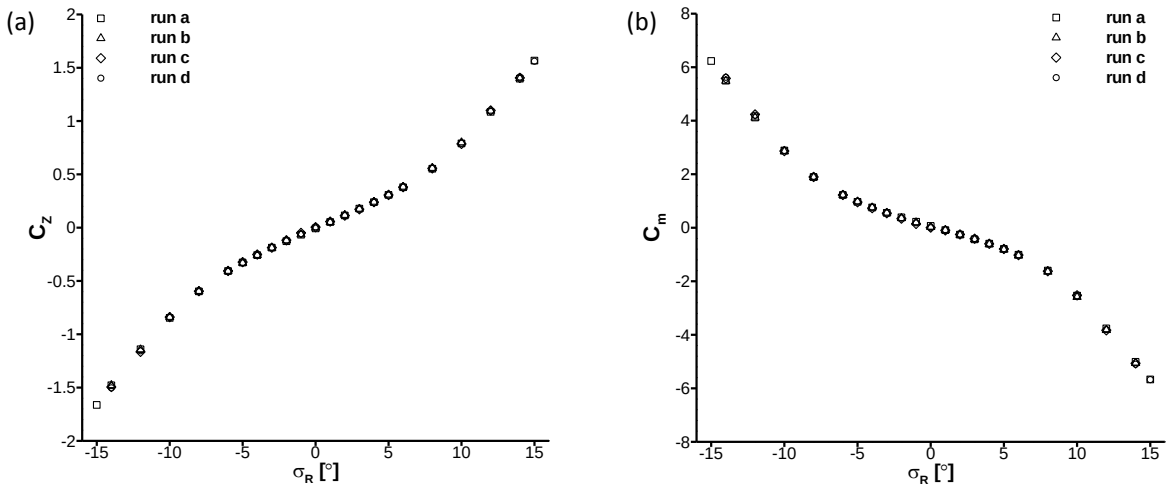

Figure B.5 Force and moment measurements on the un-finned receiver over a series of runs. (a) normal force and (b) pitching moment

Negligible differences are observed between the 4 runs for both normal force and pitching moment. This demonstrates that the original discrepancy is not due to poor measurement repeatability.

B.2.3 Tests on the tunnel centerline

All tests in the S20 SWT, except one, positioned the receiver body below the tunnel centerline. This was so that adequate space remained for the generator body to fit in the tunnel for the multi-body configurations. Small-scale, high-speed wind tunnels can have at least 1° of local flow pitch angularity away from the ideal working section flow conditions on the centerline. Consequently, the results for the un-finned receiver in isolation were compared for the nominal position in the tunnel (below the centerline) and on the centerline (Figure B.6) to evaluate whether this was a source of the original discrepancy.

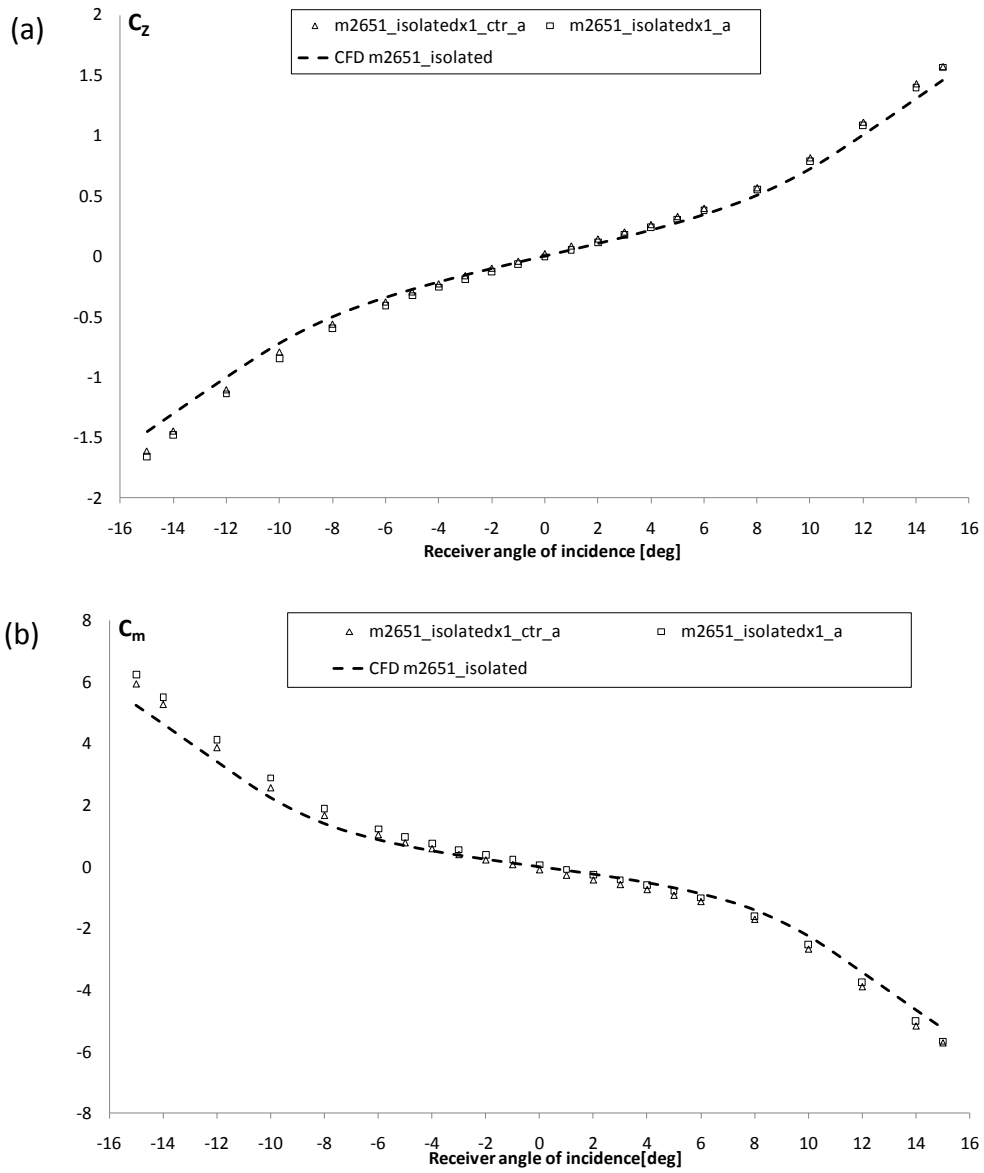

Figure B.6 Comparison of (a) normal force and (b) pitching moment measurements for un-finned receiver on and below the tunnel centreline

Although both normal force and pitching moment show a small difference on the tunnel centerline, this is very much smaller than the original discrepancy and the body test position can be discounted as a source of the discrepancy.

B.2.4 S20 SWT freestream Mach number

The freestream Mach number in the S20 SWT was checked to ensure it was equal to the assumed value of M_∞=2.43. If the ISL S20 predictions were run at the wrong Mach number this may account for the differences observed. The Mach number in the S20 SWT was estimated using two methods. The first was to calculate the angle of freestream disturbances emanating from the tunnel liner blend points suing the Mach wave relation (μ=sin-1(1/M)). On the upper linear the estimated Mach number was M=2.42 and M=2.41 for the lower liner. The second method was to measure the working section static pressure and settling chamber total pressure and use the isentropic relations to calculate the Mach number. This was only done for a single test since the working section static pressure was used to measure base pressure in all other runs. This approach measured a Mach number of M=2.4, a small amount less than M=2.43 which is due to the assumption of isentropic flow, in fact there will be a loss in the boundary-layer. Therefore, overall it is reasonable to assume that the working section Mach number is indeed M=2.43

B.2.5 Balance proof testing

The internal balance was calibrated a-priori by the balance manufacturer (Able). This calibration was proof tested for a series of known loads applied in the normal force direction under gravity. The applied load range covered the normal forces experienced by the un-finned and finned receivers in isolation up to σ=15° (up to 100N). These proof loading tests were done for the balance in the calibration rig and also in the tunnel under 'wind-off' conditions. In all cases the measured loads were less than 0.5% of the applied loads.

B.2.6 Summary

After a thorough investigation, the source of the original discrepancy has not been discovered. However, it is thought the differences were due to a systematic measurement bias in the S20 SWT force and moment measurement system. This did not affect the interference loads since the bias was present in both the isolated and multi-body measurements.

B.3 Nomenclature and definitions used in the discussion of the results

All of the notation used in this research is listed at the beginning of this thesis. This section gives additional information about the nomenclature and definitions used in the discussion of the interference aerodynamics.

B.3.1 General Language

In general, an isolated body generates *disturbance* shockwaves and expansion waves due to the leading edge and forebody. All of the disturbance waves emitted by an isolated body are termed the *disturbance flowfield* of that body (Figure B.7 (a)). In a multi-body configuration, a single disturbance from the generator body interacts with the receiver body. For a shockwave, this *interaction* occurs at a single point on the receiver body with an approximately step pressure rise. For an expansion wave fan, this *interaction* has a finite extent determined by the generator forebody shape and over which a pressure gradient acts. The interaction which occurs foremost on the receiver body is termed the *primary interaction*. Any subsequent interactions further aft are termed the *secondary* and *tertiary* interactions. Finally, the *interference flowfield* is the collective term for all interactions in a multi-body configuration (Figure B.7 (b)).

All interactions cause a pressure change on the body from the equivalent isolated configuration. This pressure change is termed a *differential pressure*. Moreover, regions where the local pressure is above the isolated values (*positive differential pressure*) or below the isolated values (*negative differential pressure*) exist over the body downstream of the impingement location. The magnitude and extent of these differential pressure regions contribute to the observed interference loads.

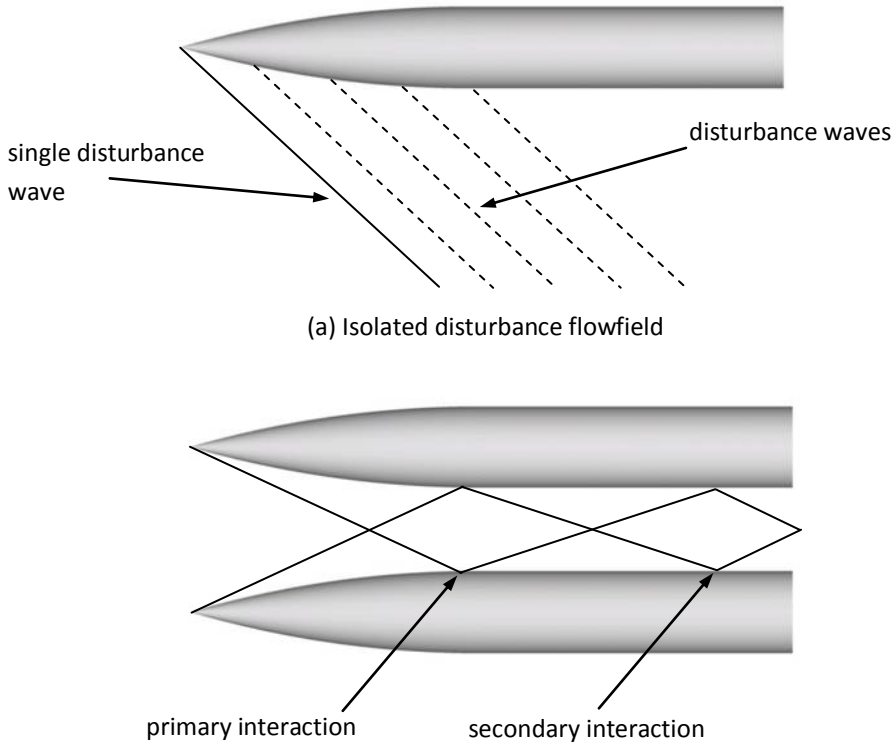

Figure B.7 Multi-body flowfield language

B.3.2 Nomenclature and definitions

Figure B.8 shows a shadowgraph image for a typical multi-body configuration. The important interaction parameters which help to analyse the problem are identified and then explained.

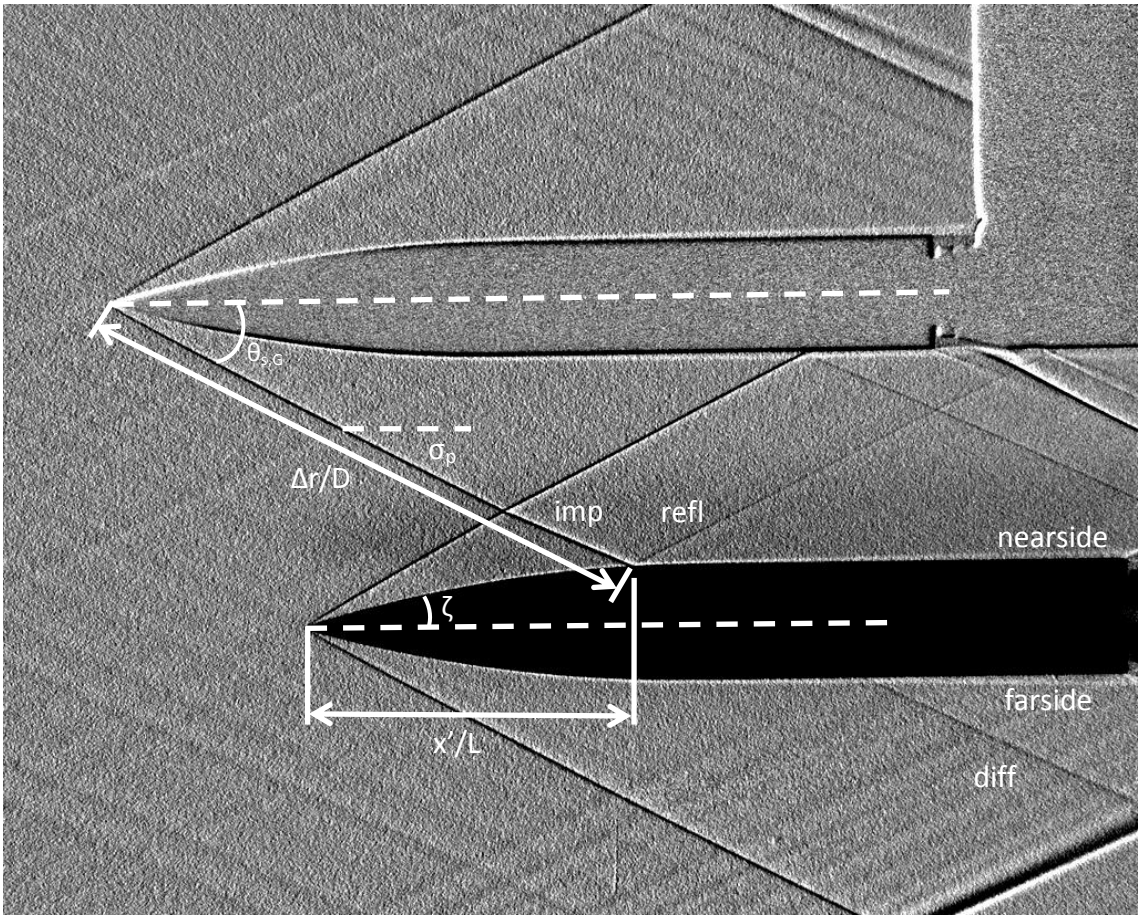

Figure B.8 Shadowgraph of a typical multi-body configuration showing parameters used in the results analysis

- Impinging shock (*imp*): the generator bow shock which interacts with the receiver body
- Reflected shock (*refl*): the reflected portion of the impinging shock
- Diffracted shock (*diff*): the diffracted portion of impinging shock
- Nearside (*near*): the nearside of the receiver body (ϕ=180°)
- Farside (*far*): the farside of the receiver body (ϕ=0°)
- Axial impingement location (x'/L): the axial distance from the leading edge of the receiver body to the primary impingement location.

- Generator shockwave angle ($\theta_{s,G}$): the included angle between the generator shockwave and the X_w-Y_w plane in the wind axes reference frame. For simplicity this is positive as shown in Figure B.8.

- Shock obliqueness angle (θ_{obl}): the included angle between the generator shockwave and the receiver body centreline $\theta_{obl}=\theta_{s,G}-\sigma_R$.

- Surface curvature angle (ε): the included angle between the local body surface at ϕ=180° and the X-Y plane (body axes reference frame). Since the body is at zero incidence in Figure B.8, $\varepsilon=\zeta$. This parameter is equal to $\varepsilon=-34.13(x/L)+16.194$ over the forebody and $\varepsilon=0$ on the afterbody ($x/L > 0.48$)

- Surface curvature angle (ζ): the included angle between the local surface at ϕ=180° and the X_w-Y_w plane (wind axes reference frame). This parameter is equal to $\zeta=\varepsilon-\sigma_R$

- Disturbance field strength (σ_p): the local flow pitch angle immediately downstream of the impinging shock. Measured from X_w-Y_w plane in the wind axes reference frame, negative downward towards the receiver body.

- δ_{refl}: the flow turning necessary to maintain a regular reflection ($\delta_{refl}=\zeta-\sigma_p$)

- ψ_{refl}: the reflected shock strength expressed as $\Delta C_{p,refl}$ across the reflected shock

- r_{sh}/D: the distance from generator leading edge to the impingement location, used to characterise the decay in disturbance field strength from the generator body ($\Delta z_{sh}/D$ used for blunt generator since the shock is not conical)

- Disturbance field strength (ψ_{imp}): the impinging shock strength expressed as $\Delta C_{p,imp}$ across the impinging shock

- Interaction shock strength (ψ): overall shock strength at the impingement point which includes both ψ_{imp} and ψ_{refl}. This is characterised by change in pressure on receiver nearside at ϕ=180° ($\Delta C_{p,near}$). $\Delta C_{p,near}\approx\Delta C_{p,imp}+\Delta C_{p,refl}$

- Disturbance expansion field strength (η): the local expansion field strength characterised by pressure gradient across the expansion fan extent $\eta = dp/dx * L/p_\infty$

B.4 CFD and PSP comparisons for the un-finned receiver body

B.4.1 Un-finned receiver and sharp generator

The following pages compare PSP and CFD results for the un-finned receiver and sharp generator configuration. This includes plots of surface pressure (p/p_∞), axial distributions of C_p at different azimuth locations ϕ=0° (farside) and ϕ=180° (nearside) and crossflow distributions of C_p at different axial locations on the receiver body over an incidence range $-15 \leq \sigma_R \leq 15°$.

At the extremes of surface curvature near the receiver leading edge ($x/L \leq 0.15$) the local surface normal was almost perpendicular to the camera line-of-sight and the data in this small region were considered to be un-reliable and excluded from the pressure plots. Due to wind tunnel debris a small amount of degradation of the PSP coating occurred during each test. In addition, the model attachment screw hole caused a local flowfield disturbance at $x/L \approx 0.55$ and ϕ=90°.

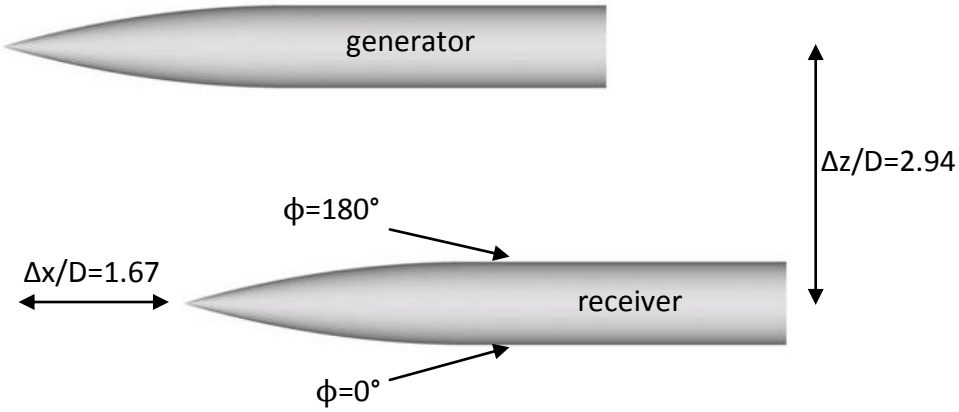

σ_R=0°

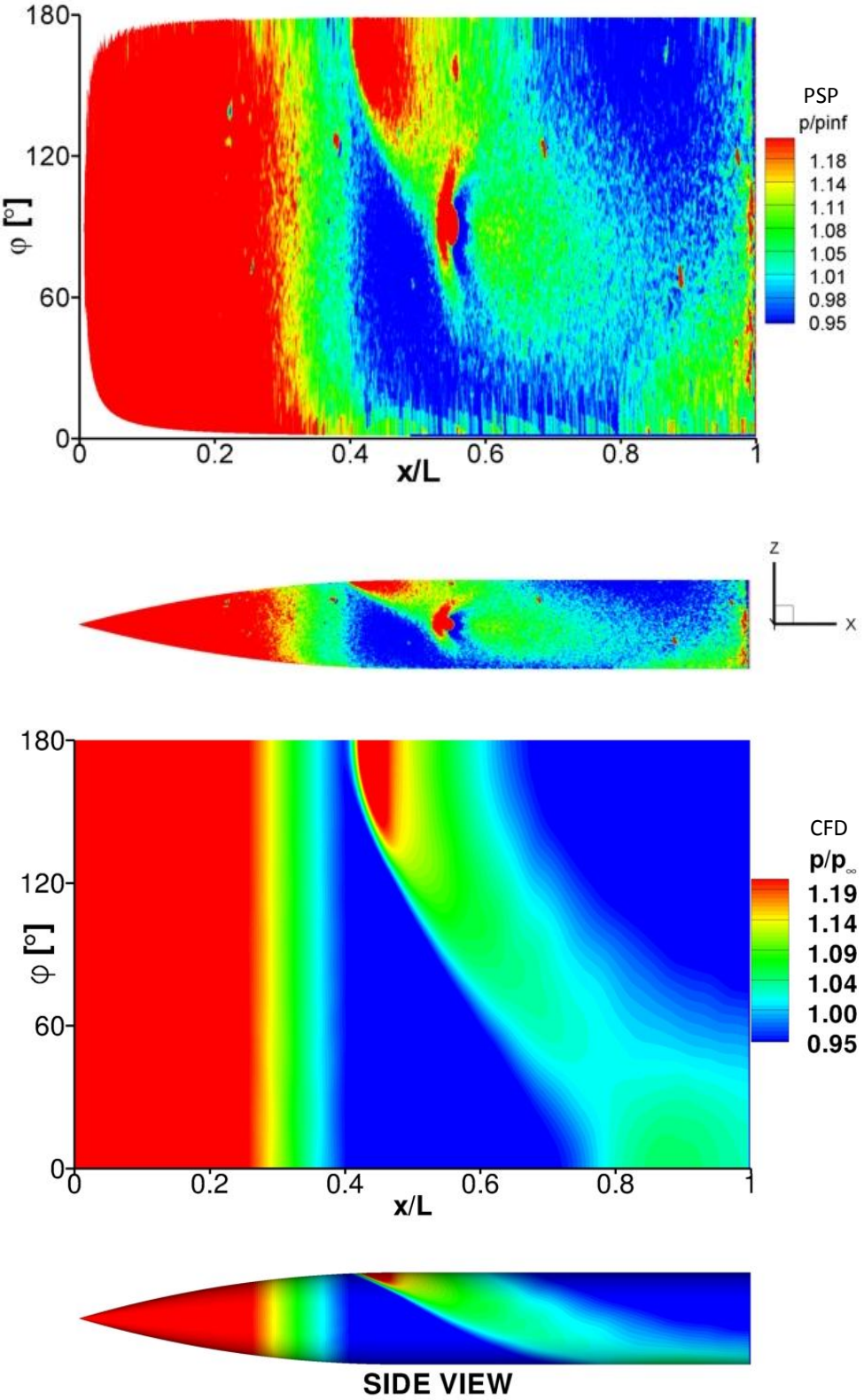
180
120
60
0
φ [°]
0
0.2
0.4
0.6
0.8
1
x/L
PSP
p/pinf
1.18
1.14
1.11
1.08
1.05
1.01
0.98
0.95
z
x
CFD
p/p∞
1.19
1.14
1.09
1.04
1.00
0.95
SIDE VIEW

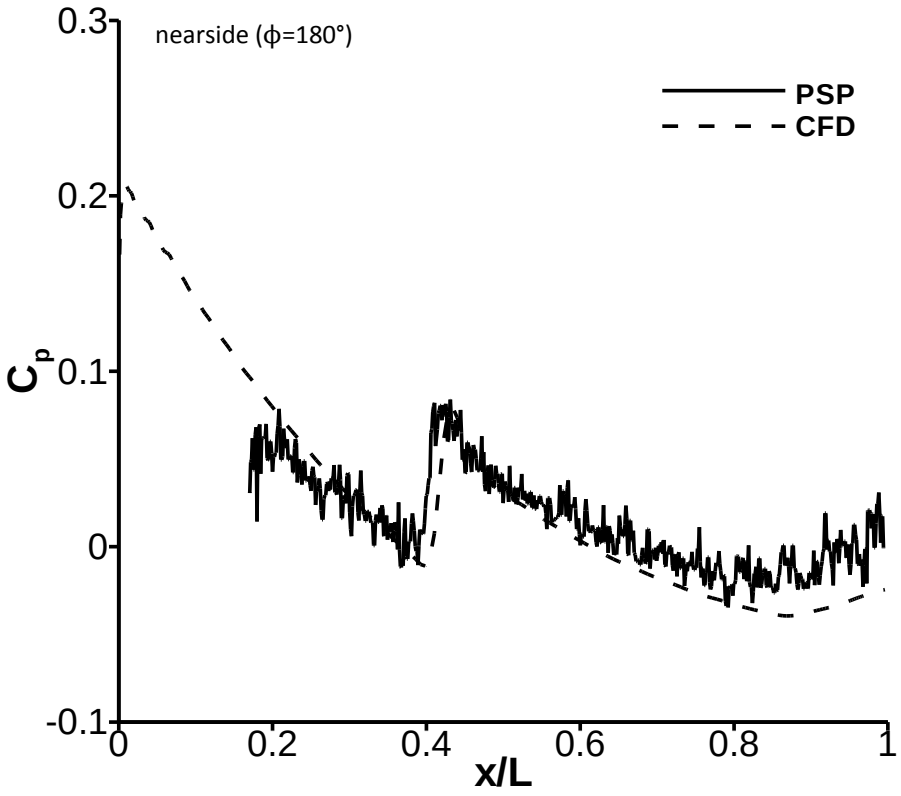
nearside (ϕ=180°)
PSP
CFD
0.3
0.2
0.1
0
-0.1
C_p
0
0.2
0.4
0.6
0.8
1
x/L

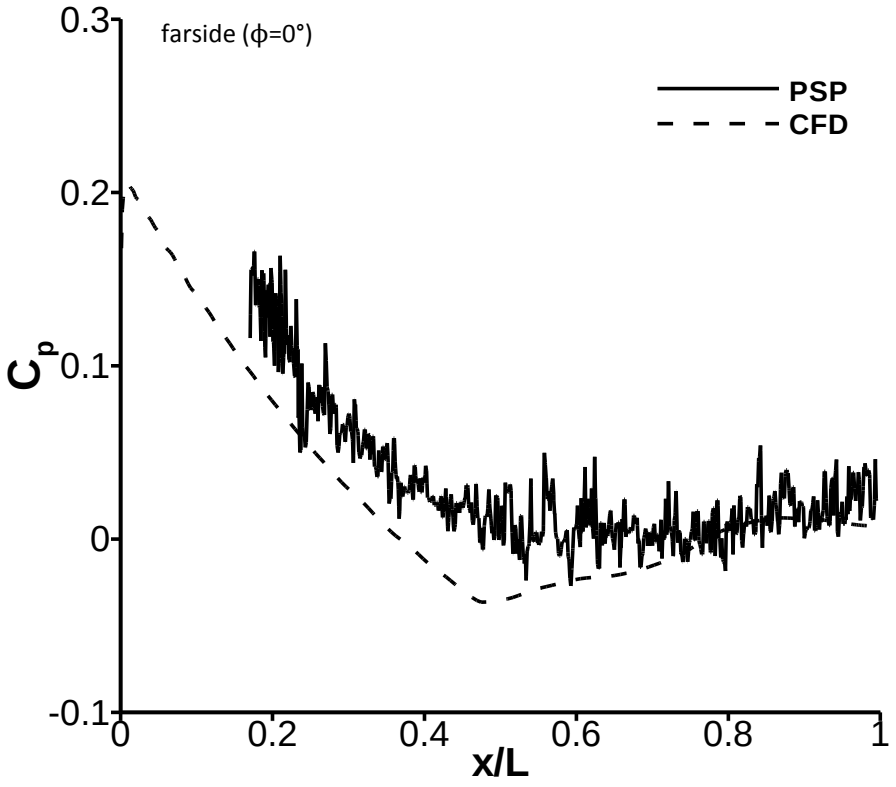
farside (ϕ=0°)
PSP
CFD
0.3
0.2
0.1
0
-0.1
C_p
0
0.2
0.4
0.6
0.8
1
x/L

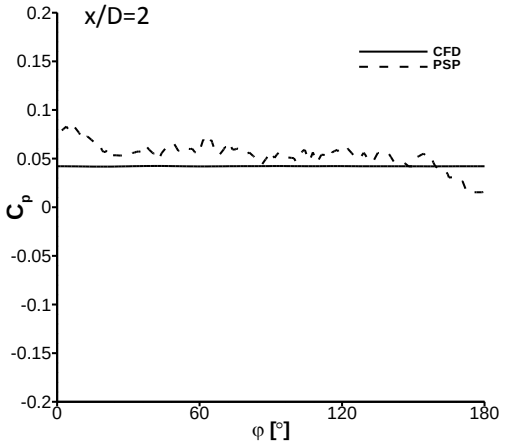
x/D=2
CFD
PSP
C_p
φ [°]

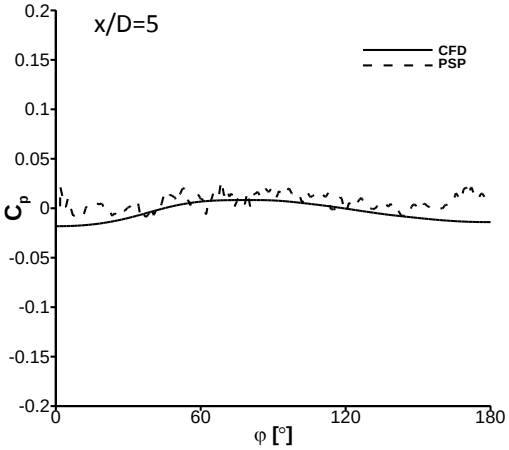
x/D=5
CFD
PSP
C_p
φ [°]

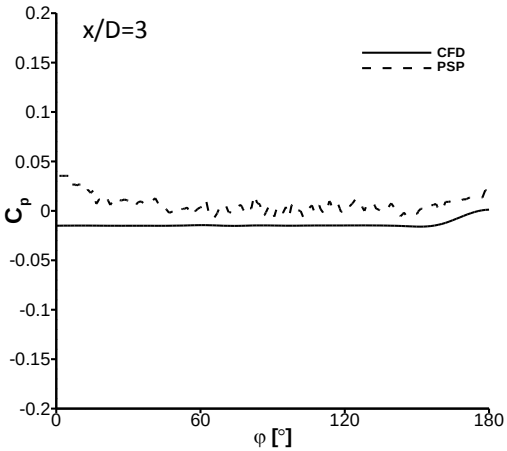
x/D=3
CFD
PSP
C_p
φ [°]

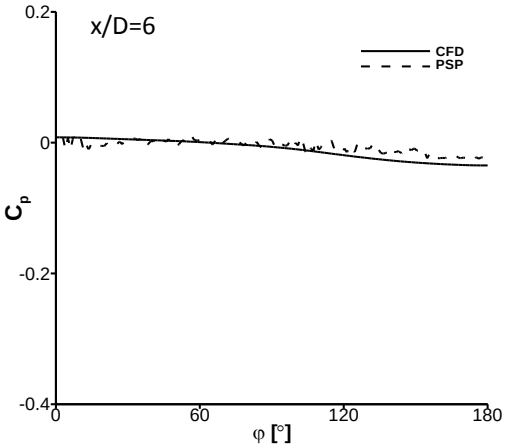
x/D=6
CFD
PSP
C_p
φ [°]

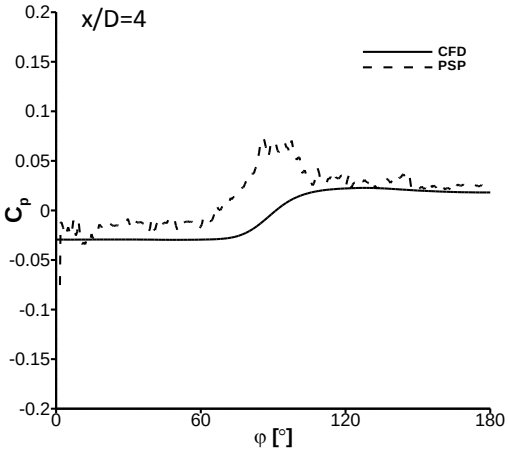
x/D=4
CFD
PSP
C_p
φ [°]

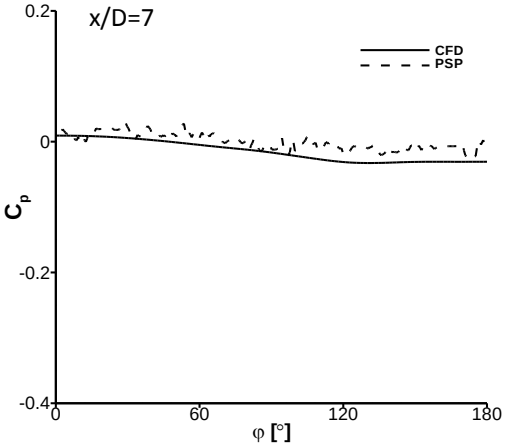
x/D=7
CFD
PSP
C_p
φ [°]

σ_R =-8°

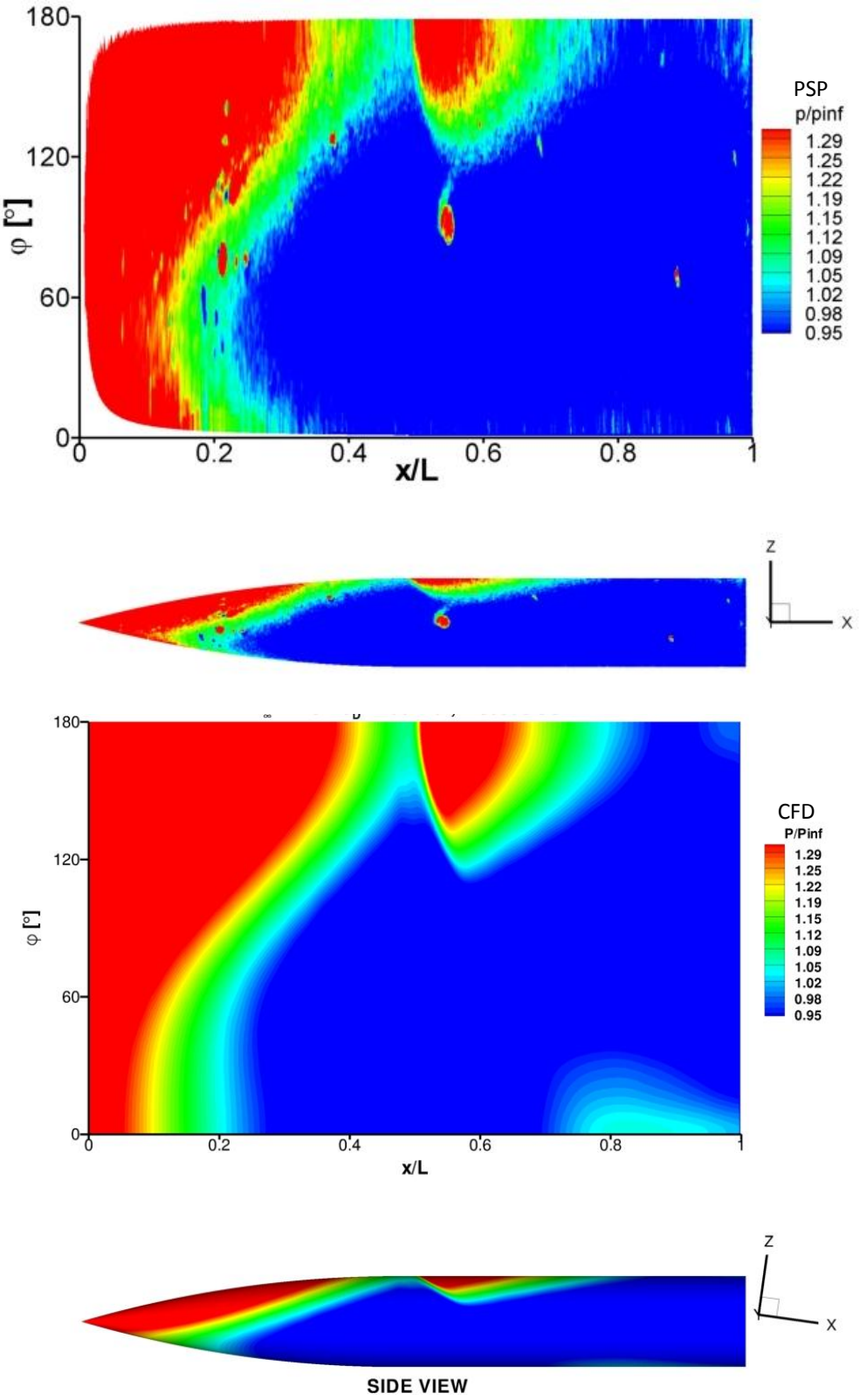
180
120
60
0
φ [°]
0
0.2
0.4
0.6
0.8
1
x/L
PSP
p/pinf
1.29
1.25
1.22
1.19
1.15
1.12
1.09
1.05
1.02
0.98
0.95
Z
X
CFD
P/Pinf
SIDE VIEW

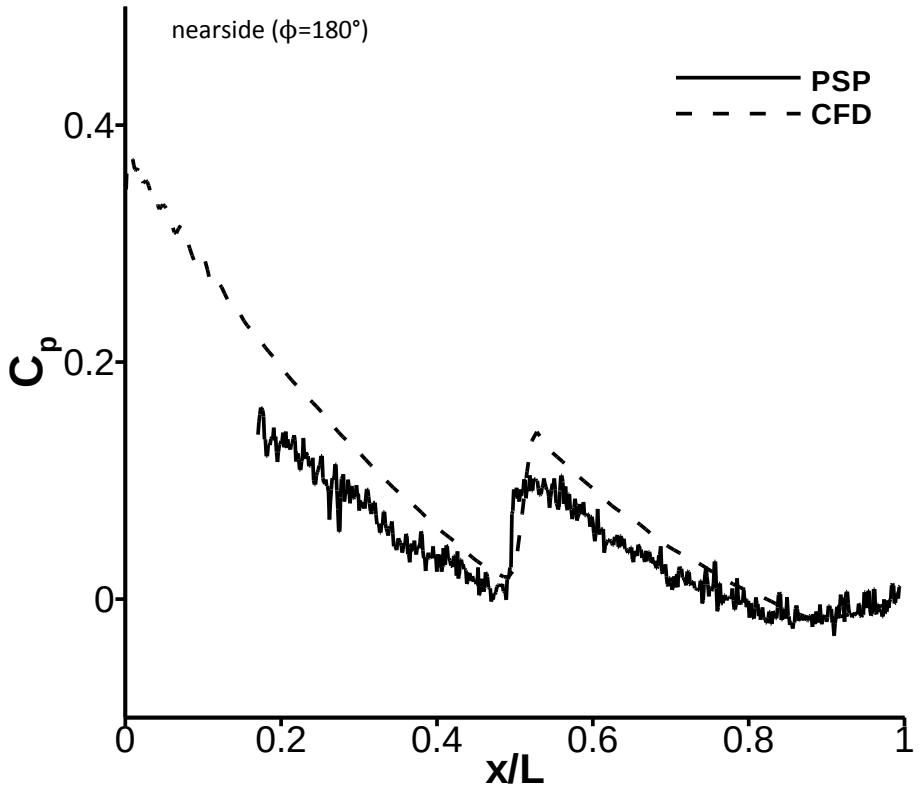
nearside (ϕ=180°)
PSP
CFD
0.4
0.2
0
C_p
0
0.2
0.4
0.6
0.8
1
x/L

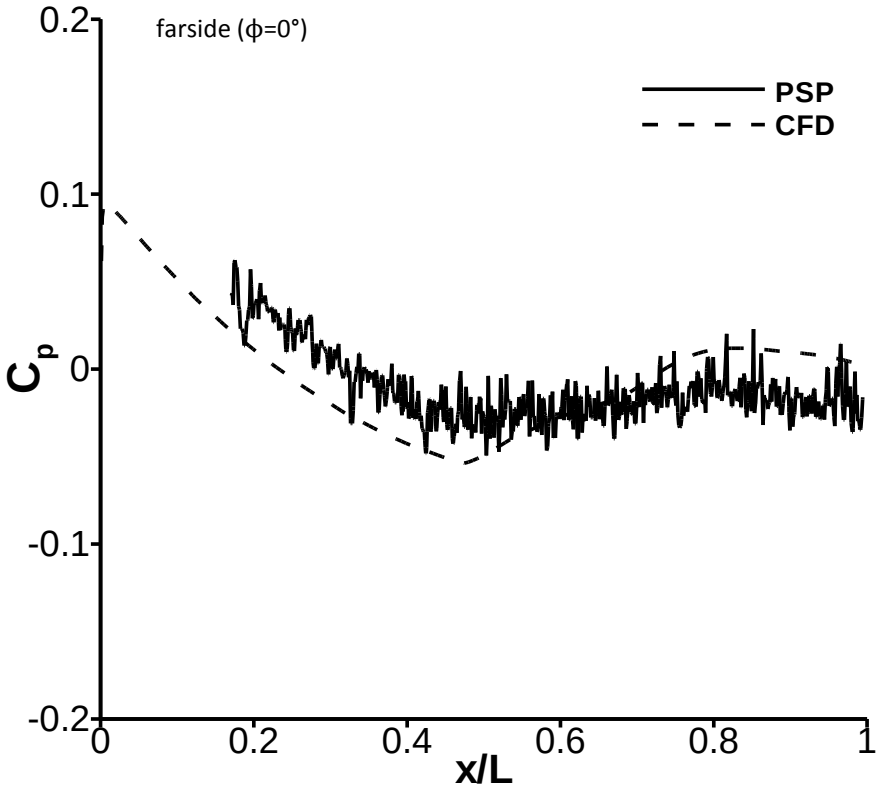
farside (ϕ=0°)
PSP
CFD
0.2
0.1
0
-0.1
-0.2
C_p
0
0.2
0.4
0.6
0.8
1
x/L

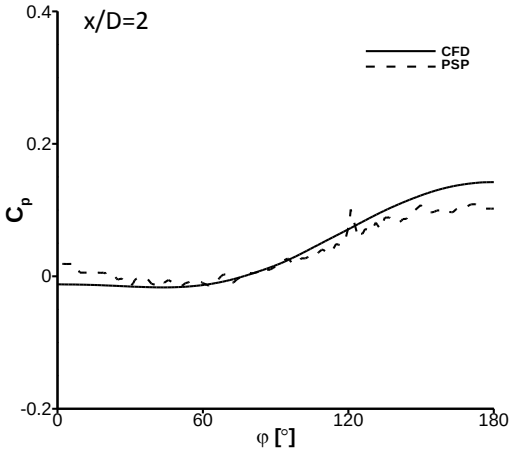
x/D=2
CFD
PSP
C_p
φ [°]

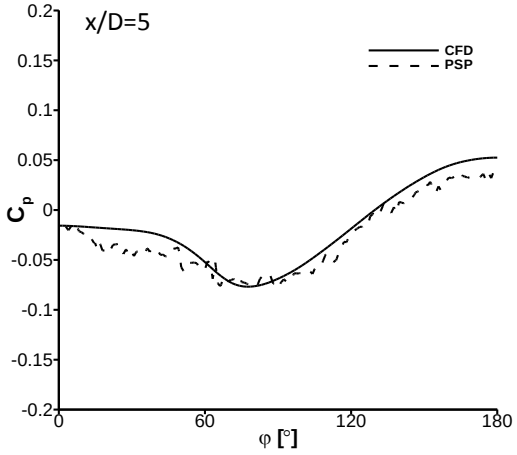
x/D=5
CFD
PSP
C_p
φ [°]

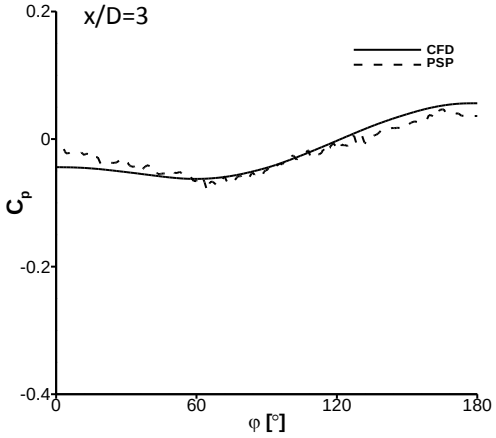
x/D=3
CFD
PSP
C_p
φ [°]

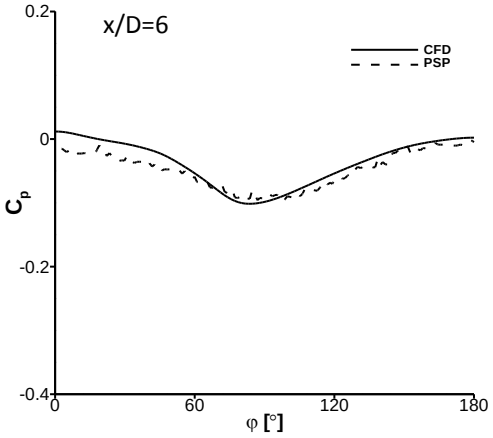
x/D=6
CFD
PSP
C_p
φ [°]

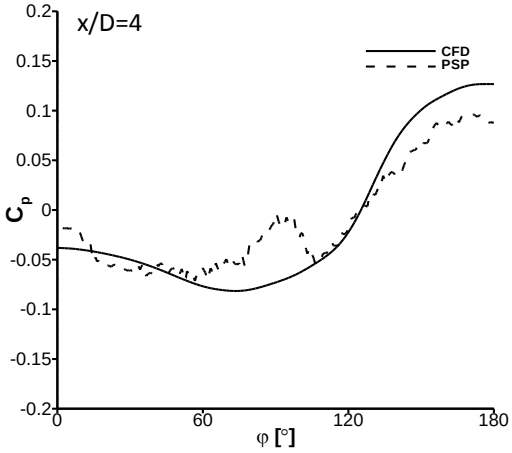
x/D=4
CFD
PSP
C_p
φ [°]

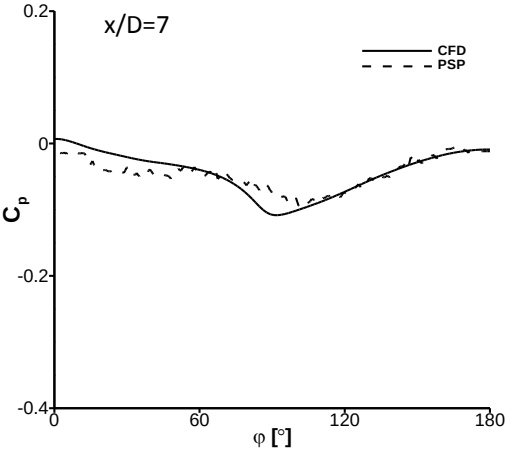
x/D=7
CFD
PSP
C_p
φ [°]

σ_R =-15°

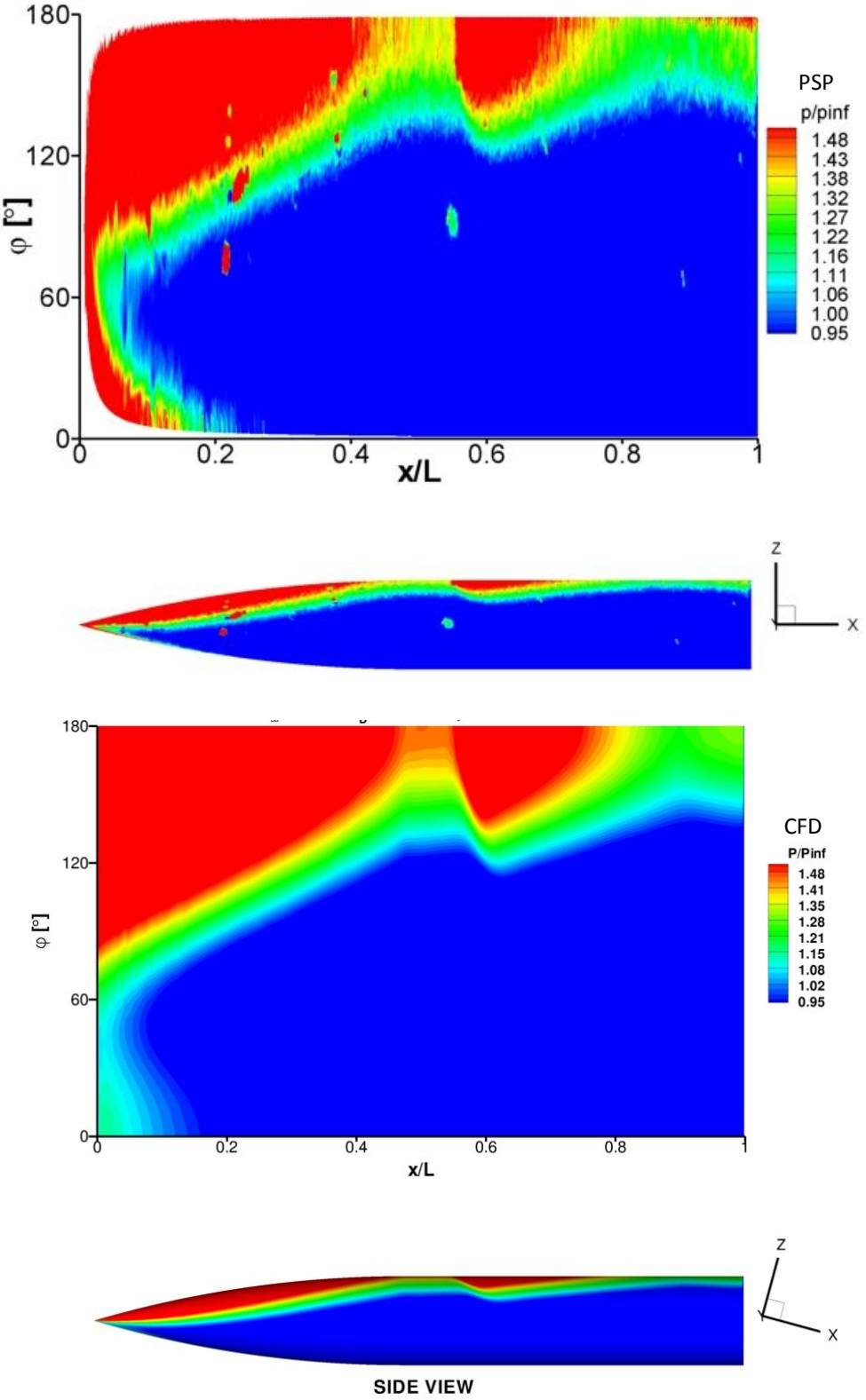
180
120
60
0
φ [°]
0
0.2
0.4
0.6
0.8
1
x/L
PSP
p/pinf
1.48
1.43
1.38
1.32
1.27
1.22
1.16
1.11
1.06
1.00
0.95
Z
X
180
120
60
0
φ [°]
0
0.2
0.4
0.6
0.8
1
x/L
CFD
P/Pinf
1.48
1.41
1.35
1.28
1.21
1.15
1.08
1.02
0.95
Z
X
SIDE VIEW

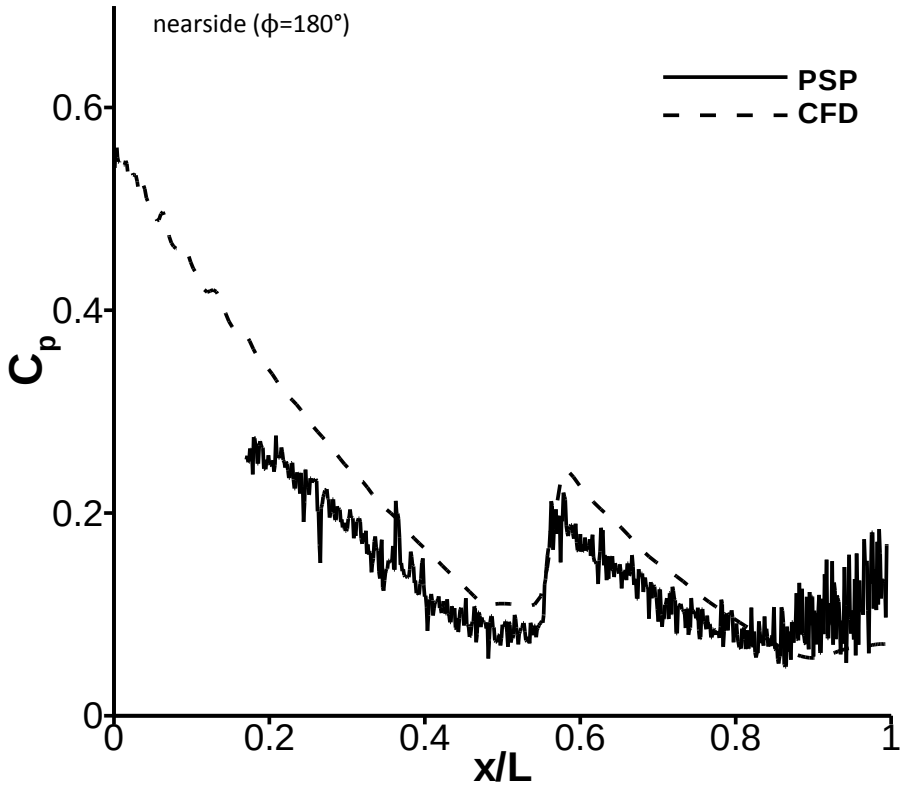
nearside (ϕ=180°)
PSP
CFD
0.6
0.4
0.2
0
C_p
0
0.2
0.4
0.6
0.8
1
x/L

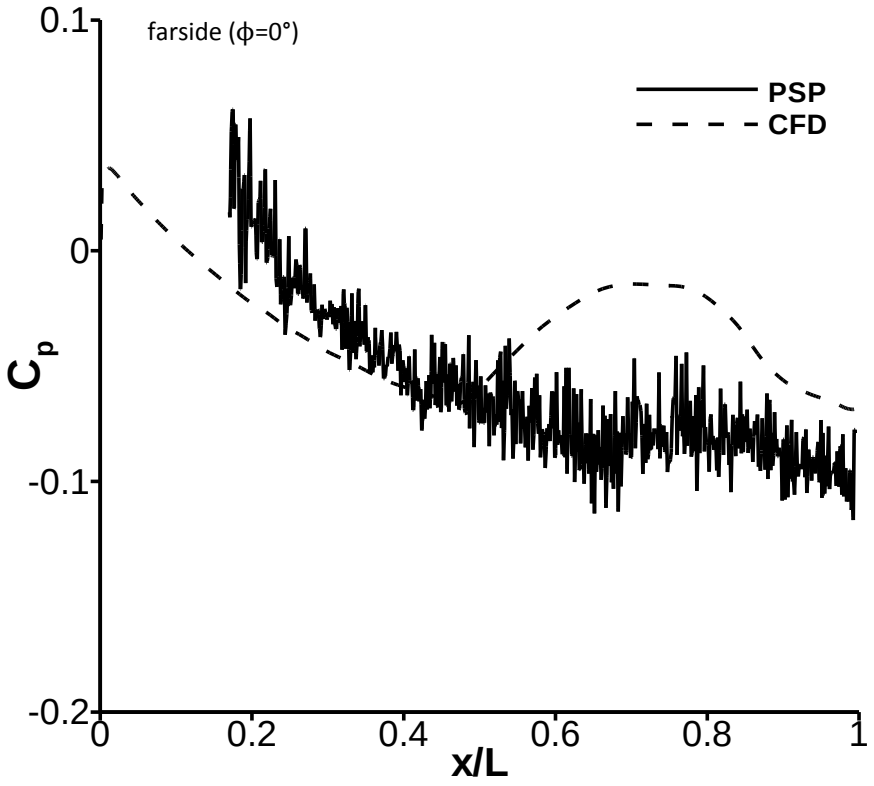
farside (ϕ=0°)
PSP
CFD
0.1
0
-0.1
-0.2
C_p
0
0.2
0.4
0.6
0.8
1
x/L

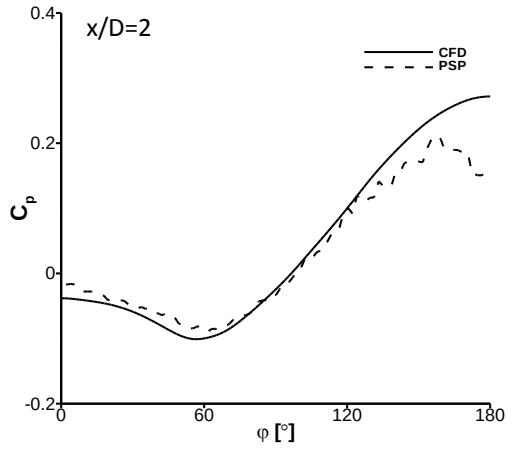
x/D=2
CFD
PSP
C_p
φ [°]

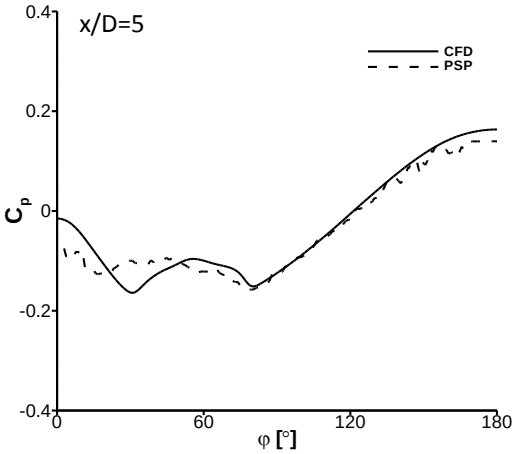
x/D=5
CFD
PSP
C_p
φ [°]

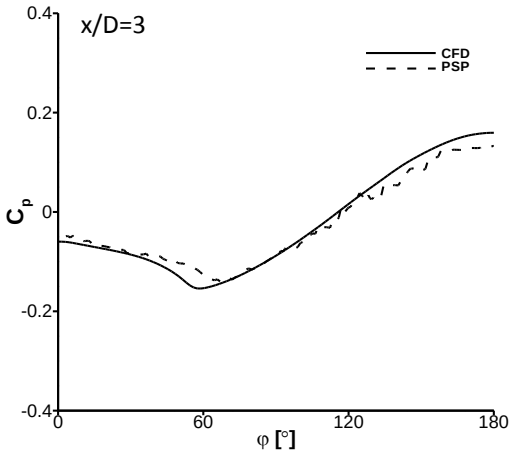
x/D=3
CFD
PSP
C_p
φ [°]

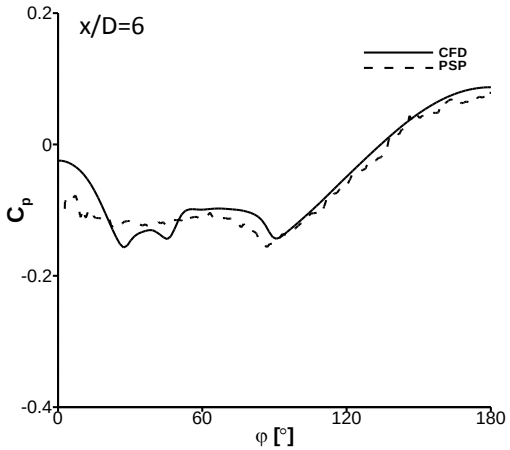
x/D=6
CFD
PSP
C_p
φ [°]

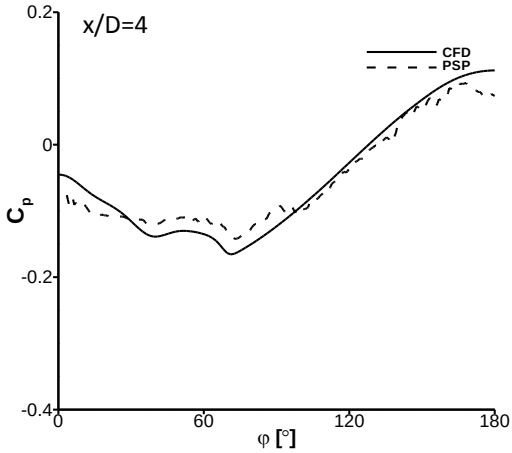
x/D=4
CFD
PSP
C_p
φ [°]

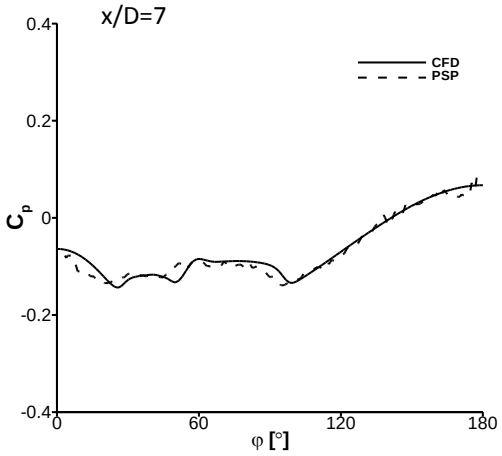
x/D=7
CFD
PSP
C_p
φ [°]

σ_R =8°

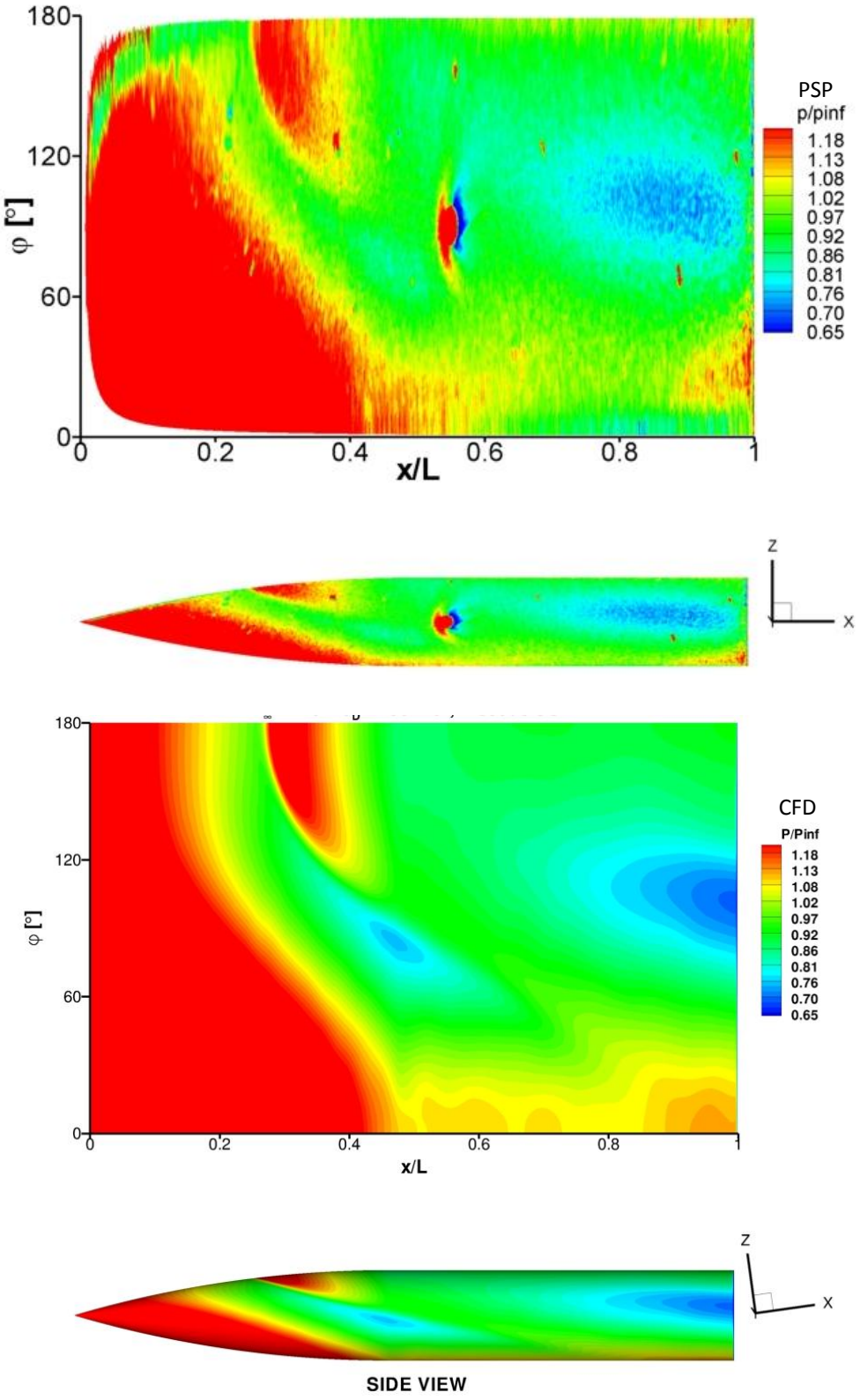
180
120
60
0
φ [°]
0
0.2
0.4
0.6
0.8
1
x/L
PSP
p/pinf
1.18
1.13
1.08
1.02
0.97
0.92
0.86
0.81
0.76
0.70
0.65
Z
X
CFD
P/Pinf
SIDE VIEW

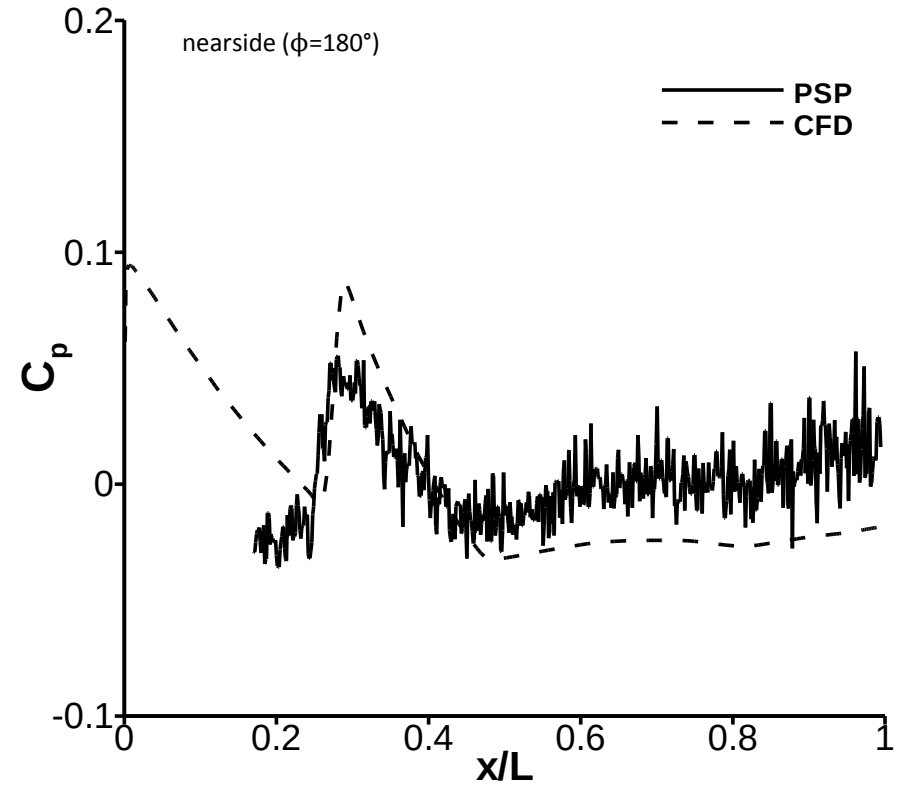
nearside (ϕ=180°)
PSP
CFD
0.2
0.1
0
-0.1
C_p
0
0.2
0.4
0.6
0.8
1
x/L

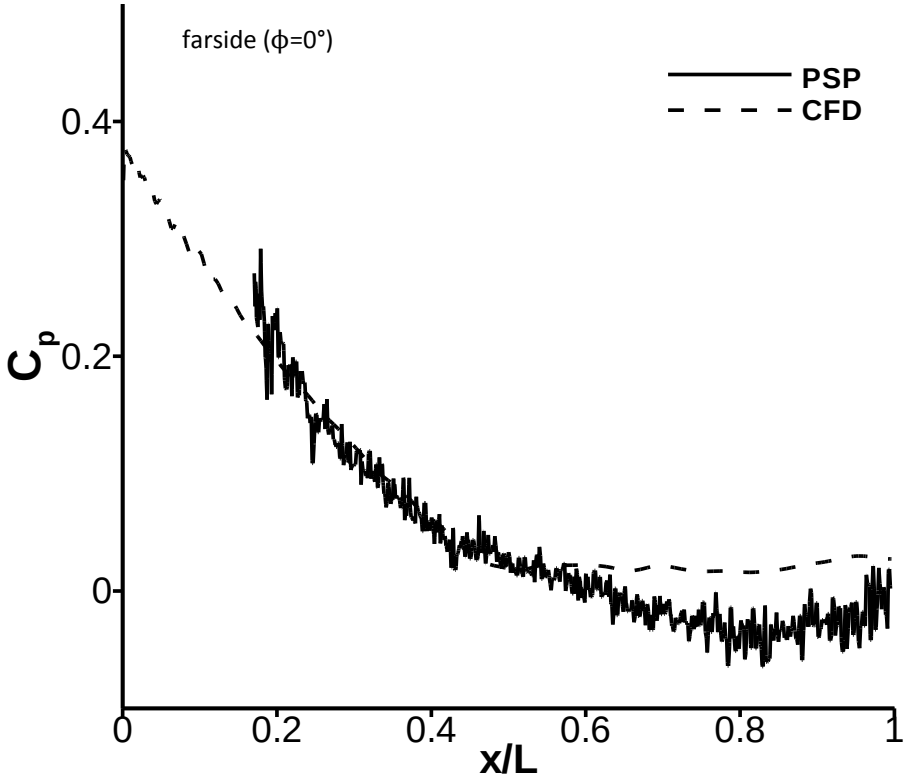
farside (ϕ=0°)
PSP
CFD
0.4
0.2
0
C_p
0
0.2
0.4
0.6
0.8
1
x/L

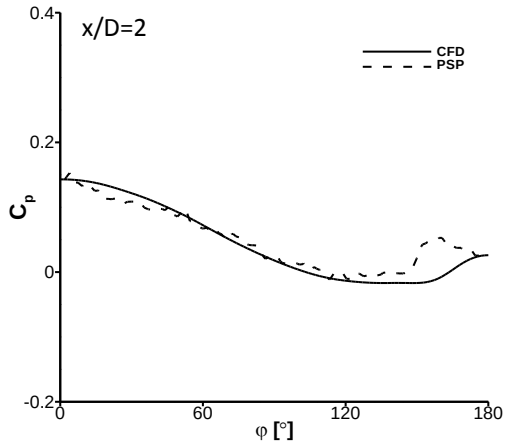
x/D=2
CFD
PSP
C_p
φ [°]

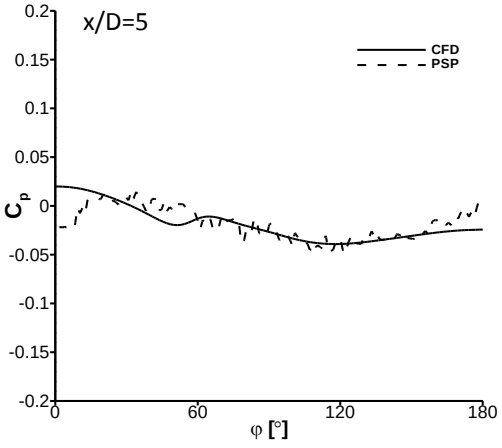
x/D=5
CFD
PSP
C_p
φ [°]

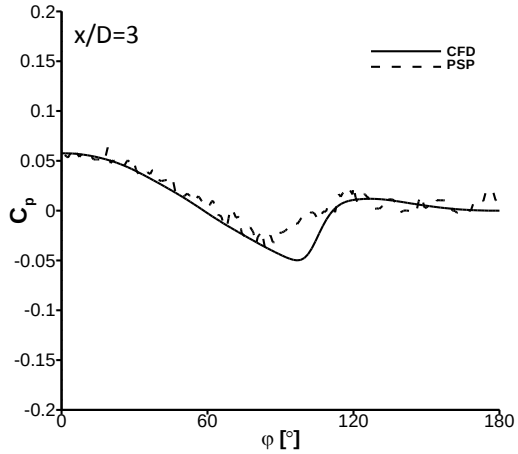
x/D=3
CFD
PSP
C_p
φ [°]

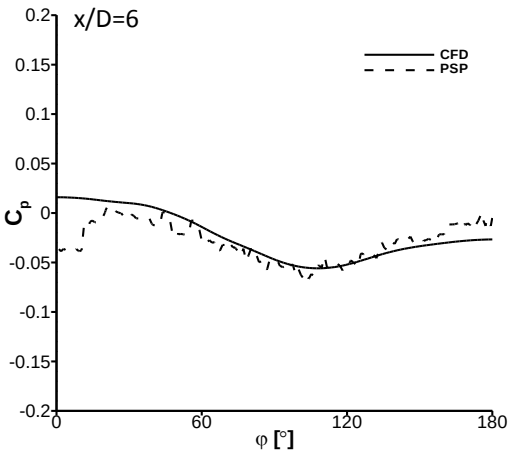
x/D=6
CFD
PSP
C_p
φ [°]

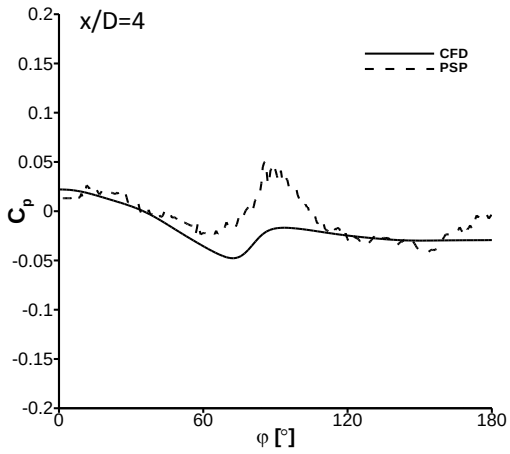
x/D=4
CFD
PSP
C_p
φ [°]

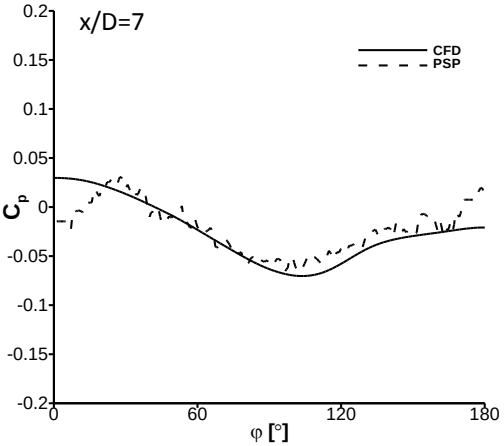
x/D=7
CFD
PSP
C_p
φ [°]

σ_R =15°

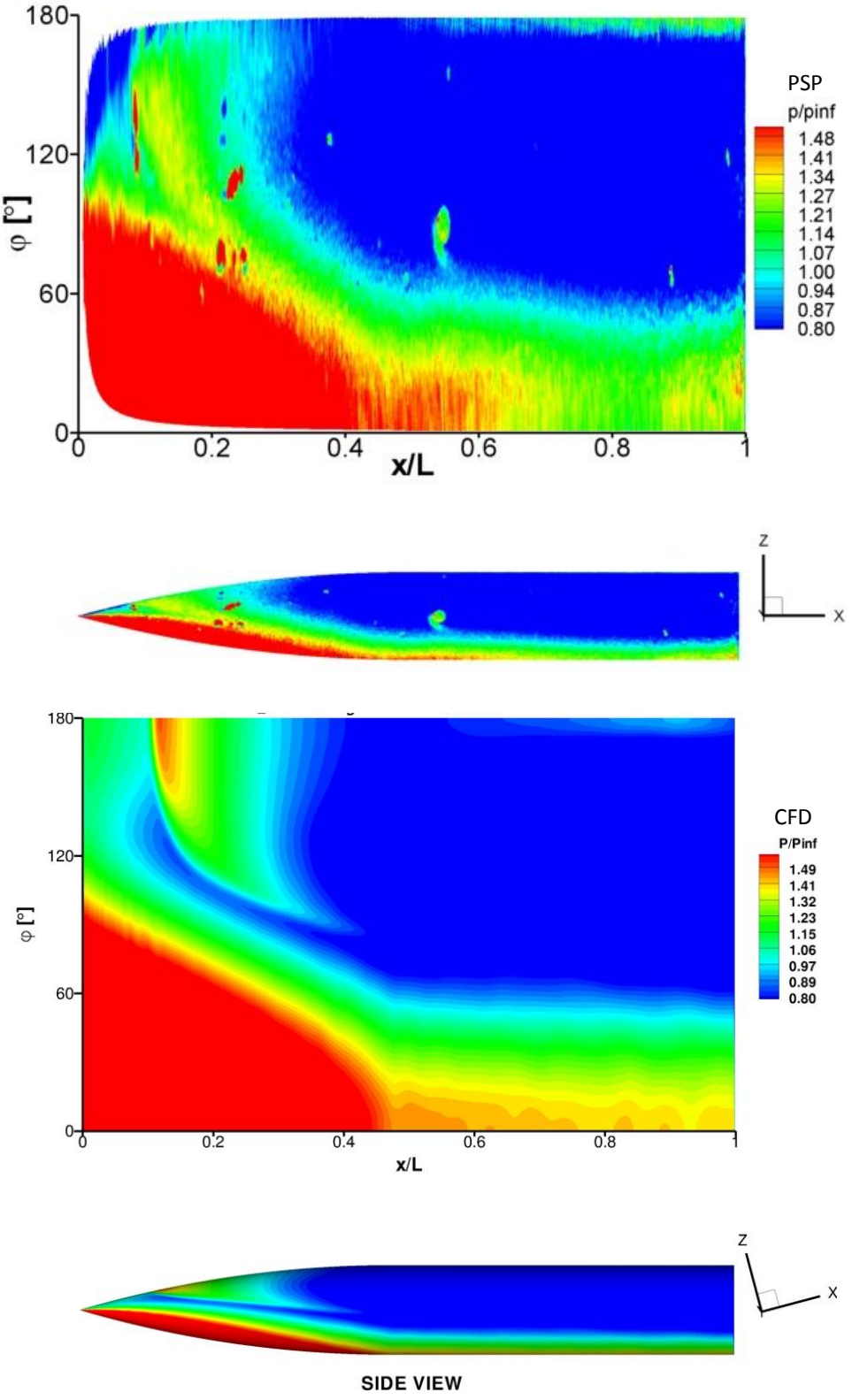

SIDE VIEW

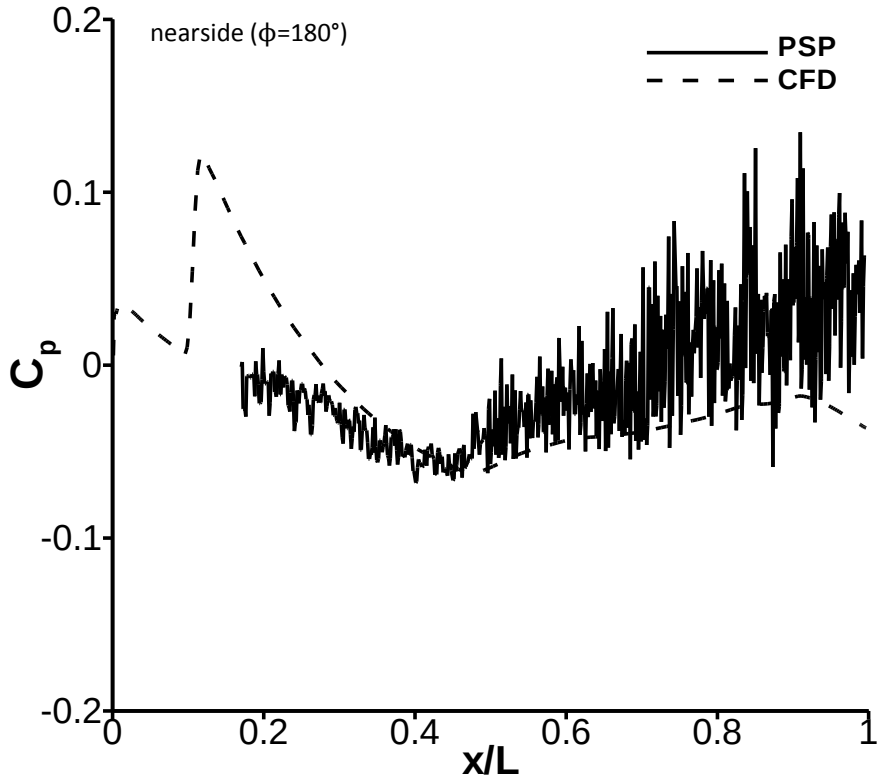
nearside (ϕ=180°)
PSP
CFD
0.2
0.1
0
-0.1
-0.2
C_p
0
0.2
0.4
0.6
0.8
1
x/L

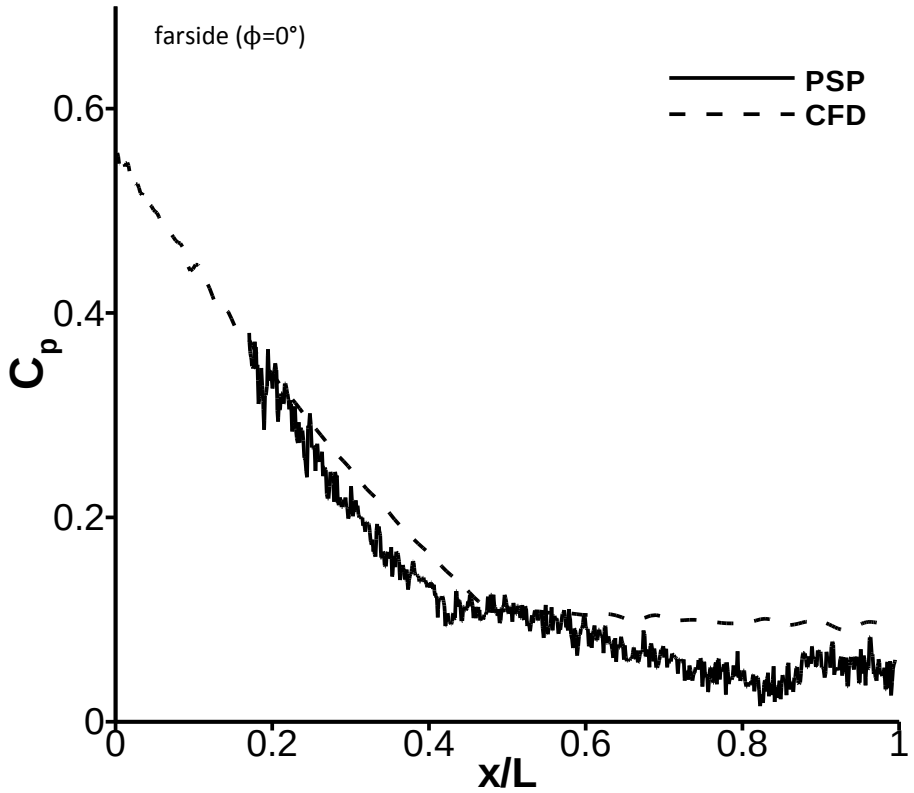
farside (ϕ=0°)
PSP
CFD
0.6
0.4
0.2
0
C_p
0
0.2
0.4
0.6
0.8
1
x/L

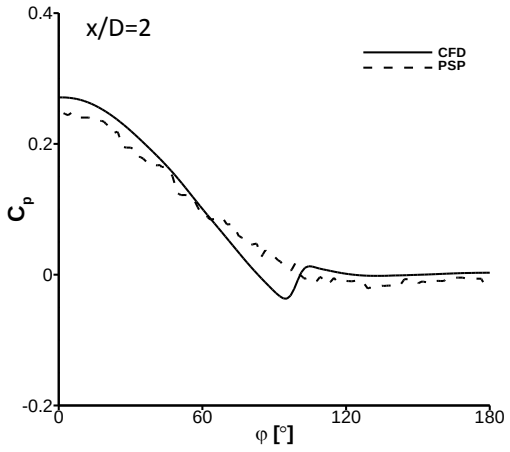
x/D=2
CFD
PSP
C_p
0.4
0.2
0
-0.2
0
60
120
180
φ [°]

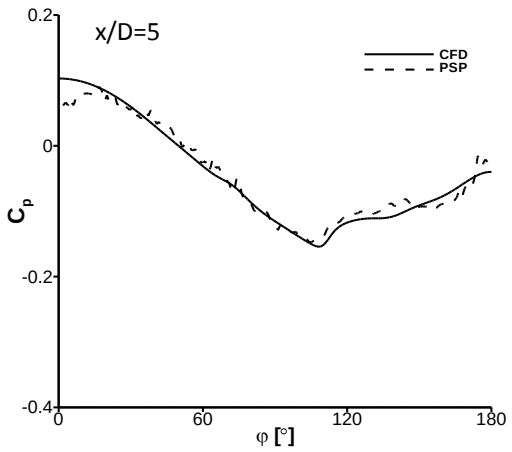
x/D=5
CFD
PSP
C_p
0.2
0
-0.2
-0.4
0
60
120
180
φ [°]

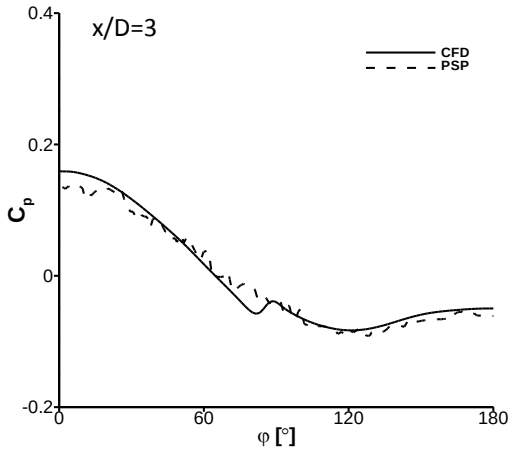
x/D=3
CFD
PSP
C_p
0.4
0.2
0
-0.2
0
60
120
180
φ [°]

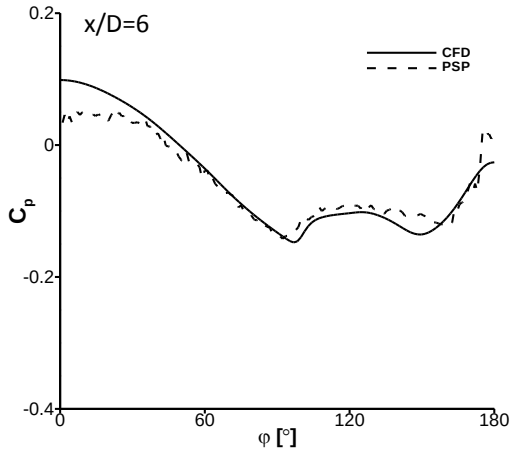
x/D=6
CFD
PSP
C_p
0.2
0
-0.2
-0.4
0
60
120
180
φ [°]

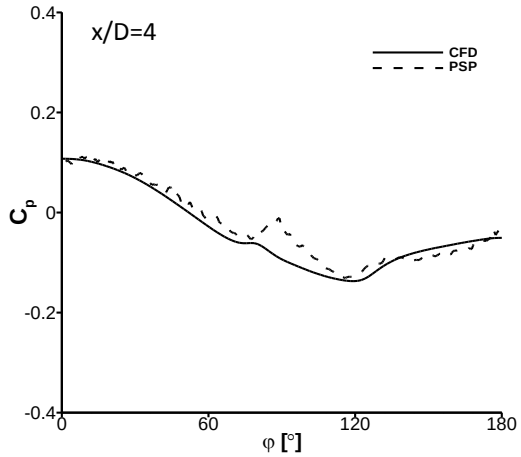
x/D=4
CFD
PSP
C_p
0.4
0.2
0
-0.2
-0.4
0
60
120
180
φ [°]

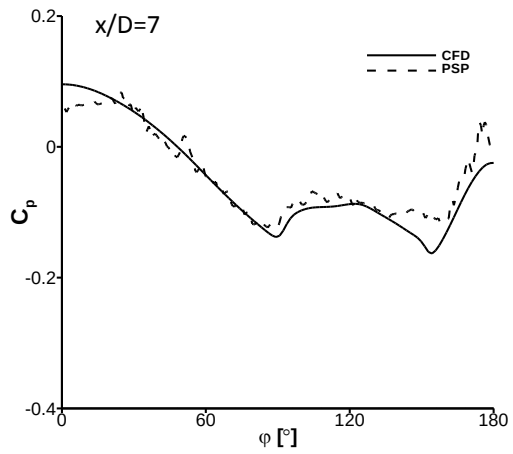
x/D=7
CFD
PSP
C_p
0.2
0
-0.2
-0.4
0
60
120
180
φ [°]

Overall, there is good agreement between the measured (PSP) and predicated (CFD) surface pressures on the un-finned receiver. In qualitative terms, the CFD predicts the location and local flow structures very well for the wide range of incidence angles tested. In quantitative terms, the CFD frequently predicts the magnitude of the interaction footprints sufficiently well. Finally, the above analysis gives confidence that that the CFD predictions of the interference loads for the un-finned receiver are based on the adequate resolution of the correct physical mechanisms.

B.4.2 Un-finned receiver and blunt generator

The following pages compare PSP and CFD results for the un-finned receiver and blunt generator configuration. This includes plots of surface pressure (p/p_∞), axial distributions of C_p at different azimuth locations ϕ=0° (farside) and ϕ=180° (nearside) and crossflow distributions of C_p at different axial locations on the receiver body over an incidence range $-15 \le \sigma_R \le 15°$.

At the extremes of surface curvature near the receiver leading edge ($x/L \le 0.15$) the local surface normal was almost perpendicular to the camera line-of-sight and the data in this small region were considered to be un-reliable and excluded from the pressure plots. Due to wind tunnel debris a small amount of degradation of the PSP coating occurred during each test. In addition, the model attachment screw hole caused a local flowfield disturbance at $x/L \approx 0.55$ and ϕ=90°.

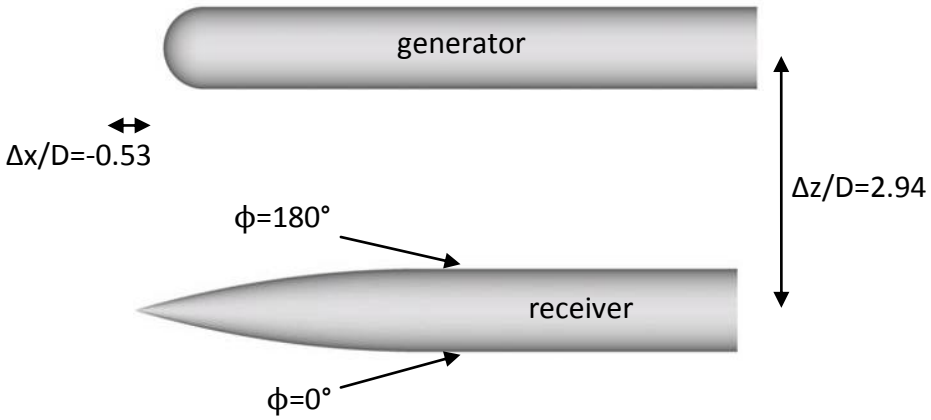

σ_R=0°

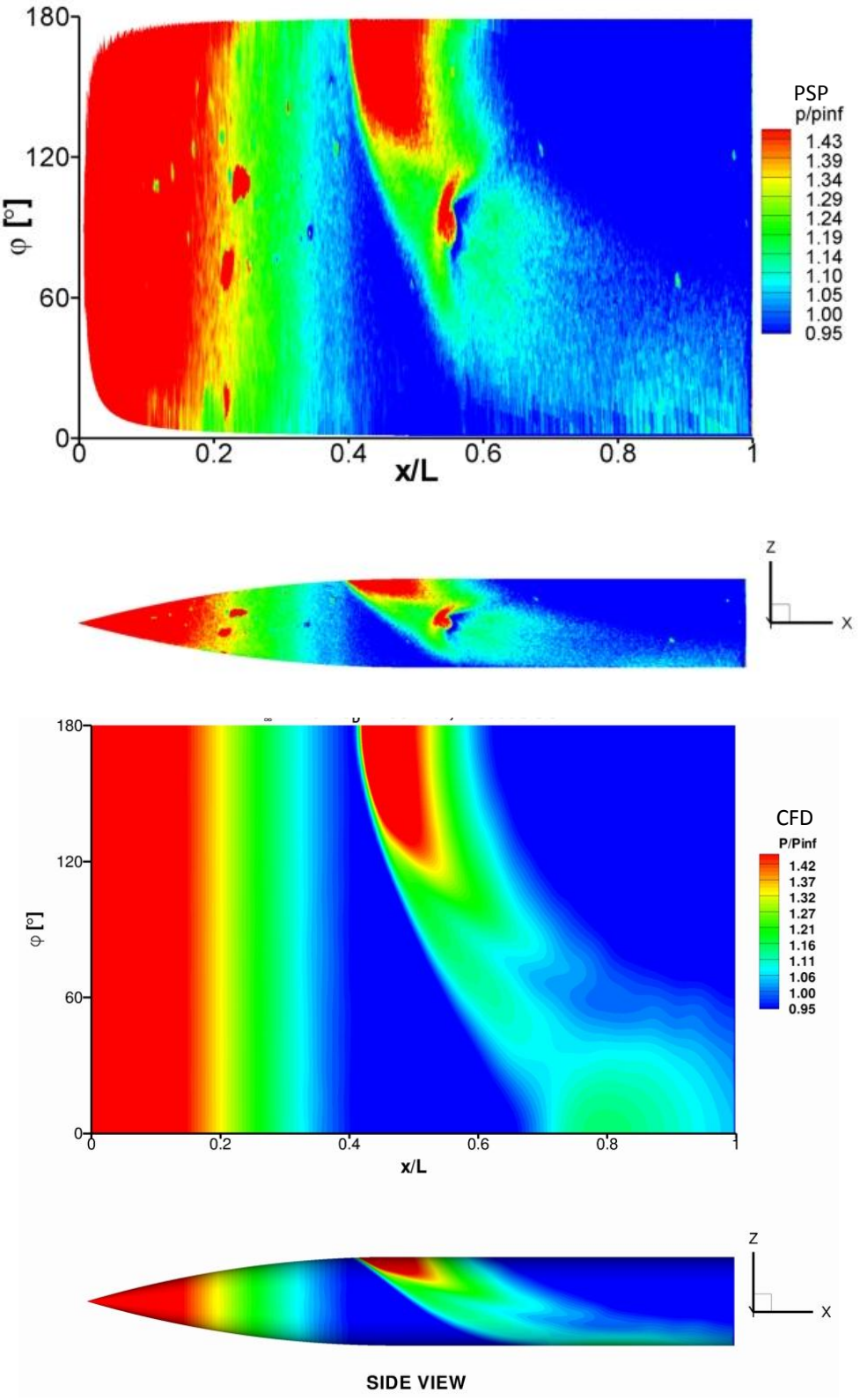
180
120
60
0
φ [°]
0
0.2
0.4
0.6
0.8
1
x/L
PSP
p/pinf
1.43
1.39
1.34
1.29
1.24
1.19
1.14
1.10
1.05
1.00
0.95
Z
X
180
120
60
0
φ [°]
0
0.2
0.4
0.6
0.8
1
x/L
CFD
P/Pinf
1.42
1.37
1.32
1.27
1.21
1.16
1.11
1.06
1.00
0.95
Z
X
SIDE VIEW

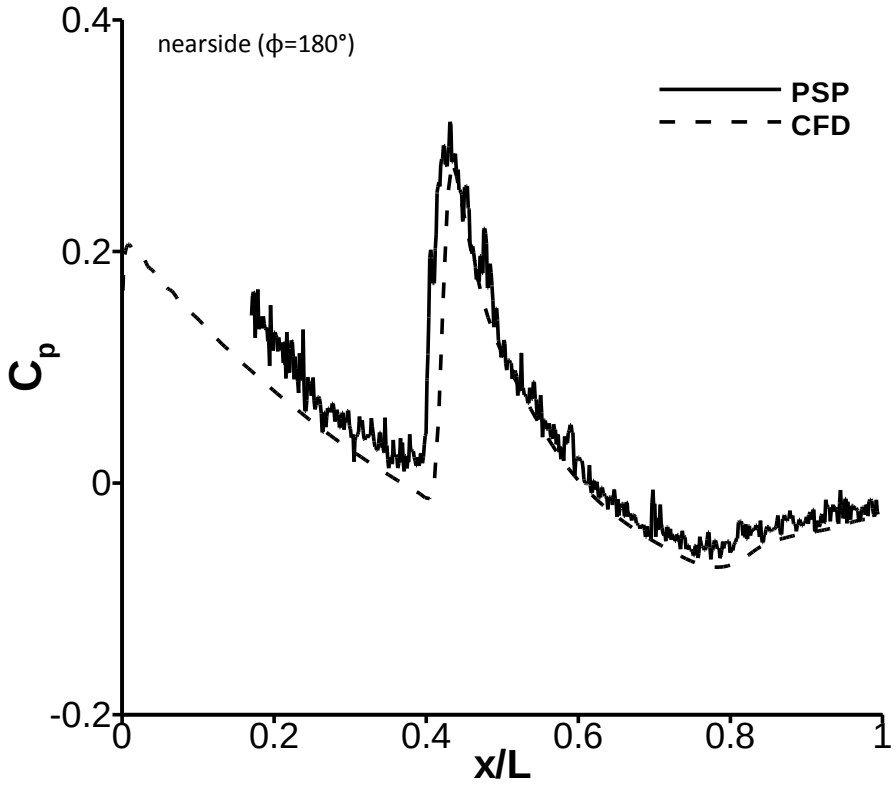
nearside (ϕ=180°)
PSP
CFD
0.4
0.2
0
-0.2
C_p
0
0.2
0.4
0.6
0.8
1
x/L

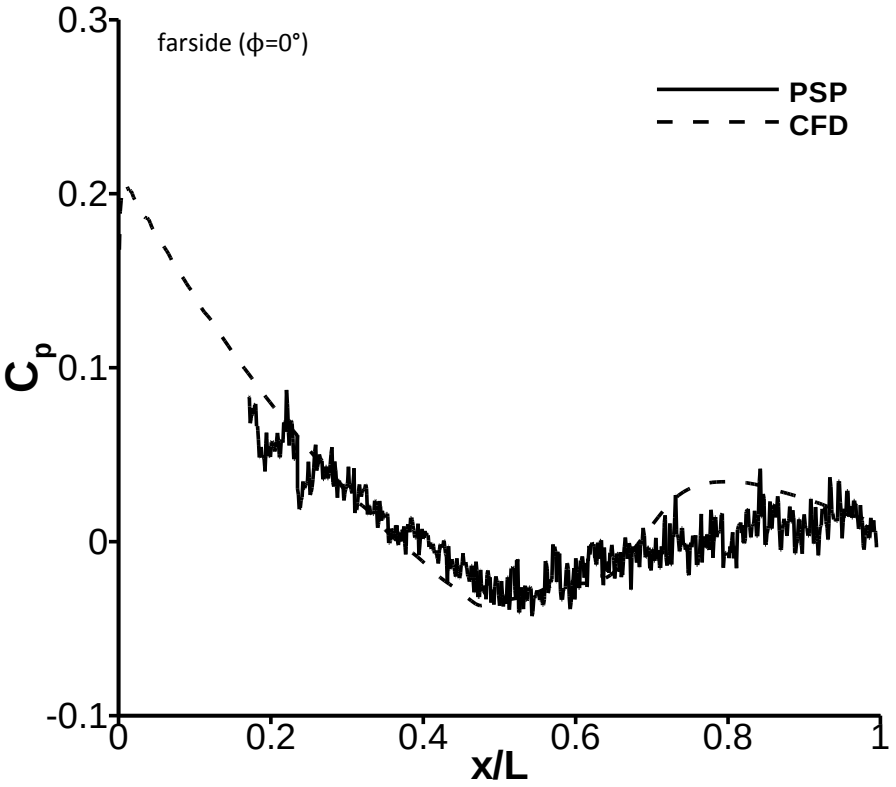
farside (ϕ=0°)
PSP
CFD
0.3
0.2
0.1
0
-0.1
C_p
0
0.2
0.4
0.6
0.8
1
x/L

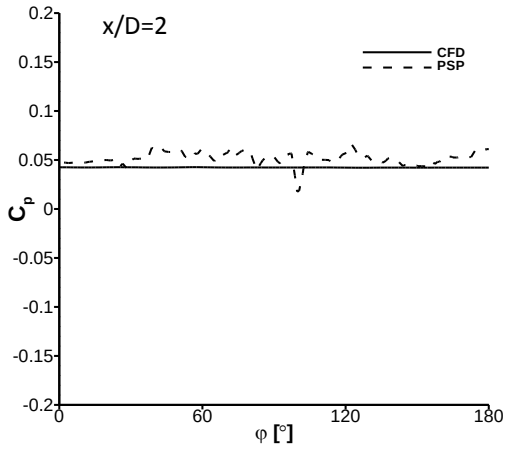
x/D=2
CFD
PSP
C_p
φ [°]

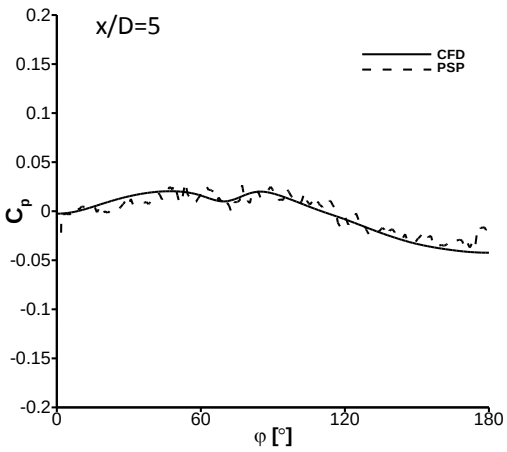
x/D=5
CFD
PSP
C_p
φ [°]

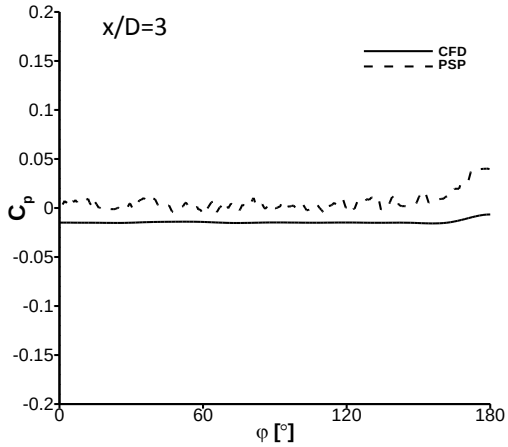
x/D=3
CFD
PSP
C_p
φ [°]

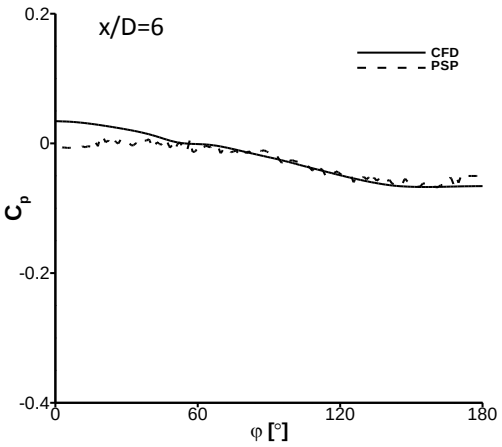
x/D=6
CFD
PSP
C_p
φ [°]

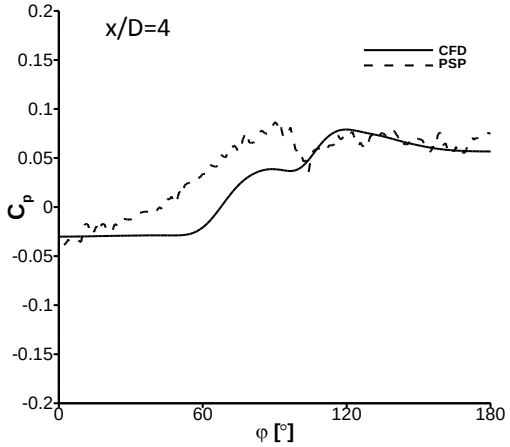
x/D=4
CFD
PSP
C_p
φ [°]

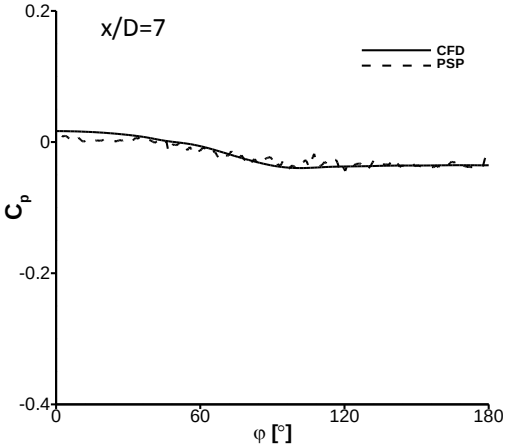
x/D=7
CFD
PSP
C_p
φ [°]

σ_R =-8°

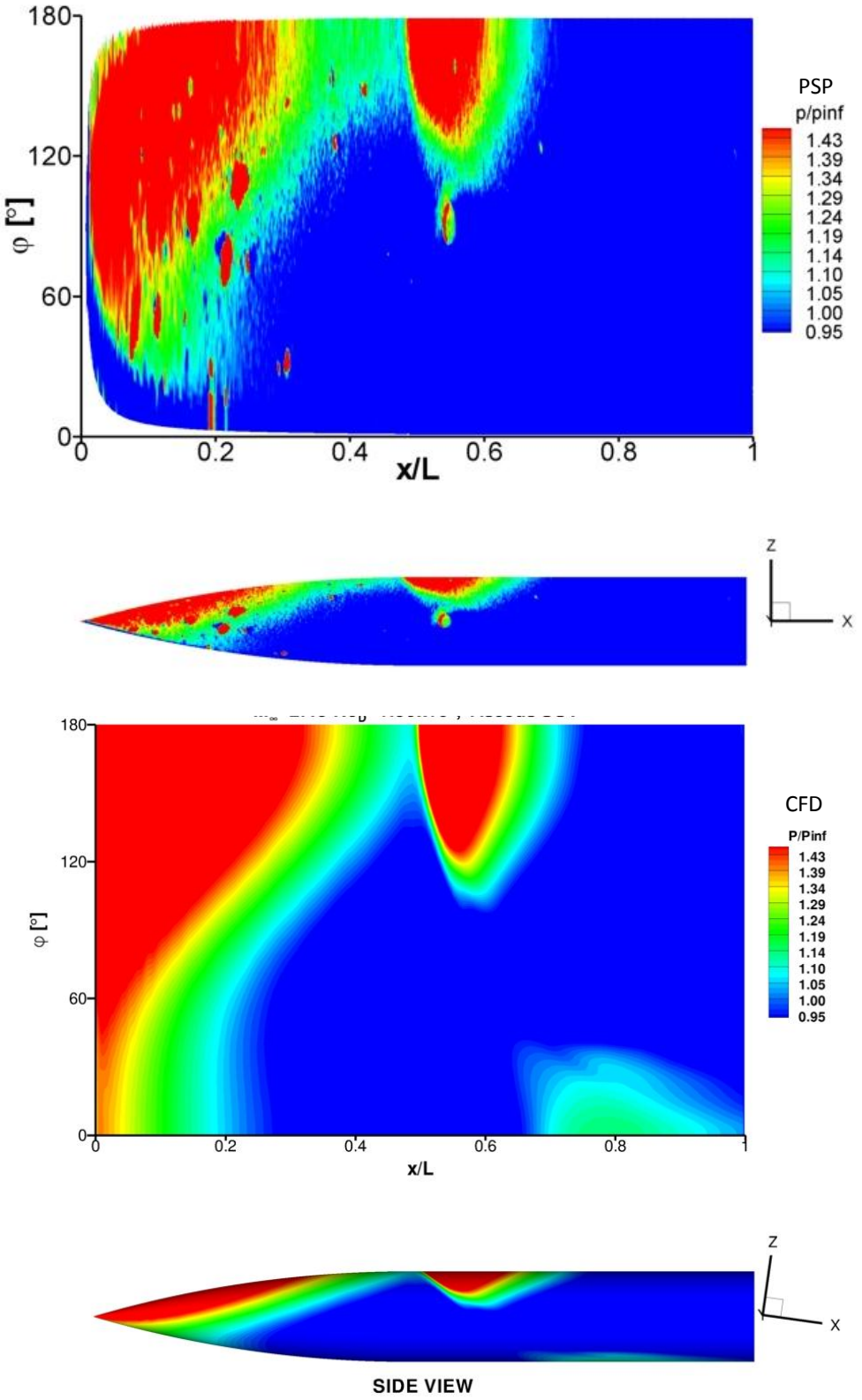
180
120
60
0
φ [°]
0
0.2
0.4
0.6
0.8
1
x/L
PSP
p/pinf
1.43
1.39
1.34
1.29
1.24
1.19
1.14
1.10
1.05
1.00
0.95
Z
X
180
120
60
0
φ [°]
0
0.2
0.4
0.6
0.8
1
x/L
CFD
P/Pinf
1.43
1.39
1.34
1.29
1.24
1.19
1.14
1.10
1.05
1.00
0.95
Z
X
SIDE VIEW

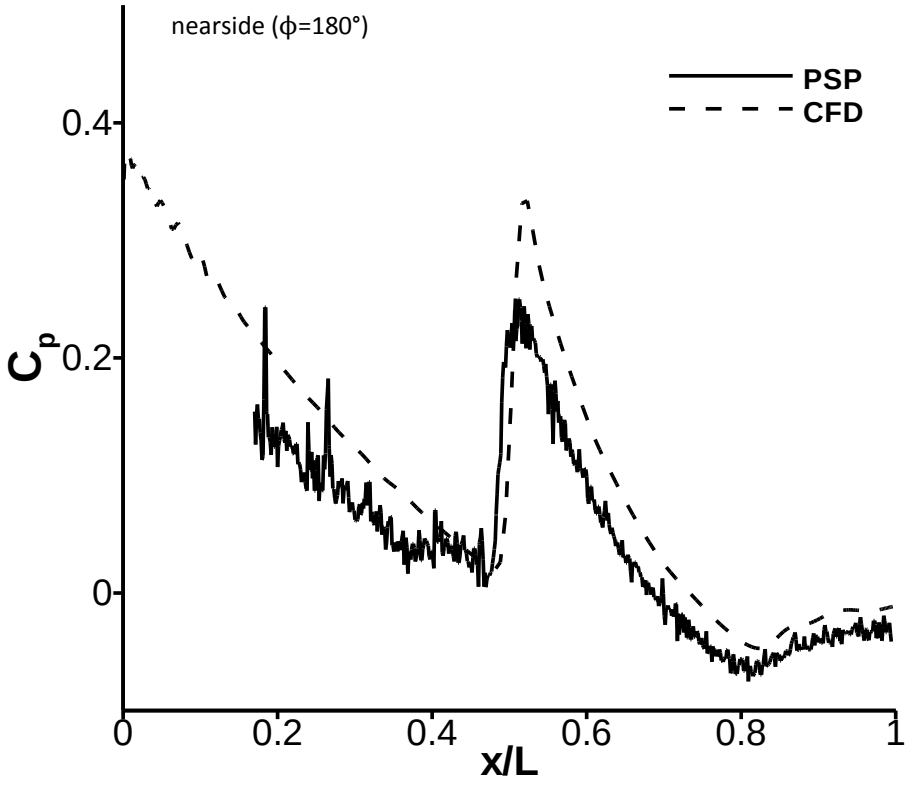
nearside (ϕ=180°)
PSP
CFD
0.4
0.2
0
C_p
0
0.2
0.4
0.6
0.8
1
x/L

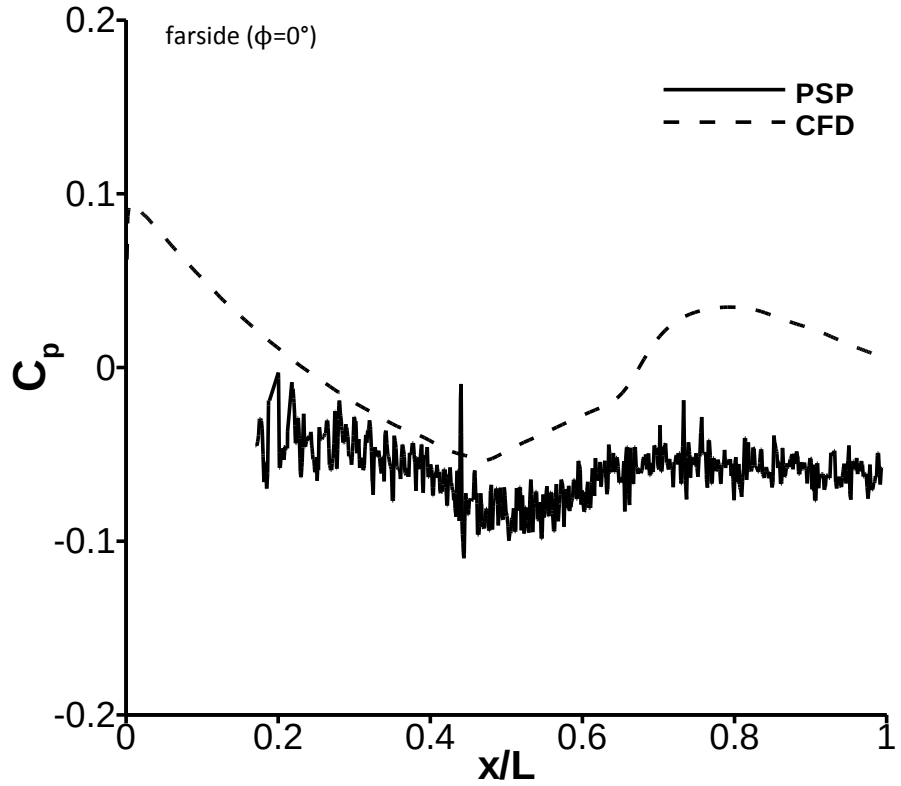
farside (ϕ=0°)
PSP
CFD
0.2
0.1
0
-0.1
-0.2
C_p
0
0.2
0.4
0.6
0.8
1
x/L

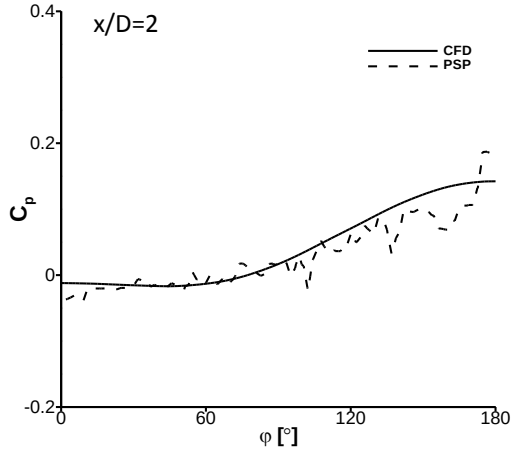
x/D=2
CFD
PSP
C_p
0.4
0.2
0
-0.2
0
60
120
180
φ [°]

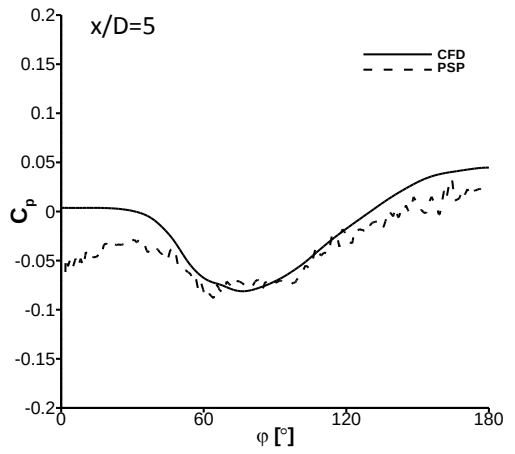
x/D=5
CFD
PSP
C_p
0.2
0.15
0.1
0.05
0
-0.05
-0.1
-0.15
-0.2
0
60
120
180
φ [°]

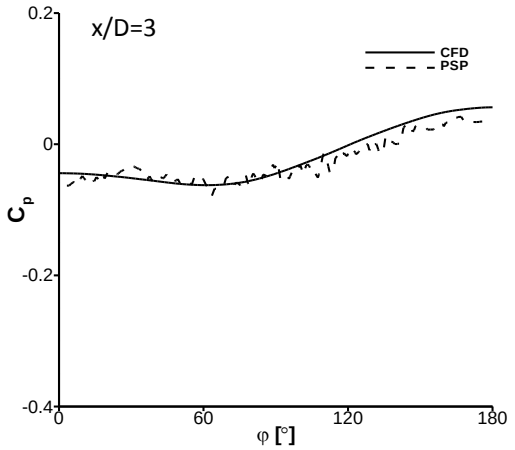
x/D=3
CFD
PSP
C_p
0.2
0
-0.2
-0.4
0
60
120
180
φ [°]

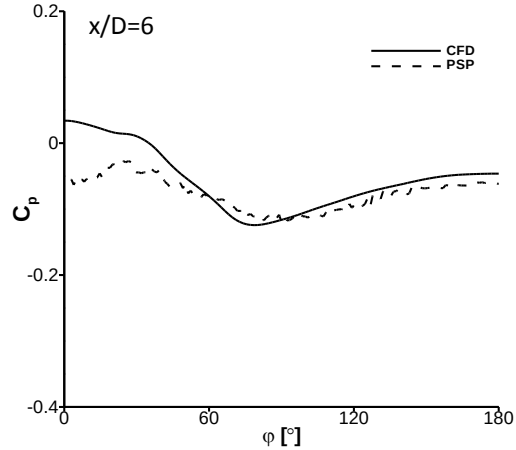
x/D=6
CFD
PSP
C_p
0.2
0
-0.2
-0.4
0
60
120
180
φ [°]

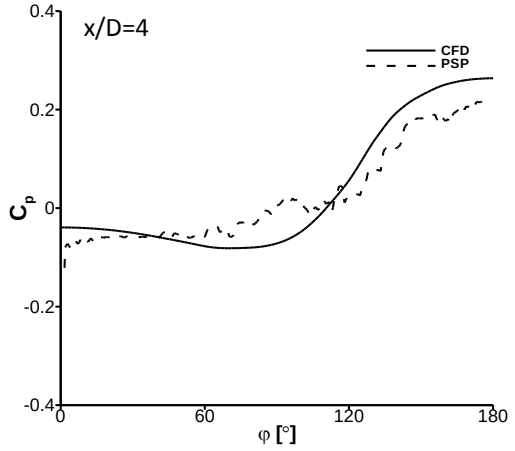
x/D=4
CFD
PSP
C_p
0.4
0.2
0
-0.2
-0.4
0
60
120
180
φ [°]

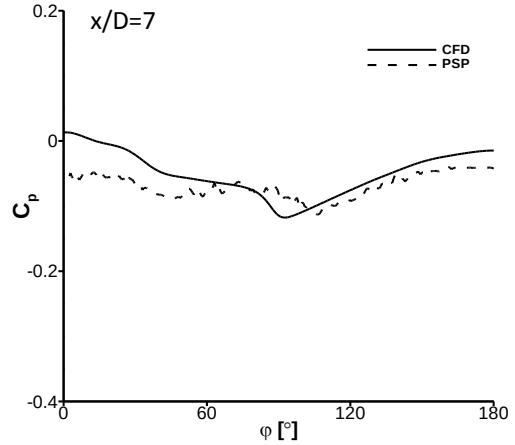
x/D=7
CFD
PSP
C_p
0.2
0
-0.2
-0.4
0
60
120
180
φ [°]

σ_R =-15°

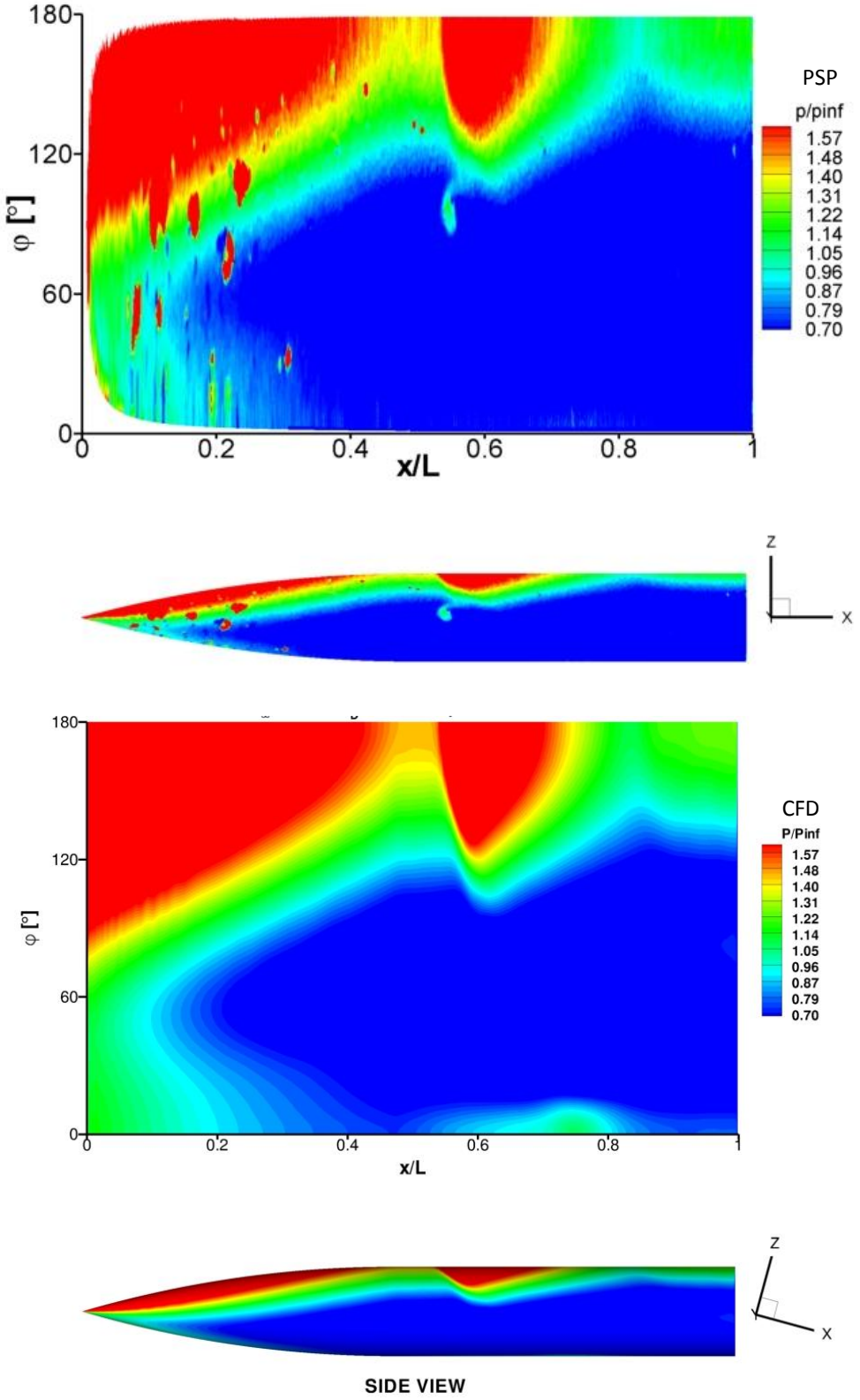

SIDE VIEW

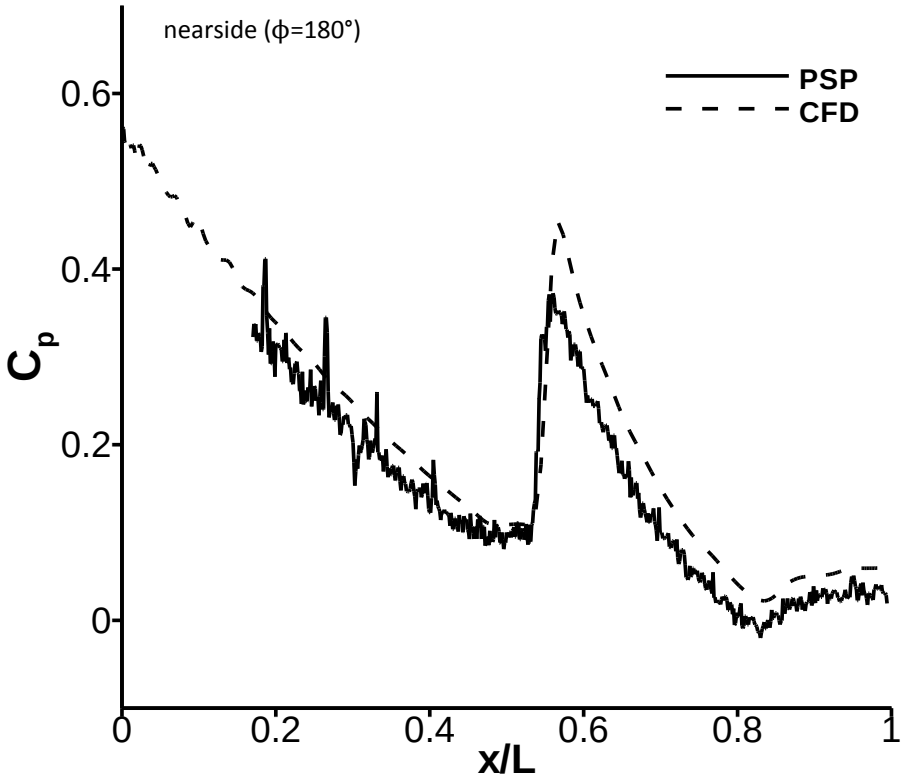
nearside (ϕ=180°)
PSP
CFD
0.6
0.4
0.2
0
C_p
0
0.2
0.4
0.6
0.8
1
x/L

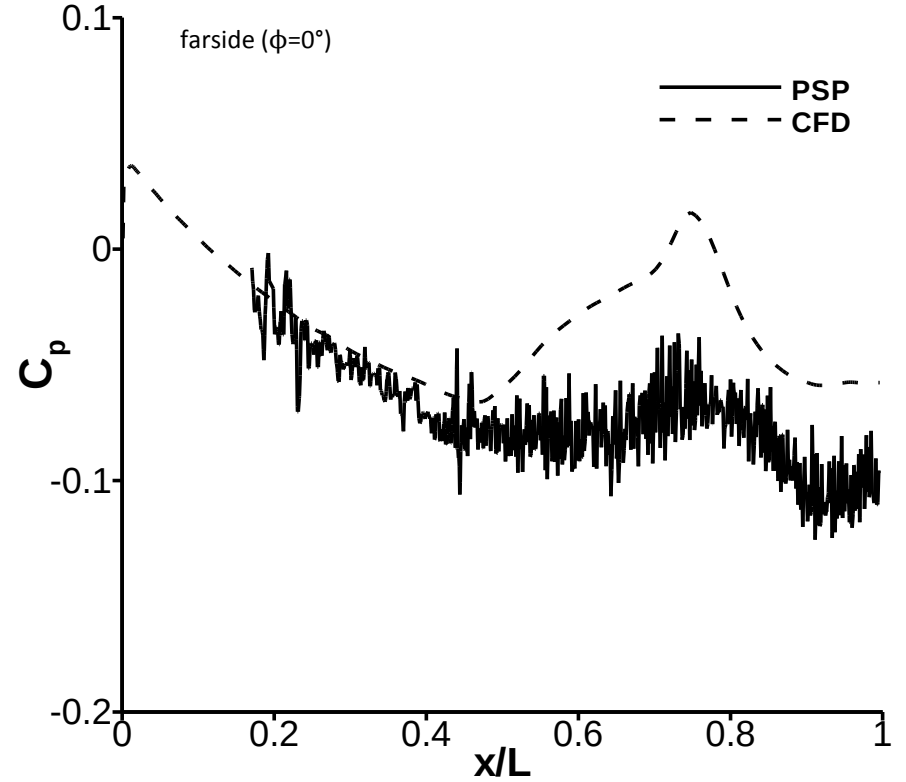
farside (ϕ=0°)
PSP
CFD
0.1
0
-0.1
-0.2
C_p
0
0.2
0.4
0.6
0.8
1
x/L

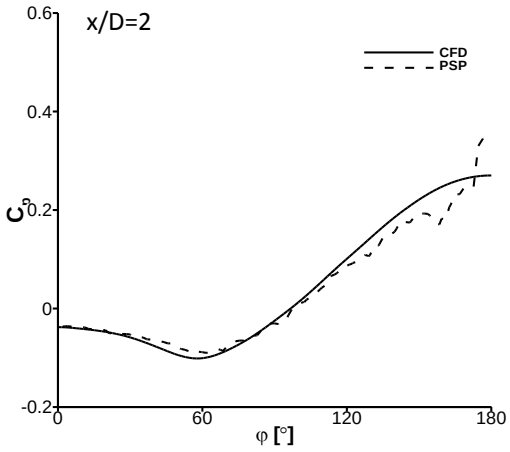
x/D=2
CFD
PSP
C_p
φ [°]

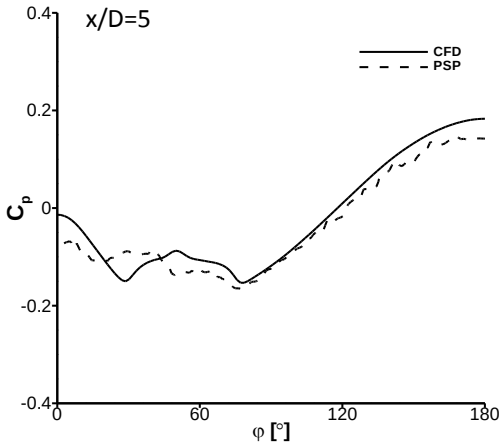
x/D=5
CFD
PSP
C_p
φ [°]

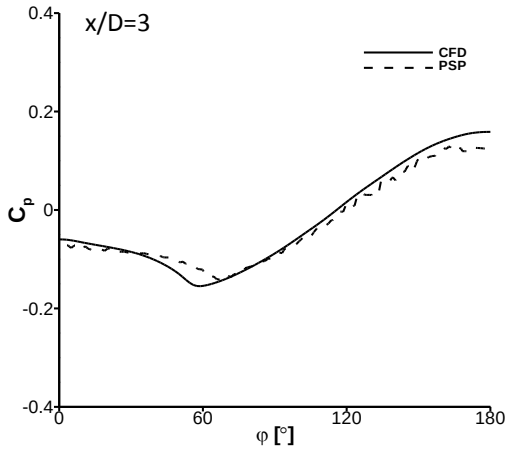
x/D=3
CFD
PSP
C_p
φ [°]

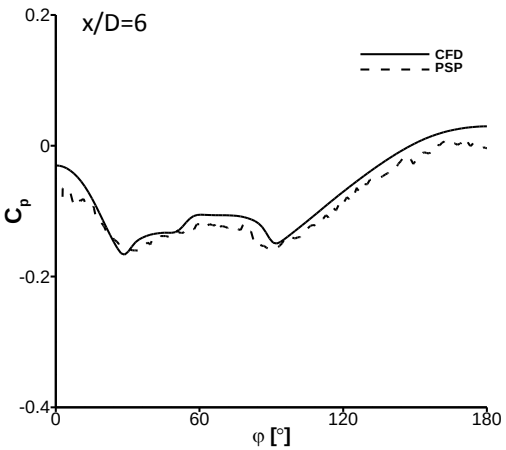
x/D=6
CFD
PSP
C_p
φ [°]

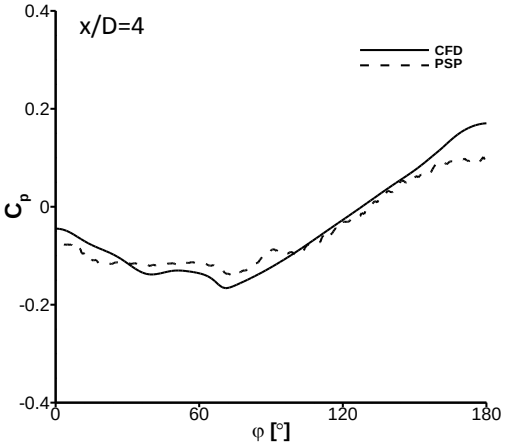
x/D=4
CFD
PSP
C_p
φ [°]

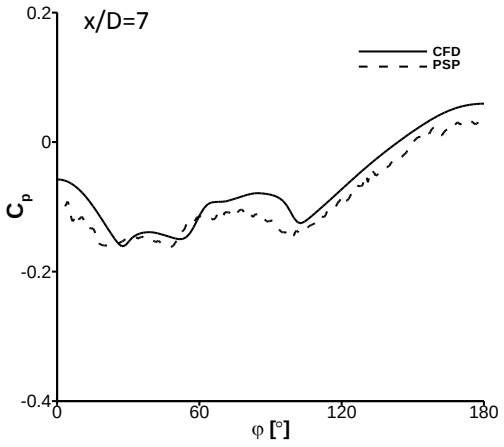
x/D=7
CFD
PSP
C_p
φ [°]

σ_R =8°

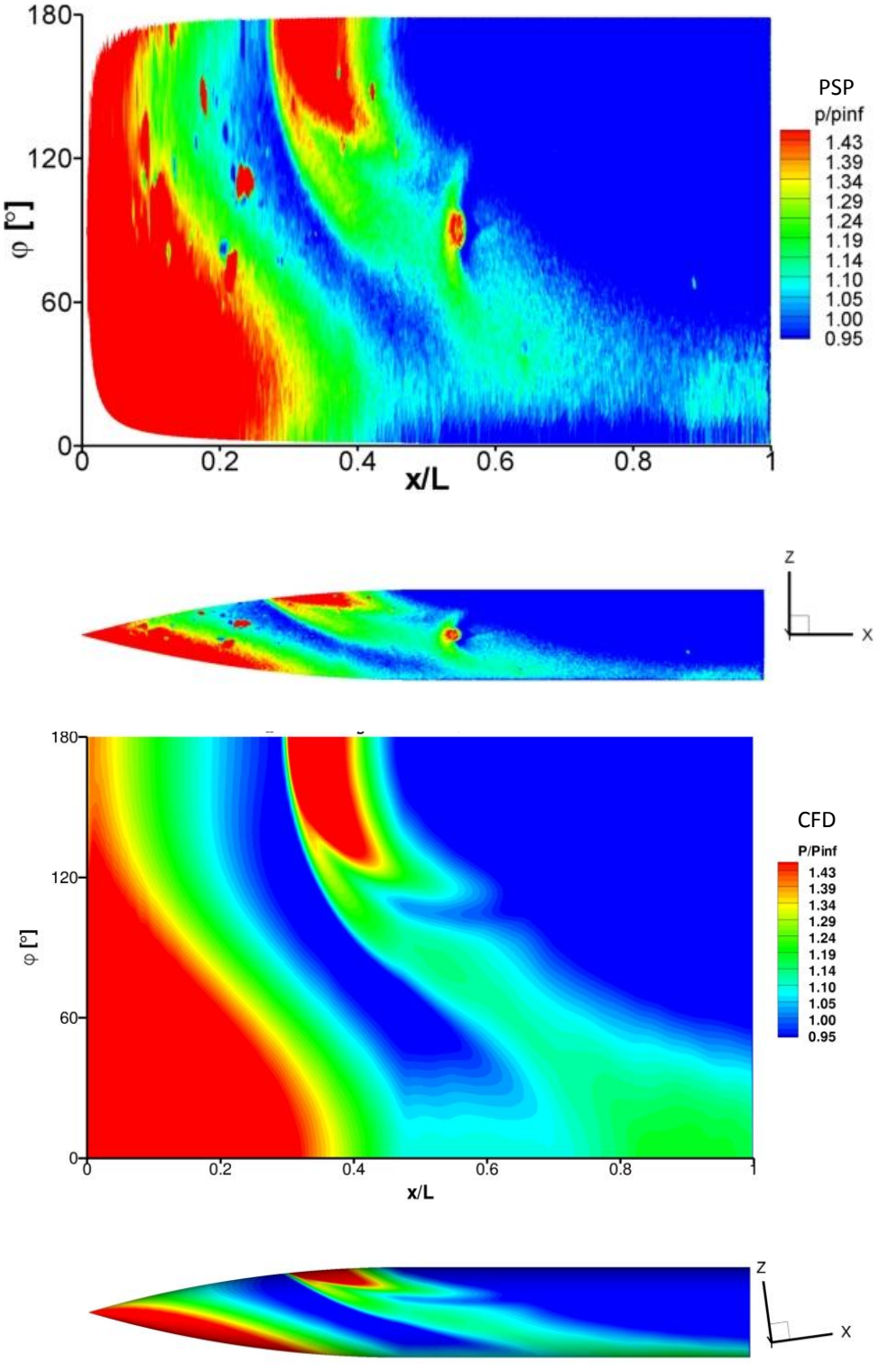

SIDE VIEW

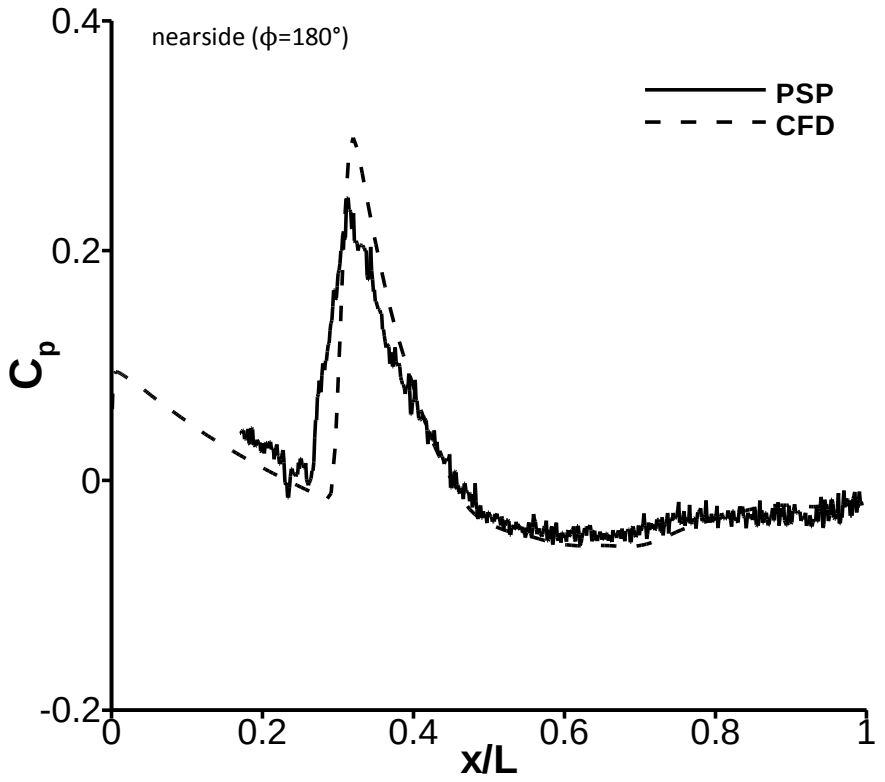
nearside (ϕ=180°)
PSP
CFD
0.4
0.2
0
-0.2
C_p
0
0.2
0.4
0.6
0.8
1
x/L

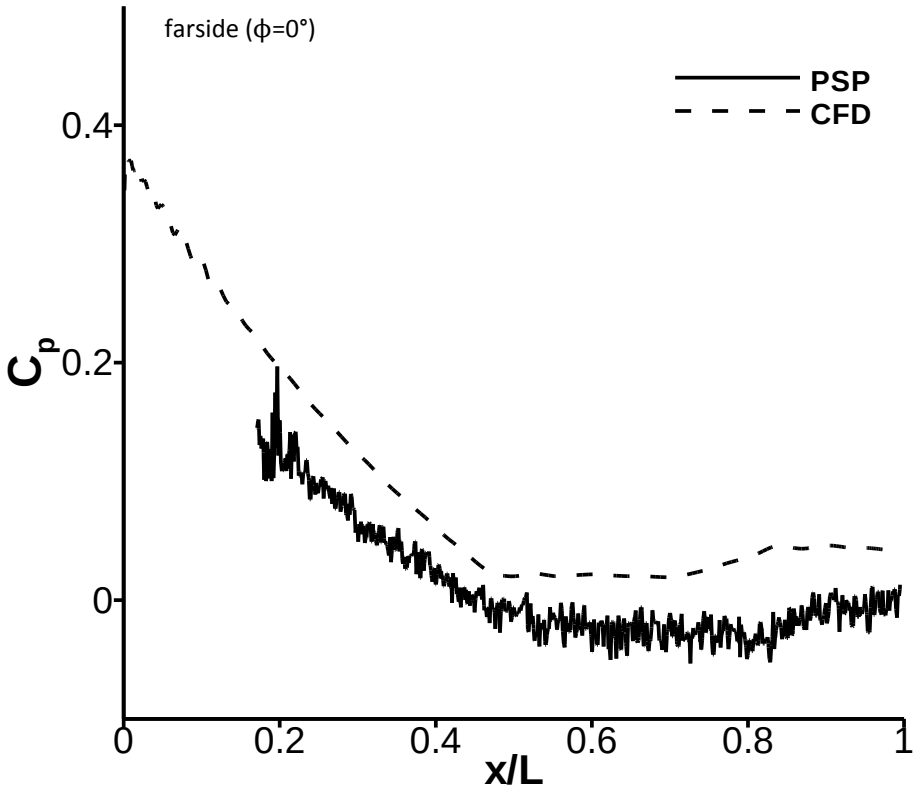
farside (ϕ=0°)
PSP
CFD
0.4
0.2
0
C_p
0
0.2
0.4
0.6
0.8
1
x/L

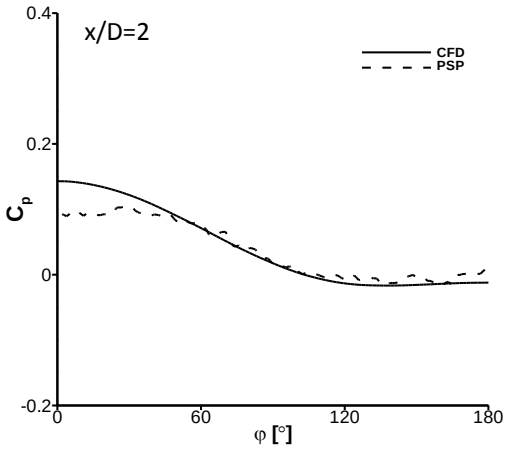
x/D=2
CFD
PSP
C_p
φ [°]

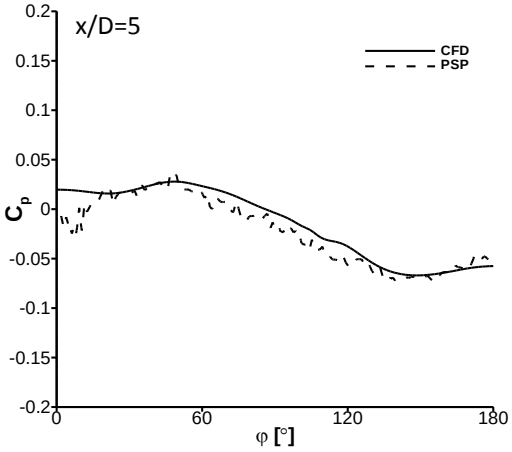
x/D=5
CFD
PSP
C_p
φ [°]

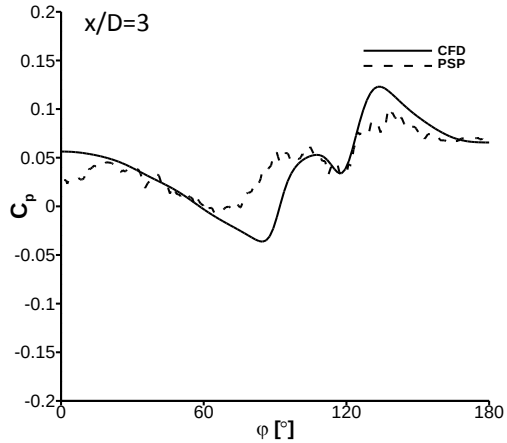
x/D=3
CFD
PSP
C_p
φ [°]

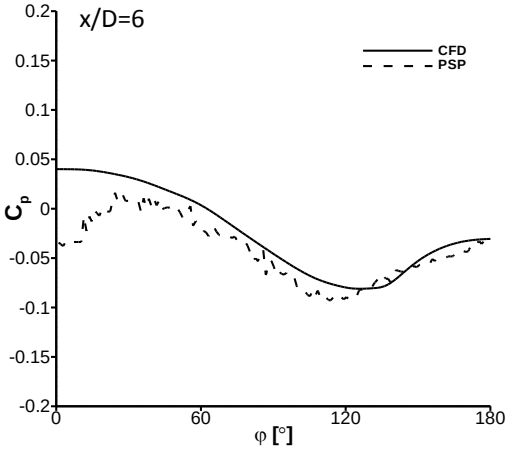
x/D=6
CFD
PSP
C_p
φ [°]

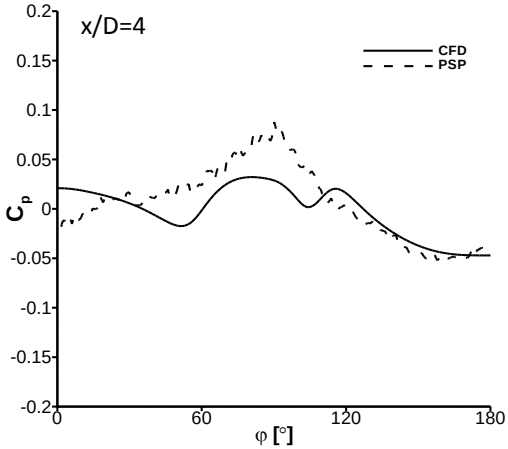
x/D=4
CFD
PSP
C_p
φ [°]

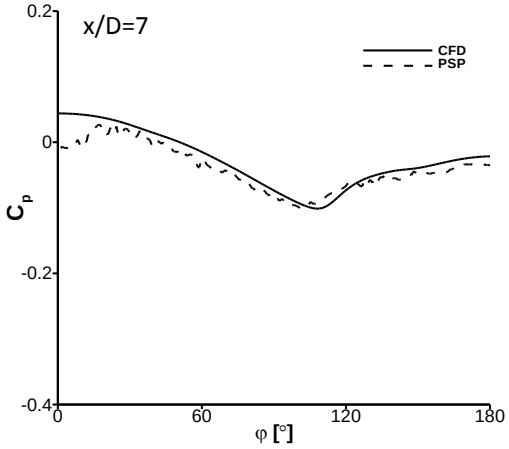
x/D=7
CFD
PSP
C_p
φ [°]

σ_R =15°

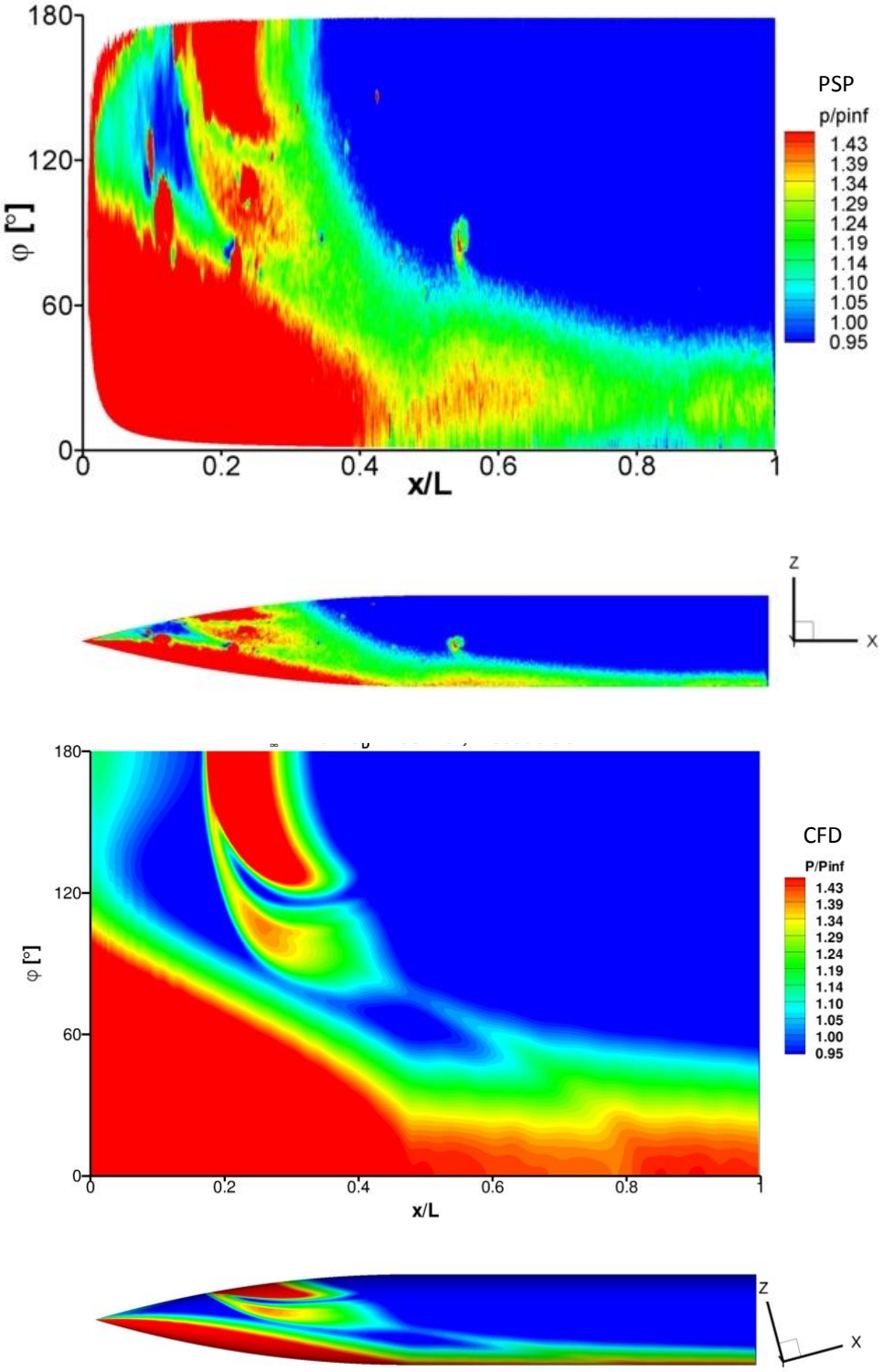

SIDE VIEW

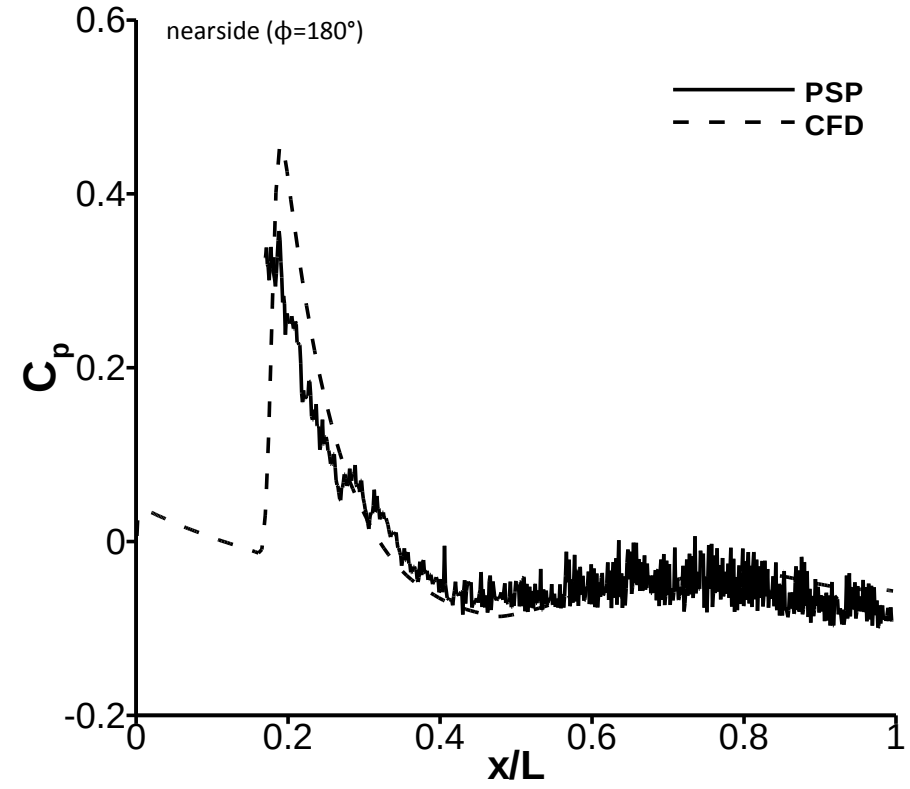
nearside (ϕ=180°)
PSP
CFD
0.6
0.4
0.2
0
-0.2
C_p
0
0.2
0.4
0.6
0.8
1
x/L

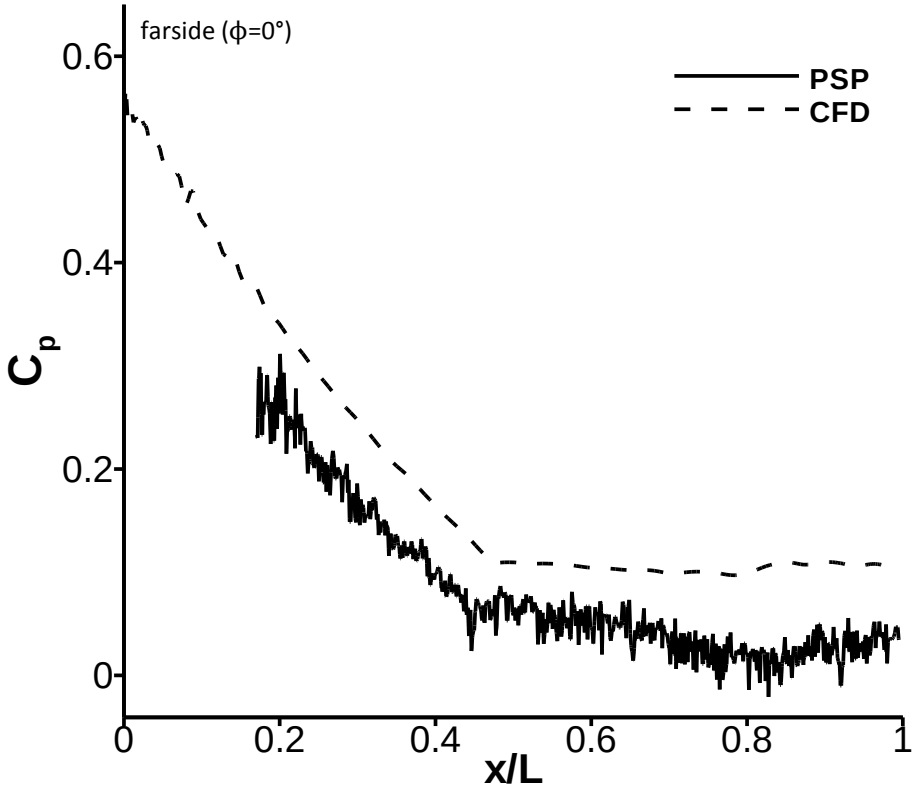
farside (ϕ=0°)
PSP
CFD
0.6
0.4
0.2
0
C_p
0
0.2
0.4
0.6
0.8
1
x/L

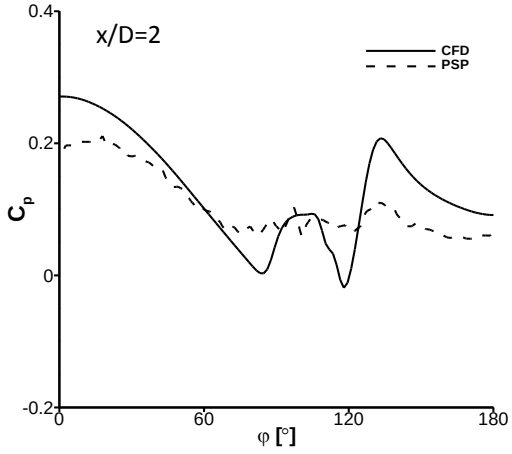
x/D=2
CFD
PSP
C_p
0.4
0.2
0
-0.2
0
60
120
180
φ [°]

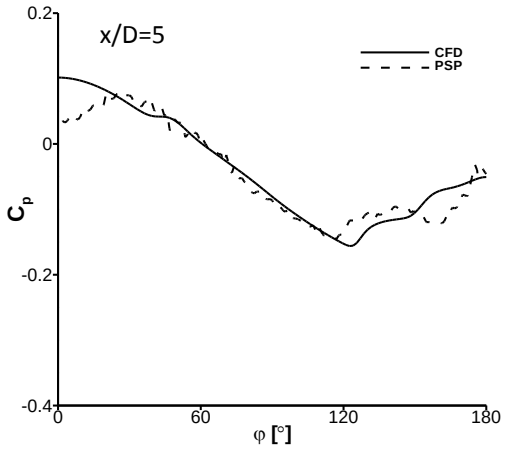
x/D=5
CFD
PSP
C_p
0.2
0
-0.2
-0.4
0
60
120
180
φ [°]

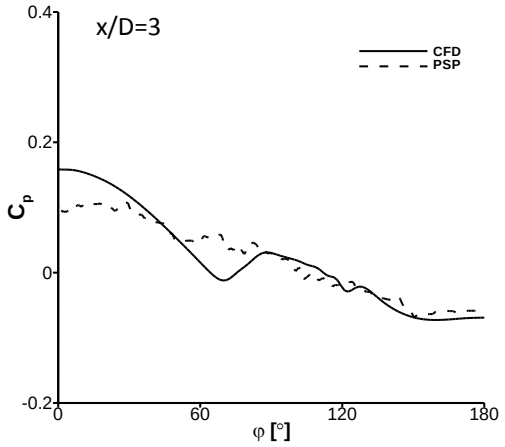
x/D=3
CFD
PSP
C_p
0.4
0.2
0
-0.2
0
60
120
180
φ [°]

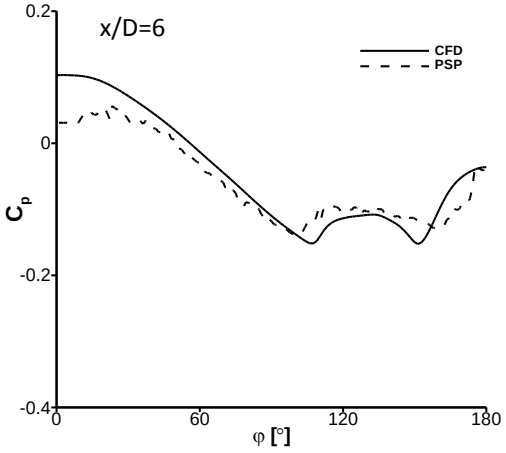
x/D=6
CFD
PSP
C_p
0.2
0
-0.2
-0.4
0
60
120
180
φ [°]

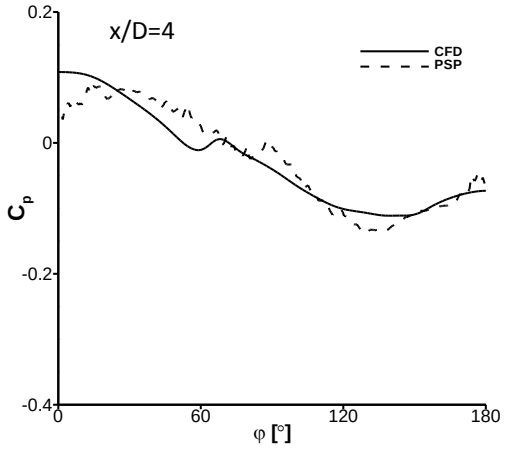
x/D=4
CFD
PSP
C_p
0.2
0
-0.2
-0.4
0
60
120
180
φ [°]

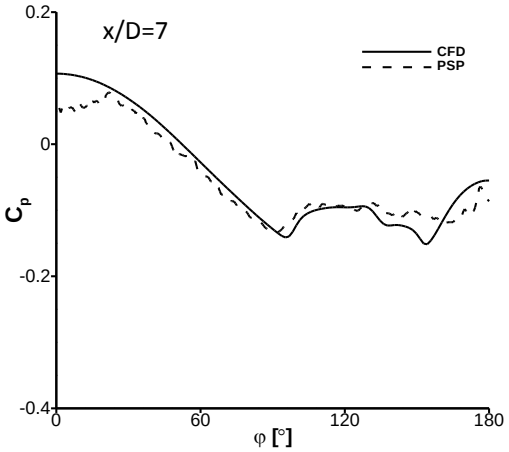
x/D=7
CFD
PSP
C_p
0.2
0
-0.2
-0.4
0
60
120
180
φ [°]

Overall, there is good agreement between the measured (PSP) and predicated (CFD) surface pressures on the un-finned receiver. In qualitative terms, the CFD predicts the location and local flow structures very well for the wide range of incidence angles tested. In quantitative terms, the CFD frequently predicts the magnitude of the interaction footprints sufficiently well. Finally, the above analysis gives confidence that that the CFD predictions of the interference loads for the un-finned receiver are based on the adequate resolution of the correct physical mechanisms.

B.5 Effect of axial impingement for the finned receiver and blunt generator

The effect of axial impingement location is evaluated for the un-finned receiver and blunt generator. Figure B.9 - Figure B.10 show a variation in axial stagger between the bodies ($\Delta x/D$) for a fixed receiver incidence (σ_R).

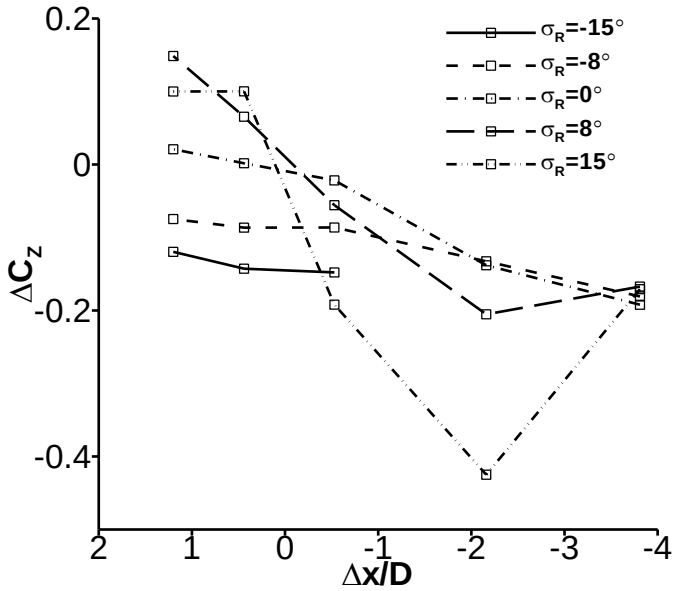

Figure B.9 Effect of axial stagger on measured normal force interference load: m2651 m2654, $\Delta z/D=2.94$, $\sigma_G=0°$

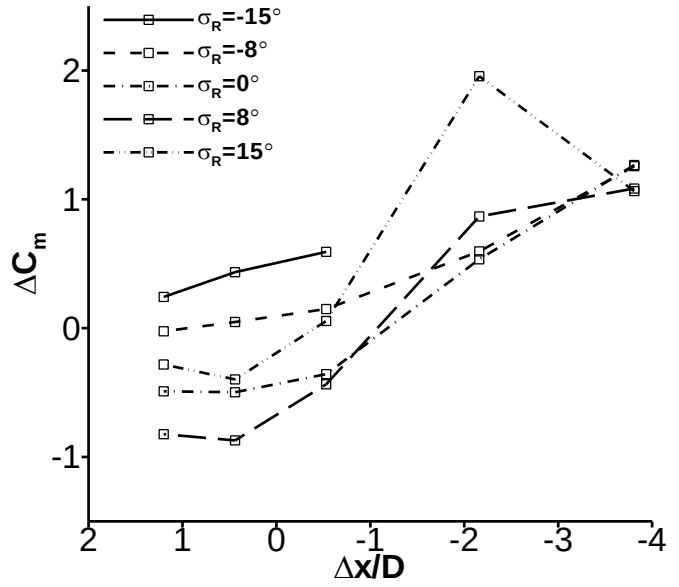

Figure B.10 Effect of axial stagger on measured pitching moment interference load: m2651 m2654, $\Delta z/D=2.94$, $\sigma_G=0°$

The above results show that the effect of axial impingement location is similar for all the incidence angles tested except σ_R=15°. The trends observed are similar to when the sharp generator is used, but the magnitude of the interference effects are amplified.

B.6 Force and moment results for the un-finned receiver and sharp generator

The interference loads are plotted as a function of receiver incidence for the un-finned receiver and sharp generator at a fixed lateral separation for different axial staggers (Figure B.11 - Figure B.14). Measured (EXP) and predicted (CFD) data are shown.

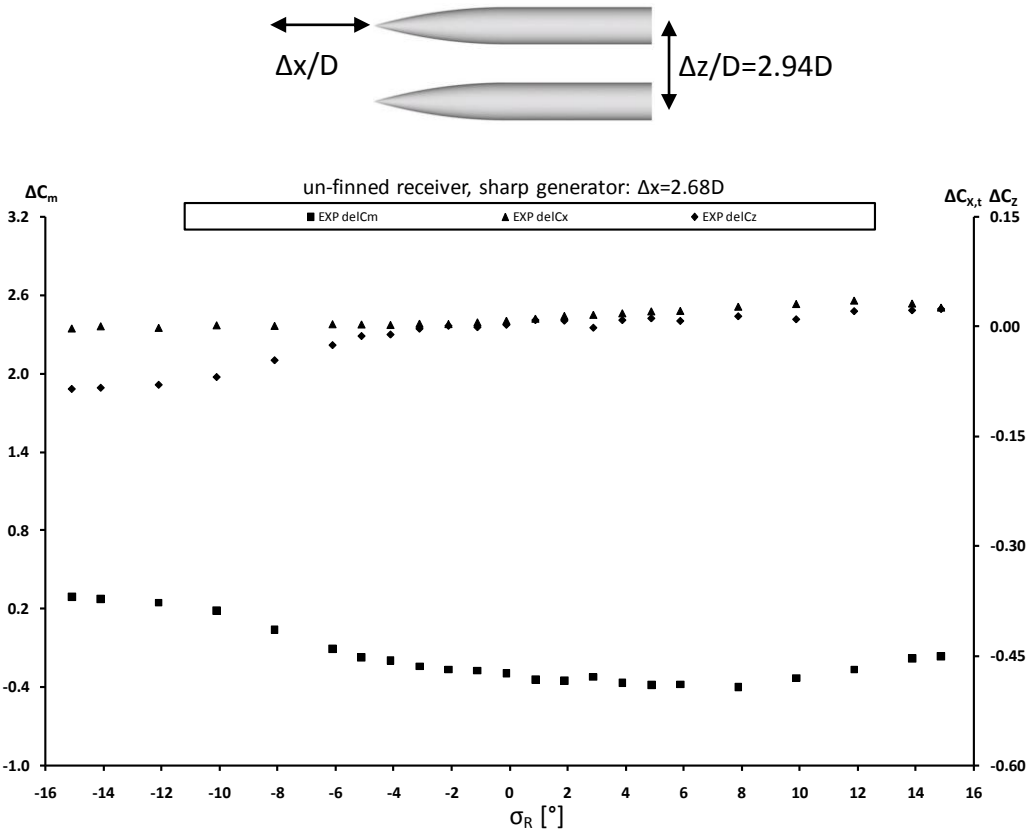

Figure B.11 Effect of receiver incidence on receiver interference loads: m2651 m2653, Δx/D=2.68 Δz/D=2.94, σ_G=0°

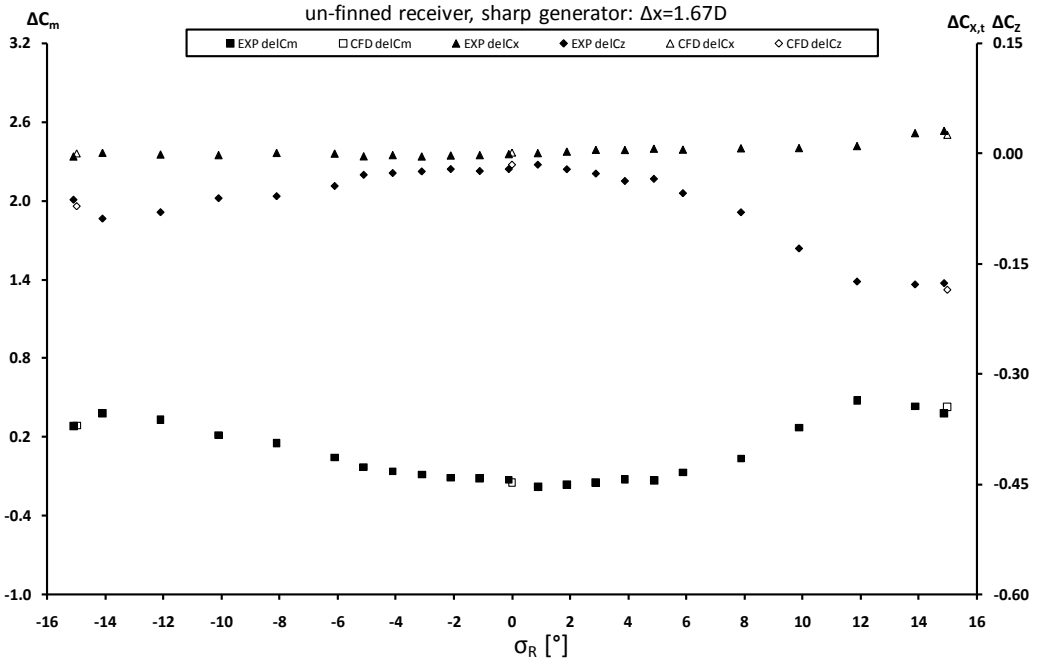

Figure B.12 Effect of receiver incidence on receiver interference loads: m2651 m2653, Δx/D=1.67 Δz/D=2.94, σ_G=0°

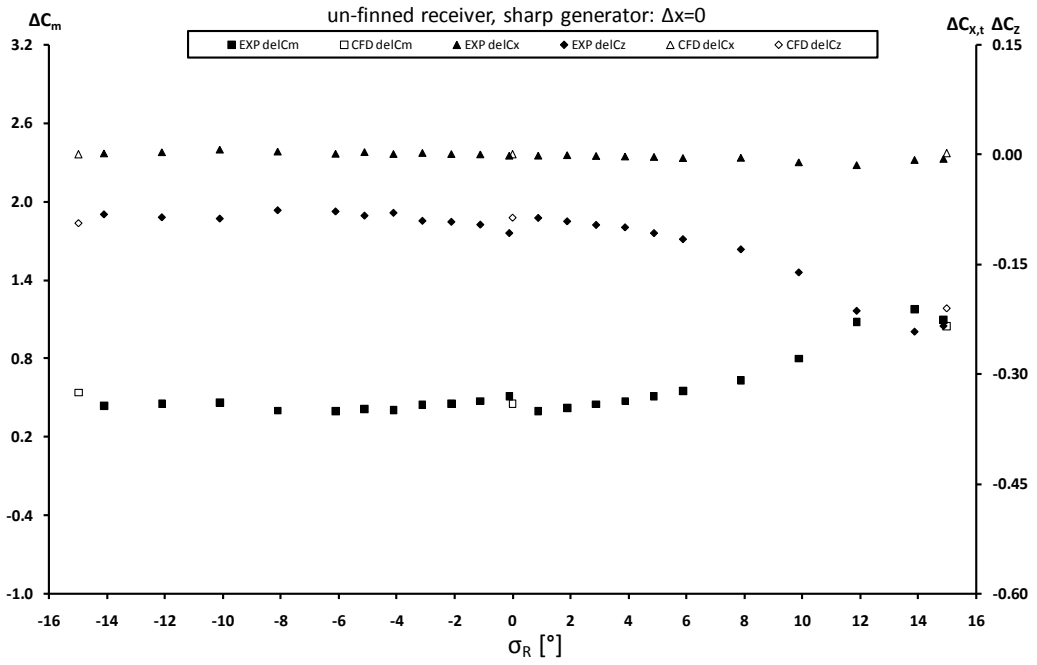

Figure B.13 Effect of receiver incidence on receiver interference loads: m2651 m2653, Δx/D=0 Δz/D=2.94, σ_G=0°

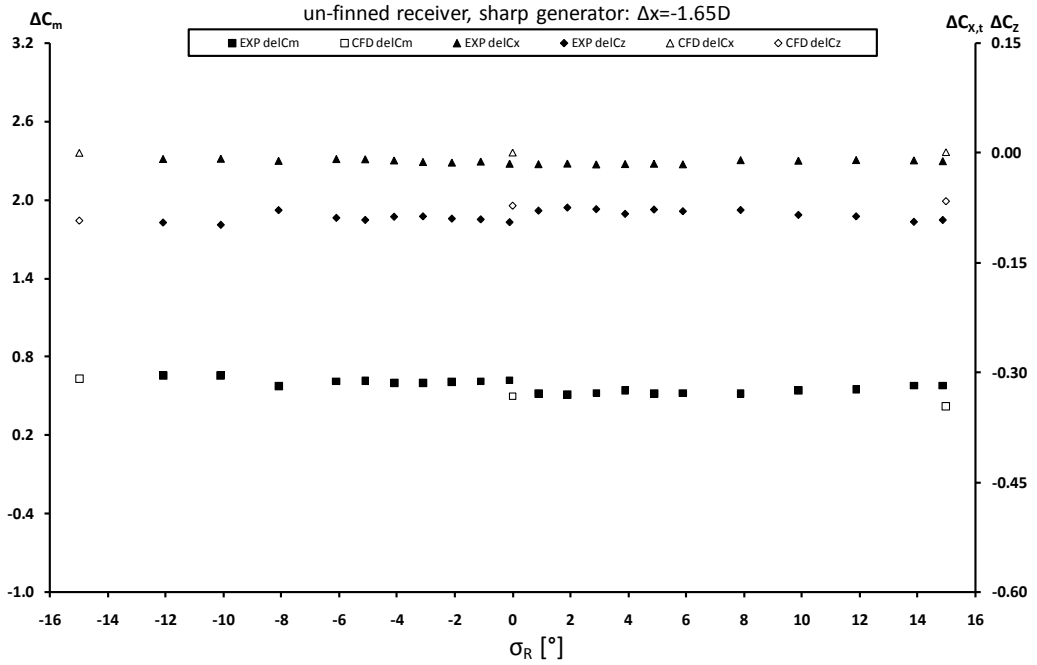

Figure B.14 Effect of receiver incidence on receiver interference loads: m2651 m2653, Δx/D=-1.65 Δz/D=2.94, σ_G=0°

B.7 Force and moment results for the un-finned receiver and blunt generator

The interference loads are plotted as a function of receiver incidence for the un-finned receiver and blunt generator at a fixed lateral separation for different axial staggers (Figure B.15 - Figure B.18).

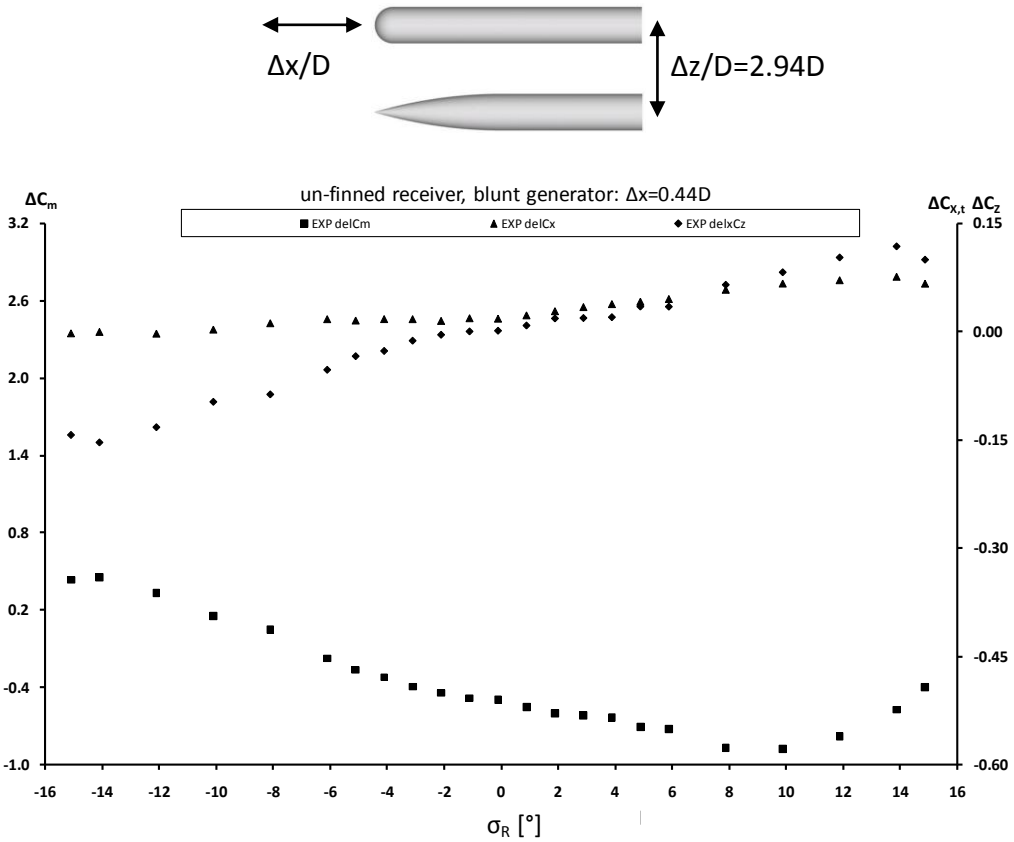

Figure B.15 Effect of receiver incidence on receiver interference loads: m2651 m2654, Δx/D=0.44 Δz/D=2.94, σ_G=0°

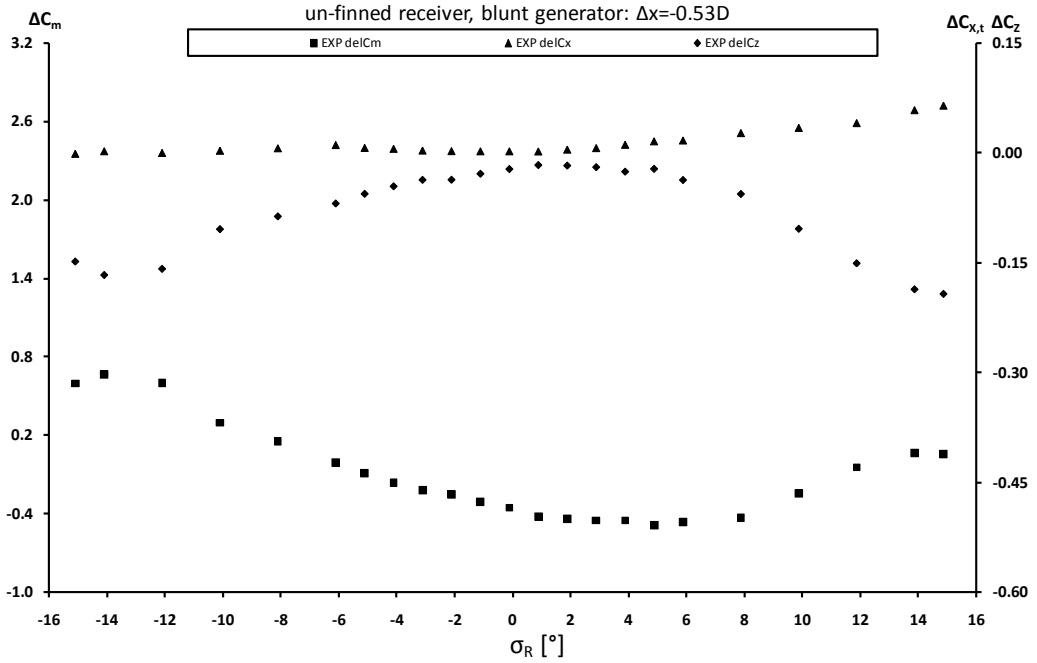

Figure B.16 Effect of receiver incidence on receiver interference loads: m2651 m2654, Δx/D=-0.53 Δz/D=2.94, σ_G=0°

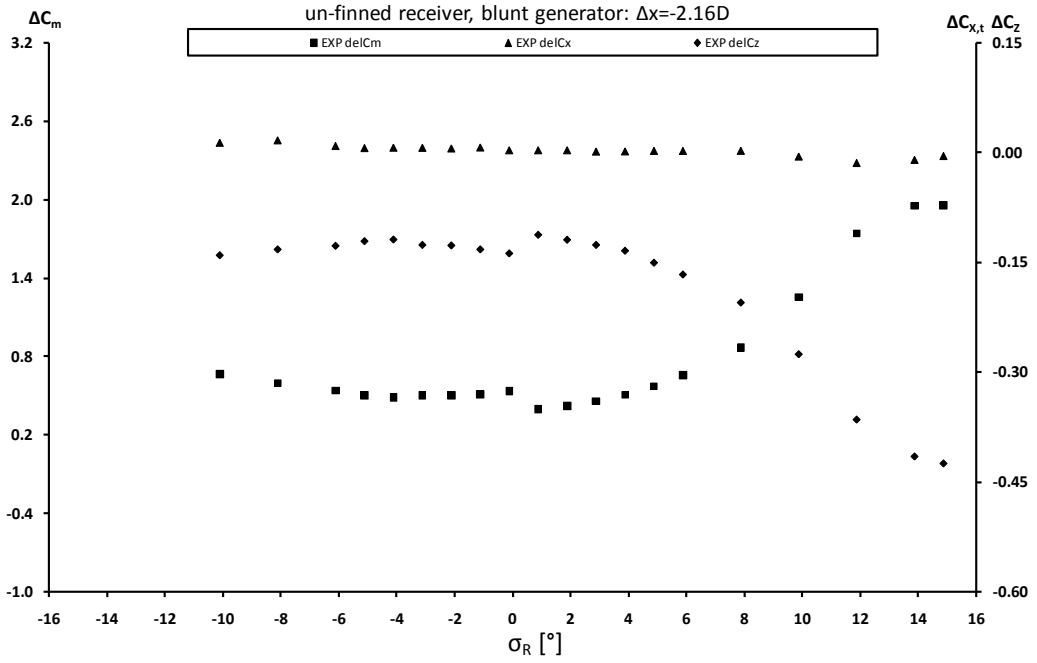

Figure B.17 Effect of receiver incidence on receiver interference loads: m2651 m2654, Δx/D=-2.16 Δz/D=2.94, σ_G=0°

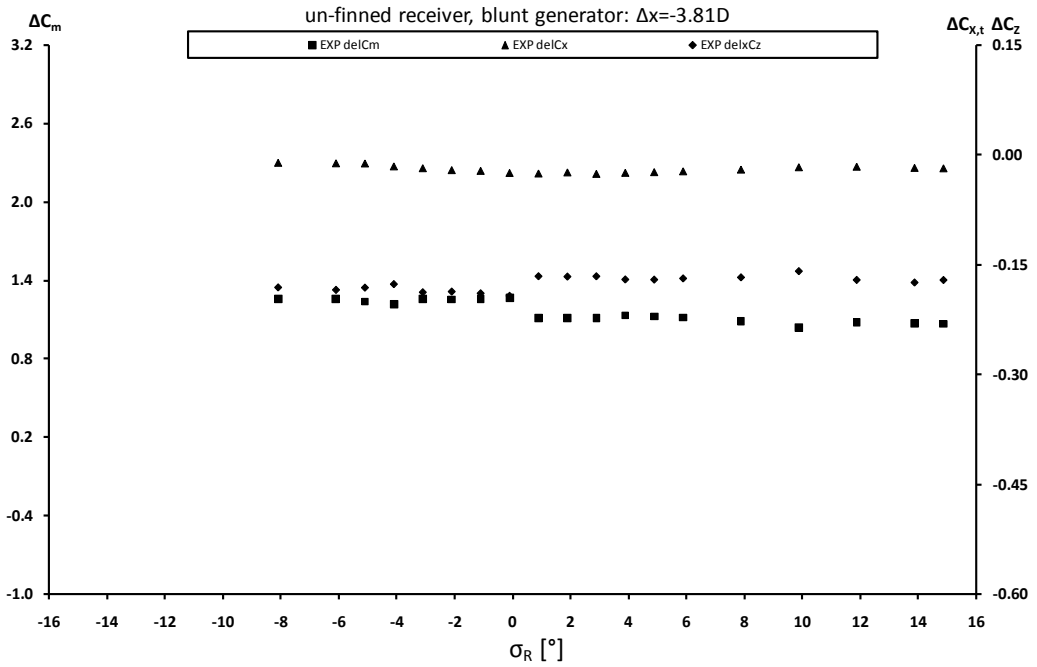

Figure B.18 Effect of receiver incidence on receiver interference loads: m2651 m2654, Δx/D=-3.81 Δz/D=2.94, σ_G=0°

Appendix C

C.1 Effect of axial impingement for the finned receiver and blunt generator

The effect of axial impingement location is evaluated for the finned receiver and blunt generator. Figure C.1 and Figure C.2 show a variation in axial stagger between the bodies (Δx/D) for a fixed receiver incidence (σ_R).

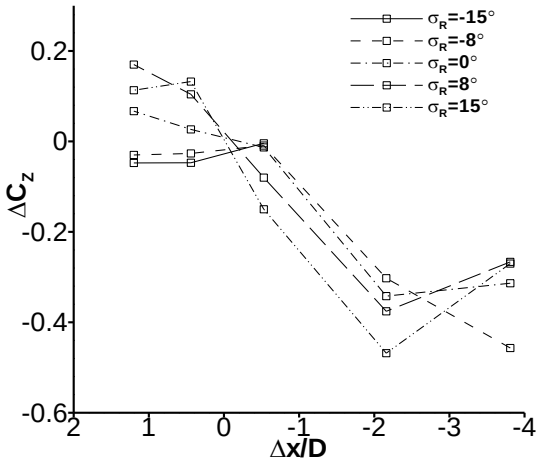

Figure C.1 Effect of axial stagger on measured normal force interference load: m2652 m2654, Δz/D=2.94, σ_G=0°

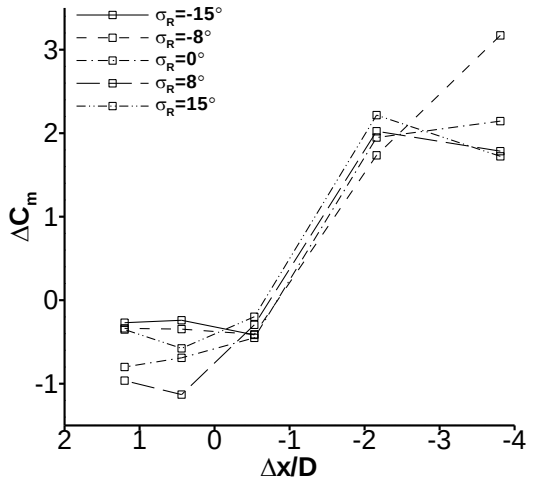

Figure C.2 Effect of axial stagger on measured pitching moment interference load: m2652 m2654, Δz/D=2.94, σ_G=0°

The above results show that the effect of axial impingement location is similar for all the incidence angles tested. The trends observed are similar to when the sharp generator is used, but the magnitude of the interference effects are amplified.

C.2 CFD and PSP comparisons for the finned receiver body

C.2.1 Finned receiver and sharp generator

The following pages compare PSP and CFD results for the finned receiver and sharp generator configuration. This includes plots of surface pressure (p/p_∞), axial distributions of C_p at different azimuth locations ϕ=0° (farside) and ϕ=180° (nearside) and crossflow distributions of C_p at different axial locations on the receiver body over an incidence range $-15 \leq \sigma_R \leq 15°$.

At the extremes of surface curvature near the receiver leading edge ($x/L \leq 0.15$) the local surface normal was almost perpendicular to the camera line-of-sight and the data in this small region were considered to be un-reliable and excluded from the pressure plots. Due to wind tunnel debris a small amount of degradation of the PSP coating occurred during each test. In addition, the model attachment screw hole caused a local flowfield disturbance at $x/L \approx 0.55$ and ϕ=90°.

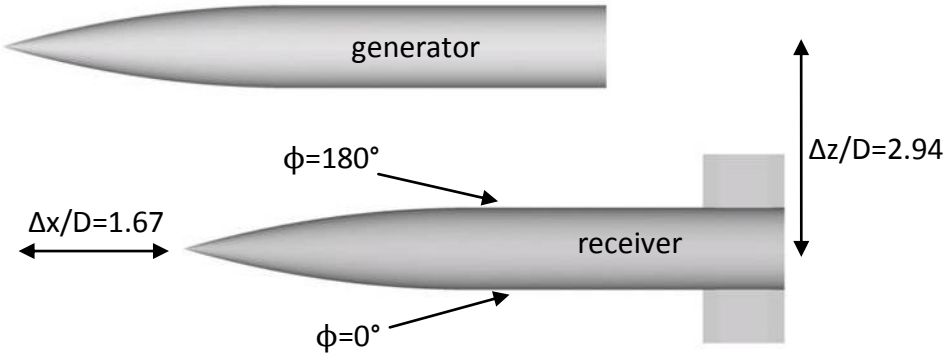

σ_R=0°

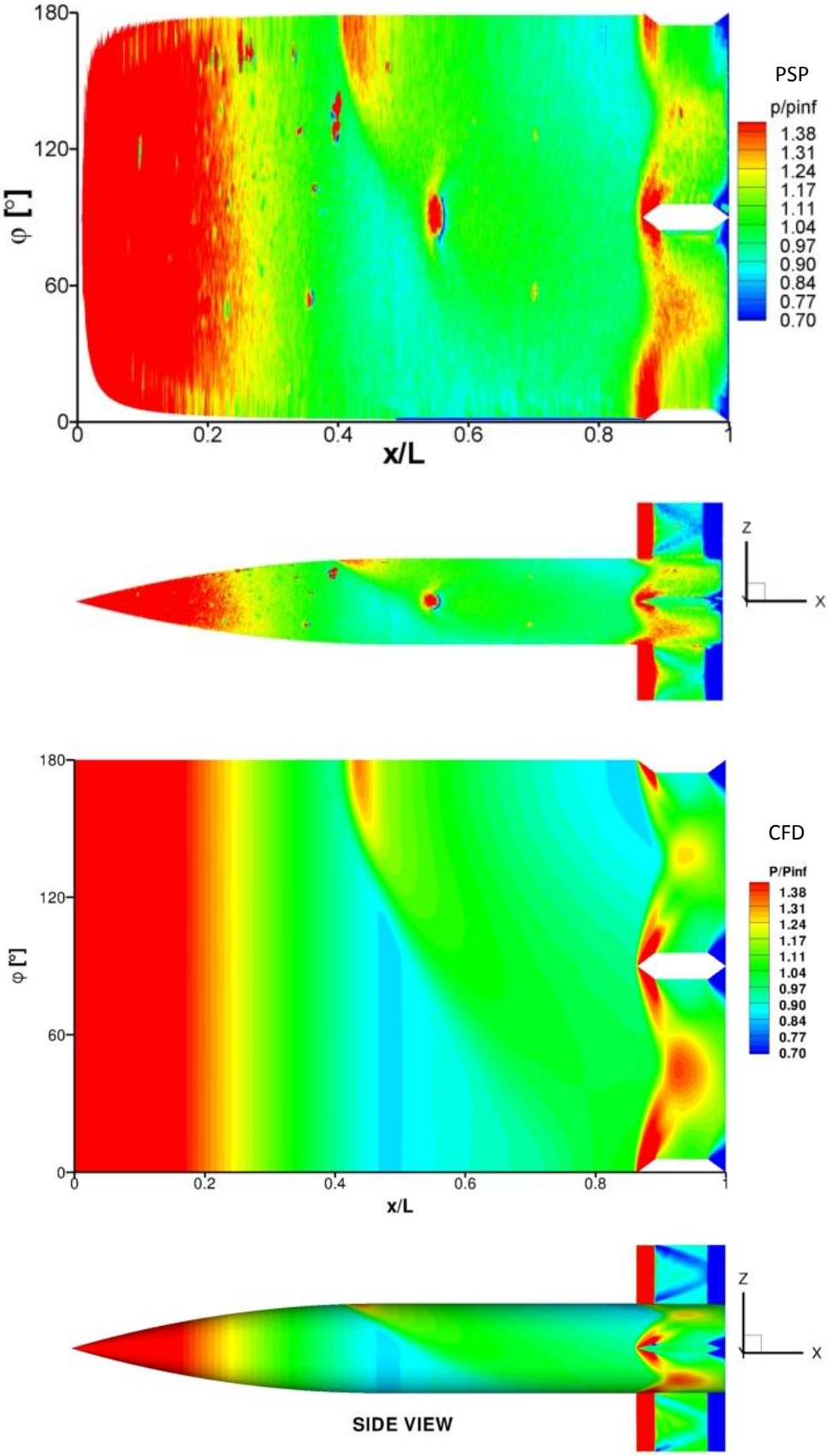
PSP
p/pinf
1.38
1.31
1.24
1.17
1.11
1.04
0.97
0.90
0.84
0.77
0.70
φ [°]
x/L
Z
X
CFD
P/Pinf
SIDE VIEW

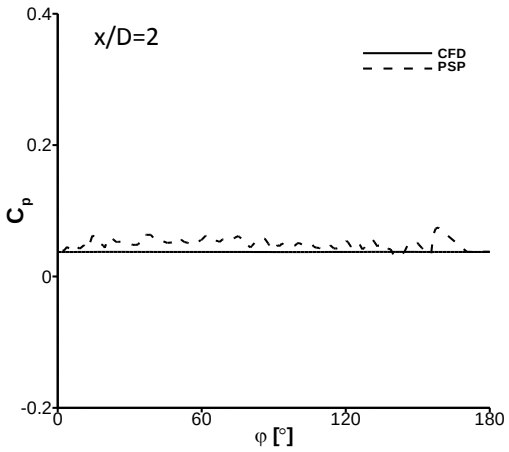
x/D=2
CFD
PSP
C_p
φ [°]

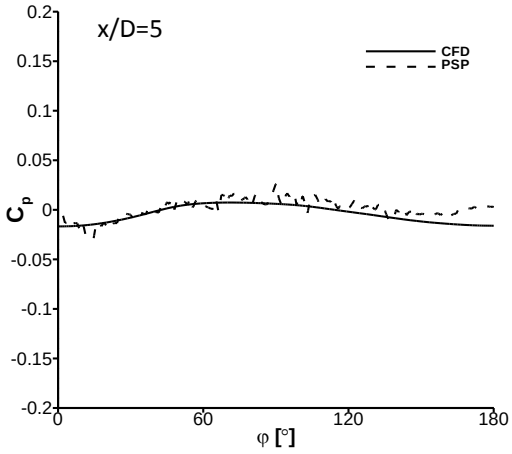
x/D=5
CFD
PSP
C_p
φ [°]

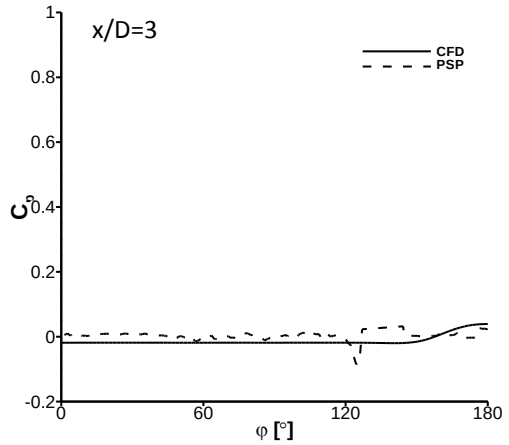
x/D=3
CFD
PSP
C_p
φ [°]

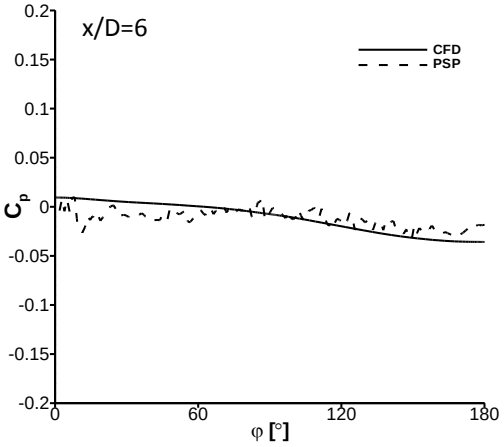
x/D=6
CFD
PSP
C_p
φ [°]

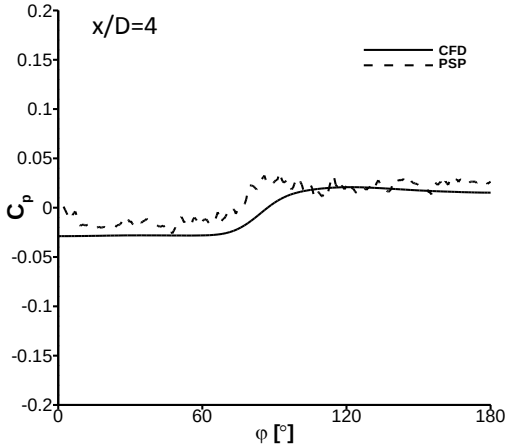
x/D=4
CFD
PSP
C_p
φ [°]

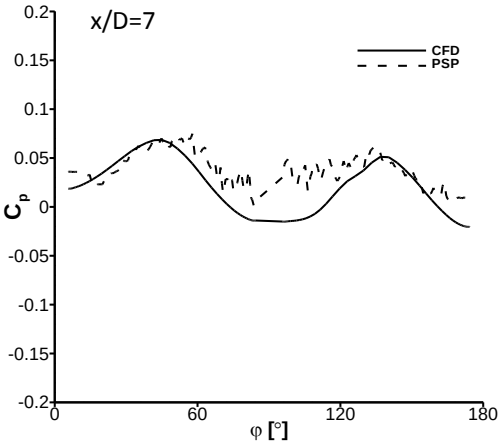
x/D=7
CFD
PSP
C_p
φ [°]

σ_R =-8°

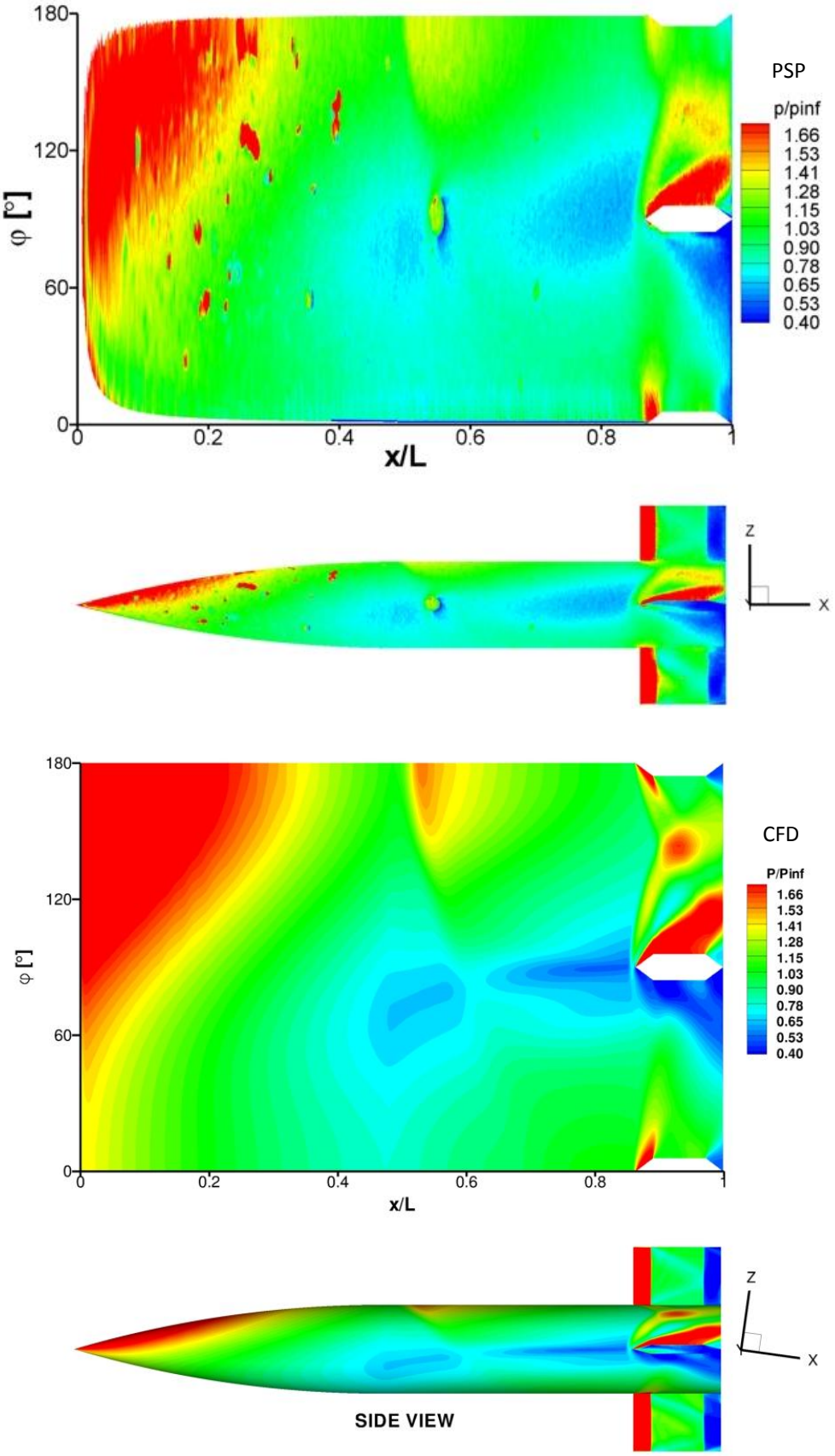
PSP
p/pinf
1.66
1.53
1.41
1.28
1.15
1.03
0.90
0.78
0.65
0.53
0.40
180
120
60
0
φ [°]
0
0.2
0.4
0.6
0.8
1
x/L
Z
X
CFD
P/Pinf
1.66
1.53
1.41
1.28
1.15
1.03
0.90
0.78
0.65
0.53
0.40
180
120
60
0
φ [°]
0
0.2
0.4
0.6
0.8
1
x/L
Z
X
SIDE VIEW

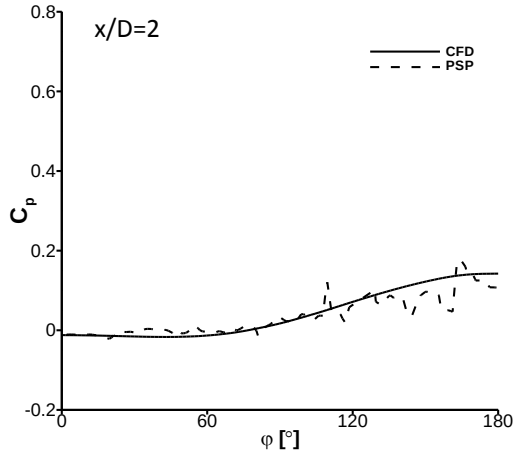
x/D=2
CFD
PSP
C_p
φ [°]

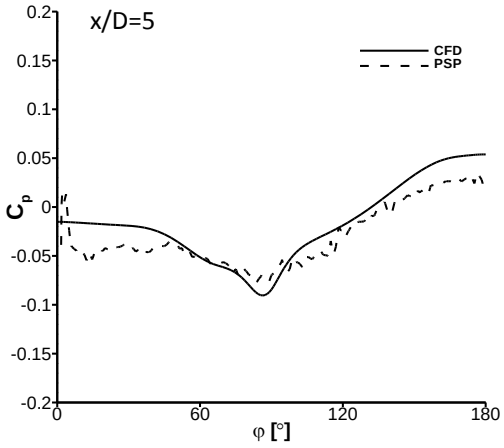
x/D=5
CFD
PSP
C_p
φ [°]

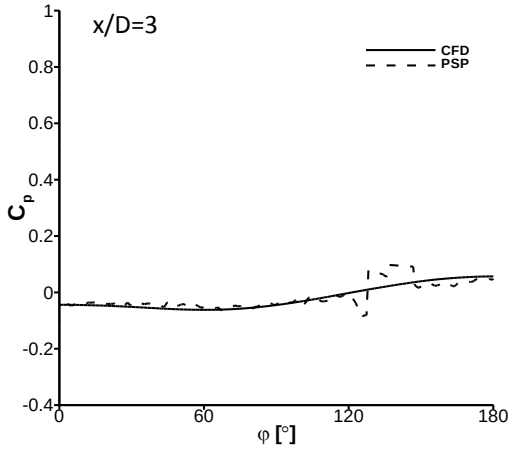
x/D=3
CFD
PSP
C_p
φ [°]

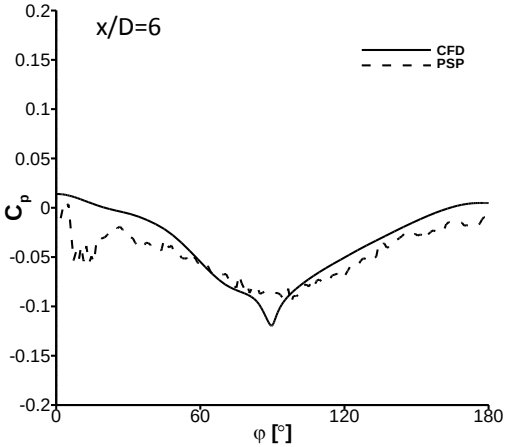
x/D=6
CFD
PSP
C_p
φ [°]

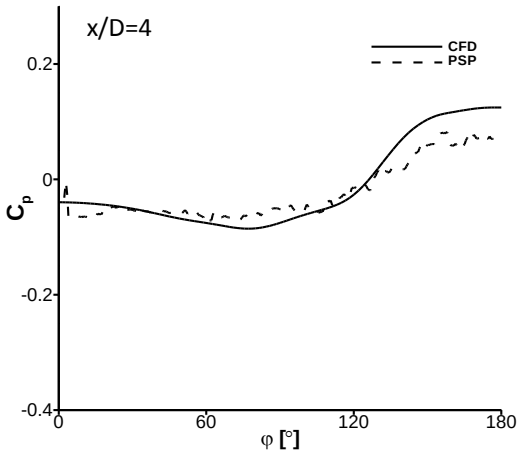
x/D=4
CFD
PSP
C_p
φ [°]

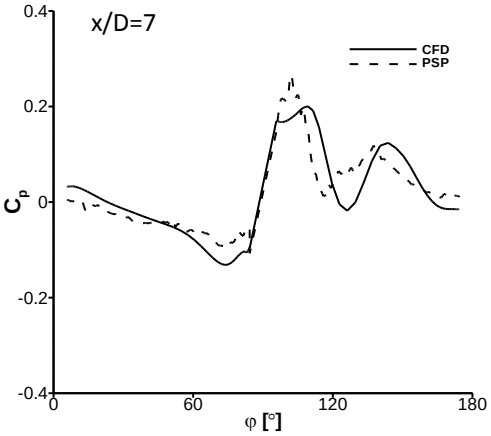
x/D=7
CFD
PSP
C_p
φ [°]

σ_R =-15°

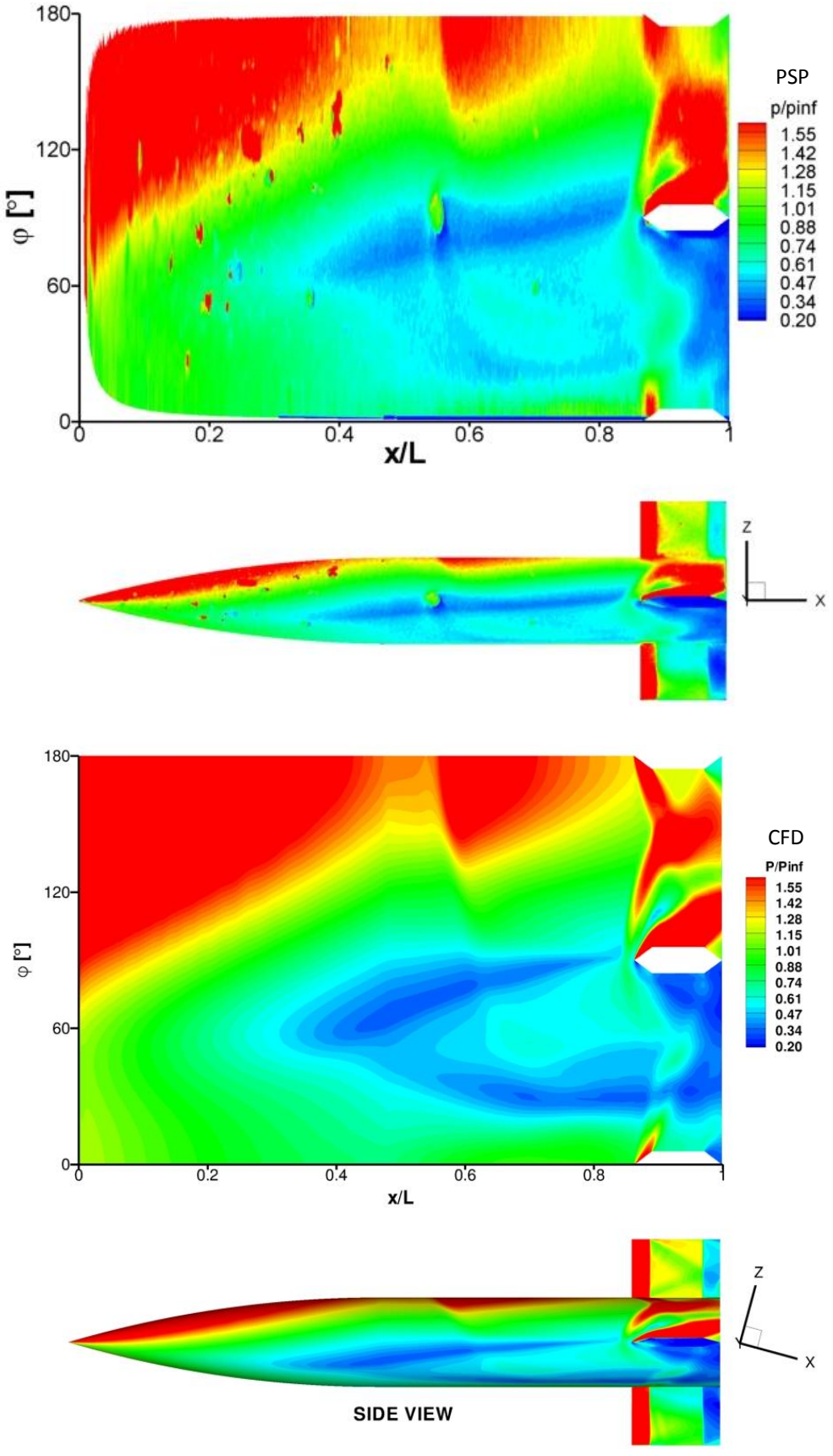
PSP
p/pinf
1.55
1.42
1.28
1.15
1.01
0.88
0.74
0.61
0.47
0.34
0.20
φ [°]
x/L
Z
X
CFD
P/Pinf
SIDE VIEW

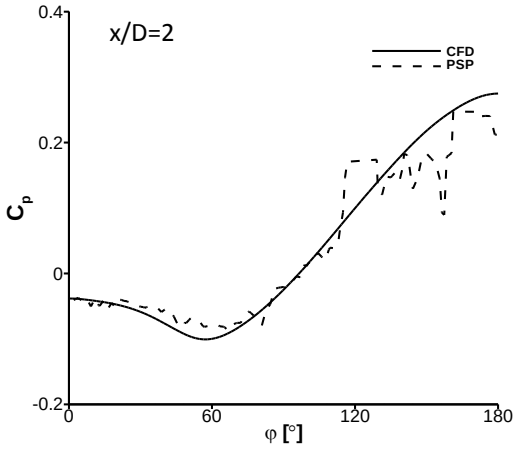
x/D=2
CFD
PSP
C_p
φ [°]

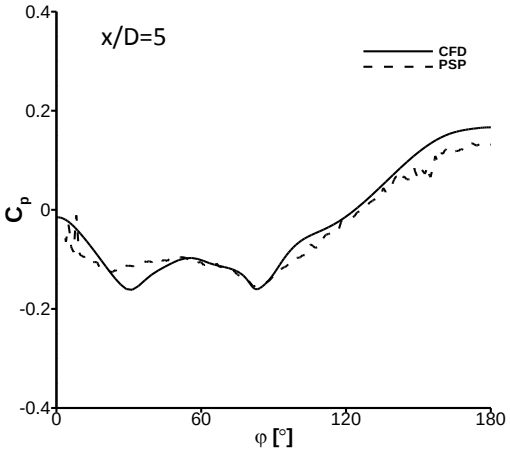
x/D=5
CFD
PSP
C_p
φ [°]

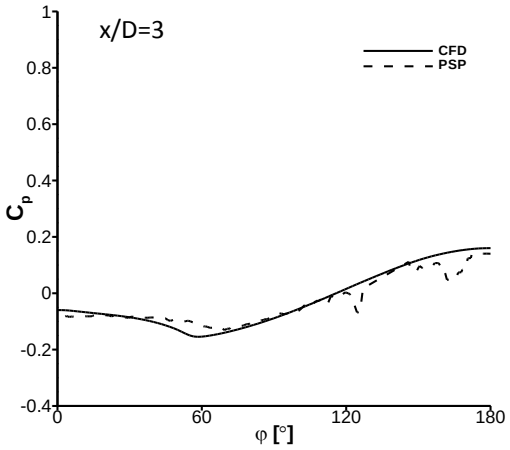
x/D=3
CFD
PSP
C_p
φ [°]

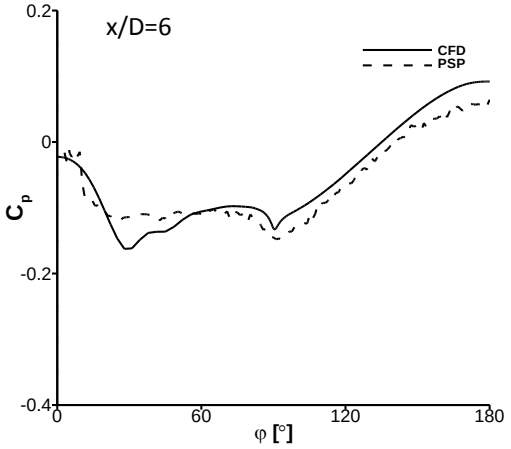
x/D=6
CFD
PSP
C_p
φ [°]

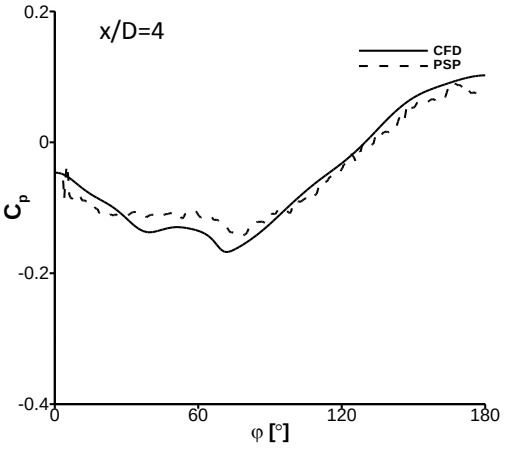
x/D=4
CFD
PSP
C_p
φ [°]

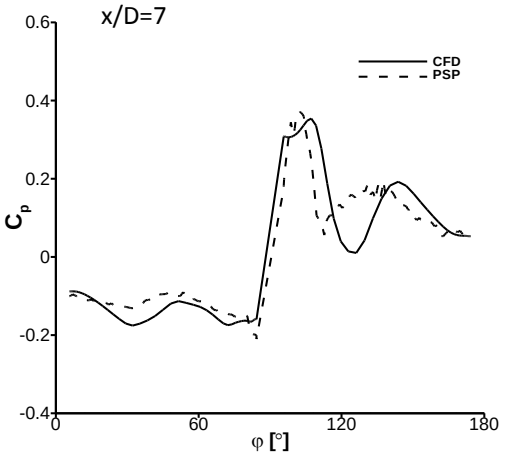
x/D=7
CFD
PSP
C_p
φ [°]

σ_R =8°

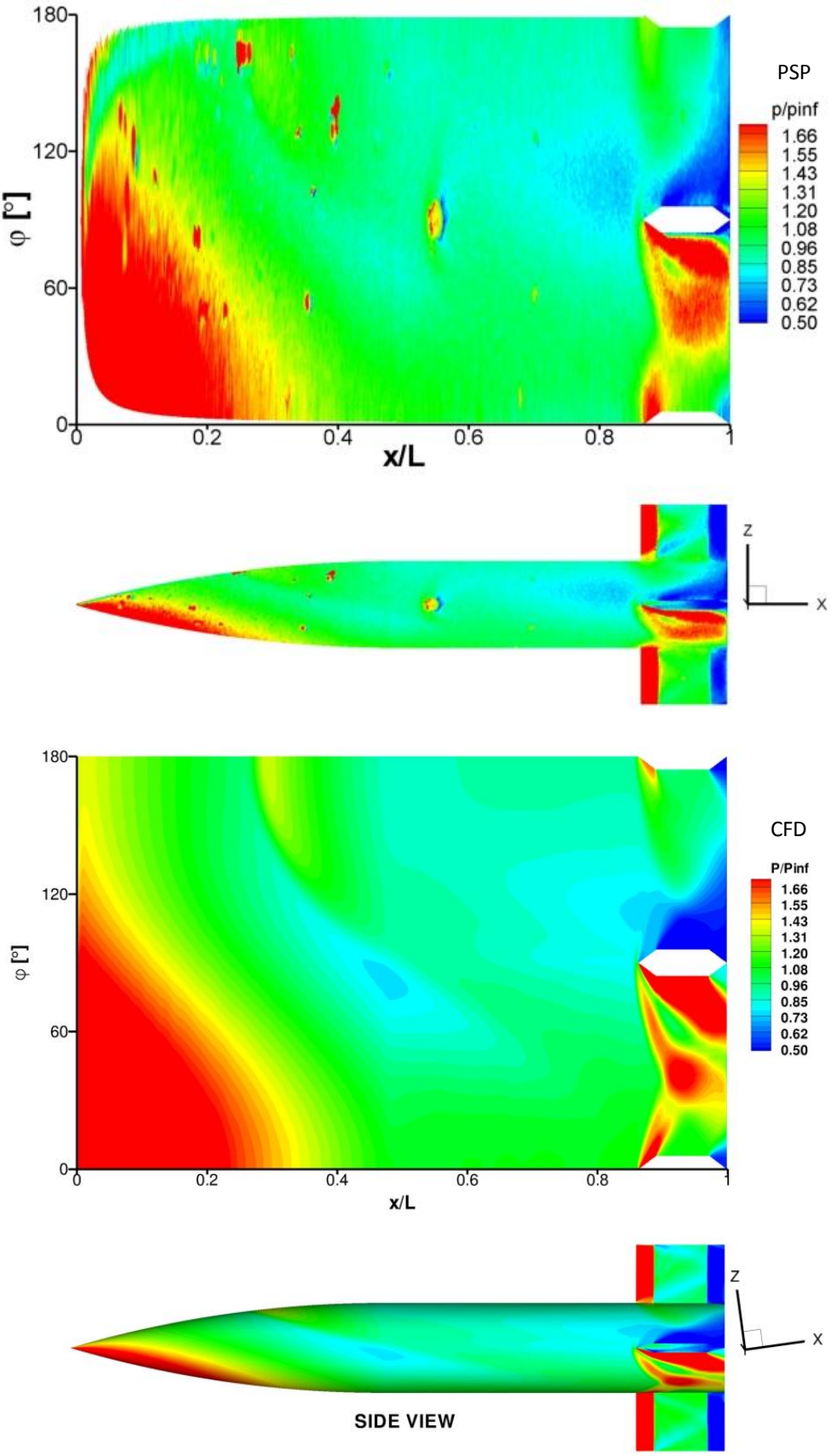
PSP
p/pinf
1.66
1.55
1.43
1.31
1.20
1.08
0.96
0.85
0.73
0.62
0.50
180
120
60
0
φ [°]
0
0.2
0.4
0.6
0.8
1
x/L
Z
X
CFD
P/Pinf
1.66
1.55
1.43
1.31
1.20
1.08
0.96
0.85
0.73
0.62
0.50
180
120
60
0
φ [°]
0
0.2
0.4
0.6
0.8
1
x/L
Z
X
SIDE VIEW

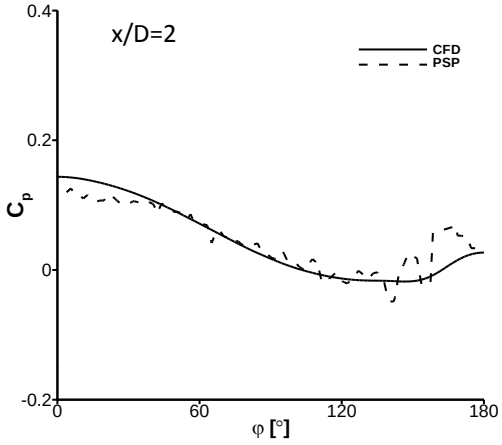
x/D=2
CFD
PSP
C_p
φ [°]

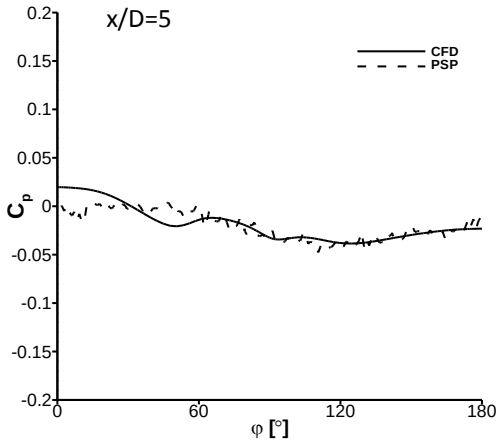
x/D=5
CFD
PSP
C_p
φ [°]

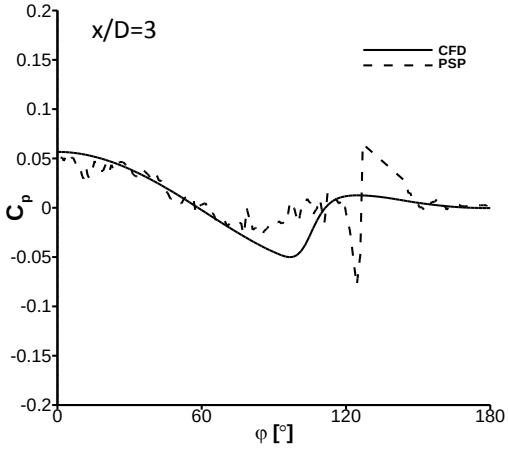
x/D=3
CFD
PSP
C_p
φ [°]

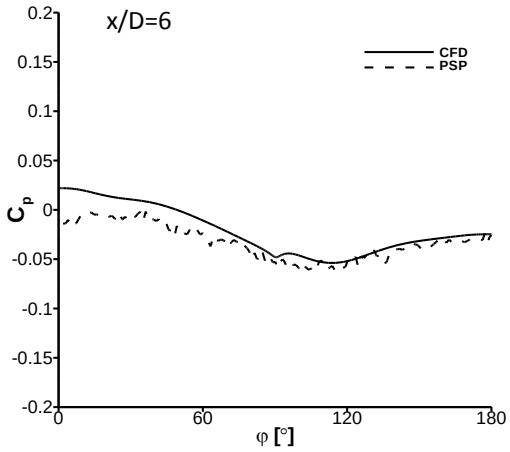
x/D=6
CFD
PSP
C_p
φ [°]

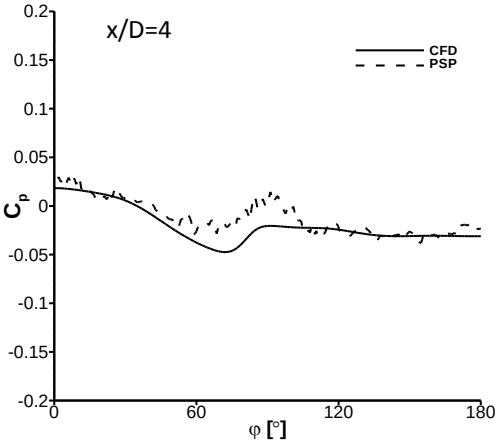
x/D=4
CFD
PSP
C_p
φ [°]

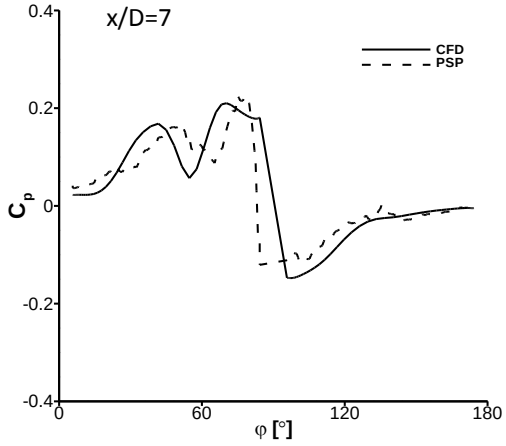
x/D=7
CFD
PSP
C_p
φ [°]

σ_R =15°

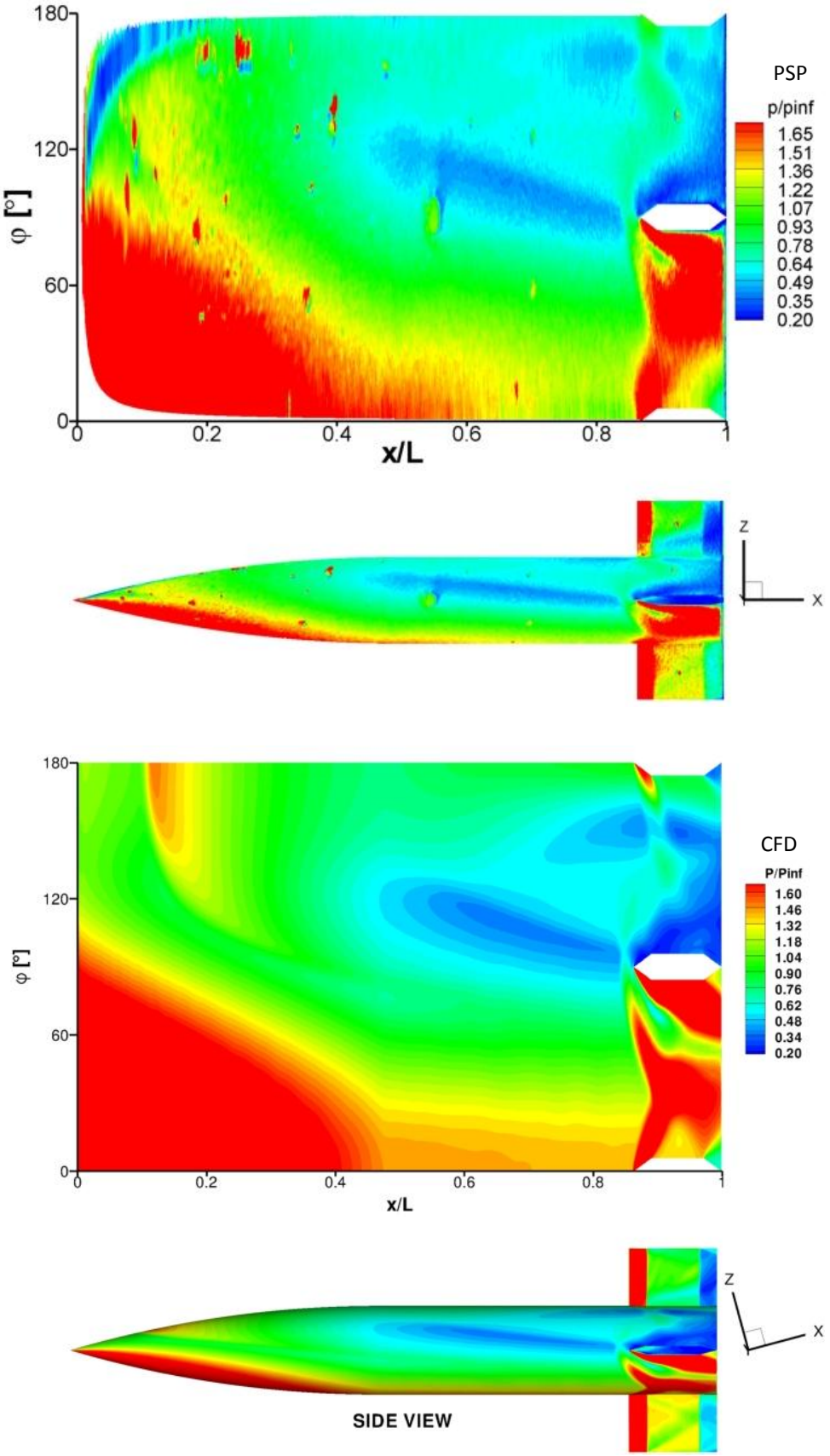
PSP
p/pinf
1.65
1.51
1.36
1.22
1.07
0.93
0.78
0.64
0.49
0.35
0.20
180
120
60
0
φ [°]
0
0.2
0.4
0.6
0.8
1
x/L
Z
X
CFD
P/Pinf
1.60
1.46
1.32
1.18
1.04
0.90
0.76
0.62
0.48
0.34
0.20
SIDE VIEW

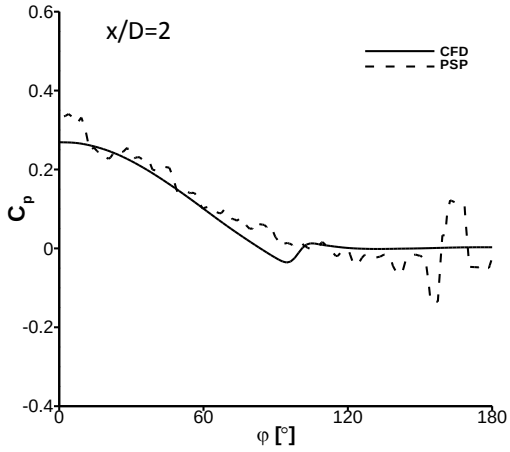
x/D=2
CFD
PSP
C_p
φ [°]
0.6
0.4
0.2
0
-0.2
-0.4
0
60
120
180

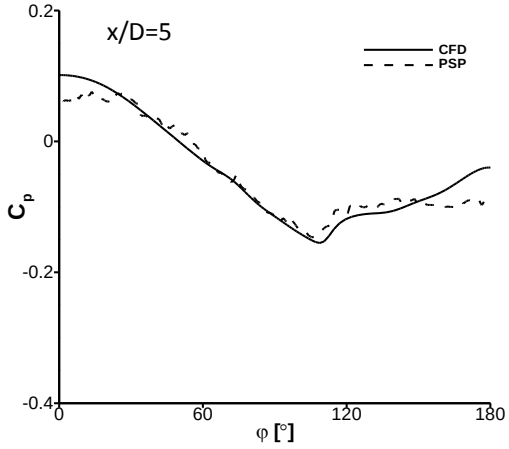
x/D=5
CFD
PSP
C_p
φ [°]
0.2
0
-0.2
-0.4
0
60
120
180

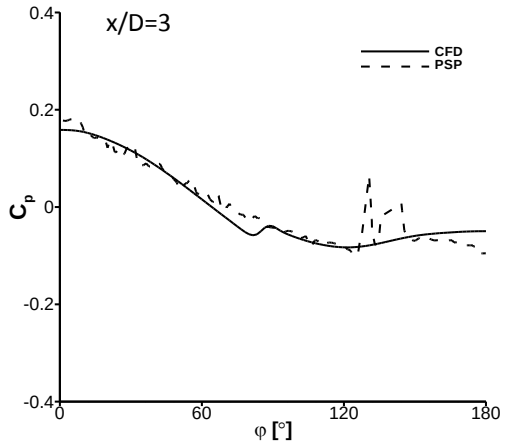
x/D=3
CFD
PSP
C_p
φ [°]
0.4
0.2
0
-0.2
-0.4
0
60
120
180

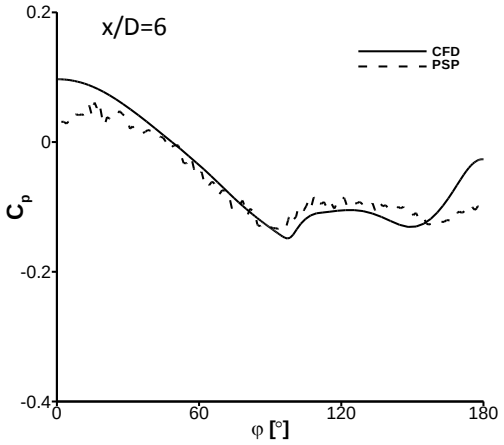
x/D=6
CFD
PSP
C_p
φ [°]
0.2
0
-0.2
-0.4
0
60
120
180

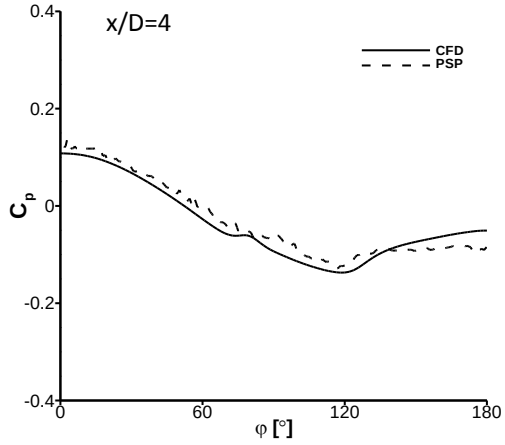
x/D=4
CFD
PSP
C_p
φ [°]
0.4
0.2
0
-0.2
-0.4
0
60
120
180

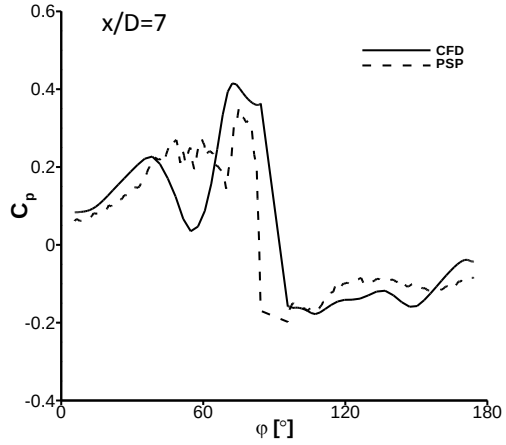
x/D=7
CFD
PSP
C_p
φ [°]
0.6
0.4
0.2
0
-0.2
-0.4
0
60
120
180

Overall, there is good agreement between the measured (PSP) and predicated (CFD) surface pressures on the finned receiver. In qualitative terms, the CFD predicts the location and local flow structures very well for the wide range of incidence angles tested. In quantitative terms, the CFD frequently predicts the magnitude of the interaction footprints sufficiently well. Finally, the above analysis gives confidence that that the CFD predictions of the interference loads for the finned receiver are based on the adequate resolution of the correct physical mechanisms.

C.2.2 Finned receiver and blunt generator

The following pages compare PSP and CFD results for the finned receiver and blunt generator configuration. This includes plots of surface pressure (p/p_∞), axial distributions of C_p at different azimuth locations ϕ=0° (farside) and ϕ=180° (nearside) and crossflow distributions of C_p at different axial locations on the receiver body over an incidence range $-15 \le \sigma_R \le 15°$.

At the extremes of surface curvature near the receiver leading edge ($x/L \le 0.15$) the local surface normal was almost perpendicular to the camera line-of-sight and the data in this small region were considered to be un-reliable and excluded from the pressure plots. Due to wind tunnel debris a small amount of degradation of the PSP coating occurred during each test. In addition, the model attachment screw hole caused a local flowfield disturbance at $x/L \approx 0.55$ and ϕ=90°.

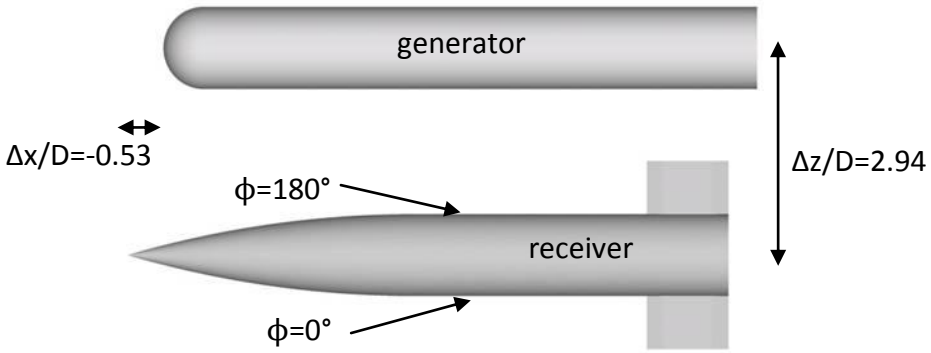

σ_R=0°

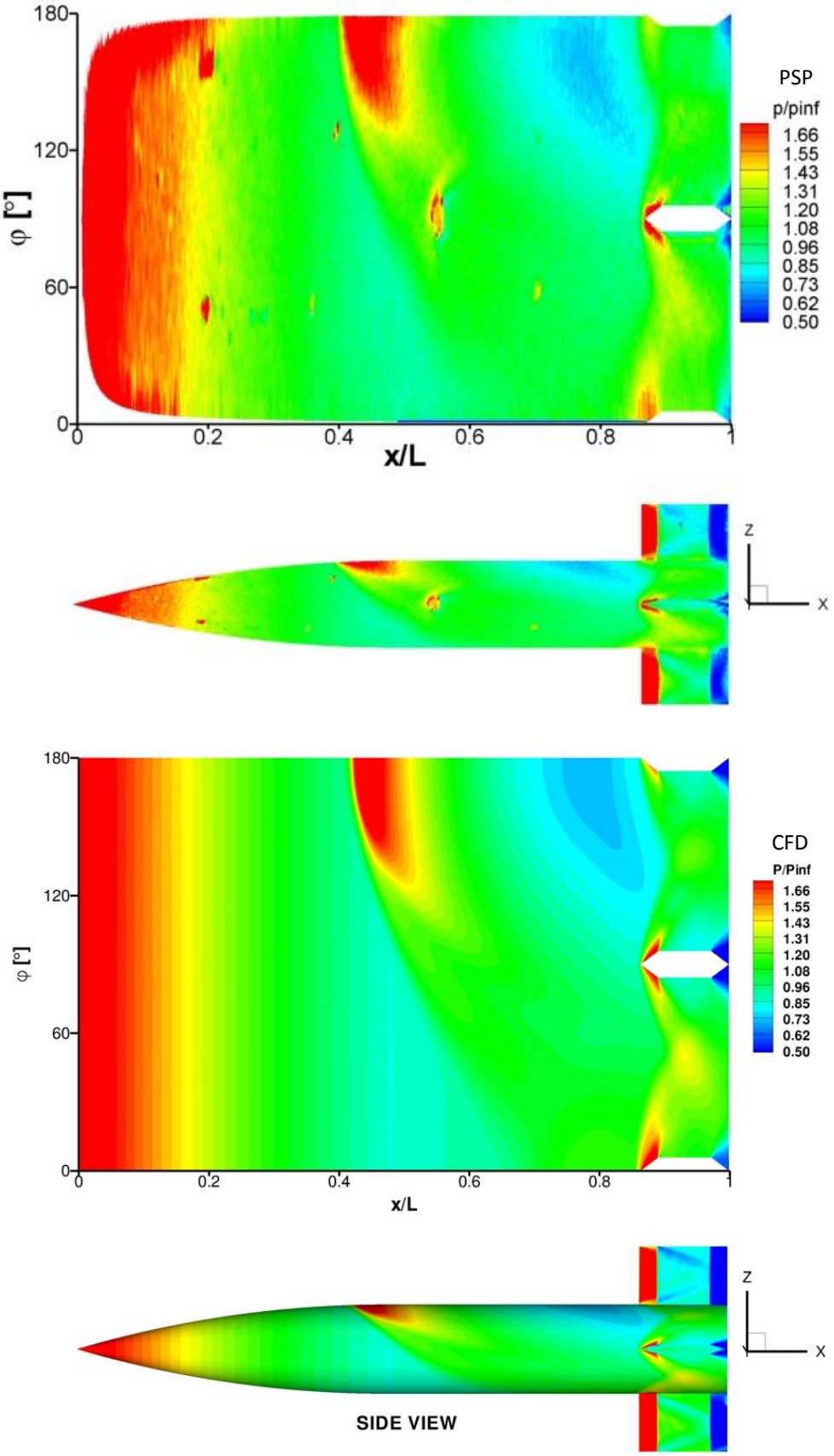
PSP
p/pinf
1.66
1.55
1.43
1.31
1.20
1.08
0.96
0.85
0.73
0.62
0.50
180
120
60
0
φ [°]
0
0.2
0.4
0.6
0.8
1
x/L
Z
X
CFD
P/Pinf
1.66
1.55
1.43
1.31
1.20
1.08
0.96
0.85
0.73
0.62
0.50
180
120
60
0
φ [°]
0
0.2
0.4
0.6
0.8
1
x/L
Z
X
SIDE VIEW

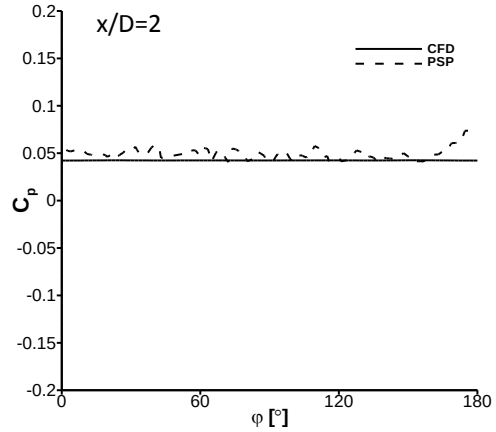
x/D=2
CFD
PSP
C_p
φ [°]

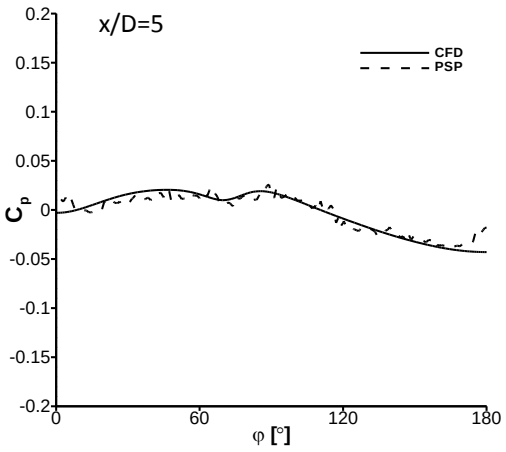
x/D=5
CFD
PSP
C_p
φ [°]

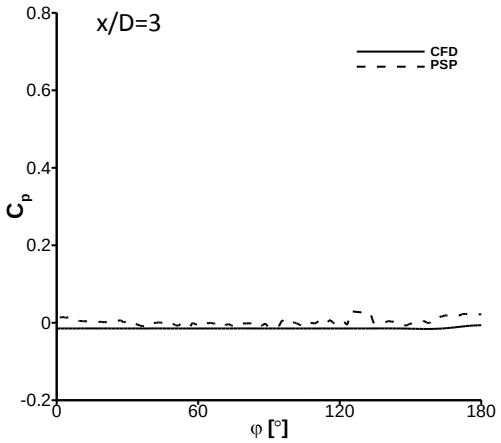
x/D=3
CFD
PSP
C_p
φ [°]

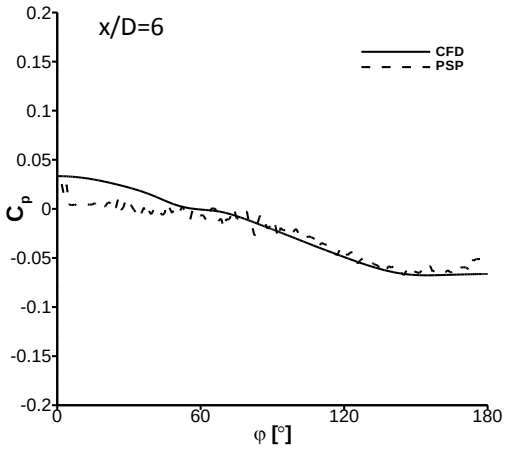
x/D=6
CFD
PSP
C_p
φ [°]

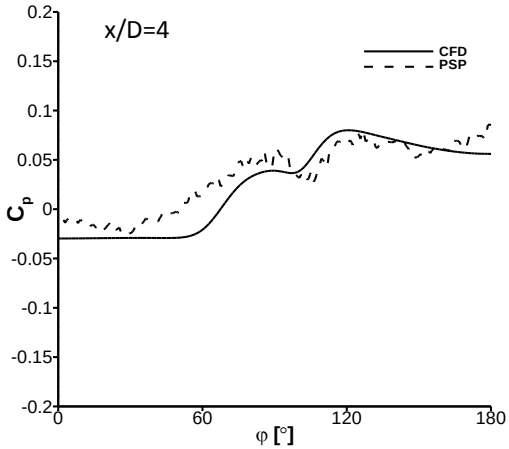
x/D=4
CFD
PSP
C_p
φ [°]

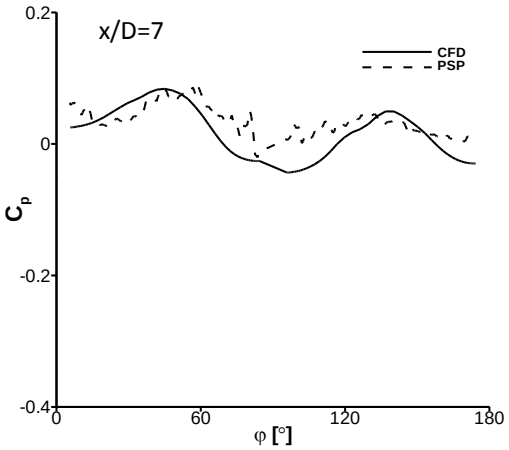
x/D=7
CFD
PSP
C_p
φ [°]

σ_R =-8°

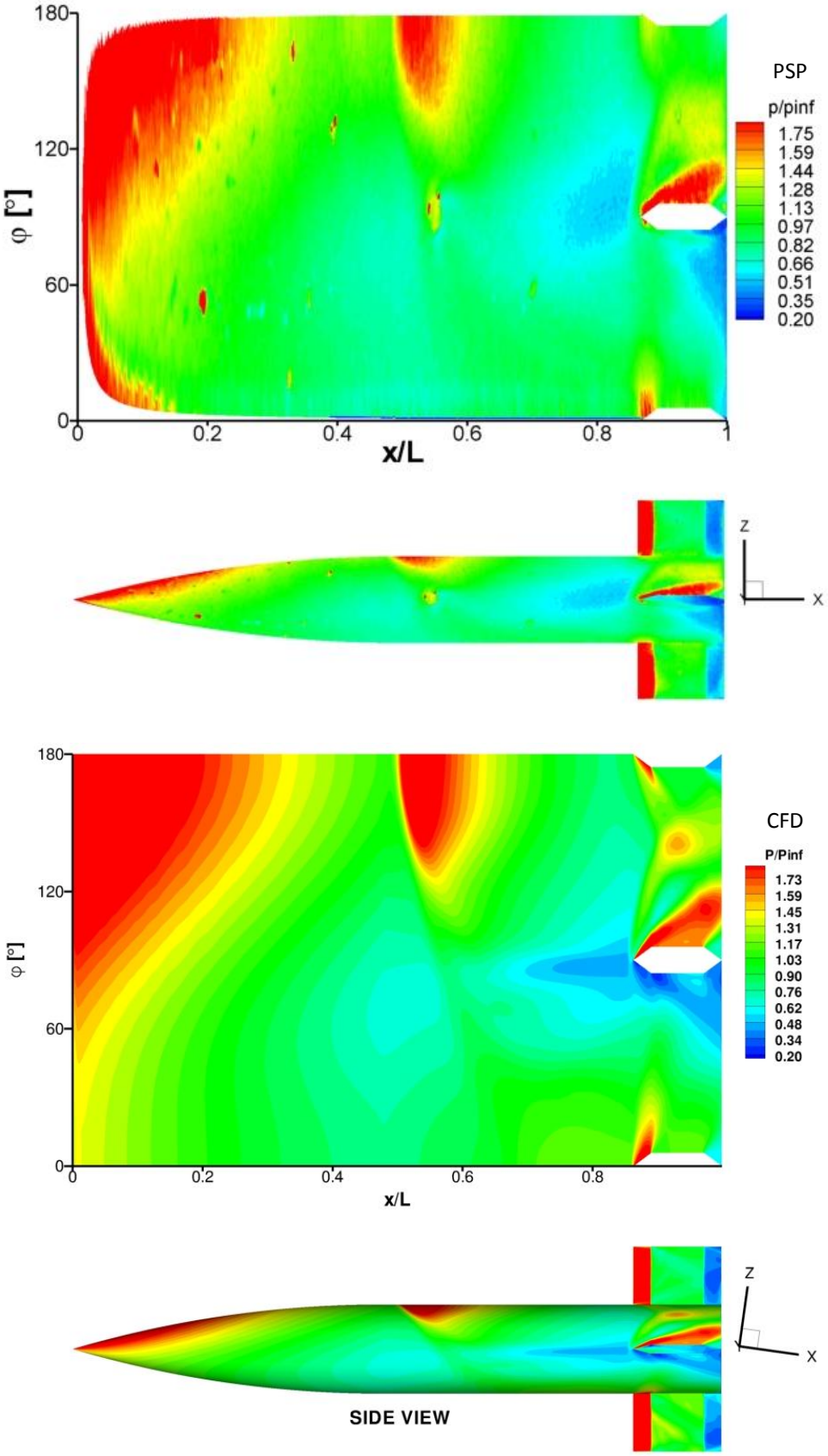
PSP
p/pinf
1.75
1.59
1.44
1.28
1.13
0.97
0.82
0.66
0.51
0.35
0.20
φ [°]
x/L
Z
X
CFD
P/Pinf
1.73
1.59
1.45
1.31
1.17
1.03
0.90
0.76
0.62
0.48
0.34
0.20
SIDE VIEW

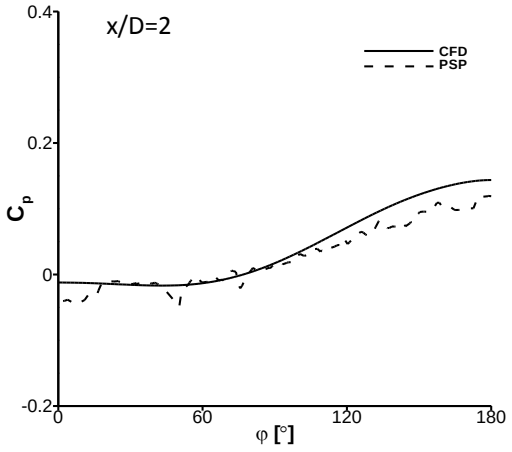
x/D=2
CFD
PSP
C_p
0.4
0.2
0
-0.2
0
60
120
180
φ [°]

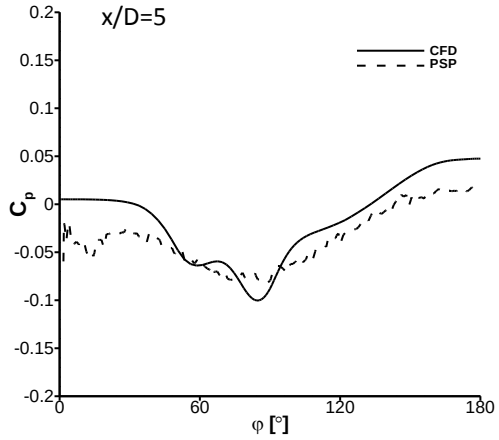
x/D=5
CFD
PSP
C_p
0.2
0.15
0.1
0.05
0
-0.05
-0.1
-0.15
-0.2
0
60
120
180
φ [°]

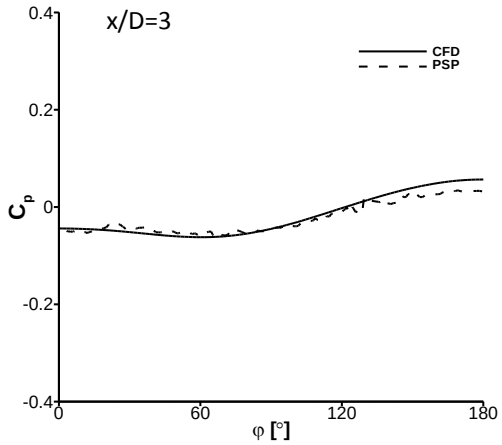
x/D=3
CFD
PSP
C_p
0.4
0.2
0
-0.2
-0.4
0
60
120
180
φ [°]

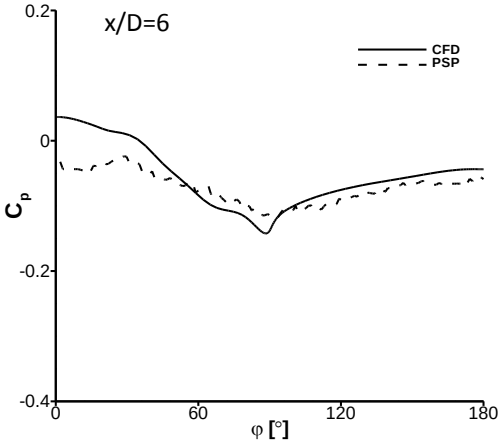
x/D=6
CFD
PSP
C_p
0.2
0
-0.2
-0.4
0
60
120
180
φ [°]

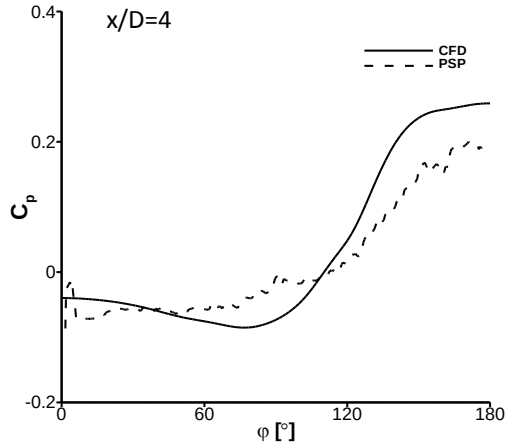
x/D=4
CFD
PSP
C_p
0.4
0.2
0
-0.2
0
60
120
180
φ [°]

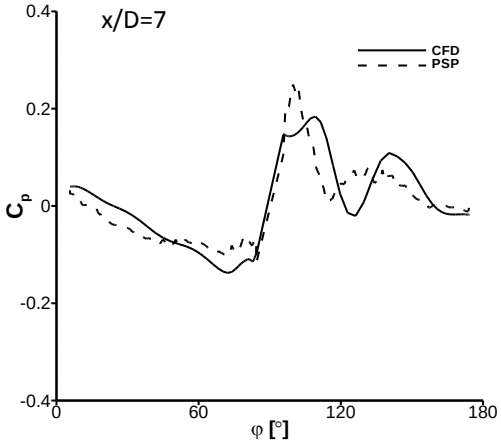
x/D=7
CFD
PSP
C_p
0.4
0.2
0
-0.2
-0.4
0
60
120
180
φ [°]

σ_R =-15°

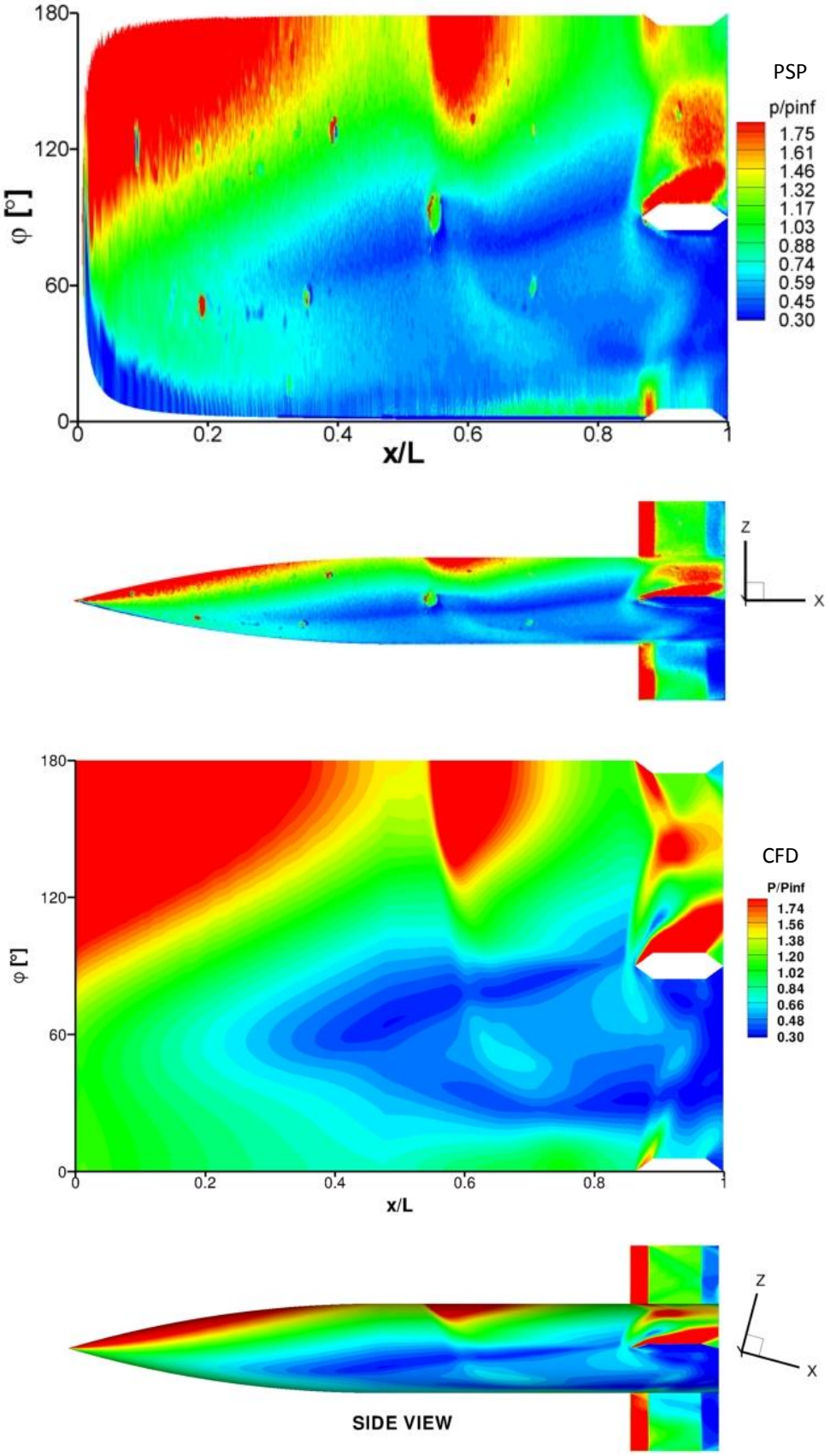
PSP
p/pinf
1.75
1.61
1.46
1.32
1.17
1.03
0.88
0.74
0.59
0.45
0.30
φ [°]
x/L
Z
X
CFD
P/Pinf
1.74
1.56
1.38
1.20
1.02
0.84
0.66
0.48
0.30
SIDE VIEW

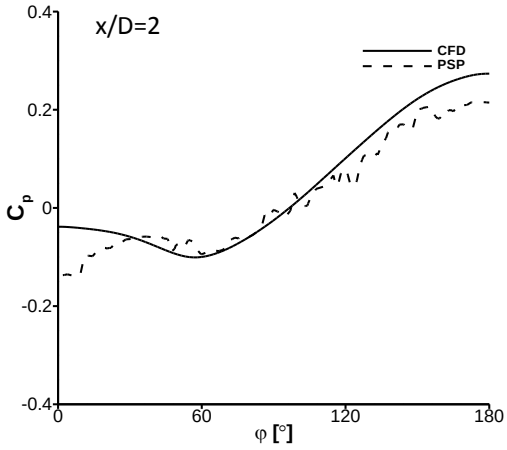
x/D=2
CFD
PSP
C_p
0.4
0.2
0
-0.2
-0.4
0
60
120
180
φ [°]

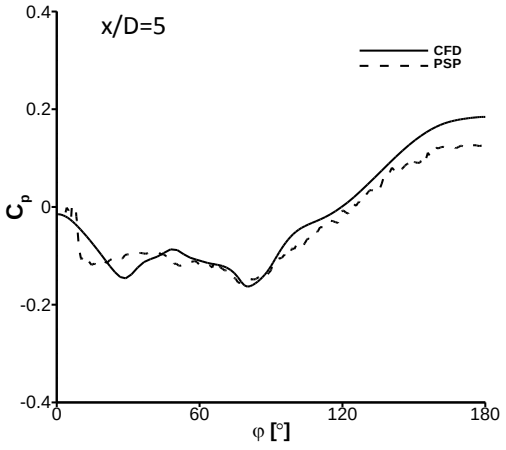
x/D=5
CFD
PSP
C_p
0.4
0.2
0
-0.2
-0.4
0
60
120
180
φ [°]

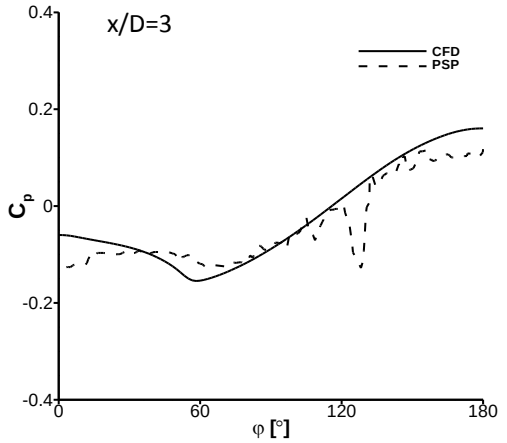
x/D=3
CFD
PSP
C_p
0.4
0.2
0
-0.2
-0.4
0
60
120
180
φ [°]

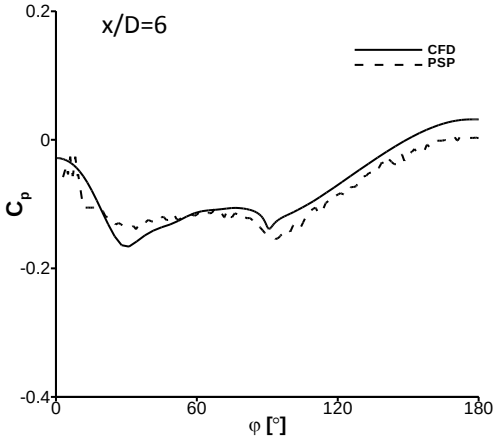
x/D=6
CFD
PSP
C_p
0.2
0
-0.2
-0.4
0
60
120
180
φ [°]

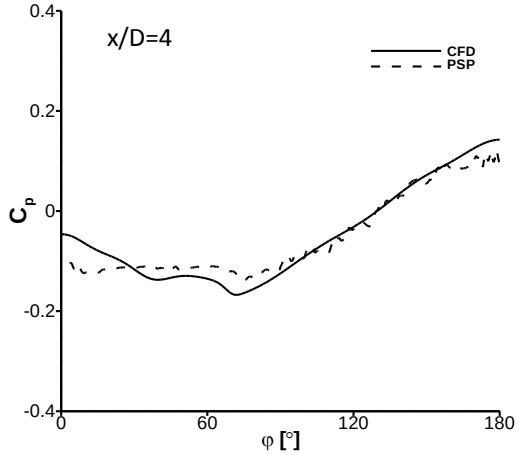
x/D=4
CFD
PSP
C_p
0.4
0.2
0
-0.2
-0.4
0
60
120
180
φ [°]

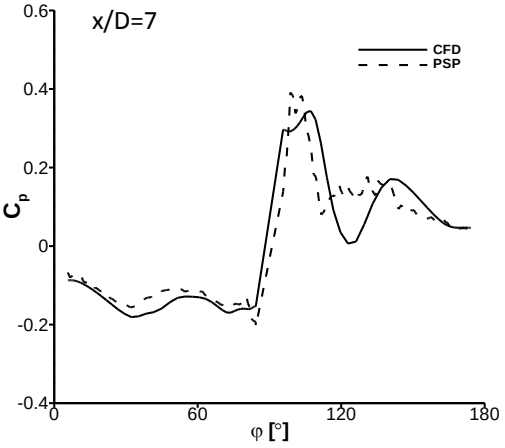
x/D=7
CFD
PSP
C_p
0.6
0.4
0.2
0
-0.2
-0.4
0
60
120
180
φ [°]

σ_R =8°

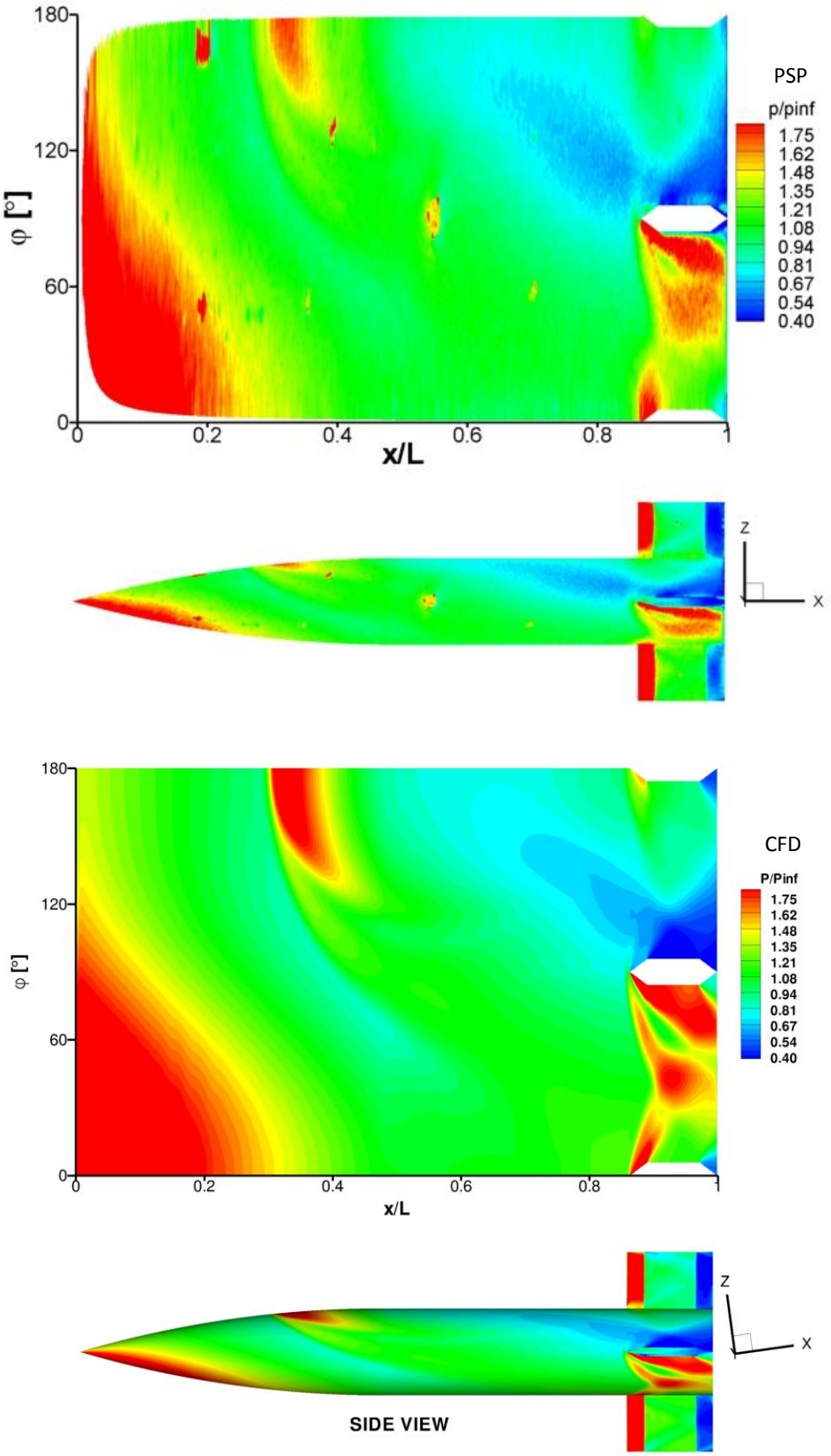
PSP
p/pinf
1.75
1.62
1.48
1.35
1.21
1.08
0.94
0.81
0.67
0.54
0.40
φ [°]
x/L
Z
X
CFD
P/Pinf
SIDE VIEW

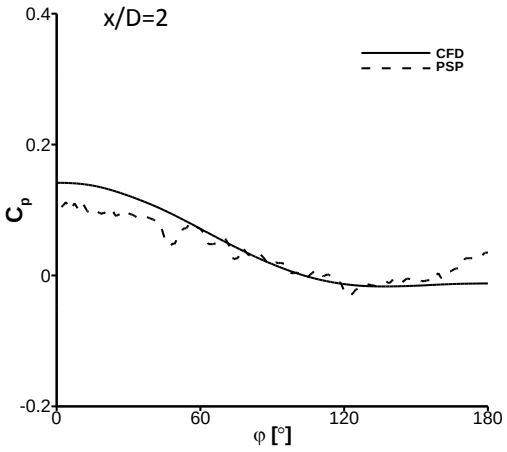
x/D=2
CFD
PSP
C_p
φ [°]

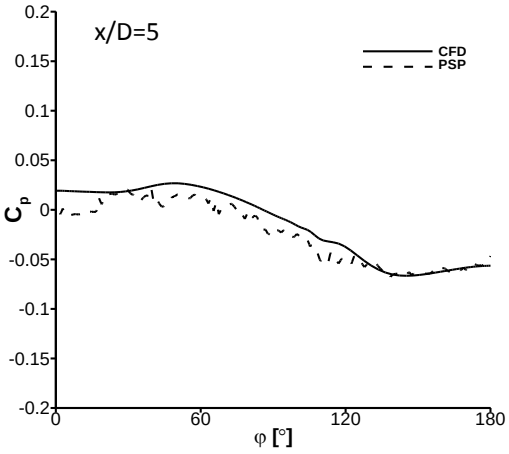
x/D=5
CFD
PSP
C_p
φ [°]

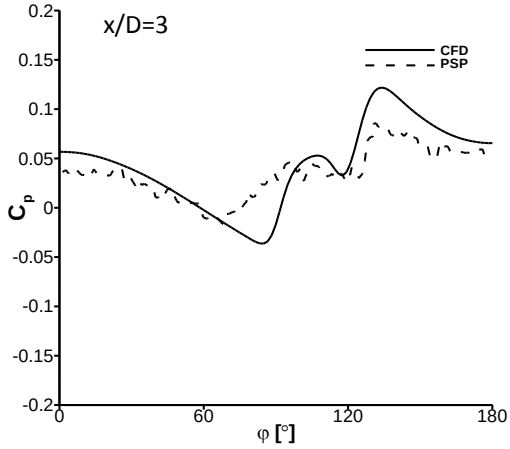
x/D=3
CFD
PSP
C_p
φ [°]

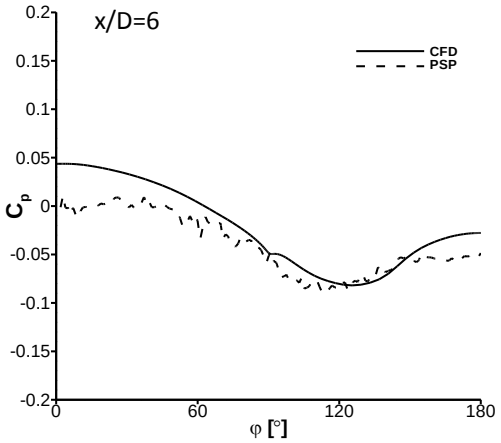
x/D=6
CFD
PSP
C_p
φ [°]

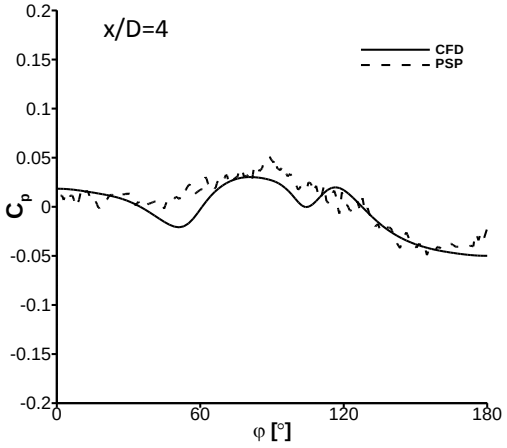
x/D=4
CFD
PSP
C_p
φ [°]

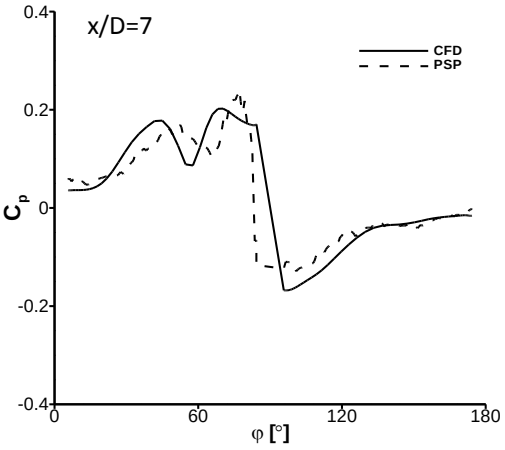
x/D=7
CFD
PSP
C_p
φ [°]

σ_R =15°

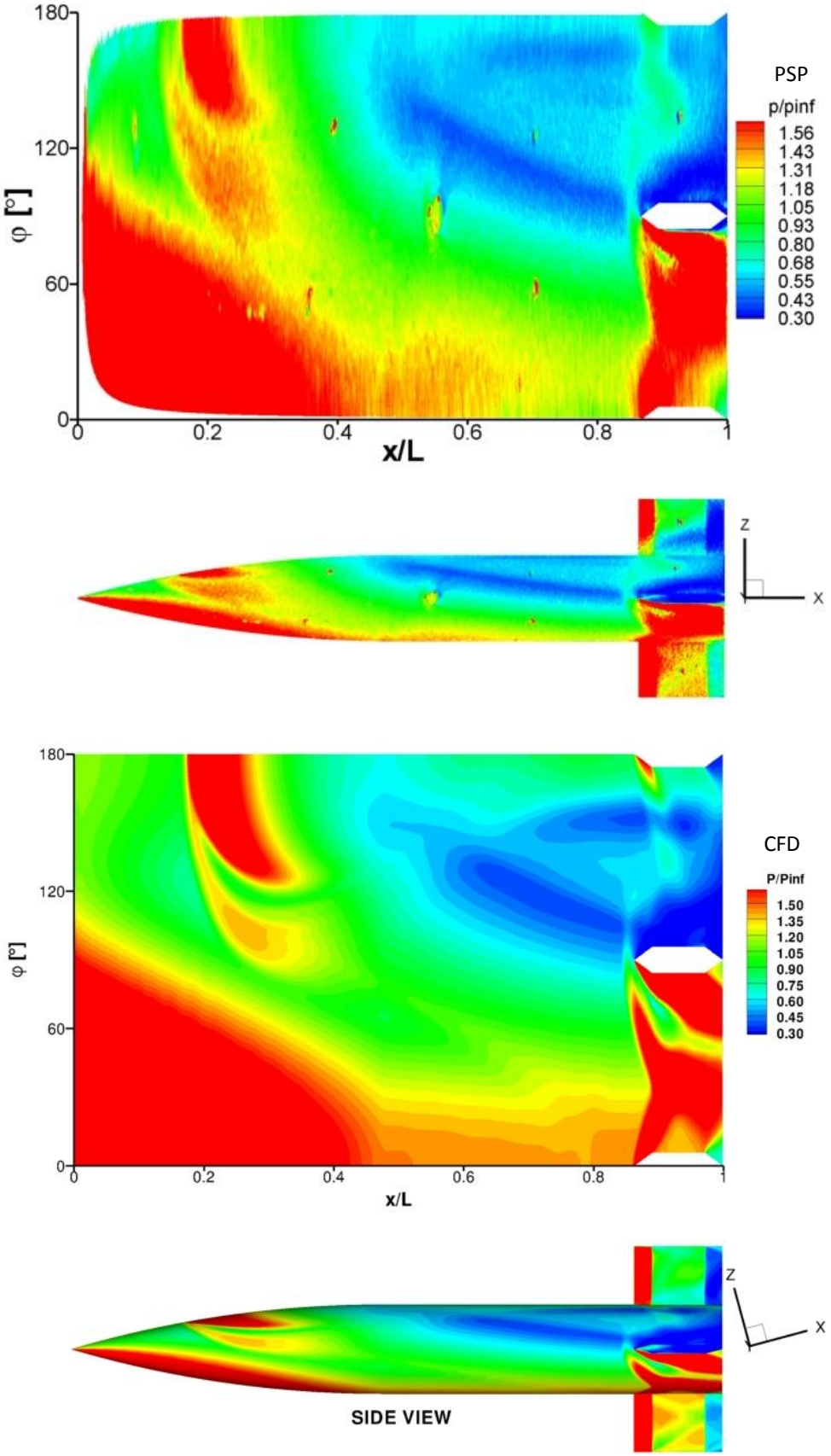
PSP
p/pinf
1.56
1.43
1.31
1.18
1.05
0.93
0.80
0.68
0.55
0.43
0.30
φ [°]
x/L
Z
X
CFD
P/Pinf
1.50
1.35
1.20
1.05
0.90
0.75
0.60
0.45
0.30
SIDE VIEW

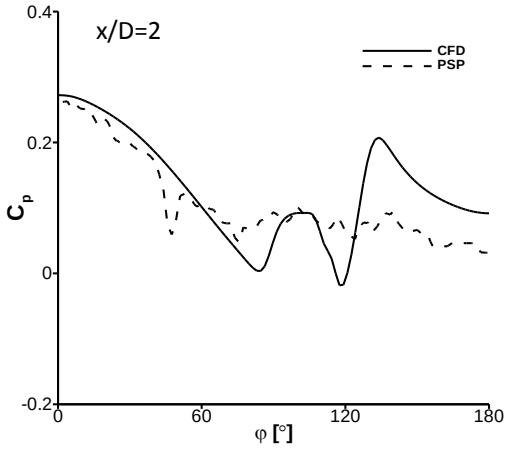
x/D=2
CFD
PSP
C_p
0.4
0.2
0
-0.2
0
60
120
180
φ [°]

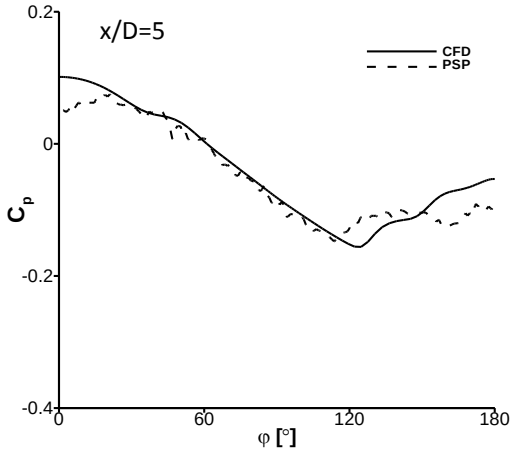
x/D=5
CFD
PSP
C_p
0.2
0
-0.2
-0.4
0
60
120
180
φ [°]

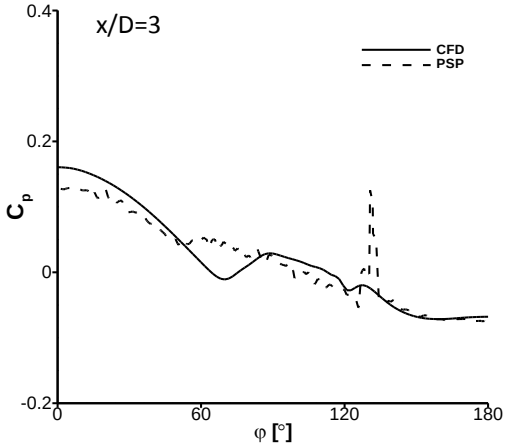
x/D=3
CFD
PSP
C_p
0.4
0.2
0
-0.2
0
60
120
180
φ [°]

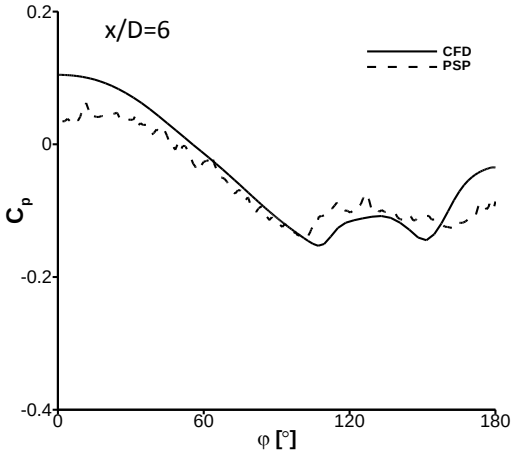
x/D=6
CFD
PSP
C_p
0.2
0
-0.2
-0.4
0
60
120
180
φ [°]

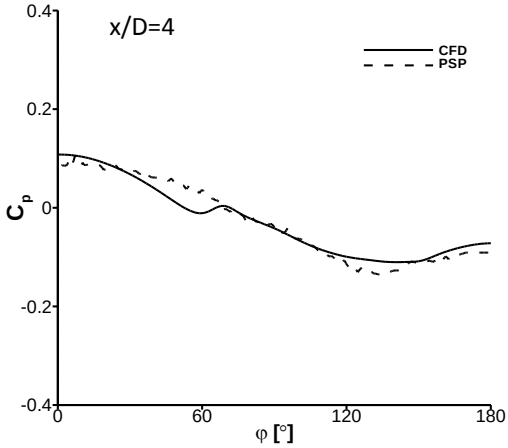
x/D=4
CFD
PSP
C_p
0.4
0.2
0
-0.2
-0.4
0
60
120
180
φ [°]

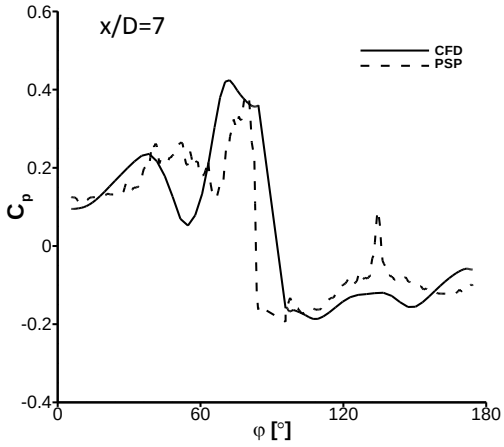
x/D=7
CFD
PSP
C_p
0.6
0.4
0.2
0
-0.2
-0.4
0
60
120
180
φ [°]

Overall, there is good agreement between the measured (PSP) and predicated (CFD) surface pressures on the finned receiver. In qualitative terms, the CFD predicts the location and local flow structures very well for the wide range of incidence angles tested. In quantitative terms, the CFD frequently predicts the magnitude of the interaction footprints sufficiently well. Finally, the above analysis gives confidence that that the CFD predictions of the interference loads for the finned receiver are based on the adequate resolution of the correct physical mechanisms.

C.3 Force and moment results for the finned receiver and sharp generator

The interference loads are plotted as a function of receiver incidence for the finned receiver and sharp generator at a fixed lateral separation for different axial staggers (Figure C.3 - Figure C.6). Measured (EXP) and predicted (CFD) data are shown.

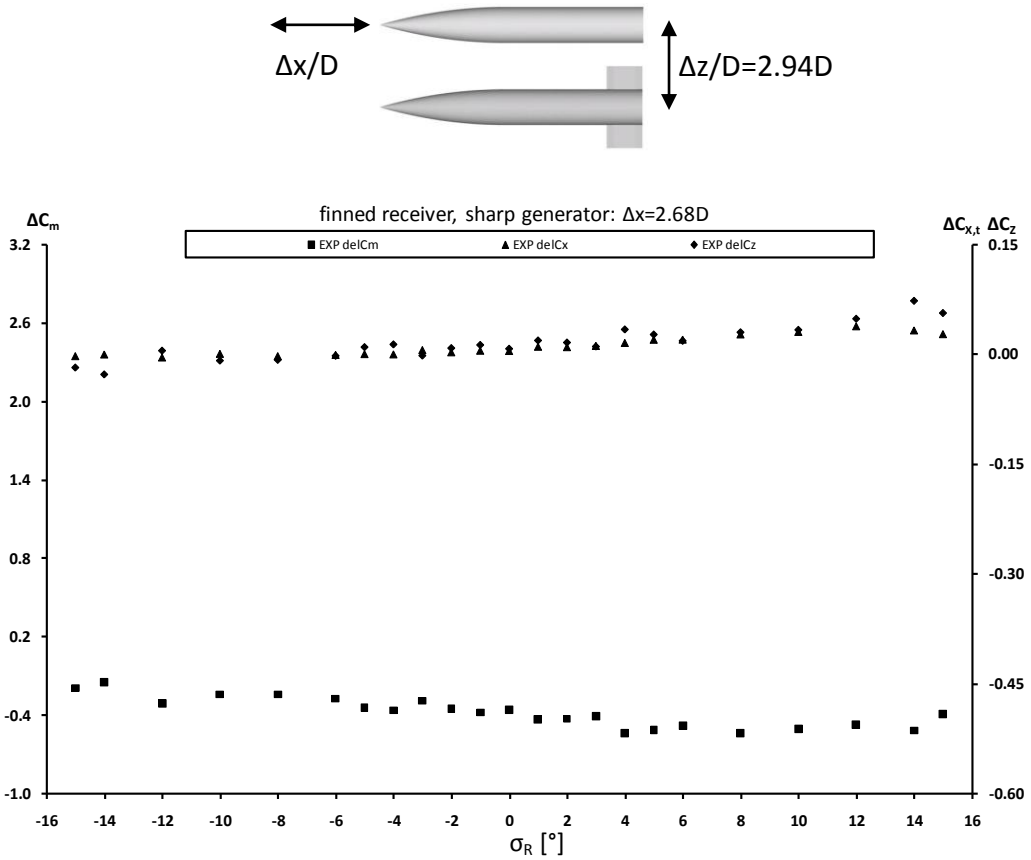

Figure C.3 Effect of receiver incidence on receiver interference loads: m2652 m2653, Δx/D=2.68 Δz/D=2.94, σ_G=0°

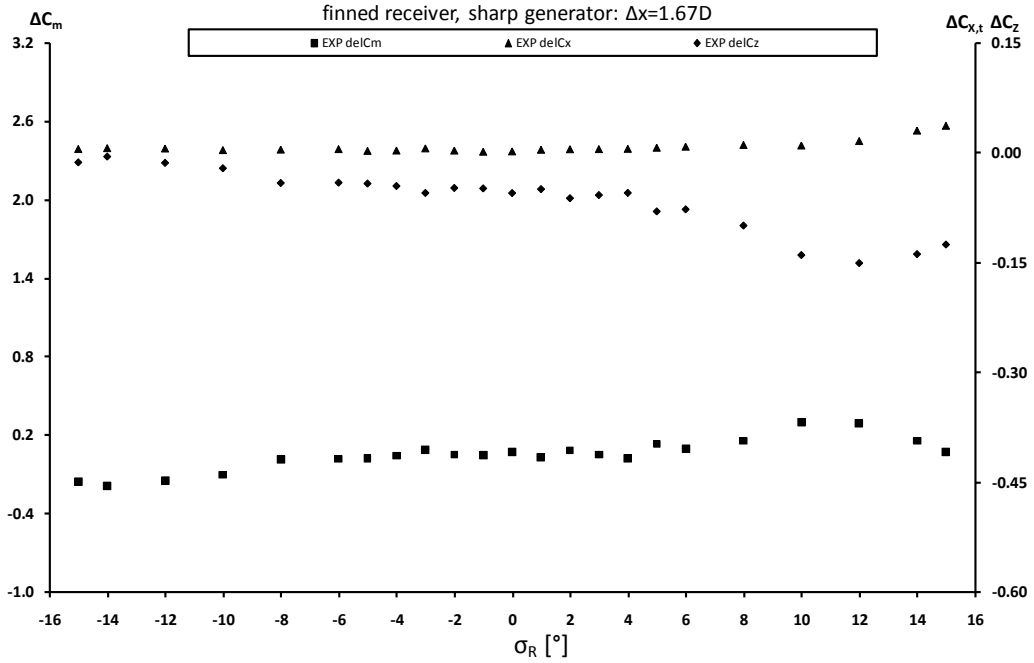

Figure C.4 Effect of receiver incidence on receiver interference loads: m2652 m2653, Δx/D=1.67 Δz/D=2.94, σ_G=0°

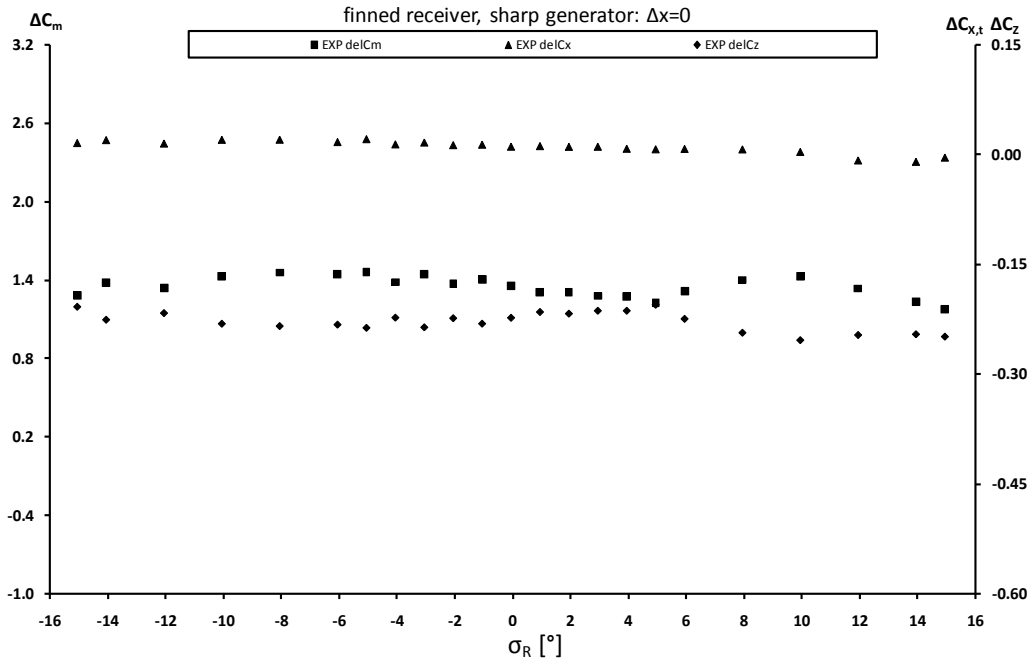

Figure C.5 Effect of receiver incidence on receiver interference loads: m2652 m2653, Δx/D=0 Δz/D=2.94, σ_G=0°

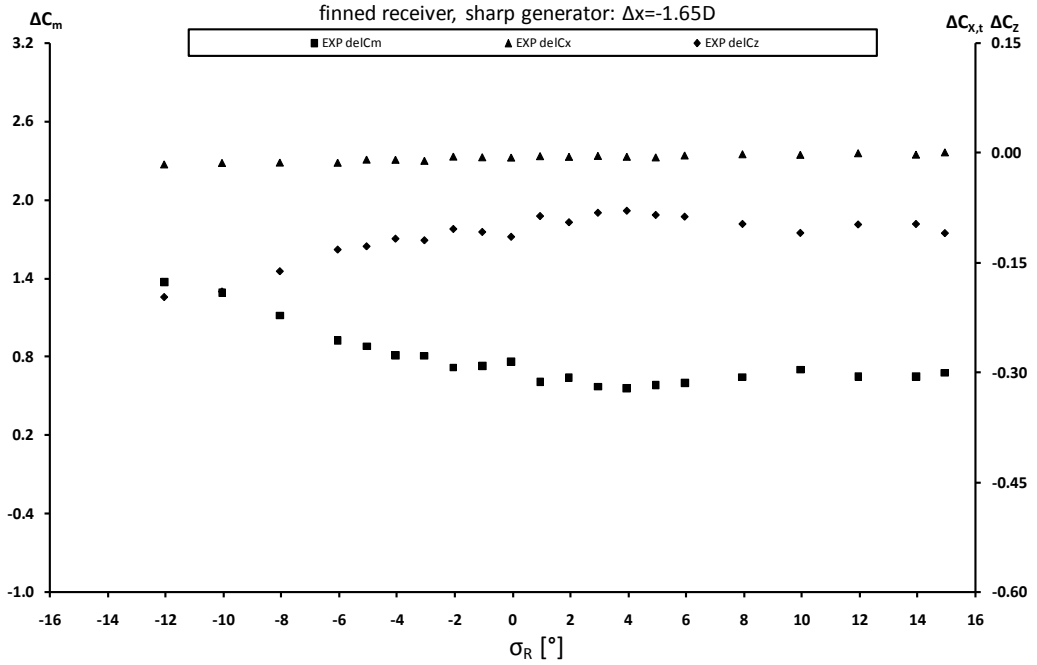

Figure C.6 Effect of receiver incidence on receiver interference loads: m2652 m2653, Δx/D=-1.65 Δz/D=2.94, σ_G=0°

C.4 Force and moment results for the finned receiver and blunt generator

The interference loads are plotted as a function of receiver incidence for the finned receiver and blunt generator at a fixed lateral separation for different axial staggers (Figure C.7 - Figure C.10).

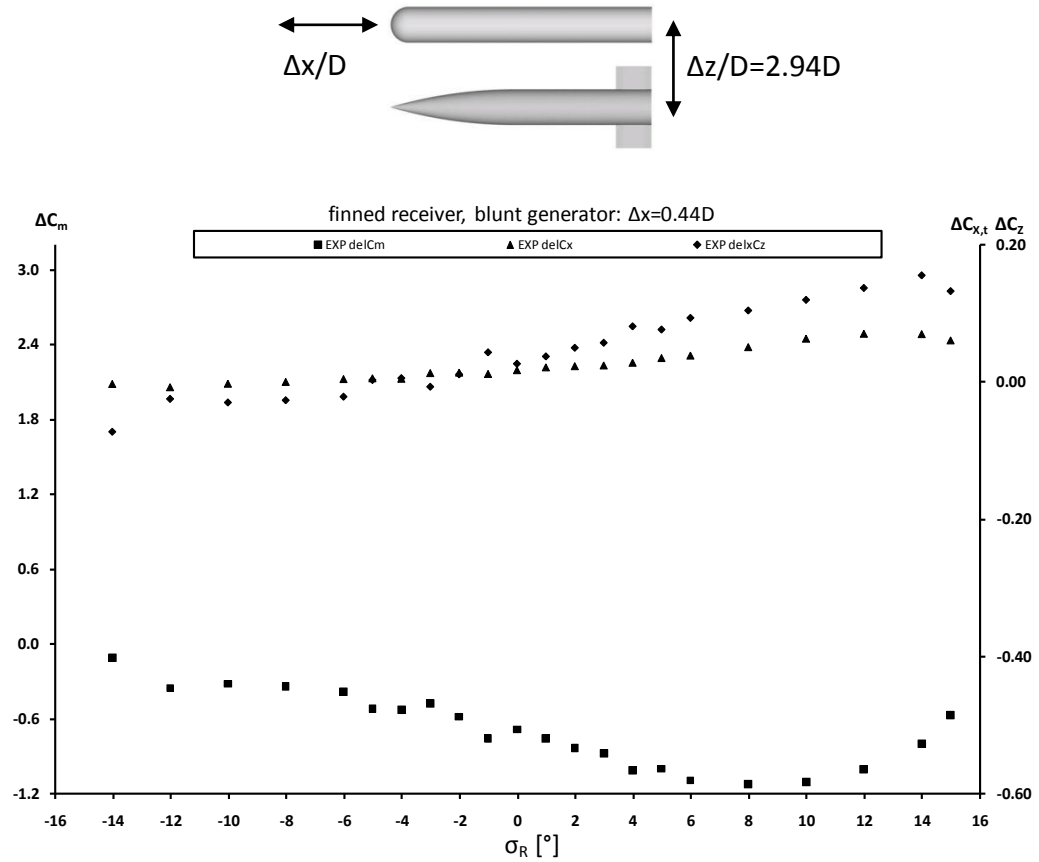

Figure C.7 Effect of receiver incidence on receiver interference loads: m2652 m2654, Δx/D=0.44 Δz/D=2.94, σ_G=0°

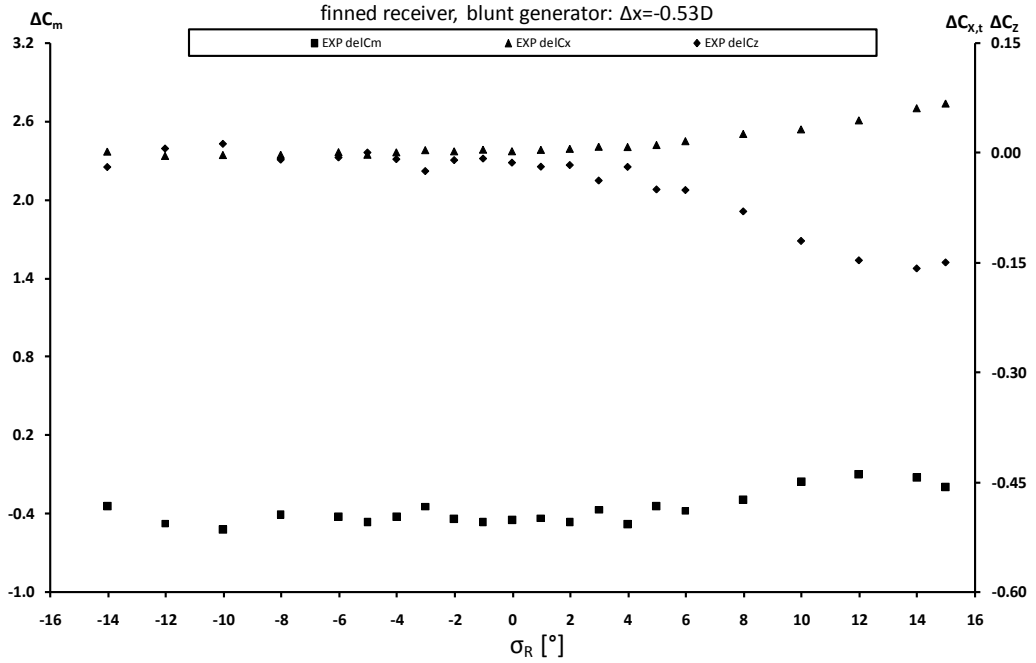

Figure C.8 Effect of receiver incidence on receiver interference loads: m2652 m2654, Δx/D=-0.53 Δz/D=2.94, σ_G=0°

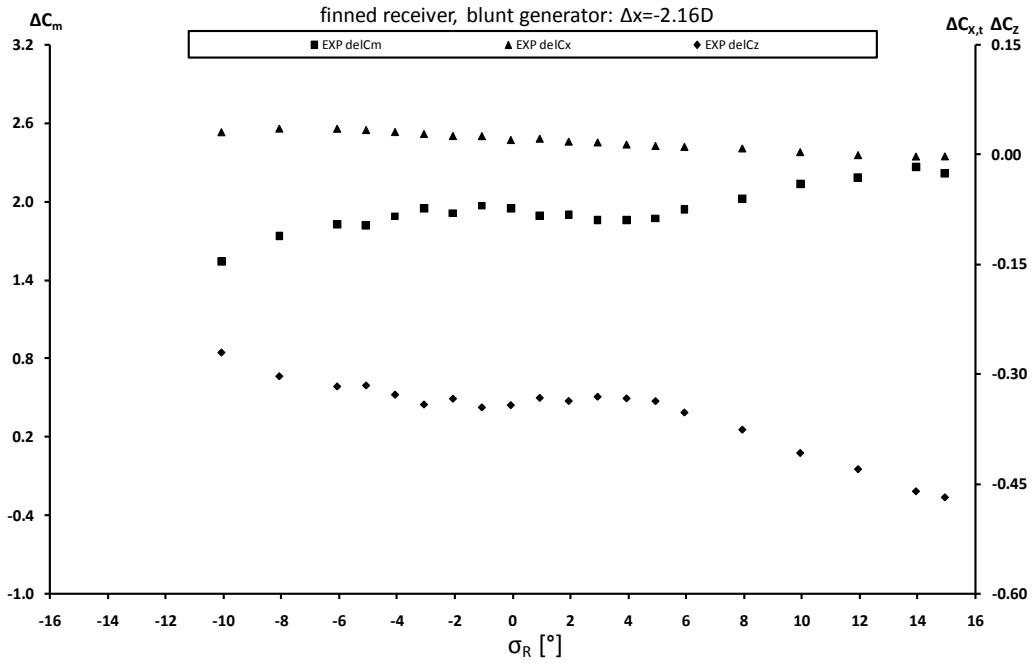

Figure C.9 Effect of receiver incidence on receiver interference loads: m2652 m2654, Δx/D=-2.16 Δz/D=2.94, σ_G=0°

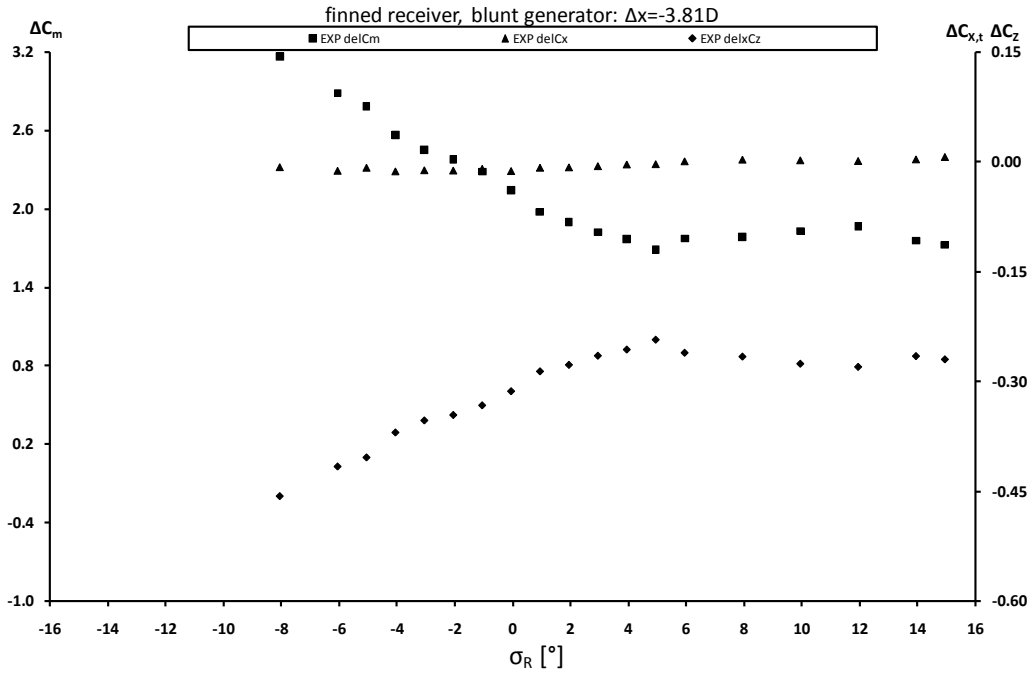

Figure C.10 Effect of receiver incidence on receiver interference loads: m2652 m2654, Δx/D=-3.81 Δz/D=2.94, σ_G=0°

Appendix D

D.1 Cobalt Overset Solver

The Cobalt overset Solver has been previously been used to predict the 6DOF trajectory of a single store as it ejects from an aircraft[62]. The solver creates a single grid from multiple overlapping grids through the grid assembly process. This assembly process involves hole-cutting, overlap regions and interpolation weights to facilitate the communication of flowfield information between the multiple original grids[44]. In this process, solution conservation is not guaranteed. .

D.1.1 Grids

In the current research, three unstructured grids were used in each computation. An empty 'background' grid of approximately 2.9m cells defined the extent of the overall computational domain and always included the other two grids throughout the solution time (Figure D.1). The 'receiver' and 'generator' grids were identical and included approximately 1.4m cells each. Each grid contained a finned body, (Figure D.2) and a small surrounding computational domain. The resolution of the background grid and finned body grids were matched as much as possible to reduce interpolation errors. The typical post assembly gird size was in the order of 5.6m cells. Due to limited resources no grid convergence study was possible.

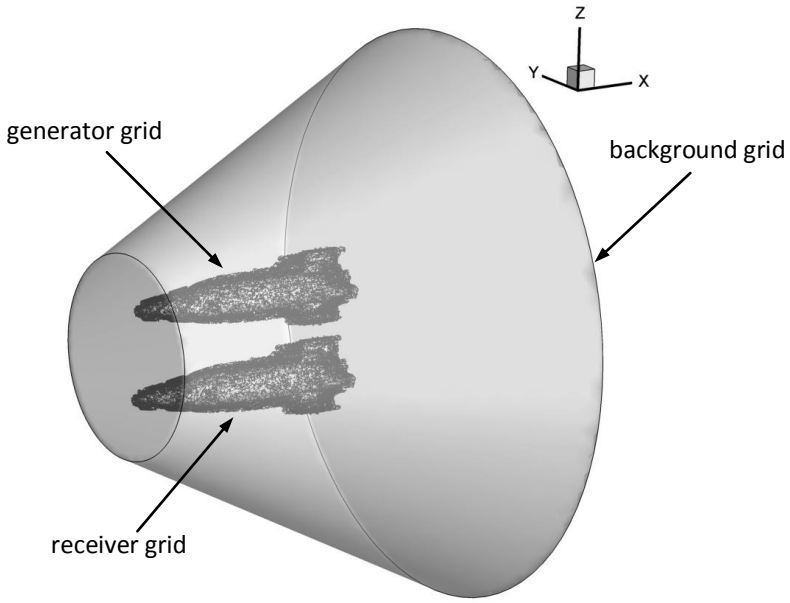

Figure D.1 Completed grid assembly, showing the outer background domain and internal receiver and generator body grids

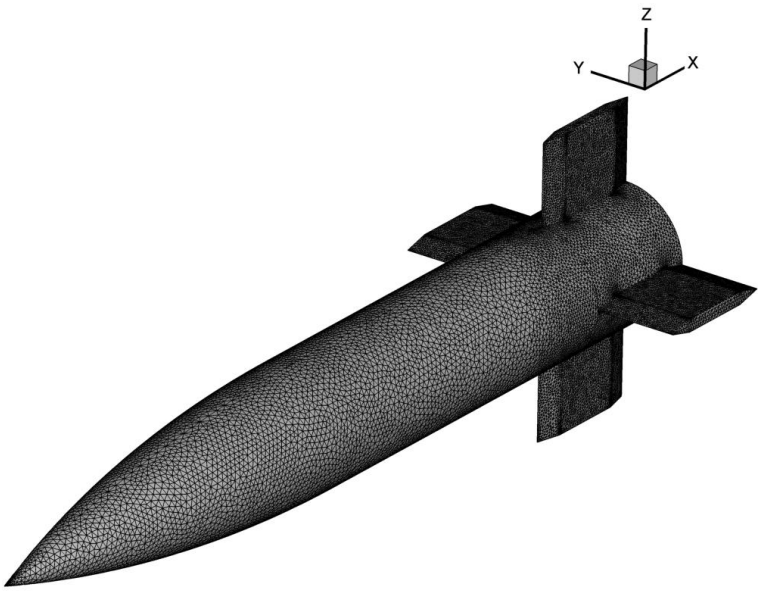

Figure D.2 Close up of the finned body surface grid

D.1.2 Boundary conditions

In all grids, a supersonic inlet boundary condition was applied to the inlet plane and surrounding farfield domain (Figure D.3). Solid slip-wall boundary conditions were applied for the receiver and generator body surfaces. Finally, the output plane values were calculated using a modified Riemann condition[44].

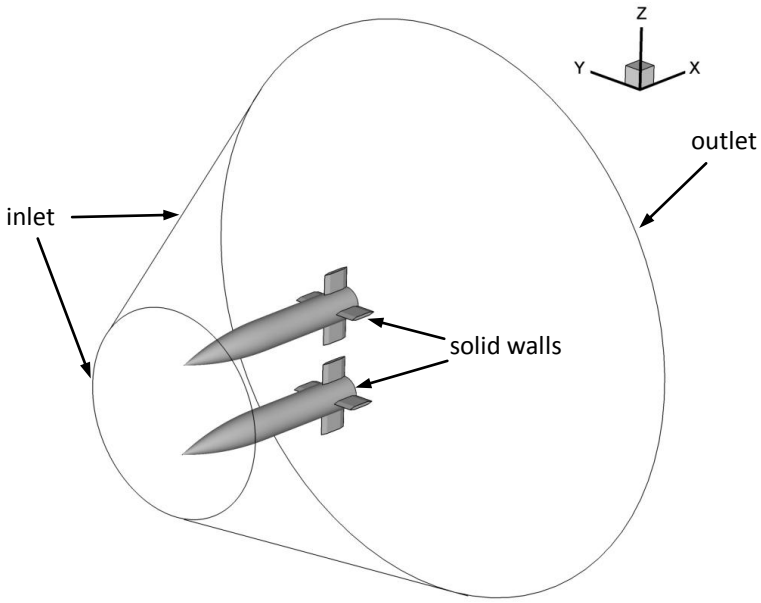

Figure D.3 Boundary conditions for the assembled grid

D.1.3 Unsteady solution parameters

The unsteady Euler equations were solved for each configuration over N=400 time-steps. A global time-step of $\Delta t=3x10^{-4}s$ was used with 5 further Newton sub-iterations computed at each time-step. Unfortunately, no convergence information was outputted by Cobalt for these sub-iterations. Rigid Body Motion (RBM) was applied to the receiver and generator grids only. The 6DOF RBM equations were solved at each time-step using a 3rd order Runge-Kutta scheme. This calculated the new position of each grid over the specified time-step, the grid assembly process was then repeated and the process repeated itself over the $\Delta T=0.12s$ solution time. Due to limited resources, no time-step convergence study was possible.

D.2 Sea Level freestream flow conditions

The freestream flow conditions used in the unsteady CFD calculations were assumed to be at Sea Level and are listed below in Table D.1.

Parameter	Value	Units
Mach number	2.43	
Stagnation pressure	1,552,378.1	Nm^{-2}
Stagnation temperature	628.4	K
Static pressure	101325	Nm^{-2}
Static temperature	288.15	K
Static density	1.225	kgm^{-3}
Velocity	826.8	ms^{-1}
Sonic velocity	340.3	ms^{-1}
Dynamic pressure	418,819.8	Nm^{-2}
Dynamic viscosity	$1.79x10^{-5}$	$kgm^{-1}s^{-1}$
Reynolds number based on diameter (D=0.1m)	$5.66x10^{6}$	
Reynolds number per meter	$5.66x10^{7}$	m^{-1}
Force coefficient denominator	3289.4	N
Moment coefficient denominator	328.9	Nm

Table D.1 Sea Level freestream flow conditions